Dynamics in Small
Confining Systems II

EDITORS

J.M. Drake

J. Klafter

R. Kopelman

S.M. Troian

MRS

Dynamics in Small Confining Systems II

Dynamics in Small Confining Systems II

Symposium held November 28–December 1, 1994, Boston, Massachusetts, U.S.A.

EDITORS:

J.M. Drake

Exxon Research and Engineering Co.
Annandale, New Jersey, U.S.A.

J. Klafter

Tel Aviv University
Tel Aviv, Israel

R. Kopelman

University of Michigan
Ann Arbor, Michigan, U.S.A.

S.M. Troian

Princeton University
Princeton, New Jersey, U.S.A.

Single article reprints from this publication are available through
University Microfilms Inc., 300 North Zeeb Road, Ann Arbor, Michigan 48106

CODEN: MRSPDH

This book has been registered with Copyright Clearance Center, Inc. For further information, please contact the Copyright Clearance Center, Salem, Massachusetts.

Contents

*Invited Paper

*Invited Paper

*Invited Paper

Preface

This symposium, the third held as part of the MRS Fall Meetings series, touched on a wide range of topics covering static and dynamic properties of small confining systems: probing of confined systems, structure and dynamics of liquids at interfaces, nanorheology, adsorption, diffusion in pores, and reactions. Participants from various disciplines shared different points of view on the questions of how ultrasmall geometries can force a system to behave in ways significantly different than its behavior in the bulk, how this difference affects molecular properties, and how it is probed.

The contributions in the book reflect the broad range of topics discussed at the meeting, all related to dynamics in small confining systems. We hope that the interdisciplinary nature of the book and the meeting will help to bridge the gap among the different approaches and methods presented. The papers appear in the book in the order of their presentation during the symposium, which was organized in sessions entitled: Probing Confined Systems; Structure and Dynamics of Thin Films; Nanorheology; Diffusion in Porous Systems; Adsorption and Phase Transitions; and Reaction Dynamics.

There appears to be a continuing interest in the dynamics and thermodynamics of confined molecular systems. The symposium was an effective way to bring together different disciplines interested in common problems. We hope to be able to organize the fourth symposium in the fall of 1996.

We would like to thank everyone who helped in the organization and execution of the 1994 MRS Fall Meeting, especially the authors and the presenters, whose work has made this book possible and the symposium successful.

<div align="right">

J.M. Drake
J. Klafter
R. Kopelman
S.M. Troian

February 1995

</div>

MATERIALS RESEARCH SOCIETY SYMPOSIUM PROCEEDINGS

MATERIALS RESEARCH SOCIETY SYMPOSIUM PROCEEDINGS

Prior Materials Research Society Symposium Proceedings
available by contacting Materials Research Society

Dynamics in Small Confining Systems II

X-RAY SCATTERING STUDIES OF MOLECULAR ORDERING PHENOMENA IN CONFINED FILMS

SUNIL K. SINHA*, M. TOLAN**, G. VACCA*, Z. LI[†], M. RAFAILOVICH[†],
J. SOKOLOV[†], H. LORENZ[††], J.P. KOTTHAUS[††], Y.P. FENG*, G. GRUBEL***,
AND D. ABERNATHY***
*Corporate Research, Exxon Research & Engineering Company, Annandale, NJ 08801
**Institut für Experimentalphysik der Universitat Kiel, 24098 Kiel, Germany
[†]Materials Science Department, SUNY, Stonybrook, NY 11794-2275
[††]Sektion Physik, Ludwig-Maximilians - Universitat München, 80539 München, Germany
***ESRF, Grenoble, France

ABSTRACT

A knowledge of the structural behavior of molecules confined in thin liquid films and the way in which they differ from bulk behavior is of great importance to a variety of technological applications. We discuss X-ray scattering studies of the conformation of liquid polymer wetting layers on laterally structured substrates in order to test theories of the conformality of the wetting layer to the substrate. Recent work on guided X-ray beams confined to the thin film opens up the possibility of detailed studies of ordering phenomena in molecular layers adjacent to solid surfaces. Recent experiments are discussed.

In this article, we take "confined geometries" to mean situations where all interfaces present have an effect on determining the structure or morphology of the fluid confined between them, as opposed to purely two-dimensional or surface behavior. Thus, thin films which have thickness comparable to or smaller than a typical interaction or correlation length in the material of the film are candidates for discussing the behavior of fluids in confined geometry, as opposed to much thicker films which reflect simply the sum of the behavior at each of the film interfaces.

Wetting of solid surfaces by liquid films is an example of such confined behavior until bulk liquid behavior is reached at large film thicknesses. A problem of continuing interest is the wetting of laterally structured (e.g., rough or periodically modulated) surfaces and the conformality to the substrate of the wetting layer. This is a problem which can be probed conveniently and accurately by X-ray scattering studies, and a few such studies have been carried out on wetting films on rough substrates by studying off-specular scattering of synchrotron X-rays [1,2]. In the first part of this paper, we discuss the use of periodically structured substrates to study the conformation of liquid polymer wetting layers. Some preliminary results have been presented earlier [3].

According to a theory proposed by Robbins, Andelman, and Joanny [4] the fluctuations of the top of a (liquid) wetting film are correlated with those on a (solid) substrate below via the relation

$$\delta z_2(\vec{q}) = \chi(\vec{q}, \ell) \delta z_1(\vec{q}) \tag{1}$$

where $\delta z_1(\vec{q})$ is the (two-dimensional) Fourier transform of the height fluctuations $\delta z_1(x,y)$ of the substrate and $\delta z_2(\vec{q})$ is the corresponding function for the top surface of the film. ℓ is the film thickness and Eq. (1) is valid in the linearized theory [4]. We may define a length given by

$$a = \left(A_{eff} / 2\pi\gamma\right)^{1/2} \tag{2}$$

where A_{eff} is the effective Hamaker constant for the Van der Waals interaction between the liquid and the substrate and γ is the surface tension between the liquid and the overlying vapor. In terms of a, we can define another length ξ given by

$$\xi = \ell^2 / a \tag{3}$$

In terms of this, the response function $\chi(q, \ell)$ is given by

$$\chi(q, \ell) = \frac{\tilde{K}(q)}{1 + q^2\xi^2} \tag{4}$$

where $\tilde{K}(q)$ is a function which can be taken as $\simeq 1$ in the so-called Deryagin approximation [4], valid when $q\ell \ll 1$.

4
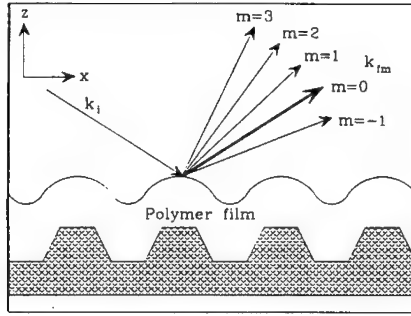
Fig. 1. Laterally structured Si diffraction grating schematic.

For a laterally structured substrate such as the diffraction grating structure indicated in Fig. 1, the relation in Eq. (1) can be tested for a discrete one-dimensional set of q-vectors, given by $q_n = n \cdot 2\pi/d$ ($\vec{q}$ normal to the strips of the diffraction grating) where d is the grating spacing. The present experiments were carried out on nanofabricated silicon gratings of spacing $d \sim 1\mu$ while the polymer films had thicknesses of ~100 Å so that the condition $q\ell \ll 1$ was satisfied for the experiments.

Consider a set of interfaces of area A given by $z_n(x)$ (n = 1, 2, 3; n = 1 corresponding to the silicon substrate height, n = 2 to the height of the oxide film on the substrate (assumed to be perfectly conformal with it), and n = 3 to the height of the top surface of the polymer film), where x is the direction normal to the grating strips. In the Born Approximation, the X-ray scattering intensity for wavevector transfer q_x in the plane and q_z normal to the surface is given by [5,6]

$$S(q_x, q_z) = \frac{4\pi^2 A}{q_z{}^4} \sum_m \sum_{j,k=1}^{3} \Delta\rho_k \Delta\rho_j e^{iq_z(\bar{z}_k - \bar{z}_j)}$$

$$(x) \, e^{-(\sigma_j{}^2 + \sigma_k{}^2)q_z{}^2/2} C_{k,m}^{*}(q_z) C_{j,m}(q_z) \delta(q_x - m \cdot 2\pi/d) \tag{5}$$

where (a) we have assumed that open detector slits in the out-of-scattering-plane direction have integrated over all q_y (b) $\bar{z}_n$ is a reference height for interface n (e.g. for n = 1, $\bar{z}_1 = 0$) (c) σ_n is the rms roughness for interface n (d) $\Delta\rho_k$ represents the difference in scattering length density (proportional to electron density difference) across interface k and

5

$$C_{k,m}(q_z) = \frac{1}{d}\int_0^d dx \; e^{-iq_z \delta z_k(x)} e^{-im\cdot(2\pi/d)x} \qquad (6)$$

where $\delta z_k(x)$ is the height of interface k relative to its reference height $\bar{z}_k$. In Eq. (5), we have neglected the diffuse scattering from random roughness fluctuations, so that the scattering exists only on "truncation rods" ($q_x = m\cdot 2\pi/d$) as a function of q_z, corresponding to the various orders of diffraction from the grating (m = 0 corresponds to the specular reflectivity).

If the top surface $\delta z_k(x)$ (k = 3) follows the lower two interfaces perfectly (conformal film), then the phase relations between the coefficients $C_{k,m}(q_z)$ will be such that modulations of $S(\vec{q}\,)$ with period $(2\pi/\ell)$ in q_z will exist for all m. (For the specular reflectivity (m = 0), these would give the usual "Kiessig fringes" superimposed on another set of fringes arising from the height of the grating strips themselves [5,6].) As the top film surface loses conformality with the substrate these fringes will "wash out" for the rods corresponding to higher m values.

The measurements were done at the X10B beamline of the NSLS Synchrotron Source at Brookhaven, using a wavelength of 1.131 Å. Data were taken along rods corresponding to the orders m = 0 through m = 4 for the bare grating (Si + oxide overlayer) plus various thicknesses of overlaid polymer films, the diffuse background (corresponding to roughness scattering) being subtracted off by measuring it along q_z-rods slightly displaced from the rod positions $q_x = m\cdot(2\pi/d)$. From these scans, using Eq. (5) and the shape of the diffraction grating strips shown in Fig. 1, the geometrical parameters for the grating, the rms roughness of its surface and the thickness and roughness of the oxide layer and the parameters corresponding to the upper film surface (see below) were determined by least squares fitting. (Note that the Born Approximation expression (Eq. (5)) works only for values of q_z larger than those corresponding to the critical angle for total external reflection.) From these, the lateral periodicity d of the grating was determined to be 9800 Å, the height of the strips to be 132 Å, the width of the grooves and bars to be 4000 Å, the thickness of the oxide layer to be 10 Å and the roughness of the Si/SiO_2 and SiO_2 surfaces to be 5 Å. These parameters are in semiquantitative agreement with those obtained from AFM studies of the substrate using a commercial Nanoscope III instrument in the contact mode. The polystyrene films were first spun onto a glass substrate to determine the thickness of the films with an ellipsometer. Afterwards, they were floated on a water surface and then picked up on the surface of the grating. Finally they were annealed for 2 hours at 185°C in a vacuum oven during which time it was assumed the liquid polymer film achieved equilibrium with the substrate. The thickness was built up by adding several such polymer films in succession and annealing each time to melt them into one film. For the top surface of the polymer film a Fourier series expansion was used for $\delta z_3(x)$, i.e.

$$\delta z_3(x) = \sum_{p>0} f_p \mathrm{Sin}(p\frac{2\pi}{d}x) \tag{7}$$

and only the terms p = 1, 3 were taken as non-zero. (From AFM studies of the top surfaces of these films, it was qualitatively seen that the surfaces became rapidly sinusoidal for increasing ℓ.)

Substituting Eq. (7) in Eq. (6), and using Eq. (5), the data along all the rods were fitted (after diffuse background subtraction) for each film thickness ℓ, and from the ratios of the f_p to the corresponding Fourier coefficients of $\delta z_1(x)$ for the grating, the values of $\chi(q_p,\ell)$ ($q_p = p.2\pi/d$) determined. Some representative data sets for the rod scans for the thinnest and thickest films and the corresponding films are shown in Figs. 2. It may be seen for the larger
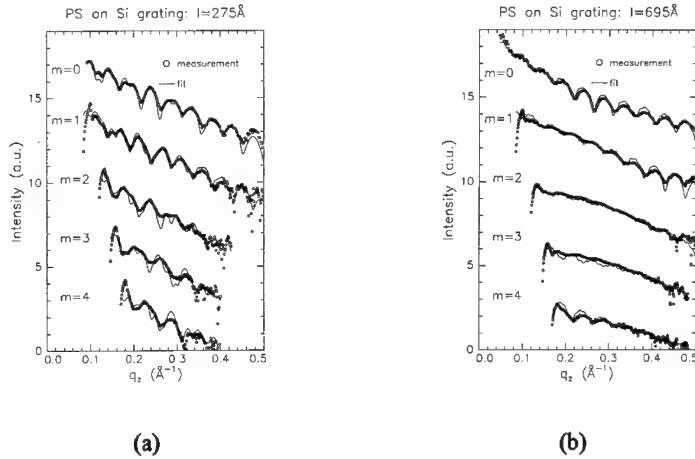
Fig. 2. Background-subtracted q_z (rod) scans corresponding to the various diffraction orders (m) for the 275 Å polymer film (a) and the 695 Å polymer film (b). The solid curves are the model fits.

thickness that the modulations in q_z are eliminated for the higher order rods showing a loss of conformal modulation of the top film surface. Fig. 3 shows the quantities $\chi(q_1,\ell)$ and $\chi(q_3,\ell)$ as a function of ℓ along with the theoretical result in the linear Deryagin approximation given by Eq. (4). The solid curve is calculated with the length a = 5 Å as expected from Eq. (2) with the known values of A_{eff} and η, and clearly does not explain the data. The expression (4) can, however, be made to fit the data if a is chosen as a_{eff} = 75 Å as seen in Fig. 3. The reasons for

this somewhat unrealistic value for the length a are not clear at present. One possible explanation could be that with the (relatively deep rectangular grooves of the grating, the linear theory of Eq. (4) is not valid and must be replaced by a full non-linear calculation, of the type done by Robbins et al. [4]. Another explanation could be that the film equilibrium is determined not purely by surface tension but by viscoelastic forces upon solidification [7]. At any rate the degree of conformality for thick films is quantitatively far greater than the simple theory would predict. In particular, the first harmonic modulation of the top film surface appears to become almost constant in amplitude (or decay very slowly) at large film thicknesses.
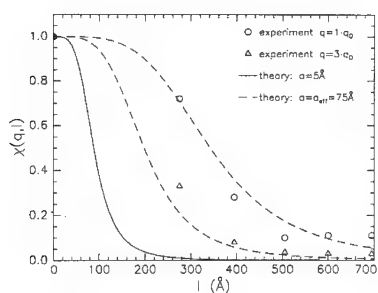
Fig. 3. Comparison of measured $\chi(q,\ell)$ for $q = q_0$ and $q = 3\ q_0$ as a function of ℓ with the theory of Eqs. (2)-(4).

In the second part of this paper, we discuss methods of using X-ray scattering to determine in-plane molecular ordering in confined thin films. Recently, several experimental and computer simulation studies of liquid films of the order of tens of molecular diameters thick and confined between two solid walls have suggested both layering and lateral ordering of the molecules in the film, particularly adjacent to the solid surfaces. Very little direct confirmation of such ordering is available by diffraction techniques, although some X-ray scattering studies of 4000 Å thick liquid crystal films between mica plates have been recently reported by Idziak et al. [8]. The problem one faces in X-ray scattering studies of very thin films between solid surfaces is the problem of getting the X-ray beam in and out of the surrounding solid medium and still being able to distinguish the relatively weak signal of a single or few layers ordering above the diffuse background from the solid. We shall outline here a possible method for doing this by utilizing the film itself as an X-ray wave guide or resonant beam coupler [9,10]. Consider a thin film of lower electron density bounded by media of higher electron density as shown in Fig. 5. Since the refractive index for X-rays (neglecting absorption effects) is given by

8

$$n = 1 - \left(\frac{e^2}{mc^2} \right) \frac{\lambda^2 \rho}{2\pi} \qquad (8)$$

where ρ is the electron density of the medium, the film can sustain modes which correspond to constructively interfering totally reflected beams from each surface, since the film has a higher refractive index than its bounding media. Now consider the case where the overlayer is very thin so that a wave incident on the top surface from air and totally reflected from it has an evanescent component in the overlayer which can tunnel into and excite one of the resonant modes in the underlying film. The situation is analogous to a one-dimensional potential well illustrated in Fig. 4, since for the direction normal to the film (z-direction) the wave equation for the X-rays maps on to the one-dimensional Schrodinger equation for particles of mass m in a potential V given by $\frac{\hbar^2}{2m} (e^2 / mc^2) 4\pi\rho$. The "particle energy" then stands for $\frac{\hbar^2}{2m} k_z^2$, k_z being the normal component of the incident X-ray wavevector in free space. The film with a dense overlayer then maps on to the square well potential shown in Fig. 4, which has bound states that correspond to

$$k_\perp = k_0 \sin(\theta_i)$$
resonance occurs if and only if:
$$k_\perp = k_\perp^m$$
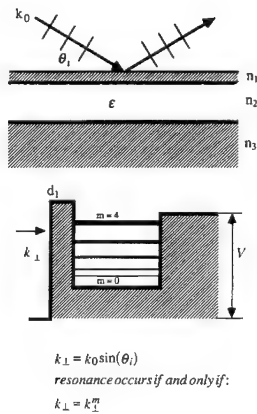
Fig. 4. Illustration of resonant tunnelling of X-rays into a thin film of refractive index (n_2) greater than those of its substrate (n_3) and overlayer (n_1).

the guided modes of the film. If the incident k_z is such that it matches one of these resonances, a wave of very large amplitude can be built up in the film. Physically this means that a plane wave of width W incident on the top overlayer can couple most of its energy into the film of thickness ℓ, achieving a flux enhancement of $\sim$ (W/ℓ) before this energy is either absorbed in the film or leaks out through the overlayer (or it can stay trapped in the film by having the overlayer become thick in the region beyond the incident beam footprint). This is the basis for optical beam thin film coupling devices developed in the 1970's [11]. The theory of this coupling and flux compression was worked out by R. De Wames and the present author around that time [12]. It should be noted that similar resonance effects in thin films were also discussed independently by Croce and Pardo [13] for both X-rays and neutrons in terms of a Fabry-Perot interferometer. Guided X-ray waves in thin films were independently demonstrated by Spiller and Segmuller in the 1970's [14]. However, it is with the advent of highly brilliant synchrotron sources and coherent beams from these that one has the hope of realizing the potentially large flux compressions with such a device (since W above cannot be larger than a coherence width of the incident beam which is also assumed to be highly collimated and monochromatic). Such flux enhancement with resonant beam couplers have been demonstrated by Feng et al. [9,15] at the NSLS and ESRF synchrotron sources. Wang et al. have also demonstrated a similar "quasi-resonant" enhancement of the flux in a thin film without an overlayer [16]. Fig. 5 shows the device used which utilized a Si substrate, a polyimide film (thickness $\sim$ 1200 Å), and a SiO_2 overlayer. Fig. 6 shows dips in the reflectivity from the overlayer below the critical angle (i.e., in the totally reflected region) corresponding to the various resonant guided modes in the film, and Fig. 7 shows the angular distribution of intensity emerging from the decoupling region corresponding to the various guided modes excited when the incident beam is set for exciting a single resonance, this being due to mode mixing effects [17]. Finally, Fig. 8 shows the far field diffraction pattern from a guided beam emerging from a truncated waveguide (i.e., exiting form the edge of the film itself instead of from a decoupling thin overlayer) together with the calculated pattern based on the field distribution for the particular modes excited [15]. With such a device to enhance the flux inside a thin film and minimize scattering from the bounding solid media (in which the field is evanescent away from the film) it should be possible to study molecular ordering conveniently and elegantly in thin confined liquid films. Such experiments are planned for the near future. In closing, we should also point out that the technique can also be used with neutrons, although the flux gain in the film is much lower due to the lower brilliance and coherence of neutron sources. Guided neutron wave propagation and resonance effects have recently been demonstrated by several groups [18-22] and remain to be explored more fully for studying confined films.
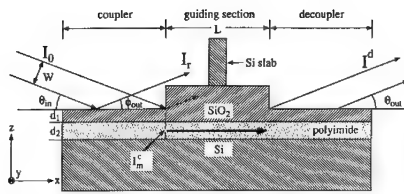
Fig. 5. Illustration of waveguide device showing the Si substrate, thin polymer film and the thin SiO$_2$ overlayer (with the thick overlayer in the guided region in the middle).
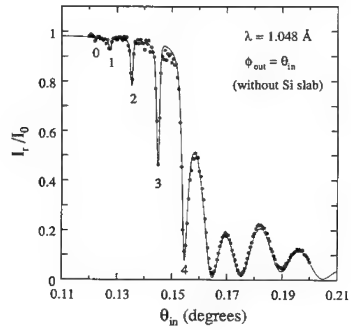
Fig. 6. The reflectivity of the Resonant Beam Coupler from the coupling region. The five dips for $\theta_{inc} < 0.16°$ signify the five TE modes. The solid line represents a fit using the standard EM theory for multilayers (from Ref. [9]).
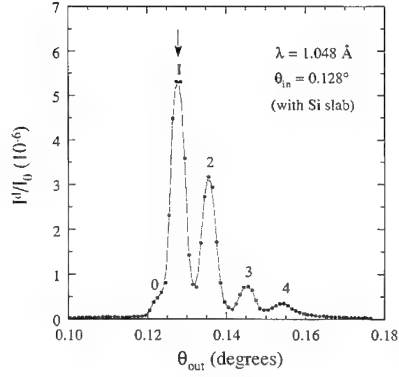
Fig. 7. The X-ray intensity exiting the decoupler with $\theta_{inc} = 0.128°$ to excite the TE1 mode only. The four peaks and the shoulder correspond to all 5 guided TE modes excited in the guide due to mode mixing. The small magnitude of I_d is primarily due to absorption in the guide (from Ref. [9]).
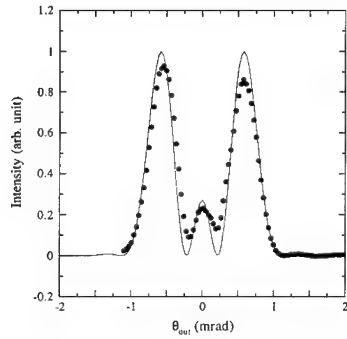
Fig. 8. Far-field intensity as a function of angle θ_{one} out of the plane of the waveguide for a guided X-ray beam exiting the truncated end of a 600 Å thin-film polymer waveguide with Si substrate and SiO_2 overlayer. The calculated curve is obtained from the Fourier transform of the electric field distribution in the guide in an excited symmetric TE mode (from Ref. [15]).

REFERENCES

1. S. Garoff, E.B. Sirota, S.K. Sinha, and H.B. Stanley, J. Chem. Phys. **90**, 7505 (1989).

2. I.M. Tidswell, T.A. Rabedeau, P.S. Pershan, and S.D. Kosowsky, Phys. Rev. Lett. **66**, 2108 (1991).

3. M. Tolan, G. Vacca, S.K. Sinha, Z. Li, M. Rafailovich, J. Sokolov, H. Lorenz, and J.P. Kotthaus, J. Phys. **D** (Appl. Phys.) to be published.

4. D. Andelman, J.-F. Joanny, and M.O. Robbins, Europhys. Lett. **7**, 731 (1988); M.O. Robbins, D. Andelman, and J.-F. Joanny, Phys. Rev. A **43**, 4344 (1991).

5. M. Tolan, G. König, L. Brügemann, W. Press, F. Brinkop, and J.P. Kotthaus, Europhys. Lett. **20**, 223 (1992).

6. M. Tolan, W. Press, F. Brinkop, and J.P. Kotthaus, J. Appl. Phys. **75**, 7761 (1994).

7. J. Hardin, Private Communication.

8. S.H. Idziak, C.R. Safinya, R.S.Hill, K.E. Kraiser, M. Ruths, H.E. Warriner, S. Steinberg, K.S. Liang, and J.N. Israelachvili, Science **264**, 1915 (1994).

9. Y.P. Feng, S.K. Sinha, H.W. Deckman, J.B. Hastings, and D.P. Siddons, Phys. Rev. Lett. **71**, 537 (1993).

10. S.I. Zheludeva, M.V. Kovalchuk, N.N. Novicova, A.N. Sosphenov, N.E. Malaysheva, N.N. Salashchenko, A.D. Akhsakhalay, and Yu. Yu. Platonov, Thin Solid Films **232**, 252 (1993).

11. P.K. Tien and R. Ulrich, J. Opt. Soc. Am. **60**, 1325 (1970).

12. R.E. DeWames and S.K. Sinha, Phys. Rev. B **7**, 917 (1973).

13. P. Croce and B. Pardo, Nuov. Rev. Opt. Appl. **1**(4), 229 (1970); see also M. Maaza, et al., J. Phys. Lett. **A** (1994).

14. E. Spiller and A. Segmüller, Appl. Phys. Lett. **24**, 60 (1974).

15. Y.P. Feng, S.K. Sinha, G. Grübel, and D. Abernathy, to be published.

16. J. Wang, M.J. Bedzyk, and M. Caffrey, Science, **258**, 775 (1992).

17. Y.P. Feng, H.W. Deckman, and S.K. Sinha, Appl. Phys. Lett. **64**, 930 (1994).

18. K.A. Steinhauser, A. Steyerl, H. Sheckenhofer, and S.S. Malik, Phys. Rev. Lett. **44**, 1306 (1980).

19. Y.P. Feng, C.F. Majkrzak, S.K. Sinha, D.G. Wiesler, H. Zhang, and H.W. Deckman, Phys. Rev. B **49**, 10814 (1994).

20. B. Pardo, M. Maaza, and C. Sella, Physica **B 198**, 235 (1994).

21. L.J. Norton, E.J. Kramer, R.A.L. Jones, F.S. Bates, H.R. Brown, G.P. Felcher, and R. Kleb, J. Phys. II (France) **4**, 1 (1994).

22. H. Zhang, P.D. Gallagher, S.K. Satija, R.M. Lindstrom, R.L. Paul, T.P. Russell, P. Lambooy, and E.J. Kramer, Phys. Rev. Lett. **72**, 3044 (1994).

SURFACE CRYSTALLIZATION AND THIN FILM MELTING IN NORMAL ALKANES

X. Z. WU[1], H. H. SHAO[2,5] B. M. OCKO[3], M. DEUTSCH[4], S. K. SINHA[5], M. W. KIM[5], H. E. KING JR.[5] AND E. B. SIROTA[5*]

[1]Physics Dept., Northern Illinois Univ. and Materials Science Div., Argonne Natl. Lab.
[2]Dept. of Physics, The Ohio State University, Columbus, OH 43210
[3]Physics Department, Brookhaven National Laboratory, Upton, NY 11973
[4]Physics Department, Bar Ilan University, Ramat Gan 52900, Israel
[5]Corporate Research Science Laboratories, Exxon Research and Engineering Co.,
    Route 22 East, Annandale, NJ 08801
[*]invited speaker

ABSTRACT

Normal alkanes of carbon number n>14 exhibit surface crystallization at their liquid-vapor interface. This has been investigated with x-ray reflectivity, grazing incidence scattering and surface tension measurements. The structure and thermodynamics of the surface layer is consistent with a monolayer of the bulk rotator phase occurring at the surface above the bulk melting temperature. On the other hand, thin films of alkanes on SiO_2, exhibit a reduction of the melting temperature. The surface crystalline phase is observed for carbon number n>14. The vanishing of surface phase for small n may be due to a transition from surface freezing to surface melting behavior. These measurements can yield the relative surface energies of the various phases.

INTRODUCTION

The normal alkanes $CH_3-(CH_2)_{(n-2)}-CH_3$ (abbr. Cn) are the most simple organic series and form the basis of lipids, surfactants, liquid-crystals and polymers. The properties of these derivative molecules, both in bulk and at interfaces, are strongly related to the properties of the alkanes. Between the low-temperature highly ordered crystalline phases of the alkanes and their high-temperature liquid phase exist a series of weakly ordered plastic-crystalline phases called the "rotator" phases, because of the *lack of long-range order in the rotational degree of freedom of the molecules about their long axes*. Some of these intermediate phases have been known and studied for a long time.[1-6] Recently, the rotator phases have been characterized in detail through x-ray scattering[7] and calorimetry[8]. Their behavior in mixtures of different carbon numbers[9,10] and their response to applied pressure and dissolved gases[11] have been studied.

Almost all materials exhibit surface melting, as the molecular entropy at the surface is higher than that in the bulk.[12,13] Liquid crystals, however, aamong the few exceptions: they often exhibit surface induced ordering effects in addition to the disorder associated with reduced dimensionality. This has been demonstrated by various experiments of freely-suspended films.[14-19] At the free surface of bulk liquid crystals in their isotropic or nematic phase, surface smectic ordering is in general observed.[20-23] Such ordering has also been studied at the solid-liquid interface.[24] The studies of alkanes[25-28] which are much simpler molecules, are a natural extension of the liquid crystal studies which showed that the methyl-group of the alkane chain

resides at the free surface. The alkane system has also been employed to further the understanding of thermally generated capillary waves, through measurements of the temperature dependence of surface roughness.[29-32]

We will discuss here, (1) the work of Wu et al.[25-28] in which surface crystallization of a 2D crystalline layer on a bulk isotropic liquid of n-alkanes was studied and (2) the work of Shao et al.[33,34] where thin films of alkanes on a SiO_2 substrate were shown to melt at lower temperatures. The surface behavior will be compared to the bulk properties.

The bulk properties of the n-alkanes are extremely rich. There are 5 rotator phases distinguished by order parameters such as distortion (D), tilt magnitude (θ) and tilt direction (ϕ).[7,8] The bulk phase diagram is shown in Fig. 1, plotted with respect to the melting temperature, T_m. The highest temperature bulk rotator phases will be the most relevant for the understanding of the surface crystalline phases. For the intermediate chain-lengths studied, it is the one with the highest symmetry (the R_{II} phase), in which the molecules are in layers, oriented along the layer normal and packed in an average hexagonal lattice. At lower chain-lengths, the bulk pure alkanes exhibit the R_I phase which differs from the R_{II} phase by a finite distortion of the hexagonal lattice. The transition from R_I to R_{II} is first-order. The distortion is strongly related to interlayer coupling, and in binary mixtures[9] where interlayer coupling is reduced, the highest temperature bulk rotator phase for the short average chain-lengths becomes the R_{II} phase. The higher chain-length alkanes ($n \geq 26$) melt from a tilted phase which (for $n \leq 30$) is called R_{IV}, where the tilt direction is toward next-nearest neighbors. This tilted phase occurs above the R_{II} both in chain-length and in temperature and has been attributed[8] to the chain-end defects which appear in the rotator phases as temperature is raised.[35,36]
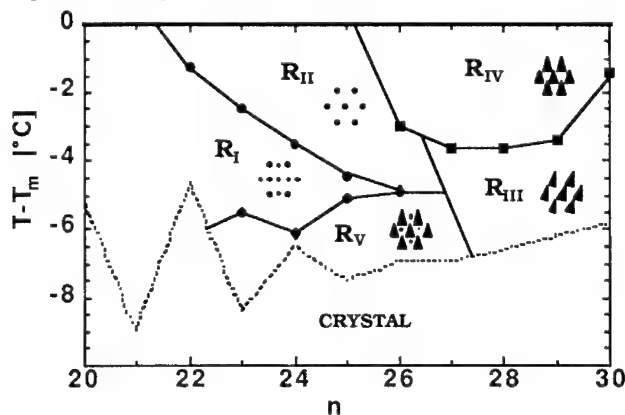
Fig 1. Phase diagram showing the rotator phases of bulk normal alkanes plotted relative to the melting temperature. The structures of the phases are shown schematically. The melting temperature T_m is shown in Fig. 8. (from Sirota et al.[7,8])

A number of complementary techniques were employed in the study of surface freezing of liquid alkanes. X-ray reflectivity and grazing incidence x-ray scattering GIXS were performed on the Harvard/BNL liquid surface spectrometer at X22B at the N.S.L.S. X-ray reflectivity measures the electron density normal to the surface and can easily determine the thickness of a

surface layer whose density is different from that of the bulk. GIXS measures the in-plane structure at a surface. Surface tension measurements were performed using the Wilhelmy plate method. The experimental details can be found elsewhere.[25-27]

Liquid Surface: Reflectivity

Shown in Fig. 2 is the x-ray reflectivity in the liquid and surface-crystal phases of C20, C30 and C44. When there is no surface crystal layer, the reflectivity, typical for a liquid surface, is well described by the smooth Fresnel reflectivity modified by surface roughness. The surface roughness has been shown to be due to capillary waves as well as an intrinsic roughness.[30-32] The surface-crystal layer produces a pronounced modulation of the reflectivity curve. The period of the oscillation yields the thickness of the layer, and a fit to a simple slab model with interface roughness yields the density and interfacial widths. The density profile derived from such a fit is shown in the inset to Fig. 2. The details of the fitting are described elsewhere.[25] These surface crystals are thermodynamically stable between the bulk freezing temperature T_f and the surface crystallization temperature T_s, which is as large as 3°C higher. The reflectivity profile does not change over that temperature range. That implies that there is no freezing of additional layers as the temperature is lowered towards bulk freezing. There is no layer-by-layer or continuous growth from the surface with decreasing temperature, as was observed in liquid crystals.[19,21,22,24]
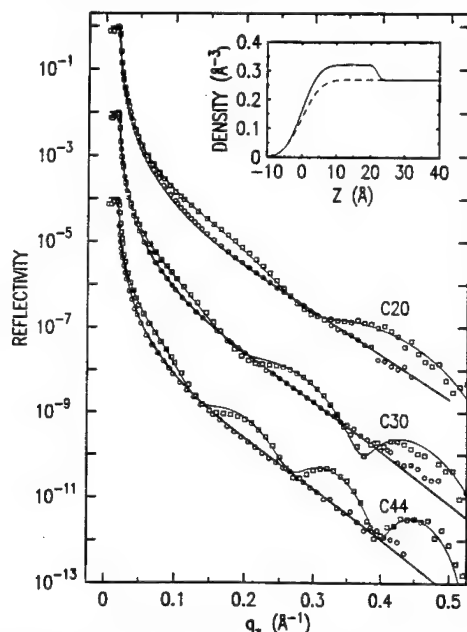
Fig. 2. Reflectivities for C20, C30 and C44. The data for the liquid surface phase are the dots and for the surface-crystal phase are the squares. The curves are shifted by 2 decades for better visibility. The solid lines are fits to the data using simple density profiles.[27] (INSERT) The surface density profile for the liquid (dashed) and crystal (solid lines) surface. (from Wu et al.[27])

17
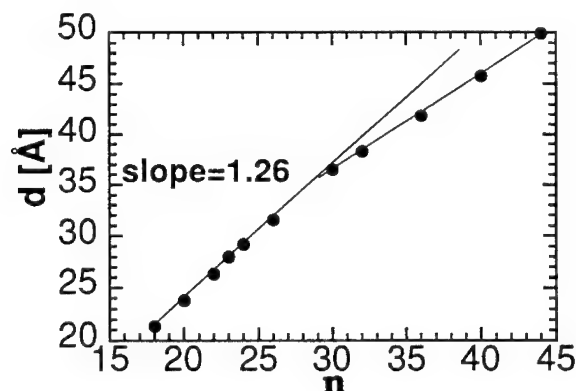
Fig. 3. The thickness of the surface-crystal layer as determined from x-ray reflectivity. (from Wu et al.[26])

Shown in Fig. 3 is the surface layer thickness (d) plotted versus chain-length. Below $n \approx 28$, d increases by about 1.26±0.02Å/carbon which is the projected length per carbon along an extended chain. Above $n \approx 28$ the slope is lower, suggesting that the molecules are tilted. We recall that the highest temperature bulk rotator phases are tilted for n>26.

Liquid Surface: GIXS

Shown in Fig. 4(a) is a grazing incidence x-ray scattering (GIXS) in-plane radial scan exhibiting a sharp peak at $q \approx 1.52$Å^{-1} in the surface-crystal phase of C20. The single peak at this position is characteristic of the hexagonal packing observed in the R_{II} rotator phase. A sample rotation scan of the liquid surface with the in-plane q vector kept fixed at the peak position is shown in Fig. 4(b). Peaks separated by 60° suggest that the structure is hexagonal and that the domain size is comparable to the surface area probed which is of order millimeters. Thus the horizontal-to-vertical dimensional ratio of this surface crystal is enormous; of order 10^6 or more.

To confirm whether or not the molecules are tilted, and to measure the tilt direction, surface-normal "rod scans" were performed at the in-plane peak positions.[27] These confirmed that the molecules are untilted for n<28 and tilted toward nearest neighbors for n>28. Note that this tilt direction is different from the R_{IV} bulk rotator phase which exhibits a tilt toward the next-nearest neighbor. We note that the surface crystalline temperatures are always above those of the bulk rotator phase, and generally, when both tilt directions occur, the nearest-neighbor tilt occurs at higher temperature.[37,38] If bulk crystallization had not limited the temperature range of stability of the surface phase, a transition to next-nearest neighbor tilt might be expected at lower temperature. Such transitions were indeed observed very recently in surface crystalline layers of binary alkane mixtures.[39]
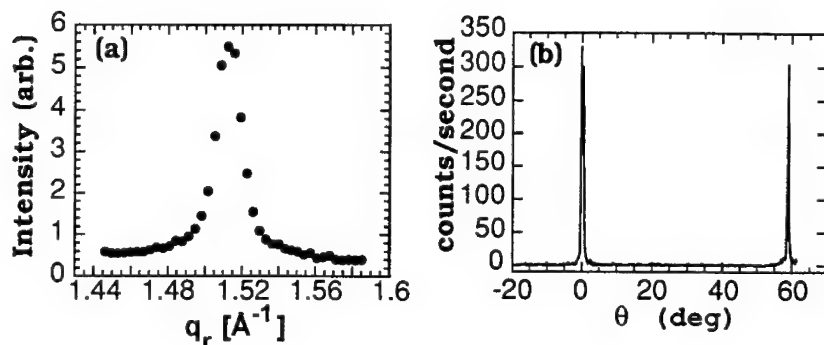
Fig. 4. (a) In-plane radial scans of C20 in the surface crystalline phase. (from Wu et al.[25]) (b) Sample rotation scan in the hexagonal surface-crystalline phase of C20. Note the peaks occur close to a 60° interval, as expected for hexagonal packing.

Shown in Fig. 5 is the spacing associated with the in-plane peak at $q_z=0$. The increase in spacing at n=30 corresponds to the onset of tilt (Fig. 3), however, since the tilt direction is toward a nearest neighbor, this spacing would not be directly affected merely by a tilt of cylinders. The increased spacing for longer chain lengths must then be related to the increasing importance of chain-end conformational disorder as n and T increase,[28] which itself is believed to be the cause of the tilt.
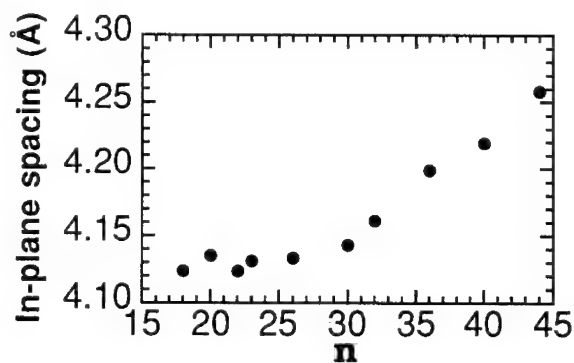
Fig. 5. The spacing $(2\pi/q)$ of the in-plane, on axis (i.e. $q_z=0$) peak as a function of chain-length. (from Wu et al.[28])

Liquid Surface : Surface Tension

Surface tension measurements were performed to study the thermodynamics of the surface.[26] In Fig. 6, the surface tension measured for C20 and C36 are displayed. The surface tension is $\gamma = \varepsilon_s - \varepsilon_B - T(S_S - S_B)$ where ε are the energies and S are the entropies of a molecule on the surface or in the bulk, (according to the subscripts). The slope of γ is then

19

$d\gamma/dT = S_B - S_S = \Delta S$. In the liquid phase (L) there is the well-known[1] behavior of a small negative slope implying greater freedom of surface molecules (i.e. $S_{SL} > S_{BL}$). The discontinuity in the slope[40] at T_s is the signature of a first-order surface transition to a phase where $d\gamma/dT > 0$. Indeed, a molecule in the crystalline surface phase is more confined than one in the bulk liquid. Hence $S_{SR} \ll S_{BL}$ (L and R denote liquid and rotator, respectively) and the slope becomes positive.

Since the structural results imply that the surface monolayer is of structure similar to that of a layer of the bulk rotator phase, the thermodynamics should be consistent as well. Assuming that $S_{SR}-S_{BR} \approx S_{SL}-S_{BL}$, a comparison can be made between ΔS obtained from the surface tension slopes and ΔS from the bulk latent heat of the rotator-liquid transition[1,8] (using the area/molecule to get moles per unit area). This is shown in Fig. 7. where the agreement is excellent, both in magnitude and in chain-length dependence.
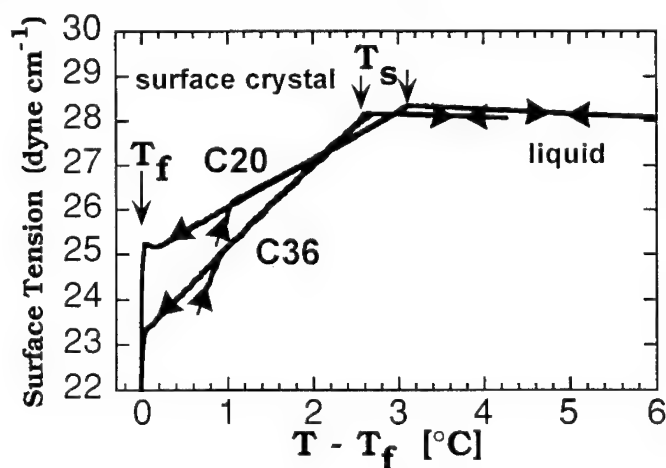
Fig. 6. The surface tensions (γ) of C20 and C36 measured in cooling and heating cycles (as denoted by arrows). The temperature is plotted with respect to the bulk freezing temperature T_f. The slope change at T_s indicates the formation of the monolayer. Note the larger slope for C36. (from Wu et al.[26])

The deviation in the figure for small n is probably related to the highest temperature bulk phase in that range. While the surface phase is R_{II}-like for all n, the highest-temperature solid bulk phase for n<21 is R_I, so that in that range, the bulk melting is R_I-to-liquid. Thus, a comparison of the bulk melting ΔS for n<21 to that of the surface phase, where the melting is R_{II}-to-liquid like, may not be completely valid. The latent heat of the R_I-R_{II} transition is strongly chain-length dependent, increasing from 0.25 kJ/mol for C25 to 1.0 kJ/mol for C22.[8] Extrapolating to lower n, this could account for the deviation.
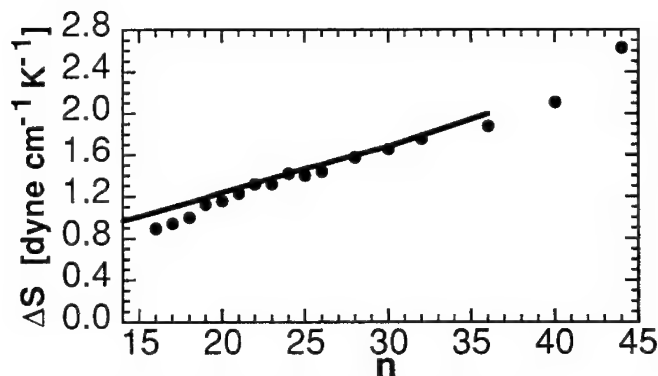
Fig. 7. ΔS, the entropy change upon surface monolayer formation, as obtained from the slope difference of the surface tension at T_s as a function of chain-length (dots) and the latent heat of the liquid-rotator melting transition per unit area (line). (surface tension data from Wu et al.[26])

Fig. 8 shows the temperature width of the surface-crystal phase as a function of chain-length. ΔT goes through zero at n=14. This can be interpreted as a crossover from the surface freezing behavior to the more common surface melting behavior. The solid line in the figure is a fit to a simple expression involving a $1/d^2$ Van der Waals interaction, discussed in detail elsewhere.[26] The deviation at long chain-length is likely due to the increasing influence of intra-chain disordering mechanisms as n increases.
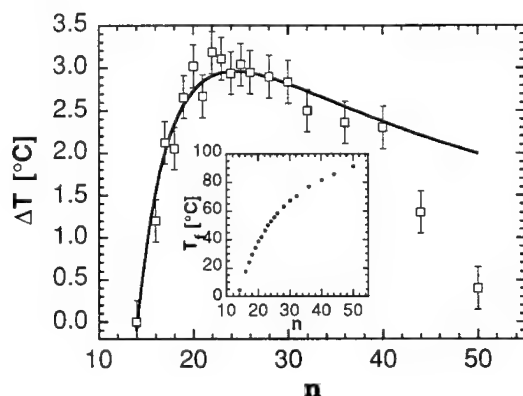
Fig. 8. The measured temperature width of the monolayer phase $\Delta T = T_s - T_f$ (squares) and a fit to the expression $\Delta T = (a/n) - (b/n^3)$ from Wu et al.[26] Note the crossover to surface melting behavior for n<14. (INSET) The bulk freezing temperature as a function of carbon number. (from Wu et al.[26])

MELTING OF THIN FILMS

Measurements were also performed on the melting of thin films of C23 on a SiO_2 substrate.[33,34] C23 films were prepared by evaporation of a dilute solution in hexane and annealing the films in the rotator phase, which produced aligned samples.[7] Thicknesses and uniformities were measured using a variety of methods including, mass balance, optical microscopy, x-ray reflectivity and intensities and peak widths from x-ray scattering. The details of the sample preparation, and thickness determination are presented by Shao et al.[34] The samples were studied using synchrotron x-ray scattering at Exxon's beamlines X10A&B at the N.S.L.S.. Melting was determined with x-rays by the disappearance of both in-plane and layering peaks, as well as by changing textures as observed by optical microscopy. A schematic of the system is shown in Fig. 9. Since in this experiment, the structure of the layer of alkane in contact with the substrate was not investigated, in this discussion we will treat such a layer, if it is different from the interior layers as part of the interface between the interior of the film and the substrate.

Vapor

top alkane layer	ε_1
	ε_2
alkane film	
	ε_3
substrate	
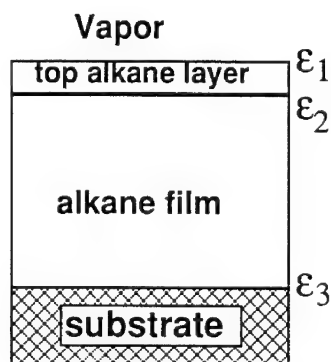
Fig. 9. Schematic of thin film.

The melting temperature of the interior of the film is shown in Fig. 10. Slightly above the melting temperature (~1°C) GIXS showed the presence of a surface crystallized monolayer, consistent with the structure observed on the bulk liquid-vapor interface by Wu et al.[26] The films macroscopically beaded-up at temperatures more than ~1°C above melting.

This system can be modeled by assuming that each layer of the alkane behaves as a layer of the bulk with a melting transition at T_f, a transition entropy of ΔS and an additional energy term if it is in contact with an interface. F_0 is the free energy per area of a N layer film which is entirely liquid. We let ε_1 be the free energy cost to have the top layer in the crystalline state ($\varepsilon_1 < 0$). ε_2 is the energy cost for an alkane liquid-solid interface, as occurs when there is a surface crystalline layer on the liquid ($\varepsilon_2 > 0$). ε_3 is the energy cost involved in having the alkane in contact with the

SiO$_2$ in the crystalline state ($\epsilon_3>0$). Thus, the free energy for an entirely crystalline film is $F_c=F_0+\epsilon_1+\epsilon_3 + N\,\Delta S(T-T_c)$ and that for a liquid film with a crystalline layer at the vapor interface is $F_s=F_0+\epsilon_1+\epsilon_2 + \Delta S(T-T_c)$. Using this simple model, the melting of the interior will occur when $F_c=F_s$. Thus, the melting temperature change in the thin films is given by $\Delta T=-(\epsilon_3-\epsilon_2)/\Delta S(N-1)$ where N is the number of layers in the film.[15] For C23, using the data in Fig. 10 and $\Delta S= 1.37$ dyne/(cm K) [1,26] we obtain $\epsilon_3-\epsilon_2=44$ dyne/cm.
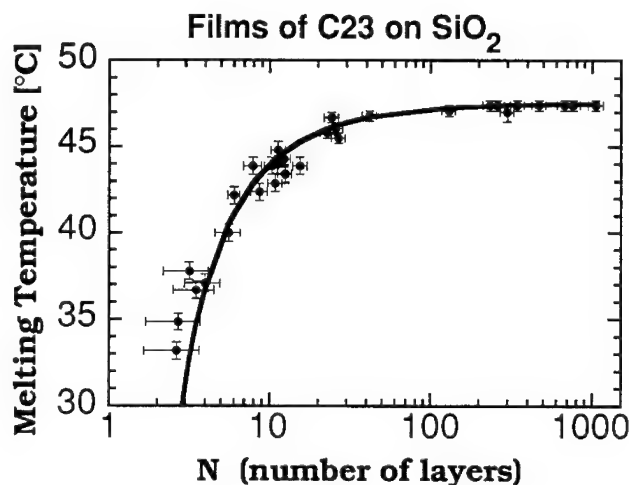
Fig. 10. Melting temperature of thin films of C23 on a SiO$_2$ substrate. The uncertainties in T and N are shown. The line is a fit yielding $T_m=47.5-32/(N-1)$. (from Shao et al.[33,34])

The melting of the surface layer will occur when $F_0=F_s$ so the temperature range of the surface-crystal phase on the semi-infinite liquid is $\Delta T=-(\epsilon_1+\epsilon_2)/\Delta S$. For C23 this yields $\epsilon_1+\epsilon_2=-4.26$ dyne/cm using the measured ΔT shown in Fig. 8. In order to independently determine ϵ_1 and ϵ_3 a third measurement would be needed. This could be either the melting temperature of the interior of freely suspended thin films where $\Delta T=\epsilon_2/\Delta S(N-2)$, or the melting temperature of a film confined between 2 solid surfaces where $\Delta T=-\epsilon_3/(N\Delta S)$. The present numbers suggest, however, that the preference of the SiO$_2$ interface for the liquid phase is much greater than the preference of the vapor interface for the rotator phase. This may be due to the preference for CH$_3$ groups at the vapor interface and a preference for CH$_2$ groups on the solid, with interaction energies much greater with the solid. To fully understand this, more detailed studies of the solid-liquid interface[24] are required.

CONCLUSIONS

Normal alkanes and their mixtures exhibit surface crystallization phenomena for chain lengths greater than 14 carbons. This phenomena has been explained with a simple thermodynamic model. The various structural properties are closely related to those of the bulk alkanes, but some unique features are also encountered. Thin films on a substrate exhibit a disordering phenomena. Such measurements can yield quantitative surface interaction energies. The rich bulk and surface properties of these simple normal alkanes will be important for understanding the properties of derivative chain molecules in bulk and on surfaces.

Related results showing new surface structures and phases have also been very recently observed in surface crystallization of pure 1-alcohols,[41] binary mixtures of n-alkanes[39] and on the thickess dependence of rotator phases in the thin films.[34]

REFERENCES

1) D. M. Small, *The Physical Chemistry of Lipids: From Alkanes to Phospholipids* (Plenum, New York, 1986).

2) A. Müller, *Proc. R. Soc. London, ser A* **138**, 514 (1932).

3) A. Craievich, J. Doucet, and I. Denicolo, *Phys. Rev. B* **32**, 4164 (1985); A. Craievich, I. Denicolo, and J. Doucet, *Phys. Rev. B* **30**, 4782 (1984); J. Doucet, I. Denicolo, A. F. Craievich, and C. Germain, *J. Chem. Phys.* **80**, 1647 (1984); I. Denicolo, J. Doucet, and A. F. Craievich, *J. Chem. Phys.* **78**, 1465 (1983); J. Doucet, I. Denicolo, and A. Craievich, *J. Chem. Phys.* **75**, 1523 (1981); J. Doucet, I. Denicolo, A. Craievich, and A. Collet, *J. Chem. Phys.* **75**, 5125 (1981).

4) G. Ungar and N. Masic, *J. Phys. Chem.* **89**, 1036 (1985).

5) G. Ungar, *J. Phys. Chem.* **87**, 689 (1983).

6) D. L. Dorset and H. Hu, *Acta Cryst.* **A47**, 543 (1991); D. L. Dorset, *EMSA Bull.* **20**, 54 (1990); D. L. Dorset, B. Moss, J. C. Wittmann, and B. Lotz, *Proc. Natl. Acad. Sci.* **81**, 1913 (1984).

7) E. B. Sirota, H. E. King Jr., D. M. Singer, and H. H. Shao, *J. Chem. Phys.* **98**, 5809 (1993).

8) E. B. Sirota and D. M. Singer, *J. Chem. Phys.* **101**, 10873 (1994).

9) E. B. Sirota, H. E. King Jr., H. H. Shao, and D. M. Singer, *J. Phys. Chem.* January (1995).

10) E. B. Sirota, H. E. King Jr., G. J. Hughes, and W. K. Wan, *Phys. Rev. Lett.* **68**, 492 (1992).

11) E. B. Sirota, D. M. Singer, and H. E. King Jr., *J. Chem. Phys.* **100**, 1542 (1994).

12) J. G. Dash, *Contemp. Phys.* **30**, 89 (1989).

13) R. Lipowsky, *J. Appl. Phys.* **55**, 2485 (1984).

14) D. E. Moncton, R. Pindak, S. C. Davey, and G. S. Brown, *Phys. Rev. Lett.* **49**, 1865 (1982).

15) E. B. Sirota, P. S. Pershan, L. B. Sorensen, and J. Collett, *Phys. Rev. A* **36**, 2890 (1987).

16) D. Y. Noh, J. D. Brock, J. O. Fossum, J. P. Hill, W. J. Nuttall, J. D. Litster, and R. J. Birgeneau, *Phys. Rev. B* **43**, 842 (1991).

17) R. Geer, T. Stoebe, and C. C. Huang, (1994).

18) E. B. Sirota, P. S. Pershan, S. Amador, and L. B. Sorensen, *Phys. Rev. A* **35**, 2283 (1987).

19) B. S. Swanson, H. Stragier, D. J. Tweet, and L. B. Sorensen, *Phys. Rev. Lett.* **62**, 909 (1989).

20) J. Als-Nielsen, F. Christensen, and P. S. Pershan, *Phys. Rev. Lett.* **48**, 1107 (1982).

21) B. M. Ocko, A. Braslau, P. S. Pershan, J. Als-Nielsen, and M. Deutsch, *Phys. Rev. Lett.* **57**, 94 (1986).

22) P. S. Pershan, A. Braslau, A. H. Weiss, and J. Als-Nielsen, *Phys. Rev. A* **35**, 4800 (1987).

23) G. J. Kellog, P. S. Pershan, E. H. Kawamoto, W. Foster, M. Deutsch, and B. M. Ocko, *Phys. Rev. E* (submitted).

24) B. M. Ocko, *Phys. Rev. Lett.* **64**, 2160 (1990).

25) X. Z. Wu, E. B. Sirota, S. K. Sinha, B. M. Ocko, and M. Deutsch, *Phys. Rev. Lett.* **70**, 958 (1993).

26) X. Z. Wu, B. M. Ocko, E. B. Sirota, S. K. Sinha, M. Deutsch, B. H. Cao, and M. W. Kim, *Science* **261**, 1018 (1993).

27) X. Z. Wu, E. B. Sirota, B. M. Ocko, S. K. Sinha, M. Deutsch, and M. W. Kim, (to be published).

28) X. Z. Wu, B. M. Ocko, E. B. Sirota, S. K. Sinha, and M. Deutsch, *Physica A* **200**, 751 (1993).

29) A. Braslau, M. Deutsch, P. S. Pershan, A. H. Weiss, J. Als-Nielsen, and J. Bohr, *Phys. Rev. Lett.* **54**, 114 (1985).

30) A. Braslau, P. S. Pershan, G. Swislow, B. M. Ocko, and J. Als-Nielsen, *Phys. Rev. A* **38**, 2457 (1988).

31) M. K. Sanyal, S. K. Sinha, K. G. Huang, and B. M. Ocko, *Phys. Rev. Lett.* **66**, 628 (1991).

32) B. M. Ocko, X. Z. Wu, E. B. Sirota, S. K. Sinha, and M. Deutsch, *Phys. Rev. Lett.* **72**, 242 (1994).

33) H. Shao, H. E. King Jr., E. B. Sirota, and D. M. Singer, *Bull. A.P.S.* **38**, 535 (1993).

34) H. Shao, H. E. King Jr., D. M. Singer, and E. B. Sirota, (to be published).

35) M. Maroncelli, H. L. Strauss, and R. G. Snyder, *J. Chem. Phys.* **82**, 2811 (1985).

36) W. L. Jarrett, L. J. Mathias, R. G. Alamo, L. Mandelkern, and D. L. Dorset, *Macromolecules* **25**, 3468 (1992).

37) E. B. Sirota, *J. Phys. (Paris)* **49**, 1443 (1988).

38) E. B. Sirota, C. R. Safinya, G. S. Smith, R. Plano, D. Roux, and N. A. Clark, in *Geometry and Thermodynamics*, edited by J. C. Toledano (Plenum, New York, 1990), p. 255.

39) X. Z. Wu, M. Deutsch, B. M. Ocko, H. Tang, E. B. Sirota, and S. K. Sinha, (to be published).

40) J. C. Earnshaw and C. J. Hughes, *Phys. Rev. A* **46**, R4494 (1992).

41) M. Deutsch, X. Z. Wu, E. B. Sirota, S. K. Sinha, B. M. Ocko, and O. M. Magnussen, *Europhys. Lett.* (submitted).

PHASE SEPARATION STUDIES OF
CONFINED THIN FILM POLYMER BLENDS

Q. PAN AND R. J. COMPOSTO
University of Pennsylvania, Department of Materials Science and Engineering,
Philadelphia, PA 19104

ABSTRACT

Using video-optical microscopy and image analysis software, the morphological development of phase separation of polystyrene (PS) and poly(vinyl methyl ether) (PVME) blends is monitored for film thickness ranging from 200 to 700nm's. In the current studies, films are confined between glass slides. For blends having a PS volume fraction of 0.30 (the critical composition), the area fraction of the PS-rich minority phase, A, decreases more rapidly as film thickness decreases. At long times, the final A achieves a constant value which is less than the bulk value. The correlation length of concentration fluctuations increases more rapidly than the bulk scaling prediction, which suggests that wetting plays a significant role in the phase separation kinetics of thin films. Because of confinement, the shape of the PS-rich phase is anisotropic, flattened along the film direction. The confinement restricts the phase growth perpendicular to the film plane, and thus hinders the development of phase separation at very late stages.

INTRODUCTION

Thin films of polymer blends have many potential applications, for example as sensors, coatings, electrodes or optical materials.[1] It is of great interest to understand how the presence of a solid boundary modifies the thermodynamic and kinetic behaviors of thin film blends with respect to that of bulk mixtures.

When a bulk mixture of two polymers is quenched rapidly from a single, homogeneous phase into the two phase region, the phase separation initiates by the destruction of the concentration homogeneity and proceeds as the local concentration fluctuations grow.[2] However, when the mixture is brought in contact with a hard wall, the concentration homogeneity has already been perturbed before the phase separation occurs, because the translational and rotational symmetries are broken near the interface. The course of phase separation may then be strongly affected in terms of thermodynamics as well as kinetics. This perturbation is only due to the geometrical constraint at the interface and defined as a confinement effect. Furthermore, if the two separated phases have different wettabilities towards the solid

surface, then the phases will spatially re-arrange to lower the total system energy including not only the polymer-polymer interaction but also the substrate-polymer interfacial free energies. Thus the pattern evolution during the late stages of phase separation is governed by the competition between the polymer-polymer interaction and substrate-polymer interfacial energies. This pattern re-arrangement caused by the difference in wettabilities is defined as a substrate effect. One would expect that both the confinement and substrate effects become significant when the binary mixture is confined to a thin film between two solid surfaces.

Recently various studies have been done on both small molecule and polymer systems in a confined geometry.[3-14] For a binary polymer blend with a lower critical solution temperature, the spinodal temperature is found to increase as the film thickness decreases,[5] which implies that the polymer system becomes more stable. In addition, surface-directed spinodal decomposition is experimentally observed where the spinodal waves grow with a dominant wave vector directed normal to the surface/interface.[12] The goal of our research is to provide a fundamental and systematic understanding of the confinement and substrate effects on the morphology, kinetics and thermodynamics of the phase separation of polymer blends.

EXPERIMENTAL SECTION

Binary polymer blends of polystyrene (PS) and poly(vinyl methyl ether) (PVME) with a lower critical solution temperature (LCST) are used in this study. The molecular weight characteristics of the polymers are shown in Table I. The thin film polymer blends have a PS volume fraction of 0.30 and are sandwiched between two hard walls, namely glass slides. The film thicknesses range from 200nm to 700nm. The phase separation behavior is studied at 135°C.

Because of the difference between the refractive indices of PS (1.59)[15] and PVME (1.47),[15] the morphology development of the phases during phase separation is easily observed using optical microscopy. The video images are analyzed by image analysis software provided by the National Institute of Health. The morphology development has been characterized by two measurable parameters, namely the area fraction of the PS-rich minority phase A and the characteristic wavelength of the concentration fluctuations ξ, i.e., the correlation length of the system. The area fraction is measured directly from the images, while the correlation length is obtained as the peak position in the frequency domain after a 2-dimensional Fourier transformation on the images.

Table I   Characteristics of Polymers

Polymer	M_w	M_w/M_n	Source
PS	65,000	1.04	Pressure Chem.
PVME	99,000	2.13	SP_2

RESULTS AND DISCUSSIONS

Fig. 1 represents the morphology evolution of polymer thin films with thicknesses of 263nm and 673nm. Both films are heated rapidly from one phase region to 135°C, a temperature inside the two phase region. Using the Becke line method, the dark phases are determined to be the PS-rich minority phase. First of all, the morphologies in both films are initially seen to be an interconnected network and finally achieve a droplet-matrix pattern. Qualitatively, the pattern evolution in the thinner film is faster than in the thicker ones. As indicated in Fig. 1(b), the PS-rich phases become isolated from each other in the 263nm film while they still remain interconnected in the 673nm film. Eventually both films, though at different times, reach a stage where the morphology no longer changes. Second, during the late stage of phase separation for both films, the lateral size scales of the phases are much larger than the film thicknesses, which implies that the phases are anisotropic in shape and the growth perpendicular to the film plane is constrained by the two hard walls. Furthermore, when both films have achieved their final pattern, for example at 180min (Fig. 1(c)), the average diameters of the PS-rich droplets in both films are about 100 times larger than the film thicknesses. This empirical result suggests that the film thickness plays an important role in controlling the finalized lateral size of the PS-rich phase, and thus the development of the phase separation.
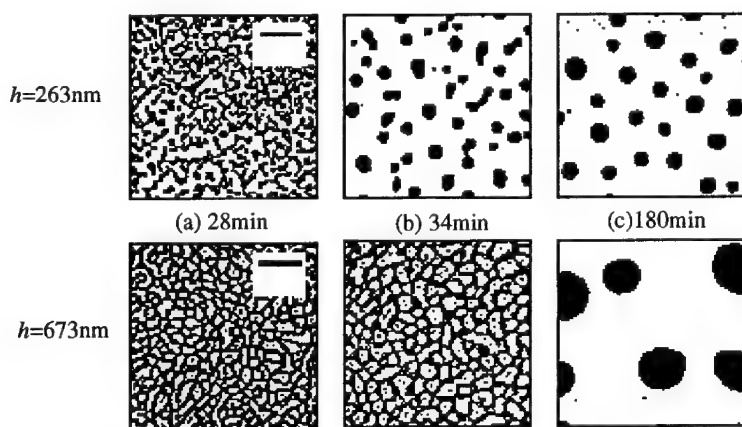
Fig.1 Morphology evolution for PS:PVME thin films with thicknesses of 263nm and 673nm, after annealing at 135°C for (a)28min, (b)34min, and (c)180min. (The scale markers in (a) correspond to 50μm.)
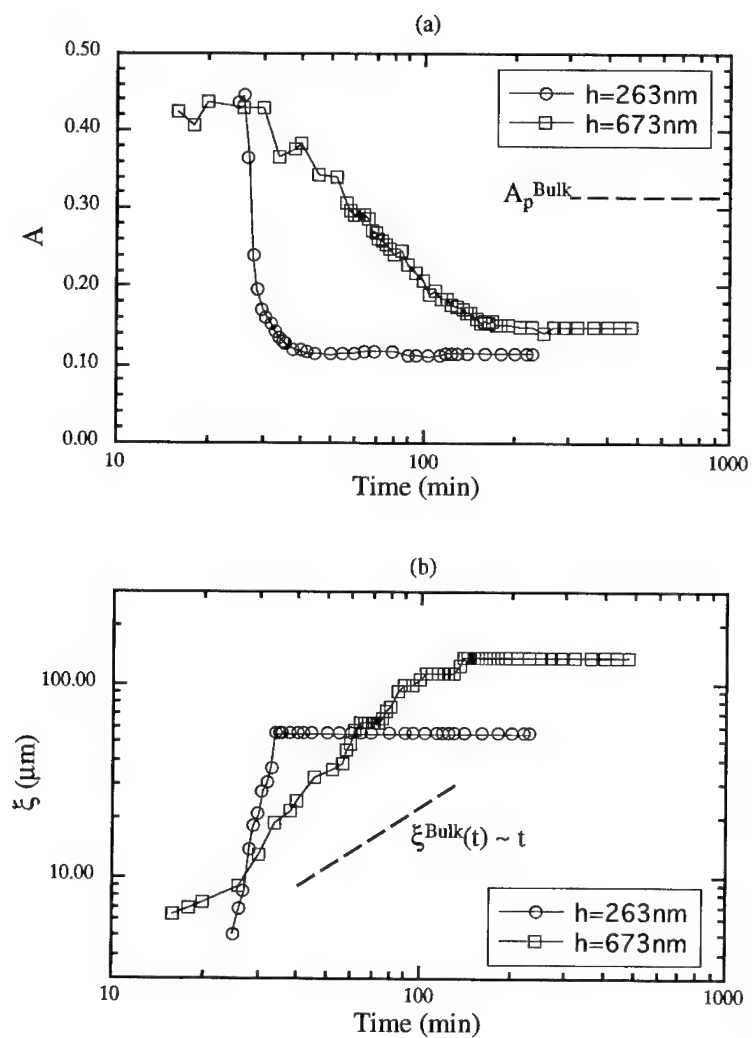
Fig.2 Time dependence of (a) the area fraction of PS-rich phase, and (b) the correlation length of the concentration fluctuations for polymer thin films with thicknesses of 263nm and 673nm during phase separation at 135°C.

Fig. 2(a) shows the time dependence of the area fraction of the PS-rich phase, A(t), for thin films with thicknesses of 263nm and 673nm, during late stages of phase separation at 135°C. Fig. 2(b) shows the time dependence of the correlation length, $\xi(t)$, for the same films. Considering both the area fraction and the correlation length, we divide the course of phase separation development into two stages, namely the evolving stage and the final plateau stage. During the evolving stage, the area fraction of the PS-rich phase decreases and the correlation length increases. The end of the evolving stage marks the start of the final stage, where the area fraction and the correlation length cease to evolve and achieve their plateau values A_p and ξ_p, respectively. As the film thickness increases, both the area fraction and the correlation length evolve more slowly and reach their final values at later times, as evidenced in Fig. 1(b). When compared with the behavior of bulk mixtures, the correlation length of thin films evolves much more rapidly and the area fraction of the PS-rich phase reaches a much lower plateau value.

The fact that the phase separation evolves faster in thinner films seems to imply that the system becomes less stable as the film thickness decreases, which is contrary to previous experimental and theoretical results.[5-7] However, PVME has a lower surface energy than PS[16] and the preferential wetting of PVME to the substrate is another driving force for the separation of PS:PVME mixture. As the film thickness decreases, this wettability effect should modify the phase separation behavior more strongly. In our film thickness range, this driving force of wettability may well outweigh the stabilizing effect due to the confinement.

In addition to the two film thicknesses being discussed, we have quantitatively studied two other thicknesses, namely 360nm and 554nm. The analysis shows that, with increasing film thickness, $\xi(t)$ slows down and becomes more similar to the scaling behavior for bulk mixture, i.e., $\xi^{Bulk}(t) \sim t$. Also, with increasing film thickness, A_p increases linearly towards the value predicted by the phase diagram of the bulk mixture. Based on these observations, a smooth transition from the thin film to the bulk mixture behavior should occur at a certain film thickness. It is of great interest to observe this transition in our future studies.

In conclusion, for a system of glass/PS:PVME(30:70)/glass, the phase separation behavior in thin film blends differs significantly from that of bulk mixtures in terms of morphology, kinetics, as well as the final stage features. In thin films, the growth of the separated phases is anisotropic due to the constraint exerted by the rigid substrates, and thus the course of phase separation is hindered at late stages. When films are thinner than 700nm, as in our studies, we observe a very strong film thickness effect on phase separation. As film thickness increases, the rate of phase separation slows down and the final area fraction increases linearly towards the predictions for the bulk mixture. Compared with bulk mixtures, the thin film blends phase separate faster in terms of the evolving rate of the correlation length of concentration fluctuations. Here the substrate effect, which draws the more wettable PVME from the mixture to the interfaces, accelerates the phase separation in the films and overwhelms the stabilizing effect from the confinement. Eventually, when the ratio of the diameter of PS-rich droplets to the film thickness

reaches the critical value, namely 100 as empirically determined from the image analysis, the stabilizing effect due to confinement and the acceleration effect due to preferential wetting become balanced, and the phase separation reaches a pseudo-equilibrium where the morphology of the phases remains unchanged.

ACKNOWLEDGMENTS

REFERENCES

1. J. D. Swalen et al., Langmuir, **3**, 932 (1987).
2. J. D. Gunton, M. San Miguel, and P. Sahni, in Phase Transition and Critical Phenomena, vol.8, edited by C. Domb and J. H. Lebowitz (Academic, London, 1983).
3. S. Mader and S. Herd, Thin Solid Films, **10**, 377 (1972).
4. J. P. Desideri and D. Scornette, J. Phys. France, **49**, 1411 (1988).
5. S. Reich and Y. Cohen, J. Polym. Sci. Polym. Phys. Ed., **19**, 1255 (1981).
6. H. Tang, I. Szleifer, and S. Kumar, J. Chem. Phys., **100**, 5367 (1994).
7. S. Kumar, H. Tang, and I. Szleifer, Molecular Physics, **81**, 867 (1994).
8. D. Katzen and S. Reich, Europhys. Lett., **21**, 55 (1993).
9. H. Tanaka, Phys. Rev. Lett., **70**, 2770 (1993).
10. H. Tanaka, Europhys. Lett., **24**, 665 (1993).
11. H. Tanaka, Phys. Rev. Lett., **72**, 1702 (1994).
12. R. A. L. Jones, L. J. Norton, E. J. Kramer, F. S. Bates, and P. Wiltzius, Phys. Rev. Lett., **66**, 1326 (1991).
13. G. Krausch, C. Dai, E. J. Kramer, J. F. Marko, and F. S. Bates, Macromolecules, **26**, 5566 (1993).
14. F. Bruder and R. Brenn, Phys. Rev. Lett., **69**, 624 (1992).
15. J. C. Seferis, in Polymer Handbook, 3rd ed., edited by J. Brandrup and E. H. Immergut (Jonh Wiley & Sons Inc., New York, 1989).
16. Q. S. Bhatia, D. H. Pan, and J. K., Macromolecules, **21**, 2166 (1988).

ADHESION FORCE BETWEEN HIGH ENERGY SURFACES IN VAPOR ATMOSPHERE.

JEROME CRASSOUS *, JEAN-LUC LOUBET ** and ELISABETH CHARLAIX *
* Laboratoire de Physique, Ecole Normale Supérieure de Lyon, 46 Allée d'Italie, Lyon, France.
** Laboratoire de Tribologie et Dynamique des Systèmes, Ecole Centrale de Lyon, 38 avenue Guy de Collongue, Ecully, France.

ABSTRACT

We report experimental measurements of the adhesion force between metallic substrates in undersaturated heptane vapor atmosphere, with a surface force apparatus. The attractive force between the substrates is strongly dependant of the condensation of a liquid bridge connecting the surfaces. The results show the importance of wetting phenomena for the maximum attractive force : we find that this maximum attraction varies as the power two-third of the curvature of the meniscus connecting the surfaces, in good agreement with the theory of Van der Waals wetting.

INTRODUCTION

The adhesion force between solid surfaces in humid atmosphere is a subject of great practical importance : it controls the cohesion of granular materials, the mechanical properties of contacts between surfaces, etc... In then presence of a condensable vapor, the adhesion force is strongly influenced by the liquid bridge that can form between the surfaces by capillary condensation. Within the framework of the classical theory of capillarity and of the Derjagin approximation, the maximum adhesion force between, for instance, a rigid sphere of radius R and a rigid plane, is [1]:

$$F = 4\pi\gamma R \qquad (1)$$

If the solid is dry, γ is the solid surface tension γ_{SV} ; if the substrates are immersed into a liquid bath, γ is the solid-liquid surface tension γ_{SL} ; finally in the presence of a liquid bridge, $\gamma = \gamma_{SL} + \gamma_{LV}\cos\theta$, where θ is the contact angle of the liquid on the solid surfaces.

When the solid surfaces are partially wetted by the liquid phase, the contact angle is given by the Young's law of capillarity $\gamma_{SL} + \gamma_{LV}\cos\theta = \gamma_{SV}$, and the adhesion force given by eq. (1) does not depend on the presence of a liquid bridge [1]. However when wetting is perfect, $\cos\theta = 1$ and $\gamma_{SL} + \gamma_{LV} < \gamma_{SV}$. A question is then [2], how does the adhesion force change from the "dry" value $F = 4\pi R\gamma_{SV}$ to the "wetted" value $F = 4\pi R(\gamma_{SL} + \gamma_{LV})$, when the pressure of the vapor is increased from zero ?

EXPERIMENTAL

We report here measurements of the adhesion force between high energy platinum surfaces in presence of heptane vapor. The measurements are made with a Surface Force Apparatus (SFA) of high rigidity [3,4]. The substrates are a plane and a sphere of millimetric radius ($R = 3.29mm$ in the following experiments), made of fired-polished pyrex coated with a $50nm$ thick layer of platinum deposited under vacuum. The roughness of those substrates, measured by atomic force microscopy, is $2nm$ peak to peak. Liquid alkanes wet completely the substrates.

The liquid n-heptane surface tension at $T = 23^oC$ (temperature of the experiments) is $\gamma_{LV} = 19.8mN/m$. When the substrates are immersed into liquid n-heptane, the interaction measured is compatible with a Van der Waals attraction : $F/R = -A_{SLS}/12\pi h^2$, where h is the minimum distance between the surfaces and $A_{SLS} = 2\ 10^{-19}J$ is the solid-liquid-solid Hamaker constant. The experimentally measured solid-liquid surface tension γ_{SL} is less than $1mN/m$. This low value is due to the roughness of the substrates.

For measuring the adhesion force in presence of n-heptane vapor, the initially dry and clean substrates are mounted on the SFA, and the pressure of n-heptane is tuned by the mean of a reservoir containing a liquid mixture of n-heptane and of non-volatil silicone oil Rhodorsil V20, whose pressure vapor is less than $.1Pa$.

RESULTS AND DISCUSSION

Figure 1 shows the force measured between the surfaces as a function of their distance h, for different values of the heptane pressure. When the surfaces are brought toward each other from a remote position where they do not interact, the force is almost zero (or very weakly attractive) up to a point of strong discontinuity (point C in the figure). This discontinuity reflects the condensation of a liquid bridge between the surfaces. When the surfaces are pulled apart, the force decreases smoothly. The liquid bridge evaporates completely at the point (E in the figure) where the force goes back to its initial zero value. In the range of distances lying between point C and point E, the force shows a strong hysteresis, corresponding to two metastable states for the system, one with and the other without the liquid bridge.

The effect of the heptane pressure on the force characteristics can be summarized as follows : when the pressure of the vapor increases, the condensation distance (abcissa of point C) and the evaporation distance (abcissa of point E) increase, while the maximum attraction experienced by the surfaces decreases. This maximum attraction however is always larger than $4\pi R(\gamma_{LV} + \gamma_{SL})$.

We interpret this interaction force in the framework of the wetting theory with Van der Waals forces. In presence of a meniscus of mean radius of curvature $r_c \ll R$, (here r_c stands for the absolute value of the radius of curvature, which is indeed negative) the attractive force predicted is [5] :

$$F = 4\pi R\gamma_{LV}(1 - \frac{h - 3e}{2r_c}) + F_{SLS}(h) \tag{2}$$

where F_{SLS} is the interaction force between the substrates through the liquid phase, and $e \ll r_c$ the thickness of the wetting films coating the surfaces far from the liquid bridge

(see fig. 2). The factor $3e$ in eq. (2) reflects the thickening of the wetting films in the region where they merge into the liquid bridge [6,7].
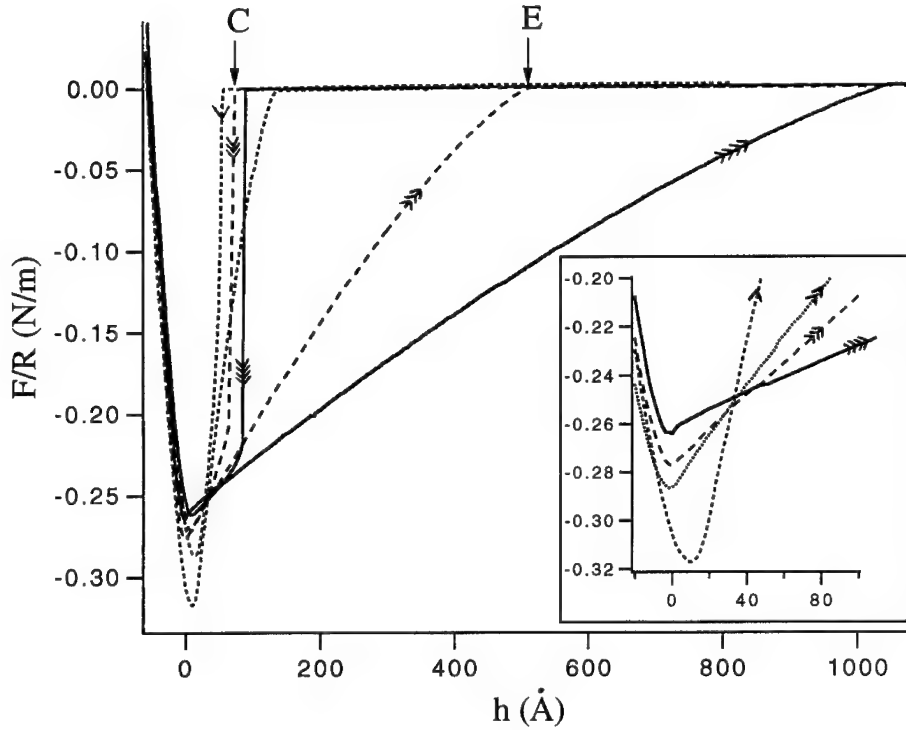
Figure1 : Variation of the force F/R measured between the sphere and the plane as a function of their distance h. The arrows on the curves show the direction of the surfaces relative motion, at a constant velocity of $1\mathring{A}/s$. The number of arrows increases with the pressure of the vapor. Inset : Magnification of the force when the surfaces are receeding, in the region of the maximum attractive force.

At equilibrium, the Laplace pressure in the bridge is equal to the disjoining pressure in the film :

$$\frac{\gamma_{LV}}{r_c} = \frac{-A_{SLV}}{6\pi e^3} \tag{3}$$

where A_{SLV} is the solid-liquid-vapor Hamaker constant. Furthermore, if the liquid phase is in equilibrium with the vapor phase, the pressure of the liquid is determined by the chemical potential of the vapor. Then r_c and e are a function of the vapor pressure only, and eq. (2) predicts that $F(h)$ depends linearly with h. The maximum attractive force predicted by (2) is :

$$F_{max} = 4\pi R[\gamma_{SL} + \gamma_{LV} + \frac{3}{2}(\frac{\gamma_{LV}}{r_c^{2/3}})(\frac{-A_{SLV}}{6\pi \gamma_{LV}})^{1/3}] \tag{5}$$

35
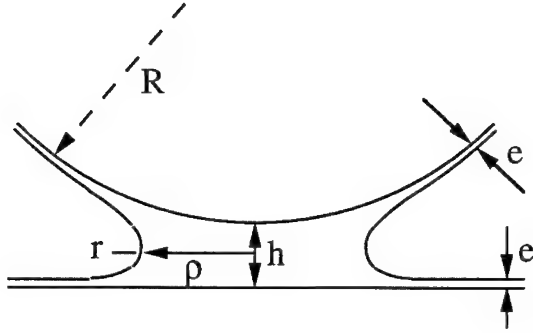
Figure 2 : Schematic illustration of a liquid bridge. The mean curvature is $1/r_c = 1/r - 1/\rho$

The force $F(h)$ measured when the surfaces are receeding has a constant slope, which does not depend on the receeding velocity, for distances ranging from small h up to about half the abcissa of point E. In this region, the liquid bridge is in equilibrium with the vapor. Close to the disparition of the liquid bridge (point E), the force $F(h)$ departs from a linear behaviour and has a slight dependence on the drift velocity. Those non-equilibrium effects appear close to the disappearance of the liquid bridge, since there is a relatively large amount of liquid to be evaporated at that point [5]. In the region of equilibrium, we derive the mean radius of curvature r_c of the meniscus, from the slope dF/dh. The different experiments shown on figure 1 correspond to r_c values of 35, 115, 175 and 377 Å.
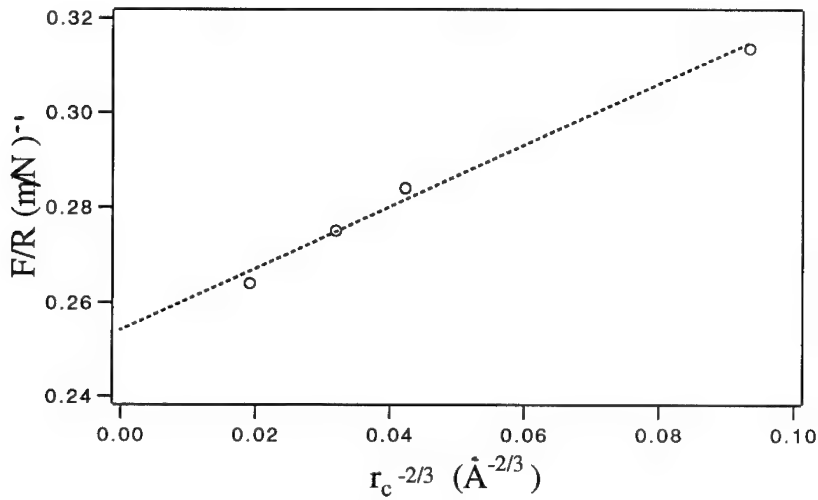
Figure 3 : The maximum attractive force F/R measured between the surfaces, as a function of the power 2/3 of the curvature of the meniscus. The dotted line corresponds to the best fit with a straight line.

Figure 3 shows the maximum attraction measured F versus $r_c^{-2/3}$. The data is in good agreement with the linear dependance predicted by eq. (5). The best fit of the data with a straight line gives values of the solid-liquid-vapor Hamaker constant and the solid-liquid surface tension. The resulting Hamaker constant is $A_{SLV} = -2.4 \pm 0.4 \ 10^{-20} J$, the large error bar coming mainly from the fact that the slope depends on $(-A_{SLV})^{1/3}$. The value of the solid-liquid surface tension found is $\gamma_{SL} = 0.5 mN/m$, which is compatible with the experiments in which the substrates are immersed into the liquid phase.

Thus, equation (5) appears as an acceptable extension of equation (1) to the case of Van der Waals wetting, i.e. to describe the adhesion of surfaces in presence of an undersaturated vapor of a wetting liquid. In our experiments the measurement of the vapor pressure P_V was not accurate enough to check directly the dependence of the maximum attraction force on P_V. However, if the mean radius of curvature of the condensed liquid bridge obeys Kelvin's law :

$$-\frac{\gamma_{LV}}{r_c} = \frac{k_B T}{v_L} Log \frac{P_V}{P_{sat}}$$

which has been shown to be valid down to very small radii of curvature [8], the dependency induced by equation (5) is :

$$F = 4\pi R(\gamma_{SL} + \gamma_{LV} + \frac{3}{2}(\frac{-A_{SLV}}{6\pi})^{1/3}(\frac{k_B T}{v_L} Log \frac{P_{sat}}{P_V})^{2/3}) \qquad (6)$$

where v_L is the molecular volume of the liquid. Equation (6) predicts that the adhesion force increases when P_V decreases, which is experimentally observed. However, it cannot be used to describe the adhesion force in the whole range of pressure $0 < P_V < P_{sat}$, since its r.h.s. diverges at $P_V = 0$. In fact, this analysis is valid only as far as the wetting films coating the surfaces actually exist. It is known however, that Van der Waals wetting films are stable only if their thickness e is larger than a minimum thickness $e^* = \sqrt{-A_{SLV}/4\pi S}$, where S is the wetting parameter $S = \gamma_{SV} - \gamma_{SL} - \gamma_{LV}$ [9]. Equation (3), together with Kelvin's law, then gives a minimum value of P_V :

$$P_V^{min} = P_{sat} \exp\{-\frac{2}{3}\frac{v_L}{k_B T}(\frac{4\pi S^3}{-A_{SLV}})^{1/2}\}$$

at which the adhesion force saturates to the value :

$$F = 4\pi R(\gamma_{SL} + \gamma_{LV} + S) = 4\pi R \gamma_{SV}$$

i.e. the adhesion force between dry solid surfaces.

References

1. J.N. Israelashvili, Intermolecular and Surface Forces, (Academic Press 1985)

2. H.K. Christenson, Journal of Colloid and Interface Science 121, 170 (1988)

3. A. Tonck, Thèse de Doctorat, Ecole Centrale de Lyon, 1989

4. J.M. Georges, S. Milliot, J.L. Loubet and A. Tonck, Journal of Chemical Physics 98, 7345 (1993)

5. J. Crassous, E. Charlaix and J.L. Loubet, in preparation

6. B. Legait and P.G. de Gennes, *J. Phys. (Paris)* **45**, L647 (1984)

7. N.V. Churaev, *Rev. Phys. Appl.* **23**, 975 (1988)

8. L.R. Fisher and J.N. Israelashvili, *Journal of Colloid and Interface Science* **80**, 528 (1981)

9. J.F. Joanny, Thèse de Doctorat d'Etat, Université Paris 6, 1984

SURFACTANT SELF-ASSEMBLIES NEAR CONTACT LINES
AND THEIR EFFECT ON WETTING BY SURFACTANT SOLUTIONS

B. FRANK AND S. GAROFF
Physics Department, Carnegie Mellon University, Pittsburgh, PA   15213

ABSTRACT

Surfactant self-assembly at the liquid-vapor, solid-liquid, and solid-vapor interfaces controls the wetting behavior of advancing surfactant solutions. While different surfactants exhibit different static and dynamic wetting properties, we show that these behaviors can be understood through an examination of microscopic structures driven by surfactant-surface interactions. We examine surfactant solutions exhibiting complete and partial static wetting as well as spreading by dendritic pattern formation and unsteady, stick-jump behavior. In each case, the observed behavior is related to the structure of the surfactant assemblies in the vicinity of the contact line.

I. INTRODUCTION

Addition of surfactants to a fluid dramatically affects the wetting and spreading of the fluid. Thus, many technologies utilize surfactants for control of wetting processes.[1-3] The ability of surfactants to control wetting arises from the their self-assembly at the solid-liquid, solid-vapor, and liquid-vapor interfaces and the resulting changes in interfacial energies. The multiple degrees of freedom of surfactant molecules cause these interfacial self-assemblies to exhibit rich structural detail and variation. The molecular structure of the self-assemblies and the effects of these structures on wetting remain topics of extensive scientific and technological interest.[4-14]

On a given surface, aqueous solutions of different surfactants exhibit widely varying wetting behaviors. Some surfactant solutions have a 0° static contact angle while others exhibit a high static contact angle. Dynamic spreading also varies widely. Surfactant solutions which spread to zero static contact angle may do so through dendritic spreading.[15-18] In contrast, solutions which have high static contact angles exhibit unsteady, stick-jump behavior when forced to advance across a surface.[19,20] This diversity in static and dynamic wetting behaviors arises from the variation of the interfacial self-assembly of the surfactant and its interaction with the surface.

Surfactant self-assembly at all three interfaces controls wetting.[8,14] The amphiphilic character of the molecule drives the assembly at the liquid-vapor interface, while the additional interactions between the surfactant head groups and the solid surface strongly influence the self-assembly at the solid-liquid interface. The self-assembly at the solid-vapor interface is very complex and can contain adsorbed surfactant as well as ultrathin precursing fluid films. While the role of these surfactant self-assemblies and fluid films in wetting has been suggested,[21] their structure is not fully determined.[1,4-6,22,23]

In this paper, we review our recent explorations of molecular structures and precursing films near contact lines of surfactant solutions as well as their effects on wetting and spreading of these solutions. We use x-ray and neutron scattering to probe the structure of: (a) surfactant assemblies left behind by contact lines forced to retreat across a surface in a dipping process and (b) the precursing films formed when these assemblies are reattached to bulk bodies of solution. The importance of the head group-surface interaction and the origin of the vast differences in mobility of different surfactants across a surface become evident (section IV). By observing

dendritic spreading of different solutions on substrates prepared in a variety of ways, we not only see the importance of surfactant mobility in dendrite formation but also confirm other aspects of proposed models for this spreading behavior (section V). In fact, we examine a suite of solutions exhibiting a continuum of behaviors between dendritic and stick-jump spreading. Any system's position within this continuum is governed by the formation of surfactant barriers on the solid surface along microscopic sections of contact lines (section VI). We report preliminary results showing that these barriers have complex structures (section VII). Often, they consist of surfactants diffusing out ahead of the contact line and separate self-assemblies of surfactants left during spontaneous retreat of the contact line. These assemblies formed on spontaneous retreat of the contact line show striking similarities to those formed on forced retreat of the solution in a dipping process (section III).

II. EXPERIMENTAL METHODS

In the studies reported, we use a variety of experimental techniques. Neutron and x-ray reflectivity and optical ellipsometry are used to probe the thickness and molecular structure of surfactant assemblies and thin precursing films.[4-6,24] Video microscopy and digital image analysis provide measurements of the lateral form and extent of moving contact lines.[24,25] The most unique aspects of our methodology, surface preparation and our use of breath figures[26,27] to measure the formation of surfactant barriers, will be briefly presented here.

The two substrates utilized in this study are silicon oxide, which is negatively charged at pH7, and sapphire, which is positively charged at pH7.[28] Our cleaning technique achieved a zero degree contact angle for water on the substrate and maintained their charged nature.[24] The silicon substrates were soaked in a sulfur-chromic acid solution, rinsed in specially purified water, and soaked in hydrochloric acid. After a final water rinse, they were coated with a protective monolayer of surfactant which prevented the adsorption of contaminants as the water dried. This monolayer was removed by UV/ozone exposure.[24,29] The sapphire substrates were treated similarly, with significantly shorter acid exposure to prevent any possible etching or roughening of the surface. The preservation of the charged nature of the surfaces after this cleaning is demonstrated by the different surfactant spreading behaviors discussed in the next section.

Depending on the wetting properties of a surface, condensing water can either spread to a uniform film or form breath figures, an assembly of microscopic drops that scatter light.[26,27] The average droplet size and polydispersity within a breath figure is associated with the contact angle of the water on the surface. The amount of light scattered is related to the droplet distribution and is therefore a function of surface wettability. Thus, by condensing water vapor on an illuminated surface, regions with different wetting properties can be observed easily.

III. MACROSCOPIC OBSERVATIONS

The macroscopic behavior of spreading surfactant solutions depends directly on the microscopic processes occurring in and around the contact line. We begin with observations of macroscopic wetting behavior of aqueous solutions of two classic surfactants: a cationic -- cetyltrimethylammonium bromide ($CH_3[CH_2]_{15}N[CH_3]_3Br$; CTAB) and an anionic -- sodium dodecyl sulfate ($CH_3[CH_2]_{11}OSO_3Na$; SDS).

We explore macroscopic wetting behaviors by placing drops of these solutions on clean surfaces and observing the results. On both silicon oxide (negatively charged) and sapphire (positively charged) surfaces, water drops spread to a 0° contact angle. In contrast, drops of solutions of the cationic CTAB at concentrations on the order of 0.1 CMC (the critical micellar concentration)[30] exhibit autophobic[31] behavior when placed on silicon oxide. The autophobing is apparent as carefully placed drops increase thier contact angle by 5-10° over the course of about

40

30 seconds. The final angle is about 25°. At the same concentrations on the same substrate, the anionic surfactant SDS spreads to a 0° contact angle. The SDS and CTAB solutions reverse their behavior on sapphire, where the charge of the substrate is opposite that of the silicon oxide, i.e., CTAB solutions exhibit 0°contact angles while SDS solutions exhibit autophobic behavior. Thus, the behavior of a spreading solution is not a property of the surfactant, but rather a property of the head group-surface interaction. When the head-surface interaction is attractive (CTAB on silicon oxide and SDS on sapphire), autophobic behavior with nonzero final contact angles occurs. When the head-surface interaction is repulsive (CTAB on sapphire and SDS on silicon oxide), complete spreading to a final contact angle of 0° occurs.

The existence of surfactant self-assemblies formed during autophobing is explicitly demonstrated by the behavior of a macroscopic meniscus of water approaching an autophobed drop. The edge of a drop of pure water spreading toward an autophobed, stationary drop of CTAB solution on a horizontal, silicon oxide surface stops advancing a fraction of a millimeter or more from the contact line of the CTAB drop. A hydrophobic barrier formed *ahead* of the CTAB drop has stopped the advance of the water contact line. Observations of the condensation of water droplets on the surface ahead of the meniscus of a CTAB solution confirm that the barrier is not wet by water and that it extends a fraction of a millimeter or more ahead of the meniscus. We discuss this barrier further in section VII. In contrast, SDS solutions do not form such barriers on silicon oxide and water drops spread freely into drops of SDS solution.

The charge interaction between the surfactant molecules and the solid surface is also displayed during the slow withdrawal of a silicon oxide surface from baths of surfactant solutions. The positively charged CTAB molecules adsorb to the substrate while it is below the surface of the bulk solution.[32,33] On withdrawal, the substrate emerges from the solution appearing dry to the eye. This indicates the formation of a monolayer of surfactant with exposed hydrophobic tails, akin to the surface formed on autophobing.[34] Breath figures on this CTAB layer indicate the hydrophobicity of the layer and the strong binding of the surfactant. In the case of the SDS molecules, no surfactant adsorbs to the substrate while it is below the surface of the bulk solution due to the repulsion between the negative head group and the negative surface. (Recent neutron reflectivity experiments show this explicitly.[5,6]) Still, deposition of surfactant occurs when the silicon oxide surface is withdrawn slowly from the SDS solution. The fully wetted substrate pulls up a thick film of surfactant solution as it is withdrawn. This film slowly thins by drainage and evaporation. The surfactant monolayer at the liquid-vapor interface of the film is deposited on the solid surface as the film reaches zero thickness in a manner similar to Langmuir-Blodgett deposition. When the SDS coatings are exposed to saturated water vapor, microdroplets do not form; rather, optical fringes appear, indicating that the surfactant is desorbed and water is spreading on the surface.

IV. MOLECULAR STRUCTURE OF DEPOSITED MONOLAYERS AND PRECURSING FILMS

Surfactant monolayers formed by forced withdrawal of a negatively charged silicon oxide substrate from solutions of SDS and CTAB exhibit similar structure despite their opposite charge interaction with the surface. We examined these structures by x-ray and neutron reflectivity.[4-6] A typical reflectivity scan is shown in figure 1. Both monolayers are deposited with their head groups adjacent to the substrate: the CTAB monolayer by charge attraction within the bulk solution, and the SDS monolayer from the liquid-vapor interface of a thinning film. The areas per molecule are 30 to 50Å^2. For both surfactants, the thickness of the tail region is considerably smaller than a fully extended, all-trans bonded hydrocarbon chain and the density of the tail regions is similar to that of the disordered, "liquid-like" tail region of the L$_\alpha$ phase of a lipid. Thus, the monolayers deposited by the forced retreat of contact lines of surfactant solutions

present disordered mixtures of methyl (-CH$_3$) and methylene (-CH$_2$-) groups to the external environment.

By reconnecting these deposited monolayers to the initial bulk solution, we produce a macroscopic meniscus of the solution with its metastable precursing film attached. This film forms the solid-vapor interfacial assembly that controls the macroscopic contact angle of the solution. Although the dry structure of the SDS and CTAB monolayers formed by a retreating contact line are similar, the precursing films of SDS and CTAB solutions are very different. The CTAB precursing film is formed as water of hydration is incorporated into the head group-substrate region of the monolayer (see figure 2). This water increases the thickness of the layer by 2-4Å, places about 5 water molecules per surfactant molecule in the head group region, and does not cause measurable restructuring of the disordered tail group region. This swelling occurs within about half an hour. In contrast, the SDS monolayer is readily desorbed from the substrate as a water core on the order of 100Å thick forms. No surfactant remains on the solid-liquid interface of the film. The evolution of the precursing film continues over days. Despite the disorder in the tail group region and the saturated vapor environment, neither the CTAB nor the SDS molecules allow detectable water into the tail group region. Therefore, the very different macroscopic contact angles of the two solutions is caused by the water incorporation in their precursing films, without compromising the hydrophobicity of the tail region.

Clearly, precursing films of SDS provide a more mobile environment for both water and surfactant molecules than the CTAB precursing films. Thus, we can interpret macroscopic wetting observations of SDS solutions in terms of a near contact line structure which allows easy movement of water and surfactant. In contrast, CTAB
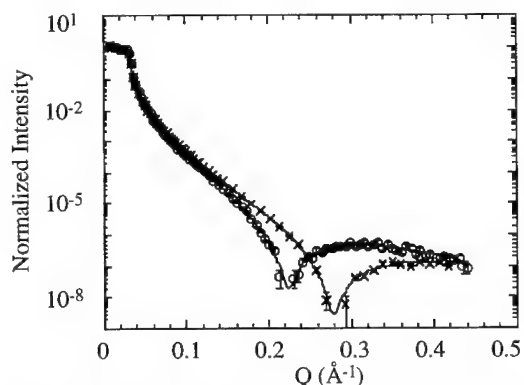
Figure 1: X-ray reflectivity data for a typical CTAB film (x) dry; (o) after connection to a bulk meniscus. Q=magnitude of scattering vector perpendicular to the substrate.
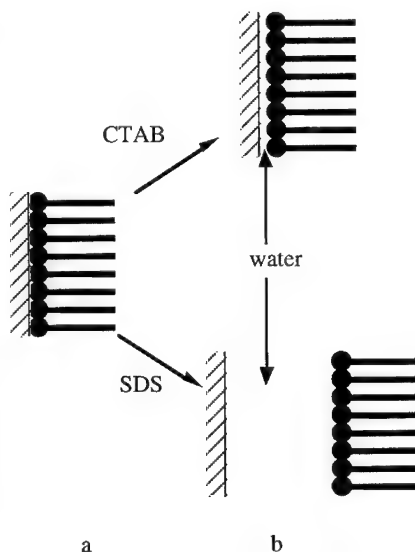
Figure 2: Schematic representation of changes in CTAB and SDS surfactant layers: (a) dry; (b) in precursing films. Note that surfactant tail groups are actually disordered, not all trans as pictured here for convenience.
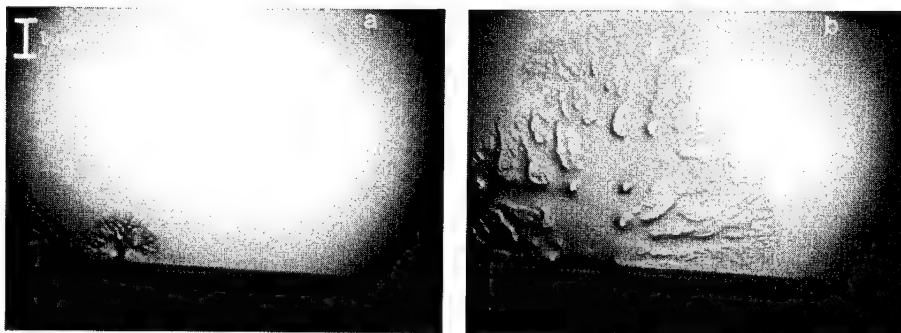
Figure 3: Development of SDS solution spreading pattern on silicon oxide. (b) is about three seconds after (a).

precursing films strongly resist incorporation of mobile water and may also be more resistant to surfactant rearrangement in the region near contact line.

V. ORIGINS OF DENDRITIC SPREADING

Some surfactant solutions spread across high energy surfaces via the rapid formation of dendrites of solution ahead of the advancing contact line.[15-18,24] For a dry, vertical substrate brought into contact with a reservoir of SDS solution, the pattern appears as in figure 3. The character of the pattern depends on the thickness of any pre-existing fluid layers, as well as the composition of the solution. Models of this phenomenon require a surfactant concentration gradient along the liquid-vapor interface near the contact line.[15,17] This gradient drives dendrite formation through Marangoni flow. Previous experimental studies are inconclusive concerning the need for a preexisting fluid layer for dendrite formation. Utilizing reflectance videomicroscopy and a variety of specially prepared substrates, we examined the origins of this spreading behavior. We provide direct evidence that a concentration gradient is needed for dendritic spreading and show that the water mobility seen in the previous section for SDS precursing films is also essential to dendrite formation.

By examining spreading SDS solutions on clean and precoated surfaces, we demonstrate the requirement of a concentration gradient for dendritic spreading. On silicon oxide surfaces precoated with a monolayer of SDS in the manner discussed in section III, solutions spread smoothly to a 0° contact angle. No dendrite formation is observed. The water mobility in the precursing film (which forms from the monolayer when the solution touches it) desorbs the surfactant. Concentration gradients are not established. The absence of a concentration gradient due to the surfactant ahead of the contact line inhibits dendritic spreading. We demonstrate the same suppression of dendrites with the SDS layer left behind after the spontaneous dendritic spreading on a clean substrate. On first contact of the clean substrate, dendritic spreading occurs. The dendrites propagate up the sample and then evaporate and drain down the surface. Ellipsometric measurements show that the receding dendrites leave an incomplete surfactant monolayer behind.[24] If the substrate is immersed further into the solution, dendrites do not form until the contact line reaches a position not previously contacted by the dendrites and coated by surfactant. Again, the readily desorbed SDS deposited ahead of the contact line by previous dendritic spreading moves to suppress any concentration gradients.

Even when a concentration gradient is present, dendritic spreading cannot occur without water ahead of the advancing front to mobilize surfactant. Using ellipsometric measurements, we have determined that the dry monolayer of SDS adsorbed to the solid surface during the retreat of

dendrites does not diffuse across the ambient surface on time scales relevant to spreading processes addressed here (on the order of a few seconds). Thus, though there is a large concentration gradient between regions of adsorbed surfactant and clean surface, no dendritic spreading is observed. We can cause the dendritic spreading to resume into a clean, uncoated area of the substrate by blowing water-saturated air onto the surface at and ahead of the position of previous dendrites, where the surfactant concentration gradient exists. As a microscopic film of water condenses, the dendritic spreading resumes. No dendritic spreading is observed when water condenses from vapor saturated air onto a surface which is clean or is uniformly precoated with an SDS monolayer.

Thus, dendritic spreading requires both a surfactant concentration gradient and water to mobilize the surfactant. However, the water does not have to be present before the surfactant solution attempts to spread. Using time resolved ellipsometry, we observe ultrathin (≈ 150Å thick) fluid films rapidly propagating across a clean surface ahead of the dendrites of an advancing solution.[24] This ultrathin precursing film is driven by the clean, high energy oxide surface and provides the fluid mobility needed for dendritic spreading.

These ultrathin films do not exist ahead of advancing CTAB solutions. The films are blocked by absorbed CTAB molecules on the solid surface ahead of the contact line. The water is unable to move within this barrier just as bulk water is halted by the barrier set up by an autophobed drop of CTAB solution (section III). This restriction of water mobility by barriers formed ahead of the advancing CTAB solution prevents the formation of dendrites which would otherwise occur due to the existing surfactant concentration gradient. We can confirm this inhibition of dendritic spreading by observing that a coating of CTAB stops an advancing SDS dendritic front in the same way that it stops an advancing droplet of water. By coating half a silicon substrate with a CTAB monolayer and allowing SDS to advance across the other half, we observe that the dendrites stop at the sharp line corresponding to the boundary of the CTAB layer. Thus, the CTAB prevents the mobility of solution required for dendritic spreading.

VI. TRANSITIONS FROM DENDRITIC TO STICK-JUMP SPREADING

While some surfactants spread through dendrite formation as described above, others spread by an unsteady, stick-jump motion.[19,20] This type of motion is shown in figure 4. In this form of spreading, the contact line pins to the surface as the solution advances. The liquid-vapor interface deforms. As the solution tries to advance farther, the line depins and jumps forward. As
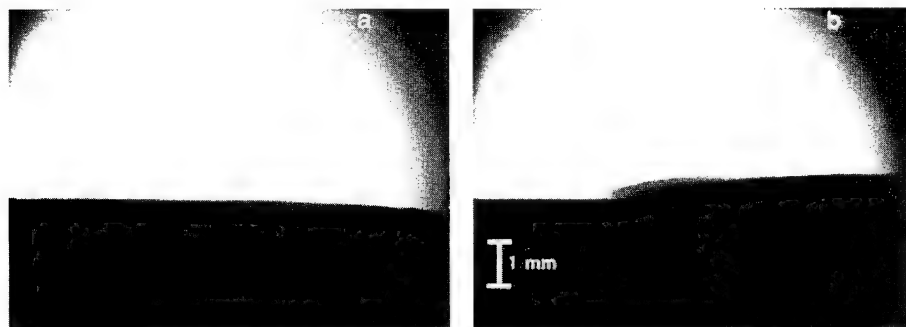
Figure 4: Contact line (a) before and (b) during the stick-jump motion of CTAB solution advancing across a silicon oxide surface. In (b) the raised part of the contact line is moving rapidly right to left across the previously pinned position of the contact line.

we shall demonstrate explicitly in the next section, this motion is caused by adsorption of a surfactant barrier on the solid surface similar to the barrier that prevents the advance of a water drop toward a CTAB solution drop (section III) and that inhibits the propagation of ultrathin fluid films ahead of a CTAB solution (section V). Although dendritic and stick-jump spreading have traditionally been examined as separate phenomena, we show that they are simply extrema in a continuum of behaviors of spreading surfactant solutions.

A strongly adsorbing surfactant such as CTAB on a silicon oxide surface advances by stick-jump spreading, while a non-adsorbing surfactant such as SDS on a silicon oxide surface advances by dendritic spreading. We can tune the adsorption strength, and thus the spreading behavior, by utilizing dipolar, nonionic surfactants instead of ionic surfactants. We used three ethylene oxide surfactants: ethylene glycol monododecyl ether ($CH_3(CH_2)_{11}OCH_2CH_2OH$; E1); triethylene glycol monododecyl ether ($CH_3(CH_2)_{11}(OCH_2CH_2)_3OH$; E3); and hexaethylene glycol monododecyl ether ($CH_3(CH_2)_{11}(OCH_2CH_2)_6OH$; E6) to adjust the interaction between the extremes of strong surface repulsion of SDS and strong attraction of CTAB. The contact angle, which serves as a qualitative measure of the adsorption strength for solutions with similar concentrations relative to their CMC, varies across these five surfactants. For 5μl drops of 0.1 CMC solutions on silicon oxide, the contact angle increases from SDS (0°) through E1 ($<2^o$), E3 (3.7 ± 4.4^o), and E6 (7.3 ± 2.8^o) to CTAB (24.3 ± 3.7^o). Thus the adsorption strength also increases from SDS through the E's to CTAB.

As the adsorption strength changes, the dendritic behavior changes. SDS exhibits dendritic spreading across a silicon oxide surface as shown in figure 3. There is no observable perturbation at the start of the dendritic spreading. During the growth, the branches join to form larger branches and also split to finer dendrites. The spreading ends as the solution evaporates from the surface and drains back down the dendrites due to gravity. In contrast, the spreading of E3 begins with a disturbance similar to the jump in CTAB spreading (figure 5a). The E3 dendrites approach each other but diverge, clearly unable to contact. The
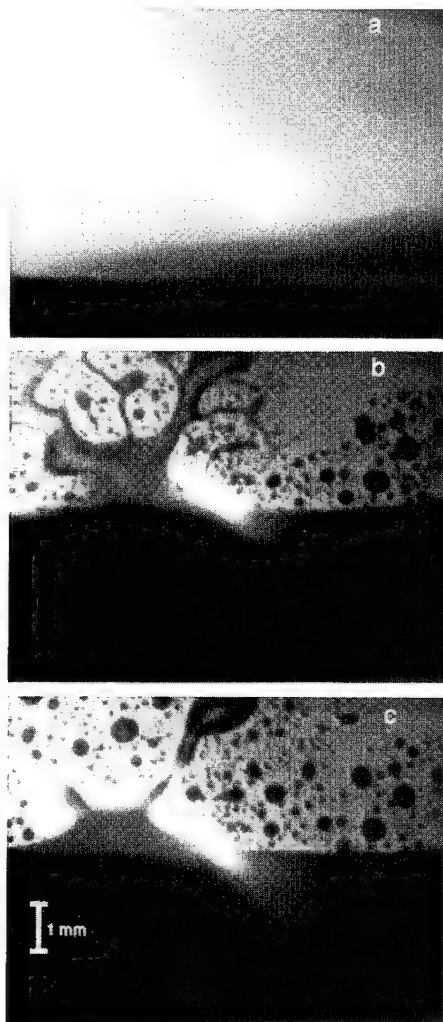
Figure 5: E3 advancing behavior. (a) Wave clearing the interface similar to CTAB behavior. (b) Formation of dendrites 1/10th of a second later, similar to SDS behavior. (c) Autophobing of dendrites into droplets. The bright flare is an artifact of the lighting.

45

spreading ends as the flow of solution is pinched off, with the pinched off portions retracting into droplets (figure 5b,c). Hence, the behavior of E3 exhibits the dendritic characteristics of SDS spreading as well as the autophobic characteristics of CTAB.

The adsorption strength of these nonionic surfactants is insufficient to produce a barrier to propagation at the rapidly advancing tip of a dendrite. However, along the sides of the dendrite where the fluid advances more slowly, adsorption is sufficient to affect the spreading behavior. The barrier strength and corresponding autophobic behavior increases as the adsorption strength increases. The autophobing leads to a pinching off of the branches and the formation of droplets. This effect is more dramatic as the dipole moment of the head group increases from E1 to E6 (figure 6), and the spreading behavior approaches the stick-jump behavior of CTAB.

Thus, dendritic spreading occurs when the surfactant does not strongly adsorb to the surface. As the affinity of the surfactant for the surface increases, the surfactant forms a barrier to fluid propagation. The strength of this barrier controls the mobility of fluid ahead of the advancing solution. In moderate cases, dendrites form but are pinched off. In the extreme case, the contact line cannot move forwardand is pinned, until stresses build up and the contact line advances via stick-jump motion.

Figure 6: (a) E1, (b) E3, and (c) E6 at the end of their spreading events. The contact line in (a) is half a millimeter below the field of view.

VII. STRUCTURE OF SURFACTANT BARRIERS

As we have seen, surfactant barriers on the solid surface near contact lines control the wetting and spreading of surfactant solutions. In particular, barriers drive macroscopic autophobing, stick-jump advance of the contact line, and changes in the dendritic patterns of spreading solutions. Combining long working distance videomicroscopy and breath figure condensation, we have discovered a complex barrier structure near the contact line for a surfactant solution with an attractive interaction with a silicon oxide surface. We partially immersed a silicon substrate into a CTAB solution, let the contact line advance via a jump motion, and allowed the system to evolve. During this evolution, the contact line retreats across the

surface. After waiting for periods ranging from 5 seconds to an hour after the jump, we probed the evolution of the barrier structure with breath figures.

The breath figures revealed several regions of differing hydrophobicity near the contact line (see figure 7) indicating regions with different mixes of methyl and methylene groups. One wettability exists between the bulk solution contact line at the time of the breath figure and the initial position of the contact line (region a in figure 7). The bulk fluid has autophobed and retreated across this region. Ellipsometric measurements of this region reveal a surfactant layer about 10-15Å thick, similar to the surfactant layer formed on forced withdrawal the substrate from a solution (section III). Thus, the deposition of surfactant from both a spontaneous and a forced retreat of the contact line produces a monolayer with head groups adjacent to the substrate and tail groups packed and away from the surface. The temporal evolution of the extent of this region is very dependent upon the concentration of the solution. Similarly, we have found that monolayers formed on forced withdrawal from bulk solution of differing concentrations show different draining behaviors.

Far from the bulk liquid (region c in figure 7), the condensing vapor spreads on the surface to form a thin film. This film indicates that no surfactant has been deposited on the surface far from the bulk.

Between these two regions, starting from the initial location of the contact line and extending to the region where no surfactant can be detected, a third region of wettability develops with time (region b in figure 7). The growth of the extent of this region follows a power law with an exponent near 1/2 (see figure 8). This exponent is consistent with growth by a diffusive process. Ellipsometric measurements of this region reveal a 3Å surfactant layer, corresponding to surfactant molecules with tail groups lying down on the surface.

Thus, the area ahead of an autophobed surfactant solution includes two regions with different surfactant orientation. We observe that the depinning of the contact line and jump of the advancing surfactant solution carries the
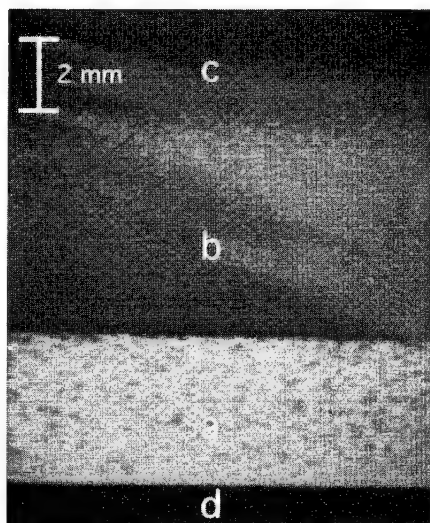
Figure 7: Condensation of microdroplets ahead of a CTAB contact line (a) autophobed region; (b) diffusion region; (c) surfactant free region; (d) bulk. The initial position of the contact line is at the boundary between regions a and b.
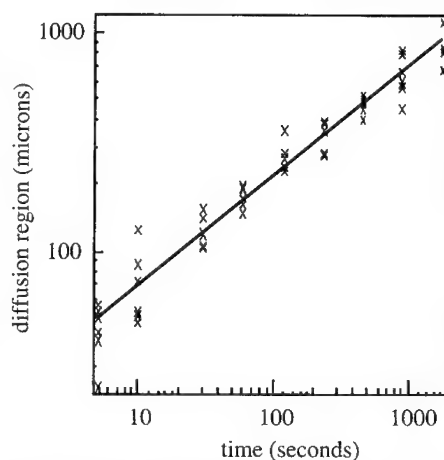
Figure 8: Development of the extent of the diffusion region with time. The line fitting the data has a slope of 1/2.

macroscopic contact line past both these regions to an uncoated area of the substrate. The contact line then pins at the new location and the regions begin to develop again. Exploring the structural and temporal evolution of these two regions will lead to a molecular scale explanation of stick-jump behavior.

VIII. CONCLUSIONS

We have presented an examination of the microscopic structure near the contact line of a surfactant solution and seen how that structure controls wetting by the solution. In the case where the surfactant head group-surface interaction is repulsive, dendritic spreading occurs. Both surfactant concentration gradients along the liquid-vapor interface and mobility of fluid on the surface are required for dendritic spreading. The latter condition is met for these surfactants because, although they deposit from a retreating contact line with head groups toward the surface, they readily desorb from the surface and form a precursing film with facile molecular mobility.

In the case where the surfactant head group-surface interaction is attractive, surfactant strongly absorbs to the surface near the contact line. The surfactant forms barriers with complex structures which evolve over time scales relevant to spreading processes. The portion of the barrier nearest the contact line contains surfactant molecules with head groups next to the surface. This region of the barrier does not allow mobile water from the bulk solution to enter the film. Thus, fluid mobility into the barrier is inhibited; and the contact line pins on the barrier. If the bulk solution tries to force the contact line forward, the liquid-vapor interface deforms causing the contact line to depin from the barrier and jump forward. Thus, theadsorption exhibited by these surfactant solutions leads to stick-jump spreading. The region of the barrier nearest the contact line develops in a complex manner over time. The portion of the barrier farther from the contact line has a different molecular configuration and grows by a diffusive process.

Tuning the strength of the attractive surfactant head group-surface interaction by varying the dipolar strength of the surfactant produces a spectrum of spreading behaviors from dendritic to stick-jump. Barriers of surfactant once again form near the contact line of the advancing solution. However, the ability of these barriers to inhibit fluid mobility varies with the head group dipole. This leads to dendritic spreading with altered dendritic patterns in the case of weaker interactions and to complete stick-jump motion in the case of the strongest dipolar interaction.

REFERENCES

[1]L. Leger and J.F. Joanny, Rep. Prog. Phys. **55**, 431 (1992).
[2]A.W. Neumann, in Wetting, Spreading, and Adhesion, edited by J.F. Padday, (Academic Press, New York, 1978), p. 3-35.
[3]R.E. Johnson Jr. and R.H. Dettre in Wettability, edited by J.C. Berg, (Marcel Dekker, Inc.: New York, 1993), Chapter 1.

[4]W.R. Birch, M.A. Knewtson, S. Garoff, R.M. Suter, and S. Satija, Coll. and Surf. **89**, 145 (1994).

[5]W.R. Birch, M.A. Knewtson, S. Garoff, R.M. Suter, and S. Satija, "Structure of Precursing Thin Films of an Anionic Surfactant on a Silicon Oxide/Silicon Surface," Langmuir, in press.

[6]W.R. Birch, PhD thesis, Carnegie Mellon University, 1993.

[7]T.D. Blake, in Wettability, edited by J.C. Berg, (Marcel Dekker, Inc.: New York, 1993), Chapter 5.

[8]T.D. Blake, In Surfactants, edited by Th.F. Tadros, (Academic Press, Inc.: New York, 1984), pp. 231-275.

[9]A. Bose, in Wettability, edited by J.C. Berg, (Marcel Dekker, Inc.: New York, 1993), Chapter 3.

[10]J.D. Swalen, et. al., Langmuir, **3**, 932 (1987).

[11]A. Ulman, S.D. Evans, Y. Shnidman, Y. Sharma, J.E. Eilers, and J.C. Chang, J. Am. Chem. Soc. **113**, 1499 (1991).

[12]G.L. Gaines, Insoluble Monolayers at Liquid-Gas Interfaces, (Interscience Publishers, New York, 1966).

[13]S. Garoff , Thin Solid Films, **152,** 49 (1987).

[14]A. Ulman, Ultrathin Organic Films, (Academic Press, New York 1991).

[15]S.M. Troian, X.L. Wu, S.A. and Safran, Phys. Rev. Lett. **62**, 1496 (1989).

[16]S.M. Troian, E. Herbolzheimer, S.A. and Safran, Phys. Rev. Lett. **65**, 333 (1990).

[17]G. Elender and E. Sackmann, J. Phys. II France, **4**, 455 (1994).

[18]A. Marmur and M.D. Lelah, Chem. Eng. Commun. **13**, 133 (1981).

[19]M.A. Cohen Stuart and A.M. Cazabat, Prog. Coll. Poly. Sci. **74**, 64 (1987).

[20]H.M. Princen, A.M. Cazabat, M.A. Cohen Stuart, F. Heslot, and S. Nicolet, J. Coll. Interf. Sci. **126**, 84 (1988).

[21]G.J. Hirasaki, in Interfacial Phenomena in Oil Recovery, edited by N.R. Morrow, (Marcel Dekker Inc., New York, 1990).

[22]S. Garoff, E.B. Sirota, S.K. Sinha and H.B. Stanley, J. Chem. Phys. **90,** 7505 (1989).

[23]F. Heslot, A.M. Caxabat, and P. Levinson, Phys. Rev. Lett. **62**, 1286 (1989).

[24]B. Frank and S. Garoff, "Origins of the Complex Motion of Advancing Surfactant Solutions," Langmuir, in press.

[25]G.D. Nadkarni and S. Garoff, Langmuir, **10**, 1618 (1994).

[26]D. Beysens and C.M. Knobler, Phys. Rev. Lett. **57**, 1433 (1986).

[27]D. Fritter, C.M. Knobler, D. Roux and D. Beysens, J. Stat. Phys. **52**, 1447 (1988).

[28]W.M. Mullins and B.L. Averbach, Surf. Sci. **206**, 41 (1988).

[29]J.R. Vig, J. Vac. Sci. Technol. A. **3**, 1027 (1985).

[30]The CMC is the concentration at which micelles form in a bulk surfactant solution. CMC's for the surfactants discussed in this work (from ref. 24) are: $CTAB \sim 10^{-3}M$; $SDS \sim 8 \times 10^{-3}M$; $C_{12}E_6 \sim 9 \times 10^{-5}M$; $C_{12}E_3 \sim 5.5 \times 10^{-5}M$; $C_{12}E_1 \sim 9 \times 10^{-5}M$.

[31]W.A. Zisman, Advances in Chemistry, **43**, 1 (1964).

[32]A.R. Rennie, E.M. Lee, E.A Simister, and R.K. Thomas, Langmuir, **6** 1031 (1990).

[33]B.H. Bijsterbosch, J. Coll. Interf. Sci. **47**, 186 (1974).

[34]The behavior described is for low concentration solutions and produces films about 10Å in thickness. At higher concentrations, a fluid film is pulled with the substrate as it is removed from solution. This film drains slowly, leaving behind a slightly thicker layer (~16Å) than that left by the rapidly autophobing withdrawal.

CRITICAL DYNAMICS OF CONTACT LINE DEPINNING

DENİZ ERTAŞ AND MEHRAN KARDAR
Department of Physics, Massachusetts Institute of Technology, Cambridge, Massachusetts 02139

ABSTRACT

The depinning of a contact line is studied as a dynamical critical phenomenon by a functional renormalization group technique. In $D = 2 - \epsilon$ "line" dimensions, the roughness exponent is $\zeta = \epsilon/3$ to all orders in perturbation theory. Thus, $\zeta = 1/3$ for the contact line, equal to the Imry-Ma estimate for equilibrium roughness. The dynamical exponent is $z = 1 - 2\epsilon/9 + O(\epsilon^2) < 1$, resulting in unusual dynamical properties. In particular, a characteristic distortion length of the contact line depinning from a strong defect is predicted to initially increase faster than linearly in time. Some experiments are suggested to probe such dynamics.

Wetting phenomena and contact lines (CLs) appear in many manufacturing processes that involve the spreading of a liquid on a solid surface [1]. Some degree of control over the spreading of the liquid and the corresponding creep of the CL is needed to optimize the desired characteristics of such processes. In particular, it is important to know the effect of surface roughness and contaminants at microscopic to mesoscopic scales on CL dynamics. Here, we study such effects at length scales from 10^{-1} down to 10^{-7} centimeters. The upper length scale is set by the droplet size or the capillary length (due to gravitation), while the lower length scale is determined by the characteristic size of the microscopic defects.

Surface impurities lead to *CL hysteresis*, i.e. a finite force is needed to start the fluid spreading. Recently, the scaling exponents of a driven elastic interface subject to quenched impurities near a similar depinning treshold have been calculated through a functional renormalization-group (RG) treatment close to four interface dimensions [2,3]. A similar treatment can be used to calculate various scaling exponents for the slowly advancing contact line [4,5]. The distinction between the two cases is that the CL is the termination of the liquid-vapor interface. We shall assume that the partially wetting fluid spreads sufficiently slowly on a heterogenous surface that the liquid-vapor interface evolves adiabatically, i.e., the it responds to changes in the CL shape instantenously. In this case, fluctuations of the CL around its time-averaged value reflect the competition between impurities on the solid surface and the liquid-vapor surface tension.

Consider a wetting front on a heterogenous surface in the x-y plane with the average orientation of the contact line in the x direction as shown in Fig. 1. In equilibrium on a *homogenous* interface, the macroscopic contact angle Θ is determined by the Young condition,

$$\gamma_{SV} - \gamma_{SL} - \gamma \cos \Theta = 0. \tag{1}$$

In the above, γ_{SV}, γ_{SL}, and γ are the interfacial tensions for the solid-vapor, solid-liquid, and liquid-vapor interfaces, respectively. The heterogeneities (i. e. defects) on the surface can be modeled as fluctuations in the difference of local interfacial energy densities,

Side View **Top View**
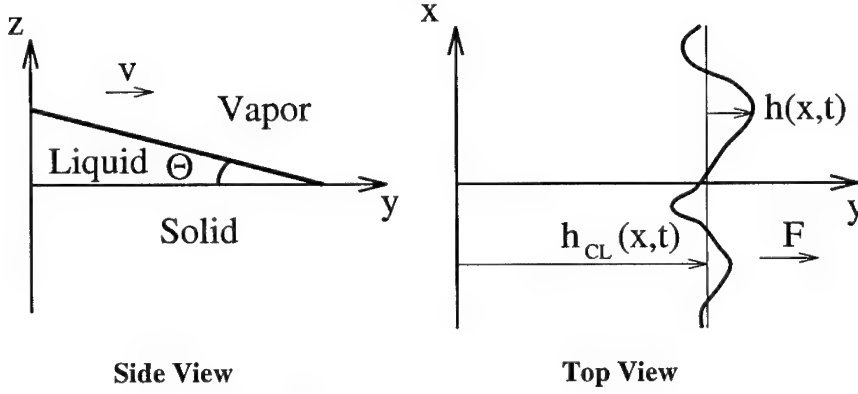
FIG. 1. Geometry of the system.

$$f(x,y) = \gamma_{SV}(x,y) - \gamma_{SL}(x,y) - \langle \gamma_{SV} - \gamma_{SL} \rangle. \tag{2}$$

The average of f is zero, while its correlations satisfy,

$$\langle f(x,y)f(x',y') \rangle = \Delta(r/a), \tag{3}$$

where $r^2 = (x-x')^2 + (y-y')^2$, a is the characteristic size of defects, and Δ is a function that decays rapidly for large values of its argument. (If the source of disorder is the roughness of the solid surface, $f(x,y)$ is proportional to the local slope [1], thus we restrict our discussion to surfaces without long-range slope correlations. For a self-affinely rough surface, Δ may have a slow algebraic decay. Such situations will not be explored here.) Fluctuations of the CL from its average position, $h_{CL}(t) = vt$, are denoted by $h(x,t)$, and thus satisfy

$$\overline{\langle h(x,t) \rangle} = 0. \tag{4}$$

(The overline denotes a *time* average.) The capillary energy associated with small deformations of a CL was calculated by Joanny and de Gennes [6] (in the $\Theta \to 0$ limit) as

$$U_{\text{cap}} = \frac{\gamma\Theta^2}{2} \int_{\frac{2\pi}{L} < |q| < \frac{2\pi}{a}} \frac{dq}{2\pi} |q||h(q)|^2 = \frac{\gamma\Theta^2}{4\pi} \int_{a<|x-x'|<L} dx dx' \frac{[h(x) - h(x')]^2}{(x-x')^2}, \tag{5}$$

where $h(q)$ is the fourier transform of the contact line profile at a given time, and a and L are the lower and upper cutoff length scales mentioned earlier. The unusual q-dependence of the energy functional, and the resulting nonlocal dynamics, reflects the fact that perturbations of wavevector q on the CL induce deformations into the liquid-vapor interface up to a distance $|q|^{-1}$. A random contribution to the liquid-surface energy comes from the defects [1],

$$U_{\text{rand}} = \int_{-\infty}^{+\infty} dx \int_{-\infty}^{h_{CL}+h(x)} dy \ f(x,y). \tag{6}$$

If the heterogeneity is strong enough, there is contact angle hysteresis [1,6]. This arises from local minima of the free energy as a function of the CL profile, since the surface tensions γ_{SL}, γ_{SV} in Eq.(1) must be interpreted as spatial averages *over the CL position*. If

a macroscopic force of F per unit length is exerted on the CL, it will move with a finite velocity v only for $F > F_c$. This occurs when the metastable state with the largest Θ, usually referred to as the advancing angle Θ_a [1,6], becomes unstable. The dynamical contact angle Θ can be expressed in terms of F through the force balance equation,

$$F - F_c = \gamma(\cos\Theta_a - \cos\Theta). \tag{7}$$

As the CL slowly advances, energy is dissipated through various mechanisms [1]. If the dissipation in the vicinity of the CL dominates for small v, the drag force at a point x on the CL is simply related to the local velocity $v + \partial_t h(x,t)$ through a microscopic mobility μ. In this case, the equation of motion for the CL is obtained by equating the drag force to the applied force, $-\delta U/\delta h(x)$, as

$$\mu^{-1}\left(v + \frac{\partial h(x,t)}{\partial t}\right) = -\frac{\gamma\Theta^2}{\pi}\int\limits_{a<|x-x'|<L} dx'\frac{h(x,t) - h(x',t)}{(x-x')^2} + f[x, vt + h(x,t)] + F. \tag{8}$$

In the above, v is determined self-consistenly by enforcing Eq.(4). Equation (8) is only valid for $v > 0$, and $F \to F_c$ from above when $v \to 0$. Recent experiments on the dynamics of CLs on clean surfaces [7,8] show agreement with the clean limit ($f = 0$) of Eq.(8).

By analogy to similar previously studied systems [2,3,9], for F slightly above F_c, we expect the average velocity of the contact line to scale as

$$v = A(F - F_c)^\beta, \tag{9}$$

where β is the *velocity exponent*, and A is a nonuniversal constant. Superposed on the steady advance of the CL are rapid "jumps" as portions of the line depin from strong pinning centers. Such jumps are similar to *avalanches* in other slowly forced systems, and have a power-law distribution in size, cut-off at a characteristic correlation length ξ. On approaching the threshold, ξ diverges as

$$\xi \sim (F - F_c)^{-\nu}, \tag{10}$$

defining a *correlation length exponent* ν. At length scales smaller than ξ, the interface is self-affine, i.e. with correlations satisfying the dynamic scaling form

$$\langle[h(x,t) - h(x',t')]^2\rangle = (x - x')^{2\zeta}g\left(\frac{t-t'}{(x-x')^z}\right), \tag{11}$$

where ζ and z are the *roughness* and *dynamic* exponents, respectively. The scaling function g goes to a constant as its argument approaches 0, ζ is the wandering exponent of an instantenous CL profile, and z relates the average lifetime of an avalanche to its size by $\tau(\xi) \sim \xi^z$.

The critical exponents defined above are not independent, they are related through exponent identities [3]:

$$\beta = (z - \zeta)\nu, \tag{12}$$
$$\nu = 1/(1 - \zeta). \tag{13}$$

The former result comes from the scaling of nonlinear response functions, requiring the fluctuations h of the CL to scale like its average position $h_{CL} = vt$. The latter results from

an exact statistical symmetry of the system that fixes the form of the static ($\omega = 0$) response function $\langle \partial h(x')/\partial f(x)\rangle$. These relations determine all exponents in terms of ζ and z.

In many aspects, Eq.(8) is similar to the model analyzed by Narayan and Fisher using the formalism of Martin, Siggia, and Rose [10] (MSR), through an expansion around a mean field solution [3]. To use this method, it is necessary to generalize to a D-dimensional "line" for a systematic computation of the exponents through an ϵ expansion. Introducing an auxiliary field $\hat{h}(x,t)$, the MSR generating functional is,

$$Z = \int [dh][d\hat{h}] \exp\left\{ i \int d^D\mathbf{x}\, dt\, \hat{h}(\mathbf{x},t)\, [\text{LHS} - \text{RHS}] \right\}, \tag{14}$$

where LHS and RHS refer to the left-hand side and right-hand side of Eq.(8), generalized to $\mathbf{x} \in \Re^D$, respectively. Mean field (MF) theory is obtained by replacing the capillary forces on a portion of the CL with Hookean springs:

$$\mu^{-1}\left(\dot{h}_{MF} + v\right) = -k h_{MF}(t) + f[vt + h_{MF}(t)] + F, \tag{15}$$

independently for each $\mathbf{x}$, and identical to the mean field model analyzed by NF [3,9]. Here again, $v(F)$ is determined by the self-consistency condition $\overline{\langle h_{MF}\rangle} = 0$.

The MF solution depends on the type of irregularity: For smoothly varying $f(x,y)$, $\beta_{MF} = 3/2$, whereas for "mesa" defects, i.e. cusped $f(x,y)$, $\beta_{MF} = 1$ [9,11]. Some recent experiments on reasonably clean surfaces by Ström et al. [12] are in agreement with Eq.(9) for $\beta = 3/2$ in the low capillary number regime. Stokes et al. [13] measure an exponent $\beta \approx 2 - 2.5$ on a hysteretic surface, using a new technique of harmonic generation. Even though it is generally believed that the scaling relation in Eq.(9) holds [14], it is clear that the prefactor is nonuniversal, and various experiments to date have obtained widely varying v-F behaviors [15]. To our knowledge, there are no experiments so far that have systematically investigated strongly heterogenous surfaces with conclusive accuracy.

Following the treatment of NF [3,9], we use the mean field solution for cusped potentials, anticipating jumps with velocity of $O(1)$, in which case $\beta_{MF} = 1$. After rescaling and averaging over impurity configurations, we arrive at a generating functional whose low-frequency form is

$$\overline{Z} = \int [dH][d\hat{H}] \exp(-S),$$

$$S = \int d^D\mathbf{x}\, dt\, (F - F_c)\hat{H}(\mathbf{x},t) + \int \frac{d\omega}{2\pi} \frac{d^D\mathbf{q}}{(2\pi)^D} \hat{H}(-\mathbf{q},-\omega)(-i\omega\eta + |\mathbf{q}|)H(\mathbf{q},\omega)$$

$$- \frac{1}{2} \int d^D\mathbf{x}\, dt\, dt'\, \hat{H}(\mathbf{x},t)\hat{H}(\mathbf{x},t') C\left[vt - vt' + H(\mathbf{x},t) - H(\mathbf{x},t')\right]. \tag{16}$$

In the above expressions, H and $\hat{H}$ are coarse-grained forms of h and $i\hat{h}$, η is a friction coefficient, and F is adjusted to satisfy the condition $\langle H\rangle = 0$. The function $C(v\tau)$ is initially the mean-field temporal correlation function $\langle h_{MF}(t)h_{MF}(t+\tau)\rangle$.

Ignoring the H-dependent terms in the argument of C results in a quadratic action S_0, which is invariant under the scale transformation $x \to bx$, $t \to bt$, $H \to b^{-(D-2)/2}H$, $\hat{H} \to b^{-(D+2)/2}\hat{H}$, $F \to b^{-D/2}F$, $v \to b^{-D/2}v$; and becomes asymptotically exact at large length and time scales for $D > D_c = 2$. The interface is then smooth at long length scales ($\zeta_0 < 0$), and the critical exponents are given by $z_0 = 1, \nu_0 = 2/D$, and $\beta_0 = 1$.

For $D < D_c$, higher order terms in S become relevant, but their contribution in the $v \to 0$ limit can be expressed as a Taylor series of the correlation function

$C[vt - vt' + H(\mathbf{x}, t) - H(\mathbf{x}, t')]$. The RG is carried out by integrating over a momentum shell and all frequencies, followed by a scale transformation $x \to bx$, $t \to b^z t$, $H \to b^\zeta H$, and $\hat{H} \to b^{\theta - D} \hat{H}$, where $b = e^l$. The renormalization of the term proportional to $F - F_c$ gives

$$\nu = 1/(z + \theta), \tag{17}$$

which holds to all orders in ϵ. The renormalization of C in $D = 2 - \epsilon$ dimensions, computed to one-loop order, gives the recursion relation

$$\frac{\partial C(u)}{\partial l} = [\epsilon + 2\theta + 2(z-1)]C(u) + \zeta u \frac{dC(u)}{du} - \frac{1}{2\pi} \frac{d}{du} \left\{ [C(u) - C(0)] \frac{dC(u)}{du} \right\}. \tag{18}$$

All higher order terms contribute to the renormalization of C as total derivatives with respect to u, thus, integrating Eq.(18) at the fixed-point solution $\partial C^*/\partial l = 0$, together with Eqs.(17) and (13), gives $\zeta = \epsilon/3$ to all orders in ϵ, provided that $\int C^* \neq 0$. For the case of a CL ($D = 1$), we thus obtain

$$\zeta = 1/3, \quad \text{and} \quad \nu = 3/2. \tag{19}$$

This value of the roughness exponent coincides with the Imry-Ma estimate for the *equilibrium* roughness with random-field disorder. This estimate gives the correct result since $C(u)$ remains short-ranged upon renormalization. Note that the disorder- averaged action S involves temporal correlations C, instead of spatial correlations Δ. Therefore, the scaling of fluctuations, and critical exponents, are independent of the type of disorder [16] (random-field or random-bond), as long as $\Delta(r)$ is short-ranged in space; in contrast with the situation in equilibrium.

Similarly, the renormalization of η fixes the dynamical exponent z, to leading order in ϵ:

$$z = 1 - 2\epsilon/9 + O(\epsilon^2). \tag{20}$$

The velocity exponent β can then be computed using Eq.(12). For the CL, the result is

$$z \approx 7/9, \quad \beta \approx 2/3. \tag{21}$$

Nattermann *et al.* [2] obtain the same results as NF for the elastic interface to $O(\epsilon)$ by a slightly different treatment.

The above scaling exponents describe a CL advancing at low capillary number on a dirty or microscopically rough surface, with uncorrelated disorder. The roughness exponent of $\zeta = 1/3$, equal to its equilibrium value, can be directly measured by microscopic imaging of a slowly advancing CL. A number of macroscopic experimental tests are also possible: the velocity of the CL is given by by $v \sim (F - F_c)^\beta$ with $\beta < 1$ (See Fig. 2a). Also, the root mean square width of the CL profile will increase like $W \sim \xi^\zeta \sim v^{-\zeta\nu/\beta} \sim v^{-3/4}$ as the threshold is approached, up to a cutoff width $l_c = \sqrt{\gamma/\rho g}$ dictated by gravity (See Fig. 2b).

A dynamical exponent of $z < 1$ suggests that the relaxation of the CL is very different on a dirty surface. Upon depinning from a strong defect, the width of the CL profile initially *accelerates*, growing with a characteristic velocity $c(t) \sim t^{(1-z)/z}$. This is, of course, not physical at arbitrarily large length and time scales, and violates the assumption that the CL velocity is low enough to allow for the liquid-vapor interface to remain in equilibrium with the instantaneous CL profile. This description will break down when characteristic velocities

become comparable to the capillary wave velocity $c_{cap} = \sqrt{\gamma/\rho}$. However, the scaling regime in between should still be accessible to experiments in which the depinning from a single strong defect is observed on a dirty or rough surface.
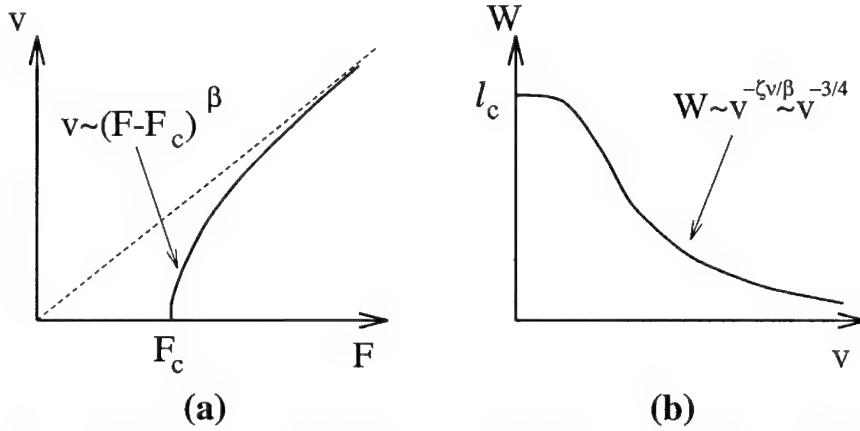
FIG. 2. (a) Predicted velocity-force behavior for a depinning contact line; $\beta \approx 2/3$. (b) Predicted width W of the CL profile as a function of velocity.

[1] P.G. de Gennes, Rev. Mod. Phys. **57**, 827 (1985).

[2] T. Nattermann, S. Stepanow, L.-H. Tang, and H. Leschhorn, J. Phys. II France **2**, 1483 (1992).

[3] O. Narayan and D. S. Fisher, Phys. Rev. B **48**, 7030 (1993).

[4] D. Ertaş and M. Kardar, Phys. Rev. E **49**, R2532 (1994).

[5] M. Kardar and D. Ertaş, to be published in Patterns and Scaling in the Growth Of Thin Films (Proceedings of the NATO ASI, Cambridge, UK, 1994).

[6] J.F. Joanny and P.G. de Gennes, J. Chem. Phys. **81**, 552 (1984).

[7] T.. Ondarçuhu and M. Veyssié, Nature **352**, 418 (1991).

[8] J.A. Marsh and A.M. Cazabat, Phys. Rev. Lett. **71**, 2433 (1993).

[9] D.S. Fisher, Phys. Rev. B **31**, 1396 (1985), O. Narayan and D.S. Fisher, Phys. Rev. B **46**, 11520 (1992).

[10] P.C. Martin, E. Siggia, and H. Rose, Phys. Rev. A **8**, 423 (1973).

[11] J.F. Joanny and M.O. Robbins, J. Chem. Phys. **92**, 3206 (1990).

[12] G. Ström, M. Fredriksson, P. Stenius, and B. Radoev, J. Colloid Interface Sci. **134**, 107 (1990).

[13] J.P. Stokes, M.J. Higgins, A.P. Kushnick, S. Bhattacharya, and M.O. Robbins, Phys. Rev. Lett. **65**, 1885 (1990).

[14] J.E. Seebergh and J.C. Berg, Chem. Eng. Sci. **47**, 4455 (1992). In their notation, $\beta = 1/B$.

[15] R.A. Hayes and J. Ralston, L. Colloid Interface Sci. **159**, 429 (1993).

[16] See Section III of Ref. [3] for a detailed discussion on random field vs. random bond disorder.

DYNAMICS OF PHASE SEPARATION OF BINARY FLUID MIXTURES IN THE PRESENCE OF SURFACTANTS

MOHAMED LARADJI*, OLE G. MOURITSEN**, SØREN TOXVAERD***,
AND MARTIN J. ZUCKERMANN****
*Center for Simulational Physics, The University of Georgia, Athen, GA 30602-2451
**Department of Physical Chemistry, The Technical University of Denmark, DK-2800 Lyngby, Denmark
***Department of Chemistry, H.C. Ørsted Institute, University of Copenhagen, DK-2100 Copenhagen, Denmark
****Center for the Physics of Materials and Department of Physics, McGill University, 3600 rue University, Montréal, Québec, Canada H3A 2T8

ABSTRACT

The dynamics of phase separation of binary fluid mixtures in the presence of surfactants is studied via molecular dynamics simulations. In contrast to phase separation in pure binary fluid mixtures, which is characterized by an algebraic time dependence of the average domain size, mixtures containing surfactants exhibit nonalgebraic slow dynamics. At very late times, the average domain size saturates at a value inversely proportional to the surfactant concentration. Despite the fact that these systems only microphase separate, a dynamical scaling was observed at late times.

INTRODUCTION

Recently, there has been an increasing interest in the dynamics of binary fluid mixtures containing surfactants, such as water/oil/amphiphiles systems or a binary homopolymer mixture containing a small amount of diblock copolymers [1, 2]. This interest results from the fact that surfactants preferentially adsorb at the interfaces, where they lower the interfacial tension, and that the growth dynamics is driven by the interfacial tension between the growing domains. In pure binary systems, where the surface tension can be thought to be a constant in time, it has been shown that the average linear size of the ordering domains evolves in time as a power-law, i.e., $R(t) \sim t^n$, where n is the growth exponent [3, 4]. When surfactants are present, the surface tension decreases with time, due to the increase in the interfacial surfactant concentration. As a result, a slowing down in the dynamics is expected. This slowing down has been recently observed in the experiment of Hashimoto and Izumitani [5]. In the present paper, we show results for the effect of surfactants on the dynamics of phase separation of a binary fluid in two dimensions by means of a molecular dynamics simulation.

We have previously proposed a time-dependent Ginzburg-Landau model for studying this dynamics and found that surfactants alter drastically the growth process to a non-power-law growth [6, 7]. These results were verified by a modified Lifshitz-Slyozov theory [8]. Kawakatsu *et al.* have also studied this dynamics using a hybrid model, in which surfactants are treated microscopically whereas water and oil are treated in a coarse-grained manner, and found an alteration of the growth dynamics [9]. Other calculations based on Monte Carlo simulations of spin models have also detected similar phenomena [10, 11]. We should note that all these studies were completely dissipative, and therefore not appropriate for fluid solutions due to the presence of hydrodynamic interactions in fluids. In fact, it has been proven that hydrodynamic interactions play an important role during the late times of phase separation in binary fluids [12, 13, 14, 15]. The molecular dynamics method used in the present paper, which takes into account hydrodynamic interactions in a natural manner, is therefore a step ahead in studying more correctly the dynamics of phase separation of binary fluids containing surfactants [16].

MODEL AND METHOD

Let us consider a system composed of N_w molecules of water, N_o molecules of oil and N_s molecules of surfactants. For simplicity, water and oil are assumed to be monoatomic molecules interacting via a special version of the Lennard–Jones potential, which was introduced earlier [15, 16, 17],

$$U(\mathbf{r}_{ij}) = 4\epsilon\left[\left(\frac{\sigma}{r_{ij}}\right)^{12} - (2\delta_{\alpha_i\alpha_j} - 1)\left(\frac{\sigma}{r_{ij}}\right)^6\right], \tag{1}$$

where $\mathbf{r}_{ij} = \mathbf{r}_i - \mathbf{r}_j$ is the distance between two interacting molecules i and j. $\delta_{\alpha_i\alpha_j}$ is the Kroneker function and α_i denotes the type of molecule i, i.e.,

$$\alpha_i = \left\{ \begin{array}{ll} 1 & \text{for a water molecule} \\ 2 & \text{for an oil molecule.} \end{array} \right. \tag{2}$$

The choice of the potential, Eq. (1), ensures that molecules of different species interact repulsively for any separation r. A surfactant molecule is assumed to be a diatomic molecule composed of a water particle connected to an oil particle by a harmonic spring. The intramolecular surfactant potential is therefore written as follows

$$U_{ss}(\mathbf{r}_{ij}) = \frac{K_s}{2}(r_{ij} - l_s)^2. \tag{3}$$

We have chosen for the harmonic potential parameters $K_s = \epsilon/\sigma^2$ and $l_s = 1.5\sigma$. The total number of particles in the system is $N = N_w + N_o + 2N_s$. In the absence of surfactants, the model exhibits both solid and fluid phases within the coexistence region. However, in this paper we shall only consider quenches into the fluid coexistence region.

The simulations are performed on two–dimensional boxes with a square geometry of linear size $L = 114\sigma$ containing $N = 10450$ particles and subject to periodic boundary conditions. We moreover consider cases of symmetric mixtures (critical quenches) where the total numbers of water and oil molecules are equal $N_w = N_o$. Five different surfactant concentrations were considered, $\rho_s = 2N_S\sigma^2/L^2 = 7.69\%$, 12.06%, 18.08%, 24.12% and 28.69% which we refer to as systems A, B, C, D and E respectively. For more details of the simulation, see Ref. [16].

Initially, the system is prepared well inside the disordered one–phase region at a very low average density ($\rho = 0.01$) and then instantaneously quenched by rescaling all spatial distances in the system so that the final density is $\rho = 0.8$. Immediately after the quench, the temperature is kept constant at $T = \epsilon/k_B$. For our simulation, we have adopted the Nosé–Hoover method [18, 19, 20, 21] with the "leap-frog" integration technique. This algorithm is time symmetrical and thus ensures time reversibility in the microscopic dynamics [21]. The integration time step is taken to be $\Delta t = 0.005\tau$ where the time scale $\tau = (m\sigma^2/\epsilon)^{1/2}$. We emphasize that Δt is much smaller than the collision time. We have made test runs with smaller values of the time step and found that the chosen value is sufficiently small.

The domain growth during the phase–separation process is monitored by calculating the real–space correlation function defined as

$$g(\mathbf{r}, t) = \langle\psi(\mathbf{r}, t)\psi(0, t)\rangle, \tag{4}$$

where $\psi(\mathbf{r}, t) = [\rho_w(\mathbf{r}, t) - \rho_o(\mathbf{r}, t)]/\rho$ is the local order parameter. $\rho_w(\mathbf{r}, t)$ and $\rho_o(\mathbf{r}, t)$ are the local concentrations of water and oil respectively (including the water and the oil parts of surfactant molecules). We have also calculated the structure factor which is defined as the Fourier transform of the correlation function. Assuming that the system is spatially isotropic at all times, the real and Fourier space correlation functions are furthermore circularly

averaged. The average domain size, $R(t)$, is then calculated from the first moment of the structure factor,

$$R(t) = 2\pi \frac{\sum_{q=0}^{q=q_c} S(q,t)}{\sum_{q=0}^{q=q_c} qS(q,t)}, \tag{5}$$

where q_c is a large–wave–number cutoff taken to be $2/\sigma$. This choice assures that we avoid the time–independent broad peak due to the short–range liquid ordering.

All measured quantities are averaged over 10 independent quenches with different initial conditions, and each quench is performed over a time period of $t = 2000\tau$.

System B   System E
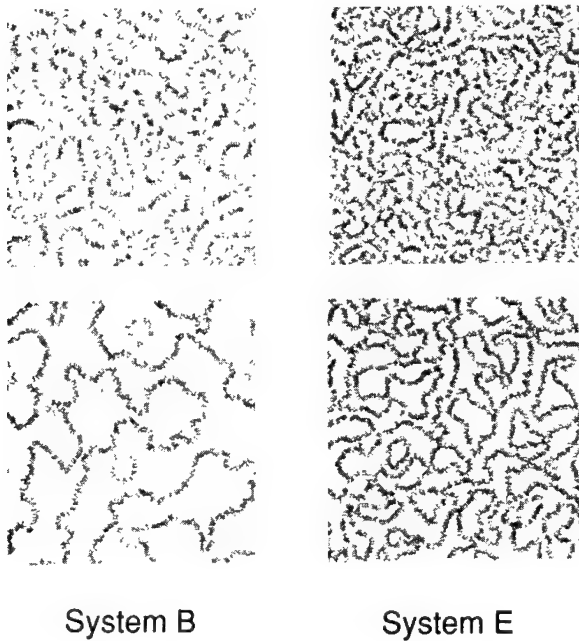
FIG. 1. Snapshots of the domain structure formed during the phase separation process. For each system, the top snaphot correspond to time $t = 100\tau$ and the bottom one to $t = 2000\tau$. Surfactants are shown by the dark dots, and water particles are shown by the grey dots.

DOMAIN GROWTH

Figure 1 shows the spatial configurations of systems B and E at an early time and a late time. We first notice that a phase separation process is taking place. Due to their structure, surfactants rapidly adsorb at the newly formed interfaces. Notice also, that because system E has a larger concentration of surfactants than system B, the interfacial density of surfactants in the earlier system is larger than that in the later one. We also notice that the domain size in system B is on the average larger than that in system E. This difference becomes even more apparent at later times. This qualitative observation already shows that surfactants slow down the domain growth. We have done a simulation of a pure binary fluid under the same conditions, and found that it completely phase separates within the same period of time.

The non–equilibrium structures are interconnected and therefore similar to bicontinuous microemulsions [2]. Since the domain growth has practically stopped after 2000τ, especially in systems C, D and E, the final phase to which the systems will equilibrate presumably corresponds to microemulsions [2]. It is important to note that in microemulsions, the average domain size also decreases with increasing surfactant concentration [2].
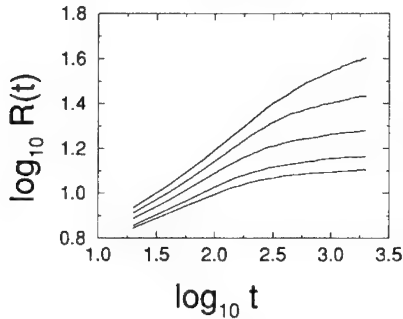
FIG. 2. Time evolution of the average domain size $R(t)$ in a double logarithmic plot. Curves from top to bottom correspond to systems A, B, C, D and E.
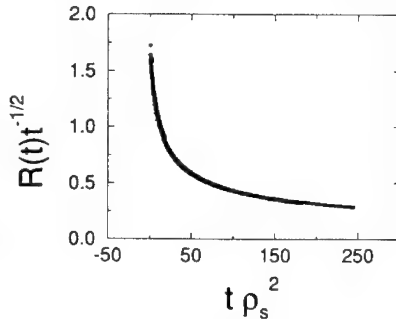
FIG. 3. Crossover scaling function $f(t\rho_s^2)$ versus $t\rho_s^2$ plotted for all five systems.

The average domain size calculated from Eq. (5) is shown in Fig. 2 for the five systems in a double logarithmic plot. At early times, the domain growth is relatively fast, but it slows down at later times. A local growth exponent defined as $n_{\mathrm{loc}} = d\log_{10} R(T)/d\log_{10} t$ was found to decrease with both time and surfactant concentrations. As time diverges, n_{loc} converges to zero, indicating that the domain growth is nonalgebraic, and that the larger the surfactant concentration is, the slower is the domain growth.

In Fig. 1, we observe that all surfactants are adsorbed at the interfaces. This is because the quenches performed in the present simulations are quite deep. We speculate that the average domain size will eventually cease growing when all interfaces are coverd by surfactants. At saturation, the interfacial length per unit of area $L(t \to \infty)$ (in three dimensions, the interfacial area per unit of volume) scales as $1/\rho_s$. Moreover, since the average domain size scales as $1/L(t)$, we expect the final domain size to scale as $1/\rho_s$. This relation was found to hold rather well for the present set of data.

While non–zero surfactant concentrations lead to slow non–algebraic growth, pure binary fluids exhibit a power–law growth with an exponent $n = 1/2$ at intermediate times, crossing over to a faster power–law growth with $n = 2/3$ as has been predicted by the dimensional analysis by Furukawa [22] and the recent simulation of Velasco and Toxvaerd [15]. A crossover between this power–law growth and a slow growth in the presence of surfactants is therefore expected. Besides, since the final domain size is inversely proportional to ρ_s, we propose the following scaling ansatz, $R(t) = t^n f(t\rho_s^{1/n})$, where the function $f(x)$ is equal to a constant for $x = 0$ and is proportional to x^{-n} for large x with n being the growth exponent in the system without surfactants. We have tested the existence of this scaling with $n = 1/3$, $n = 1/2$ and $n = 2/3$, but the scaling was found to hold only when $n = 1/2$ as shown in Fig. 3. In contrast, in our previous studies [6, 7, 8], we found a crossover scaling with $n = 1/3$ due to the fact that these studies did not take into account hydrodynamic modes, and therefore the domain growth was due to the long range diffusion process [23]. In the present simulation, the growth exponent $n = 1/2$ is an indication to the presence of hydrodynamic modes.

At late times, pure binary systems undergoing phase separation commonly exhibit a

self–similar behavior due to the presence of one characteristic length scale, corresponding to the average domain size, which scales all other spatial dpendencies in the system [3, 4]. Consequently, the structure factor can be written in this scaling form, $S(q,t) = R(t)^d F(\chi)$ where d is the spatial dimension ($d = 2$ in our case) and $\chi = qR(t)$ is the scaled wavenumber. There is an important difference between our systems and pure binary systems: Binary systems undergo a complete phase separation, and therefore small distances, such as the interfacial width, become vanishingly small compared to the average domain size at late times, whereas systems containing surfactants undergo a microphase separation. We tested the presence of dynamical scaling in our systems, and we indeed found that scaling sets in from about $t = 200\tau$ as shown in Fig. 4. We have moreover observed that the scaling function F is independent of surfactant concentration. The recent experiment of Hashimoto and Izumitani also found that the scaling function is independent of the blockcopolymer concentration [5].
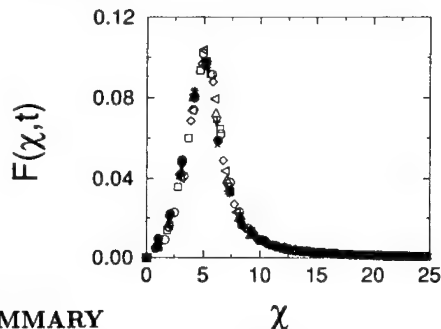
FIG. 4. Scaled structure factor, $F(\chi, t) = R(t)^{-2} S(q,t)$, in system C with $\chi = qR(t)$. The times shown are from $t = 200\tau$ to 2000τ in step of 200τ corresponding to to the symbols in the sequence: $\circ, \Box, \Diamond, \triangleleft, \triangle, \nabla, +, \times, *, \bullet$.

SUMMARY

In this paper, we have presented the results of a molecular dynamics simulation of the phase separation process in a binary fluid containing a small amount of surfactants. The main result of this paper is that surfactants alter the power–law growth in a pure binary fluid to a slow non-algebraic growth. Moreover, the larger the surfactant concentration, the slower is the dynamics. This phenomenon results from the molecular structure of surfactants which favors interfacial adsorption and then leads to the reduction of the effective interfacial tension. During the phase separation process, the surfactant density at the interfaces increases due to the decrease in the amount of interfaces, leading to a decrease in the average surface tension between the growing domains. The domain growth stops when all interfaces are covered by surfactants. These findings are in agreement with our previous results based on the time–dependent Ginzburg–Landau model and the modified Lifshitz Slyozov theory. However unlike these calculations, surfactants in the present model are treated more realistically, and the dynamics is examined by a real–time molecular dynamics method which takes into account hydrodynamic interactions in a natural manner.

We also found that at late times, the average domain size saturates at a value which is inversely proportional to the surfactant concentration. This also agrees with our previous studies. Moreover, a crossover scaling form which unifies the domain growth in pure binary fluids with the phase separation in the presence of surfactants was also found.

Finally, as in pure binary fluids, a dynamical scaling was observed to hold at late times. In addition, the scaling function is independent of the surfactant concentration.

ACKNOWLEDGMENTS

References

[1] T. Kawakatsu, K. Kawasaki, M. Furusaka, H. Okabayashi, and T. Kanaya, J. Phys.: Condens. Matter **6**, 6385 (1994).

[2] M. Laradji, H. Guo, M. Grant, and M.J. Zuckermann, Adv. Chem. Phys. Vol. LXXXIX, 159 (in press, 1994).

[3] J.D. Gunton, M. San Miguel, and P.S. Sahni, in *Phase Transitions and Critical Phenomena*, edited by C. Domb and J.L. Lebowitz, Vol. 8 (Academic Press, New York, 1983), p.265.

[4] O.G. Mouritsen, in *Kinetics of Ordering and Growth at Surfaces*, edited by M.G. Lagally (Plenum Publ. Co., New York, 1990), p.1.

[5] T. Hashimoto and T. Izumitani, Macromolecules **26**, 3631 (1993).

[6] M. Laradji, H. Guo, M. Grant, and M.J. Zuckermann, J. Phys. A: Math. Gen. **24**, L629 (1991).

[7] M. Laradji, H. Guo, M. Grant, and M.J. Zuckermann, J. Phys.: Condens. Matter **4**, 6715 (1992).

[8] J.H. Yao and M. Laradji, Phys. Rev. E **47**, 2695 (1993).

[9] T. Kawakatsu, K. Kawasaki, M. Furusaka, H. Okabayashi, and T. Kanaya, J. Chem. Phys. **99**, 8200, 1993.

[10] T. Kawakatsu and K. Kawasaki, J. Colloid Sci. **148**, 23 (1991).

[11] D. Moraietz, D. Chowdhury, S. Vollmar, and D. Stauffer, Physica A **187**, 126 (1992).

[12] E.D. Siggia, Phys. Rev. A **20**, 595 (1979).

[13] N.-C. Wong and C. Knobler, Phys. Rev. A **24**, 3205 (1981).

[14] T. Koga and K. Kawasaki, Phys. Rev. A **44**, R817 (1991).

[15] E. Velasco and S. Toxvaerd, Phys. Rev. Lett. **71**, 388 (1993).

[16] M. Laradji, O.G. Mouritsen, S. Toxvaerd, and M.J. Zuckermann, Phys. Rev. E **50**, 1243 (1994).

[17] M. Laradji, O.G. Mouritsen and S. Toxvaerd, Europhys. Let. (in press, 1994).

[18] S. Nosé, Mol. Phys. **52**, 255 (1984).

[19] W.G. Hoover, Phys. Rev. A **31**, 1695 (1985).

[20] S. Toxvaerd, Mol. Phys. **72**, 159 (1991).

[21] S. Toxvaerd, Phys. Rev. E **47**, 343 (1993).

[22] H. Furukawa, Adv. Phys., **34**, 703 (1985).

[23] I.L. Lifshitz and V.V. Slyozov, J. Phys. Chem. Solids **19**, 35 (1962).

CHEMISORPTION OF SELF ASSEMBLED ALKYL THIOL ON AU(111)

M. S. Yeganeh, S. M. Dougal, R. S. Polizzotti and P. Rabinowitz
Exxon Corporate Research, Annandale, New Jersey 08801

ABSTRACT

We have used infrared-visible sum-frequency generation (SFG) to spectroscopically probe the interfacial structure of a self assembled monolayer (SAM) of alkyl thiol on a Au(111) surface. The SFG spectra of the CH_3 group measured as a function of azimuthal angle indicates that sulfur atoms cannot be situated at sites of a single type, e.g., hollow or bridge, but must be in a mixed arrangement. SFG is also used to study the reconstruction of the gold substrate by alkyl thiol.

INTRODUCTION

Self assembled monolayer (SAM) are potentially useful for corrosion inhibition, wear protection, and organic sensors [1]. Perhaps the best characterized SAM system is $CH_3(CH_2)_{n-1}SH$, (C_n), adsorbed on a Au surface. The C_n/Au system, specifically its surface and chain orientation, have been widely studied. He [2] and x-ray [3] scattering studies have shown that the CH_3 outer surface has a rectangular unit cell which includes four tilted hydrocarbon chains. Infrared spectroscopy [4], in agreement with Raman scattering [5] and ellipsometry [6], as well as an earlier SFG study [7], suggest that the chains are densely packed and the number of the gauche defects is insignificant. Despite all the available experimental results, the location of sulfur chemisorption sites is known only by inference. The conventional belief has been that the S atoms reside at hollow sites of the gold substrate, generating a simple $(\sqrt{3} \times \sqrt{3})R30°$ structure. The location of these sites is essential for a detailed evaluation of Au-S, Au-Au and S-S bonds at the interface.

In this work infrared-visible sum-frequency generation (SFG) was used to probe the structural symmetry of the C_{18}/Au(111) interface. Our experiments reveal an unexpected three-fold rotational symmetry at the sulfur adsorbate sites of the C_{18}/Au(111) system. This result precludes the sulfur atoms being located solely at the hollow sites of the gold substrate. Such a configuration would give rise to an isotropic SFG signal. Recently, we learned of an elegant x-ray experiment that independently produced results leading to the same conclusion [8]. The experimenters suggest a disulfide configuration with sulfur in the hollow and bridge sites. This arrangement would produce SFG results consistent with ours.

In addition to adsorbate site geometry, the effect of the thiol chemisorption on the surface stress of the gold substrate was also examined. Measured SFG rotational anisotropy of the gold substrate is consistent with $(\sqrt{3} \times 23)$ and (1×1) reconstruction patterns for air/Au(111) and C_{18}/Au(111). These measurements show that the surface lattice of clean Au(111) is stable in air and relaxes upon the chemisorption of S atoms.

EXPERIMENTAL

Our samples consist of a monolayer of octadecanethiol (ODT) on a Au(111) single crystal. The gold substrate was cleaned in a UHV chamber and its surface contamination checked using XPS. The Au(111) substrate was then immersed into a 100 μM solution of ODT in
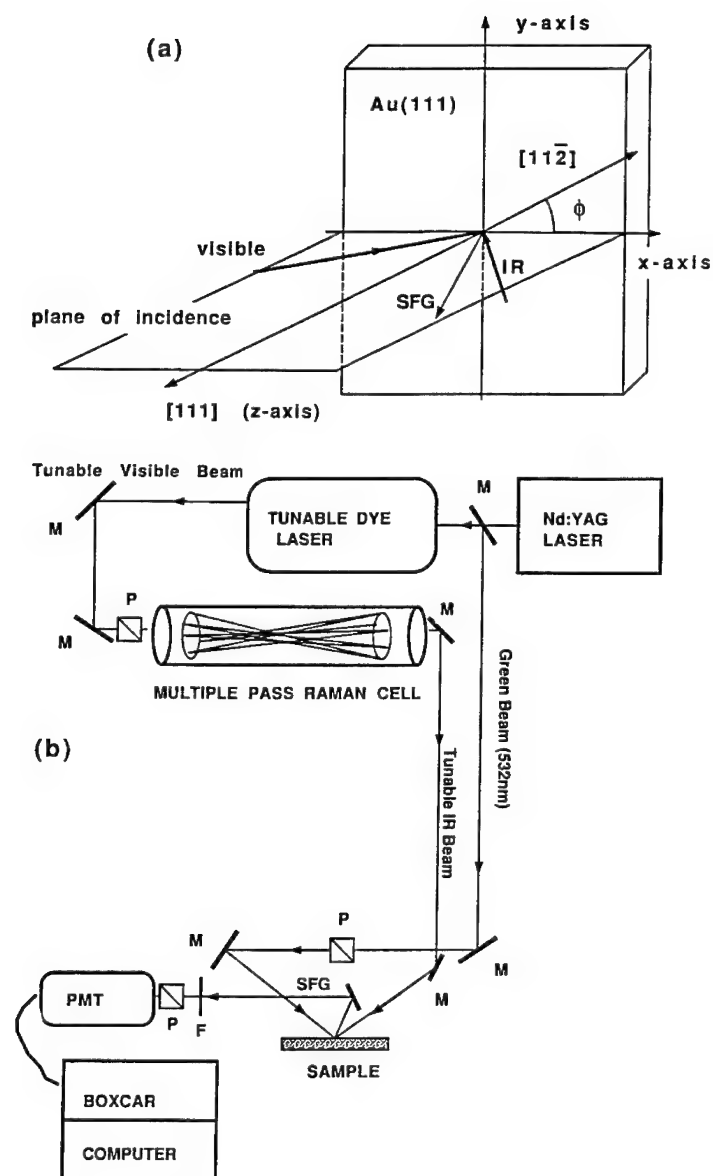
Figure 1: (a) Schematic of SFG measurements. ϕ is the angle between a mirror plane of the Au(111)(1 × 1) and the plane of the incidence. (b) Optical setup for SFG measurements: P, polarizer; M, mirror; F, spectral filter; PMT, photomultiplier tube.

ethanol for ~16 hours. The layout of the experimental apparatus and a rough schematic of the optical setup for SFG measurements are displayed in Fig. 1. The SFG measurements were made in air with a visible laser beam at 532 nm and a tunable infrared beam, both beams incident at 60° in a counter propagation geometry. In this arrangement, the resonance and background components of the nonlinear susceptibility are phase additive [9]. The infrared light was generated by stimulated Raman scattering of a doubled-Nd:YAG pumped dye laser in a multi-pass H_2 cell [10]. A portion of the output of the doubled-Nd:YAG laser was used as the visible light source. The incident light pulses had a duration of ~7 nsec and a fluence of ~15 mJ/cm^2 for both visible and IR beams. The intensity of the laser radiation was measured to be at least an order of magnitude below the sample damage threshold. Additionally, changes in the spectra of the system were not observed after a month of study with the same sample.

RESULTS AND DISCUSSION

The frequency dependence of the SFG signal at $\phi = 37°$ is shown in Fig. 2. Where ϕ is the angle between a mirror plane of the Au(111) (1×1) substrate and the plane of incidence. The SFG spectrum of the sample was measured at different azimuthal angles, ϕ. Each spectrum was fit to a standard model consisting of a constant background and a Lorentzian resonance [11]. In this way, the angular dependence of the background and the resonance signals was determined. Since the relative phase between the resonance and the background varies as a function of ϕ, this procedure is essential for separating the background and the resonance contribution from the total radiation intensity. The dependence of the relative phase between the background and the resonance signals is demonstrated in Fig. 2.

The resonance SFG signal is generated at the air/monolayer interface by CH_3 groups, and its dependence on the sample orientation is directly related to the position of the sulfur atoms at the Au interface. This results from the fact that the position of the S atoms, taken with a specific chain geometry and domain distribution, uniquely determines the position of the CH_3. We have calculated the total SFG polarization generated at the surface of the sample for a specific domain configuration [12]. As shown in the insert of Fig. 3, the *surface* of each domain is C_1 symmetric. This is resulting from the lack of a center of inversion, a plane of reflection, and proper and improper axes of rotation. This system carries all 27 elements of the second-order nonlinear susceptibility tensor, χ_{ijk}. With both p-polarized infrared and visible beams the polarization of the SFG output, generated by the tilt-domains, in the plane of incidence is

$$\sum_{all\ tilt\ direction} \mathbf{P} = \{-E_{1z}E_{2z}\chi_{yzz}\sin(\phi) - E_{1z}E_{2x}[\chi_{xxy}\cos(\phi)^2\sin(\phi) +$$
$$\chi_{xyz}\cos(\phi)^2\sin(\phi) + \chi_{yxz}\cos(\phi)^2\sin(\phi) + \chi_{yyy}\sin(\phi)^3] + E_{1x}E_{2z}[\chi_{xzz}\cos(\phi)^2 +$$
$$\chi_{yyz}\sin(\phi)^2] + E_{1z}E_{2z}[\chi_{xzx}\cos(\phi)^2 + \chi_{yzy}\sin(\phi)^2]\}\hat{x} + \{E_{1z}E_{2z}\chi_{zzz} - E_{1x}E_{2z}$$
$$\chi_{zyz}\sin(\phi) - E_{1z}E_{2x}\chi_{zzy}\sin(\phi) + E_{1x}E_{2x}[\chi_{zxx}\cos(\phi)^2 + \chi_{zyy}\sin(\phi)^2]\}\hat{z}. \qquad (1)$$

Here $\mathbf{P}$ is the SFG polarization vector in the plane of incidence produced by a single domain. The unit vector $\hat{x}$ ($\hat{y}$) is parallel to the short (long) side of the rectangular unit cell and $\hat{z}$ is normal to the surface, see the insert in Fig. 3. If all the S atoms were located at the hollow sites of the gold surface, the total SFG intensity, I^{SFG}, would be
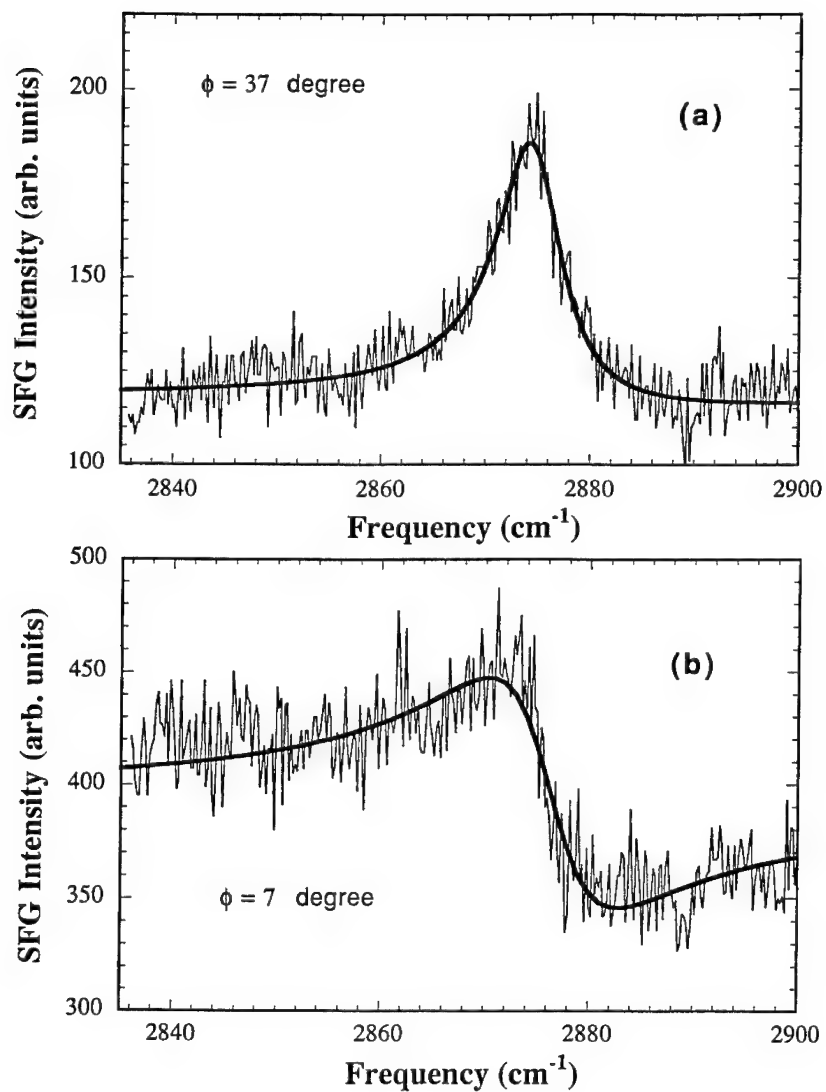
Figure 2: (a) SFG spectrum of ODT/Au(111) in ppp-polarization at $\phi = 37°$. (b) The same spectrum at $\phi = 7°$. The marked difference in the spectra results from the dependence of the relative phase between the background and resonance signal on the azimuthal angle, ϕ.
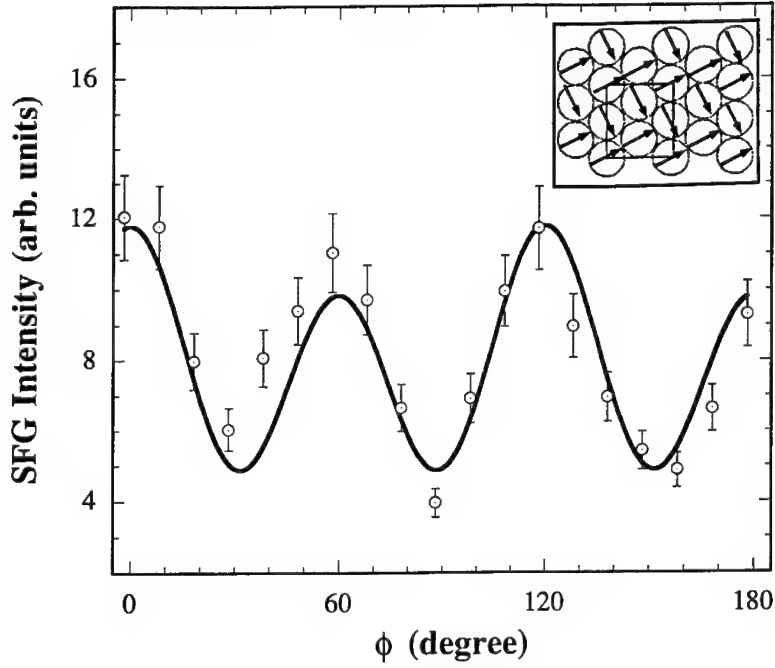
Figure 3: Resonance SFG intensity of the C_{18}/Au(111) as a function of the rotation angle, ϕ. Here ϕ is the angle between a mirror plane of the Au(111)(1 × 1) and the plane of the incidence. The solid line is the theoretical fit to the data. Insert: Surface structure of C_{18}/Au(111). The rectangular unit cell contains four chains with two different chain configurations in each unit cell [2,3]. These hydrocarbon chains are related to one another by a rotation about the chain axis. The arrows indicate the direction of the C-C bonds at the methyl groups of the monolayer.

$$I^{SFG} \propto |\sum_{n=0}^{n=5} \sum_{all\ tilt\ direction} \mathbf{P}(\phi + n\pi/3) \cdot \hat{e}(sfg)|^2 = C_0 \qquad (2)$$

where $\hat{e}(sfg)$ is the unit vector in the SFG polarization direction and C_0 is a constant, independent of ϕ, and hence the signal is isotropic. The same results are obtained if all the S atoms reside at bridge or top sites of the substrate.

The variation of the resonance SFG intensity as a function of the azimuthal angle is shown in Fig. 3. Our data is not isotropic but exhibits a three-fold symmetric pattern which shows that the S atoms cannot all be at the same sites of the Au(111) surface. To generate such three-fold symmetry, the sulfur atoms must be located at either bridge and hollow sites, at two different bridge sites, or at two different hollow sites [13]. These new geometries only allow $2n\pi/3$ rotations of the unit cell. The detected signal intensity,

67
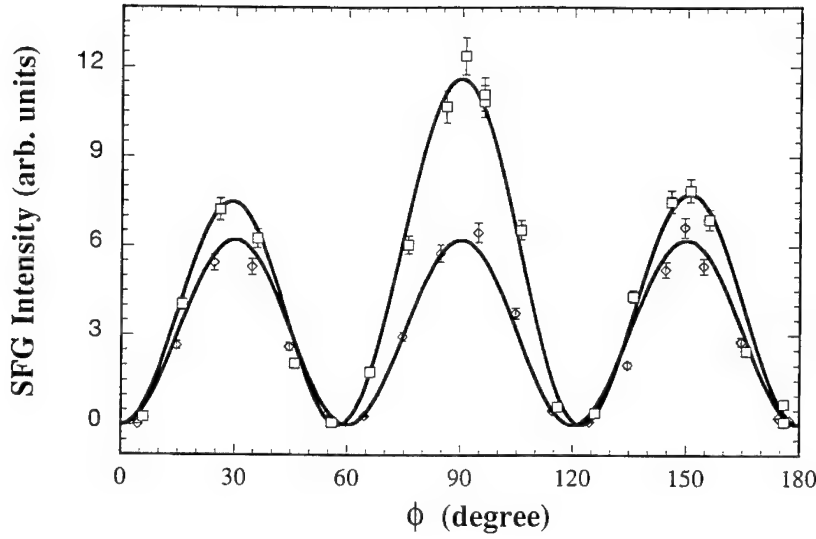
Figure 4: Variation of SFG intensity with azimuthal angle, ϕ, at 2800 cm^{-1} in sss-polarization for ODT/Au(111) ($\diamond$), and air/Au(111) ($\square$). The solid lines are the theoretical fit based on $(1 \times 1)C_{3v}$ structure for ODT/Au(111) and $(\sqrt{3} \times 23)$ structure, for air/Au(111).

I^{SFG}, is

$$I^{SFG}(\phi) = |C_1 e^{i\psi} \sum_{n=0}^{n=2} \sin^3(\delta + \phi + 2n\pi/3) + C_2|^2. \qquad (3)$$

Here C_1 and C_2 are constants which are related to the second-order susceptibilities, δ is an angular offset and ψ is the relative phase. The solid line in Fig. 3 is our best fit of the data to Eq. (3) and is in good agreement with our model.

To study the effect of thiol adsorption on the gold surface structure, the SFG intensity at 2800 cm^{-1} was measured in sss-polarization as a function of ϕ for both air/Au(111) and ODT/Au(111) systems. The results, depicted in Fig. 4, show a marked difference between the gold surface structure before and after the thiol adsorption. This difference is understood in the following context: A clean surface of gold (111) has three rotational domains generated by a rectangular $(\sqrt{3} \times 23)$ unit cell at room temperature. This reconstruction was observed by electron, He, and x-ray scattering, as well as by STM under UHV conditions [14, 15, 16, 17]. The reconstruction is caused by a stressed top surface

layer. The surface layer relaxes upon the adsorption of thiol and produces a C_{3v} symmetric (1×1) structure. The solid lines in Fig. 4 are the theoretical fit using three-fold (1×1) and one-fold $(\sqrt{3} \times 23)$ symmetric unit cells for ODT/Au(111) and air/Au(111) systems, respectively. Agreement between the experimental results and the model is excellent and illustrates that the $(\sqrt{3} \times 23)$ structure of a clean gold surface is stable in air, for at least the three hours of the measurement time.

SUMMARY

SFG spectroscopy has been used to study the interfacial structure of an ODT/Au(111) system. The substrate and adsorbate structures were differentiated by utilizing the frequency dependence of the technique. Our results corroborate a new model for the sulfur sites at the interface and show that the sulfur atoms are not all located at the hollow sites of the Au(111) substrate. A distinctive structure for a clean Au(111) surface in air and the gold substrate surface at the ODT/Au(111) interface was found. Our measurements show that the $(\sqrt{3} \times 23)$ structure of the Au(111) surface is stable in air. This structure changes to (1×1) after chemisorption of alkyl thiol on the surface.

References

[1] R. G. Nuzzo, and D. L. Allara, J. Am. Chem. Soc. **105**, 4481 (1983).

[2] Camillon, C. E. D. Chidsey, G. Liu, G. Scoles, J. Chem. Phys. **98**, 3503 (1993).

[3] P. Fenter, P. Eisenberger and K. S. Liang, Phys. Rev. Lett. **70**, 2447 (1993).

[4] R. G. Nuzzo, L. H. Dubois, and D. L. Allara, J. Am. Chem. Soc. **112**, 558 (1990).

[5] M. A. Bryant and J. E. Pemberton, J. Am. Chem. Soc. **113**, 8284 (1991).

[6] M. D. Proter, T. B. Bright, D. L. Allara, C. E.D. Chidsey, J. Am. Chem. Soc. **109**, 3559 (1987).

[7] A. L. Harris, C. E. D. Chidsey, N. J. Levinos, D. N. Loiacono, Chem. Phys. Lett. **141**, 350 (1987).

[8] P. Fenter, A. Eberhardt and P. Eisenberger, Science (submitted).

[9] A. L. Harris, private communication.

[10] P. Rabinowitz, B. N. Perry, and N. Levinos, J. Quantum Electron. **22**, 797 (1986).

[11] See, for example, R. Superfine, J. Y. Huang, and Y. R. Shen, Phys. Rev. Lett. **66**, 1066 (1991), and references therein.

[12] M. S. Yeganeh, S. M. Dougal, R. S. Polizzotti and P. Rabinowitz, Phys. Rev. Lett. (submitted).

[13] There are two different hollow sites on a (111) fcc surface. The difference between these sites is the presence or absence of a second layer atom directly below the sites.

[14] J. C. Heyraud and J. J. Metois, Surf. Sci. **100**, 519 (1980).

[15] U. Harten, A. M. Lahee, J. P. Toennies, and Ch. Woll, Phys. Rev. Lett. **54**, 2619 (1987).

[16] K. G. Huang, D. Gibbs, D. M. Zehner, A. R. Sandy and S. G. J. Mochrie, Phys. Rev. Lett. **65**, 3313 (1990).

[17] Ch. Woll, S. Chiang, R. J. Wilson, and P. H. Lippel, Phys. Rev. B, **39**, 7988 (1989).

DEWETTING OF POLYMER BILAYERS: MORPHOLOGY AND KINETICS

ALESSANDRO FALDI[*1], KAREN I. WINEY[*], AND RUSSELL J. COMPOSTO[*]
[*]Department of Materials Science and Engineering and Laboratory for Research on the Structure of Matter, University of Pennsylvania, Philadelphia, Pennsylvania, 19104.

ABSTRACT

The kinetics of de-wetting a polycarbonate (PC) film from a poly(styrene-co-acrylonitrile) (SAN) copolymer film was monitored using optical microscopy. Whereas the SAN layer was stable upon annealing at 190°C, the PC layer dewetted the SAN and formed holes whose diameter increased linearly with time. Auger electron spectroscopy measurements confirmed that PC was fully removed from the interior of the hole. Upon varying the AN content, the dewetting velocity was found to be a minimum near 0.27 weight percent AN. This result is consistent with the interfacial thermodynamics between PC and SAN. Atomic force microscopy was used to provide a unique image of the hole profile.

INTRODUCTION

Polymer thin films are of fundamental importance to many areas of science and technology which involve, for example, coatings, drying, lubrication, and colloidal systems. Thin film stability is of particularly importance because many applications involve producing films under non-equilibrium conditions (e.g., spin-coated films). Thus, a fundamental study of the molecular parameters which control thin film stability is of practical interest. Within the past several years, the study of polymer films deposited on a non-wettable inorganic surface has received widespread attention.[2-9] These films are either unstable or metastable depending on film thickness.[10] If a hole forms, either spontaneously or by nucleation, the hole will grow because of the interfacial driving forces; we refer to this process as dewetting. Until recently, most experiments have involved films on rigid substrates.[2, 5-8] One study, though, has examined polymer dewetting from a microphase separated block copolymer film.[9]

The present study is concerned with polymer-polymer dewetting. We observed that a film of bisphenol A polycarbonate (PC) spontaneously develops holes and dewets an underlayer of poly(styrene-co-acrylonitrile) (SAN) when the bilayer structure is annealed above the glass transition temperatures of both PC and SAN. In the following paper, we present measurements of the dynamics of hole growth as well as a description of the hole morphology. To the best of our knowledge, this research is the first attempt to study the dewetting of a polymer melt from another polymer melt. A recent theoretical analysis of liquid-liquid dewetting[11] suggests that polymer-polymer dewetting will behave in a fundamentally different manner than polymers dewetting rigid substrates.

EXPERIMENTAL

A film of SAN (~200 nm thick) was spin-coated on a silicon wafer and then dried at 80 °C under vacuum. A film of PC (~200 nm thick) was spin-coated on a glass slide. The film was scored at the edges, floated on a water bath, and recovered on top of the SAN-covered wafer to form a polymer bilayer. The samples were dried at 80 °C for 8-12 hours under vacuum. The polymer characteristics are reported in Table I.

Dewetting was monitored in real time using an optical microscope equipped with a hot stage and a video system. The hole dimensions were recorded as a function of time until neighboring holes impinged on one another. Atomic force microscopy (AFM) was used to image the surface topology of samples quenched at intermediate stages of hole growth.

Table I. Polymer Characteristics.

Sample	$\overline{M}_w$	$\overline{M}_w / \overline{M}_n$	AN content (w%)	Source
SAN17	172,000	2.26	17	Monsanto
SAN27	242,000	2.98	27	Monsanto
SAN33	118,000	2.24	33	Monsanto
PC	19,100	2.94		General Electric

RESULTS AND DISCUSSION.

Figure 1 displays an optical micrograph of holes in the PC layer of a PC/SAN17 bilayer after 2.7 hours of annealing at 190 °C. The holes are circular and their rims almost touch each other. This hole is representative of the very latest stage of development that we've analyzed. The dark spot in the middle of the holes will be discussed later. Auger electron spectroscopy (AES) studies show that the polymer on the hole floor is exclusively SAN, whereas the surface outside the hole is PC.[12]

The dewetting velocity is determined by measuring the hole radius as a function of time. Within the range of our experimental data, the PC dewetting proceeds with constant speed. Figure 2 shows how the dewetting velocity depends on the acrylonitrile content of the SAN layer. A minimum velocity is observed for AN weight fractions in the 25-30% range. Callaghan et al.[13] and Willet and Wool[14] report that the PC-SAN Flory-Huggins interaction parameter, χ, is a minimum in the same AN range. As a result of this behavior of χ, PC on SAN has the lowest contact angle in the 25-30% range, and correspondingly the slowest dewetting velocity.[2,4,8]
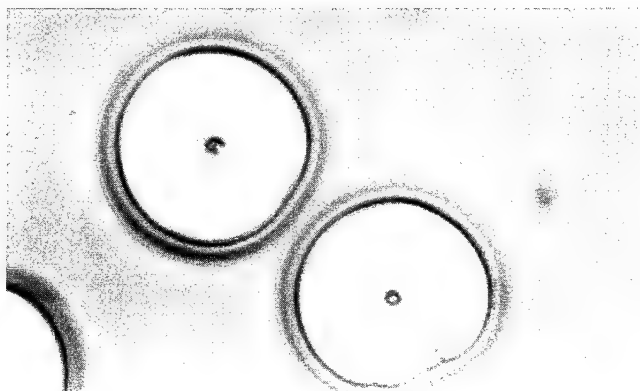
Figure1: Optical micrograph of PC holes after 2.7 hours at 190°C. The average hole diameter is 127µm's. The dark center spots are dimples which are 50nm deep.
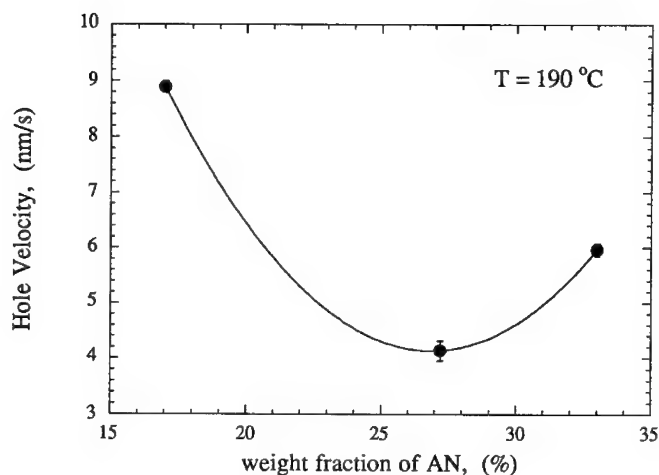
Figure 2: Hole velocity as a function of AN content in theunderlying SAN layer. The solid line is a guide to the eye.

A detailed image of the surface topology of a dewetted sample can be obtained using AFM. Figure 3 shows a cross-sectional trace across the center of a hole after annealing a PC/SAN27 bilayer at 190 °C. This figure clearly shows the morphology that develops during the dewetting process. The hole diameter corresponds to 35 μm, in good agreement with optical microscopy measurements. The PC from the hole is raked into the rim around the hole which has a height of about 400 nm with respect to the top of the bilayer far from the hole. The AFM trace also shows that the dewetted SAN layer is not flat, but rather has a 50 nm depression in the middle of the hole. This hole corresponds to the dark spot seen in Figure 1 and is the likely nucleation site for dewetting. Every hole displays this nucleation site. The various hole dimensions are given in Table II.

Table II. Hole dimensions

Hole diameter	35 μm
Rim top to unperturbed PC	400 nm
Rim top to interior (close to rim base)	740 nm
Rim top to interior (center)	790 nm

These AFM dimensions are in reasonable agreement with those obtained from scanning electron microscopy (SEM) images. The SEM results will be discussed elsewhere.[12]

The AFM values in Table II reveal an interesting characteristic of the hole morphology. Knowing that the initial bilayer thickness is 400nm, the thickness of the SAN layer which remains inside the hole can be estimated from the AFM trace. The resulting thickness, 40 nm, is much smaller than the original SAN thickness of 200 nm. Experiments are in progress to determine how the SAN redistributes during dewetting.
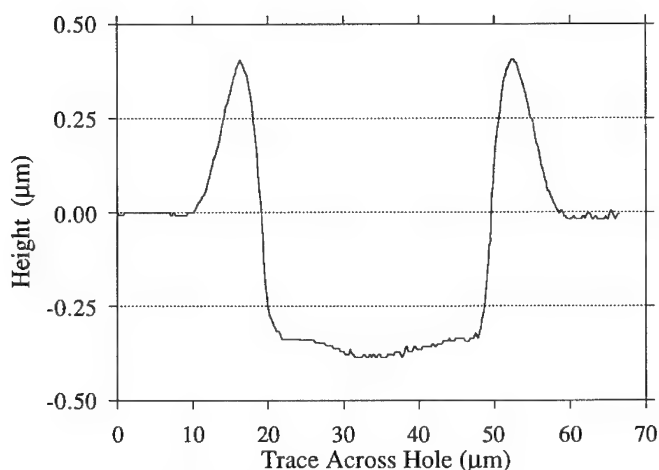
Figure 3: Cross-sectional trace across PC hole using AFM. The hole dimensions are given in Table II.

CONCLUSIONS.

- Spontaneous dewetting of PC from SAN of various AN contents is observed at 190°C.

- The dewetting velocity is slowest when the AN weight content in the SAN copolymer is 25-30%.

- The hole interior consists of a pure SAN layer which is thinner than the original film thickness and a dimple at the center of the hole. The PC rim around the hole is steep on the inside and decays slowly on the outside.

REFERENCES

(1) Exxon Chemical Co., P.O. Box 5200, Baytown, Texas 77522-5200

(2) Redon, C.; Brochard-Wyart, F.; Rondelez, F. *Phys. Rev. Lett.* **1991**, *66*, 715

(3) Safran, S.A.; Klein, J. *J. Phys. II France* **1993**, *3*, 749

(4) Brochard-Wyart, F.; de Gennes, P.-G. *Adv. Coll. Interface Sci.* **1992**, *39*, 1

(5) Reiter, G. *Phys. Rev. Lett.* **1992**, *68*, 75

(6) Reiter, G. *Langmuir* **1993**, *9*, 1344

(7) Zhao, W.; Rafailovich, M. H.; Sokolov, J.; Fetters, L. J.; Plano, R.; Sanyal, M. K.; Sinha, S. K.; Sauer, B. B. *Phys. Rev. Lett.* **1993**, *70*, 1453

(8) Shull, K. R.; Karis, T. E. *Langmuir*, **1994**, *10*, 334

(9) Liu, Y.; Rafailovich, M. H.; Sokolov, J.; Schwarz, S. A.; Zhong, X.; Eisenberg, A.; Kramer, E. J.; Sauer, B. B.; Satija, S. *Phys. Rev. Lett.* **1994**, *73*, 440

(10) Brochard-Wyart, F.; Daillant, J. *Can. J. Phys.* **1990**, *68*, 1084

(11) Brochard-Wyart, F.; Martin, P.; Redon, C.; *Langmuir*, **1993**, *9*, 3682

(12) Faldi, A.; Winey, K.I.; Composto, R. J., to be published

(13) Callaghan, T.A.; Takakuwa, K.; Paul, D.R.; Padwa, A.R. *Polymer*, **1993**, *34*, 3796

(14) Willet, J.L.; Wool, R.P. *Macromolecules*, **1993**, *26*, 5336

LOCAL FIELD EFFECTS NEAR SURFACES OF SMALL SYSTEMS

DAVID BEAGLEHOLE
Department of Physics, Victoria University of Wellington, P.O.Box 600, Wellington, New Zealand.

ABSTRACT

The interaction of light with a system of molecules depends upon the polarisation induced by an external electric field, which depends not only upon the external field but also upon the local fields due to neighboring polarised molecules. These local fields result in the traditional Clausius-Mossotti (CM) dielectric constant for a molecule deeply imbedded in a medium. Near the surface the local fields are altered, and the dielectric constant becomes anisotropic and dependent upon depth into the medium. The local fields are shape dependent in small systems and differ substantially from the CM value.

A self-consistent computer calculation of the local fields has been implemented, and these effects will be shown using molecule positions and polarisabilities typical of liquids and crystals. The shape dependence of small systems, the reflection of light from liquids with fluctuating surfaces, and the effect of supporting substrates will be described.

INTRODUCTION

The work I wish to describe today is the result of an attempt to get a better understanding of the way in which light interacts with the molecules in a liquid - especially when the liquid forms a thin layer on a substrate or forms islands of finite extent. There are several questions I wish to answer which arise in the interpretation of ellipsometry and other optical studies of liquid and solid surfaces - ellipsometry has sensitivity to study surfaces with sub monolayer sensitivity, but its usefulness is limited by the uncertainty in interpretation. The questions are the following:

(i)   If the optical response of a medium is described by a dielectric constant, to what extent is it anisotropic and varies with depth near the surface of the medium; also how does it depend upon the thickness of the medium?

(ii)   What is the influence of an underlying supporting substrate?

(iii)   What is the best description of the response of a medium consising of objects of finite size such as small liquid droplets on a substrate?

(iv)   If the medium is a disordered liquid, what is the best way to take into account the optical response of themolecules in the inhomogeneous transition region at the surface?

Drude[1] proposed that the surface of a medium should be represented by a dielectric constant $\varepsilon(z)$ which varied continuously between the limits ε_1 and ε_2, these being the values on

each side of the interface. Drude assumed that this "transition" layer was isotropic, though the model can be generalised[2] to an anisotropic $\varepsilon_y(z)$, $\varepsilon_z(z)$. An alternative approach for liquids was proposed by the author[3] based upon the thermally excited capillary wave model of liquid surface excitations. This approach uses a sharp discontinuity between the dielectric constants of the bounding media following a displacement $\zeta(x,y)$ from the mean. The present discussion is aimed at clarifying which of these is the best model - which reproduces best the optical response of dipoles in the region of a liquid surface. To a first approximation the dipoles of a medium are polarised by the external electric field, and this produces a dielectric constant given by $\varepsilon = 1 + n\alpha$. However this approximation neglects the local fields due to surrounding polarised dipoles which alter the net local field. The best model is the one which gives the best representation of local field effects.

To study the local field effects a self-consistent computer calculation has been implemented using a set of dipoles placed on sites which correspond to those of crystal or liquid molecules. An external field E_0 is applied to this set, and the dipoles have been allowed to develop an induced polarisation resulting from the sum of the applied field and the local fields of the neighboring dipoles. The size and shape dependence of the induced polarisation has been studied as well as disordered configurations.

Lekner and Castle[4] have considered the surface variation problem analytically, and obtained a formulation of the dipole sums for a slab-shaped cubic lattice. They have assumed that the system is of infinite dimension in the xy plane, and thin in the z direction. The induced dipoles are taken to be parallel to the applied field, with no finite size fringing field effects. They have separated the summations into those contributed by each plane. Briefly, they predict anisotropy and surface variation of the dielectric constant of the order of one percent. Castle and Lekner[5], and Lekner[6] have applied a similar formulation to the surface-variation of the dielectric constant of a simple liquid, and have shown again that in-plane summations dominate the local field corrections, and that (with approximations) the anisotropy of the dielectric constant in the surface region is weak.

Our present simulation reproduces their results, and we find that the induced dipoles will saturate for slab samples of dimension n x n x k (k the slab thickness) when Bk/n<<1, where B is in the range 0.3 to 1. Small samples show large depolarising field size effects. If a medium dielectric constant is used, as is done in the capillary wave model, then the surface waves need to satisfy the condition $\zeta_q q \ll 1$. Surface fluctuations on a shorter scale are best handled with the anisotropic Drude model, but we observe deviations from a dielectric constant $\varepsilon(z)$ whose dependence on z is based solely upon a density n(z).

INDUCED POLARISATIONS AND DIELECTRIC CONSTANT

When a medium with n dipoles per unit volume each of polarisability α is in an applied field E_0 and the induced polarisation of each dipole is p, then the polarisation density P is given by $P = n\, p = n\alpha\, \varepsilon_0\, E_{loc}$, where E_{loc} is the field acting on each dipole. P is also given by $P = \varepsilon_0 (\varepsilon - 1)\, E_{av}$, where E_{av} is the average electric field in the medium, defining the dielectric constant ε. E_{loc} and E_{av} are both proportional to E_0, the relationship depending upon the medium geometry. For an infinite homogeneous medium

$$E_{loc} / E_{av} = (\varepsilon + 2)/3 , \quad E_{loc} / E_0 = (\varepsilon + 2)/3\varepsilon , \tag{1}$$

which leads to the Clausius-Mossotti expression for the relative dielectric constant

$$\varepsilon = 1 + \frac{n\alpha}{(1 - n\alpha/3)}. \tag{2}$$

The denominator here is due to the local fields due to surrounding dipoles. Since these fields are relatively long-ranged, decaying as $1/r^3$, the shape, substrate and local configurations are each important in determining the dielectric constant in inhomogeneous media.

When light is reflected at an arbitrary angle of incidence from a semi-infinite medium with a flat surface, two cases are considered, E_0 parallel and E_0 perpendicular to the surface. In the Fresnel theory for an isotropic semi-infinite medium it is assumed that ε is independent of both depth and electric field polarisation. We have:

(a) E_0 parallel to the surface.

When the external field E_0 is parallel to the surface (direction y) the fields associated with polarisation charges on the xz surfaces are negligibly small, and the average field in the medium E_{av} equals E_0, so from (1)

$$p_y = E_{loc}/E_0 = (\varepsilon-1)/n\alpha. \tag{3}$$

If $\varepsilon = \varepsilon_{CM}$ then we would expect

$$E_{loc}/E_0 = 1/(1-n\alpha/3). \tag{4}$$

(b) E_0 normal to the surface.

The polarisation surface charges on the xy surfaces reduce the internal fields substantially. We have $\varepsilon E_{av} = E_0$, which follows also from continuity of D, so that

$$p_z = E_{loc}/E_0 = (\varepsilon-1)/\varepsilon n\alpha. \tag{5}$$

If $\varepsilon = \varepsilon_{CM}$ then we would expect

$$E_{loc}/E_0 = 1/(1 + 2n\alpha/3). \tag{6}$$

These expressions for p_y and p_z apply equally to the local fields associated with a slab of material much wider and longer than it is thick. Note that if the ratios p_y and p_z are known for the slab geometry then a dielectric constant can be found in each case. We have

$$\varepsilon_y = 1+n\alpha p_y , \quad \varepsilon_z = 1/(1 - n\alpha p_z). \tag{7}$$

REFLECTION OF LIGHT BY DIPOLES

A dipole p_i situated at ρ_i gives a radiating far-field at a point P a distance r far from the dipole $E_{r,i} = (1/4\pi\varepsilon_0)(\omega^2/c^2)(1/r) |p_i| \sin\gamma_i \exp(-i\rho_i.\Delta k)$. Δk is $k' - k$, the change in wavevector between the outgoing and incoming fields. γ_i is the angle between p_i and k'. With the small

samples used here $\rho_i.\Delta\mathbf{k}$ is small for all dipoles, and the phase factor is unity. The total radiating field is then proportional to $\Sigma\,E_{r,i} \propto \Sigma\,p_i\,\sin\gamma_i$.

If light is incident at angle θ, polarised in the p direction, then $E_{oz}= E_o\sin\theta$, and $E_{oy}= E_o\cos\theta$. The induced dipoles are then p_yE_{oy} and p_zE_{oz} in the y and z directions respectively. The orientation of the induced dipole measured from the surface normal is given by $\tan\theta_i = p_yE_{oy} / p_zE_{oz} = \cot\theta\,p_y/p_z = r\cot\theta$ if $r = p_y / p_z$.

For a sample where r has the same value for all dipoles (a uniform dielectric constant) the radiating p field is zero when the angle of reflection, which equals the angle of incidence, is also equal to θ_i, ie when $\tan^2\theta = r$. This angle of incidence is the Brewster angle. Surface dipoles which have a different value for r will give a radiating field at the Brewster angle. The strength of the radiating field will be proportional to $\cos^2\theta\,\Sigma\,p_{iz}\,(r_i - \tan^2\theta)$, which becomes at the Brewster angle (r_p and r_s are the p and s amplitude reflectivities respectively)

$$r_p /r_s \;\propto\; 1/(1+\varepsilon)\,\Sigma\,(\,p_{iy} - \varepsilon\,p_{iz}). \tag{8}$$

If we use the relation between p and ε then the summation here is identical to the surface integral in Drude's homogeneous transition region model appropriately generalised for anisotropy, namely

$$\int dz\,\{\varepsilon_y + \varepsilon\,/\,\varepsilon_z - \varepsilon -1\}. \tag{9}$$

In the Drude theory the dielectric constants would be evaluated using a surface-averaged $\overline{n}(z)$.

CALCULATION OF LOCAL FIELDS

The external electric field $\mathbf{E}_o$ initially produces an induced dipole $\mathbf{p}_{io}$ on the ith molecule, where $\mathbf{p}_{io}= \alpha_i\varepsilon_o\,\mathbf{E}_o$. The net field on this molecule due to all other dipoles is the local field
$\Sigma_j\,\mathbf{E}_{ji}$ where $\mathbf{E}_{ji} = 1\,/(4\pi\varepsilon_o\,r_{ji}{}^3\,)[3\,\mathbf{r}\,(\mathbf{r}.\mathbf{p}_j) - \mathbf{p}_j\,]$; $\mathbf{r}$ is a unit vector in the direction of $\mathbf{r}_{ji}$. Together the local field and the external field determine the resultant polarisation of each molecule

$$\mathbf{p}_i = \alpha_i\varepsilon_o\,(\mathbf{E}_o + \Sigma_j\,\mathbf{E}_{ji}\,). \tag{10}$$

With r_{ji} in reduced units of the lattice constant a

$$(\mathbf{E}_{loc}/\mathbf{E}_o)_i = 1+\Sigma\beta_j(1/r_{ji}{}^3)(\mathbf{E}_{loc}/\mathbf{E}_o)_j\;\;f(\theta_{ji}). \tag{11}$$

Here $f(\theta_{ji})$ depends upon the angle between $\mathbf{p}_i$ and $\mathbf{p}_j$, and $\beta_j = \alpha_j/4\pi a^3$.
The calculation of $\mathbf{E}_{loc}/\mathbf{E}_o$ starts assuming an initial configuration given solely by the external field $\mathbf{E}_{loc} = \mathbf{E}_o$, then procedes using iterative steps to add the local fields calculated with the current value until convergence is obtained. For a particular molecule the value either follows an oscillatory path with decreasing-amplitude to the convergence value, or follows a monotonic trend to the convergence value. In both cases the path can be speeded using "acceleration" techniques[7] where the iteration values are assumed to follow a simple series. Three iterations yield an initial estimate for the convergence value. Two subsequent iterations yield a second estimate, etc. Convergence is assumed when the final average value departs from the previous by less than 0.01%, and typically 7 iterations have been needed for this accuracy. On occasions,

when the molecules are close or β is large the interactions can be so strong that the values divergence. This is a ferroelectric transition, where the local field effects in the denominator of the expression for ε become greater than unity, causing ε to diverge. Two values of β have been used in the calculations, $\beta = .034$ and $\beta = 0.1$. The first corresponds to the dielectric constant of liquid argon near its triple point $\varepsilon = 1.5$, while the second is a substantially larger value so that ε is part way between the values for glass and silicon, Table I.

Table I   Dielectric constant parameters

The dielectric constants for some liquids and solids, along with estimates for the strength of the local field corrections based upon the Clausius-Mossotti expression $1/(1-n\alpha/3)$, and the parameter $\beta = n\alpha/4\pi$. For the slab geometry $p_y = 1/(1-n\alpha/3)$ and for the Clausius-Mossotti dielectric constant $p_z = p_y / \varepsilon$.

	ε	$n\alpha$	$1/(1-n\alpha/3)$	β	p_y	p_z
liquid argon	1.5	.4286	1.167	0.034	1.167	.778
CCl_4	2.13	.8201	1.377	0.065	1.377	.647
glass	2.25	.8823	1.417	0.070	1.417	.630
	3.163	1.257	1.721	0.1	1.721	.544
silicon	16	2.50	6.0	0.199	6.000	.316

SURFACE VARIATION AND ANISOTROPY OF THE DIELECTRIC CONSTANT

Lekner and Castle [4] have obtained an analytic formulation of the dipole sums for cubic crystal (and disordered media[5]) in the slab geometry. They have assumed that the system is of infinite dimension in the xy plane, and thin in the z direction. The induced dipoles are taken to be parallel to the applied field, with no finite size fringing effects. For a single layer with the field in the z direction their theory can be written $p_z = E_{loc}/ E_0 = 1/(1-\beta S_0)$ and $p_y = (1+ \beta S_0/2)$, for two layers $p_z = 1/\{1-\beta (S_0 +S_1)\}$ and $p_y = \{1+\beta (S_0 +S_1) / 2\}$. Here $S_0 = -9.0336$, and $S_1 = 0.3275$ with S_0 determining the in-layer contribution and S_1 the adjacent layer contribution. Their estimate for the dielectric constant using the slab relations above, and for the anisotropy, are shown in Table II. Note that substantial anisotropy is predicted for the silicon surface.

Table II Estimate for ε_y and ε_z and the anisotropy $A = (\varepsilon_y- \varepsilon_z)/ (\varepsilon_y+ \varepsilon_z)$ for a molecule at the surface of a single layer and at the surface of a slab, calculated with the Castle-Lekner expressions. The anisotropy is small for the materials with dielectric constants not far from unity, but very substantial for the more polarisable materials.

	single layer			slab surface		
	ε_y	ε_z	A	ε_y	ε_z	A
argon	1.5066	1.4873	.0064	1.5033	1.4936	.0032
CCl_4	2.1643	2.0670	.0230	2.1468	2.0979	.0115
glass	2.2933	2.1734	.0266	2.2706	2.2107	.0134
silicon	25.653	9.412	.4631	19.625	11.7970	.2491

Figure 1 shows the computer calculations for p_y and p_z for the central dipole on the outer layer of a slab of size n x n x k (in units of lattice constant a) as a function of the size n and thickness

k, for $\beta = 0.034$.   As n increases the polarisations tend to a limiting value characteristic of large slabs, reaching the limiting value more slowly as k increases.   The convergence follows a function $p_\infty(1 \pm B'/n)$ for large n[8], with B' roughly proportional to k for thin slabs.   Writing B' = Bk, we find B ~-0.2 for p_y and ~0.2 for p_z for $\beta = 0.034$, and ~ -1.5 and ~0.3 respectively for $\beta = 0.1$.   Bk/n must satisfy the condition Bk/n << 1 for p to be close to p_∞.

Figure 1
p_y and p_z for the central dipole of the outer layer of the n x n x k lattice
(A of Figure 3) as a function of n and k
 for $\beta = 0.034$.
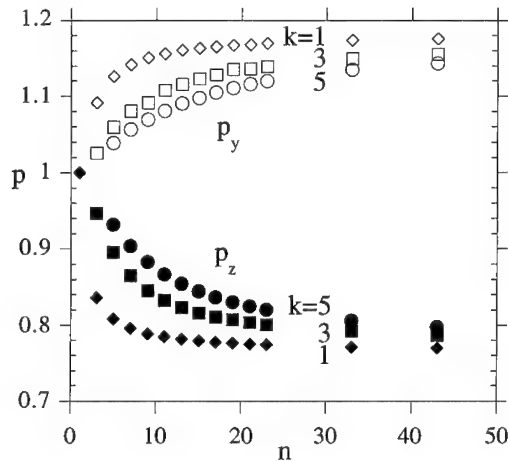
Table III gives the convergence values. A dielectric constant can be determined from these p_y, p_z using the slab expressions given above, and these values are also shown in the table. A denotes the anisotropy $A = (\varepsilon_y - \varepsilon_z)/(\varepsilon_y + \varepsilon_z)$.   These calculations are in good agreement with the work of Lekner and Castle. For thicker samples most of the surface variation takes place in the first two layers. Deviations from ε_{CM} and the anisotropy are seen to vary as β^2.

Table III Convergence values for large n for p_y and p_z for a dipole at the center of the appropriate layer for an n x n x k lattice estimated from calculations for n in the range 11 to 43. $\beta = 0.034$

	p_y	p_z	r	ε_y	ε_z	A
n x n x 1	1.182	.765	1.546	1.507	1.487	.006
n x n x 2	1.173	.771	1.522	1.503	1.493	.003
n x n x 3 layer 1	1.171	.771	1.518	1.502	1.494	.003
n x n x 3 layer 2	1.164	.777	1.499	1.499	1.499	.000
n x n x 5 layer 1	1.166	.773	1.510	1.500	1.495	.002
n x n x 5 layer 2	1.160	.776	1.495	1.497	1.499	.000
n x n x 5 layer 3	1.161	.775	1.497	1.497	1.498	.000

$\beta = 0.1$

	p_y	p_z	r	ε_y	ε_z	A
n x n x 1	1.823	.526	3.468	3.291	2.946	.055
n x n x 2	1.759	.535	3.290	3.211	3.048	.026
n x n x 3 layer 1	1.736	.534	3.250	3.182	3.043	.023
n x n x 3 layer 2	1.685	.542	3.108	3.118	3.137	-.003
n x n x 5 layer 1	1.671	.532	3.139	3.100	3.021	.013
n x n x 5 layer 2	1.626	.534	3.043	3.044	3.045	.000
n x n x 5 layer 3	1.630	.532	3.063	3.048	3.018	.005

THE EFFECT OF SUBSTRATES

The Lekner-Castle (LC) approach has shown that the in-plane summations dominate the calculation of E_{loc}, and this suggests that a substrate will have only a small effect on the polarisation of an overlying layer. Their expresssion above can be generalised for an A layer on a B substrate to $p_z = E_{loc} / E_o = 1/(1-\beta_A\, S_o - \beta_B\, S_1)$ for the A layer, with βA and βB interchanged for the B substrate, and similarly for p_y. The LC values for an infinite layer of A on B calculated with $\beta_A = .034$ and $\beta_B = 0.1$ are $p_{yA} = 1.159$, $p_{zA} = 0.785.$, $p_{yB} = 1.805$, $p_{zB} = .528$. Our calculation for the convergence values gives $p_{yA} = 1.143$, $p_{zA} = .777$, $p_{yB} = 1.810$, $p_{zB} = .530$. Figure 2 shows the size variation of a single A layer and an A layer on a B substrate It can be seen that the depolarising substrate fields have a large effect on the A polarisations when the size is small.

Figure 2
The variation of p_y and p_z for an n x n system as a function of n for an A layer alone and an A layer on a B substrate, with $\beta_A = 0.034$ and $\beta_B = 0.1$.
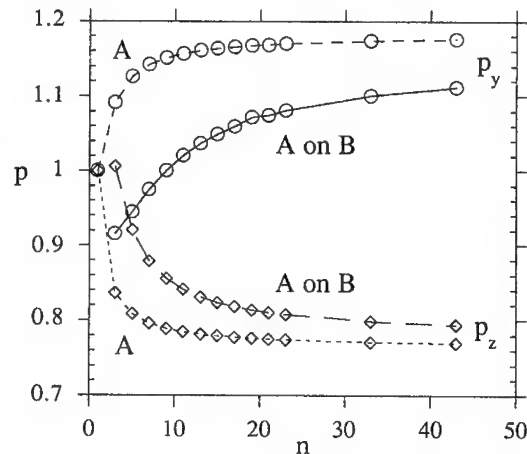
SMALL SYSTEMS AND HEMISPHERICAL BOSSES

A major implication of the calculations shown here is that for slab-shaped systems with n/k smaller than ~10 the depolarisation fields must be taken into account when estimating the

radiation fields. Figure 3 shows the how the depolarising fields develop in the sequence of thickening slab, single layer to cube, for the point A on the center of the outer face, and also shows an example of the variation along the line AO, for a 7 x 7 x k lattice (O the center of the slab).
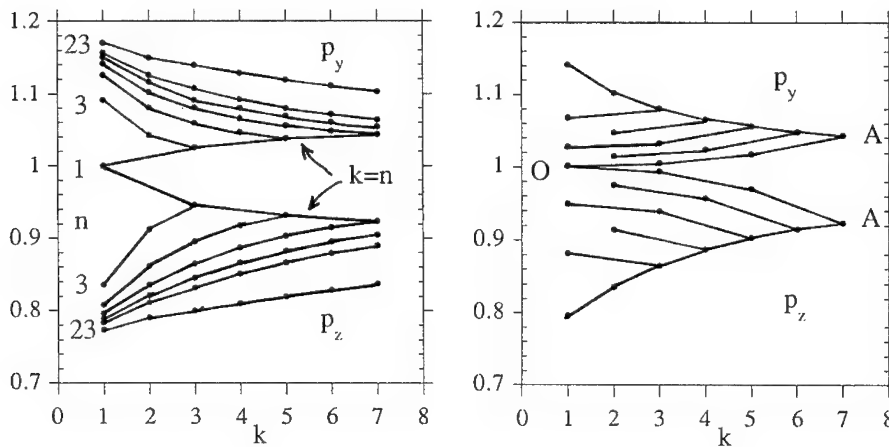
Figure 3 Slab geometry;
p_y and p_z for the point A on the center of the outer face as a function of n and k, for
n = 1, 3, 5, 7, 9, 11and 23, and k = 1 to 7;
and variation along the line AO, for a 7 x 7 x k lattice.
The slab becomes a cube for k = 7.
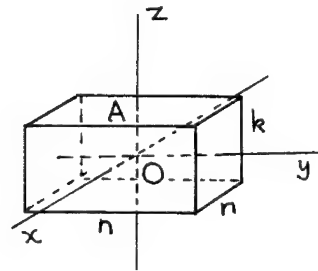
Liquid drops spreading or sitting on solids can be modelled by hemispheres placed on a flat surface. Berreman[9] used a sphere half submerged in a plane semi-infinite medium and found an approximate analytic solution, neglecting the interaction between the sphere and the medium. Spheres near a flat conducting surface were shown by Hunderi and Beaglehole[10] to explain the reflectivity of rough metal surfaces when roughness induced coupling into surface plasmons. Spheres and hemispheres show resonance effects for small negative ε which are equivalent to short range surface plasmons on metal surfaces and resonance effects are also observed in restrahlung structure.

Figure 4 shows the variation of p_y and p_z along the x, y and z axes for a hemisphere of diameter 6 sitting on an 11 x 11 x 1 flat surface (in units of a) placed at z= 0. p_y values are lower and p_z values higher for the dipoles within the hemisphere (shown by the z axis locus) than they are for a flat surface with the same β. The local field within the hemisphere is reduced by the depolarising fields of the charges on the hemisphere surface
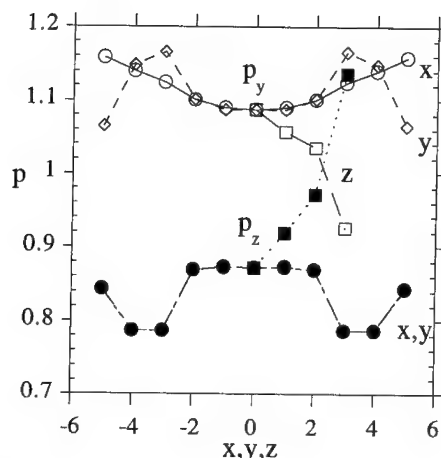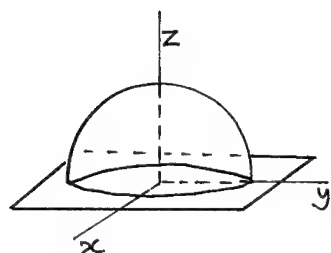
Figure 4   Hemisphere geometry and the variation of p_y and p_z along the x, y and z axes.

The average values for p_y and p_z for the dipoles in the hemisphere are given in Table IV. The values are close to unity. The "flat" columns in the table give the values the dipoles would have if these dipoles were placed on the flat surface. p values near unity produce an equivalent dielectric constant which is very anisotropic (we have assumed $\bar{n}$ for the hemisphere dipoles equals 0.39 that for the layer, corresponding to the ratio 47/121 of the number of dipoles in the hemisphere to the number in the layer).

Table IV Average polarisations for the hemisphere on a plane.

β	$<p_y>$	$<p_z>$	r	p_y flat	p_z flat	ε_y	ε_z
0.034	1.032	.954	1.082	1.156	.785	1.17	1.19
0.1	1.117	.905	1.234	1.649	.553	1.55	1.80

RESPONSE OF THE SURFACE OF A DISORDERED MEDIUM

The capillary wave model has been used in the past to estimate the ellipticity of liquid surfaces, but we show here that this is not a satisfactory procedure. There are clearly two conditions that must be satisfied if the continuum dielectric constant is to be used. The first requires the local fields acting on the dipoles of the medium be unaltered by the roughness. This implies that the surface look flat over lengths no shorter than the typical convergence length ζ_c found in the flat surface simulations. We have found above that these are about 20a. This condition is thus $\zeta_q / \zeta_c \ll 1$. The second condition is that the wavelength of the surface fluctuations is much greater than ζ_c, i.e $q\zeta_c \ll 1$. Together these two conditions require $q \xi_q \lll 1$. In fact for capillary waves on a typical liquid near the triple point q ζ_q has a value ~ 1, and the inequality is not satisfied. We have therefore looked at the local field effects using the self-consistent calculations using dipoles on typical configurations for molecules in a disorderd medium.

85

The first step is the calculation of typical configurations for disordered dipoles near surfaces. One approach we tried was to estimate a surface displacement $\zeta(x,y)$ using the capillary wave theory with summations over waves ζ_q (with random phases) up to a cut-off given by $qd=1$ (with d the molecular diameter). It was thought that we could then fit spheres representing the molecules under this envelope. In fact this was impossible, since the resulting $\zeta(x,y)$ can vary rapidly with x and y, and no sensible distribution of spheres maintaining the medium's density will fit under the envelope. This is therefore a second reason for cutting off the capillary wave spectrum at much longer wavelengths, and using an intrinsic model for the short wave molecule displacements.

We have generated configurations starting with hard spheres on a n x n x k lattice and allow them to move following the standard MC techniques[11]. We have prevented the molecules from diffusing into a vapour space on each side of a slab of dipoles using a confining surface potential $U(z_i) \propto (abs(z_i)-z_0)^2$, where z_0 is given by $k = 2z_0+1$. Once the configuration is randomised we calculate p_{iy} and p_{iz} and r_i for each dipole in the usual way, and have determined $<p_y(z)>$, $<p_z(z)>$ and $<r(z)>$. We have summed only the central portion of dipoles to eliminate the edge effects. These have been compared with values based on the Drude expression found by evaluating $\bar{n}(z)$ and $\varepsilon(z)$, and from these $p_y(z)$ and $p_z(z)$ and r_{CM} using the Clausius-Mossotti slab relationship between ε, $\bar{n}(z)$ and p.

Figure 5 shows an example of 5 configurations of $\bar{n}(z)$ and r(z) for a set of dipoles placed initially on a 43 x 43 x 3 lattice and allowed to relax by the Monte Carlo method. The study of dipoles on the lattice suggests that for this size of slab the polarisations should be within 5% of their saturation value. α in this calculation is $1.26a^3$. The density after relaxation was about $0.5a^{-3}$. The fluctuations in r(z) are much smaller than those in $r_{CM}(z)$ which follow the fluctuations in $\bar{n}(z)$, and this must be due to a smoothing effect of the surrounding dipoles in the z direction.
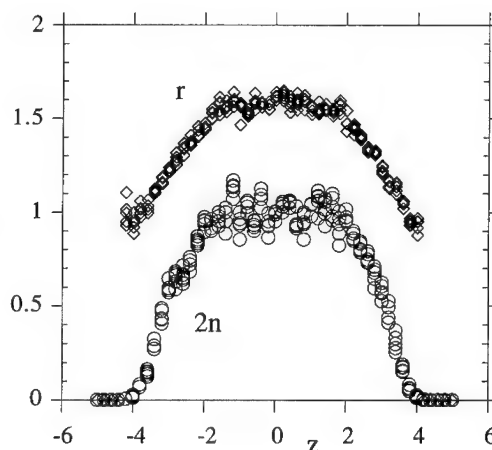
Figure 5
r(z) and n(z) (the latter scaled by a factor of 2) for 5 configurations of the disordered system.

Figure 6 shows r, r_{CM}, p_y, p_z and the CM values for these as a function of density. It can be seen that r initially follows parallel to r_{CM} at low densities, but breaks away and grows less

rapidly as the density increases. This difference is mainly due to $p_z(z)$ being larger than $p_z(CM)$. r becomes closer to r_{CM} at low densities as the length of the slab increases. From this figure it is also clear that the summation entering the ellipticity $\Sigma\ (p_{iy} - \varepsilon\ p_{iz}\ )$ will have a smaller value than estimated from CM values for p. In practice a measured ellipticity is interpreted as an interface thickness uing the Drude expression. The calculations here suggest that the thickness will be underestimated this way.
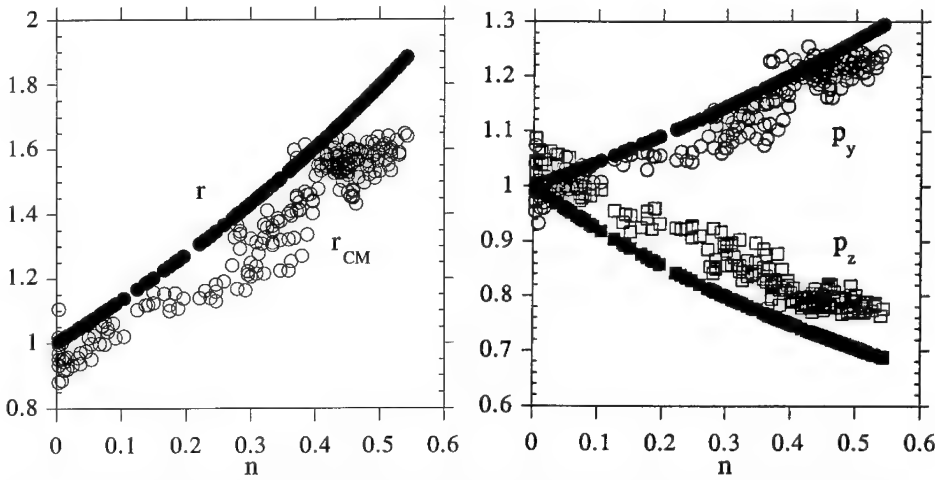
Figure 6 shows r and r_{CM} (left) and p_y and p_z and the CM values for these (right) as a function of density.

There are substantial fluctuations in the magnitude and direction of the individual induced dipoles as the local fields vary from one dipole to another. Figure 7 shows a scatter plot of the x-z projection (p_{ix}, p_{iz}) for the applied field in the y direction with an average $p_{iy} \sim 1.2$. The scatter indicates fluctuations in orientation of the induced dipoles of up to 20° from the y direction, and a similar scatter is found for the electric field in the z direction.
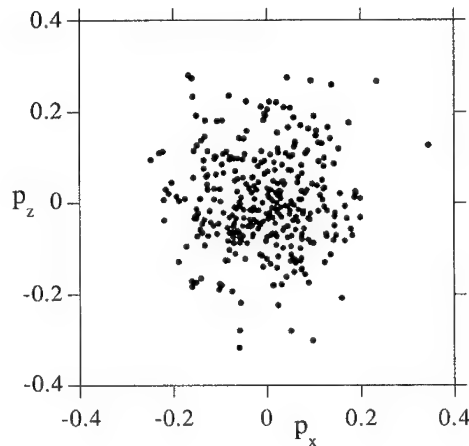
Figure 7 Fluctuations in the direction of p_{iy} are indicated by a scatter plot of p_{iz} versus p_{ix}, with $p_{iy} \sim 1.2$.

SUMMARY

We have seen that for small systems the depolariing fields can alter the local field acting on a dipole in a major way. It is essential to take this into account rather than use the macroscopic dielectric constant when analysing optical surface studies. One particular example we have given is of a hemisphere on a flat surface, which models liquid drops and surface roughness. We have also looked at the surface of a disordered medium such as a liquid where disordered surface dipole experience fields different from those inside the medium. Here the Drude transition layer approach should provide an estimate of the reflectivity which is better than that based on the capillary wave model, but a dielectric constant which depends solely upon an average depth-dependent density omits disorder-induced fluctuations of the dipoles. Bottcher[12] gives a discussion of some of the limitations of the Clausius-Mossotti theory, and of Kirkwood's statistical extension.

ACKNOWLEDGEMENTS

REFERENCES

1   P.Drude, Theory of Optics (Dover,New York 1959).

2   see references in J.Lekner, Mol.Phys.**49**, 1385 (1983).

3   D.Beaglehole, Physica **100B**, 163 (1980).

4   J.Lekner and P.J.Castle, Physica **101A**, 89-98 (1980).

5   P.J.Castle and J.Lekner, Physica **101A**, 99-11 (1980).

6   J.Lekner, Mol.Phys. **49**, 1385-1400 (1983).

7   W.H.Press, S.A.Teukolsky, W.T.Vetterling and B.P.Flannery, Numerical Recipies in C, 2nd ed (Cambridge University Press, London,1992) p166.

8   A. Seleznyova (private communication).

9   D.W. Berreman, Physical Review **163**, 855 (1967).

10   O.Hunderi and D.Beaglehole, Physical Review **B2**, 321 (1970).

11   M.P. Allen and D.J. Tildesley, Computer Simulation of Liquids (Clarendon Press, Oxford, 1987)

12   C.J.F.Bottcher, Theory of Electric Polarisation (Elsevier, Amsterdam, 1952), Chapter 7

THE MESOSCOPIC DESCRIPTION OF PRESSURE AND VELOCITY PROFILES NEAR PLANAR WALL IN WATER SOLUTIONS

ANATOL BRODSKY AND WILLIAM P. REINHARDT
Department of Chemistry, University of Washington, Seattle, WA 98195, USA

Abstract

The stress tensor for polar solutions is constructed starting from a nonlocal and nonlinear Landau free energy functional. Explanations of some puzzling properties of liquids near interfaces are proposed.

1. Introduction. Among intriging new experimental results concerning properties of water, water solutions, and other liquids near interfaces are discoveries of sharp desnity increases near metallic surfaces [1] and the singular dynamics of confined liquids under shear [2]. The latter experiments show a substantial increase of the effective viscosity η_{eff} near surfaces and a non-Newtonian behavior which displays a flow-dependent η_{eff}:

$$\eta_{eff} \sim \left(\frac{|v|}{d}\right)^{-a} \tag{1}$$

where v is the shear velocity and d the film thickness. Reported values [4] of the exponent a have been around $a \simeq 2/3$, although higher values $a \simeq 1$ have been also observed.

The most advanced theoretical descriptions of liquid properties near walls are based on an introduction of Landau order parameter free energy functionals and time-dependent Ginzburg-Landau equations [1,3]. In this communication we formulate and apply a mesoscopic order paramter description of water near an electrical surface. As the vector order parameter we will take polarization (polarization density) $\bar{P}(\bar{r})$ since the electrostatic interactions in a polar fluid system have the longest range. With nonpolar liquids the longest correlation lengths correspond to the orientational order parameters. In contrast to previous analyses we will not assume, in view of results of [1], that water on mesoscopic distances from surfaces is incompressible. Another principal new element is a parameterization of properties of surface layers, which allows the possibility of a continuous ordering transition at the surface. Such surface layer behavior were confirmed earlier in our computer calculations and is in agreement with electrochemical experiments [4].

2. The Landau Functional. We take the Landau free energy density functional $F_B\{\bar{P}(\bar{r})\}$ for a polar bulk liquid in the following form

$$F_B = F_{BO}(\bar{r}) + F_{B\bar{P}}\{\bar{P}(\bar{r})\} ;$$

$$F_{BP} = \frac{\bar{D}^2}{8\pi} - \bar{P}\bar{D}_{(\bar{r})} + \frac{2\pi\varepsilon(\rho,T)}{\varepsilon(\rho,T)-1}\left[\bar{P}^2 + V^B(\bar{P}) + \zeta^2(\rho,T)\left(\frac{\partial P_i}{\partial r_k}\right)^2\right],$$

$$i, k = 1,2,3 . \tag{2}$$

Here and in what follows summation over repeated indexes is assumed. In (2) F_{BO} is the Helmholtz free energy density in the absence of mesoscopic polalization and $\bar{D}(\bar{r})$ is the dielectric displacement. The nonlinear "potential"

$$V^B(\bar{r}) = a_2(\rho,T)(\bar{P}^2)^2 +... \tag{3}$$

takes into account the dielectric saturation effect and $a_2 \sim P_M^{-2}$ where P_M is the maximum possible value of the polarization. The function $\zeta(\rho,T)$ of density $\bar{\rho}(\bar{r})$ and temperature T is the longest correlation length in the bulk solution. For $\zeta 2 = 0$ and $V^B = 0$ the minimumization of (2) with respect to $P(\bar{r})$ leads to the standard macroscopic expression for F_B if $\varepsilon(\bar{r})$ is assumed equal to the dielectric constant of linear macroscopic electrostatics. The important point is that $\bar{P}(\bar{r})$ is assumed to be a superposition of only long-wave components of polarization in the sense developed in [5]. At the same time the coefficients $\varepsilon(\rho,T)$, $\zeta(\rho,T)$, $a_n(\rho,T)$ depend only on short range interactions and are correspondingly considered as independent of the values of $\bar{P}(\bar{r})$. The expression (2) can give a reasonable description of solution behavior only at mesoscopic distances from interfaces. In order to describe surface layer properties we introduce the surface part of the full free energy functional in the form of a two-dimensional integral over the surface density $F_S\{\bar{P}^0(\bar{r}'')\}$, $\bar{r}'' = (r_1, r_2)$, where $\bar{P}_i^0(\bar{r}'')$ (i = 1,2,3) is the averaged polarization vector near the interface. Averaging is over mesoscopic distances in the directions $\bar{r}''$ parallel to the interface and over the surface layer width, λ, in the normal (r_3) direction. In the case of sufficiently concentrated strong electrolyte solutions λ can be taken as equal to the width of the Helmholtz dense double layer, and thus may be as small as two to four water molecule diameters. In the generalized surface capacitor model F_S can be represented as follows

$$F_S = \lambda \left(2\pi Q^2 - \overline{QP}^0 + V^S(\bar{P}^0) + \zeta_s^2 \left(\frac{\partial P_i^0}{\partial r_k''} \right)^2 \right) \tag{4}$$

where Q is the surface charge density and ζ_s is the surface correlation length. The general strucure of the surface potential $V^S(\bar{P}^0)$ for water solutions is in accord with results [4] related to the formation of surface liquid crystal-like structures. V^S can be represented in parameter intervals near surface transition points $Q = Q_{cr}^\kappa$ in the following form

$$V^S = \alpha^\kappa(\rho, T)\left(Q - Q_{cr}^\kappa\right)\left(P_i^0\right)^2 + \beta^\kappa(\rho, T)\left(\left(P_i^0\right)^2\right)^2 , \tag{5}$$

where Q_{cr}^κ is the critical surface charge. We will connect the functions $\bar{P}(\bar{r})$ and $\bar{P}^0(\bar{r}'')$ by the "matching" condition

$$P_i(\bar{r})\Big|_{r_3 = 0} = P_i^0(\bar{r}_\parallel) . \tag{6}$$

Equilibrium is determined by vanishing variations of the full grand free energy functional Ω constructed from (2) and (4) with additional conditions (6) near interfaces. We find the variational solutions in two steps, I and II below, by determining first the optional value of P_{opt} with fixed $\bar{P}^0$, and then $\bar{P}^0$ itself.

I.
$$h_i(\bar{r}) \equiv \frac{\delta}{\delta P_i} \int_V \Omega_B(\bar{r}) d^3\bar{r} = 0 \Big|_{T,D,\mu,\bar{P}^0}$$

90

II.
$$\frac{\delta}{\delta P_i^0}\left[\left.\int\limits_V \Omega(\bar{r})\middle|d^3r + \int\limits_s \Omega_s(\bar{r}'')d^2r''\right]\right|_{T,D,\mu,\bar{P}=\bar{P}_{opt}\{\bar{P}^0\}} = 0 \qquad (7)$$

where $\Omega_{B,S}$ are the bulk and surface grand free energy densities , $\bar{P}_{opt}(\bar{P}^0)$ is the solution of the equation I, and μ is the water chemical potential. The equation II in (7) has a quasi-twodimensional form.

3. The Stress Tensor. Near equilibrium it is possible to interpret nonzero $h_i(\bar{r},t)$ as a mesoscopic molecular polarization field impeding dynamical processes which would take the system away from equilibrium. The Ginzburg-Landau equation for $P_i(\bar{r},t)$ has the following form

$$\gamma \frac{dP_i(\bar{r},t)}{dt} = \gamma\left(\frac{\partial P_i}{\partial t} + \text{div } \bar{v}\, P_i\right) = -h_i\{P_i\} \qquad (8)$$

where $\bar{v}_{(\bar{r})}$ is the flow velocity and coefficient γ is of dynamical origin and has the order of magnitude of dipole relaxation time. It is necessary to consider Eq. (8) in combination with the hydrodynamical equations

$$\frac{\partial \bar{D}}{\partial t} = 4\pi \ \bar{j}; \quad \frac{\partial \rho v_i}{\partial t} = \frac{\partial \sigma_{ik}}{\partial r_k}; \quad \frac{\partial \rho}{\partial t} + \text{div } \rho\bar{v} = 0 \ ;$$

$$\frac{dS}{dt} = \frac{\partial S}{\partial t} + \text{div } S\bar{v} = \frac{2R}{T} \qquad (9)$$

where S is the entropy density, $\bar{j}$ is the sum of the ion currents and the displacement current, σ_{ik} is the stress tensor and R is the dissipation function. Analysis of the energy conservation equation, analogous to that performed in liquid crystal theory [6], leads to the following expression for σ_{ik}.in the case of small deviaitons from the equilibrium

$$\sigma_{ik} = \delta_{ik}\left(-p_0(\rho,T) + F_{BP} - \rho\left.\frac{\partial F_{BP}}{\partial\rho}\right|_{T,\bar{P}} - \frac{1}{4\pi}E_\ell D_\ell\right) -$$

$$-\rho v_i v_k + \frac{1}{2\pi}(E_k D_i + E_i D_k) - 2\zeta^2\frac{\partial P_\ell}{\partial r_k}\frac{\partial P_\ell}{\partial r_i} \ ;$$

$$E_i = \frac{1}{4\pi}\left.\frac{\partial F_B}{\partial D_i}\right|_{\rho,T,\bar{P}} \qquad (10)$$

where $p_0(\rho,T)$ is the pressure in the liquid bulk with density ρ and temperature T in the absence of external fields and polarization. The details of the technically complicated derivation of (10) will be published elsewhere.

4. Force. Density. Pressure and Viscosity. In the case of equilibrium when $\bar{v} = 0$ and $h_i = 0$ it follows from (10) that, at constant temperature T under conditions of charge neutrality in the bulk,

91

$$-\rho \ \mathrm{grad}_i\,\mu \ = -\rho \ \mathrm{grad}_i\!\left[\mu_0 - \left.\frac{\partial F_{BT}}{\partial\rho}\right|_{T,\overline{P}}\right] = 0 \tag{11a}$$

and correspondingly

$$\mu = \mu_0(\rho,T) - \left.\frac{\partial F_{BT}}{\partial\rho}\right|_{T,\overline{P}} = \mu_0(\rho,T) \ - $$

$$-2\pi\left\{\frac{\partial}{\partial\rho}\,\frac{\varepsilon(\rho,T)}{\varepsilon(\rho,T)-1}\left[\overline{P}^2 + V^B(\overline{P}) + \zeta^2(\rho,T)\left(\frac{\partial P_i}{\partial r_k}\right)^2\right] + $$

$$+\frac{\varepsilon(\rho,T)}{\varepsilon(\rho,T)-1}\left[\frac{\partial\zeta^2}{\partial\rho}\left(\frac{\partial P_i}{\partial r_k}\right)^2 + \frac{\partial a_2}{\partial\rho}(\overline{P}^2)^2 + ...\right]\right\} = \mathrm{const.} \tag{11b}$$

where $\mu_0(\rho,T)$ is the bulk chemical potential. The equations $h_i = 0$, (6) and (11) allow calculation of both $\rho(\bar{r})$ and $\bar{P}(\bar{r})$. The expression (11b) is a generalization of the corresponding Helmholtz expression for electrostatic forces in the media [7]. In contrast to the Helmholtz expression it depends not only on $\frac{\partial\varepsilon(\rho,T)}{\partial\rho}$ but on the derevatives $\frac{d\zeta^2(\rho,T)}{d\rho}$, $\frac{\partial a_n(\rho,T)}{\partial\rho}$ as well. Since these derevatives in (11) give the contributions of different signs, the mesoscopic electrostatic forces can have, in different parameter ranges, different behavior and are not only repulsive as in classical *DLVO* theory [8].

Due to the finite correlation length Eq. (11a) predicts that $\rho(\bar{r})$ increases near an electrode. Such an increase is especially significant if there are nonuniformities parallel to the electrode surface, which can exist even on atomically flat surfaces due to spontaneous symmetry breaking in surface liquid crystal phases. In such a case, simple estimates give the value of the effective pressure p_{ef} near the wall

$$p^{ef} \sim \frac{\zeta^2}{\delta^2}\,P_M^2 \tag{12}$$

which corresponds to the very high value $\sim 10^4$ atm if the correlation length δ along the surface is of the same order as ζ. It follows from (7), that near surface phase transition points, $Q \cong Q_{cr}$, the behavior of the inverse differential capacitance C^{-1} must be singular

$$C^{-1} \sim \frac{\partial^2\Omega}{\partial Q^2} \sim \frac{1}{|Q-Q_{cr}|^{1-\alpha}} \tag{13}$$

where α is the critical index of the surface phase transition.

In the presence of flows even if $v(\bar{r}) = 0$ on the boundaries the dependence on velocity derivative $\frac{dv_i}{dr_k}$ in the bulk will enter in the solution of equations (7)-(10). In the case of shear viscosity, the quantaty $\frac{v}{d}$ will enter in this step as a governing parameter. Thus, by analogy with (13),

$$\eta_{\text{eff}} \sim \frac{\partial^2 \Omega}{\partial \left(\frac{\nu}{d}\right)^2} \sim \frac{1}{\left| Q - Q_{cr} + k\zeta\sqrt{\rho}\,\frac{\nu}{d} \right|^{1-\alpha}} \sim$$

$$\sim \begin{cases} \dfrac{1}{\left| Q - Q_{cr} \right|^{1-\alpha}} & \text{for} \quad \left| \dfrac{Q - Q_{cr}}{k\sqrt{\rho}} \right| > |\nu| \dfrac{\zeta}{d} \\[4mm] \dfrac{1}{|\nu|^{1-\alpha}} & \text{for} \quad \left| \dfrac{Q - Q_{cr}}{k\sqrt{\rho}} \right| < |\nu| \dfrac{\zeta}{D} \end{cases} \tag{14}$$

where k is a dimensionless constant, thus reproducing (1) by noting, for example, that for the two dimensional Ising model $\alpha = 0$, and for the hard hexagon model $\alpha = 1/3$ [9]. The result thus encompasses both behavior (η_{eff} independent of ν) and the anamolous behavior of Eq. (1).

References

1. M. Toney, et.al., Nature **368**, 444 (1994). A large water density increase near walls has also been found in computer simulation: e.g., E. Spohr, Chemical Physics **191**, 87 (1990).

2. S. Granick, Science **253**, 1379 (1992).

3. P. Hohenberg and B. Halperin, Rev. Mod. Phys. **49**, 435 (1977); T. Koga, et. al., Physica **A198**, 473 (1993) and literature therein.

4. A. Brodsky, M. Watanabe and W. Reinhardt, in Microscopic Models of Electrode-Electrolyte Interfaces, edited by J. Kalley and L. Blum, (The Electrochemical Society, Inc., Pennigton, 1993) pp. 115 and literature therein.

5. L. Landau and E. Lifshitz, Statistical Physics, Part I, (Pergamon, Oxford, 1984) Ch. 14.

6. L. Landau and E. Lifshitz, Theory of Elasticity, 3rd ed. (Pergamon, Oxford, 1986) Ch. 6.

7. L. Landau and E. Lifshitz, Electrodyanmics of Continuous Media, 2nd ed. (Pergamon, Oxford, 1984) p. 62.

8. J. Israelachvili, Intermolecular and Surface Forces, 2nd ed., (Academic, London, 1992).

9. R. Baxter, Exactly Solved Models in Statistical Mechanics, (Academic, London, 1982).

MONTE CARLO SIMULATION OF A LATTICE MODEL OF MICROEMULSIONS IN POROUS MEDIA

PARISA NOWROOZI AND MUHAMMAD SAHIMI
Department of Chemical Engineering, University of Southern California, Los Angeles, CA
90089-1211

ABSTRACT

Monte Carlo simulations are used to study various properties of a new lattice model of microemulsions. In particular, we calculate the critical exponent β of the order parameter (water concentration) and the correlation length exponent ν, and find them to be in excellent agreement with those of the 3D Ising model, and also in agreement with the experimental measurements. However, when the same exponents are calculated for the microemulsions in a porous medium, they do *not* agree with those of either the dilute or the random-field Ising model.

INTRODUCTION

Microemulsions are complex fluids that contain large amounts of two immiscible liquids such as water and oil and one or more surfactants. The surfactant molecule has a polar, hydrophilic head group attracting water and an apolar, hydrophobic tail more attracted by oil. Microemulsions exhibit very complex phase behavior [1], and show a rich variety of self assembly of complex structures such as micelles (oil droplets immersed in water, or vice versa) and bicontinuous regions [2]. Because of their chemical nature surfactant molecules tend to be localized at the water-oil interface, thereby reducing the interfacial tension to very small values. For this reason, microemulsions have also been advocated as agents for enhanced oil recovery from underground reservoirs [3]. Moreover, surfactant flushing of porous media is currently being considered [4] as a method of remediating contaminated soils. Knackstedt and Ninham [5] suggested recently that variation of component ratios in a class of microemulsions can yield *parameter-free* model porous media of prescribed microstructure, thereby allowing for the first time *independent* measurements of transport and elastic properties in a well-defined porous medium.

Many models have been proposed for microemulsions [1]. Some of the most interesting ones are lattice models, the simplest of which was first proposed by Wheeler and Widom [6,7], which was a spin-$\frac{1}{2}$ Ising model with nearest-neighbor ferromagnetic interactions. In this model molecules resided on the bonds of a lattice, with a pair of up spins representing water, and pairs of down spins and antiparallel spins corresponding to the oil and surfactant, respectively. Extensive Monte Carlo studies of this model [8] indicated that it can predict some qualitative features of microemulsions. However, in this model all molecules had the same length of one bond. Recently, Stauffer *et al.* [9] generalized the original Wheeler-Widom model by allowing the amphiphilic polymers to have lengths longer than one bond. A somewhat different model was proposed by Larson [10] in which diagonal interaction between the spins was also allowed. The purpose of this paper is two-fold. (1) We study the scaling properties of this model near a critical temperature and compare the results with the experimental data [11], to demonstrate the capability of the model for reproducing such

data. (2) We investigate the same scaling properties in a disordered porous medium since, as discussed above, microemulsions have been advocated as enhanced oil recovery and soil remediation agents. A lattice model of microemulsions in a porous medium also represents a spin model in a disordered system, a notoriously difficult problem, and we show that the scaling properties of this model do *not* agree with those of Ising models in a disordered medium [12], or with those of random-field Ising models [13]. Thus, new theories may have to be developed for explaining our results.

THE MODEL AND MONTE CARLO SIMULATION

The model consists of a $L \times L \times L$ simple-cubic lattice in which each site is either an Ising spin up or down, or it may belong to a polymer chain representing the amphiphilic molecules. Each chain is a constrained self-avoiding walk of n sites in which the first site is an up spin, the last site a down spin, and the remaining $n - 2$ interior sites are neutral (zero spin). The interaction energy is $E = -J \sum S_i S_j$, with $S_i = \pm 1$, with the sum running over all nearest-neighbor sites on the lattice. This same equation also holds for the polymer chains and their interactions with themselves and with other neighboring molecules. The interior sites of the polymer always have $S_i = 0$, and the chain ends and other molecules always have $S_i = \pm 1$. Since there is no "magnetic field" in the system, the chemical potentials of oil and water can be chosen such that they are in coexistence at temperatures T below the critical demixing temperature T_c. We flip the spins not attached to the polymer chains with a probability proportional to $\exp(-\Delta E_s/kT)$ (i.e., Glauber dynamics), where ΔE_s is the energy change caused by the spin flip. To move a polymer chain, one end of it is selected randomly and is moved to a randomly-selected neighbor. If that neighbor belongs to another polymer or, in the case of microemulsions in a porous medium, belongs to the solid matrix of the medium, the chain does not move, but if it does move, its remaining $n - 1$ sites trail the moving end like a slithering snake. The site made free by the motion of the polymer is given the previous spin value of the site now occupied by the moving end. The probability of moving the polymer is $\exp(-\Delta E_p/kT)$, where ΔE_p is the energy change caused by the movement of the whole chain. Thus, the sites associated with the polymers are updated with a Kawasaki dynamics. Helical boundary conditions in one direction and periodic ones in the other two are used. The concentration of the polymers is taken to be small, typically 10% of the lattice sites belonged to the polymers, randomly distributed throughout the lattice. As the model of a porous medium we use a percolation system [14] in which a randomly-selected fraction q of the sites are designated as the solid matrix of the medium, and the rest represent the pore space. Thus, $1 - q$ is the porosity of the system, and we vary q between 0 and q_c, the percolation threshold above which no sample-spanning pore space exists. No interaction was allowed with the matrix sites. The critical demixing temperature now depends on q.

Two critical exponents were calculated and were found to depend on q. One was ν, the critical exponent of the correlation length ξ, defined by

$$\xi \sim [T_c(q) - T]^{-\nu(q)} , \tag{1}$$

for T close to $T_c(q)$. To estimate $\nu(q)$ we used the standard finite-size scaling theory according to which

$$T_c(q, L \to \infty) - T_c(q, L) \sim L^{-1/\nu(q)} , \tag{2}$$

where $T_c(q, L)$ is the effective critical temperature of a $L \times L \times L$ lattice. Various values of L were used and the results were averaged over 100 different realizations of the system.
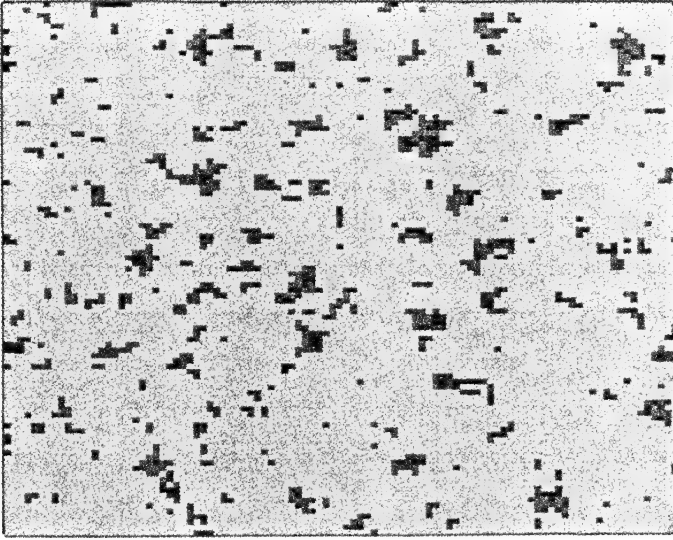
Figure 1: The equilibrium distribution of the oil (dark gray), water (the light gray background) and polymer (black) molecules in the middle plane of a $150 \times 150 \times 150$ cubic lattice.

We then plotted $T_c(q, L)$ versus $L^{-1/\nu(q)}$, and found that value of $\nu(q)$ which made the plot a straight line, which also yielded an estimate of $T_c(q, \infty) = T_c(q)$. We also calculated β, the exponent associated with the order parameter M, which in our model is just the water concentration. Near $T_c(q)$ one has

$$M \sim [T_c(q) - T]^{\beta(q)} . \tag{3}$$

To estimate β, we calculated M for several temperatures close to $T_c(q)$. A plot of $\ln M$ versus $\ln [T_c(q) - T]$ would then yield an estimate of β. To eliminate finite-size effects, we used $150 \times 150 \times 150$ lattices, and averaged the results over up to 150 different realizations. In all cases a very large number of iterations (time steps) were used to allow the system reach equilibrium. Some of our results were published in a recent Letter [15].

RESULTS AND DISCUSSION

Figure 1 shows the equilibrium distribution of water, oil, and the polymers in the middle plane of a $150 \times 150 \times 150$ cubic lattice. As expected, the amphiphilic molecules distribute themselves at the interface between the oil and the water. Our extensive simulations yielded $\nu(q = 0) \simeq 0.625 \pm 0.003$ and $\beta(q = 0) \simeq 0.335 \pm 0.015$, in excellent agreement with those of the 3D Ising model [16], $\nu \simeq 0.6305 \pm 0.0025$ and $\beta \simeq 0.3265 \pm 0.0025$. Moreover, our estimate of $\beta(q = 0)$ is in good agreement with the experimental estimate of Aschauer and Beysens [11] who used a ternary microemulsion consisting of water, benzene, and benzyldimethyl-n-hexadecyl ammonium chloride, and estimated that $\beta \simeq 0.34$. It has been argued by some researchers [17] that the critical exponents of ternary fluid mixtures
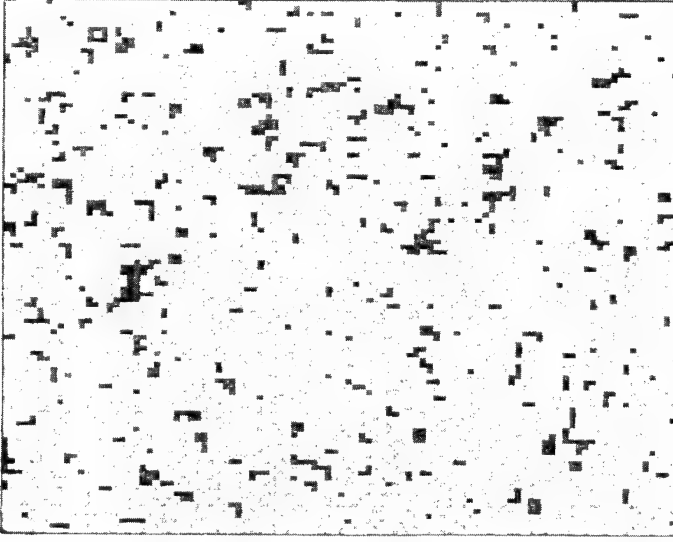
Figure 2: The equilibrium distribution of the oil (light gray), water (the white background) and polymer (dark gray) molecules in a porous medium with a porosity of 0.70. Black area denotes the solid matrix of the medium.

should be Fisher-renormalized, i.e. β(ternary)= β(Ising)/[1-α(Ising)], where α is the critical exponent of the specific heat. This relation then predicts that β(ternary)$\simeq 0.37$, in disagreement with our result. One might argue that the net effect of having fixed spins at either end of the polymers might be making the observation of the Fisher-renormalized exponents more difficult. However, our extensive simulations provided no evidence for such exponents, although we cannot rule this possibility out completely.

Figure 2 shows the equilibrium distribution of the oil, water and amphiphilic molecules in the middle plane of a $150 \times 150 \times 150$ cubic lattice, in which 30% of the sites have been designated as the solid matrix of a porous medium (thus the porosity of the medium is 0.70). Although the Widom model [7] was previously studied in a percolation system [18], no critical exponent was calculated. Our simulations of the present model show that for all values $0 < q < q_c$ one obtains the *same* $\beta(q)$ and $\nu(q)$ which are, however, different from the corresponding values for $q = 0$. For example, Fig. 3 presents our results for $q = 0.25$, from which we obtain $\beta(q) \simeq 0.47 \pm 0.01$, while our results for $T_c(q = 0.25, L)$ yielded $\nu(q) \simeq 0.575 \pm 0.015$. These results do not agree with those of the 3D dilute Ising model, obtained by Heure [12] with extensive simulations. Field-theoretic renormalization [12] also predicts universal exponents for the dilute Ising model for $0 < q < q_c$, and in particular $\nu \simeq 0.67$ and $\beta \simeq 0.35$ for the 3D case, also in disagreement with our results. At $q = q_c$, where one has percolating fractal structures, we expect to have a different set of critical exponents than that for $0 < q < q_c$, although our results for $q = q_c$ are not yet accurate enough to yield precise estimates of the exponents. We point out that near and at q_c one has anomalous diffusion which makes the motion of the polymers very difficult, and thus one needs very long simulations to achieve equilibrium. Note that unlike the 3D dilute
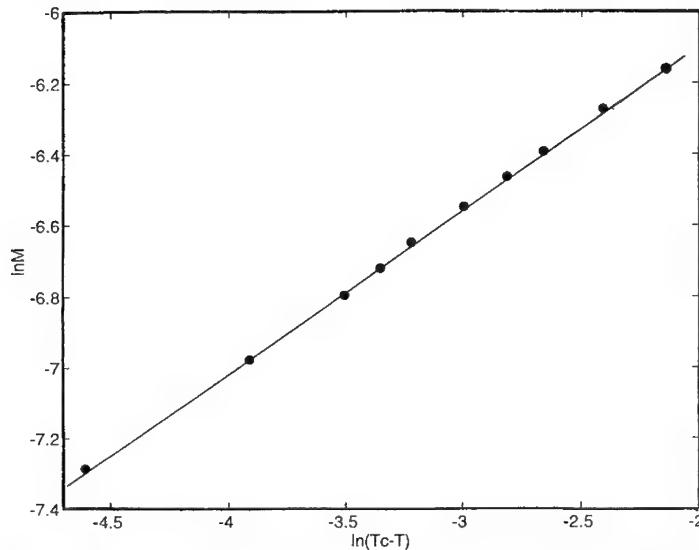
Figure 3: The equilibrium magnetization (water concentration) M versus the temperature T in a porous medium whose porosity is 0.75.

Ising model whose scaling properties were controversial for several years [12], and until very recently had appeared to be continuously varying with q for $0 < q < q_c$, our results provide clear evidence for *three* distinct sets of critical exponents, one for $q = 0$, one for $0 < q < q_c$, and one for $q = q_c$.

de Gennes [19] suggested that fluid mixtures in disordered porous media may be described by the random-field Ising (RFI) model [13] (i.e., disorder is equivalent to a random field). There has been experimental evidence both in favor of his proposal [20] and against it [21], and thus the matter has remained controversial. Since in the present model one has fixed spins at either end of the polymer chains, one might argue that the model is some sort of annealed (coupled) RFI model. The coupling is caused by the fact that each up spin has a down spin not too far away. However, our results, obtained with a well-defined and realistic model of a ternary fluid mixture in a well-defined model porous medium indicate that, at least for our system there seems to be no relation between the scaling behavior of our ternary fluid mixture in the porous medium and that of RFI model for which [13] $\nu \simeq 1.5$. This does not exclude the possibility that some aspects of fluid mixtures in porous media might be described by a RFI model. In a future paper [22] we will present the complete details of our simulations and results for $0 \leq q \leq q_c$, and investigate other aspects of this problem.

ACKNOWLEDGMENTS

REFERENCES

1. W. M. Gelbart, A. Ben-Shaul and D. Roux (eds.), *Micelles, Membranes, Microemulsions, and Monolayers* (Springer Verlag, Heidelberg, 1994).

2. L. E. Scriven, *Nature* **63**, 123 (1976).

3. R. L. Reed and N. R. Healy, in *Improved Oil Recovery by Surfactant and Polymer Flooding*, edited by D. O. Shah and R. S. Schechter (Academic Press, London, 1977).

4. A. S. Abdul and C. C. Ang, *Ground Water* **32**, 727 (1994).

5. M. A. Knackstedt and B. W. Ninham, *Phys. Rev. E* **50**, 2839 (1994).

6. J. C. Wheeler and B. Widom, *J. Am. Chem. Soc.* **90**, 3064 (1969).

7. B. Widom, *J. Chem. Phys.* **84**, 6943 (1986).

8. For a review see, D. Chowdhury and D. Stauffer, *Physica A* **186**, 70 (1992).

9. D. Stauffer, N. Jan and R. B. Pandey, *Physica A* **198**, 401 (1993); D. Stauffer, N. Jan, Y. He, R. B. Pandey, D. G. Marangoni, and T. Smith-Palmer, *J. Chem. Phys.* **100**, 6934 (1994); N. Jan and D. Stauffer, *J. Physique II* **4**, 345 (1994).

10. R. G. Larson, *J. Chem. Phys.* **96**, 7904 (1992).

11. R. Aschauer and D. Beysens, *Phys. Rev. E* **47**, 1850 (1993); *J. Chem. Phys.* **98**, 8194 (1993).

12. H.-O. Heuer, *J. Phys. A* **26**, L333 (1993).

13. H. Rieger and A. P. Young, *J. Phys. A* **26**, 5279 (1993).

14. M. Sahimi, *Rev. Mod. Phys.* **65**, 1393 (1993); *Applications of Percolation Theory* (Taylor and Francis, London, 1994); *Flow and Transport in Porous Media and Fractured Rock* (VCH, Weinheim, Germany, 1995).

15. M. Sahimi and P. Nowroozi, *Phys. Rev. Lett.* **73**, 1182 (1994).

16. J. C. Le Guillou and J. Zinn-Justin, *J. Physique Lett.* **46**, L137 (1985).

17. P. Honorat, D. Roux, and A.-M. Bellocq, *J. Physique Lett.* **45**, L961 (1984).

18. D. Stauffer, J. S. Ho, and M. Sahimi, *J. Chem. Phys.* **94**, 1385 (1991).

19. P. G. de Gennes, *J. Phys. Chem.* **88**, 6469 (1984).

20. S. B. Dierker and P. Wiltzius, *Phys. Rev. Lett.* **58**, 1865 (1987); B. J. Frisken and D. S. Cannell, *Phys. Rev. Lett.* **69**, 632 (1992); A. P. Y. Wong, S. B. Kim, W. I. Goldburg, and M. H. W. Chan, *Phys. Rev. Lett.* **70**, 954 (1993).

21. F. Aliev, W. I. Goldburg, and X.-l. Wu, *Phys. Rev. E* **47**, R3834 (1993).

22. P. Nowroozi and M. Sahimi, *J. Chem. Phys.* (to be published).

THE APPLICATION OF THE X-RAY SURFACE FORCES APPARATUS (XSFA) TO STUDIES OF CONFINED COMPLEX FLUID SYSTEMS.

I. KOLTOVER*, S. H. J. IDZIAK*, C. R. SAFINYA*
S. STEINBERG**, J. N. ISRAELACHVILI** and K. S. LIANG***
*Materials and Physics Departments, University of California at Santa Barbara, Santa Barbara, CA 93106
** Chemical Engineering and Materials Departments, University of California at
Santa Barbara, Santa Barbara, CA 93106
*** Exxon Research and Engineering Co., Annandale, NJ 08801

ABSTRACT

We report here on the application of the new technique of the X-Ray Surface Forces Apparatus[1-3] (XSFA) to the study of the smectic liquid crystal 8CB (4-cyano-4'-octylbiphenyl) and a zwitterionic polyisoprene melt. The XSFA allows one to study the structure of fluid films under confinement and flow using intense synchrotron x-ray radiation. The above systems were investigated with the distances between the confining surfaces ranging from 0.4μm to a few tens of microns. Two different kinds of confining surfaces were used leading to different structural behavior of the samples as a function of the confining gap.

INTRODUCTION

The new X-Ray Surface Forces Apparatus (XSFA) developed by our groups allows the study of very thin confined complex fluid films under well-controlled experimental conditions of precisely measured confining gaps and variable shear flow applied to the sample. In particular, we can conduct synchrotron x-ray diffraction studies of fluids in the "meso-scale" size regime between about 4000 Å and tens of micrometers. The first application of this technique to investigate the structure of a smectic liquid crystal under confinement and flow[1-3] has shown unexpected and interesting results. The behavior of the confined liquid crystal under flow turned out to be very different from the previously studied bulk non-equilibrium behavior,[4] with the effects of confinement dominating the flow-induced alignment at small confinement gaps.

Confinement of complex fluid systems between two surfaces or in narrow pores is expected to strongly alter the collective structure of the trapped molecules of either simple or complex fluids composed of molecular aggregates such as polymers, vesicles, biomembranes, or colloidal particles suspended in a liquid.[5-10] Molecular dynamics simulations[11] indicate that an increased confinement may change the density and positional order, in addition to the molecular orientational order of molecules and aggregates, especially as the decreasing gap size approaches an inherent length scale such as the diameter of suspended colloidal particles or the radius of gyration of dissolved polymer coils, or ultimately, the diameter of the trapped solvent molecules.

Structural rearrangements within complex fluid systems may also be induced by flow,[4,9-13] but such flow-induced effects do not require confinement and occur throughout the bulk fluid, as shown in studies of bulk nematic[4] and smectic[14] liquid crystals under shear. An important difference between the confinement-induced and the flow-induced effects is that in the latter case

the changes in the structure are non-equilibrium. Obviously, it would be interesting to simultaneously study the competition of the effects of confinement and flow in the same system. An understanding of the properties of complex fluid systems in this regime is of fundamental scientific interest and also of importance to many technological fields such as lubrication, the flow of colloidal and biological particles through narrow channels or biological pores, and the processing of ceramic and polymer composite materials and films.

The effects of confinement on molecular conformations and transport, as well as the phase behavior of liquids in small pores (with a pore size distribution), have recently been studied with spectroscopic,[9] calorimetric,[10] and neutron scattering techniques.[15] At the molecular level, the Surface Forces Apparatus (SFA) technique has allowed for direct force, friction, and rheological measurements of liquid films.[5-8] However, until recently, complex fluids confined between two surfaces of well characterized physico-chemical origin with precisely controllable separations have not been studied with a direct imaging probe such as x-ray or neutron diffraction. Such a probe would clearly allow investigations of a number of important physical phenomena. First, by controlling the nature of the confining surfaces, it would be possible to separate the effects induced by a surface-specific interactions[8] from effects purely due to confinement. Second, by modifying the experimental apparatus so that the confining surfaces can be moved with respect to each other, one could study the effects of shear on the structure of a fluid in this very clean geometry. Conceivably, by moving the surfaces fast enough and by decreasing the separation between the surfaces to a few angstroms one could achieve extremely high shear rates.

In this paper we describe the present state of the art of XSFA technology developed since the first application[1-3] and report new results on the alignment of 8CB between different types of surfaces and on the alignment of a zwitterionic compound under confinement.

EXPERIMENTAL

The X-ray SFA is based on a conventional SFA Mk III,[16] which was modified for simultaneous on-line use with an intense synchrotron x-ray beam passing through the sample and the confining surfaces. In this device, the confining gap thickness between two atomically smooth surfaces can be continuously adjusted from a few angstroms to $>10\mu m$, with control to $\pm 10 Å$ by means of a three-stage coupled micrometer/differential micrometer/differential spring mechanism. The surfaces used are freshly-cleaved silvered mica sheets in a crossed-cylinder geometry with various radii of curvature (as described below). The curvature allows the surfaces to be brought into single point contact, but also requires the use of very small diameter x-ray beams in order to image the volume of the sample close to the point of contact. For our experiments the apparatus is mounted on a stepper-motor driven XYZ translation stage fitted onto a Huber four-circle x-ray scattering diffractometer (Figure 1). During the experiments the scattering volume of the sample is fixed in the center of rotation of the diffractometer.

The measurements were conducted on beamline 6-2 at the Stanford Synchrotron Radiation Laboratory (52-pole wiggler x-ray source). A Si(111) double-bounce monochromator was used at 8keV with the beam focused at the sample position. A $125\mu m$ pinhole was placed several centimeters before the sample in order to provide a proper collimation of the incident x-ray beam. The diffraction patterns were observed with a 180mm MAR image-plate 2D detector. The incoming resolution was determined by the slits on the diffractometer and the outgoing resolution by the pixel size of the image-plate ($150\mu m$) and the distance from the sample to the detector. In the experiments described here the in-plain longitudinal and transverse resolutions were $\delta h=\cos(2\theta/2)\delta q$ and $\delta k=\sin(2\theta/2)\delta q$ respectively, out-of-plane resolution δl was equal to the in-plain longitudinal resolution. Here $\delta q=0.001 Å^{-1}$ and 2θ is the scattering angle.
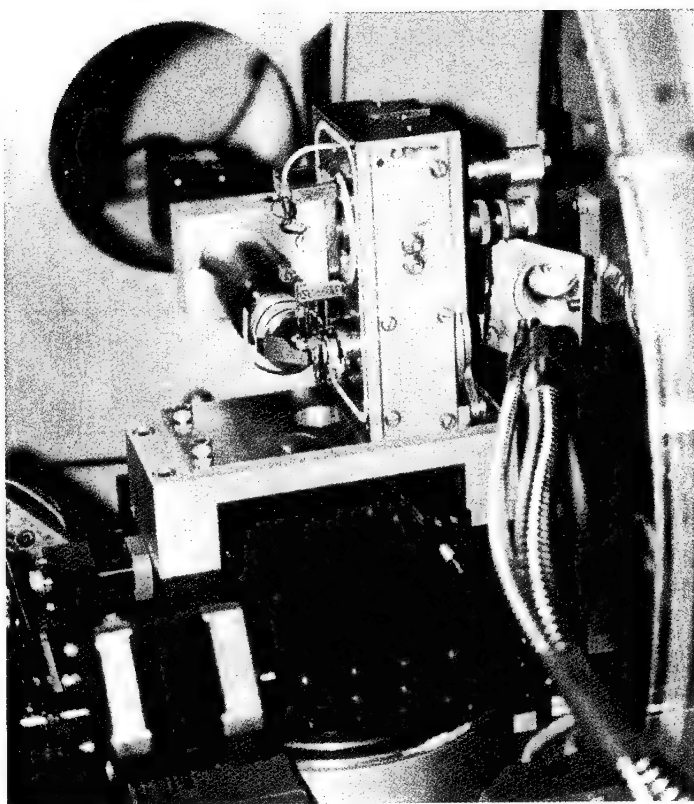
Figure 1. A photograph of the experimental setup of the XSFA experiment. The XSFA itself is the box-like apparatus in the center with two micrometers for changing the gap size on the right and a piezoelectric bimorph device for applying shear to the samples on the left. One can see the two mylar mirrors and a fiber-optic guide used for the optical gap measurements. The sodium light of the guide was directed to the bigger mirror on the right of the apparatus and, after passing through the sample, was reflected by a smaller mirror to the 5x long working distance objective. The apparatus is mounted on a stepper-motor driven XYZ translation stage.

The gap between the two confining cylindrical surfaces was monitored simultaneously with the x-ray measurements by observing the Newton fringes created when the light from a sodium lamp was passed (coaxially with the x-ray beam) through the back-silvered mica surfaces and the thin, confined, sample. In order to monitor the fringes simultaneously with the x-ray measurements we used a system of two 5mil thick aluminized mylar mirrors (see Figure 1). The mirrors attenuated the x-ray beam by about 20% and did not contribute to the background scattering at the angles of interest for the systems studied. The Newton fringes were observed using a Nikon 5x long working distance objective and a CCD camera connected to a TV-monitor and video-recorder.

The cylindrical holders in our experiments were oriented so that the x-ray beam first passed through a surface with a vertically-oriented cylindrical axis, then through the sample and then through a horizontally-oriented surface. The latter was mounted on a special piezoelectric bimorph sliding device[16], whereas the former was kept stationary. This allowed us to apply a variable shear to our samples.

The confining surfaces used in this experiments must be transparent to x-rays and partially transparent for the visible sodium light to allow simultaneous x-ray access and optical gap measurements. In order to satisfy these requirements we have developed three different kinds of surfaces. In the first kind, thin (about $1\mu m$), freshly-cleaved silvered mica sheets were glued silvered side down on a pair of 2mm diameter quartz capillary tubes with a wall thickness of 0.01mm.[1] The second kind of surfaces, which we refer to as "the soft surfaces", were prepared by gluing a 5-6μm mica sheet on a cylindrical lens made of aluminum with a 45° conical hole of 1mm diameter opening drilled through the center of the lens. The mica was glued over the hole using a UV-cured optical glue (Figure 2). The third kind, referred to as "the hard surfaces", were prepared by first gluing a 4-8μm thick piece of quartz over the hole in the aluminum cylindrical-lens holder and then gluing a 3-5μm thick piece of mica over the supporting quartz. In both the soft and the hard surfaces the cylindrical lenses had 20mm radius of curvature. In the experiments described here we have used the soft and the hard surfaces, because they have a larger radius of curvature then the capillaries. Both hard and soft surfaces have little glue present in the path of the x-ray beam (no glue at all in the case of soft surfaces), and the amount of glue present proved not to give any background scattering for the angles of interest.

RESULTS AND DISCUSSION

We have applied the XSFA technique to study the structural behavior under confinement and shear flow of two systems - the thermotropic liquid crystal 8CB and a zwitterionic polyisoprene melt (Figure 3).

The liquid crystal 8CB (4-cyano-4'-octylbiphenyl) is a compound consisting of rod-like molecules and has a smectic-nematic phase transition at 32.5°C.[4] In our experiments the sample was kept in the smectic phase. On the extremely hydrophilic freshly-cleaved mica surfaces, such as used in our experiments, 8CB molecules are known to orient with their long axis parallel to the surface[17] (planar orientation). In this case the smectic layers are oriented perpendicular to the confining surfaces, allowing us to see a diffraction pattern corresponding to the scattering from the layered smectic structure in our experimental geometry.

Figure 4(a) shows a typical 2D image of a diffraction pattern from 8CB confined in the XSFA. The two symmetric arc-like spots are the characteristic x-ray scattering peaks of 8CB, arising from the layered smectic structure. By taking appropriate cuts through the points of the 2D image one can extract information corresponding to the various 1D x-ray scans obtainable with a conventional scintillation point detector. For example, by taking the scattering intensities
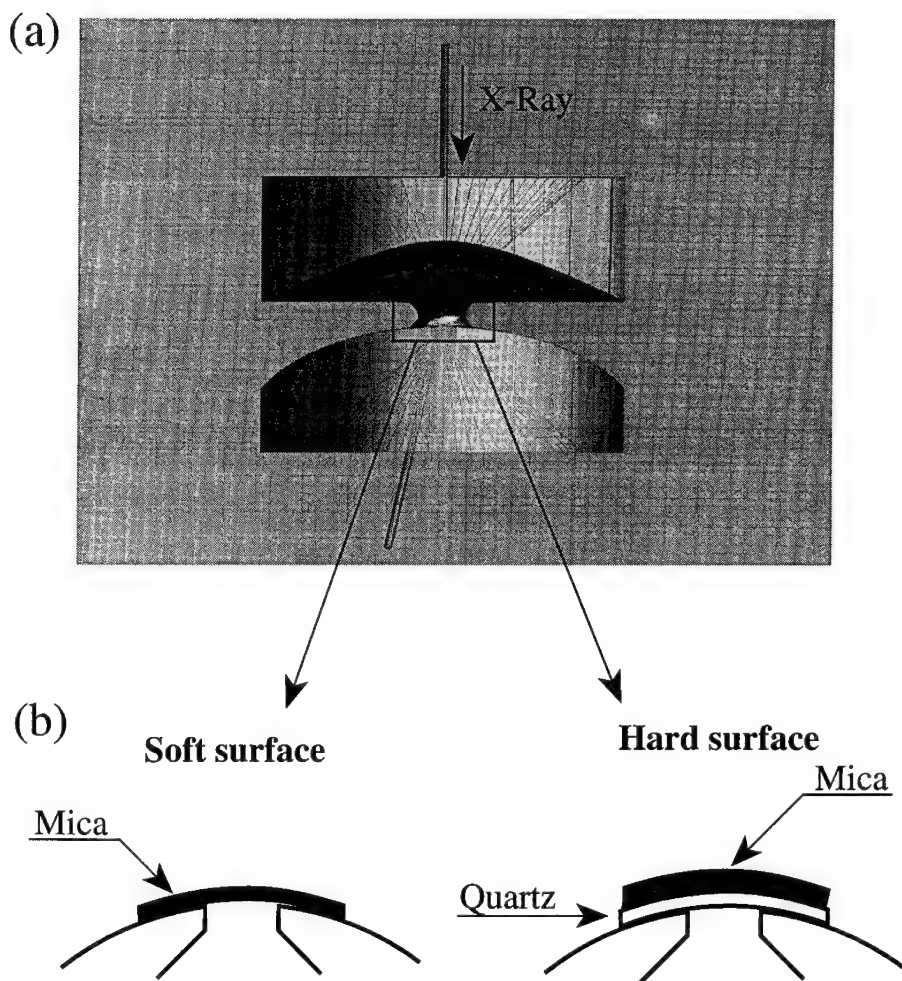
Figure 2. (a) A view of the aluminum cylindrical lenses with conical holes used as a support for both soft and hard surfaces in the XSFA experiments. (b) Blow-up of the contact region of the lenses in (a) shows a schematic of the soft and hard surfaces.

(a) smectic liquid crystal:

8CB C_8H_{17} —⬡—⬡— CN
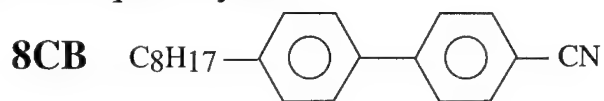
forms layered structure:
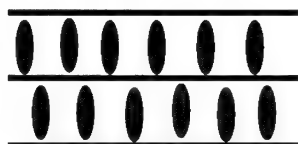
(b) Zwitterionic polyisoprene, MW=4650

$$= \quad \begin{array}{c} CH_3 \\ | \\ + CH_2 - CH = C - CH_2 \ ]_X \end{array}$$

$$= \quad \begin{array}{c} CH_3 \\ | \\ N - (CH_2)_3 - SO_3 \\ | \\ CH_3 \end{array}$$
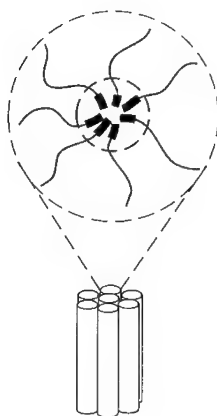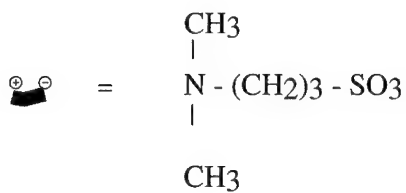
Forms hexagonal lattice of tubules:

Figure 3. The two systems studied using the XSFA technique. (a) A smectic liquid crystal 8CB (4-cyano-4'-octylbiphenyl). (b) A zwitterionic polyisoprene which forms a tubular hexagonal-packed structure.

of the points of 2D image lying on a circle, centered on the incident x-ray beam, in the direction of the χ arrow on Figure 4(a), one would obtain a conventional mosaic χ-scan (Figure 4(b)). This scan could be obtained with a point detector by fixing the detector and rotating the sample about the axis of the incident x-ray beam. A powder sample, consisting of many small, randomly oriented domains, would appear as a flat line in this scan. A partially ordered sample would produce two broad peaks, where the peak widths would indicate the degree of orientation present. Finally, an extremely ordered sample would manifest itself in two very sharp peaks. The angular positions of the peaks on the χ-scan correspond to a preferred direction of orientation in the sample. In the case of 8CB, the peak positions indicate the orientation of the normal to the smectic layers. Thus the broad angular extent of peaks in Figure 4(b) indicates that the sample consists of many domains with their layers aligned slightly off-axis with the cylindrical confining surfaces and with the mosaic spread of the domain orientations of 35°.

In our experiments with 8CB confined between the soft surfaces we have observed dramatic changes in the degree of orientation of the sample as a function of the gap size and the applied shear.[3] Moreover, the effects of confinement were very different for the soft and hard surfaces (Figure 5). In the case of the soft surfaces we observe a continuous improvement in the degree of alignment as we decrease the gap from 1mm to a few microns, with the best alignment achieved for a 3-4µm gap (Figure 5(1a)). However, as we decrease the gap size below this critical value, we observe a sudden change to a less aligned state of the sample (Figure 5(1b)). This means that for the gap size below critical the sample breaks into multiple domains with a significant spread of the layer-normal directions, as manifested by the broader peaks on the χ-scan. This is consistent with our previous observation of discrete orientations present in 8CB at a gap size of 3900 Å.[1] It is interesting that we observe a deformation of the Newton fringes from circular to a distorted oval shape at about the same size of gap as the orientational transition is observed with the x-rays. It is also important to note that this transition is *reversible*, that is, it happens any time when the gap is either increased or decreased through the critical value.

In the case of hard surfaces we do not observe any significant changes in the orientational state of the sample as a function of the gap size. Figure 5(2a) and (2b) show the χ-scans for the gaps similar to those shown in Figure 5(1) for soft surfaces. There is no change in either the peak widths or the overall lineshape even for the gaps smaller then 1µm.

The above results suggest that the nature of the surfaces greatly affects the sample alignment for small gaps. The difference is that the soft surfaces are somewhat flexible and can bend and flatten as one tries to confine the sample to very small gaps. The hard surfaces are not flexible at all and can not be flattened. This is consistent with the observation of the Newton fringes, which remain circular for the hard surfaces, whereas the fringes of the soft surfaces become distorted to a shape corresponding to the surfaces flattening near the point of contact. This also suggests that the orientation transition might be happening when the sample suddenly becomes harder to squeeze - that is when the fringes of the soft surfaces become distorted. A possible explanation would be that the transition occurs when the size of the gap becomes comparable with the size of the domains (defects) present in the sample. Further reduction of the gap would then require a rearranging of the domains between the two mica surfaces and, in the case of the soft surfaces, leads to a distortion of the surfaces and breaking of the domains into smaller and less oriented ones. In the case of the hard surfaces the domains are squeezed out from the contact area of the curved surfaces to a region away from the point of contact, instead of being trapped between two approaching flattened surfaces.

We have also applied the XSFA technique to study the effects of confinement on a zwitterionic polyisoprene polymer melt with the molecular weight MW=4650. The molecules of this polymer consist of a polar headgroup and a hydrocarbon tail (Figure 3). This compound is
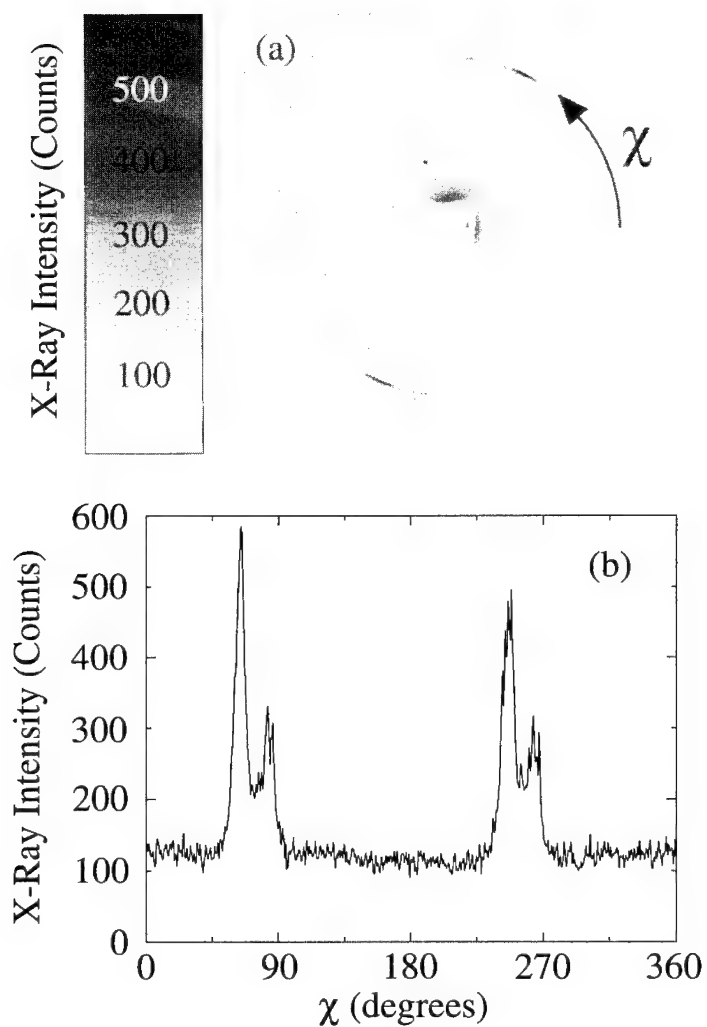
Figure 4. (a) A typical 2-dimensional X-ray diffraction image showing alignment in an 8CB sample. The white square in the center of the image is the lead beam-stop. The black dot above it corresponds to a "dead-spot" in the center of the detector. The darker points of the image correspond to a higher X-ray intensity. (b) To convert the image data to a one-dimensional orientational scan we draw a circle through the peaks on the image as shown by the arrow in (a). The resulting one-dimensional data corresponds to the χ scan which could be obtained with a point detector by rotating the sample about the axis of the incident X-ray beam.
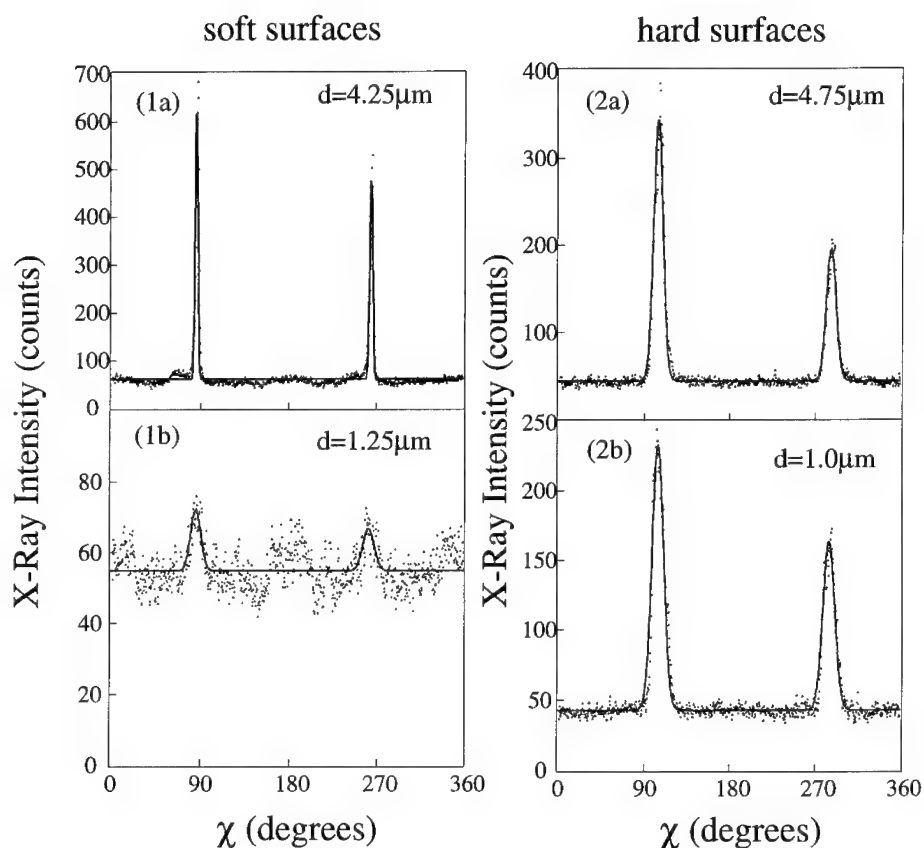
Figure 5. The difference of the sample alignment as a function of the gap size "d" for the soft and hard surfaces. In the case of the soft surfaces one can clearly see the broadening of the peaks as d is decreased below a certain critical value, indicating a decrease in the alignment of the sample. The widths of the peaks are 2° for d=4.25μm (1a) and 8° for d=1.25μm (1b). For the hard surfaces (2a and 2b) the peak intensities decrease as a function of the decreasing gap, but the widths and overall shape of the peaks remain similar. The solid lines are the fits to the data using a linear combination of two gaussians. The peaks at 0 and 180° in (1a) and (1b) arise because of a shadow from the sample holder. The technique was later improved to elliminate this shadow for the hard surface experiments.

(a)

(b)
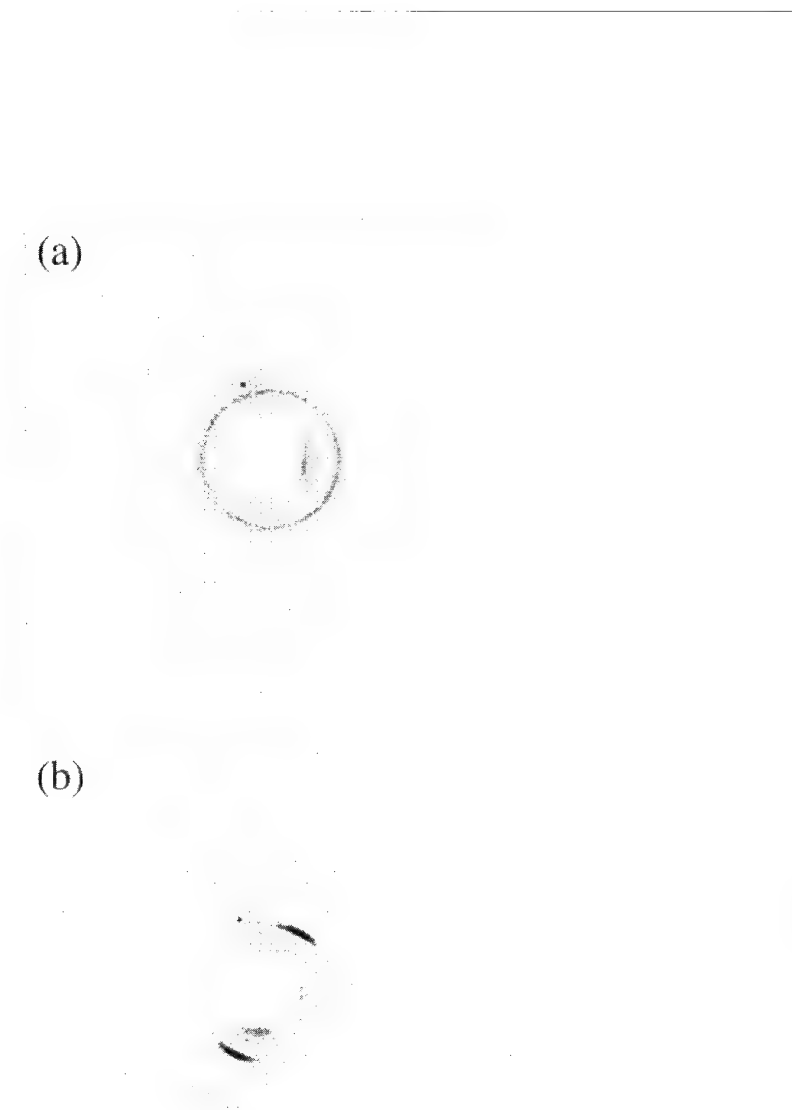
Figure 6. 2D x-ray diffraction images showing scattering patterns of the zwitterionic polyisoprene compound (a) in a bulk disordered state (thick sample, d≈1mm) and (b) in a partially aligned state (thin sample, d several microns). The clearly visible full circle in (a) corresponds to the (1 0) peak of a powder sample with hexagonal crystalline structure. The peaks in (b) correspond to (1 0), (1 1) and (2 0) peaks of a significantly aligned sample with a small angular mosaicity. The large white squares in the center of the images are the shadows of a lead beam stop.

known to form a tubular structure with the tubes arranged in a hexagonal lattice with a lattice constant of 102Å.[18] Figure 6 shows two diffractograms of this system. The image in Figure 6(a) is from a thick sample ($d \approx 1$mm). It shows a (1 0) diffraction ring of a powder sample. The image in Figure 6(b) is from a sample confined to a gap size of several microns between the soft surfaces. One can see the (1 0), (1 1) and (2 0) peaks. The sample is clearly in an aligned state. The arrangement of the peaks on the 2D image suggests that the tubules are oriented along the mica surfaces with their axis in a direction almost exactly at a 45° angle to the directions of the two cylindrical axis of confining surfaces. The sample mosaic is about 30° as determi.ied from the corresponding χ-scans. This high degree of alignment in a preliminary experiment is just slightly larger than the one obtained by shear-alignment on a similar viscous polymer systems (approximately 25°).[19] This is one of few experiments where one could achieve alignment in such viscous ordered polymer systems for x-ray diffraction studies. Thus, confinement turns out to be a valuable technique for the preparation of a highly aligned sample in systems which are otherwise difficult to align for the x-ray experiments.

CONCLUSION

The results described above show that the new XSFA technique is an exciting probe for investigating the structure of fluids under confinement. We were able to directly investigate the structure of the smectic liquid crystal 8CB under confinement and flow with well-characterized experimental conditions, such as the nature of the confining surfaces and the gap size. We were also able to show that the XSFA can be valuable for the preparation of thin, well aligned films of complex fluids. Future investigations may include experiments with various chemically modified surfaces, i.e. by depositing thin monolayer films of various materials on the mica surfaces. Clearly, it would be interesting to apply the XSFA technique to other complex fluid systems.

ACKNOWLEDGMENTS

REFERENCES

1. S. H. J. Idziak, C. R. Safinya, R. S. Hill, K. E. Kraiser, M. Ruths, H. E. Warriner, S. Steinberg, K. S. Liang and J. N. Israelachvili, Science **264**,1915 (1994).
2. S. H. J. Idziak, C. R. Safinya, E. B. Sirota, R. F. Bruinsma, K. S. Liang and J. N. Israelachvili, in Structure and Flow in Surfactant Solutions, edited by C. A. Herb and R. K. Prud'homme (American Chemical Society, Washington, DC, 1994).
3. S. H. J. Idziak, I. Koltover, K. S. Liang, J. N. Israelachvili and C. R. Safinya, International Journal of Thermophysics, (in press).
4. C. R. Safinya, E. B. Sirota, R. Plano, R. F. Bruinsma, J. Phys. Condens. Matter **2**,SA365 (1990); C. R. Safinya, E. B. Sirota, R. Plano, Phys. Rev. Lett. **66**, 1986 (1991).
5. J. N. Isrealachvili, "Intermolecular and Surface Forces," Academic Press, London & New York, 1985 (1st edition), 1991 (2nd edition).
6. J. Van Alsten and S. Granick, Phys. Rev. Lett. **61**, 2570 (1988).

7. J. Klein, D. Perahia, S. Warburg, Nature **352**, 143 (1991); J. N. Israelachvili, A. M. Homola, P. M. McGuiggan, Science **240**, 189 (1988).

8. J. Als-Nielsen, Topics in Current Physics, W. Schommers and P. V. Blackenhagen, Eds. (p. 181, Springer-Verlag, Verlin 1987); P. S. Pershan, J. Physique Coll. **50**, C7 1 (1989); B. Jerome, Rep. Prog. Phys. **54**, 391 (1991) and references therein.

9. See e.g. J. M. Drake and J. Klafter, Physics Today **43** (5), 46 (1990) and references therein; J. M. Drake, J. Klafter, P. Levitz, Science **251**, 1574 (1991).

10. T. Bellini et al., Phys. Rev. Lett. **69**, 788 (1992).

11. M. Schoen, D. J. Diestler, and J. H. Cushman, J. Chem. Phys. **87**, 5464 (1987); C. L. Rhykerd Jr., M. Schoen, D. J. Diester, and J. H. Cushman, Nature **330**, 461 (1987); P. A. Thompson, M. O. Robbins, G. S. Grest, Phys. Rev. Lett. **68**, 3448 (1992).

12. K. Weissenberg, Nature **159**, 310 (1947); R. F. Bruinsma and C. R. Safinya, Phys. Rev. A **43**, 5377 (1991).

13. N. A. Clark, and B. J. Ackerson, Phys. Rev. Lett. **44**, 1005 (1980).

14. C. R. Safinya, E. B. Sirota, R. Plano, R. F. Bruinsma, C. Jeppesen, R. J. Plano, and L. J. Wenzel, Science **261**, 588 (1993).

15. M.Y. Lin, S.K. Sinha, J.M. Drake, X.-I. Wu, P. Thiyagarajan, and H.B. Stanley, Phys. Rev. Lett. **72**: 2207 (1994).

16. J. N. Israelachvili and P. M. McGuiggan, J. Mater. Res. **5**, 2223 (1990).

17. P. Pieranski and B. Jerome, Phys. Rev. A **40**,317 (1989).

18. Y. Shen, C. R. Safinya, L. Fetters, M. Adam, T. Witten and N. Hadjichristidis, Phys. Rev. A **43**(4), 1886 (1991).

19. K. A. Koppi, M. Tirrell, F. S. Bates, K. Almdal, and R. H. Colby, J. Phys. **2**, 1941 (1992); K. A. Koppi, M. Tirrell, F. S. Bates, Phys. Rev. Lett. **70**, 1449 (1993).

NANORHEOLOGY

OF POLYMERS, BLOCK COPOLYMERS, AND COMPLEX FLUIDS

A. LEVENT DEMIREL, LENORE CAI, ALI DHINOJWALA,
AND STEVE GRANICK
Department of Materials Science and Engineering
University of Illinois
Urbana, IL 61801

and

J. M. DRAKE
Exxon Research & Engineering Corp.
Annandale, NJ 08801

ABSTRACT

The shear rheology of molecularly-thin films of fluids has been studied experimentally as it depends on sinusoidal frequency (linear response) or on sliding velocity (nonlinear response). Building upon previous identification of a solid-like state that is induced by confinement, we find the shear-induced transition to a sliding state in which the viscous dissipation is essentially velocity-independent. The mechanism appears to involve wall slip but Fourier transforms of the response reveal fluctuations, intrinsic to the sliding state, over all accessible frequencies. Other ongoing studies involve shear-induced changes in the fluorescence of confined fluorescent probes, shear dilatancy, and the contrast between the shear of simple nonpolar fluids, and block copolymers.

INTRODUCTION

Nanorheology -- the rheology of substances confined in one or more directions to molecular dimensions -- is in an active state of development. In a major recent surge of activity, new experimental methods have been developed to measure dynamic interfacial forces of confined fluids in shear [1-4] and compression [5-6]. Other related methods of nanorheology include atomic force (AFM) and friction force microscopy (FFM) [7,8] and the quartz-crystal microbalance [9]. Theoretical calculations and molecular dynamics simulations are also emerging [10-19].

In the present studies, the experimental approach was based on confining fluids between atomically smooth, step-free, single crystals of muscovite mica that were close to one another but not actually touching; the mica substrate was also modified by deposition of self-assembled organic monolayers so that the surface chemistry was transformed [20]. In such experiments, the area of contact between the solid surfaces is vast compared to the thickness between them; the extent of confinement differs in this respect fundamentally from the tip-surface interactions studied by atomic force microscopy and friction force microscopy. The contrasting calorimetric, NMR, and fluorescence depolarization investigations of fluids in porous media [21] constitute another important approach to these questions.

To summarize a large literature, the main dynamical findings are the following:

(1) Two qualitatively different responses to shear in ultrathin liquid films are observed -- liquid-like and solid-like. In the liquid-like shear response, a liquid film liquid eases deformations by flowing at some rate. Solid-like response is characterized by the observation that deformation over macroscopic distances will not occur unless a certain shear stress (or "yield stress") is exceeded. Interesting patterns of "stick" and "slip" result.

(2) The dynamic perturbations appear to be smaller in measurements of liquids confined in porous media and in measurements of drainage rates as opposed surfaces are brought together [21,22]. It suggests something special about a molecularly-thin film in a tight space between two solid plates -- a kinetically trapped state of some kind.

(3) Features of the molecular make-up come into play. Linear and branched chain molecules have been compared experimentally and in computer simulations [23,24]. In a homologous series of confined polymers, chain molecules are found to relax more sluggishly, the longer the chain length [25-27]. Polymer brushes in good solvent display normal forces that far exceed the shear forces [28,29].

(4) A limitation has been the rheological experiment itself; direct response on the scale of individual molecules was not measured. This report includes description of the first experiments to compare the rheological response, i.e. the stresses characteristic of the entire contact region, and the spectroscopic response of individual molecules.

EXPERIMENTAL

A surface forces apparatus with oscillatory shear attachment was employed [1,4]. The film thickness and area of flattened contact were measured by multiple beam interferometry. Sinusoidal shear forces were applied by a piezoelectric element. A second sensor piezoelectric element was used to detect the resulting response, and this response was compared with the force required to deform this element when no liquid was present. The temperature was 27°C.

For fluorescence experiments, an alternative technique, described below, was used in place of interferometry between reflective silver coatings.

For shear experiments, device compliance was accounted for by a mechanical circuit in which the calibrated properties of the device and glue were combined with the mechanical response of the sample of interest. Here the mechanical impedance of the piezoelectric device itself (Z_D), and of the serial contribution of the glue and the sample of interest (Z_G and Z_L, respectively), respond to applied forces in parallel. The applied force then divides into some portion which acts to deflect the piezoelectric device, and some portion which acts to deflect the serial combination of glue and sample. The measured deflection of the receiver bimorph is equal to the sum of the deflections within the glue and within the sample of interest [25].

FLUORESCENCE SPECTROSCOPY OF CONFINED LIQUIDS

The desirability of spectroscopic measurements of confined liquids, in the geometry of a surface forces apparatus, has long been clear, but faces three central difficulties:

(1) Signal to noise. The meager abundance of sample, buried between two bulk condensed phases with thickness ≈1-2 nm, sets harsh requirements on the experimental methods that would be sensitive to this small sample size. The mass present is no more than approx. i.e. ≈1-2 μg-cm^{-2}. Methods of fluorescence spectroscopy satisfy this requirements.

(2) Needle-in-a-haystack syndrome. The tiny sample area, ≈10 μm on a side, is difficult to distinguish from adjoining areas in the apparatus. This sets harsh requirements on positioning the sample optics. Methods of deliberate alignment in the optical train satisfy this requirement.

(3) Optical interferometry with concomitant fluorescence spectroscopy. The classical surface forces apparatus, which involves optical interferometry between silvered layer on the back sides of mica sheets [30], is unsuitable for fluorescence experiments because the silver coatings are opaque to most fluorescence emission wavelengths of interest. Replacement of the mica by soft dielectric coatings [31] rectifies this deficiency.

These three difficulties have now been overcome by an apparatus in operation at Exxon Research and Engineering. The fluorescence decay of pyrene molecules, dissolved in squalane and confined between methyl-terminated self-assembled monolayers [31], shows interesting differences from fluorescence decay in bulk samples.

SHEAR DILATANCY

The desirability of measuring changes in film thickness, in the course of shear displacement, has long been apparent. Clearly stick-to-slip shear transitions should be accompanied by changes in sample thickness. But these changes have, so far, been surmised only from computer simulations [14]; they are too small to measure by the interferometric techniques that are traditionally used in a surface forces experiment.

This limitation has been overcome by mounting the lower mica surface on a boat of two piezoelectric bimorphs similar to that used for the shear experiment. Distance changes of <0.01 angstroms have been detected. Their amplitude and phase can be analyzed to give in-phase and out-of-phase responses, with analysis closely analogous to analysis of the shear experiments [4] and confirming earlier work of Montfort, Georges, and coworkers [5,6]. The stick-to-slip transition, discussed further in the following section, involves a substantial increase of film thickness.

FINE STRUCTURE OF FRICTION

The shear-induced transition, from confinement-induced solidity (at rest), to a sliding state in which the viscous dissipation is essentially velocity-independent [32], involves the passage from a state of static friction to one of kinetic friction.

Detailed analysis of the friction traces shows the dissipative stress building smoothly but dropping abruptly, breaking time-reversal symmetry. The rate of smooth stress buildup shows a narrow distribution around a constant level, but this level seems to change with the amplitude of the drive. There is small structure nested within larger structure. Quantitative analysis suggests a power law distribution of events, i.e. self-affine scaling. Preliminary data also shows that increasing strain during a cycle of oscillation, the noise is punctuated by intervals of flat baseline(see raw data Fig.1).
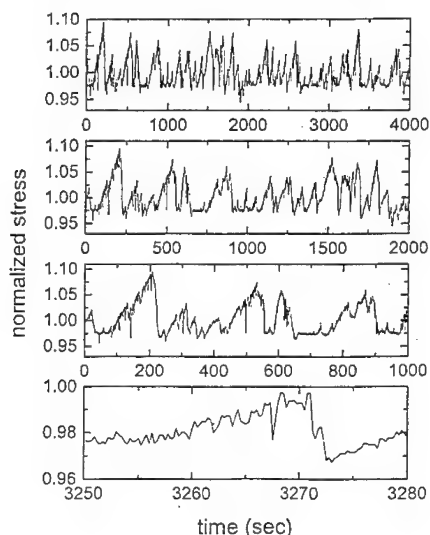
Figure 1. Giant fluctuations in the dissipative sliding state. The sample is squalane confined to a thickness of 16 Å between parallel mica sheets ($\approx$20 μm on a side) and subjected to repetitive sinusoidal forces of large amplitude at 250 Hz. The response is measured both in-phase and out-of-phase with the drive. The out-of-phase (dissipative stress) is shown here.

Two principal questions are raised by this provocative data:

(1) What is the fluctuation mechanism? Coherent dissipative structures must extend over distances huge compared with molecular dimensions; otherwise they would average out over the sample dimension of 20 μm. What types of defects extend over such distances? What is the mechanism of slow stress build-up followed by sudden drop to a relatively constant baseline? Can the avalanche-like events be

117

described as some sort of marginally-stable driven self-organization; or do they reflect large-scale metastable states already present without driving?

(2) Why are these fluctuations so phenomenologically reminiscent of noise in other systems? The avalanche-like events are reminiscent of earthquake models, sandpiles, and contact angle depinning, to pick a few examples. Are the similarities among these driven systems superficial or deep?

SHEAR OF BLOCK COPOLYMERS IN SOLUTION

Polymer "brushes," end-attached to a surface under conditions where one block adsorbs negligibly, have been of major interest in polymer physics in recent years. The structural properties have been investigated rather thoroughly and are well understood. But as concerns the dynamical structure there has been hardly any experimental work, with the exception of the recent study of friction by Klein and coworkers [28]. Lately it has seemed profitable to measure the dynamical shear properties of polymer brushes in solution, with the hope of drawing conclusions as to the dynamical structure.

The PS-PVP (polystyrene-polyvinylpyridine) block copolymers were allowed to adsorb onto mica from dilute solution below the critical micelle concentration in toluene. The molecular weight and molecular weight distribution is specified in the caption of Fig. 2. The experiments were conducted in trans-decalin at $24°C$, which is $≈4°C$ above the theta temperature of a bulk solution. Interpenetration of the opposed layers can be expected near the theta point.

The force-distance profile can be fit quantitatively to well-known theoretical expressions [33]. These static forces, required to compress the films to a given thickness, we denote as static *normal* forces. The ratio of *dynamic oscillatory shear* (at fixed frequency) to *static normal forces* is plotted against film thickness in Fig. 2. While it is true that these ratios are proportional to strain (the dynamic oscillatory shear forces, but not the static normal forces, are proportional to strain), the relative values are strain-independent.

By systematically sweeping the frequency at fixed film thickness, one concludes that the longest relaxation time shifts to longer times as the brushes are compressed.
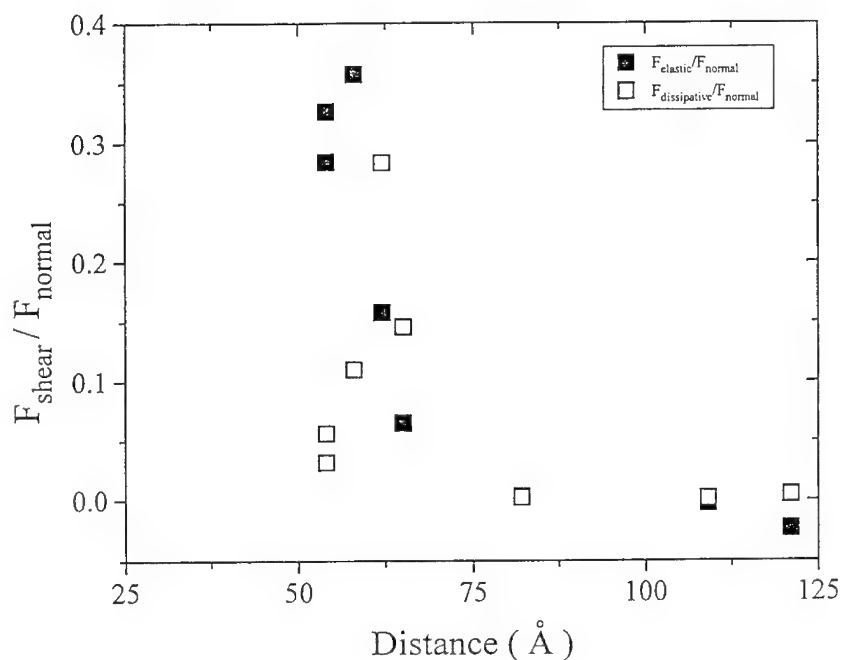
Figure 2. Shear dynamics of PS-PVP polymer brushes in decalin at 24°C, measured at 1 Hz, with amplitudes of oscillation chosen to give linear viscoelastic response. The diblock copolymers of polystyrene and polyvinylpyridine (PS-PVP) were generously donated by Professor Hiroshi Watanabe of the Institute of Chemical Research at Kyoto University. The molecular weights were 32,300 (PS) and 32,700 g-mol^{-1} (PVP) the ratio of weight-average to number-average molecular weight were $M_w/M_n = 1.05$. The ratio of shear forces (dissipative and elastic) to normal forces is plotted against film thickness.

In Fig. 2 one observes that large increases of the dynamic oscillatory shear forces (at 1 Hz) and of the static normal forces occurred at the same film thickness. This we interpret as reflecting interpenetration of the chains from opposed layers.

An interesting implication of the data in Fig. 2 comes when one compares tanδ (from shear rheology) and F/R (from static normal forces). Here tanδ is defined as the ratio of the dissipative to elastic shear forces. In Fig. 3 one observes a sharp peak of tanδ at the point of moderately strong compression. The position of this peak changes, however, according to the frequency of shear oscillation; tanδ peaks at larger distances, the higher the frequency of oscillation.
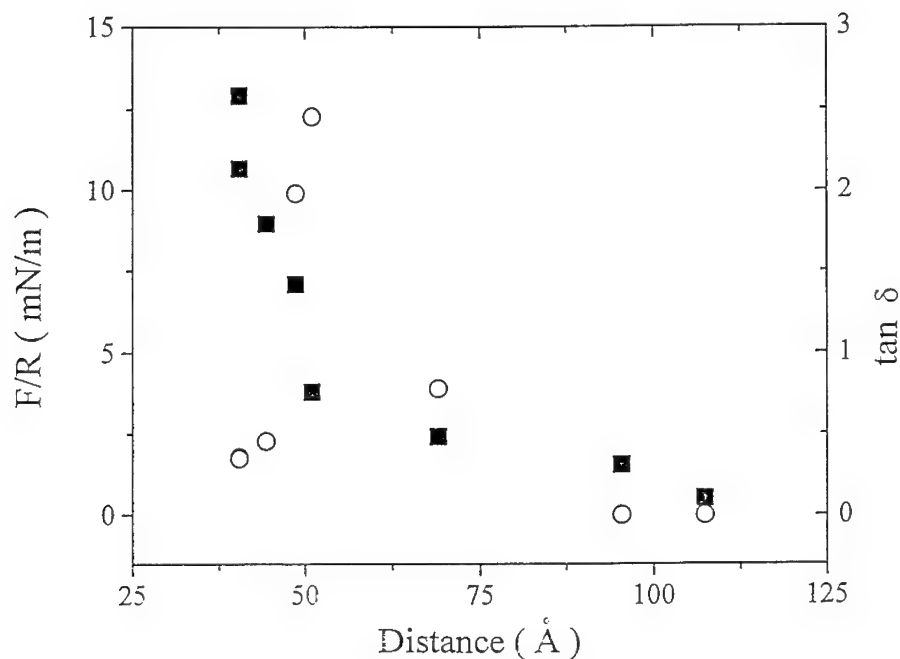
Figure 3. Shear dynamics of PS-PVP polymer brushes in decalin at 24°C. The diblock copolymers are identified in the caption of Fig. 2. Filled squares indicate the static force-distance profile, F/R, where F is the force required to compress the films to the given thickness, and R is the mean radius of curvature of crossed mica cylinders. Open circles indicate tanδ, the ratio of the dissipative to elastic shear forces, measured at 1 Hz.

The data in Figs. 2 and 3 shows that under weak compression (relatively large film thickness), the magnitude of the dissipative shear forces at 1 Hz exceeded both the elastic shear forces and the static normal forces. But elastic shear forces dominated at lesser film thickness. In other words, it was easier to compress these brushes than to shear them at this frequency; under strong compression the inverse experimental frequency exceeded the longest relaxation time of the brush layers.

It is remarkable that the longest relaxation time of the opposed brush layers was so slow. Of course, with polystyrene (PS) brushes, one can be concerned that the brush could become compressed to the point of becoming glassy. This point was considered in detail with the conclusion that the volume fraction of PS was 30% at the point of strongest compression, and less than this for most of the measurements, so that glassy behavior of PS in concentrated solution would not intervene.

PROSPECTS

The nanorheology of complex liquids is in a period of rapid development. New instrumental approaches are allowing concomitant measurements of fluorescence spectroscopy. Other new instrumental approaches are allowing the concomitant study of shear and normal forces.

Provocative and unexpected results have been obtained as concerns intrinsic fluctuations and noise of friction (in deformations far from equilibrium) and as concerns the linear viscoelastic response (of block copolymers in solution).

REFERENCES

1. J. Van Alsten; S. Granick, *Phys. Rev. Lett.* <u>61</u>, 2570 (1988).
2. J. N. Israelachvili, P. M. McGuiggan, A. M. Homola, *Science* <u>240</u>, 189 (1988).
3. A. M. Homola, H. V. Nguyen, G. Hadziioannou, *J. Chem. Phys.* <u>94</u>, 2346 (1991).

4. J. Peachey, J. Van Alsten, S. Granick, *Rev. Sci. Inst.* 62, 463 (1991).
5. A. Tonck, J. M. Georges, J. L. Loubet, *J. Coll. Interface Sci.* 126, 150 (1988).
6. E. Pelletier, J. P. Montfort, F. Lapique, *J. Rheol.* 38, 1151 (1994).
7. C. M. Mate, G. M. McClelland, R. Erlandsson and S. Chiang, *Phys. Rev. Lett.* 59 1942 (1987).
8. R. Erlandsson, G. Hadziioannou, C. M. Mate, G. M. McClelland, and S. Chiang, *J. Chem. Phys.* 89, 5190 (1988).
9. J. Krim, D. H. Solina, and R. Chiarello, *Phys. Rev. Lett.* 66, 181 (1991).
10. U. Landman, W. D. Luedtke, and M. W. Ribarsky, *J. Vac. Sci. Technol.* A7, 2829 (1990).
11. U. Landman, W. D. Luedtke, N. A. Burnham, and R. J. Colton, R.J., *Science* 248, 454 (1990).
12. J. B. Sokoloff, *Phys. Rev. B* 42, 760 (1990).
13. C. L. Rhykerd, Jr., M. Schoen, M., D. J. Diestler, J. H. Cushman, *Nature* 330, 461 (1987).
14. P. A. Thompson, M. O. Robbins, *Science* 250, 792 (1990).
15. M. W. Ribarsky, U. Landman, *J. Chem. Phys.* 97, 1937 (1992).
16. P. A. Thompson, G. S. Grest, M. O. Robbins, *Phys. Rev. Lett.* 68, 3448 (1992).
17. S. Gupta, et al., *J. Chem. Phys.* 100, 8444 (1994).
18. Y. Braiman, I. Goldhirsch, J. Klafter, *Phys. Rev. E.* 50, 838 (1994).
19. B. N. J. Persson, *Phys. Rev. B* 50, 4771 (1994).
20. C. Kessel and S. Granick, *Langmuir* 7, 532 (1991); J. Peanasky et al., *Langmuir*, in press.
21. see other articles in this volume.
22. D.Y.C. Chan, R. G. Horn, *J. Chem. Phys.* 83, 5311 (1985).
23. Y. Wang, K. Hill, J. G. Harris, *J. Chem. Phys.* 100, 3276 (1994).
24. S. Granick, A. L. Demirel, L. Cai, J. Peanasky, *Israel J. Chem.*, in press.
25. S. Granick, H.-W. Hu, *Langmuir* 10, 3857 (1994).
26. S. Granick, H.-W. Hu, G. A. Carson, *Langmuir* 10, 3867 (1994).
27. J. Peanasky, L. Cai, C. R. Kessel, S. Granick, *Langmuir* 10, 3874 (1994).
28. J. Klein, E. Kumacheva, D. Mahalu, D. Perahia, L. J. Fetters, *Nature* 370, 634 (1994).
29. L. Cai and S. Granick, submitted.
30. J. N. Israelachvili and G. E. Adams, *J. Chem. Soc. Faraday Trans. II* 74, 975 (1978).
31. J. M. Drake, to be published.
32. G. Reiter, A. L. Demirel, S. Granick, *Science* 263, 1741 (1994).
33. for a review, see A. Halperin, M. Tirrell, T. Lodge, *Adv. Polymer Sci.* 100, 31 (1991).

ENERGETICALLY AND PRESSURE DRIVEN LIQUID-SOLID TRANSITIONS IN MOLECULARLY THIN HYDROCARBON FILMS

RAVI K. BALLAMUDI AND IOANNIS A. BITSANIS
Department of Chemical Engineering, University of Florida, Gainesville, FL32611

ABSTRACT

In this study we used molecular dynamics simulations to investigate the structural changes in nanoscopically thin n-octane films confined between smooth solid surfaces as a result of a) increasing solid-methylene unit affinity and b) increasing pressure. Increasing solid-methylene unit energetic affinity resulted in the solidification of the film at a critical value. A similar transition is observed at a critical value of pressure. Bulk n-octane was a liquid in both cases. The transition was signaled by an abrupt increase in the intermolecular order and was facilitated by a precipitous extension of the octane molecules, which adopted almost fully extended configurations. A discontinuous jump in the film density at the critical values of solid affinity and pressure was evident. The characteristics of the transitions showed that it was a mild first order transition from a highly ordered liquid to a poorly organized solid.

I. INTRODUCTION

In the recent past several experiments reported solid like features in alkane films [1,2]. We investigated the effect of pressure and solid-methylene unit energetic affinity on the solidification of nanoscopically thin films by studying n-octane chains confined between smooth solid surfaces. The choice of the solid surfaces deprived of any topographical features was motivated by the fact that solid like thin film behavior was observed for a variety of liquids whose molecular structure was not particularly commensurate with the underlying solid substrate (cleavage plane mica).

The choice of n-octane was due to the availability of extensive data on bulk n-octane and wider films from previous simulation studies [3,4]. Furthermore, several experiments investigated films of short linear alkanes [5].

II. THE MOLECULAR MODEL AND SIMULATION METHOD

In all simulations the octane films were confined between two parallel, geometrically flat solid planes. The segment density normal to the solid surfaces always exhibited the usual oscillatory behavior [6]. The distance between the solid walls was chosen so that, a) three distinct methylene layers were formed b) pressure normal to the solid surface attained a prespecified value. Furthermore, the temperature was kept constant by velocity scaling. Therefore, our simulations were performed in a constant N, V, T (canonical) ensemble. The fixed film thickness was chosen to yield the same selected value of the (normal) pressure. This implies that all films were at thermodynamic equilibrium with a bulk reservoir at the same temperature and a bulk pressure equal to the normal component of the pressure tensor inside the film. Hence, the film and the bulk reservoir have the same chemical potential.

The effect of pressure was studied by fixing the solid-methylene unit energetic affinity to a constant value. The distance between the solid walls was adjusted to yield different normal pressures.

The model of the octane chain uses the "United Atom" approach, which treats CH_2 and CH_3 groups as identical spherically symmetric units. The connectivity of the molecules was maintained using the following potentials: a) a harmonic bond length potential [3]. b) a harmonic bond angle potential [3]. c) a torsional potential [3].

The interactions between segments of different chains as well as segments of the same chain separated by more than three bonds were of the 12-6 Lennard-Jones type. The value of the inter-segment Lennard-Jones parameter for methyl and methylene units was 60.1K. The segment-solid wall interactions were modeled by a 10-4 Lennard-Jones potential

$$U_{sl}(z/\sigma_{sl}) = 2\pi\rho_s\varepsilon_{sl}\{0.4(z/\sigma_{sl})^{-10} - (z/\sigma_{sl})^{-4}\}$$

In the above equation z is the surface-segment distance, ρ_s is the number density of the solid layer, ε_{sl} is the Lennard-Jones energy parameter for the interaction between segments and a (fictitious) surface atom and σ_{sl} is the arithmetic average of the Lennard-Jones length parameters for segments and surface "atoms" and segments over an entire solid layer. After the smearing of solid atoms the resulting surface becomes perfectly smooth and lacks any topographical features.

In what follows we discuss the results of the simulations performed at the following conditions: a) temperature 300.5K and (normal) pressure close to 0 bar for the following values of the solid-segment energy parameter ε_{sl}: 180.3K, 240.4K, 300.5K, 360.6K and 480.8K. b) temperature 360.6K and solid-segment energy parameter (ε_{sl}) 601K for the following values of pressure: -300 bar, -40 bar, 170 bar, 400 bar, 820 bar, 900 bar, 1050 bar, 1500 bar.

Bulk octane was a liquid at all the above conditions. The freezing point and boiling point of n-octane are 216.4K and 398.8K at standard conditions (1 bar pressure). Estimates using the Clausius-Clapeyron equation showed that increasing the pressure on bulk n-octane to 1500 bar elevates its melting point by only 10 to 20 K.

III. RESULTS AND DISCUSSION

In this section we discuss the effect of both pressure and solid-segment affinity ε_{sl} in inducing structural transitions of the thin films studied. Since both pressure and ε_{sl} induce qualitatively similar features in the films, we discuss their effect simultaneously.

In figure 1a we show the average film density as a function of the solid surface affinity ε_{sl}. The overall shape of the curve in fig. 1a is similar to typical high adsorption isotherms. We observe an abrupt densification of the film between the ε_{sl} values 300.5K and 360.6K. We see in figure 1b that increasing pressure has a similar effect on film density with a sharp densification between pressures 820 bar and 900 bar.
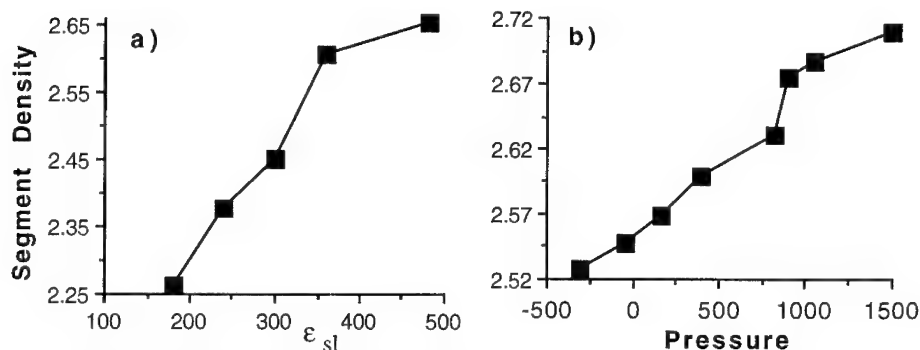
Figure 1. Average segment density of the film as a function of a) ε_{sl} b) pressure.

The in-layer pair correlation function (PCF) offers insight into the structural properties of the film layers. Figures 2a and 2b show the first and middle layer PCF's for various ε_{sl} values.

Figures 3a and 3b show the PCF's for several values of pressure. The initial part of the pair correlation function which mostly reflects trivial intrachain correlations, has been omitted.
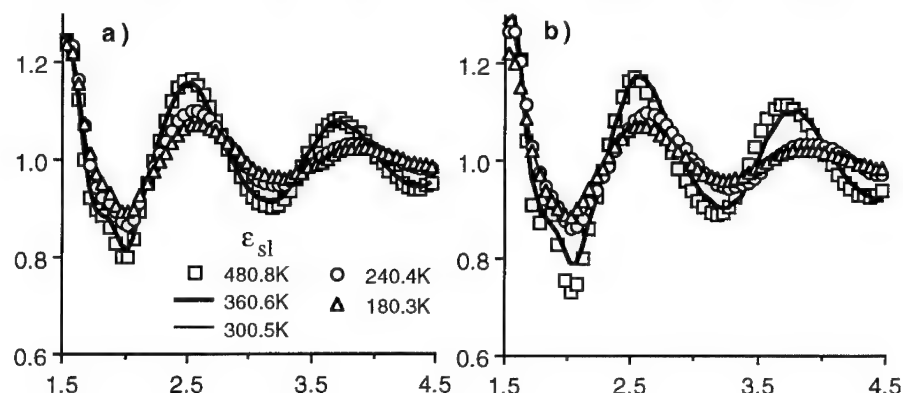
Figure 2. Pair correlation function curves for different solid-segment affinities a) first layer b) middle layer.
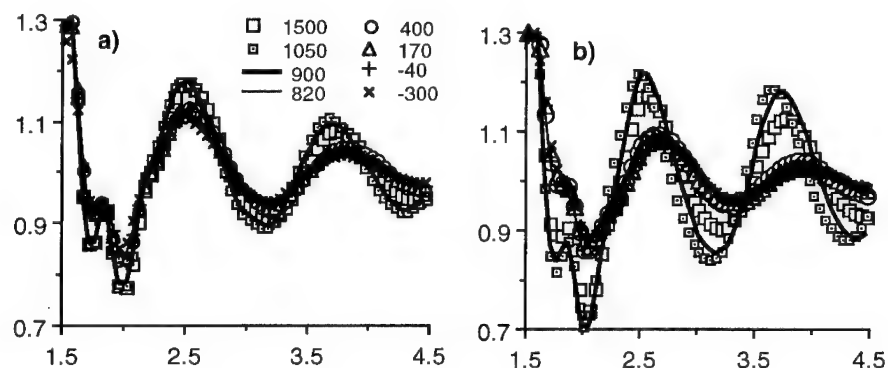
Figure 3. Pair correlation function for several values of pressure, a) first layer b) middle layer.

A common feature of all the above figures is that, the PCF curves belong to one of two distinct groups. In fig 2 the shape of the PCF of both the first and middle layers undergoes an abrupt change at some critical ε_{sl} value (between 300.5K and 360.6K). A similar change occurs for a critical pressure between 820 bar and 900 bar (fig 3). Such abrupt changes in the shape of the PCF's are representative of first order phase transitions. Another important feature in figs. 2 and 3 is the formation of well defined second and third peaks. Such peaks indicate regular packing of n-octane molecules, which is possible only if they adopt extended, rod-like configurations.

The fraction of trans angles in the octane chains showed an abrupt jump corresponding to the precipitous change in the shape of the curve of the pair correlation functions. Figure 4 depicts the percentage of trans angles as a function of ε_{sl} and pressure. Between the ε_{sl} values of 300.5K and 360.6K the fraction of trans angles sharply raises from 0.83 to 0.90. A similar jump occurs (0.85 to 0.90) between the pressures 820 bar and 900 bar. Above the critical ε_{sl} and pressure

values, over half the octane chains are in all trans configuration, while the rest of the chains usually end up with a gauche sequence.
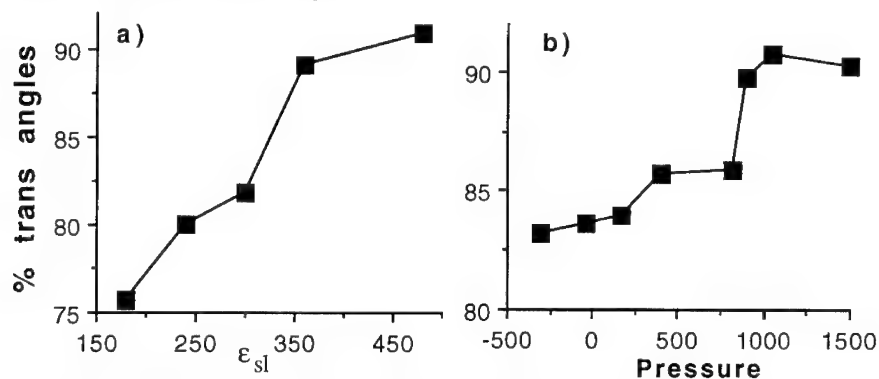
Figure 4. Percentage of trans angles in the film as a function of a) ε_{sl} b) pressure.

The discontinuous structural changes are accompanied by the freezing of molecular translation and rotation in the case of ε_{sl} dependence [6]. The mean square displacement and the time correlation function of molecular end-to-end vector are good measures of molecular mobility. Above the critical ε_{sl} the mean square displacement of the chain centers of mass were much smaller than the molecular dimensions over a period of 0.25 nsec. The decay of the chain end-to-end vector time correlation function was also negligible over the same time period. Below the critical ε_{sl} value the chains were mobile with significant molecular translation and rotation. Near the transition pressure the mean square displacement and the rotational correlation function exhibit similar characteristics. Nevertheless, the effect of pressure in freezing molecular motion is not as sharp as in the case of ε_{sl} dependence.

The cleavage plane of mica used in most SFA experiments is a strongly adhesive surface. Estimates of its effective ε_{sl} range from 360K to 600K, which places it well above the transition threshold for the "room condition" simulations. Though the effect of normal pressure could have been investigated at a lower temperature, we chose to simulate a system at a temperature considerably over the room temperature (360.6K). The effect of pressure in inducing structural transitions even at such an elevated temperature emphasizes the critical role normal forces play in SFA experiments.

We now examine more closely the ordered phases formed above the critical conditions. Figure 5 contains typical snapshots of the first layer molecules at four different ε_{sl} values: ε_{sl} =180.3K, 300.5K, 360.6K and 480.8K. These include the two values below and two above the transition threshold. Figure 6 contains typical snapshots for the following pressures: -40 bar, 820 bar, 900 bar and 1500 bar.

One conspicuous characteristic of the most ordered configurations (fig 5d and 6d) is the presence of two distinct domains with their directors approximately normal to each other. The formation of two such domains is apparent in many such ordered phases. The domains were stable over the time scale of the simulations (1-2 nsec). The presence of the ordered domains instead of a uniform ordered phase lead to the formation of two "grains" through out the whole film. Each grain typically contained about 20-50 octane molecules. Simulations of smaller systems with periodic dimensions 6σ (2.4 nm) always led to the formation of a uniform ordered phase. Therefore, we can conclude that the linear dimensions of these domains should be intermediate between 2 to 3 nm. This is close to the domain size inferred from Scanning Tunneling Microscopy experiments of oligomer monolayers deposited on metal surfaces. However, it is possible that the domains are frozen metastabilities that cannot relax on the time scale of the simulations.

Above the transition values of ε_{sl} and pressure the film can be characterized as a solid. The presence of orientational order and considerable translational order perpendicular to the molecular end to end vector are characteristic of a 2-dimensional smectic. However, no order in the direction parallel to the chain end to end vector, can be observed (figs 5c, 5d, 6c, 6d). So we can safely characterize the film as a solid or a granular solid similar to the "rotator phases" of bulk hydrocarbons. Nevertheless, it is a poorly organized solid (figs 5c, 6c) as manifested by the presence of a few large defects (i.e, presence of partial chains) and numerous small defects (i.e, gauche sequences of ordered chains).

Immediately below the transition thresholds the film is clearly a liquid. This can be readily inferred from the high degree of molecular diffusion and rotation. However, it is a considerably more "viscous" and considerably more "ordered" liquid than bulk octane. Fig 5b and 6b illustrate the presence of strong intermolecular order just below the transitions (ε_{sl}=300.5, P=820 bar).

a) ε_{sl} = 180.3K

b) ε_{sl} = 300.5K

c) ε_{sl} = 360.6K

d) ε_{sl} = 480.8K
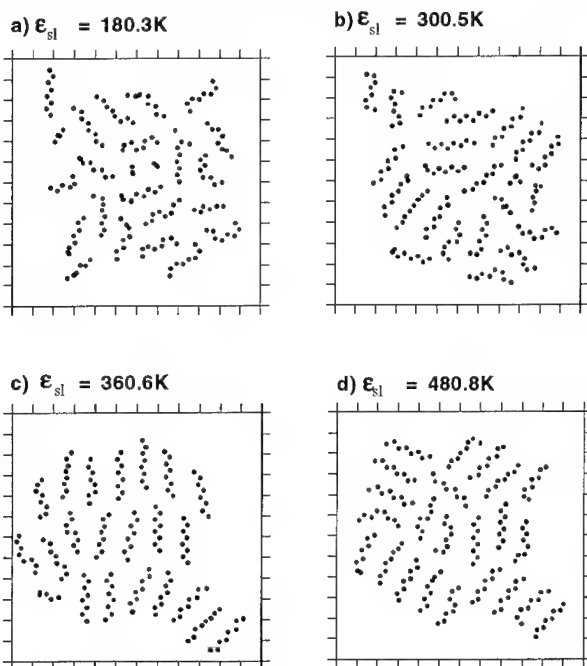
Figure 5. Typical snapshots of the octane chains next to the solid surface for several ε_{sl} values. The dots represent the centers of mass of the segments. The ticks on the axes are spaced one segment diameter apart.

In summary, we have presented results of two sets of molecular dynamics simulation studies designed to explore the effect of increasing solid-segment affinity and increasing pressure in thin n-octane films. The solid surfaces were devoid of any topographical features and were modeled as atomically smooth 10-4 Lennard-Jones planes.

In both simulations we observed a sharp transition in the structural features of the film at some critical value of ε_{sl} and pressure. The transition is signaled by a discontinuous change in the intermolecular order and is facilitated by a sharp extension of the n-octane molecules. The transition is a first order phase transition from a strongly ordered liquid to a weakly organized solid. The molecules formed stable microdomains over the time scale of the simulation (~2 nsec).

These findings demonstrate that the solidification of nanoscopically thin films of short, linear alkanes under the conditions where the bulk is a liquid is a generic, energetically driven phenomenon. Normal pressure has a similar effect on solidifying the thin films. The solidification does not require the aid of commensurate surface topography of the underlying

solid substrate, though it may be promoted or suppressed by the topography of the confining surfaces.

Our simulations provide a natural explanation to the solid like features reported in several experimental studies of thin linear alkane films.

a) P=-40 bar

b) P=820 bar

c) P=900 bar

d) P=1500 bar
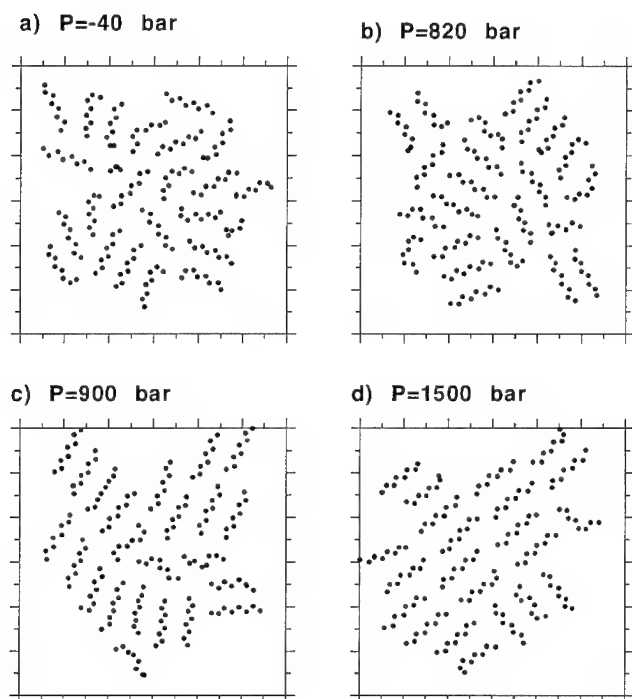
Figure 6. Typical snapshots of the octane chains next to the solid surface for several values of pressure.

ACKNOWLEDGMENTS

REFERENCES

1. J.N. Israelachvili, P.M. McGuiggan, A.M. Homola, Science **240**, 189 (1988).
2 S. Granick, Science, **253**, 1374 (1991).
3. S. Gupta, D.C. Koopman, G.B. Westermann-Clark and I.A. Bitsanis, J. Chem. Phys. **100**, 8444 (1994).
4. D.C. Koopman, S. Gupta, R.K. Ballamudi, G.B. Westermann-Clark and I.A. Bitsanis, Chem. Eng. Sci. **49**, 2907 (1994).
5. D.Y. Chan, R.G. Horn, J. Chem. Phys. **83**, 5311 (1985).
6. R.K. Ballamudi and I.A. Bitsanis, J. Chem. Phys., submitted (1994).

FRICTIONAL FORCES IN THIN LIQUID FILMS

MICHAEL URBAKH, JOSEPH KLAFTER AND LEONID DAIKHIN
School of Chemistry, Tel-Aviv University, Tel Aviv 69978, Israel

ABSTRACT

Shear thinning of confined liquids is studied in the framework of the time dependent Ginzburg-Landau equation coupled to a shear-induced velocity field. Scaling relationship between the effective viscosity and the shear rate is analytically derived with an exponent which depends on the velocity profile within the liquid and on the boundary conditions. The velocity profile is derived in the limit of low shear rate. Thinning is observed for shear rates faster than typical liquid relaxation rates. Relevance to existing systems and predictions amenable to new experiments are discussed.

1. INTRODUCTION

Understanding the properties of liquids in contact with solid surfaces has been a long standing problem with relevance to a broad range technological questions as well as to basic issues in theories of interfaces [1,2]. Changes in the nature of liquids at the liquid-solid interface have been observed experimentally and through molecular dynamics calculations. While the peculiarities of the changes in liquid structure near surfaces are quite well documented and understood, much less is known about the dynamical behaviors of liquids under shear [1-4].

In this paper we concentrate on confined liquids under shear, a problem known as the Couette flow. There has been a revival of interest in this problem, which directly reflects on the fields of tribology and on the general aspects of fluid rheology, following some intriguing experimental results on thin films [3,4]. The latter have stimulated detailed molecular dynamic studies [5-7] and some general theoretical arguments [8]. The main features observed experimentally and through calculations have been: (a) Structural inhomogeneities induced by the surfaces (layering), (b) Substantial increase of the effective viscosity, η_{eff}, relative to the bulk and (c) a non-Newtonian

behavior which displays a flow-dependent effective viscosity [4],

$$\eta_{eff} \sim (\dot{\gamma})^{-\alpha} \tag{1}$$

where $\dot{\gamma}$ is the shear rate, $\dot{\gamma} = V/d$; V being the shear velocity and d the film thickness. The scaling in Eq.(1) corresponds to what is known as shear thinning, namely reduction of the initial effective viscosity with the increase of the shear rate. The reported values of the exponent α have been around $\alpha \cong 2/3$, although higher values, $\alpha \cong 1$, have been also observed [4].

Previous studies have focused on molecular dynamics calculations [5-7] and have contributed important microscopic scale information. Here we introduce a theoretical approach to describe the shear-induced properties of confined liquids, which is based on the coupling between the time-dependent Ginzburg-Landau (TDGL) equation for the order parameter $S(\mathbf{r},t)$ and a velocity field [9,10]. The nature of the velocity field can be dictated, as an example, by the Navier-Stokes equation, or can mimic some known behavior

related to the structure of the confined liquid. The approach is the extension, to include dynamics, of studies of the Landau-Ginzburg equations for equilibrium properties of confined liquids [10,11]. What we obtain is an analytical derivation of Eq.(1) with an exponent α which depends on the velocity profile and on the boundary conditions. We emphasize that our approach is not an atomistically realistic description of the system but we rather derive a reasonable continuum description which holds for a large class of systems independent of molecular details.

2.   THE MODEL

We consider two walls separated by a liquid film. The planes $z = 0$ and $z = d$ are chosen to coincide with the wall surfaces. A flow is generated in the liquid by moving the bottom wall at a constant velocity V in the direction along the axis y. In order to describe the dynamics under shear we start from the TDGL equation for the local order parameter $S(\mathbf{r},t)$

$$\frac{\partial}{\partial t} S(\mathbf{r},t) = - \Gamma \ \mu(\mathbf{r},t) - \nabla \ [S(\mathbf{r},t)\mathbf{v}(\mathbf{r},t)] \tag{2}$$

where Γ is the kinetic coefficient which describes relaxation of the order parameter, $\mathbf{v}(\mathbf{r},t)$ is the local velocity and $\mu(\mathbf{r},t)$ is the local chemical potential, which is expressed as

$$\mu(\mathbf{r},t) = \frac{\delta \ H\{S\}}{\delta \ S(\mathbf{r},t)} \ . \tag{3}$$

Here $H\{S\}$ is the Ginzburg-Landau type free-energy functional

$$H\{S\} = \int d\mathbf{r} \ \left[\frac{a}{2} \ [\nabla \ S(\mathbf{r},t)]^2 + \frac{\tau}{2} \ S(\mathbf{r},t)^2 + ... \right] \tag{4}$$

where a and τ are positive coefficients. As we aim at a general continuum description, the order parameter may mimic liquid density, polarization of liquid molecules, their orientation, local number of near neighbors, etc. The effect of the substrate on the liquid structure is introduced by adding surface terms to the free-energy of the system

$$H_s\{S\} = \sum_{i=1,2} \int d\mathbf{r} \delta(z-z_i)[- h_i(\mathbf{R} - \delta_{i,1} Vt) S(\mathbf{r},t) + \frac{1}{2} C_i S^2(\mathbf{r},t) + ...] \tag{5}$$

where $z_1 = 0$ and $z_2 = d$ and $\mathbf{R} = (x,y)$. A similar model, with uniform interactions along the interfaces, h_i , has been used to study wetting phenomena [12]. The free-energy functional in Eq.(5) introduces the preferred value of the order parameter at the surface, $S(z = z_i, \mathbf{R}) = h_i(\mathbf{R})/C_i$, i = 1,2. The values of the parameters h_i /a and C_i /a determine the equilibrium state at the interface [12]. Here we take into account the lateral nonunifomity of the liquid-solid interactions which plays an essential role in dynamics of confined liquid. The importance of this new aspect has been emphasized in recent molecular dynamic calculations [5-7]. As an example we assume periodically varying liquid-substrate interactions along the interfaces, $h_i(\mathbf{R}) = h \sin(2\pi y/l)$.

The calculations have been done for the quadratic form of the free-energy, Eq.(4), which is simple to handle but yet rich enough to lead to novel shear-induced effects. In this case the parameters $(a/\tau)^{1/2}$ and $1/(\Gamma\tau)$ are the correlation length and relaxation time in the liquid.

The boundary conditions for the order parameter $S(r,t)$ at the two walls, the movable and fixed, follow from the Eqs.(4) and (5) for the free energy and are

$$a \frac{\partial}{\partial z} S(z = 0, \mathbf{R}, t) = C_1 S(z = 0, \mathbf{R}, t) - h_1(\mathbf{R} - Vt) \qquad (6)$$

$$a \frac{\partial}{\partial z} S(z = d, \mathbf{R}, t) = - C_2 S(z = d, \mathbf{R}, t) + h_2(\mathbf{R}) \qquad (7)$$

In order to study the dynamics of the order parameter one needs the velocity distribution in the liquid film. We assume that the liquid is incompressible and that the velocity obeys the modified Navier-Stokes equation

$$\rho \frac{\partial}{\partial t} \mathbf{v}(\mathbf{r},t) = \eta \nabla^2 \mathbf{v}(\mathbf{r},t) - \nabla P(\mathbf{r},t) + \mathbf{f}(\mathbf{r},t) \qquad (8)$$

where ρ is the density, η is the shear viscosity P is the pressure and $\mathbf{f}$ is the force associated with a local stress created by the inhomogeneous order parameter [9]

$$\mathbf{f}(\mathbf{r},t) = \mu(\mathbf{r},t) \nabla S(\mathbf{r},t) \qquad (9)$$

For the velocities within the liquid we use the stick boundary conditions. It should be emphasized that considering the Navier-Stokes equation should be viewed only as an example of how velocities can be coupled to the liquid order parameter (although molecular dynamic studies in thin films [5] which show that $\eta_{eff} \neq$ const, still exhibit a Navier-Stokes - like behavior of the velocity field). The approach is more general, as will be shortly shown, and different velocity distributions can be deduced from other equations relevant to the problem.

The frictional force per unit area, F, which is the experimental observable, can be found from the energy balance in the system. Equation (2) for the order parameter and the Navier-Stokes equation lead to the following expression for the frictional force

$$F = \frac{1}{VL^2} \left\{ \eta \int d\mathbf{R} \left[\mathbf{v}(\nabla\mathbf{v}) + (\mathbf{v}\nabla)\mathbf{v} \right] \Big|_{z=0} - a \int d\mathbf{R} \left[\frac{\partial}{\partial z} S(z = 0, \mathbf{R}, t) \right] \frac{\partial}{\partial t} S(z = 0, \mathbf{R}, t) \right\} (10)$$

where L^2 is the surface area. The first term in Eq.(10) describes the usual viscous friction at the solid-liquid interface and the second term gives an additional contribution associated to the dynamics of ordering in the liquid film. Below we focus on the latter contribution which depends strongly on the liquid-substrate interaction and on the thickness of the film. The effective viscosity of the sheared liquid film, η_{eff}, is defined [3,4] as $\eta_{eff} = Fd/V$. Experimentally it has been observed that η_{eff} of confined liquids is usually $\sim 10^4 \eta$ which means that the second term in Eq.(10), on which we concentrate, dominates. The main effect here is a boundary effect which induces some structure in the confined liquid represented by the order parameter. In the limit

of d $\rightarrow \infty$, where there is no boundary effect, one recovers the bulk behavior, in which only the first term in Eq.(10) contributes and the order parameter is zero.

Equations (2) and (8) have to be solved self-consistently. In the case of zero force, associated with the order parameter, the solution of Navier-Stokes equation with no-slip boundary conditions gives a linear velocity distribution in the film. Both molecular dynamics simulations [5-7] and the results of self-consistent calculations [13] (see Fig.4) show that flow near solid boundaries depends on the strength of the wall-liquid interaction. For strong interactions, of interest in the present paper, the liquid layers adjacent to the two interfaces may be partially locked to the solid walls and the velocity profile is close to linear between these layers [5-7].

We do not solve the problem self-consistently, but instead present the results of an approximate solution for two limiting velocity distributions. Based on the considerations given above we have chosen the following two distributions: (1) a linear one which is reasonable for thick enough "liquid-like" films and (2) a step-wise distribution ($v = V$ for $z \leq d/2$ and $v = 0$ for $z > d/2$) which simulates velocity profile in thin "solid-like" films. In both cases the problem is solved analytically. For this purpose it is convenient to Fourier transform the order parameter $S(r,t) \rightarrow S(z, K, \omega)$. The solutions are expressed in terms of two dimensionless parameters

$$u = d/l_{eff} \qquad \text{and} \qquad g = |\omega| \; (\tau\Gamma)^{-1} \; \frac{l_{eff}^2}{a/\tau} \qquad (11)$$

where $l_{eff} = ((\tau/a) + K^2)^{-1/2}$ is the effective length which characterizes the lateral nonuniformity of the liquid film caused by the "bulk" fluctuations of the order parameter and by nonuniformity of the liquid-substrate interactions. In contrast to the equilibrium properties which are determined mostly by the vertical nonuniformity of liquid films [11], the energy dissipation in our dynamical system is affected by the lateral nonuniformity. For the particular sinusoidal choice mentioned above, with period l , of the liquid-solid interaction one obtains $K = 2\pi/l$ and $\omega = -(KV)$. The parameter u is the ratio of the transversal length d and the lateral length l_{eff} and the parameter g is proportional to the ratio of the liquid relaxation time, $(\Gamma\tau)^{-1}$ and the characteristic time of the wall motion, l/V. The parameter g in Eq.(11) is proportional to the shear rate $\dot{\gamma}$ and can be rewritten as $g = \dot{\gamma}/\dot{\gamma}_0$ where $\dot{\gamma}_0 = al\Gamma/(2\pi d l_{eff}^2)$ and characterizes the relaxation rate in the liquid. Within our model the rate $\dot{\gamma}_0$ is related to relaxation of some lateral structure.

Linear velocity distribution (liquid-like film)

The solution of the dynamic equation for the Fourier component of the order parameter is expressed in terms of Airy functions and leads to the following asymptotic behavior for the effective viscosity at low and high shear rates (see Appendix A)

$$\eta_{eff} = \eta_{eff}^0 \left\{ \begin{array}{ll} 1 & \text{at } \dot{\gamma}/\dot{\gamma}_0 \ll 1 \\[3em] \dfrac{4\pi(\delta + 1)^2 u^{2/3}}{3^{1/6} \; \Gamma(1/3)^2} \left(\dfrac{\dot{\gamma}}{\dot{\gamma}_0} \right)^{-2/3} \left| \delta - \dfrac{\pi(1 + i/\sqrt{3})}{\Gamma(1/3)^2} \left(\dfrac{3 \; \dot{\gamma}}{u\dot{\gamma}_0} \right)^{1/3} \right|^{-2} & \text{at } \dot{\gamma}/\dot{\gamma}_0 \gg 1 \end{array} \right. \qquad (12)$$

Here η^0_{eff} is the maximum value of the effective viscosity

$$\eta^0_{eff} = \frac{\pi^2 h^2 l^4_{eff}}{2\ a^2 l^2 \Gamma}\ (\delta + 1)^{-2} \tag{13}$$

Equation (12) demonstrates that the viscosity reaches its maximum value at low shear rates and remains almost constant in this region ($\dot\gamma/\dot\gamma_0 \ll 1$); in the high shear rate limit ($\dot\gamma/\dot\gamma_0 > 1$) the viscosity exhibits shear thinning according to Eq.(1) with a characteristic exponent, α, which depends on the parameter $\delta = Cl_{eff}/a$. For $\delta \ll 1$ we obtain $\alpha = 4/3$ while for $\delta > 1$ we obtain in the region of intermediate asymptotics ($1 \leq \dot\gamma/\dot\gamma_0 < u\delta^3$) $\alpha = 2/3$ as observed in experiments and in molecular dynamics simulations [4,5]. It should be pointed out that our calculations assume a constant film thickness, while the 2/3 power-law observed in experiments and simulations corresponds to the condition of constant normal pressure. However the experiments were unable to detect a variation of the layer thickness with shear rate and similar results for the exponent were obtained in simulations for the constant thickness [4,5]. The dependence of the effective viscosity on the shear rate calculated over a broad range of $\dot\gamma$ values for different values of the parameter δ is shown in Fig.1. Our calculations also show that the effective viscosity of the liquid-like films only slightly depends on the thickness d, demonstrating power law dependence.

While in the above discussion we have assumed the velocity profile relevant for the experimental realization, one can actually derive the profile within the Navier-Stokes assumption for the low shear rate limit.

Step-wise velocity distribution (solid-like film)

For the step-wise velocity profile, which represents two locked regions, we arrive at the following asymptotic behavior,

$$\eta_{eff} = 2\ \eta^0_{eff}\ u\ e^{-u} \begin{cases} 1 & \text{at}\ \dot\gamma/\dot\gamma_0 \ll 1 \\ \\ 4\sqrt{2}\ (\dot\gamma/\dot\gamma_0)^{-3/2} & \text{at}\ \dot\gamma/\dot\gamma_0 \gg 1 \end{cases} \tag{14}$$

As before the viscosity reaches its maximum value at low shear rates and exhibits shear thinning in the high shear rate limit. In contrast to the liquid-like films the characteristic exponent here is $\alpha = 3/2$ and is independent of the parameter δ . The dependence of the effective viscosity on the shear rate for the solid-like films is presented in Fig.2. Equation (14) is characterized by an exponential dependence of the effective viscosity of a solid-like film on its thickness (see Fig.3). We note that the step-wise velocity distribution may be appropriate for the description of ultrathin surface layers in which the molecules are chemically attached to the surfaces, a case which has been recently studied experimentally [14]. In this case we have a definite plane of slippage as assumed in the model discussed above. Experimental studies indicate that under high pressures ultrathin layers of liquids also show solid-like behavior [14].

133
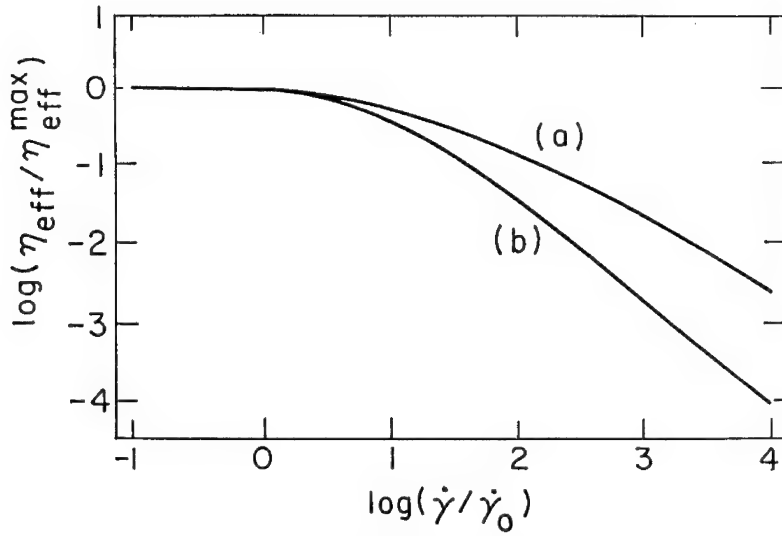
Figure 1. Log-log representation of the reduced effective viscosity as a function of the reduced shear rate obtained for liquid-like films with the thickness $d = 4\, l_{eff}$ and (a) $\delta = 10$, for which $\alpha \approx 2/3$ and (b) $\delta = 0.1$, for which $\alpha = 4/3$.
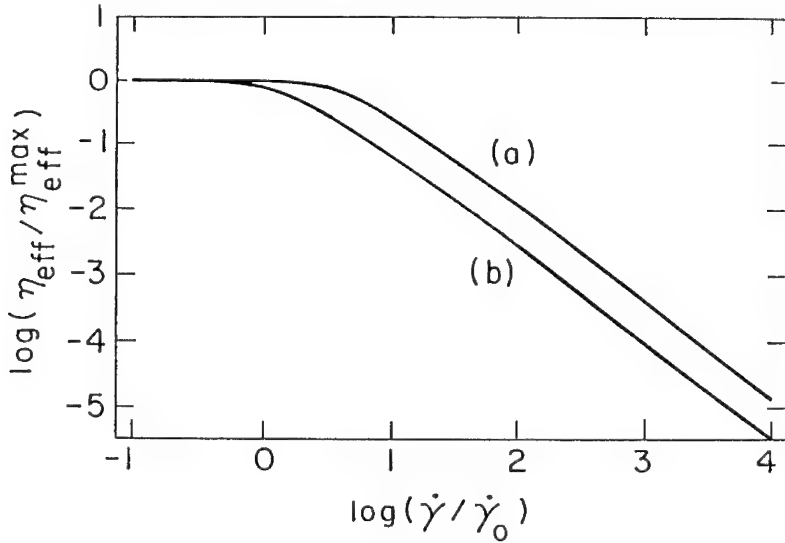
Figure 2. Log-log representation of the reduced effective viscosity as a function of the reduced shear rate obtained for solid-like films with the thickness $d = 2\, l_{eff}$ and (a) $\delta = 10$ and (b) $\delta = 0.1$. In both cases $\alpha = 3/2$.
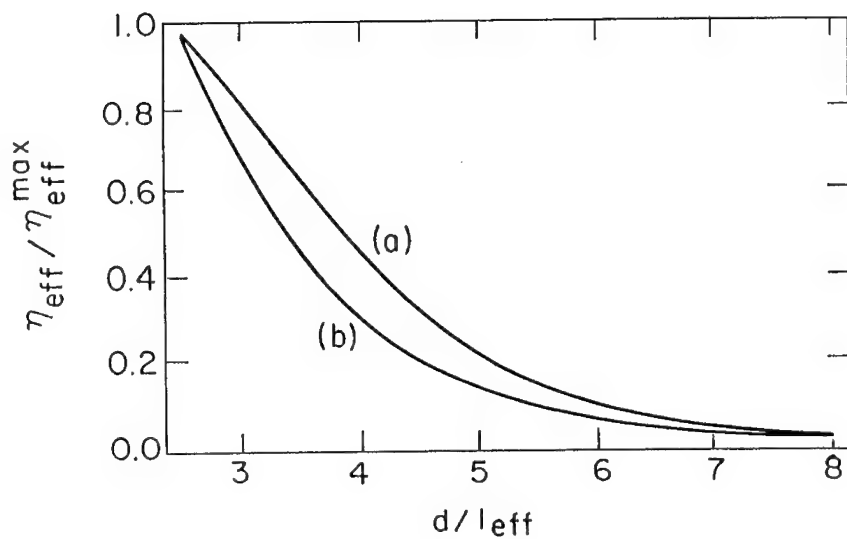
Figure 3. Variation of the reduced effective viscosity of solid-like films with the reduced thickness at low shear rates for (a) $\delta = 10$ and (b) $\delta = 0.1$.
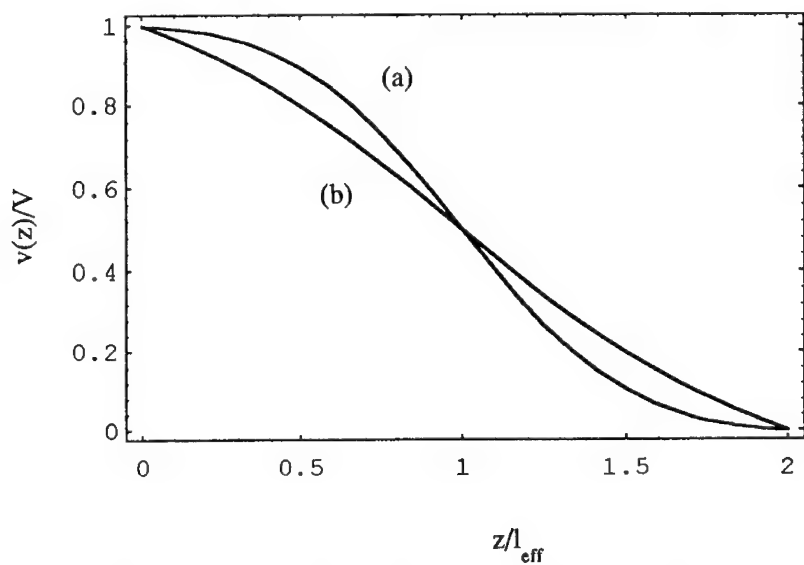
Figure 4. Variation of the reduced velocity $v(z)/V$ within the liquid film with the thickness $d = 2\, l_{eff}$ for two values of the parameter ε: (a) $\varepsilon = 0.01$ and (b) $\varepsilon = 0.1$.

While in the above discussion we have assumed the velocity profile relevant for experimental realization , one can actually derive the profile within the Navier-Stokes assumption. Based on Eqs.(3), (4) and (9) the force $f(r,t)$, induced by the inhomogeneous order parameter $S(r,t)$, which appears in Navier-Stokes Eq.(8), can be written as

$$f(r,t) = - \frac{1}{\Gamma} \int \frac{dK}{(2\pi)^2} \frac{d\omega}{2\pi} \, K \left[\omega + (v(z)K) \right] S(-K, -\omega, z)S(K, \omega, z) \qquad (15)$$

For the calculation of the force $f(r,t)$ in the low shear rate limit ($\dot{\gamma}/\dot{\gamma}_0 < 1$) we need only the static (at $V \equiv 0$) order parameter S . As a result in this limit we arrive at the following equation for the velocity profile in the liquid film, averaged over the plane parallel to the walls,

$$\varepsilon \frac{\partial^2 v(t)}{\partial t^2} - v(t) \, q_1(t) + V \, q_2(t) = 0 \qquad (16)$$

Here we introduced the dimensionless normal coordinate $t = z/l_{eff}$ and the small parameter

$$\varepsilon = \eta/4\eta^0_{eff} , \quad \varepsilon \ll 1 \qquad (17)$$

The averaged velocity is parallel to the wall surfaces. The functions $q_1(t)$ and $q_2(t)$ differ from zero only in the interfacial regions of thickness l_{eff} at the walls and can be written for the liquid films with $d > l_{eff}$ in the form

$$q_1(t) = \exp\left[- 2t \right] + \exp\left[- 2 \, (d/l_{eff} - t) \right]$$

$$q_2(t) = \exp\left[- 2t \right] \qquad (18)$$

Fig.4 exhibits two different velocity profiles which correspond to different values of the small parameter ε. The behavior of the velocity profiles predicted here is in agreement with the results of molecular dynamics calculations [5,6].

4. DISCUSSION

The results in Eqs.(12) and (14) demonstrate that shear thinning is a quite general phenomenon and does not depend on the details of intermolecular interactions in the liquid and between the liquid and the substrate. The non-Newtonian behavior arises when the relaxation time of the liquid structure induced by the interaction with the laterally nonuniform interfaces becomes larger than the time at which the wall passes the length characterizing the lateral ordering, namely $g = \dot{\gamma}/\dot{\gamma}_0 > 1$. The value of the exponent α, the maximum value of the effective viscosity, and the magnitude of critical

136

shear rate $\dot{\gamma}_c$ at which the non-Newtonian behavior starts, depend on the properties of the system : the film thickness, the boundary conditions on the order parameter and the velocity distribution in the liquid film. Our calculations show that the exponent α spans the interval $2/3 \leq \alpha \leq 3/2$. The exponent reaches the lower and upper bound values in the two limiting cases, respectively: the liquid-like films with the linear velocity distribution and the solid-like films with the step-wise velocity distribution. For intermediate velocity distributions, which we do not discuss in detail here, we expect the exponent α to lie between 2/3 and 3/2. It should be stressed that the exponents discussed above describe the asymptotic behavior of the effective viscosity for high shear rates. The values found from the experimental data could be smaller if the asymptotic region is not reached during the measurements. The predicted values of the exponent α depend on the velocity profiles which should be obtained in self consistent way from Eq.(2) and the Navier-Stokes equation. The velocity profile itself may change with the shear rate. Here we presented only the approximate solution of the equations which holds for the given velocity profiles. The self-consistent solution may still change the values of the exponent.

The experimental observation [4] of a strong dependence of η_{eff} on thickness for very thin films can be explained under the assumption that the step-wise velocity distribution is applicable. With the increase of the thickness the velocity distribution changes to the linear profile and the film passes from the solid-like to liquid-like state. As a result the effective viscosity loses its pronounced dependence on the film thickness, as observed experimentally [4]. It should be mentioned that within our model this transition is not related to any phase transition in the system. The observation of the exponent $\alpha \approx 2/3$ may indicate that the film is close to the liquid-like state and that $\delta > 1$ (see Eq.(12)). It is important to note that this value of the exponent has been obtained in the region of the thicknesses where the effective viscosity only slightly depends on the thickness that gives additional support to the above statement.

In conclusion, shear thinning is obtained in the framework of the TDLG equation coupled to a velocity field for shear rates faster than relaxation rates in the liquid. The scaling relationship, Eq.(1), emerges naturally from the model with a scaling exponent which depends on the nature of the velocity field and on the boundary conditions. Our results demonstrate that the thinning is enhanced in the step-wise velocity case ($\alpha = 3/2$) relative to the hydrodynamic, liquid-like case ($\alpha = 4/3$ or $\alpha = 2/3$). In the liquid-like regime dependence on surface wetting is predicted, which should be amenable to experimental observation by changing the liquid-wall interactions. The experimental findings of thinning with $\alpha \approx 2/3$ and the dependence η_{eff} on liquid thickness concur with a possible solid-like to liquid-like transition.

ACKNOWLEDGEMENTS

APPENDIX

For the linear velocity distribution, $v(z) = V(1 - z/d)$, the dynamical equation (2) takes the following form in the $(z, \mathbf{K}, \omega)$ - representation

$$\left[\frac{\partial^2}{\partial z^2} - \left(\frac{\tau}{a} + \mathbf{K}^2 + \frac{i\omega}{a\Gamma} \right) - \frac{i(\mathbf{KV})}{a\,\Gamma}(1 - z/d) \right] S(z, \mathbf{K}, \omega) = 0 \qquad (A1)$$

The boundary conditions (6) and (7) transforms to

$$a\,\frac{\partial}{\partial z} S(z = 0, \mathbf{K}, \omega) = C_1 \, S(z = 0, \mathbf{K}, \omega) - h_1(\mathbf{K})\,\delta(\omega + (\mathbf{KV})) \qquad (A2)$$

$$a\,\frac{\partial}{\partial z} S(z = d, \mathbf{K}, \omega) = -C_2 \, S(z = d, \mathbf{K}, \omega) + h_2(\mathbf{K})\,\delta(\omega) \qquad (A3)$$

For the particular form of the liquid-substrate interaction $h_i(\mathbf{R}) = h \ \sin(2\pi y/l)$ considered here the wave vector $\mathbf{K}$ takes the values $\mathbf{K} = (0, \pm 2\pi/l)$.

The solution of Eq.(A1) is expressed through the Airy functions [15]

$$S(z, \mathbf{K}, \omega) = D_1 \, \mathrm{Ai}(\xi) + D_2 \, \mathrm{Bi}(\xi), \qquad (A4)$$

where

$$\xi = -(igu^2)^{1/3}\left[\frac{z}{d} + ig^{-1} \right] \qquad (A5)$$

The prefactors D_1 and D_2 are obtained from the boundary conditions (A2) and (A3) :

$$D_1 = A_{11}(\mathbf{K})h_1(\mathbf{K})\delta(\omega + (\mathbf{KV})) - A_{12}(\mathbf{K})h_2(\mathbf{K})\delta(\omega) \qquad (A6)$$

$$D_2 = A_{21}(\mathbf{K})h_1(\mathbf{K})\delta(\omega + (\mathbf{KV})) + A_{22}(\mathbf{K})h_2(\mathbf{K})\delta(\omega) \qquad (A7)$$

Here

$$A_{11}(\mathbf{K}) = [-\kappa \mathrm{Bi}'(\xi_2) + C_2\mathrm{Bi}(\xi_2)]/\mathrm{Det} \ , \ A_{12}(\mathbf{K}) = [\kappa \mathrm{Bi}'(\xi_1) + C_1\mathrm{Bi}(\xi_1)]/\mathrm{Det} \ ,$$

$$A_{21}(\mathbf{K}) = [\kappa \mathrm{Ai}'(\xi_2) - C_2\mathrm{Bi}(\xi_2)]/\mathrm{Det} \ , \ A_{22}(\mathbf{K}) = [\kappa \mathrm{Ai}'(\xi_1) + C_1\mathrm{Ai}(\xi_1)]/\mathrm{Det}$$

$$\kappa = [i(\mathbf{KV})/(a\Gamma d)]^{1/3} \ ,$$

$$\xi_1 = \xi(z = 0) = (i^{-1}g^{-1}u)^{2/3} \ , \ \xi_2 = \xi(z = d) = -(igu^2)^{1/3}[\ 1 + ig^{-1}],$$

$$Det = \left[\ \kappa Ai'(\xi_1) + C_1 Ai(\xi_1)\ \right]\left[\ -\kappa Bi'(\xi_2) + C_2 Bi(\xi_2)\ \right] -$$

$$\left[\ -\kappa Ai'(\xi_2) + C_2 Ai(\xi_2)\ \right]\left[\ \kappa Bi'(\xi_1) + C_1 Bi(\xi_1)\ \right] \qquad (A8)$$

and prime denotes the derivative with respect to ξ .

Substitution of Eqs.(A4), (A6) and (A7) into Eq.(10) leads to the following expression for the frictional force

$$F = -\frac{a\pi h^2}{1}\ Im\left\{\ \kappa\ \left[\ |A_{11}(2\pi/l)|^2\ Ai'(\xi_1)Ai^*(\xi_1) + |A_{21}(2\pi/l)|^2\ Bi'(\xi_1)Bi^*(\xi_1) + \right.\right.$$

$$\left.\left. A_{11}{}^*(2\pi/l)\ A_{21}(2\pi/l)Bi'(\xi_1)Ai^*(\xi_1) + A_{11}(2\pi/l)\ A_{21}{}^*(2\pi/l)Ai'(\xi_1)Bi^*(\xi_1)\right]\right\} \qquad (A9)$$

Using the asymptotic expressions for the Airy functions [15] in Eq.(A9) we arrive at the Eq.(12) for the effective viscosity.

Similar calculations have been carried out for the step-wise velocity distribution.

REFERENCES

1. I. L Singer and H. M. Pollock, Eds. Fundamentals of Friction, NATO ASI Proceedings, (Kluwer, Dordrecht, 1992) .
2. MRS Bulletin, **18** (5) (1993), see pages 15-59.
3. (a) M.L. Gee,P.M. McGuiggan and J.N. Israelachvili, J. Chem. Phys. **93**, 1895 (1990); (b) H. Yoshizawa, P.M. McGuiggan and J.N. Israelachvili, Science **259**, 1305 (1993).
4. (a) J. Van Alsten and S. Granick, Phys. Rev. Lett. **61**, 2570 (1988); (b) H-W. Hu, G.A. Carson and S. Granick Phys. Rev. Lett. **66**, 2758 (1991); (c) S. Granick, Science **253**, 1374 (1992)
5. (a) P.A. Thompson and M.O. Robbins, Phys. Rev. A **41**, 6830 (1990); Science **250**, 792 (1990); (b) P.A. Tompson, G.S. Grest and M.O. Robbins, Phys. Rev. Lett. **66**, 3448 (1992).
6. (a) I. Bitsanis, J.J. Magda, H.T. Davis and M. Tirrell, J. Chem. Phys. **87**, 1733 (1987); (b) I. Bitsanis, S.A. Somers, H.T. Davis and M. Tirrell, J. Chem. Phys. **93**, 3427 (1990).
7. L. Bocquet and J.-L. Barrat, Phys. Rev. Lett. **70**, 2726 (1993); Phys. Rev. B **49**, 3079 (1994).
8. Y. Rabin and I. Hersht, Physica A **200**, 708 (1993).
9. (a) K. Kawasaki, Ann. Phys. (NY), **61**, 1 (1970); (b) T. Koga and K. Kawasaki, Physica A **196**, 389 (1993); (c) T. Koga, K. Kawasaki, M. Takenaka and T. Hashimoto, Physica A **198**, 473 (1993).
10. P.C. Hohenberg and B.I. Halperin, Rev. Mod. Phys. **49**, 435 (1977).

11. (a) S. Marcelja and N. Radic, Chem. Phys. Lett. **42**, 129 (1976); (b) M.E. Fisher and H. Nakanishi, J. Chem. Phys. **75**, 5857 (1981); (c) R. Evans, J. Phys.: Condens. Matt. **2**, 8989 (1990); (d) S. Dietrich, in: Phase Transitions and Critical Phenomena, vol. 12, ed. by C. Domb and J. L. Lebowitz (Academic Press, New York, 1988) p.1.
12. P.G. de Gennes, Rev. Mod. Phys. **57**, 827 (1985).
13. The detail discussion of the results of the self-consistent solution of the Navier-Stokes equation will be presented in a future publication.
14. G. Reiter, A. L. Demirel, J. Peanasky, L. L. Cai and S. Granick, J. Chem. Phys. **101**, 2606 (1994).
15. M. Abramovitz and I. Stegun, Eds. Handbook of Mathematical Functions (Dover, New York, 1965).

MIXTURES IN SLIT-MICROPORES WITH PORE-WALLS STRUCTURED ON BOTH THE ATOMIC AND NANOSCALE

J.E. CURRY AND J.H. CUSHMAN
Center for Applied Mathematics, Math Sciences Building, Purdue University, West Lafayette, IN 47907

ABSTRACT

The grand canonical Monte Carlo method is used to study a binary mixture of Lennard-Jones atoms confined to various corrugated slit-micropores which are in thermodynamic equilibrium with their bulk phase counterpart. The micropore walls have the structure of the (100) face of an fcc lattice. In addition to this atomic scale structure, one wall possesses nanoscale structure in the form of rectilinear grooves (corrugation). The grooved surface divides the confined fluid film into two strip shaped regions. The confined film is studied in each region as a function of groove width, bulk phase composition, and the size of the wall atoms.

INTRODUCTION

Significant progress has been made in simulating fluid behavior on a molecular. Of most importance in this regard is the marked progress made in the use of computer simulation to study fluids confined to systems of molecular dimension[1]. Such simulations have shown that fluids confined to spaces of molecular dimension behave significantly different from their bulk-phase counterparts[2]. From these simulations it has been clear for many years[3,4] that the discrete molecular-scale lattice structure in the walls of a slit-micropore impacts a significant perturbation on the structural and dynamical character of the pore fluid. Specifically, recent work[5] has illustrated the role corrugation in one of the confining walls of a slit-micropore plays in determining the character of the pore fluid. In this article we expand on previous efforts and study the effect the size of the wall defect (corrugation) size of wall atoms, and bulk phase composition has on species segregation and phase in different regions of the pore.

In earlier work[5] the authors studied a single component Lennard-Jones (LJ) fluid confined to an infinite corrugated slit-micropore. We found that under appropriate alignment of the surfaces the fluid film froze epitaxially to the wall lattice, and that a subsequent slight misalignment (change in registry) of the surfaces could result in liquid and solid phases coexisting in separate regions of the pore. More significant misalignment results in liquefaction of the entire film. In another study[6] the authors examined a binary mixture of different sized LJ molecules confined to an atomically structured slit-micropore without any nanoscale corrugation. Molecular sieving (segregation based on size exclusion) was observed much as it was in Somers et al.[7]. In addition we observed a significant compositional sensitivity to the relative alignment of the two walls. With these studies as motivation we

next investigated the properties of binary mixtures confined to corrugated micropores with fixed size of corrugation[8]. The grooved surface divides the confined fluid film into two strip shaped regions, that inside and that outside the grooves. Transverse solid-like order in the film gave rise to shear stress. Transverse order coupled with packing restrictions gave rise to a difference between the bulk and pore fluid mixture compositions. Solid-like order could appear within the grooves only, outside the grooves only, or in both regions simultaneously. As the relative alignment of the walls was shifted the pore fluid underwent freeze-thaw cycles in one or both regions with associated changes in the shear stress and pore fluid composition.

Model

Our nanostructued model (see Fig. 1) is a modification of the prototypal slit-pore[3] (hereafter referred to as the "prototype"), whose walls consist of atoms rigidly fixed in the (100) plane of the face-centered-cubic (fcc) lattice. As an approximation we have neglected the motion of the wall atoms. One wall of the nanostructured model is identical with the prototypal wall. The other wall is constructed by removing portions of one or more layers of atoms from the (100) face of the fcc lattice to create rectilinear grooves (i.e. corrugation)[5]. The lattice constant ℓ is $1.5985\sigma_w$ where σ_w is the diameter of a wall atom. The dimensions of the groove are specified by its width, s_b, and depth, h_b. The infinite corrugated pore is simulated by applying periodic boundary conditions on the edges of the simulation cell whose dimensions are s_x by s_y. The separation between the walls is h in the narrow regions and h + h_b in the wide regions where h is measured from the center of the wall atoms. The relative lateral alignment of the walls in the x-direction, or the registry, α, is given in the narrow region in terms of the coordinates of the corresponding atoms: $x_i^{(2)} = x_i^{(1)} + \alpha\ell$; $y_i^{(2)} = y_i^{(1)}$; $z_i^{(2)} = z_i^{(1)} + h$ where the superscripts (1) and (2) refer to the lower and upper walls respectively. Note that the walls are kept permanently aligned in the y-direction. We set α to zero when the walls are precisely in registry and to 0.5 when they are completely out of registry. In the wide region of the pore the relationship of the coordinates of wall atoms depends on the depth of the groove. If the groove is an odd number of solid layers deep, (i.e. $h_b = \ell/2, 3\ell/2, ...$), the registry in the wide region of the pore is (0.5 - α), whereas if the groove is an even number of layers deep (i.e. $h_b = \ell, 2\ell$, ...), the registry is α throughout the pore. For the cases considered here, $h_b = 0.5\ell$, and corresponding wall atoms in the wide region of the pore are thus related by $x_i^{(2)} = x_i^{(1)} + (0.5 - \alpha)\ell$; $y_i^{(2)} = y_i^{(1)}$; $z_i^{(1)} + h + h_b$.

The fluid and wall atoms are spherical, nonpolar, Lennard-Jones (LJ) atoms characterized by diameters σ_i and interaction energies ε_i where i indicates the fluid species (i = 1, 2) or wall atom (w). The total potential energy of the confined fluid mixture is approximated as a pairwise sum of shifted-force LJ (12,6) interactions with cylindrical cutoff $3\sigma_{ij} = 3/2 (\sigma_i + \sigma_j)$. The interaction energy between atoms of species i and j is thus given by[6]

$$u^{SF}\left(r_{ij}\right) = 4\varepsilon_{ij}\left[\left(\frac{\sigma_{ij}}{r_{ij}}\right)^{12} - \left(\frac{\sigma_{ij}}{r_{ij}}\right)^{6} - C_1 - C_2\left(\frac{r_{ij}}{\sigma_{ij}} - 3\right)\right]$$
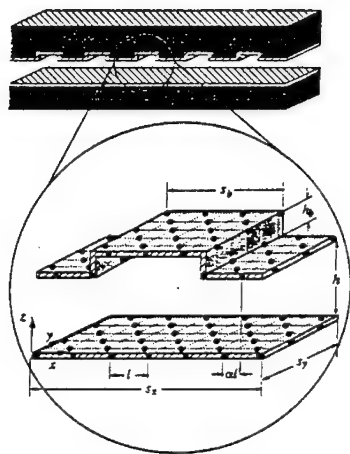
Figure 1. Schema of the corrugated slit-pore; inset details the simulation cell. The origin of the coordinate system lies at the intersection of the vectors labeled x, y and z. Reprinted from J.E. Curry and J.H. Cushman, J. Chem. Phys. (Submitted, 1994).

where $C_1 = -0.001370$, $C_2 = 0.002736$, and $\varepsilon_{ij} = (\varepsilon_i\varepsilon_j)^{1/2}$. The explicit value of the cutoff radius has been substituted into the shifted force expression to obtain C_1 and C_2. The cutoff distance depends on σ_{ij} and therefore varies for different sized atoms.

The temperature for all simulations is 119.8 K. To completely specify the thermodynamic state of the bulk mixture we must choose the chemical potential, size and potential energy well depth of the mixture components (μ_1, μ_2, σ_1, σ_2, ε_1, ε_2). Our goal is to investigate the role wall atomic and nanoscale structure has on the selectivity of one species over another from a bulk binary mixture and the effect of mixture composition and structure on shear-stress. The atom size and the strength of the interaction potential of both fluid and wall species are important parameters. Our mixture consists of two different sized species σ_1 = 3.405Å and σ_2 = 2.55Å with the same interaction potential well depth ε_1 and ε_2 = 1.654 $\times 10^{-21}$J. This choice of LJ parameters was motivated in part because of the similarity with a mixture of octamethyltetracyclosiloxane (OMCTS) and cyclohexane, a common mixture used in SFA experiments, whose LJ parameters are taken to be σ_2/σ_1 = .70 and $\varepsilon_2/\varepsilon_1$ = 0.94[7]. We determine the chemical potential for each component as discussed in reference[6] to give each of the bulk mixtures at two different compositions, 15% large atoms, $X_1 = 0.15$ ($\mu_1/\varepsilon_1 = -11.48$, $\mu_2/\varepsilon_2 = -9.513$), and 86% large atoms, $X_1 = 0.86$ ($\mu_1/\varepsilon_1 = -10.093$, $\mu_2/\varepsilon_2 = 11.864$), where X_1 is the fraction of the large atoms. For simplicity, the mass of all fluid atoms is taken as that of argon.

Two different models of the corrugated surface, schematically illustrated in Fig. 2, are used to study the effect σ_w has on the fluid. In the first (system I) the wall atoms are identical to the large fluid species, σ_w = 3.405Å, sx = 10ℓ (period of corrugation is 10ℓ), s_y = 5ℓ and s_b = 5ℓ. In the second (system II) the wall atoms are identical to the small fluid species, σ_w = 2.55Å, s_x = 14ℓ (period of corrugation is 14ℓ), s_y = 7ℓ and s_b = 7ℓ. The period of corrugation is similar for the two systems. Two other systems are used to study the

role the groove width has on confined fluid composition and phase. System III is similar to system I except $s_b = 2\ell$ and $s_y = 10\ell$. System IV is similar to system II except $s_b = 3\ell$ and $s_y = 14\ell$.
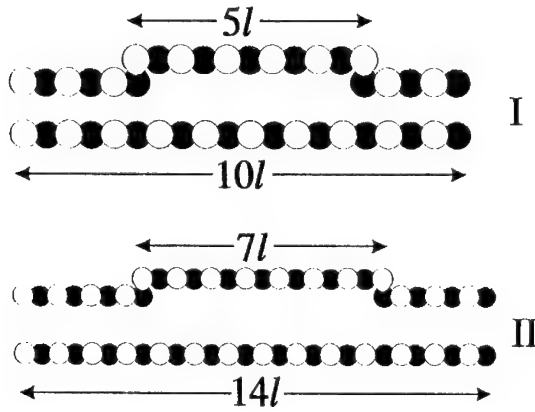
Figure 2. Schematic diagrams for the corrugated pores I and II of Fig. 1. Reprinted from J.E. Curry and J.H. Cushman, J. Chem. Phys. (Submitted, 1994).

Computational Methods and Properties

We examine the behavior of the confined mixture as the walls are quasistatically displaced (strained) relative to one another; all the while the components of the confined mixture are kept in equilibrium with their bulk phase counterparts. That is, we study the behavior of the film as the registry, α, is systematically varied at fixed temperature (T), chemical potentials (μ_1, μ_2), and pore width (h). We apply the grand-canonical ensemble Monte Carlo (GCEMC) method following the prescription of Adams[9] as outlined in reference[6]. By sliding the walls over one another in the x-direction, we vary the registry incrementally from $\alpha = 0.0$ to $\alpha = 0.5$. We choose $h = 1.7\sigma_1$ for all simulations reported here, as the character of the prototypal fluid for these parameter values is know from previous work[6]. For each GCEMC simulation the system was equilibrated for an average of 1×10^6 steps followed by a production run of length 1×10^7 steps.

Structural features of the pore fluid are presented in terms of partially averaged local density profiles, $\overline{\rho^{(1)}}$. The partially averaged local density, $\overline{\rho_i^{(1)}(z)}$, for species i, is calculated separately for the narrow and wide regions of the pore fluid and is given by

$$\overline{\rho_i^{(1)}(z)} = \langle N_i(z) \rangle / s_y \Delta x \Delta z ,$$

where $\langle N_i(z) \rangle$ is the average number of film atoms of species i in a layer of thickness $\Delta z = 0.02\sigma_1$ about z and $s_y \Delta x$ is the area of the layer. To avoid spurious effects attributable to the interface between narrow and wide regions, we consider only atoms in a central strip of each region; Δx, the x dimension of that strip, is taken to be $s_b/2$ and is centered on $x = 0.0$ for the narrow region and on $x = s_x/2$ for the wide region.

The shear stress is the average force per unit area exerted by the film on either wall in the x-direction and is expressed as

$$T_{zx}^k = \sum_{i=1}^{N} \sum_{j=1}^{N_s^k} \langle x_{ij} u'(r_{ij})/r_{ij} \rangle / s_x s_y$$

where N is the number of film atoms and N_s^k is the number of solid atoms in wall k ($k = 1$ or 2). To enhance statistical accuracy we set

$$T_{zx} = \left(T_{zx}^1 + T_{zx}^2 \right) / 2 .$$

The normal stress T_{zz} is similar to T_{zx} only x_{ij} is replaced by z_{ij}.

Results and Discussion

Epitaxial alignment of one or both species within one or both regions of the pore gives rise to shear stress[10]. Solid-like order of one or both species causes the pore fluid composition to shift toward the component which becomes structured[8]. Here we study eight examples (15% or 86% large atoms in the bulk phase for each of systems I-IV) of binary mixtures confined in corrugated slit-pores subject to an incremental change in registry from $\alpha = 0.0$ to $\alpha = 0.5$. The composition, normal and shear stress change between cases with changes in registry.

In system I the mixture which is 86% large atoms (Figs. 3, 4) in the bulk, is confined in a pore whose walls are constructed from atoms which are the same size as the large mixture species. Fig. 3 shows the normal and shear stress for each species, fraction of large atoms within the wide and narrow regions and the average number of particles of each species within the wide and narrow regions as the registry is varied from $\alpha = 0.0$ to $\alpha = 0.5$. The pore width is such that one layer of large atoms fits in the narrow region and two layers fit in the wide region. Figure 4 displays density plots for each species in the wide and narrow regions of the pore. When $\alpha = 0.0$ the large atoms solidify into a single layer solid in the narrow region and a two layer solid in the wide region, as evinced by the sharp peaks in the density profiles in Fig. 4. The lower panel in Fig. 3 indicates though the large species is frozen a few small atoms remain in each region of the pore, i.e. there is not complete exclusion of the small species. The panel second to the bottom in Fig. 3 indicates that the large atom species is preferentially adsorbed when $\alpha = 0.0$ in both regions of the pore relative to the bulk phase with which it is in equilibrium. As α increases the preferential adsorption decreases until around $\alpha = 0.25$, where the small atom begins to preferentially adsorb in both regions of the pore. As the walls are shifted out of alignment (α increases)

the fluid melts as indicated by the decrease in the intensity of the density peaks of Fig. 4. The melting is not abrupt however as evinced by the gradual change in atom number as indicated in the lowest panel of Fig. 3. Thus, strain inducted melting in this case is not first-order. The gradual transition here is attributable to the presence of small atom impurities in the large atom lattice, which we believe decreases large atom long range cooperativity. As the structure of the frozen film is strained the magnitude of the shear stress increases elastically until $\alpha \approx 0.3$, at which point it begins to decrease linearly as a result of liquification of the film. The compressive stress depicted in the top panel of Fig. 3 increases with increasing strain on the film until $\alpha \approx 0.3$ and then it becomes relatively constant. Thus though the film is behaving elastically in shear-stress it is not dilating as an elastic material would be expected to.
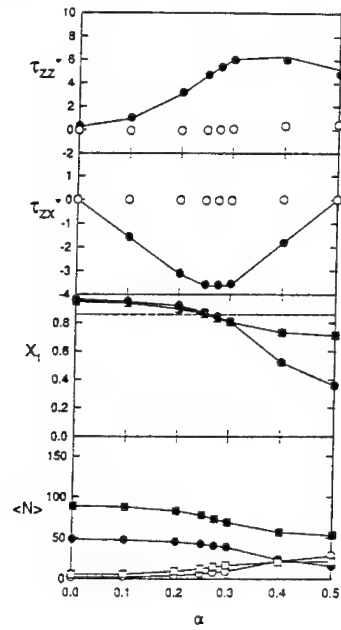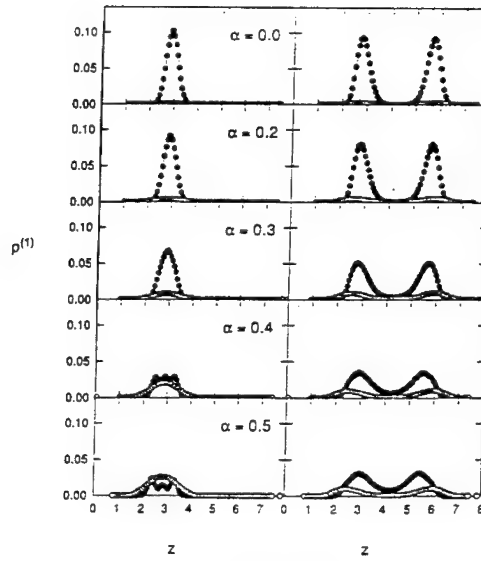
Figure 3   Figure 4

Figure 3. Normal and shear stress, fraction of large atoms and atom number by region and species for 86% bulk mixture in system I. (Top panel) Normal stress: total (-), large component (●) and small component (○). (Second panel) Shear stress: total (-), large component (●) and small component (○). (Third panel) Fraction of large atoms in the narrow (●) and wide (■) regions. (Bottom panel) Average number of atoms in the narrow region, large (●) and small (○), and in the wide region, large (■) and small (□).

Figure 4. Local density profiles, $\rho^{(1)}$, for large atoms (●) and small atom (○) calculated separately for the narrow (left) and wide (right) regions for avarious registries with an 86% large atom bulk mixture in corrugated pore I.

Figures 5 and 6 are similar to Figs. 3 and 4 only now the bulk phase with which the pore phase is in equilibrium is 15% large atoms. In the wide region the fraction of large atoms remains constant, near the bulk value. The two layer large atom solid present in the previous case is not present here. The density profile peaks of Fig. 6 show the fluid in the wide region to be two layer liquid-like and only slightly affected by registry. At $\alpha = 0.0$ the large atoms in the narrow region form a one layer solid as in the previous case, however the number of large atoms participating in the structure is small compared to the smaller liquidic atoms in the same region. With increasing registry the shear stress changes sign and increases in magnitude as the small atoms arrange into a two layer solid in the narrow region at $\alpha = 0.5$. A qualitatively similar trend is observed in the normal stress associated with the small atoms. Snapshots (not shown) suggest the small atoms are epitaxially aligned with the large atom surface and are not able to pack as tightly as in their natural close packed structure and therefore do not sustain as much shear stress. This example is novel because only the fluid in the narrow region changes; the fluid in the wide region is only slightly affected by strain.
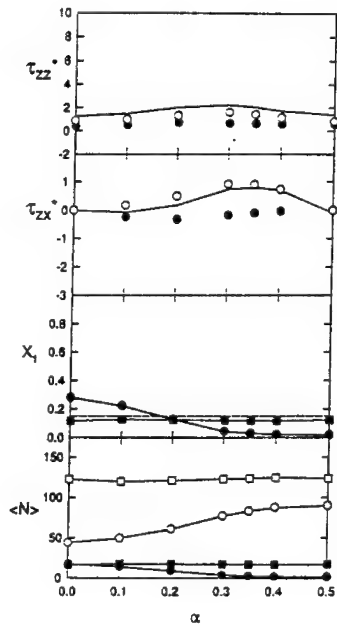
Figure 5   Figure 6

Figure 5. As for Fig. 3 with 15% large-atom bulk phase.
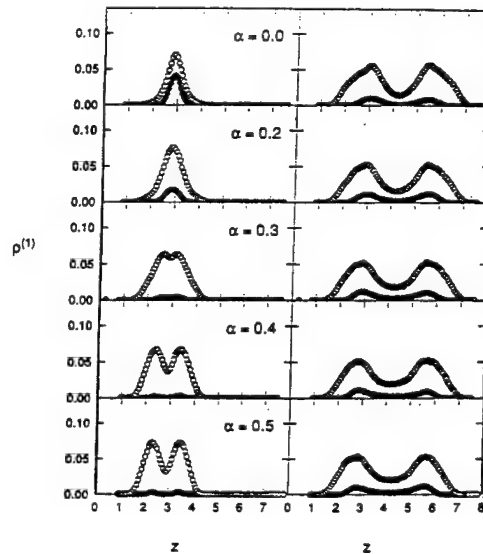
Figure 6. As for Fig. 4 with 15% large-atom bulk phase.

The third pore studied is identical to the first except the walls are now composed of small atoms rather than large atoms. Figs. 7 and 8 are similar to Figs. 3 and 4 respectively. The main point to be observed in Fig. 7 is the formation of at two-layer solid at $\alpha = 0.5$ while the narrow region remains liquidly. Such a phenomena was not observed[5]. The broad density profile peaks for the wide region at $\alpha = 0.0$ indicate a mixed two-layer fluid. Snapshots not shown show that as $\alpha \to 0.5$ the large atoms form an epitaxial fcc structure rotated $45°$ with respect to the wall lattice with lattice constant $\sqrt{2}\ell$. This is a loosely packed structure which according to Fig. 7 does not support much shear stress but it does lead to significant normal stress. The wide region large atom fraction is less than the bulk but increase as $\alpha \to 0.5$. On the other hand, the narrow region fraction of large particles remains nearly the same as the bulk phase.
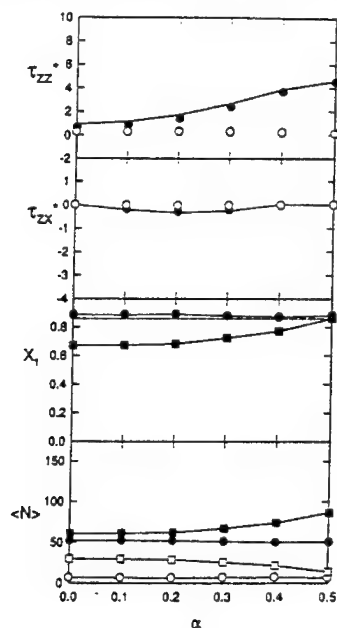
Figure 7

Figure 8

Figure 7. As for Fig. 3 with system II.
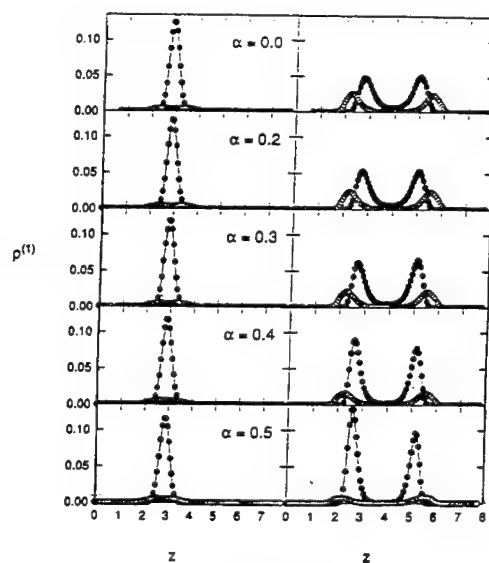
Figure 8. As for Fig. 4 with system II.

Figures 9 and 10 are similar to Figs. 7 and 8 only now the pore phase is in equilibrium with a 15% large atom fraction in bulk. Large atoms are favored in the narrow region relative to the bulk since the pore width is optimum for a one layer large atom fluid. Figure 10 shows the small component to be in transition between a one and a two layer fluid. The wide region is relatively unaffected by α and it is of composition similar to the bulk. Both the shear and normal stresses are qualitatively similar to the previous two figures.

148
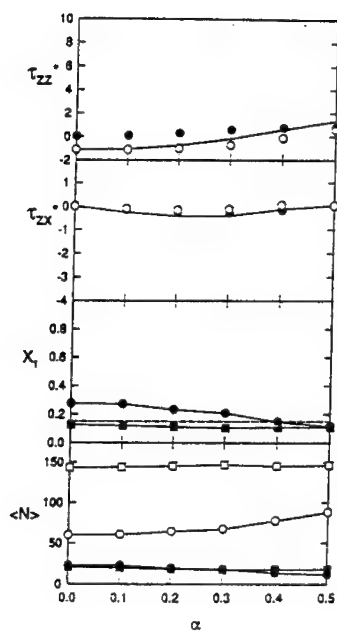
Figure 9

Figure 10

Figure 9. As for Fig. 7 with 15% large-atom bulk phase.
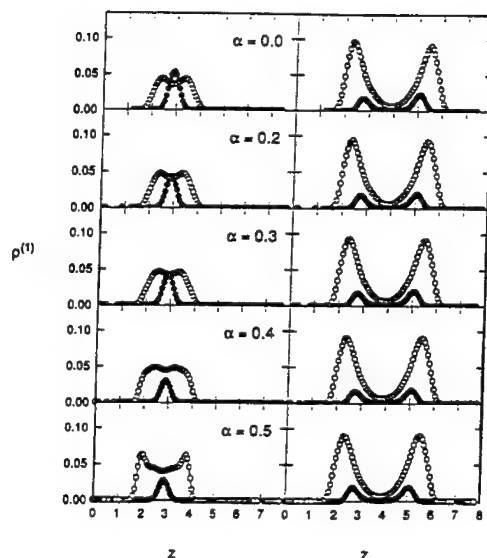
Figure 10. As for Fig. 8 with 15% large-atom bulk phase.

Figures 11 and 12 have the pore walls made of large atoms and the pore fluid in equilibrium with a bulk mixture having 86% large atoms. The difference between this setting and that depicted in Figs. 3 and 4 is that the groove width has been reduced here to 2ℓ . Qualitatively the graphs in Fig. 3 and Fig. 11 are similar however there is a subtle quantitative difference. The magnitude of the normal and shear stresses are larger when the groove width is small, owing to increased epitaxial arrangement. At $\alpha = 0.0$ a two-layer large atom solid exits in the groove and a one-layer large atom solid exists outside the groove. In both areas small atom impurities remain. Figures. 4 and 12 are also qualitatively similar, however there again exists one subtle difference. The symmetry of the wide region large atom peaks is destroyed when the groove width is 2ℓ. A similar phenomena was observed[5]. Figures 13 and 14 correspond to the same setting as Figs. 11 and 12 except now the bulk solution has 15% large atoms. Comments similar to the previous two figures are apropos here as well.
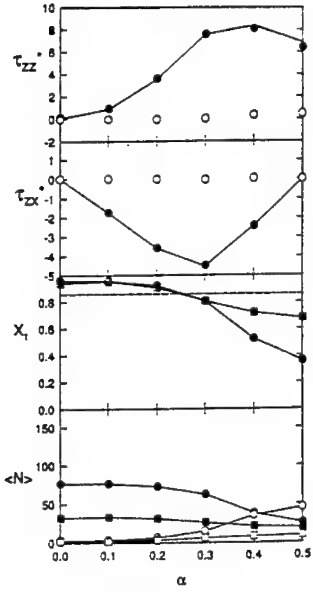
Figure 11. As for Fig. 3 in system III.
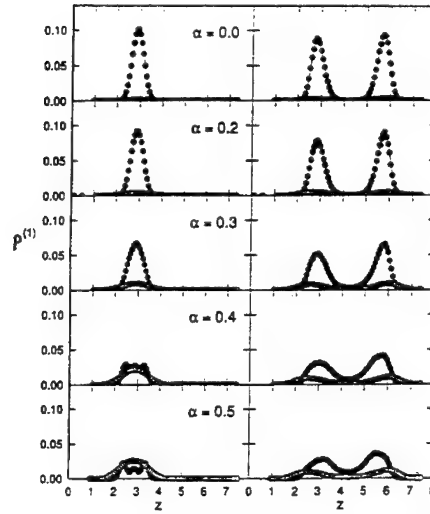
Figure 12. As for Fig. 4 with system III.
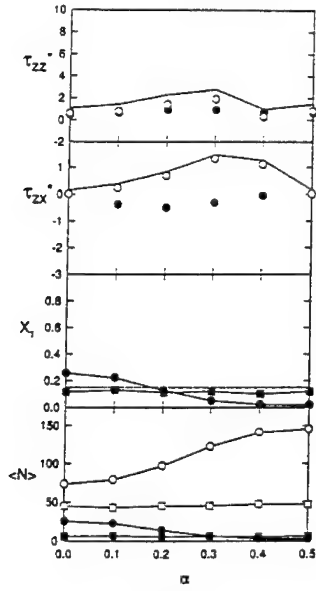
Figure 13
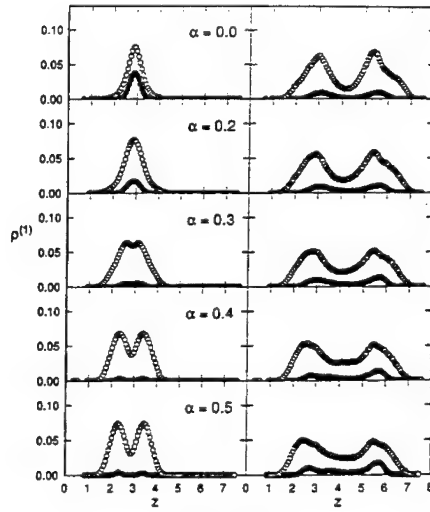
Figure 14

Figure 13. As for Fig. 11 with 15% large-atom bulk phase.

Figure 14. As for Fig. 12 with 15% large-atom bulk phase.

Figures 15 and 16 are similar to Figs. 7 and 8. The walls now consist of small atoms and the bulk phase is 86% large atoms. The groove width has been reduced from 7ℓ to 3ℓ. The only significant difference between the results presented in Fig. 15 when compared to those of Fig. 7 is the magnitude of the large atom shear stress which is larger in Fig. 15 than in Fig. 7. This again is a result of increased large-atom structure. When comparing density profiles in Fig. 8 with Fig. 16 one notes more significant asymmetry in the wide region at $\alpha = 0.5$ for Fig. 8. The final two figures (17 and 18) are similar to 15 and 16 except the bulk phase has 15% large atoms. Little difference in shear stress and composition exists between Figs. 17 and 9 however there is a difference in normal stresses. There is also a significant difference in narrow region density plots between Figs. 18 and 10. The two layer small atom liquid is less distinct in Fig. 18 than in Fig. 10. From these latter results it appears that groove width is less important than either wall structure or bulk composition in determining the character of the pore fluid.
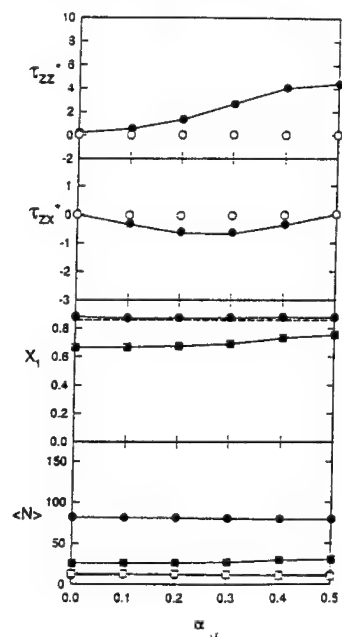
Figure 15

Figure 16

Figure 15. As for Fig. 3 with system IV.
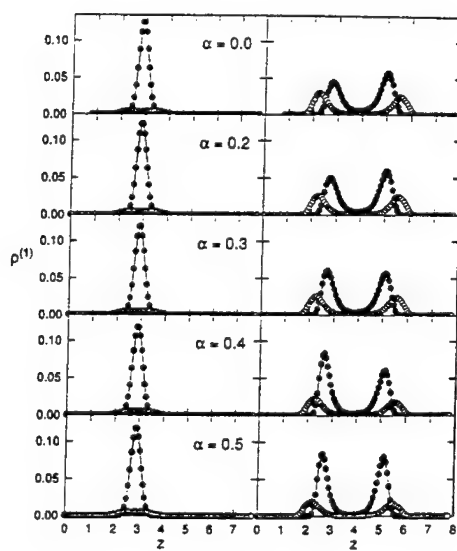
Figure 16. As for Fig. 4 with system IV.
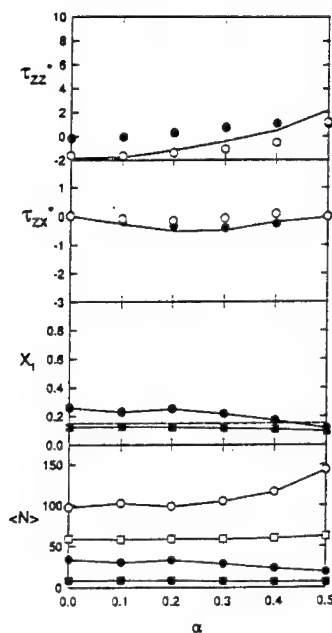
Figure 17
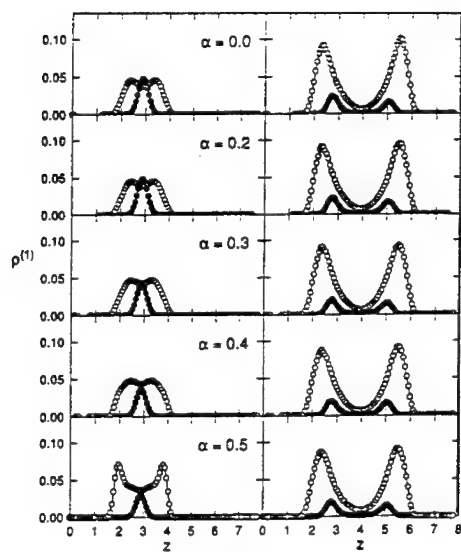
Figure 18

Figure 17. As for Fig. 15 with 15% large-atom bulk phase.

Figure 18. As for Fig. 16 with 15% large-atome bulk phase.

REFERENCES

1. M.P. Allen and D.J. Tildesley, Computer Simulation of Liquids (Oxford University Press, 1989)
2. M. Schoen, Computer Simulation of Condensed Phases in Complex Geometric (Springer-Verlag, Heidelberg, 1993)
3. M. Schoen, D.J. Diestler, and J.H. Cushman, J. Chem. Phys. 87, 5464 (1987)
4. M. Schoen, J.H. Cushman, D.J. Diestler, and C.L. Rhykerd, Jr., J. Chem. Phys. 88, 1394 (1988)
5. J.E. Curry, F. Zhang, J.H. Cushman, M. Schoen, and D.J. Diestler, J. Chem. Phys. (1994), in press
6. J.E. Curry and J.H. Cushman, Mol. Phys. (1994), submitted
7. S.A. Somers, A.V. McCormick, and H.T. Davis, J. Chem. Phys. 87, 5464 (1987)
8. J.E. Curry and J.H. Cushman, J. Chem. Phys. (1994), submitted
9. D.J. Adams, Mol. Phys. 29, 307 (1975)
10. M. Schoen, C.L. Rhykerd, Jr., D.J. Diestler, and J.H. Cushman, Science 245, 1223 (1989)

ACKNOWLEDGMENTS

ASYMMETRIC DRAINAGE IN FOAM FILMS
N4.1

Jean-Luc Joye; George J. Hirasaki, and Clarence A. Miller, Department of Chemical Engineering, Rice University, P. O. Box 1892, Houston, TX 77251

ABSTRACT

Drainage of circular foam films is much more rapid when the drainage is asymmetric. The same basic mechanism is responsible for asymmetric drainage of thin circular films and marginal regeneration. A linear stability analysis showed that these phenomena are caused by a hydrodynamic instability that is produced by a surface-tension-driven flow and stabilized by surface viscosity, surface diffusivity and system length scale. A criterion for the onset of this instability was derived. Experiments performed on small circular films of aqueous solutions of SDS and SDS:1-dodecanol demonstrated the strong stabilizing effect of surface viscosity. Experimental results were found to be in good agreement with the predictions of the linear stability analysis. Finite difference simulations demonstrate the validity of the linear stability analysis for when the radius of curvature of the "barrier ring" is large compared to the transverse wave length of the instability. These simulations also show the circulation cells that relax the surface tension gradient and thus accelerate the drainage of the film.

REFERENCE

1. J.-L. Joye, G.J. Hirasaki, and C.A. Miller, Langmuir **10**.9, 3174 (1994).

LIGHT SCATTERING STUDIES OF AN ELECTRORHEOLOGICAL FLUID IN OSCILLATORY SHEAR

JAMES E. MARTIN AND JUDY ODINEK
*Advanced Materials Physics Division, Sandia National Laboratories, Albuquerque, New Mexico 87185-0345

ABSTRACT

We have conducted a real time, two-dimensional light scattering study of the nonlinear dynamics of field-induced structures in an electrorheological fluid subjected to oscillatory shear. We have developed a theoretical description of the observed dynamics by considering the response of a fragmenting/aggregating particle chain to the prevailing hydrodynamic and electrostatic forces. This structural theory is then used to describe the nonlinear rheology of ER fluids.

INTRODUCTION

Electrorheological (ER) fluids are particle suspensions that undergo dramatic rheological changes when subjected to strong electric fields. [1,2] The rheology of these fluids at low to moderate volume fractions is due to the aggregation of particles into volatile chain-like structures whose size adjusts in response to the flow, fragmenting and aggregating as the shear rate increases or decreases.

Structural studies on ER fluids have focused on the quiescent state and on stationary flows. Optical studies of the quiescent ER fluid have elucidated both the kinetics of structure formation [3] and the final equilibrium state. [4] Light scattering studies of an ER fluid in steady shear [5] have determined the manner in which the chain size and orientation increases with shear rate, confirming earlier experiments and theory of the power-law shear thinning viscosity. [6]

Although some experimental work has been done on fluid structure in stationary flows, the chain dynamics has not yet been determined in nonstationary flows such as oscillatory shear. Because an understanding of electrorheology in nonstationary flows is essential to modeling the behavior of ER devices, we have undertaken a study of the chain dynamics in oscillatory shear. We have discovered a new class of nonlinear dynamics that is dominated by fragmentation/aggregation events occurring during each shear cycle, and have used our observations to develop a theory of nonlinear rheology. Direct rheological measurements [7,8] show that the framework of linear viscoelasticity- a phase-shifted stress proportional to an applied strain- is of limited utility for ER fluids, so a nonlinear theory is appropriate.

EXPERIMENTAL

Sample and Apparatus

Our sample is a transparent model silica fluid developed for light scattering and electrorheology studies. [3] The 700 nm spheres are coated with a silane coupling agent and dispersed in 4-methylcyclohexanol to 7.5 wt % silica. Aggregation is reversible by Brownian motion.

The scattering cell consists of an inner 40x2 mm circular disk electrode that is concentric to a 42 mm hole in an outer electrode, thus creating a radial electric field in a 1 mm gap. The outer electrode is sandwiched between plastic, and both are embedded between glass plates, with a fluid-filled 2 mm gap between the electrodes glass plates. The inner electrode is oscillated by a rod connected to a 25 mm lever on the electrode shaft, driven by an eccentric on a 300 oz.-in. microstepping motor.

The electric field is a 1 kHz square wave from a Trek™ power supply driven by Wavetek™ signal generator. Voltages are reported peak-to-peak.

Scattering data are captured by a Pulnix™ video camera, and stored on video tape. Data were then real-time digitized by a Perceptix™ frame grabber on a Macintosh Quadra 950™. Optical corrections were then made to the scattering data. [3]

A problem in this experiment is the phasing of the applied strain with the scattering data. We devoted a small corner of the scattering screen to an optical "strain phase clock" created by rotating a prism in synchrony with the stepping motor. The prism deflects a He-Ne laser beam that thus scribes a circle on the scattering screen, encoding the absolute strain phase on each image.

Data analysis

A scattering image contains a pair of scattering lobes [3] and the strain phase clock. These scattering lobes are tilted relative to the orientation of the scattering lobes obtained for the quiescent fluid, which are *orthogonal* to the electric field. The orientation of the scattering lobes reflects the orientation of the chains.

The rotation angle θ of the chains was determined by dividing the scattering image into 360 wedges, each subtending $1°$ of arc, and then integrating to find the average intensity in each wedge. [5] The orientation of the scattering lobes was then obtained by: locating the intensity maximum, θ_{max}; or finding the median, θ_m, that divides the integrated scattered intensity into equal halves, so $\int_{\theta_m}^{90°} I(\theta)d\theta = \int_{-90°}^{\theta_m} I(\theta)d\theta$. The median is useful when the dynamics is strongly nonlinear, but gives an orientation angle about five times smaller than θ_{max}.

MEASUREMENTS

At low strain amplitudes $\gamma_0 \ll 1$ the response of the orientation angle θ_{max} to the shear strain $\gamma = \gamma_0\sin(2\pi\omega t)$ was nearly sinusoidal. This sinusoidal response is exemplified in Fig. 1, where clockwise Lissajous plots of $\tan(\theta_{max})$ against γ are shown to be nearly elliptical. At high frequencies the shear rate, $\dot{\gamma} = 2\pi\omega\gamma_0\sin(2\pi\omega t)$, is large, and the chain orientation is nearly in phase with the fluid shear, since the hydrodynamic dominates electrostatic torque. Affine deformation is nearly achieved, as shown by the dashed line.

At low shear frequencies the chain orientation leads the strain by $57°$ and thus lags the strain rate by $33°$. In this regime electrostatic torque evidently dominates the hydrodynamic torque.

156
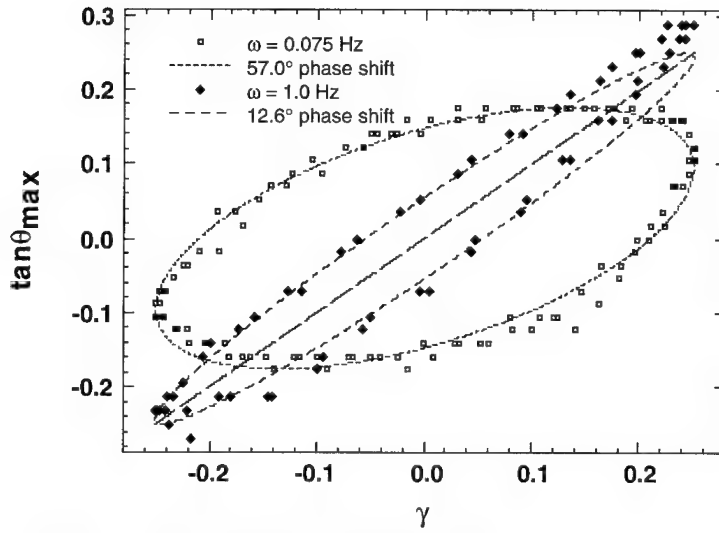
Figure 1: Clockwise Lissajous plots of $\tan(\theta_{max})$ against γ.
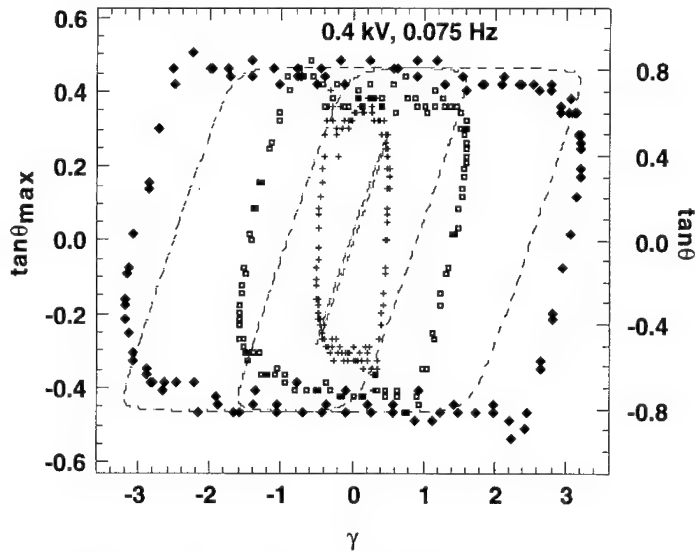
Figure 2: Lissajous plots at strain amplitudes of γ_0 = 0.5, 1.6, and 3.2 have parallelogram shapes that indicate a "clipping" of the angular motion. The theoretical curves are computed in the instantaneous 'equilibrium' limit where k is large.

At higher strain amplitudes, Fig. 2, the sinusoidal motion becomes "clipped" as the chains fragment and aggregate during a cycle to maintain good field alignment, giving parallelogram Lissajous plots.

At lower voltages we observe a highly nonlinear fluid response, as shown in Fig. 3. Starting at maximum positive strain, the chain half cycle can be described as follows. As the strain reverses, the chains co-move with the fluid, tilt to a maximum angle at half maximum strain, whereupon they fragment and undergo retrograde motion to realign with the electric field. Analysis shows that as they co-move with the shearing fluid, the chains aggregate, and indeed the scattering lobes brighten considerably during this time. These observations of chain motion have led us to propose the following model of ER fluid microstructure and rheology.
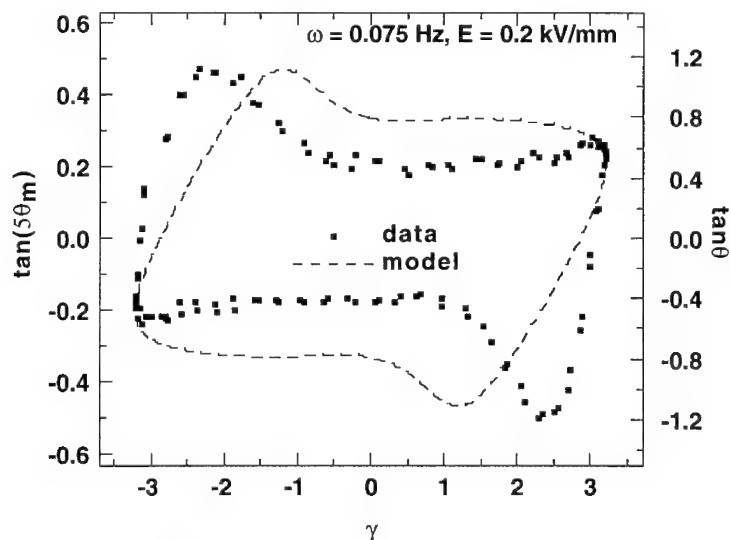
Figure 3: At low voltages a novel retrograde motion of fragmenting chains can be observed (dashed line is theory). The amplitude of motion is sensitive to the dipolar model and the method of data reduction.

THEORY

The salient features of experimental results we have shown can be understood in terms of a kinetic model of the dynamics of volatile chains. In this model we assume that dipolar interactions and hydrodynamic forces dominate thermal forces, which is certainly true in our experiments. This kinetic chain model differs from the elliptical droplet model, which minimizes a free energy and is thus is an equilibrium model.

Although it is not appropriate to give a full derivation of the model here, a brief description will aid the reader. We consider a linear chain of $2N+1$ spheres of radius a in an ocillatory shear field. The chain has a rotational velocity $\dot{\theta}$ and makes an angle θ to the electric field. The hydrodynamic force the fluid exerts can be decomposed into a

tangential component that causes chain rotation, and a radial component that causes tension or compression. The tangential force is a maximum at the chain center, where in low Reynolds number flow is balanced by the tangential component of the dipole-dipole interaction force[11] Balancing the tangential hydrodynamic and electrostatic forces at the chain center [9] gives the oscillator equation [10]

$$\dot{\theta} + \omega_d \sin 2\theta = \dot{\gamma}\cos^2\theta, \quad \text{where} \quad \omega_d = \dot{\gamma}\Big/16MnN^2.$$
(1)

Here $Mn=\mu_0\dot{\gamma}/2\varepsilon_0\varepsilon_c\beta^2 E_0^2$ is the Mason number, which expresses the ratio of hydrodynamic to electrostatic forces, β is the dielectric contrast factor $(\varepsilon_p\text{-}\varepsilon_c)/(\varepsilon_p+2\varepsilon_c)$, ε_c and ε_p are the liquid and particle dielectric constants. [11]

The oscillator frequency ω_d depends strongly on chain size. Physically acceptable values of N must correspond to mechanically stable chains or fragmentation will occur. The radial component of the hydrodynamic force is a maximum at the chain center, puts the chain in tension when $\theta\dot{\gamma} > 0$ and under compression when $\theta\dot{\gamma} < 0$. For the chain to be stable to fracture this hydrodynamically induced force must be smaller than the radial component of the electrostatic interaction [11]. The maximum stable chain number is determined by balancing these forces at the chain center.

$$N_{\max} = \begin{cases} \sqrt{\dfrac{2}{Mn}\dfrac{3\cos^2\theta-1}{\sin 2\theta}} & \dot{\gamma}\theta \geq 0 \\[4mm] \infty & \dot{\gamma}\theta < 0 \end{cases}$$
(2)

N_{max} is dependent on chain orientation and strain rate, causing nonlinear response when driven by oscillatory shear $\dot{\gamma}=2\pi\omega\gamma_0\cos(2\pi\omega t)$. The maximum stable chain length diverges when the chain is aligned with the field, when the instantaneous strain rate is zero, and when the chain is under compression.

If a chain finds itself far from its maximally stable size then its size will adjust by aggregation or fragmentation. The kinetics of aggregation and fragmentation can be described by the phenomenological formula

$$\frac{dN(t)}{dt} = \frac{k}{N(t)}\left[1 - \frac{N(t)^2}{N_{\max}^2(t)}\right]$$
(3)

where because induced dipolar forces drive aggregation the rate constant $k=k_0$ $(8\varepsilon_0\varepsilon_c\beta^2 E_0^2/\mu_0)$ where k_0 is a concentration dependent constant. When the chain is at its maximum length no aggregation or fragmentation occurs since $dN(t)/dt =0$. When the chain is much smaller than its maximum stable length, the chain will aggregate according to $N(t) = \sqrt{N(0)^2 + 2kt}$, in agreement with the root time prediction of See and Doi. [12] Thus aggregation is a slow power law growth process that is independent of the often divergent size N_{max}. If the chain is much larger than its stable length, then it

will fragment exponentially quickly according to $N(t) = N(0)e^{-kt/N_{max}^2}$. Note that the fragmentation rate k/N_{max}^2 is proportional to the strain rate and is *independent* of the electric field.

Equations 1-3 are a set of coupled nonlinear equations that model the dynamics of chains in shear flow. There are four independent parameters in the system; Mn, ω, γ_0, and k_0. A simplification occurs by noting that solutions to the kinetic equation are of the form $N(t) = (\dot{\gamma}/16\omega Mn)^{1/2}n(\omega t)$. The reduction to a two parameter (γ_0, k_0) model is a result of the rate equation we have chosen. Because the strain amplitude is fixed by experiment, this is really a single free parameter model.

Before showing the behavior of these equations we would like to discuss the predicted rheology. The stress σ in the sample is the hydrodynamic torque density, which equals the electrostatic torque density since inertia is small. In terms of the volume fraction ϕ of spheres this is $\sigma = 6\mu_0 N^2\phi(\dot{\gamma}\cos^2\theta - \dot{\theta}) = \frac{3}{4}\varepsilon_0\varepsilon_c\beta^2 E_0^2\phi\sin 2\theta$. This equation demonstrates that the stress is nearly proportional to the angle θ, so light scattering is an indirect probe of stress. [13] Furthermore, it is apparent that when $\theta = 0$, the chain is comoving with the fluid so $\dot{\gamma}\cos^2\theta = \dot{\theta}$.

Because the dynamics of chain orientation $\theta(s)$ is independent of electric field and shear frequency, we conclude that the stress scales purely as the square of the electric field. In steady shear it is readily shown that $\sin 2\theta = 2\sqrt{6}/5$, so the solution viscosity thus has the shear thinning form

$$\mu = \frac{3\sqrt{6}}{10}\varepsilon_0\varepsilon_c\beta^2 E_0^2\phi\dot{\gamma}^{-1}. \tag{5}$$

The result $\mu \propto \dot{\gamma}^{-1}$ has been obtained in many experiments, including those conducted on our silica fluid. [6] However, for the silica fluid at low fields we find $\mu \propto \dot{\gamma}^{-2/3}$, a result consistent with the elliptical droplet model. [6]

The nature of the nonlinear response is illustrated in Fig. 4 (small strains give a sinusoidal response). For $k = 0$ the oscillator reorientation rate ω_d is constant, and the remaining nonlinearities in Eq. 1 are small enough that a nearly elliptical response is observed. As k increases, the chains fragment and aggregate to achieve mechanical stability while trying to maximize their length, and Lissajous plots approach a parallelogram, as in Fig. 2. Finally, for intermediate values of k an interesting crossover to retrograde motion is observed. This is observed in our data at low fields, as illustrated in Fig. 3.

CONCLUSIONS

We have conducted light scattering studies that show that ER fluids can have strongly nonlinear behavior in oscillatory shear. The dipolar kinetic chain model gives a qualitative account of the nonlinearities observed in our data, without generating behaviors that we have not observed. However, it makes a number of quantitative
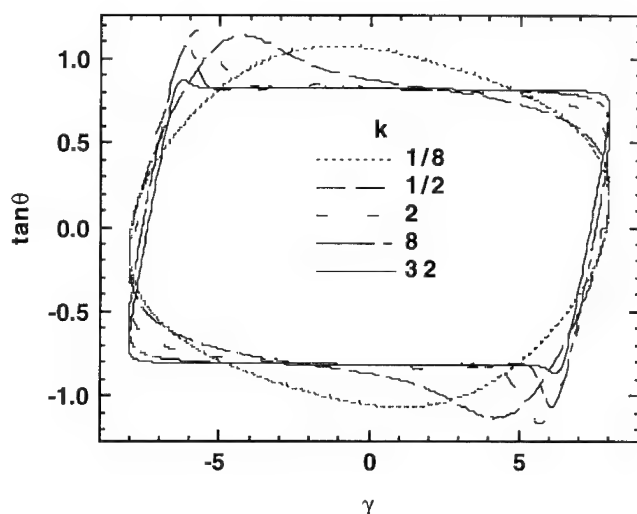
Figure 4: Lissajous plots change unexpectedly as the rate constant k is varied. For $k =$ 0 the oscillator reorientation rate ω_d isconstant, and the nonlinearity is small. For large k Lissajous plots approach a parallelogram, whereas for intermediate k values retrograde motion is observed.

predictions that are not correct, such as predicting chain angles that are too large and not accounting for residual field/frequency trends in the data. It is easy to modify the theory to give much better fits to the data, for example by rescaling n_{max}, but only at the expense of introducing arbitrary parameters. What are the problems? Multipolar interactions will probably renormalize the tangential and radial components of the electrostatic forces incommensurately, decreasing the chain angle if the tangential component increases more. The distribution of chain sizes has been ignored, yet light scattering samples all chains and thus *understimates* the maximum chain orientation. Nonetheless, we feel that this model provides a framework that captures the essence of the observed dynamics.

REFERENCES

1. H. Block and J.P. Kelly, J. Phys. D: Appl. Phys. **21**, 1661 (1988).
2. A.P. Gast and C.F. Zukoski, Adv. Coll. Inter. Sci. **30**, 153 (1988).
3. J.E. Martin, J. Odinek and T.C. Halsey, Phys. Rev. Lett. **69**, 1524 (1992).

4. T. Chen, R.N. Zitter and R. Tao, Phys. Rev. Lett. **68**, 2555 (1992).
5. J.E. Martin, J. Odinek and T.C. Halsey, to appear in Phys. Rev. E.
6. T.C. Halsey, J.E. Martin and D. Adolf, Phys. Rev. Lett. **68**, 1519 (1992).
7. J.E. Martin, D. Adolf and T.C. Halsey, J. Coll. Inter. Sci. **167**, 437 (1994)
8. T.C.B. McLeish, T. Jordan, M.T. Shaw, J Rheol. **35**, 427 (1991); T. Jordan, M. T. Shaw, and T.C.B. Mcleish J. Rheol. **36**, 441 (1992).
9. Balancing the force along the chain gives a chain shape that resembles an arcsine; Linearity avoids a dynamical system of 2N+1 coupled nonlinear equations.
10. A similar result is obtained from the droplet model in Ref 6.
11. D.J. Klingenberg and C.F. Zukoski, Langmuir **6**, 15-24 (1990).
12. H. See and M. Doi, J. Phys. Soc. Jpn. **60**, 2778 (1991).
13. Analogous to the Stress-Optical Theorem, which relates birefringence to stress.

DYNAMICAL BUCKLING TRANSITIONS OF A CONFINED COLLOIDAL MONOLAYER

CHERRY A. MURRAY, WOLFGANG SPRENGER *, RAJ SESHADRI **, and JANE E. CERISE ***
*AT&T Bell Laboratories, 600 Mountain Ave., Murray Hill, NJ 07974
**Stanford University, School of Business, Stanford, CA 94305
***University of Houston, Department of Physics, Houston, TX 77204-5506

ABSTRACT

When a rigid two-dimensional triangular crystalline layer of colloidal spheres confined between two smooth repulsive walls is gradually given freedom to move out of plane, it buckles dynamically undergoing several Peierls transitions involving different soft phonon modes before forming a two layer crystal with square in-plane symmetry. We have mapped out the complex phase diagram of the buckling transitions as a function of sphere density and wall separation. Digital imaging is used to study the instantaneous particle positions and trajectories of the uniform, highly charged 0.3 μm diameter polystyrene spheres that comprise the crystalline layer in water suspension. Brownian motion of the spheres creates a true thermodynamic system with a real temperature, which is studied using video microscopy. We follow the collective dynamics of the system as well as individual particle motions and the motions and rearrangements of topological defects and domains. At sufficiently low sphere densities the system melts into a fluid. As the wall separation increases to the point of two layer formation we observe square symmetry in the fluid correlation volumes.

INTRODUCTION

Layering transitions of monolayer crystals have been investigated in both experimental and theoretical work in the past decade. [1-5] These are analogous to the layering of molecular systems that have been observed in narrow pores in experiments [6] and simulations, [7] but have not been extensively studied in the limit of a single layer. In the layering process a two-dimensional, single-layer array undergoes a transition to a three-dimensional, two-layer structure. Preliminary experimental observations of confined colloidal crystals, an excellent model system for observation of collective manybody phenomena, [8] indicate that a monolayer triangular array of polystyrene spheres undergoes a transition to a two-layer square array as the separation h between the smooth confining walls is increased. [1-3] However, in past experiments the transition was not studied in any detail. In this experiment we observe the equilibrium state of the system of colloidal spheres confined between two smooth walls at a large range of densities and wall separations in order to map out a more complete picture of both the statics and dynamics of the buckling transition. A preliminary account of a portion of our results was reported elsewhere. [9] Since the experiment is carried out at a finite temperature, T, the equilibrium buckled states of the monolayer at certain fixed wall separations are in constant dynamic motion due to thermal fluctuations.

We became interested in studying the details of this transition because the confined

triangular colloidal monolayer could be thought of as an analog of a two-dimensional membrane confined to the three-dimensional space between two parallel hard repulsive walls, which is predicted to melt as it is allowed freedom to move out of plane due to the lowering of the core energy of dislocations when they can distort out of plane. [10] In fact, we have observed a lowering of the in-plane translational correlation length of the triangular colloidal monolayer after it was allowed to buckle out of plane in earlier studies. [8] However, it appears that over the greater part of the phase diagram we have studied (varying both sphere density and wall separation) that the buckling transition is less representative of a generalized Kosterlitz-Thouless transition involving buckled dislocation pair breaking and better described by a Pierls transition driven by soft phonon modes of the triangular layer. Predictions for the nature of this Pierls transition have been made in several theoretical studies. [4-5] We are surprised by the richness and complexity of the phase diagram we have found. We describe the overview of the equilibrium phase diagram in this paper and will describe the details and the dynamics of the transition in later publications.

EXPERIMENT

Charged polystyrene spheres (diameter d = 0.300 ± 0.003 μm) suspended in a water electrolyte at a volume fraction of 1-2 % interact primarily via screened Coulomb repulsion. [8] In the colloidal suspension the surface sulfonate groups on the spheres dissociate to produce highly charged monodisperse spherical macroions (of effective charge $Z \sim 10^3$ electrons per sphere, uniform to ± 1%) each screened by roughly Z positive microscopic H^+ counterions in solution. The counterion concentrations are regulated by mixed-bed H and OH ion-exchange resins that occupy about a fourth of the total suspension volume. We confine the spheres into a single layer between two repelling charged glass walls of separation h that are smooth on the colloidal scale (see Fig. 1) in a specially designed cell described in detail elsewhere. [11]
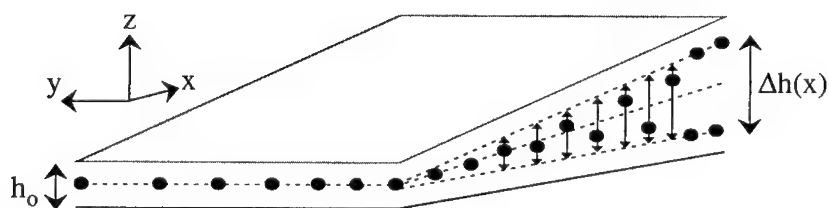
Fig. 1. Diagram of the wedge geometry of the experiment.

In order to study the equilibrium phases of the colloidal monolayer as a function of wall separation h, we created a gradual wedge angle dh/dx ~ 10^{-3} - 10^{-4} rad between the confining walls by gently pumping on the cell and bowing the thin bottom window. The wedge angle between the walls in the perpendicular direction, dh/dy, was roughly ten times smaller. The cell was filled with a three-dimensional reservoir of colloid surrounding the thin region and then allowed to equilibrate for ~ 2 months at temperature T = 22.11 ± 0.6 ° C. The cell temperature was maintained at this value for the duration of the experiments to avoid creating spurious ion gradients. Any density gradients in the system after equilibration varied slowly on the scale of the lateral field-of-view (roughly 30 µm X 22 µm .) The wall separation varied sufficiently slowly along the wedge that the system can be considered to be an ensemble of equilibrated smaller systems, each with a slightly different fixed wall separation, that can be studied separately by moving specific distances along the wedge. Here, we define the system equilibrium time to be the time it takes a relevant defect (for example a dislocation in the layer) to move either a translational correlation length or the size of the field-of-view, whichever is larger. [8,12] The small systems along the wedge will be effectively independent of each other if the correlation length of each system is smaller than the separation of the systems. We studied the wedge in this manner with seven different reservoir densities so that the in-plane density of spheres, n, varied between 1-6 μm^{-2}, or in reduced units of sphere diameters, 0.1 d^{-2} < n < 0.6 d^{-2}. Along the wedge, the separation between the walls varied between 1.5 to 4 µm, or in reduced units, 4d < h < 12 d.

The spheres were observed at video rates using diffraction-limited optical microscopy (depth of focus $\pm$ 0.2 µm and position of focal plane adjustable to 0.1 µm,) and their positions analyzed using computer-video techniques. [13] Each sphere is directly imaged as a Gaussian spot due to Mie scattering of the visible light from a Xe arc lamp, filtered to remove UV and IR light (which is absorbed by the spheres and could cause local heating of the system.) Because the depth of focus of the objective lens is comparable to the sphere diameter, we could observe the displacements out-of-plane of each sphere as a scattering intensity change, providing the extent of the displacements out-of-plane were comparable in size to the focal depth ~ 0.1-0.2 µm. By focussing the lens slightly above or below the midplane of the colloidal layer we could observe only the most buckled spheres and their dynamics, while focussing directly at midplane included all of the spheres in the sample volume and revealed the topology of the layer in the x-y plane.

RESULTS

The observed phase diagram of the equilibrium buckled monolayer is summarized by the plot of in-plane density n of the system versus wall separation h in Fig. 2. We have observed roughly 10 distinct phases of the system, between which we have drawn tentative phase boundaries in the Figure. These boundaries are only approximate due to the coarseness of the data points on the diagram. Also, we may have missed a phase or two for the same reason. We will describe the results in three sections - at intermediate, high and low in-plane densities.

Intermediate in-plane densities

At intermediate in-plane densities such that 0.2 < n < 0.3 d^{-2}, beginning at low separations h ~ 6 d^{-2} we observe as h increases first a rigid single layer triangular crystal phase (1Δc), followed by a gradual transition to a dynamically correlated buckled state (R) in which

primarily "regions" of the triangular layer defined by lattice circuits (such as those shown in Fig. 3) move simultaneously out of plane. The underlying triangular crystal maintains its long in-plane translational correlation lengths of $\xi \sim 15$ a, where a is the nearest neighbor spacing. The buckling does not appear to preferentially take place at topological defects of the underlying crystal, so the lattice is not softening due to the reduced core energy of dislocations. [10]

For h > 8.6 d, a qualitative change takes place in the buckling out of plane, which is now correlated into a specific 2X1 vertical phonon mode of the lattice, as shown in Fig. 4. This soft phonon corresponds to an edge instability of the two-dimensional Brillouin zone of vertical phonon modes of a triangular crystal of particles interacting with nearest neighbor and next nearest neighbor repulsive screened Coulomb potentials, predicted to go unstable by Chou and Nelson in a small amplitude Landau theory analysis in which only vertical motion of the spheres is considered. [4] As h increases further, we observe this mode becoming progressively more rigid, distorted slightly in plane and longer ranged (Fig. 4). The average residence time of a sphere in a focal volume centered 0.2 μm above the center of the layer varies monotonically from 0.1 sec at h = 9d to .9 sec at n = 12d. For 11d < h > 12d we observe two phase coexistence of the now rigid 2X1 buckled mode (which retains its in-plane hexagonal symmetry)
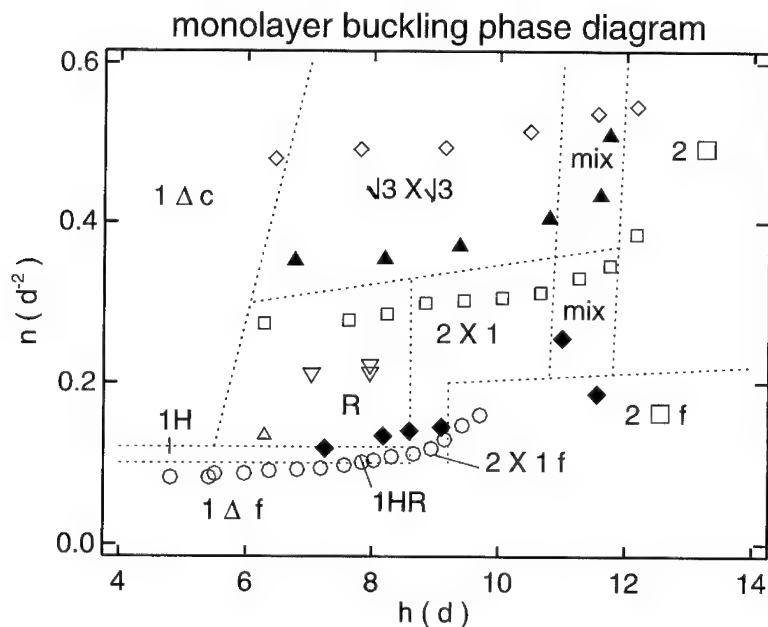
Fig. 2. Experimental monolayer buckling phase diagram. Here the in-plane sphere density, n for 7 different experimental runs (different symbols for each run) is plotted against the wall separation, h. Approximate phase boundaries are marked by the dotted lines and phases are labeled as described in the text.

and 2 □ symmetrical domains. The 2 X 1 → 2 □ transition is a symmetry-breaking Martensitic transition and strongly first order, involving in-plane phonons. We do not observe the 2 X 2 buckled state predicted by Chou and Nelson for an asymmetric potential between the two walls. A long range 2 □ crystal exists for n > 12d.

High in-plane densities

At higher densities n > 0.3 d^{-2}, the transition proceeds somewhat differently (see Fig. 2): no "regions" phase is observed within our experimental runs, but instead a $\sqrt{3} X \sqrt{3}$ phonon mode goes soft at h ~ 6, corresponding to a corner instability in the Brillouin zone in the model of Chou and Nelson. This phase belongs to a xy-cos (6 θ) universality class. [4] Interestingly, in their mean field model, valid for small amplitude motion out of plane, this phonon mode becomes unstable when they consider only nearest neighbor interactions on the triangular lattice. On the contrary, we observe this mode at the highest densities we have studied where next-nearest-neighbor interactions become more important. Also, the experimental buckled out of plane motion is large: $1d < \delta h < 5d$, up to 1.5 times larger vertical motion than the nearest neighbor distance in the top layer. The $\sqrt{3} X \sqrt{3}$ domains are rather small, never larger than roughly ten superlattice constants across, and move extremely rapidly on a video timescale. A snapshot of such a single domain is shown in Fig. 5. The mean particle residence time in the upper layer is faster than 30 msec in the $\sqrt{3} X \sqrt{3}$ domains throughout this region of the phase diagram. For h > 11d and n > 0.4 d^{-2}, we observe a complicated mixture of three phases: the $\sqrt{3} X \sqrt{3}$, the rigid 2 X 1, and regions of 2 □ c.
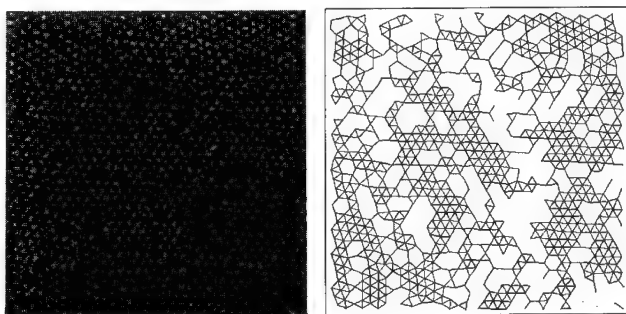
Fig. 3. An example of sphere positions in a snapshot of a portion of the field of view of the system in the "regions" phase, marked 'R' in Fig. 2. At left is a photograph 0.2 μm above the midpoint of the layer. The spheres that are above the midpoint appear brighter than those at the midpoint or below. These are highlighted in the right diagram, which shows only the spheres above the layer and their nearest neighbor bonds to other spheres also above the midpoint. The density and wall separation for this snapshot are n = 0.28 d^{-2}, h = 8.2 d.

For $n \leq 0.1\ d^{-2}$ the phase diagram becomes even more complex. Some examples of the
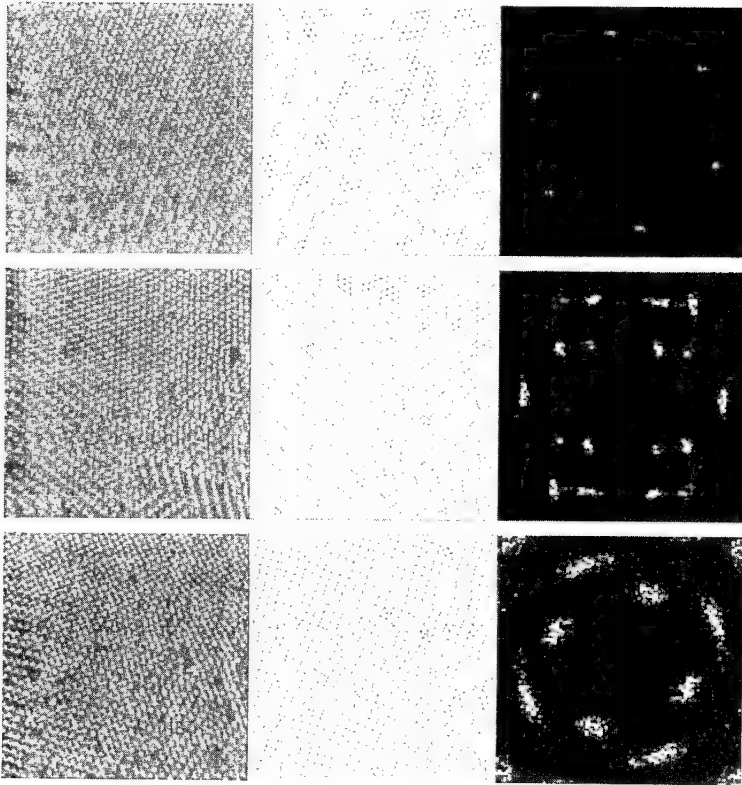
Fig. 4. Examples of the instantaneous structure of the system in the 2X1 buckled phase (top and center rows) and the 2 □ crystal phase, 2 □ c, (bottom row). In the left column are snapshots of a portion of the field of view of the system just ~ 0.2 μm above the midpoint of the layer. In the center column are plotted only the nearest neighbor bonds of the spheres above the midpoint of the layer. In the right-most column are displayed the in-plane structure factors for the layer at its vertical midpoint between the walls, show-ing the difference in symmetry between the 2X1 phase (slightly distorted hexagonal) and 2 □ c phase (square). The densities and wall separations for these images are: top: (n = 0.285, h = 9.4d) fast 2X1; center: (n = 0.345, h = 11.8d) slow 2X1; bottom: (n = 0.38, h = 12.2d) 2 □ c.

instantaneous structure of the layer in the major phases are shown in Figs. 2 and 6. For low separations h ≤ 7d, the system is in a 1 layer triangular fluid phase (1 Δ f). Uncorrelated buckling of the fluid is observed above h ≥ 6d. For 7d ≤ h ≤ 8.5d, the system exhibits hexatic[8,12] symmetry, and correlated buckling in a "regions" type mode (1HR). Above h~ 8.6d the hexatic symmetry is lost and the symmetry of the correlated hopping takes on more 2 X 1 character (1f 2X1). Above h ~ 9.2 d we observe a two layer fluid with translational correlation length about 2-3a, but square in-plane symmetry in regions 3-8a across which last for several seconds (2 □ f). Fig. 7 shows the in-plane translational correlation length of the system as a function of wall separation in the lowest density experimental run depicted by the open circles in Fig. 2. [14]

The 2 □ fluid freezes at a density somewhere near n ≥ 0.2 d^{-2}, but this region of the phase diagram and the freezing transition has not yet been fully explored.
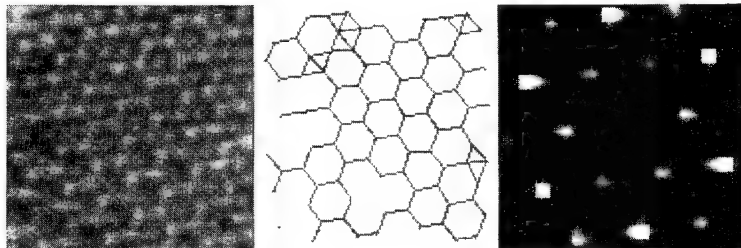
Fig. 5. An example of the instantaneous structure of the buckling in the $\sqrt{3} X \sqrt{3}$ region of the phase diagram. At left is an image of a single domain of the $\sqrt{3} X \sqrt{3}$ structure taken ~ 0.2 μm above the vertical midplane of the layer. In the center, only the nearest neighbor bonds to spheres that are above the midplane are plotted. At right, the structure factor of the entire layer shows the $\sqrt{3} X \sqrt{3}$ superlattice spots inside the bright ring of 1 X 1 diffraction peaks. The image is taken at density n = 0.37 d^{-2} and h = 8.2 d.

CONCLUSIONS

The equilibrium buckling transition from one to two layers of a colloidal system confined between two smooth repulsive walls is surprisingly complex. The detailed mechanisms of the observed transitions are not completely understood, although two of the observed phonon instabilities are those predicted by the mean field Landau theory of Chou and Nelson that considers only small amplitude out-of-plane motions. The real experimental crystalline triangular monolayer is two-dimensional, and has been shown to have a power-law

decay of translational order, and also melts through a hexatic phase. [15] Fluctuations, neglected in the theory, are thus very important in the experimental system. Thus the dynamic critical behavior of the transitions we observe should be modified by fluctuations and thus quite interesting.
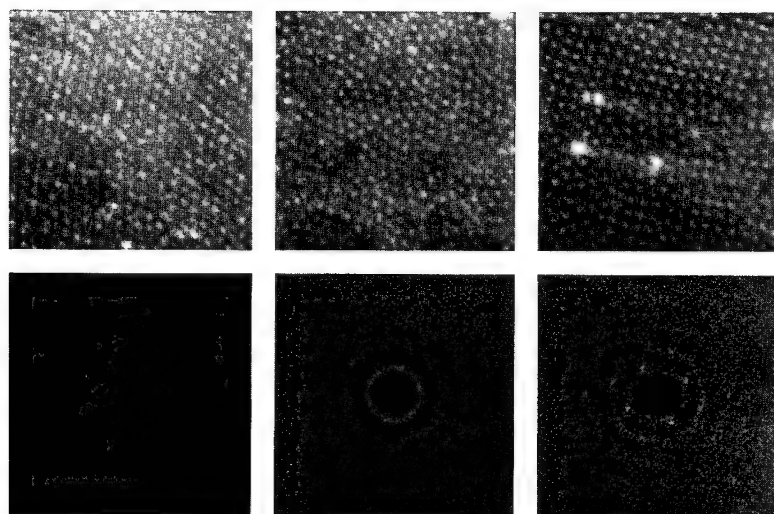
Fig. 6. Top row: Examples of instantaneous structure of the low density buckled phases. The snapshots are taken of a portion of the field of view ~ 0.2 μm above the vertical midplane of the layer so that those spheres buckled up out of the midplane are somewhat brighter. At left is a snapshot of the spheres in the hexatic "regions" phase at $n = 0.01\ d^{-2}$ and h = 8.05 d. At center is a snapshot of the phase of fluid 2X1 - R at $n = 0.012\ d^{-2}$ and h = 8.5 d. At right is a snapshot of the upper layer of a 2 □ fluid at $n = 0.016\ d^{-2}$ and h = 9.5 d. Larger bright spots in the image are large particles aggregated on one of the walls of the cell. Bottom row: structure factors of the vertical midpoint of the system (which includes all of the spheres) at the same density and wall separation as the snapshots in the column directly above showing the in-plane symmetry and order.

A thorough search for the enhanced melting of a buckled monolayer predicted by Morse and Lubensky has not yet been made, but in our present restricted data set it has not been observed. The melting of a two-layer square crystal has also not been thoroughly studied, and should prove quite interesting. Simulations [16] of a single layer square lattice find a first order melting transition. There is, however, a possibility that in the experiment a two-layer square

"quadratic" phase exists in the uncharted region at the lower right of Fig. 2.
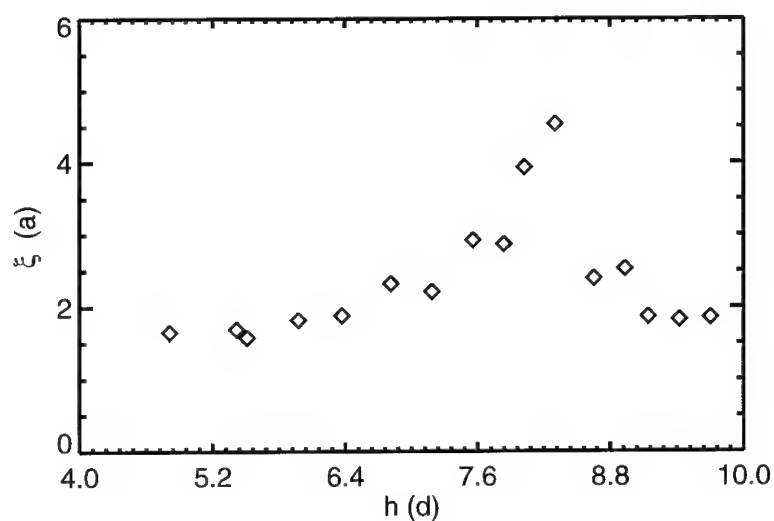
Fig. 7. In-plane translational correlation lengths ξ, in units of nearest neighbor distances for the lowest density experimental run depicted by the open circles in Fig. 2.

ACKNOWLEDGEMENTS

REFERENCES

1. P. Pieranski and J. Finney, *Acta. Cryst.* **A35,** 194 (1979).

2. P. Pieranski, L. Strzelski and B. Pansu, *Phys. Rev. Lett.* **50,** 900 (1983).

3. D. H. Van Winkle and C. A. Murray, *Phys. Rev.* **A34,** 562 (1986).

4. T. Chou and D. R. Nelson, *Phys. Rev.* **E48,** 4611 (1993).

5. M. Warner and M. Hornreich, *J. Phys. A: Math. Gen.* **18,** 2325 (1985). J. Berger, R. M. Hornreich and M. Warner, *Physica* **A 194,** 199 (1993).

6. J. N. Isrealachvili and P. M. McGuiggan, *Science* **241,** 795 (1988).

7. W. J. Ma, J. R. Banavar and J. Koplik, *J. Chem. Phys.* **97,** 485 (1992).

8. C. A. Murray, in *Bond-Orientational Order in Condensed Matter Systems,* edited by K. Strandburg (Springer, NY, 1991).

9. R. Seshadri, W. O. Sprenger and C. A. Murray, presented at the March American Physical Society Meeting, (1993).

10. D. Morse and T. Lubensky, *J. de Physique* **II 3,** 531 (1993); H. S. Seung and D. R. Nelson, *Phys. Rev.* **A38,** 1005 (1988).

11. D. H. Van Winkle and C. A. Murray *J. Chem. Phys.* **89,** 3885 (1988).

12. D. R. Nelson, in *Phase Transitions and Critical Phenomena, Vol 7,* eds. C. Domb and J. L. Lebowitz (Academic, London, 1983).

13. D. G. Grier and C. A. Murray, "Direct imaging of the local dynamics of colloidal phase transitions, to be published in *Ordering and Phase Transitions in Colloidal Suspensions,* ed. A. K. Arora, (VCH Publishers, New York 1995)

14. J. E. Cerise and C. A. Murray, unpublished.

15. C. A. Murray, W. O. Sprenger, and R. A. Wenk, *Phys. Rev.* **B 42** 688 (1990).

16. T. A. Weber and F. H. Stillinger, *Phys. Rev.* **E 48,** 4351 (1993).

DYNAMICS OF NANOMETER SiO2 PARTICLES AND THEIR COALESCENCE CHARACTERISTICS

ESTELA BLAISTEN-BAROJAS[*], LING LIU[*], AND MICHAEL ZACHARIAH[**]
[*]Institute for Computational Sciences and Informatics, George Mason University, Fairfax, VA 22030
[**]National Institute of Standards and Technology, Gaithersburg, MD 20899

ABSTRACT

Various mechanisms of glassy transformations involving computational annealing were investigated by Molecular Dynamics simulations. Large clusters of silicon dioxide ranging from sub to nanometer size regime were considered. Silica is both a prototype ceramics and glassy material. Silica particles are fabricated in flow and flame reactors to design novel granular materials which depend strongly on the heating and cooling processes. During these processes extensive thermally driven relaxation in growing clusters allow for configurational changes from a liquid-like cluster to a glassy cluster. Crystal-like structures were investigated as well. Cooling rates comparable to experimental rates were achieved in these simulations. We find that the glass transition temperature decreases with decreasing cluster size. Calculations were performed by implementing a massively parallel particle decomposition schema of Molecular Dynamics with an excellent speedup and a significant decrease of complexity.

INTRODUCTION

Formation of ceramic particles from the products of combustion mechanisms in flow and flame reactors is one of the novel techniques used to fabricate granular thin films and coatings.[1-5] The building blocks of these films are particles in the nanometer size regime fabricated with the aim to enhance and control their properties.[6] In the gas phase solid cluster structures are formed at temperatures characteristic of the flame or above (2000K to 3000K) and later deposited on surfaces undergoing a fast cooling process. Both mechanisms, particle growth in the gas phase and cluster deposition to yield a final thin film are not fully understood. In this arena the atomistic approaches are very scarce.[6] The aim of this work is to build understanding in this direction by investigating some mechanisms by which either crystalline, polycrystalline or glassy particles may be obtained from the liquid-like state.

A number of Molecular Dynamics simulations have been performed to simulate bulk related properties of crystalline and glassy SiO_2 using effective pairwise additive interatomic potentials.[7-13] Recently Tsuneyuki et al[7,10] have developed an optimized two-body potential fitted on ab initio calculations of tetrahedral SiO_4^{4-} clusters including long range Coulomb interactions between localized effective charges. This potential has been used in crystalline and glassy bulk simulations in recent years.[10,13] In this work we use this potential to model the interactions of Si-Si, Si-O and O-O in clusters containing tens to hundreds of SiO_2. Results presented here on the liquid glass transition and structural properties of silica particles are our first attempts in the study of the agglomeration and coalescence mechanisms of particle deposition.

MODEL POTENTIAL

The atomic interactions are modeled through a sum of pairwise additive terms, each of them containing a Born-Mayer-type repulsion, Coulomb interaction and a dispersion term[7] between every pair of atoms:

$$U = \sum_{i<j} \{ f_0 (b_i + b_j) \exp[(a_i + a_j - r_{ij}) / (b_i + b_j)] + u_{ij}^{Coulomb} (r_{ij}) - c_i c_j / r_{ij}^6 \}$$

Here r_{ij} is the distance between atoms and a_i (b_i) are the effective radius (softness parameter) of the ith atom and $f_0 = 1$ kcal/A/mol. Molecular Dynamics is used to follow the time evolution of the system by solving the classical equations of motion of every atom in the cluster. Due to the nature of the proposed potential, these equations are second order ordinary differential equations containing highly non-linear terms. These ode's are solved numerically by third order finite difference methods and a time step of 3.5 fs to ensure conservation of energy.[14] The initial configurations are spherical structures of SiO_2 arranged in the positions of the α-quartz crystal at room temperature. Typical runs to bring the system to equilibrium were conducted over several tens of thousands of time steps.
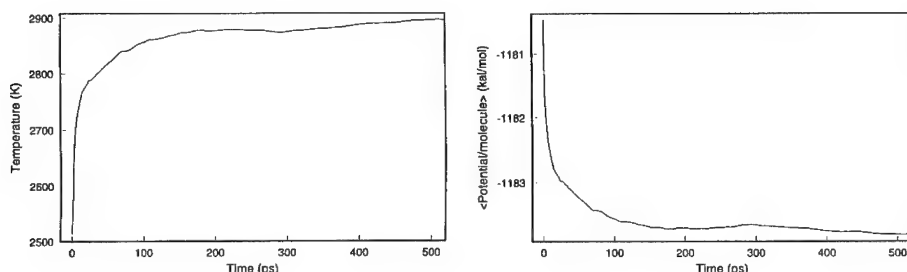
Fig. 1 Temperature (left) and average potential energy (right) as a function of time after the collision of two 64-molecule clusters that coalesce into a large 124-molecule cluster. The temperature of the colliding clusters and the collision energy was 2500K.

THE GLASSY STATE

Our search of the glass transition in these silica particles was based on two pre-cooling strategies to reach the liquid state. In the first the particles were grown larger by previous collision between smaller particles.[6] The small particles stick together and give rise to larger particles at higher temperatures.[6,15] Results from a typical collision between two 64 SiO_2 is depicted in Fig. 1. The temperature increases after the collision (1a) whereas the potential energy (1b) decreases accommodating the collision energy. The collision process was continued until reaching temperatures of about 2600K to ensure that particles are liquid-like. The second heating strategy was based on the scaling of the atomic velocities of a cluster previously equilibrated at a lower temperature until the 2600K were attained.

Once the particles are hot and in the liquid state they were subjected to an annealing process that initiates by cooling the liquid particles in a step-like manner with a scaling of the particle velocities. The first 10,000 steps of each cooling step were used to reach equilibrium whereas energy averages were calculated on the last 5,000 steps. A cooling rate of 200K/ns was achieved. Fig. 2 shows the cooling curves for three cluster sizes. The liquid to glass transition is identified at the point where the slope of the energy versus temperature presents a change. This change in the slope is however small and takes place in a smooth fashion around the transition temperature. More noticeable are the fluctuations that become smoother as temperature decreases. Cooling processes starting from clusters heated in the two different fashions gave rise to almost indistinguishable curves for internal energy as a function of temperature indicating that the history behind the liquid state is not important in the formation of the glass.

The transition temperature depends strongly on the size of the cluster. Small clusters with
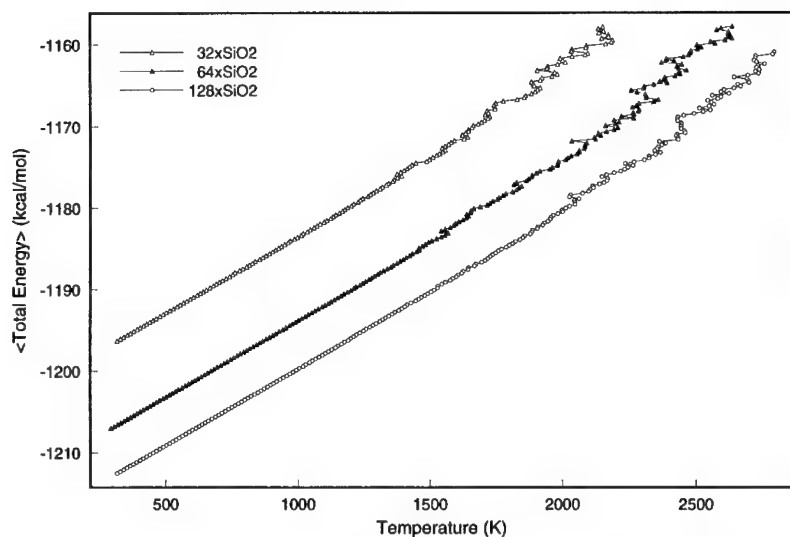
FIG.2 Total cluster energy as a function of temperature for clusters with 32 (top), 64 and 128 (bottom) SiO_2 molecules.

tens to one hundred SiO_2 molecules exhibit the glass transition at temperatures up to 20% below the equivalent bulk transition temperature of 2200K. When the cluster reaches a size of 128 molecules, the discrepancy is of only 5%. In Table I we report the region of temperatures around the glass transition for particles containing 32, 64 and 128 SiO_2 molecules. We arbitrarily estimated the glass transition temperatures as the center of that region. Below the transition temperature region the atoms are oscillating about fixed positions indicating that the molecules are locked into a solid-like configuration. The constant volume heat capacity $C_v = 0.0185 \pm 0.0008$ kcal/mol K was obtained from the low temperature portion of the curves in Fig.1 for all the cluster sizes investigated in this work This value is consistent with $9k_B$, the classical limit of a harmonic solid.

TABLE I. Glass transition temperature and temperature regions within which the glass transition is located as a function of the cluster size

No. of SiO_2 Molecules in Cluster	Transition Temperature Region (K)	Glass Transition Temperature (K)
32	1400-1750	1550
64	1550-1850	1700
128	2000-2200	2100

CLUSTER STRUCTURE

Glass and liquid structure are best visualized through the radial distribution functions. Since a number of equilibration processes were investigated, for each of them we calculated the pair distribution functions g_{Si-Si}, g_{Si-O} and g_{O-O} as a function of size and temperature. In Fig 3 the pair distribution functions of two sets of simulations are shown and compared to the crystal-like

ones for the 32-molecule cluster. Figures on the top of Fig. 3 show g_{Si-Si} (left), g_{O-O} (center) and g_{Si-O} (right) for a spherical cluster in the α-quartz configuration, whereas the other figures show the changes to the structure when the clusters are equilibrated at 300K before (middle) and after annealing (bottom).
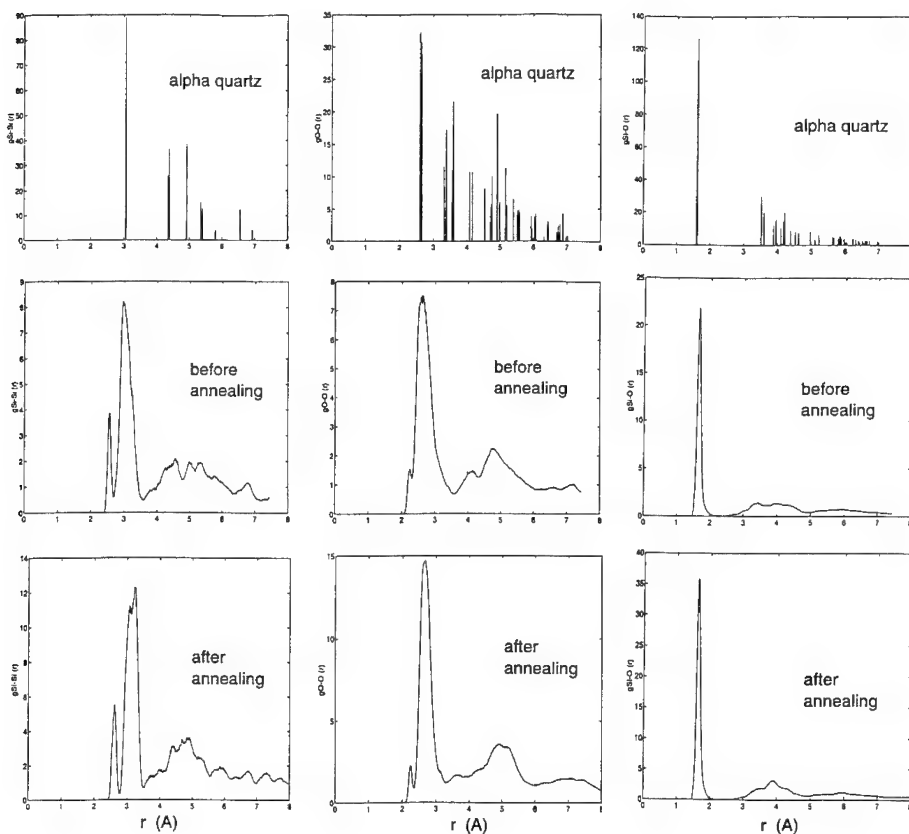
FIG 3. Pair distribution functions g_{Si-Si} (left), g_{O-O} (center) and g_{Si-O} (right) for 32-molecule clusters in the α-quartz configuration (top) and at 300K before annealing (center) and after annealing (bottom).

Both g_{Si-Si} and g_{O-O} pair distribution functions show a distinct peak at short distances which is absent in the crystalline configuration. The novel short distance features prevail in the 64 and 128-molecule clusters. We attribute this new feature to re-arrangements of Si-O bonds into 4-member rings. These peculiar rings, absent in the α-quartz, are primarily formed at the surface of the clusters. It is important to note that these novel ring formations are also present in the glassy clusters (bottom figures). The g_{Si-O} function for any cluster size does not present major changes when passing from crystal to glass (see left column in Fig. 3). This fact indicates that

the first-neighbor bonding structure is not significantly affected by either the annealing process nor the thermal surface reconstruction.

At the glass transition temperature (or above) the short distance peaks of the pair distribution functions are smeared out into one broad first peak with a prominent tail at short distances. In Fig. 4 the three pair distribution functions at 2200K for a large 128-molecule cluster are reported. The position of the first peak in the three cases is remarkably close to the calculated[13] and experimental[16,17] values reported for bulk silica. On this basis we conclude that the mechanism of thermal surface reconstruction in small clusters is extremely strong and that glassy transformations initiate at temperatures well below the glass transition.

Radial distribution function for 128 SiO2 cluster at Tg=2200K
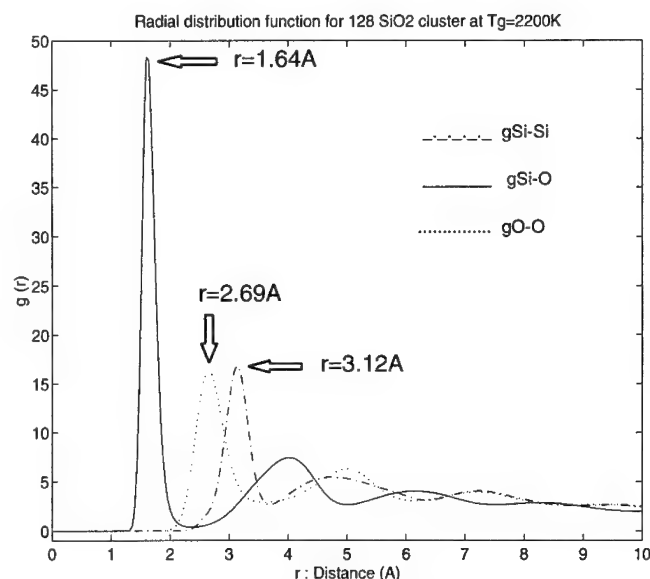
Fig. 4 Pair distribution functions g_{Si-Si} (-·-·-), g_{O-O} (····) and g_{Si-O} (——) for the 128-molecule cluster at T=2200K.

SINTERING OF CLUSTERS

Sintering simulations were conducted to investigate the time and temperature dependence of voids created between three clusters physisorbed on a surface. Assuming that glassy particles are formed in the gas phase, during the process of surface deposition voids are inevitably generated. We have modelled simple voids at room temperature by placing three clusters of the same size radially located from the center of an empty circle of diameter d. Typically the sintering process of these simple voids lasted a few ps. The long range interactions are extremely important during the process of sintering. Due to these interactions the clusters around the void have the ability to increment their temperature by 200 to 300K in less than 10 ps. The behavior is depicted in Fig. 5a. Since the mobility of the atoms is larger, they start migrating towards the center of the void with a peculiar deformation of the cluster shape. Very fast, in just a few ps, the shape deformation is so strong that the void is filled with atoms. Si-O bonds are formed locking the structure into large agglomerates of three clusters. The rate of sintering is fast at the beginning of the process and remains a constant after the first few ps (see Fig. 5b). Sintering rates are slightly slowed down when the void is made up of crystal-like clusters.

177
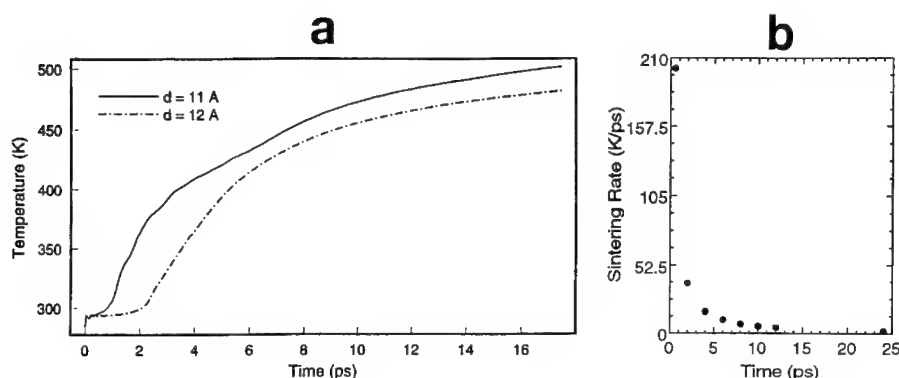
Fig. 5 Sintering of three 64-SiO$_2$ clusters. (a) Internal temperature of the void as a function of time. (b) Sintering rate as a function of time.

CONCLUSION

In conclusion, we have conducted Hamiltonian molecular dynamics simulations of the liquid-glass transition in silica clusters. The transition temperature decreases with the size of the silica particle up to 20% less than in the bulk material temperature. In turn this is an indication of the strong influence of that the thermal reconstruction of the cluster surface plays in the glass transition. The surface reconstruction is mainly lead by the formation of 4-member rings which are absent in the crystalline allotropes of SiO$_2$. The computational strategy used in the above computations allowed us to implement the particle decomposition parallel strategy in the Intel Paragon at George Mason University. This computational schema gave rise to a significant reduction in the complexity of the problem and an almost ideal speedup.

REFERENCES

1.   M. R. Zachariah and H. G. Semerjian, AIChE. J. 35, 2003 (1989).
2.   S. L. Chung and J. L. Katz, Combust. Flame 61, 271 (1985).
3.   F. Gelbard F.,Y. Tambour, and J. H. Seinfeld, J. Colloid Inteface Sci. 76, 541 (1980).
4.   S. H. Bauer and D. J. Frurip, J. Phys. Chem. 81, 1015 (1977).
5.   R. A. Dobbins and G. W. Mulholland, Combust. Sci. Technol. 40, 175 (1985).
6.   E. Blaisten-Barojas and R. M. Zachariah, Phys. Rev. B 44, 4403 (1992).
7.   S. Tsuneyuki, M. Tsukada, H. Aoki, and Y. Matsui, Phys. Rev. Lett 61, 869 (1988).
8.   J. R. Rustand, D. A. Yuen, and F. J. Spera, Phys. Rev. A 42, 2081 (1990).
9.   J. S. Tse, D. D. Klug, Y. Le Page, Phys. Rev. Lett. 69, 3647 (1992).
10.   S. Tsuneyuki, H. Aoki, and M. Tsukada, Phys. Rev. Lett. 64, 776 (1990).
11.   B. P. Feuston and S. H. Garofalini, J. Chem. Phys. 89, 5818 (1988).
12.   G. J. Kramer et al., Phys. Rev. B 43, 5068 (1991).
13.   R. G. Della Valle and H. C. Andersen, J. of Chem. Phys. 97, 2682 (1992).
14.   E. Blaisten-Barojas and D. Levesque, Phys. Rev. B 34, 3910 (1986).
15.   J. G. Gay and B. J. Berne, J. Colloid Interface Sci. 109, 90 (1986).
16.   J. H. Konnert.and J. Karle, Acta Crystallogr. A 29, 702 (1973).
17.   D. I. Grimley, A. C. Wright, and R. N. Sinclair, J. Non-Cryst. Solids 119, 49 (1990).

Anomalous Phase Separation Kinetics Observed in a Micelle System

J. P. Wilcoxon and J.E. Martin*
*Organization 1153, Sandia National Laboratories, Albuquerque, NM 87185

Abstract:
We report a real-time, two-dimensional light scattering study of the evolution of structure of a two component nonionic micelle system undergoing phase separation. The micelles act like molecular slug-a-beds whose domain growth is pathetically lathargic (i.e. slower than the cube root of time prediction for simple binary fluids). In fact, the growth kinetics can be empirically described as a stretched exponential approach to a pinned domain size. Although the kinetics are not yet understood, this anomalous behavior may be due to the ability of the spherical micelles to reorganize into more complex structures.

Introduction:

Micelles are surfactant aggregates with a droplet-like structure that can form in either polar or nonpolar solvents. In nonpolar solvents such as oils the hydrophobic (lyophilic) surfactant tails are exposed to form *reverse* or *inverse* micelles. Micelles formed of nonionic surfactants often phase separate when the temperature is increased or decreased (inverse systems). The critical point behavior of these systems has been the subject of several investigations[1-5] and it has been established[2-5] that they fall into the same universality class as simple binary fluids, although the critical concentration is quite low due to the large size of the micelles compared to the solvent. In particular, static properties, such as the divergence of the correlation length and the osmotic compressibility, can be expressed as power-laws in the reduced temperature with Ising exponents.

However, the universal Ising-type critical behavior of these systems does not extend deeply into the two phase region. Several years ago we observed [6] that a sample equilibrated in the two-phase region exhibits unusually strong scattering due to structures of enormous size. This novel scattering occurs in both inverse and normal micelles. It is reasonable to expect the formation of large structures to affect the kinetics of phase separation. In this paper we report the first study of the evolution of structure in a micelle system in an attempt to understand the origin of these structures.

Results and Discussion:

To study the kinetics of phase separation requires the ability to determine structure as a function of time. Traditional one-dimensional light scattering instruments must repetitively scan through a sequence of angles, with the result that data are acquired in an interval during which the structure is evolving, so that the temporal resolution is compromised. In these experiments we used a two-dimensional, time-resolved light scattering instrument that is based on currently available video and computer technology.

Radially-averaged scattering data taken during a 9 mK quench are shown in Fig. 1 (although our time resolution is 33 ms we have only shown a few data sets for clarity). An unstable concentration fluctuation that intensifies with time and moves toward q=0 is clearly observed. A significant feature of the data is the pronounced maximum, or spinodal ring, that occurs at a scattering wavevector q_{max} and has an intensity I_{max}. The peak position and amplitude have simple physical interpretations: the characteristic domain size is just $L(t) = 2p/q_{max}$ and the characteristic domain mass- i.e. the domain mass within a domain size, is just proportional to I_{max}. Key issues are the structure of the domains and their growth kinetics.

A salient feature of these data is that as soon a ring can be resolved its peak position is already moving toward q=0, in contradiction to the linear Cahn-Hilliard theory, which predicts exponential growth of a stationary ring at early times. In real space, the Cahn-Hilliard description corresponds to phase separation into domains of fixed size but of increasing concentration difference. Despite our best efforts to find this linear regime we were unsuccessful. Of course, one can always postulate that the linear regime occurs on time scales shorter than can be resolved, so although we can't rule out Cahn-Hilliard, we can't measure it either.

Having resolved that the domains grow from the earliest observable times, an obvious issue is whether the domain structures grow by simple enlargement, while their morphology is statistically constant. If this is case then the scattering data will collapse onto a master curve when plotted on the universal axes I/I_{max} versus q/q_{max}. In fact, a good data collapse, shown in Fig. 2, is obtained, indicating that the expected scaling of the structure does occur, at least for shallow quenches. However, the form of the collapsed data differs in some regards from standard results, as we shall now discuss.
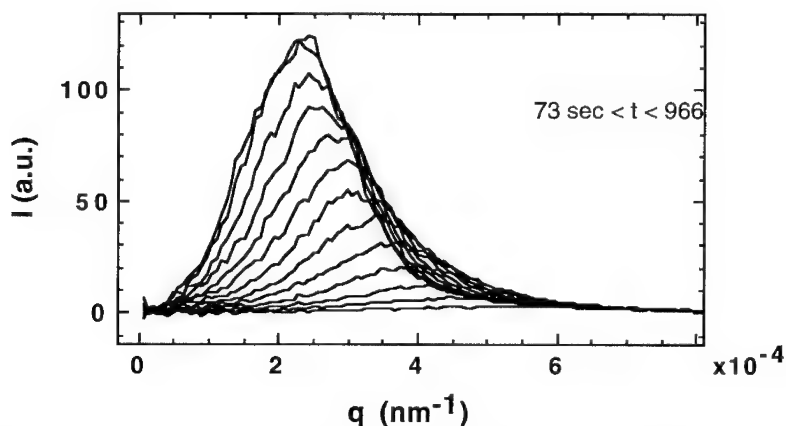
Figure 1. The growth of the radial-averaged intensity with time, as a function of the momentum transfer q, for a critical quench of 9 mK.

For spinodal decomposition in simple liquids (as well as other systems) Furukawa [7] has presented heuristic arguments that the scattered intensity I(q,t) has the universal scaling form:

$$I(q,t) \sim q_{max}^{-3} f(x),$$

(1)

where $x=q/q_{max}$ and q_{max} is a function of time. The scaling function depends on whether the quench is along the critical isochore and has the form

$$f(x) = \frac{4x^2}{3+x^8}; \quad \text{critical quench}$$
$$= \frac{3x^2}{2+x^6}; \quad \text{off – critical quench}$$

(2)

These functions have simple limiting behaviors at small and large wavevectors,

$$f(x) \sim x^2 \quad x \ll 1$$
$$\sim x^{-6} \quad x \gg 1; \quad \text{critical quench}$$
$$\sim x^{-4} \quad x \gg 1; \quad \text{off – critical quench}$$

(3)

that can easily be discerned in the data. At small q the structure factor increases as q^2, which is simply the result of having a conservation law. For large q there is a q^{-4} decrease for an off-

critical quench, which is simply Porod's scattering law for sharp interfaces. The q^{-6} fall-off is for critical quenches and is apparently due to a more complex interface.

The data of figure 2 do increase as q^2 for $q<q_{max}$ and fall-off as q^{-6} for $q>q_{max}$, in agreement with Eq. 3. However, at higher values the q^{-6} fall-off crosses over to q^{-2}, possibly indicating the formation of more complex structures, such as micellar aggregates. Alternatively, this cross-over may be due to the fact that a system near the critical point has a substantial correlation length beneath which Ornstein-Zernike scattering can be observed. In other words, critical opalescence occurs within the domain structures once the domain size is greater than the correlation length.
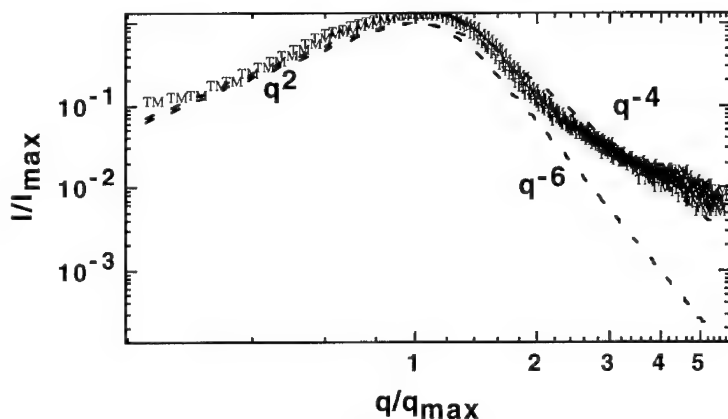
Figure 2. When the normalized intensity I/I_{max} is plotted against the normalized momentum transfer q/q_{max} for the 9 mK quench a master curve results that is well described by the Furukawa [10] function for a critical quench. However, at large wavevectors a q^{-2} tail is observed that is not predicted. This tail may be due to critical opalecscence within the phase separated domains.

The next issue is how the domain size depends on the domain mass. For non-mass fractal objects in three dimensions it is expected that the mass increases as the cube of a length. Since the peak intensity is a domain mass and the inverse of the peak position is the domain size we expect to observe, $I_{max}(q) \sim q_{max}^{-3}$. Observation of this relation would imply that the coarsening of non-mass fractal domains is taking place during the phase separation process, independent of quench depth.

Scattering data for all quench experiments with 2 mK<DT<38 mK were quantitatively similar to the shallow quench data, albeit a crossover from critical quench to off-critical quench behavior was seen at large times (eq. 3), and this will be discussed later. In particular, a cubic dependence of the domain size on the domain mass was observed, and the structure factor was found to scale on dimensionless axes, with q^2, q^{-6} and q^{-2} regimes. Evidently, the integrated measure of structure (eq. 4) is much less sensitive to morphology than the structure factor itself. However, as we shall now discuss, the kinetic data show large differences between the shallow and deeper quenches.

Following a suggestion of S. Glotzer, who has simulated spinodally decomposing systems that exhibit pinning, we then attempted to analyze our data in terms of an asymptotic approach to some pinning length, $L(\bullet)$, i.e.

$$L(t) = L(\infty)(1 - e^{-(\frac{t}{t})^b}) \qquad (5)$$

As in the case of both power law and logarithmic fits, this function has 3 adjustable parameters, $L(\bullet)$, t, and b. Analysis demonstrated that the optimal stretched exponential exponent b was very close to 0.5 for all quench depths, while the pinning length $L(\bullet)$ was nearly constant at a value of ~25 mm. We thus chose to fix these parameters and let only the characteristic time t vary with quench depth.   These fits are shown as solid lines through the experimental data of Fig. 3 and demonstrate that eq. 5 is a good description of all our data. An important point, however, is that a functional form that approaches an asymptote can be a misleading fit unless the pinning length is reasonably close to the largest length scale in the experimental data. Our data approaches 80% of the pinning length, so we do not think that the pinning interpretation can be rejected out of hand.
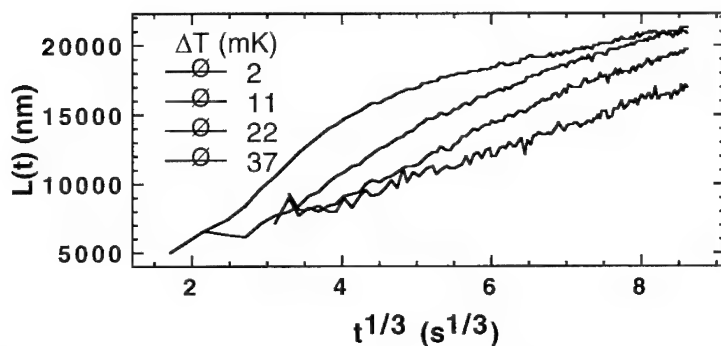
Figure 3 . The growth of the domain size as a function of time t for four quench depths is plotted against $t^{1/3}$ to determine deviations from Lifshitz-Slyozov growth. Significant deviations in the form of an apparent slowing down occur at large times for deep quenches. The solid lines are best fits to the stretched exponential form of eq. 5.

The stretched exponential analysis doesn't resolve the question of whether the postulated pinning is extrinsic- due perhaps to impurities- or intrinsic, due to the ability of the spherical micelles to restructure into more complex morphologies. We do not expect impurities of a chemical nature in our samples, and this assumption is fortified by previous HPLC analysis of the surfactant used. Furthermore, any impurities would probably be quickly encapsulated by surfactants and thus rendered benign in their ability to moderate interactions between micelles. We suspect that the flattened portion of the phase diagram near the critical point leads to phases with large concentration differences even for relatively small quenches.

Acknowledgement:

References:
1. M. Corti and V. Degiorgio, Phys. Rev. Lett. **55**, 2005, (1985).
2. J.P. Wilcoxon and E.W. Kaler, J. Chem. Phys. **86**, 4684, (1987).
3. G. Dietler and D.S. Cannell, Phys. Rev. Lett. **60**, 1852, (1988).
4. K. Hamano, N. Kuwahara, I. Mitsushima, K. Kubota, and T. Kamura, J. Chem. Phys., **94**, 2172, (1991).
5. K. Hamano, N. Kuwahara, I. Mitsushima, K. Kubota, and J. Ito, Phys. Lett. A **150**, 405, (1990).
6. J.P. Wilcoxon, J. Phys. Chem. **94**, 7588, (1990).
7. H. Furukawa, Physica, **123A**, 497, (1984).

DEPRESSION OF THE GLASS TRANSITION TEMPERATURE IN ULTRA-THIN, GRAFTED POLYSTYRENE FILMS

J.L. KEDDIE and R.A.L. JONES
Polymer and Colloid Group, Cavendish Laboratory, University of Cambridge,
Madingley Road, Cambridge CB3 0HE, UK

ABSTRACT

We have used ellipsometry to measure the glass transition temperature (T_g) of ultra-thin films of polystyrene (PS) (less than 10 nm thick) obtained by grafting PS-COOH on the native oxide of Si. We find that T_g in these ultra-thin films is depressed from the bulk value by as much as 35 K. This is in qualitative accord with our earlier results on thicker non-grafted films of PS.

INTRODUCTION

The dynamic properties of amorphous polymers at surfaces control many important processes, such as welding, adhesion and melt-pressing. Additionally, an understanding of size effects can cast light onto the fundamental nature of the glass transition. Our past and present studies[1,2] in which we probe size-effects on glass transition temperature (T_g) - as well as the effects of an air surface and an interface with a solid substrate - thus have both technological and scientific implications.

Earlier we reported that the T_g of polystyrene (PS) decreases as film thickness is reduced.[1] We explained this finding by proposing that a liquid-like layer exists at the surface and its size diverges as T_g is approached from below. These previous experiments were conducted on PS spun-cast on a hydrogen-passivated silicon substrate, a surface that the polymer wets. In this work we have studied ultra-thin films of PS prepared by grafting carboxy-terminated molecules onto a hydrophilic oxide. Our preparation technique enables us to produce - in a controlled manner - films that are thinner than what is usually possible with spin-casting[3] and that are of a lower molecular weight than what is normally possible without de-wetting of the substrate.[4]

EXPERIMENTAL PROCEDURE

Preparation of Ultra-thin Films

Monocarboxy-terminated polystyrene (PS-COOH) (used as received from Scientific Polymer Products, Inc.) in toluene was spun-cast from solution onto the native oxide surface of (111) silicon. We deposited films between 200 and 300 nm thick for three molecular weights (13,000 50,000 and 225,000) of monodisperse PS-COOH. For the samples with MW = 13,000, we created a smooth, hydrophilic oxide by alternating several times between an oxide etch (NH_4/HF 7:1 solution) and an "RCA clean"[5] of the recently-etched surface to re-grow an oxide with a hydoxylated surface. In the RCA
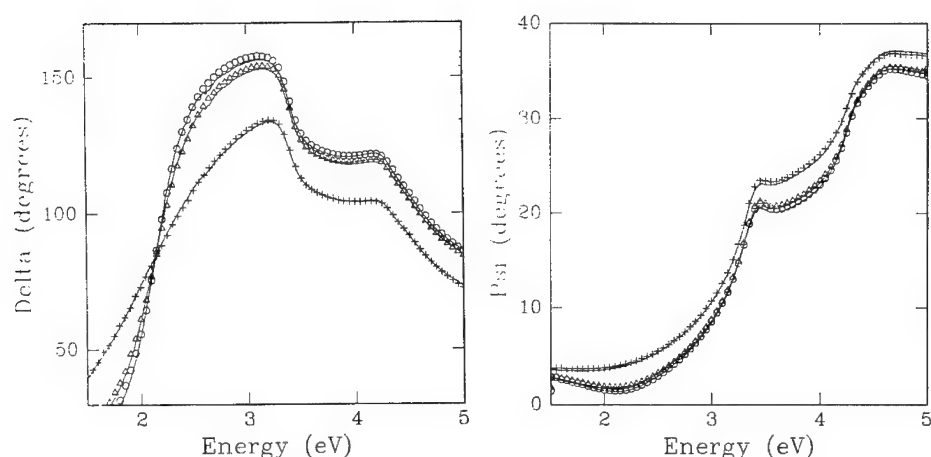
Figure 1. Spectroscopic scans (showing the ellipsometric angles ψ and Δ as a function of the energy of the incident light) for a bare Si substrate with 1.75 nm native oxide (o); after a film of PS-COOH (MW = 225,000) was spun-cast and rinsed with toluene (Δ); and after a PS-COOH film was annealed in vacuum at 433 K for 12 hours and then rinsed with toluene (x). Solid lines are best fits to the data corresponding to 1.75 nm thickness of native oxide and 3.98 nm of grafted PS-COOH after heating. The angle-of-incidence is 72 ° for all scans shown. On re-heating the volume of the glass falls slightly below that of the equilibrium liquid but then rises to meet it, as is expected from relaxation phenomena.

clean, the substrate was heated to 343 K for 20 minutes in a solution of NH_4OH, H_2O_2 and H_2O in a ratio of 1:1:5.

Zhao and co-workers[6] have proposed that PS-COOH is grafted on hydroxylated oxide via the reaction:

$$SiOH + R(COOH) <====> R(COOSi) + H_2O, \tag{1}$$

where SiOH represents a hydroxyl group on the oxide surface. They found that the grafting density of PS-COOH increases with temperature and that the enthalpy of the grafting reaction is +7.4 kcal/mole. To graft the PS-COOH to the substrates, we heated the samples in vacuum at 433 K, a temperature well-above the bulk T_g, for varying lengths of time - from one hour to four days. After quenching to room temperature, we repeatedly soaked and rinsed with toluene to remove any non-grafted and non-adsorbed polymer. We concluded the sample preparation with a final heat treatment to ensure that the polymers were at equilibrium and had a well-known thermal history. Samples were held at 433 K in vacuum for five hours and cooled slowly (0.25 K/minute).

184

By this procedure, we produced ultra-thin PS films, having a thickness less than 10 nm, according to our ellipsometry measurements. Regardless of MW, the grafted polymer film thickness was less than the radius of gyration of a polymer chain measured in a three-dimensional glass.[7] If the thicker, initial PS film was not heated prior to rinsing with toluene, we found that only a small amount of polymer, if any, adsorbed or grafted on the oxide surface. This finding is demonstrated by the ellipsometry measurements in Figure 1.

Measurements of Glass Transition Temperature

We used the same procedure described elsewhere[1,2] for determining T_g. Samples were heated or cooled at 2 K/minute while we continuously determined the ellipsometric angles (ψ and Δ) using a phase-modulated spectroscopic ellipsometer (Jobin-Yvon UVISEL). For the small changes with temperature found in the ultra-thin films, ψ and Δ are nearly linear functions of thickness and refractive index. From the discontinuity in thermal expansivity we can determine T_g.

RESULTS AND DISCUSSION

Thermal expansivity in the substrate results in linear changes in the ellipsometric angles with temperature. Although the expansivity of a polymer **glass** has little effect on the temperature-dependence of ψ and Δ, we observe a marked departure from linearity at T_g, even for films with thickness of only a few nm, as shown in Figure 2.
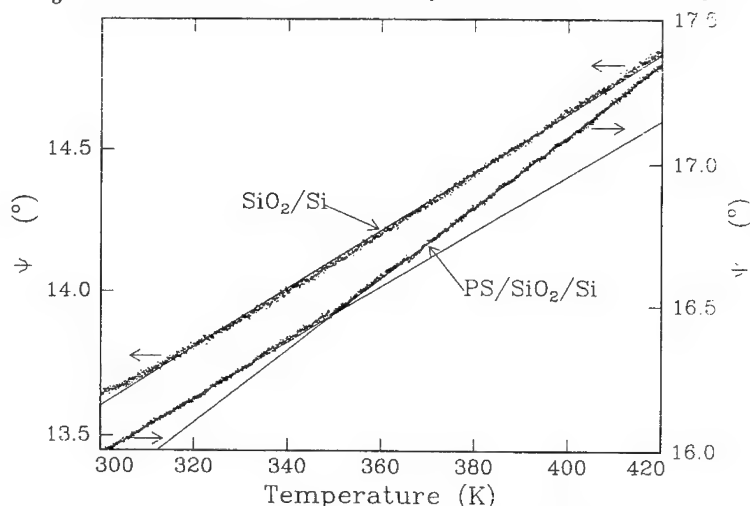
Figure 2. A comparison of kinetic scans from a bare Si substrate with native oxide and one with a 5.46 nm film of grafted PS-COOH (MW= 225,000). The substrate has a linear dependence of ψ on temperature. The scan of the film shows an inflection indicating a T_g of 349.7 K. The straight lines are the best fits through the linear regions above and below Tg. Angle-of-incidence of radiation is 72 ° and its energy is 3.2 eV.
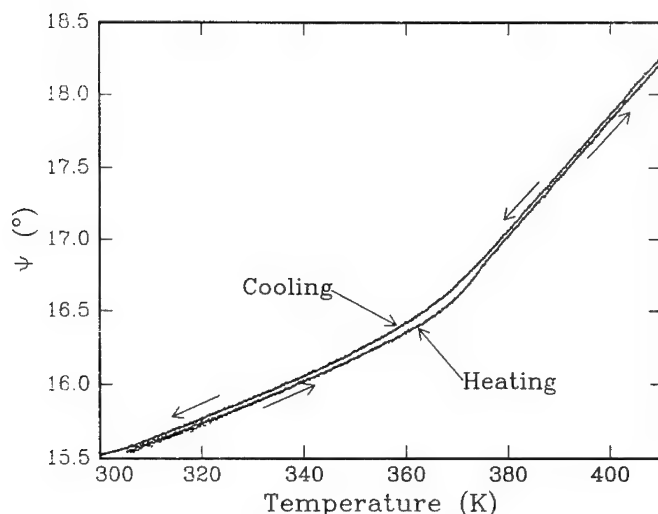
Figure 3. Scans showing the result of the thermal cycling of a 210 nm PS-COOH spun-cast film. Sample was cooled from the melt at 2 K/min. then re-heated and cooled again at the same rate during these scans. The linear regions of the plots are parallel, resulting in similar values of T_g for both heating and cooling (about 368 K).

We explored whether T_g differed during heating and cooling, as might be expected if there is a significant thermal lag between the temperatures of the substrate and sample surface. Figure 3 indicates that in thicker films (200 - 300 nm) T_g is similar regardless of whether the sample is being heated or cooled but that T_g obtained during heating tends to be slightly higher. Table I summarises the findings of thermal cycling experiments for PS-COOH of three molecular weights. The table also lists T_g obtained from DSC using a heating rate of 2 K/min. (the same as in ellipsometry). Values obtained with DSC are between 8 and 10 K higher than those obtained with ellipsometry. Both techniques reveal a dependence of T_g on molecular weight, as is predicted by the Flory-Fox equation for PS.[8] Note in Table I that the T_g values obtained with ellipsometry are in better agreement with the Flory-Fox equation, which uses empirical values derived from thermal expansivity, than are the DSC values.

Table I. Bulk Glass Transition Temperatures* of PS-COOH
as Determined by Ellipsometry on Relatively Thick Films and by DSC.

Molecular Weight	Thickness (nm)	T_g (heating) (K)	T_g (cooling) (K)	T_g (DSC) (K)	T_g (Flory-Fox) (K)
225,000	210	368.8	367.5	377.4	372.4
50,000	180	365.2	363.1	374.7	369.6
13,000	130	359.4	360.7	369.0	359.3

* Each value listed is an average of at least two measurements.

The thickness of the grafted polymer film depends on the size of the PS chain and on the grafting density, and so films of a thickness between 1.5 and 2.5 nm are obtained with MW = 13,000, whereas thickness varies between 5 and 10 nm for MW = 225,000. Grafted PS-COOH films, regardless of their thickness, consistently have a T_g well below that found for the "bulk" film. Typical results for films of different thickness are shown in Figure 4. The left axis corresponds to scan "a" which is from a film with thickness of 8.7 nm (MW = 225,000) showing a Tg of 347.8 K, corresponding to a depression of $\approx$ 20 K from the bulk value. The right axis is for a much thinner film (1.7 nm; MW = 13,000) with an apparent T_g of 331.7 K (scan "b"), which is depressed nearly 30 K from the bulk. In agreement with the thickness-dependence of Tg observed earlier for spun-cast PS, we find that T_g is depressed from the bulk value by a greater amount in thinner films, even when taking MW-effects into account.

These data support our previous finding for spun-cast PS[1] that Tg is size-dependent and follows an expression of the form:

$$T_g = T_g(\infty)\left[1-\left(\frac{A}{d}\right)^{\delta}\right]$$

(2)

where Tg(∞) is the T_g of the bulk material, A is a characteristic length fitted to 3.2 nm, δ = 1.8, and d is film thickness. We find that the thickness dependence of the grafted-PS films is not as strong as predicted by Equation 2 using values obtained for spun-cast PS. We plan to discuss this result further in a forthcoming paper.
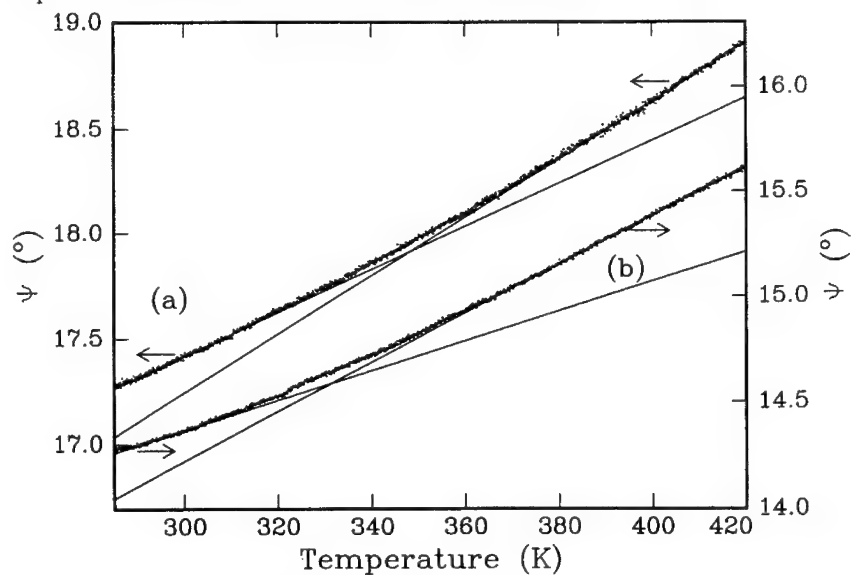
Figure 4. Ellipsometric scans of ultra-thin films of grafted PS-COOH. Lines are best fits through the linear regions corresponding to the glass and the melt. Angle-of-incidence of radiation is 72 ° and its energy is 3.2 eV.

We also found previously that the T_g of poly(methyl methacrylate) cast on the native oxide of silicon does not decrease as the film thickness is reduced.[2] We explained this result by suggesting that interaction between the polymer and the substrate outweighed the effect of the air surface in depressing T_g. PS is not expected to interact strongly with a silicon dioxide surface; if not grafted, low MW PS de-wets the surface. Thus, we suggest that the effects of the free surface dominate the T_g behaviour of PS, even in the case of low-MW, grafted polymer chains studied here. Whereas, PMMA chains might be attracted to an oxide surface along their entire length, grafted PS-COOH chains are attached to the substrate only at their ends.

CONCLUSIONS

We have extended our earlier study of spun-cast PS thin films by determining with ellipsometry the T_g of ultra-thin films of grafted PS-COOH. As with thicker films, we find two linear regions of thermal expansivity corresponding to the polymer glass and to the melt. Values of T_g obtained with ellipsometry for the ultra-thin films are up to 35 K below the value for the bulk. As found with spun-cast PS, T_g decreases as film thickness is reduced.

ACKNOWLEDGMENTS

REFERENCES

1. J.L. Keddie, R.A. L. Jones, and R.A. Cory, *Europhys. Lett.* **27**, 59 (1994).
2. J.L. Keddie, R.A. L. Jones, and R.A. Cory, *Disc. Faraday Soc..,* **98**, to be published.
3. T.G. Stange, R. Mathew, D.F. Evans, and W.A. Hendrickson, *Langmuir* **8**, 920 (1992).
4. G. Reiter, *Langmuir* **9**, 1344 (1993).
5. W. Kern, *J. Electrochem. Soc.* **137**, 1887 (1990).
6. X. Zhao, W. Zhao, X. Zheng, M.H. Rafailovich, J. Sokolov, S.A. Schwarz, M.A.A. Pudensi, T.P.Russell, S.K. Kumar and L.J. Fetters, *Phys. Rev. Lett.* **69**, 776 (1992).
7. G.D. Wignall, D.G.H. Ballard and J. Schelten, *Eur. Polym. J.* **10**, 861 (1974).
8. T. G. Fox and P.J. Flory, *J. Appl. Phys.* **21**, 581 (1950).

MOLECULAR DYNAMICS OF MONOMER, OLIGOMER, AND POLYMER LIQUIDS IN POROUS MEDIA: A FIELD-CYCLING NMR RELAXOMETRY AND NMR FIELD-GRADIENT DIFFUSOMETRY STUDY

R. KIMMICH,* S. STAPF,* R.-O. SEITTER,* P. CALLAGHAN,** AND E. KHOZINA*
*Universität Ulm, Sektion Kernresonanzspektroskopie, 89069 Ulm, Germany
** Massey University, Department of Physics and Biophysics, Palmerston North, New Zealand

ABSTRACT

The molecular dynamics of fluids in porous media has been studied using field-cycling NMR relaxometry and NMR field-gradient diffusometry. The frequency dependences of the ^{1}H and ^{2}H spin-lattice relaxation times T_1 of various liquids in porous glass reveal weak and strong adsorption behaviour depending on the polarity of the adsorbates. Correlation times eight orders of magnitude longer than in bulk have been observed. The T_1 dispersion moreover reflects geometrical details of the matrix in a length scale three orders of magnitude longer than the adsorbate molecules. The mean-square displacements of adsorbate molecules on the surface are only one order of magnitude less than in bulk. The global diffusivity is reduced by tortuosity and porosity effects. The observed phenomena may be explained by bulk-mediated surface diffusion, i.e., Lévy walks. The dynamics of polymer chains much longer than the pore size is characteristicly different from that in bulk melts. There is evidence that the reptation mechanism explains at least a part of the phenomena observed for the porous matrix in contrast to findings with bulk polymer melts.

INTRODUCTION

Continuous translational and rotational diffusion of spherically shaped molecules in an unrestricted homogeneous medium are described by the well-known diffusion equations leading to the displacement probability density (or "propagator")

$$P(\boldsymbol{r},t) = \left(\frac{3}{2\pi\langle r^2\rangle}\right)^{3/2} \exp\left\{-\frac{3r^2}{2\langle r^2\rangle}\right\} \quad \text{where} \quad \langle r^2\rangle = 6Dt \tag{1}$$

and the nuclear magnetic resonance (NMR) autocorrelation function for intramolecular dipolar or quadrupolar interactions [1]

$$G(t) = e^{-t/\tau_c} \quad \text{where} \quad \tau_c = \frac{4\pi\eta a^3}{3k_BT} = \frac{a^2}{6D_r} \tag{2}$$

The quantities D and D_r are the translational and rotational diffusivities, respectively, of a molecule with radius a in a medium with viscosity η at an absolute temperature T. These laws change dramatically in liquids confined in media such as porous glasses, fine-particle agglomerates, and globular-protein powders.

Systems of this sort are characterized by a large specific surface giving rise to interactions with the molecules of the liquid which is dispersed in the medium. Adsorption/desorption processes take place. While adsorbed, molecules tend to adopt a preferential orientation relative to the surface as revealed by ^{1}H or ^{2}H NMR line-splitting studies of hydrated lipid bilayers [2,3] or hydrated collagen [4], for instance. The consequence is that the frequency dependence of the spin-lattice relaxation time, the so-called T_1 dispersion, of polar fluids

incorporated in such matrices indicates correlation times up to eight orders of magnitude longer than in the bulk [5,6].

Translational displacements of molecules in confining systems are not only affected and possibly slowed down by surface interactions. The second kind of restraint refers to the geometry of the pore space. A tortuosity factor, τ, has been introduced [7,8] globally taking into account the distribution of pore orientations, the connectivity, and the pore size variation. A notion of the order of magnitude of τ is already provided by the consideration of the simplest situation, that is, randomly oriented uniform cylindrical capillaries with polar angles ϑ. In this case, one expects $\tau = \langle \cos^2 \vartheta \rangle^{-1} = 3$.

Assuming furthermore a two-site fast-exchange model for the "bulk" and "adsorbed" phases of the fluid in the pore space leads to an effective diffusivity

$$D = \frac{\epsilon_p}{\tau}[p_a D_a + (1 - p_a)D_b] \tag{3}$$

p_a is the weight fraction of the adsorbed phase, D_a and D_b are the diffusivity within the adsorbed and the bulk phase, respectively. The porosity, ϵ_p, is defined as the ratio of the pore space and the matrix volumes.

This formula implies a simplified, crude view: In reality, the time dependence of the mean-square displacement tends to become anomalous, that is, the linear relationship in eqn 1 is not fulfilled anymore. Modified power laws as expected for fractal percolation clusters, that is,

$$\langle r^2 \rangle \propto t^\kappa \qquad (\kappa < 1) \tag{4}$$

are discussed theoretically in [9] and experimentally in [11,12], for instance. In [10] a general propagator for anomalous displacements is given.

Furthermore, diffraction-like effects due to defiles in the pore network have been observed in echo-attenuation curves recorded in pulsed-gradient spin-echo (PGSE) diffusometry [13]. That is, strictly speaking, there is no simple way to characterize fluid diffusion in porous media by a single coefficient.

In the present paper we report on the influence of the adsorbate polarity, the pore size, and the chain length of adsorbed polymers on T_1 and translational diffusion of fluids in porous glasses. The techniques which we have predominantly employed are field-cycling NMR relaxometry [14] and the supercon fringe field variant [15] of PGSE diffusometry [16].

SAMPLES AND INSTRUMENTS

The field-cycling data were recorded with home-built instruments. Spin-lattice relaxation times at higher frequencies were recorded with Bruker SXP 4-100 and MSL 300 spectrometers. The total frequency ranges were for ^{1}H $3 \times 10^3 \ldots 3 \times 10^8$ Hz and for ^{2}H $3 \times 10^2 \ldots 4 \times 10^7$ Hz. All relaxation curves were found to decay monoexponentially within the experimental error over at least 1 decade. The measurements were carried out at 293 ± 1) K if not specified otherwise.

Vycor Porous Glass (VPG, # 7930, 96 % SiO_2) was purchased from Corning Inc., Corning, NY 14831, USA. The average pore diameter was specified by the manufacturer as 4 nm (96 % of the pore volume is within 4 ± 0.6 nm), the porosity as 28 % and the specific surface as 250 m^2/g. Note, however, that literature values of the specific surface of this material are considerably smaller [17]. This material tends to adsorb organic vapors from the air. In order to remove such impurities and following the recommendations of the manufacturer, the samples were boiled in 30 % H_2O_2 for 20 minutes before lyophilizing the material overnight and filling it with fluids using the bulk-to-bulk method. The VPG rods were carefully dried with tissue to avoid any artifacts by bulk liquid outside

of the pores. The measurements were performed immediately thereafter, and could be reproduced several months later using the same samples. Replacement of surface OH groups by propyl groups leads only to minor changes of T_1 [6].

Bioran porous glass was purchased from Schott Glaswerke, Mainz, Germany. The mean pore diameters are specified by the manufacturer as 30, 50, 70, 100, and 200 nm with a narrow pore size distribution (90 % within ± 5 %). In the following, the samples are denoted as B30, B50, B70, B100, and B200, respectively. The porosities are specified in the range $0.67\ldots 0.69$. The samples were prepared in the same way as the Vycor samples. The relaxation data were reproducible after several months using the same samples.

Monodisperse silica fine-particles were purchased from Cabot GmbH, Hanau, Germany. The registered product name is Cab-O-Sil EH-5. The specific surface was specified as (380 ± 30) m^2/g, the mean fine-particle diameter as 7 nm.

DIFFUSION

Evidence of anomalous diffusion

In previous papers [18,11,12], we have already reported that fluid diffusion in fine-particle agglomerates and in protein aerogels tends to be anomalous in the sense of eqn 4. The degree of anomaly is a matter of the displacement length scale probed in the experiments: Above the correlation length of the particle clusters, diffusion becomes more or less normal with an effectively reduced D value. This is confirmed by directly evaluating the mean-square displacement from PGSE attenuation curves (fig. 1). The evaluation procedure is described in [19].
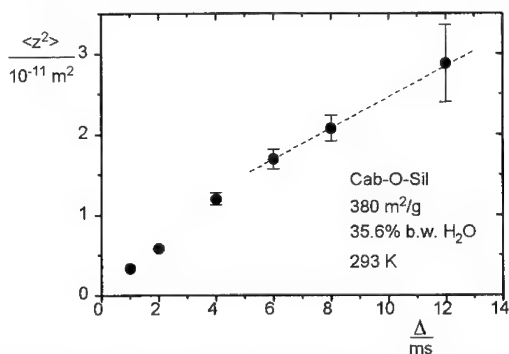
Figure 1: Mean-square displacement of water in silica fine-particle agglomerates

Fluids with different polarities

In the long-time limit where root mean-square displacements exceed the correlation length of the matrix structure, diffusivities in the proper sense may be evaluated. This was done with a series of different adsorbates filled in porous glasses. The results are listed in tab. 1. Obviously there is no significant influence of the polarity of the adsorbate. It rather appears that these diffusivities are of an effective nature and are determined by geometrical factors such as the tortuosity, the porosity and the mean pore size (see eqn. 3) [20].

Diffusion in the adsorbed phase

The freezing or - more generally - the solidification temperature of the fluid is normally much lower in the adsorbed phase than in bulk. This permits one to freeze the bulk phase

Table 1: Diffusivities D in 10^{-11} m^2/s at 294 K of different fluids filled in porous glasses

liquid	pure	in B30	in Vycor	pure/B30	pure/Vycor
Acetone	416	253	65.0	1.64	6.4
Hexane	389	251	73.8	1.55	5.3
Water	191	140	37.8	1.36	5.1
Cyclohexane	126	82.0	22.2	1.54	5.7
Ethanol	92.8	58.5	13.4	1.59	6.9
Tetradecane	49.0	27.6	6.47	1.78	7.6
Hexanol	17.6	10.1	1.84	1.74	9.6

while the adsorbed fluid layers are still liquid. NMR diffusometry then yields direct information on the displacement characteristics within the adsorbed phase. Corresponding measurements of the water diffusivity within the hydration layers of agglomerates of globular protein macromolecules are reported in [11,12]. The results agree very well with the conclusion from a NMR relaxation experiment concerning diffusion near protein surfaces [21] and with a molecular dynamics study of hydration water [22]. In the hydration layers, the diffusivity is roughly one order of magnitude less than in bulk.

Vapor-phase enhancement of diffusion

There is evidence that the vapor phase in partially filled pores contributes to the diffusivity by rapid exchange of adsorbate molecules between the adsorbed phase and the gaseous phase [23,24]. The effective diffusivity is then much higher than the bulk value. The vapor-phase enhancement was proven by showing that compression of silica fine-particle samples, that is, reduction of the vapor volume fraction, lowers the diffusivity down to the bulk value [25]. Fig. 2 shows water D values recorded in silica fine-particle agglomerates. At low water contents, the D is eight times higher than in bulk water.

SPIN-LATTICE RELAXATION DISPERSION

Figure 3 shows the ^{1}H and ^{2}H T_1 dispersions of water in porous glass (Bioran B30). In order to eliminate the nucleus and interaction specific parameters, the relaxation times are given as the ratio of the fluid spin-lattice relaxation times in the confined state and in the bulk, T_1 and T_1^{bulk}, respectively. Note that the latter are independent of the frequency in the shown range. The data indicate the appearance of low-frequency plateaus. This may be due to the influence of local fields which obtain a dominant influence in the limit of very low external fields B_0. It is nevertheless obvious that water relaxation implies correlation times as long as 1 ms, that is, there are motional components eight orders of magnitude slower than rotational diffusion in the bulk. It should be noted that intermolecular interactions cannot play a major role at low frequencies because ^{2}H relaxation is governed by quadrupole interaction, a purely intramolecular phenomenon.

Reorientations mediated by translational displacements (RMTD)

The apparent discrepancy of relatively fast translational diffusion in the adsorbed phase (see above) while molecular reorientations are extremely slow can be explained as reorien-
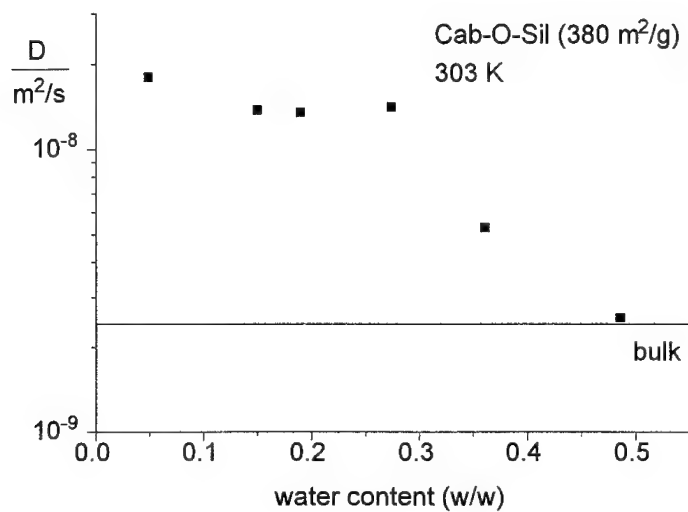
Figure 2: Water diffusivities in Cab-O-Sil in dependence on the water content
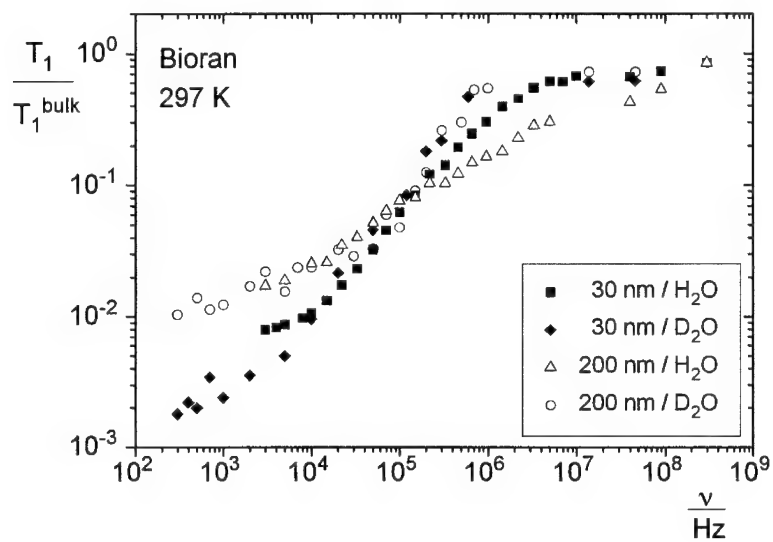
Figure 3: Water ^{1}H and ^{2}H T_1 dispersion in B30

tations mediated by translational displacements. The notion is that polar molecules have a relatively long residence time in the adsorbed phase. At very small fluid contents and in the absence of perceptible vapor contributions this may be even the only fluid phase existing in the system [5]. As outlined above, molecules tend to be oriented relative to the surface. Molecular reorientation is then governed by surface diffusion taking place within the adsorption layers or bulk mediated [26]. Figure 4 shows an illustration of the proposed mechanism.

A formalism has been developed for the representation of the T_1 dispersion in terms of the surface structure [2,6]. The molecular orientation is given by the azimuth and polar angles defining the vector $\vec{\Omega} = (\varphi, \vartheta)$. The NMR correlation function describing molecular reorientations, that is, the autocorrelation function of spherical harmonics of second order, is then [1]

$$G(t) = \left\langle Y_2^{(m)}\{\vec{\Omega}(0)\} \; Y_2^{(-m)}\{\vec{\Omega}(t)\} \right\rangle = \int g_{2,m}\left(\vec{r}\right) \; P\left(\vec{r}, t\right) \; d^z r = \int \tilde{S}\left(\vec{k}\right) \; e^{-Dtk^2} \; d^z k \quad (5)$$

where $\vec{k}$ is the wave-number vector of the surface structure. z is the topological dimensionality of the space within which the translation takes place, i. e., in our case $z = 2$. The surface "roughness" with respect to orientations is described by the spatial correlation function $g_{2,m}(\mathbf{r})$. For simplicity, we furthermore use the propagator eqn 1, that is, a Gaussian probability distribution. The orientational structure factor is then $\tilde{S}\left(\vec{k}\right) = (2^z \pi)^{-1} \int g_{2,m}\left(\vec{r}\right) \exp\{-i\vec{k} \cdot \vec{r}\} \; d^z r$, that is, in an isotropic topologically two-dimensional space $S(k) = \pi k \int_0^\infty r \; g(r) \; \mathcal{J}_0(kr) \; dr$, where $\mathcal{J}_0(kr)$ is the Bessel function of zeroth order. On this basis, the spectral density turns out to be

$$I(\omega) = \int_0^\infty S(k) \frac{2\tau_k}{1 + \omega^2 \tau_k^2} \; dk \qquad (6)$$

where the "mode" correlation times are given by $\tau_k = 1/(Dk^2)$. The application of this formalism to experimental relaxation dispersion data leads to a new representation characterizing the surface structure by a distribution of surface "modes" [6,25].

Fluids with different polarities
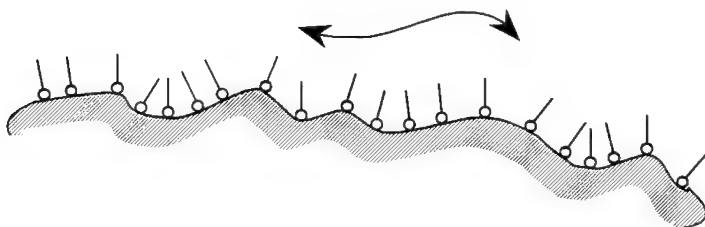
Figure 4: The RMTD mechanism

Figure 5 shows the dispersion of the relative T_1 values of various fluids in porous glass B30.

Two groups of liquids may be distinguished. Depending on the polarity, either a strong or an almost negligible frequency dependence appears. These findings may be attributed to "weak" and "strong" adsorption [26]. Only in the latter case, surface diffusion can take place so that the RMTD mechanism becomes effective.
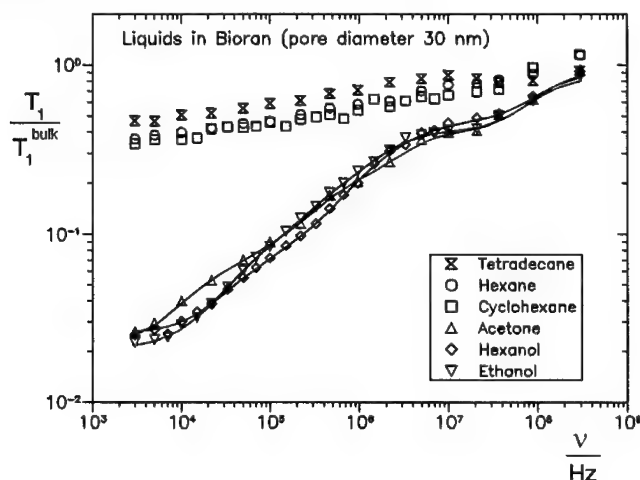
Figure 5: ^{1}H T_1 dispersion of various fluids in porous glass B30

The lines in fig. 5 correspond to the evaluation using the orientational structure factor formalism (see above). A representative example of the wave number distribution is shown in fig. 6. At low wave numbers an equipartition is found indicating an entirely random
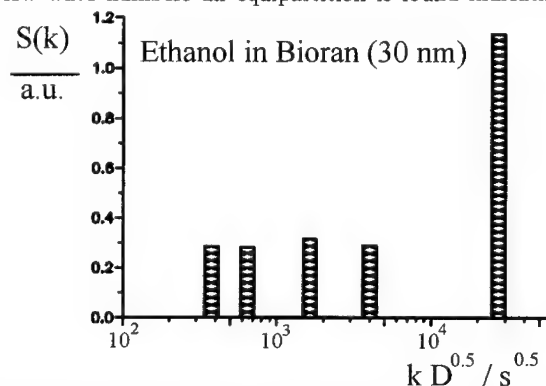
Figure 6: Orientational structure factor $S(k)$ for ethanol in B30 (solid line in fig. 4)

surface structure with respect to orientations of adsorbate molecules. The corresponding range of the wavelengths may be estimated using the D value given in tab. 1. We find $15nm < \lambda < 1.5\mu m$ in accordance with the order of magnitude of the characteristic pore

195

structure lengths.

<u>Matrices with different pore sizes</u>

Figure 7 shows the ^{1}H T_1 dispersion of water confined in porous glass with different pore sizes. As the pores were completely filled, the fraction of adsorbed water is a function of the pore size. Therefore the relaxation times were reduced to values corresponding to the first monolayer on the surface using the two-site fast exchange formula

$$\frac{1}{T_1^{ML}} = \frac{1}{p^{ML}} \left(\frac{1}{T_1} - \frac{1 - p^{ML}}{T_1^{bulk}} \right) \tag{7}$$

where T_1 is the spin-lattice relaxation time globally measured in the porous glass. The data
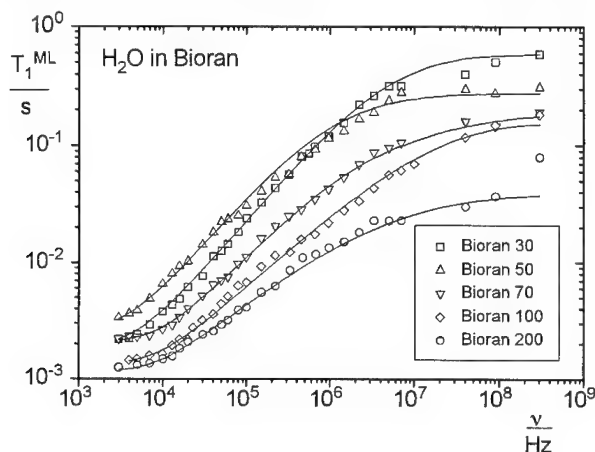
Figure 7: ^{1}H T_1 dispersion of adsorbed water in porous glass

indicate a clear dependence on the pore size. The evaluation of the orientational structure factor gives some insight in the nature of the structural changes accompanying the variation of the pore size. Examples of this evaluation are shown in fig. 8. The solid lines in fig. 6 correspond to these distributions of the structure factor. The wave number dependence of the orientational structure factor can be represented by power laws $S(k) \propto k^{-\chi}$ (solid lines in fig. 7) The exponent χ as well as the absolute values of the monolayer relaxation times depend on the pore size in a characteristic way (fig. 9). This pronounced pore size dependence gives evidence of the fact that T_1 is sensitive to the pore structure.

<u>Alkanes and polymers in porous glass</u>

Figure 10 shows the T_1 dispersions of two alkanes in porous glasses in comparison to the bulk data. Molecular dynamics computer simulations [27,28] predict a flat, relatively ordered arrangement of the alkane chains on surfaces. The NMR relaxation data do show an effect of the surfaces on the alkane reorientation dynamics. It is, however, much less pronounced than with polar adsorbates.

Much stronger frequency dependences were found with polydimethylsiloxanes (PDMS) in Vycor. A molecular weight dependence of the T_1 dispersion slopes was only found below
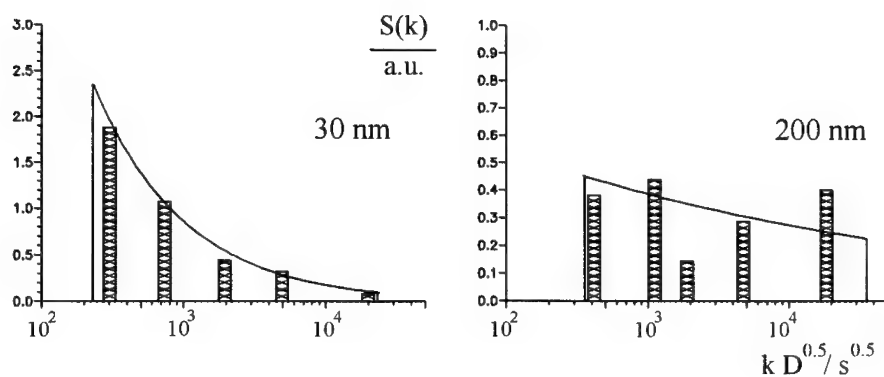
Figure 8: $S(k)$ for water in Bioran
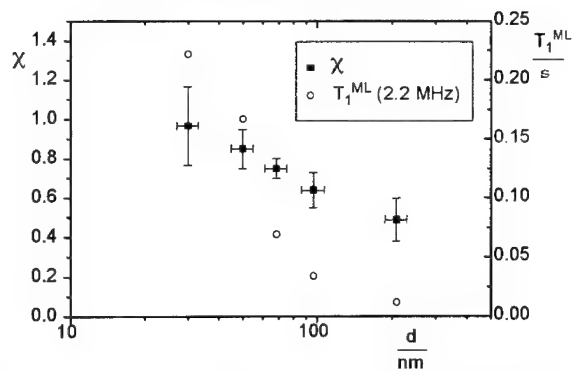
Figure 9: Pore size dependences of χ and T_1^{ML} at 2.2 MHz
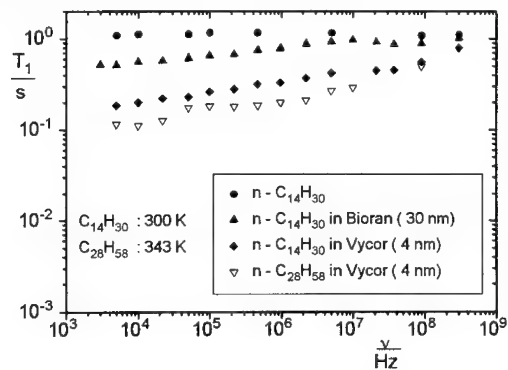
Figure 10: ^{1}H T_1 dispersion of alkanes in porous glasses

the critical value M_c. Figure 10 shows two typical data sets for PDMS 340 and PDMS 115 000 in Vycor.
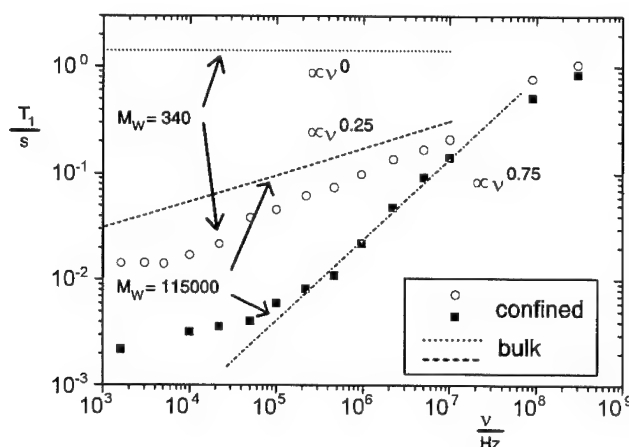
Figure 11: ^{1}H T_1 dispersion of PDMS in Vycor at 293 K

The chain dimensions of PDMS 340 are below, those of PDMS 115000 above the pore size (tab. 2). The bulk T_1 dispersions of the same polymers are represented by the indicated

Table 2: Dimensions of the system PDMS/Vycor

	$M_w = 340$	$M_w = 115000$
chain diameter	0.8 nm	0.8 nm
chain length	1 nm	300 nm
radius of gyration	0.5 nm	9 nm
mean pore diameter	4 nm	4 nm

lines. Compared with these, the dispersion slopes of the polymers confined to pores are considerably steeper. In the case of PDMS 340, the reason for this appears to be the interaction with the inner surfaces: The slope is between those of the polar and apolar solvents in fig. 5. An additional constraint obviously is effective with PDMS 115000: The interaction with the surfaces should be the same as with the low molecular weight. The T_1 frequency dependence nevertheless is much stronger. As an explanation we suggest that the chain modes are affected by the confinement of the chains in the rigid geometry of the pore network.

DISCUSSION

The dynamic behaviour of fluids in porous media is determined by processes in the bulk and the adsorbed phases only [29]. Translational diffusion of fluids in porous materials is astonishingly fast. The diffusivity in the adsorbed phase of polar liquids on polar surfaces is merely reduced by one order of magnitude relative to the bulk value. However, there is

evidence for tortuosity and porosity reductions of the average diffusivity in porous media. Diffusion also tends to be anomalous in short length/time scales.

On the other hand, the T_1 dispersions of ^{1}H as well as ^{2}H indicate extremely slow molecular reorientation processes. In contrast to translational diffusion, there is a strong influence of the polarity of the adsorbate, that is, "weak" and "strong" adsorption [26] reveals itself in such experiments. The T_1 dispersion also reflects geometrical details of the matrix which are three orders of magnitude larger than the molecules. These findings may be explained by the RMTD mechanism. A corresponding formalism analyzing the T_1 dispersion in terms of structural surface modes has been presented [6,25].

There is evidence that molecules persistently diffuse along the matrix surface after having been adsorbed. An explanation may be given by "bulk mediated surface diffusion" (BMSD) [26]. That is, molecules once adsorbed underlie many desorption/readsorption cycles before they are able to escape eventually to the bulk. The statistics of this effective surface diffusion process corresponds to Lévy walks [30,31]. There is an interesting implication connected with this mechanism: The mean-square displacement along the surface is predicted to be effectively anomalous. It is expected that this affects the T_1 dispersion characteristics of the RMTD mechanism. Considerations, whether BMSD can be proven in this way, are in progress.

The T_1 dispersion of polymers in narrow pore networks is of particular interest with respect to polymer theories. Chain dynamics in entangled polymer melts are alternatively discussed in the frame of the so-called "tube" models of chain dynamics [32,33] or with memory-function formalisms [34]. In our previous work [35,36] we have shown that T_1 dispersion of polymer melts is compatible with the renormalized Rouse theory [34] and contradicts to the Doi/Edwards tube concept [33] in the time scale of these experiments. Following de Gennes' reptation theory [32], a proportionality $T_1 \propto \nu^{3/4}$ would be expected in the latter case. By contrast a $\nu^{0.25}$ law was observed in accordance with the renormalized Rouse theory. In porous media, however, the situation appears to be quite different. The data presented in this paper are compatible with a $T_1 \propto \nu^{3/4}$ dispersion. That is, the reptation model is suitable for the description of chain dynamics under these circumstances.

REFERENCES

1. A. Abragam, The Principles of Nuclear Magnetism (Clarendon Press, Oxford, 1961).

2. R. Kimmich and H. W. Weber, Phys. Rev. B **47,** 11 788 (1993).

3. S. König, E. Sackmann, D. Richter, R. Zorn, C. Carlile, and T. M. Bayerl, J. Chem. Phys. **100,** 3307 (1994).

4. C. Migchelsen and H. J. C. Berendsen, J. Chem. Phys. **59,** 296 (1973).

5. R. Kimmich, W. Nusser, and T. Gneiting, Colloids and Surfaces **45,** 283 (1990).

6. S. Stapf, R. Kimmich, and J. Nieß, J. Appl. Phys. **75,** 529 (1994).

7. J. Kärger and M. Ruthven, Diffusion in Zeolites (Wiley, New York, 1992).

8. F. A. L. Dullien, Porous Media, Fluid Transport and Pore Structure (Academic Press, New York, 1979).

9. R. Orbach, Science **231,** 814 (1986).

10. J. Klafter, G. Zumofen, and A. Blumen, J. Phys. A: Math. Gen. **24,** 4835 (1991).

11. F. Klammler and R. Kimmich, Croat. Chem. Acta **65,** 455 (1992).

12. R. Kimmich, F. Klammler, V. D. Skirda, I. A. Serebrennikova, A. I. Maklakov, and N. Fatkullin, Appl. Magn. Reson. **4,** 425 (1993).

13. P. T. Callaghan, A. Coy, D. MacGowan, K. J. Packer, and F. O. Zelaya, Nature **351,** 467 (1991).

14. F. Noack, Progr. in NMR Spectr. **18,** 171 (1986).

15. R. Kimmich and E. Fischer, J. Magn. Reson. A **106,** 229 (1994).

16. J. Kärger, H. Pfeifer, and W. Heink, Adv. Magn. Reson. **12,** 1 (1988).

17. P. Levitz, G. Ehret, S. K. Sinha, and J. M. Drake, J. Chem. Phys. **95,** 6151 (1992).

18. R. Kimmich, Magn. Reson. Imag. **9,** 749 (1991).

19. J. Kärger, H. Pfeifer, and G. Vojta, Phys. Rev. A **37,** 4514 (1988).

20. J. Kärger, J. Lenzner, H. Pfeifer, H. Schwabe, W. Heyer, F. Janowski, F. Wolf, S. Ždanov, J. Am. Ceram. Soc. **66,** 69 (1982).

21. C. F. Polnaszek and R. G. Bryant, J. Chem. Phys. **81,** 4038 (1984).

22. P. Ahlström, O. Teleman, and B. Jönsson, J. Am. Chem. Soc. **110,** 4198 (1988).

23. J. Kärger, H. Pfeifer, E. Riedel, and H. Winkler, J. Coll. Interface Sci. **44,** 187 (1973).

24. F. D'Orazio, S. Bhattacharja, W. P. Halperin, and R. Gerhardt, Phys. Rev. Lett. **63,** 43 (1989).

25. R. Kimmich, S. Stapf, P. Callaghan, and A. Coy, Magn. Reson. Imaging **12,** 339 (1994).

26. O. V. Bychuk and B. O'Shaughnessy, J. Chem. Phys. **101,** 772 (1994).

27. T. K. Xia, J. Ouyang, M. W. Ribarsky, and U. Landman, J. Chem. Phys. **69,** 1967 (1992).

28. R. Hentschke and R. G. Winkler, J. Chem. Phys. **99,** 5528 (1993).

29. K. Overloop and L. Van Gerven, J. Magn. Reson. A **101,** 147 (1993).

30. O. V. Bychuk and B. O'Shaughnessy, J. Phys. II **4,** 1135 (1994).

31. A. Blumen, G. Zumofen, and J. Klafter, Phys. Rev. A **40,** 3964 (1989).

32. P. G. de Gennes, J. Chem. Phys. **55,** 572 (1971).

33. M. Doi and S. F. Edwards, The Theory of Polymer Dynamics (Clarendon Press, Oxford, 1986).

34. K. S. Schweizer, J. Chem. Phys. **91,** 5802 (1989).

35. N. Fatkullin and R. Kimmich, J. Chem. Phys. **101,** 822 (1994).

36. R. Kimmich, N. Fatkullin, H. W. Weber, and S. Stapf, J. Non-Cryst. Solids **172-174,** 689 (1994).

EXPERIMENTAL STUDY OF ELECTROKINETICS
IN POROUS MEDIA

DAVID B. PENGRA, LIANG SHI, SIDNEY XI LI, AND PO-ZEN WONG
Department of Physics and Astronomy, University of Massachusetts,
Amherst, MA 01003, U.S.A.

ABSTRACT

In brine-saturated porous media the existence of a space-charge layer at the solid/liquid interface leads to a coupling between fluid and electric currents. This coupling is seen as a *streaming potential* (STP) across a porous plug when the fluid flows through it, or conversely, as *electroosmosis* (ELO) of the fluid when an electric field is applied. The magnitude of these electrokinetic effects depends on the thickness of the space-charge layer relative to the pore size, which in turn depends upon the salinity of the brine. From electrokinetic measurements one can obtain an effective hydraulic radius R_{eff} and an effective zeta-potential at the slip-plane ζ_{eff}. We have developed a high-sensitivity AC technique that can detect these small coupling effects, and have measured them in a suite of natural and artificial rock samples. We find that R_{eff} and ζ_{eff} depend on salinity in ways which may be attributed to the roughness of the pore surfaces.

INTRODUCTION

In a brine-saturated porous material, both fluid and electric currents may be induced by externally applied pressure and electric fields. The system's response depends on the microgeometry of the material and the chemistry at the interface. Because both types of currents flow through the same pore space, one expects the electric and fluid currents to be related. Here, we examine the phenomena where a current of one type is induced by a field of the *other* type—this is the subject of electrokinetics.

Electrokinetic phenomena result from the electrochemical double-layer that exists at the boundary between a dielectric solid and an electrolyte [1, 2]. Typically, one of the ionic species preferentially adsorbs at the surface; to preserve charge-neutrality, other species form a diffuse screening layer with screening length λ next to this charged layer. The mobility of the bound species is reduced relative to the diffuse species. Because of viscous forces, pressure-induced fluid flow will carry the charge in the diffuse layer; this charge current is called the *streaming current*. Conversely, charge currents induced by electric fields carry fluid with them, which is *electroosmosis*.

The screening length λ is calculated by applying the Debye-Hückel theory of ionic distributions to a flat interface [2]. Dimensional analysis gives

$$\lambda = \left(\frac{\epsilon k_{\mathrm{B}} T}{2 N_0 q^2} \right)^{1/2} , \qquad (1)$$

where we assume a binary electrolyte (such as NaCl in water); ϵ is the dielectric constant of the solution, N_0 is the salt concentration, and q is the ionic charge. All else being equal, the strength of electrokinetic effects depend on λ, which varies as $N_0^{-1/2}$.
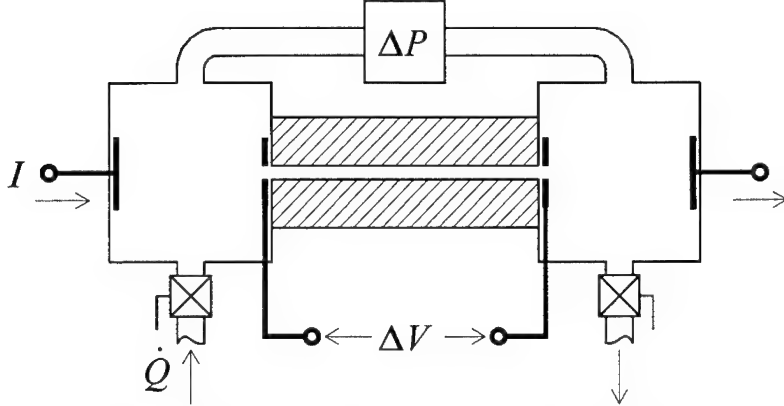
Figure 1: Schematic of typical electrokinetic measurement cell.

We may write the transport of charge and fluid in a general way which includes the electrokinetic couplings [3]:

$$\mathbf{J}_e = -\sigma_0 \nabla \Phi - L_{12} \nabla P , \tag{2}$$

$$\mathbf{J}_f = -L_{21} \nabla \Phi - \frac{k_0}{\eta} \nabla P , \tag{3}$$

The diagonal terms are Ohm's law and its hydraulic analog Darcy's law, giving the electric and fluid current densities $\mathbf{J}_e$ and $\mathbf{J}_f$ in terms of the potential and pressure gradients $-\nabla \Phi$ and $-\nabla P$. The constants σ_0 and k_0 are the zero-pressure-gradient conductivity and the zero-electric-field permeability, respectively. Permeability has the units of area, and is typically expressed in darcys (1 D = 1.0133 μm^2) [4]. The fluid viscosity is labeled η. The off-diagonal terms represent the electrokinetic couplings.

ELECTROKINETICS IN A CAPILLARY TUBE

To establish the physics of electrokinetics in porous media, we first examine an experiment on a simple system: a cylindrical capillary. Consider an apparatus where a capillary connects two brine-filled cavities of an experimental cell, as shown in Figure 1. If a pressure drop ΔP_a is applied across the tube, the charge displacement arising from the streaming current along the tube wall creates a voltage drop ΔV_s, known as the *streaming potential* (STP), that drives an ohmic counter-current in the bulk electrolyte in the opposite direction. Conversely, if a voltage ΔV_a is applied across the tube, electroosmosis (ELO) produces a counter-pressure ΔP_e that opposes the fluid flow; this is the *electroosmotic pressure*. Both STP and ELO are characterized by their steady-state coupling coefficients: $K_S = -\Delta V_s / \Delta P_a$ and $K_E = -\Delta P_e / \Delta V_a$.

We may calculate K_S and K_E for a capillary tube of length ℓ and radius R by integrating Eqs. (2) and (3) with the help of a model for L_{12} and L_{21}. If we assume that the space-charge distribution is given by the Debye-Hückel theory with $\lambda \ll R$, the fluid velocity field is described by Poiseuille flow, and the bulk electric current density is uniform, then the total electric current I and fluid current $\dot{Q}$ are

$$\frac{I}{\pi R^2} = -\frac{\sigma_w}{\ell}\Delta V - \frac{\epsilon\zeta}{\eta\ell}\Delta P , \tag{4}$$

$$\frac{\dot{Q}}{\pi R^2} = -\frac{\epsilon\zeta}{\eta\ell}\Delta V - \frac{R^2}{8\eta\ell}\Delta P , \tag{5}$$

where ζ is the electric potential at the slip-plane relative to the average potential over the cross-section, σ_0 equals the conductivity of the brine σ_w, and $L_{12} = L_{21} = \epsilon\zeta/\eta$ holds [2]. The STP and ELO coefficients are found when the associated current is equal to zero:

$$K_S^{\text{cap}} = -\Delta V/\Delta P|_{I=0} = L_{12}/\sigma_0 = \epsilon\zeta/\eta\sigma_w , \tag{6}$$

$$K_E^{\text{cap}} = -\Delta P/\Delta V|_{\dot{Q}=0} = L_{21}\eta/k_0 = 8\epsilon\zeta/R^2 . \tag{7}$$

The ζ-potential depends on the surface charge density qN_s of the adsorbed ions. By equating $-qN_s$ with the line-integral of the diffuse-layer charge density ρ_e normal to the surface, the Debye-Hückel approximation gives $\zeta = qN_s\lambda/\epsilon$ [1]. If the surface density N_s is independent of the brine concentration N_0, we would have $\zeta \propto \lambda \propto N_0^{-1/2}$, according to Eq. (1). In addition, since $\sigma_w \propto N_0$ for dilute electrolytes, we expect

$$\zeta \propto \sigma_w^{-1/2} . \tag{8}$$

It follows from Eqs. (6) and (7) that

$$K_S^{\text{cap}} \propto \sigma_w^{-3/2} , \tag{9}$$

$$K_E^{\text{cap}} \propto \sigma_w^{-1/2} . \tag{10}$$

By eliminating ζ from Eqs. (6) and (7), we find that the capillary radius is given by

$$R^2 = 8\eta\sigma_w K_S^{\text{cap}}/K_E^{\text{cap}} . \tag{11}$$

These predictions for cylindrical capillaries have been verified in our laboratory [5].

ELECTROKINETICS IN RANDOM POROUS MEDIA

For the general case of random porous media, the capillary-tube expressions for L_{12} and L_{21} may no longer hold, but we can still define the electrokinetic coefficients K_E and K_S with the first parts of Eqs. (6) and (7). Further, we benefit from the well-known Onsager's relation of linear nonequilibrium thermodynamics [6] which requires $L_{12} = L_{21}$ in the steady state. This allows us to prove $k_0 = \eta\sigma_0 K_S/K_E$ [3].

In the usual practice, measurements of conductivity or permeability ignore the electro-kinetically-produced complementary fields. In these instances, what would be regarded as the "ordinary" Darcy permeability k_d and rock conductivity σ_r would differ from their zero-complementary-field counterparts k_0, and σ_0 according to the strength of the off-diagonal terms. It can be shown that the conductivity σ_r of the system under the condition $\mathbf{J}_f = 0$ is actually given by $\sigma_r = \sigma_0(1 - K_S K_E)$. Likewise, $k_d = k_0(1 - K_S K_E)$ when $\mathbf{J}_e = 0$. As a result, the "ordinary" permeability k_d is rigorously determined by the values of K_S, K_E and the "ordinary" conductivity σ_r [3]:

$$k_d = \eta\sigma_r K_S/K_E . \tag{12}$$

Typically, one expresses σ_r in terms of the brine conductivity σ_w alone: $\sigma_r = \sigma_w/F$, where the factor F is known as the *formation factor*. Theoretical and experimental work have shown that k_d and F are related, once a basic length such as the average grain size or pore size is known [7, 8, 9]. One such relation, suggested by Johnson, Koplik and Scwartz, is [10]

$$k_d \approx \Lambda^2/8F \ . \tag{13}$$

where Λ is the effective throat radius in a porous material. For a cylindrical capillary, $\Lambda = R$ is exact. By analogy with Eqs. (6) and (7) for a capillary, we can *define* effective parameters R_{eff} and ζ_{eff}:

$$R_{eff}^2 \equiv 8\eta\sigma_w K_S/K_E \ , \tag{14}$$
$$\zeta_{eff} \equiv \eta\sigma_w K_S/\epsilon \ . \tag{15}$$

Comparison of Eqs. (12) and (14) with (13) suggests $\Lambda \approx R_{eff}$.

One measure of the importance of electrokinetics in the transport processes is the dimensionless quantity $K_S K_E$. By using Eqs. (14) and (15) and an effective surface charge density qN_{eff} defined as $qN_{eff} \equiv \epsilon\zeta_{eff}/\lambda$, we have

$$K_S K_E = \frac{8q^2 N_{eff}^2}{\eta\sigma_w} \left(\frac{\lambda}{R_{eff}}\right)^2 \ . \tag{16}$$

This shows that electrokinetic effects are stronger in smaller-pored material.

The principle difficulty in measuring K_S and K_E is that they are often small quantities in comparison to other sources of noise in the experimental environment: in our samples, $K_E \approx 1$ Pa/V and $K_S \approx 10^{-9}$ V/Pa. To improve the signal to noise ratio, we use an AC lock-in amplification technique, measure the response over a range of frequencies, and extrapolate to the DC limit where Onsager's relation is strictly valid. Details are reported elsewhere [5].

We have carried out measurements on a suite of 12 samples: 6 sandstones, 2 carbonates, and 4 artificial samples made of fused-glass beads. They are cylindrical in shape (4 cm long by 2 cm diameter) and range in permeability from 2 to 4000 mD. By using a cell similar to that in Fig. 1, we measured K_S, K_E, and σ_r with brine concentrations of 0.05M, 0.1M, 0.2M, 0.4M, and 0.8M NaCl. We have also measured k_d directly and verified Eq. (12). The results will be reported elsewhere [3, 5]. Here, we report on the effects of changing the salinity to test Eqs. (8)–(11).

Figure 2 shows the data for a Berea sandstone ($k_d \approx 27$ mD), which are typical of all of the samples. We observe in Fig. 2a and 2b that $K_S \propto \sigma_w^{-1.02}$ and $K_E \propto \sigma_w^{-0.43}$; both deviate noticeably from the simple capillary-tube behavior of Eqs. (9) and (10). As a result, R_{eff} calculated from Eq. (14) is not constant, but increases with increasing conductivity: $R_{eff} \propto \sigma_w^{0.21}$ (Fig. 2c). We have also made direct measurements of k_d, calculated R_{eff} from $\sqrt{8k_d F}$ and found the same result. In Fig. 2d, we show that ζ_{eff} calculated from Eq. (15) is independent of σ_w, in contrast to the expectation that $\zeta_{eff} \propto \sigma_w^{-1/2}$. We note that the data for the other samples show similar deviations from Eqs. (8)–(11): they exhibit power-law dependencies on σ_w but the exponents vary from sample to sample. The trend that R_{eff} increases with increasing σ_w mostly holds in all the samples.
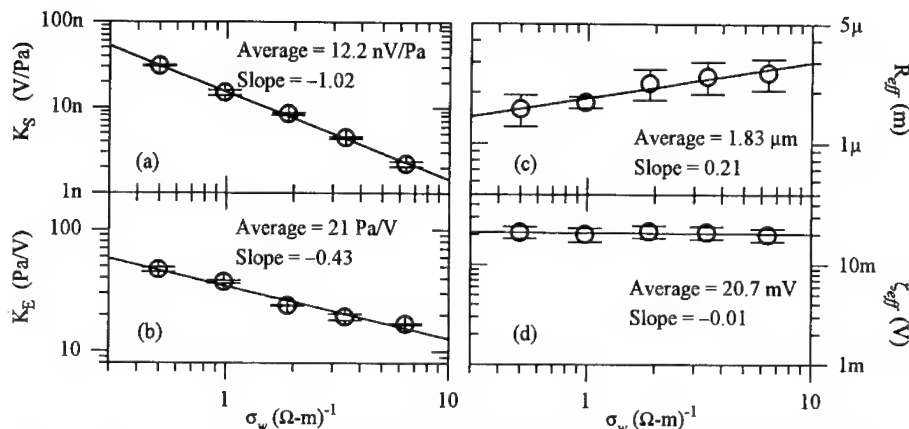
Figure 2: Brine conductivity dependence of electrokinetic parameters for a Berea sandstone of permeability $k_d \approx 27$ mD.

DISCUSSION

There are several possible explanations of the anomalous power-law behavior. First, the Debye-Hückel approximation is only valid when $q\zeta \ll k_B T$, but our data in Fig. 2d show that $q\zeta \simeq k_B T$. This implies that the charge-density profile in the screening layer does not decay exponentially. Nonetheless, $\lambda \propto N_0^{-1/2}$ should still hold, because it comes from dimensional analysis. So this is not a likely explanation.

Second, there may be physical changes in the sample, as suggested by the increase of R_{eff} with increasing salinity. These changes may be reversible or irreversible. A type of reversible change would be salinity dependent swelling of clay minerals embedded in the rock [11]. A type of irreversible change would be the flushing of small particles from the samples as the experiment progresses, which we are currently investigating. One expects both mechanisms to be inoperative in glass-bead samples, yet we do find some change in R_{eff} for these, so these are also unlikely explanations.

Third, the assumption that qN_{eff} is constant could be invalid for a number of reasons: the existence of other ionic species native to the sample may complicate the surface chemistry; the composition of the immobile charged layer may change due to salinity dependent adsorption; and the slip-plane may not be located in the diffuse layer, but may lie within the charged boundary layer [1, p.426]. All of these effects render $\lambda \propto \zeta_{eff}$ invalid and allow ζ_{eff} to vary in an unknown way. These possibilities cannot be ruled out.

Finally, we consider effects of the interfacial geometry itself. The capillary-tube theory presented above requires that the interface be locally flat, and that $\lambda \ll R$. But in sedimentary rock, it is common to find fractally rough pore surfaces for length scales above a few ångstroms [12, 13]. The screening length λ provides a natural length scale to measure any property of the surface. Since a fractal surface is expected to exhibit scaling behavior, one expects K_S, K_E to scale as a power-law in λ, and hence in σ_w. The same trend should hold for R_{eff} and ζ_{eff}, and all the exponents should be related to the fractal dimension.

This scaling behavior does not tell us the physical mechanism, however. One expects R_{eff} and k_d to depend only on the geometry of the pore for a fluid with no space charge, so how

can we account for the large change we observe by the presence of a very thin space-charge layer? We note that for the brine concentrations used, $\lambda = 3.5$–14 Å, while $R_{eff} \approx 2$ μm or $\lambda \approx 10^{-3} R_{eff}$. What mechanism can change R_{eff} by 1 μm when λ changes by only 10 Å?

A likely explanation involves the flow pattern produced by electrokinetic currents coupled with the interfacial roughness. In a capillary, electroosmotic pressure is produced when electrokinetic flow along the wall is counterbalanced by bulk flow along the center; the flow field is not strictly given by the Poiseuille form. So even though the total flow is zero, locally the fluid circulates between the wall and the center. The flow field incorporates the entire radius R and is affected by the screening layer [2]. In a fractally-rough rock, similar flow circulation between the pore surface and pore volume occurs over a wide range of length scales. One may imagine that small, viscous-flow eddies are superimposed on larger and larger circulatory fields. The result is to widen the influence of a 10 Å boundary layer to the entire pore volume in a way which correlates with the interfacial roughness. It would not be surprising, then, that the micro-circulations impede the average flow and hence affect k_d and R_{eff} significantly. This would be an interesting phenomenon to investigate further.

ACKNOWLEDGEMENTS

References

[1] G. Kortüm, *Treatise on Electrochemistry*, 2nd revised English edition (Elsevier, Amsterdam, 1965).

[2] J. S. Newman, *Electrochemical Systems* (Prentice-Hall, Engelwood Cliffs, 1973).

[3] S. X. Li, D. B. Pengra and P.-z. Wong, Phys. Rev. Lett. (submitted 1994).

[4] See, for example, F. A. L. Dullien, *Porous Media: Fluid Transport and Pore Structure* (Academic Press, San Diego, 1979).

[5] D. B. Pengra, S. X. Li, and P.-z. Wong, to be published (1994).

[6] See, for example, S. R. deGroot and P. Mazur, *Non-Equilibrium Thermodynamics* (North-Holland, Amsterdam, 1962).

[7] P.-z. Wong, J. Koplik, and J. P. Tomanic, Phys. Rev. B **30**, 6606 (1984).

[8] A. J. Katz and A. H. Thompson, Phys. Rev. B **34**, 8179 (1986).

[9] P.-z. Wong, MRS Bull. **19** (5) p.32 (1994).

[10] D. L. Johnson, J. Koplik and L. M. Schwartz, Phys. Rev. Lett. **57**, 2564 (1986).

[11] N. Wada in *Physics and Chemistry of Porous Media II*, edited by J. R. Banavar, J. Koplik, and K. W. Winkler (AIP Conf. Proc. **154**, New York, 1987) p. 195.

[12] P.-z. Wong, Phys. Today **41** (12) p.24 (1988); P.-z. Wong, J. Howard, and J.-S. Lin, Phys. Rev. Lett. **57**, 637 (1986).

[13] A. H. Thompson, A. J. Katz and C. E. Krohn, Adv. in Phys. **36**, 625 (1987).

ROBUSTNESS OF METHANE DIFFUSION IN GEOMETRICALLY RESTRICTED MOLECULAR SIEVE PORES

Sriram S. Nivarthi, H. Ted Davis and Alon V. McCormick
Department of Chemical Engineering and Materials Science, University of Minnesota
421 Washington Avenue S.E., Minneapolis, MN 55455

ABSTRACT

NMR measurements of sorbate mobility in zeolites are especially attractive because of their capability of measuring multicomponent and anisotropic self-diffusion. We have recently reported the application of the pulsed field gradient NMR technique using very large zeolite crystals to study how easily methane can diffuse when we attempt to slow its migration by crowding the pore space. Here we analyze the implications of these PFG NMR experiments involving (i) ethylene blocking of methane in zeolite NaY; and (ii) methane molecules trying to pass one another in the molecular sieve $AlPO_4$-5.

INTRODUCTION

The study of the mobility of sorbates in molecular sieves is important because of their application as selective adsorbents and shape selective catalysts [1]. NMR methods provide accurate and detailed information on the molecular translations and reorientations of guest molecules in zeolite micropores [2]. The pulsed field gradient NMR (PFG NMR) technique in particular allows a direct measurement of sorbate displacement over a specified time interval, and is a powerful tool to probe diffusion in zeolites [3].

Multicomponent diffusion of sorbates in molecular sieves is particularly germane in this regard because the feed streams encountered in industry almost always contain more than one chemical component [1]. The PFG NMR technique is particularly well suited to measuring the diffusion of coadsorbed molecules in zeolites especially when the coadsorbed components have clearly distinguishable chemical shifts [4]. Several recently synthesized molecular sieves (e.g., ZSM-12, $AlPO_4$-5) possess pore networks that are highly anisotropic and hold promise for exciting potential applications. Understanding and measuring the anisotropic properties in these molecular sieves is key to tailoring them for specific applications.

In this paper, we report PFG NMR studies on two systems: methane and ethylene coadsorbed in NaY; and methane singly adsorbed in $AlPO_4$-5. NaY is a large pore zeolite (7.3 Å in diameter) with a tetrahedral pore network, whereas $AlPO_4$-5 is a large pore molecular sieve (7.3 Å) with one-dimensional channels running along the length of the crystals (with no interconnections). Specifically, we are interested in learning how molecules behave in constricted pores when mobile

"obstacles" are encountered in their diffusive paths. In NaY, we are interested in seeing the effect of a strongly adsorbed molecule like ethylene on the mobility of methane, while in the case of the $AlPO_4$-5, we are interested in finding out if individual methane molecules are able to pass one other in the unidirectional pores.

EXPERIMENTAL

Large crystals of NaY (average diameter ~30 μm, Si/Al = 1.8) and $AlPO_4$-5 (average length ~30 μm) were provided by M.E. Davis (Caltech) and D. Young (U. of Toronto). Figure 1 shows SEM micrographs of the NaY and $AlPO_4$-5 crystals. A known quantity of the molecular sieve crystals was outgassed under vacuum, following which the desired quantity of sorbate gas was introduced. The procedure followed in preparing the samples for NMR has been reported in ref. [5] and [6].

In the PFG NMR experiment [7], the spin echo was accumulated 1000 to 3000 times, followed by Fourier transformation of the second half of the echo. The stimulated spin echo pulse sequence $(\pi/2\text{-}\pi/2\text{-}\Delta\text{-}\pi/2)$ was employed in the multicomponent experiment (on account of the low transverse relaxation time of the adsorbed components) whereas the spin echo pulse sequence $(\pi/2\text{-}\Delta\text{-}\pi/2)$ was adequate for the methane in $AlPO_4$-5 sample. In both cases, the intracrystalline diffusivities were independent of the observation time as expected for ordinary diffusion. Further details of the PFG NMR experiment are available in ref. [8]. All the spectra were acquired on a Nicolet NT-300 Fourier transform spectrometer equipped with a field gradient probe from Doty Scientific.
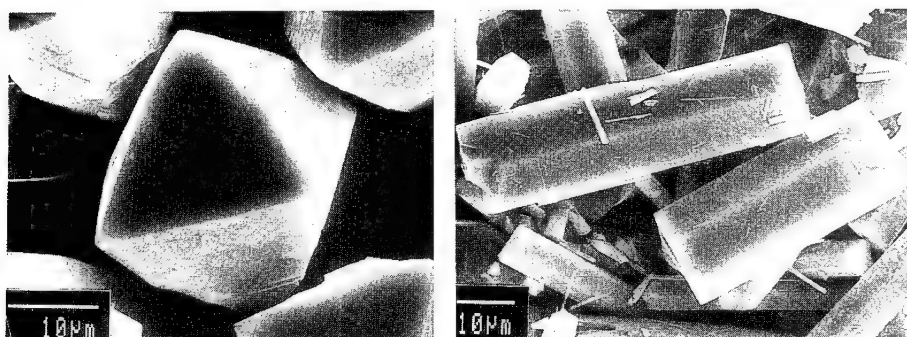
(a)   (b)

Figure 1. Scanning electron micrographs of (a) NaY crystals and (b) $AlPO_4$-5 crystals.

The PFG NMR Experiment

In a PFG NMR experiment, the intracrystalline self-diffusion of a sorbate is determined by monitoring the intensity of the NMR signal (called the spin echo) as a function of the duration of the field gradient pulses (δ) or the magnitude of the field gradient pulse (G).

In an isotropic system, the NMR spin echo attenuation follows the relation [7]

$$A = \exp\left(-\gamma^2 G^2 \delta^2 \Delta\, D \right), \tag{1}$$

where A is the spin echo intensity relative to that when G = 0. γ is the gyromagnetic ratio of the nucleus under observation, Δ is the time allowed for diffusion and D is the self-diffusion coefficient of the molecule carrying the nucleus.

In the case of anisotropic diffusion in $\underline{one}$ direction (unidirectional diffusion), the NMR spin echo attenuation follows the relation [9,10]

$$A = \int_0^1 \exp(-\gamma^2 G^2 \delta^2 \Delta D x^2)\, dx. \tag{2}$$

Thus the spin echo attenuation shows a characteristic decay depending on the anisotropy prevalent in a system.

Note that Eqs (1) and (2) are powder average expressions derived for zeolite crystals that are randomly oriented, as in an NMR tube. Both expressions are valid for Brownian motion of the sorbates. In the unidirectional channels of $AlPO_4$-5, the motion of the methane molecules would be Brownian only if they are able to pass each other in the pores. In the event that they are not able to pass each other, motion would cease to be simply Brownian and would become "single-file" [11]. In this case, the mean square displacement would be proportional to the square root of the observation time, leading to very small effective diffusion coefficients [12].

EXPERIMENTAL RESULTS

PFG NMR measurements on methane (1.1 molecules per supercage) and ethylene (1.8 molecules per supercage) coadsorbed in NaY revealed the methane self-diffusivity to be higher than ethylene by a factor of thirty. The diffusion coefficients were determined to be $D_{methane} = (9.6 \pm 1.0) \times 10^{-9}$ $m^2 s^{-1}$ and $D_{ethylene} = (3.1 \pm 0.5) \times 10^{-10}$ $m^2 s^{-1}$ at 298 K. In each case, the root mean square displacement of the molecules was less than the average diameter of the NaY crystals, so that the majority of the molecules diffuse only inside the crystals. The use of large zeolite crystals enables us to discount surface mass transfer resistances [3].

In both cases, the spin echo decay followed the behavior predicted by Eq.(1) indicating diffusion is isotropic. This may be expected given the tetrahedrally connected NaY supercages. Further details on the measurement of these diffusivities and the spin echoes generated in such a two-component sample are provided in ref. [5].

The spin echo attenuation produced by methane (0.7 molecules per unit cell) singly adsorbed in $AlPO_4$-5 followed Eq. (2) establishing that the diffusion was unidirectional, but not single file. The intracrystalline diffusivity of methane was determined to be 2.9 x 10^{-9} m^2s^{-1} at 300 K. A more detailed analysis of the diffusivity data is presented in ref. [6].

DISCUSSION

The difference in the measured diffusivities of methane and ethylene coadsorbed in NaY is a consequence of the interaction of the π-electron cloud in ethylene with the Na ions in NaY [2, 13]. This is also reflected in the higher adsorption heat of ethylene in NaY compared to methane [14]. Given this situation, one might expect ethylene to be very effective in blocking the motion of methane through the NaY pores. Comparison with single-component diffusivities at the same total sorbate loading, though, show that this is not the case. The diffusivities of methane and ethylene coadsorbed in NaY and their single-component diffusivities *at the same total sorbate loading* (2.9 molecules per supercage) are listed below in Table I.

Table I. Single and multicomponent diffusivities of methane and ethylene in NaY

Sorbate/Zeolite System	Self-Diffusivity
Methane in NaY, 25 °C	2.0 x 10^{-8} m^2s^{-1} [15]
Ethylene in NaY, 25 °C	~3.0 x 10^{-10} m^2s^{-1} [13]
Methane in NaY (coadsorbed with ethylene), 25 °C	~9.6 x 10^{-9} m^2s^{-1} (this work)
Ethylene in NaY (coadsorbed with methane), 25 °C	3.1 x 10^{-10} m^2s^{-1} (this work)

Thus we find that the methane diffusivity in NaY in the presence of coadsorbed ethylene is lower than its single component value by a factor of approximately two. This is certainly not as drastic a reduction as one might expect based on previous coadsorption studies [16] and shows that ethylene poses a minor obstruction to methane in its diffusive motion in NaY. This may be rationalized by considering the open pore structure of NaY. Due to its specific interaction with the Na ions, the ethylene molecules are probably localized close to the Na^+ ions near the wall of the NaY supercage. The methane molecules, on account of the large pore size of NaY and high

connectivity, are able to find several diffusion paths. We believe this points out how important it will be, when considering multicomponent diffusion, to assess where cosorbates are placed in the pore.

Since diffusion of methane in $AlPO_4$-5 is not single file, methane molecules must be able to pass one another in the $AlPO_4$-5 channels. Thus even in 7.3 Å (diameter) sized unidirectional pores with no interconnections, 3.8 Å sized methane molecules do not pose a very stringent obstruction to one another in their diffusive motion. This surprising result reemphasizes the difficulty in predicting the diffusive properties of sorbates in molecular sieves based purely on the pore sizes determined from X-ray crystallographic data. It is probably important to consider the detailed zeolite structure and perhaps even to consider flexibility of the zeolite (as in ref. [17])

SUMMARY

In two PFG NMR studies on methane and ethylene coadsorbed in NaY and methane singly adsorbed in $AlPO_4$-5, we have demonstrated the robustness of the methane diffusivity in overcoming mobile obstacles placed in its diffusive path. In NaY, due to the localized interaction of the ethylene molecules, and the large, well connected pores, methane is able to find alternate paths for diffusion. In $AlPO_4$-5 which has unidirectional channels without any interconnections, methane is squishy enough to be able to pass other methane molecules in the $AlPO_4$-5 pores.

ACKNOWLEDGMENTS

REFERENCES

1.   D.M. Ruthven, Principles of Adsorption and Adsorption Processes, (Wiley, New York, 1984).
2.   H. Pfeifer, Phys. Reports **26C**, 293 (1976).
3   J. Kärger and D.M. Ruthven, Diffusion in Zeolites and Other Microporous Solids, (Wiley, New York, 1992).
4.   U. Hong, J. Kärger, H. Pfeifer, J. Am. Chem. Soc. **113**, 4812 (1991).
5.   S.S. Nivarthi and A.V. McCormick, J. Phys. Chem. submitted.

6. S.S. Nivarthi, A.V. McCormick, H.T. Davis, Chem. Phys. Lett. **229**, 297 (1994).

7. E. O. Stejskal and J. E. Tanner, J. Chem. Phys. **42**, 288 (1965).

8. J. Kärger, H. Pfeifer, W. Heink, Adv. Magn. Res. **12**, 1 (1988).

9. P.T. Callaghan, Aust. J. Phys. **37**, 359 (1984).

10. B. Zibrowius, J. Caro, J. Kärger, Z. Phys. Chem. (Leipzig) **269**, 1101 (1988).

11. D. G. Levitt, Phys. Rev. A **8**, 3050 (1973).

12. J. Kärger, Phys. Rev. E **47**, 1427 (1993).

13. C.J. Wright and C. Riekel, Mol. Phys. **36**, 695 (1978).

14. D.W. Breck, Zeolite Molecular Sieves, (Wiley, New York, 1974).

15. J. Caro, M. Bülow, W. Schirmer, J. Kärger, W. Heink, H. Pfeifer, S.P. Zdanov, J. Chem. Soc., Faraday Trans. I **81**, 2541 (1985).

16. for example, J. Kärger and H. Pfeifer, Zeolites **7**, 90 (1987).

17. P. Demontis, G.B. Suffritti, S. Quartieri, E.S. Fois and A. Gamba, Zeolites **7**, 522 (1987).

REORIENTATIONAL DYNAMICS OF A NEMATOGENIC LIQUID IN POROUS SOL-GEL-GLASSES: SURFACE AND PORE SIZE EFFECTS

F.W. DEEG AND G. SCHWALB
Institut für Physikalische Chemie, Universität München, Sophienstrasse 11, D-80333 München, Germany

ABSTRACT

Time-resolved transient grating optical Kerr effect experiments on a nanosecond timescale were used to investigate the reorientational dynamics of pentylcyanobiphenyl (5CB) confined in the nanometer lengthscale pores of silica glasses. Pore size dependent studies (25 Å $\leq$ d $\leq$ 100 Å) over a large temperature range from the bulk phase transition temperature T_{ni} = 35.2 $^\circ C$ up to 115 $^\circ C$ demonstrate a drastic influence of geometrical restriction on the cooperative reorientational motion in the nematogenic liquid. At temperatures far above the phase transition (T $\geq$ 70 $^\circ C$) a bulk phase and a distinct surface layer with different dynamic properties are observed. With pore size reduction to 25 Å, a decrease of the surface layer thickness and an increase of the surface layer relaxation time are found. This is associated with the modification of the surface layer structure by geometrical factors, e.g., the pore curvature. Measurements at lower temperature in the range $T_{ni} \leq$ T $\leq T_{ni}$ + 30 $^\circ C$ show a drastic decrease of the mean relaxation time τ of the order parameter fluctuations compared to the bulk. The relaxation dynamics exhibit a pronounced pore size dependence which can be explained by a crude correlation length cutoff model as well as a modified Landau-deGennes ansatz. However, these approaches cannot reproduce the nonexponentiality of the observed decays suggesting the importance of interporous interactions.

INTRODUCTION

The isotropic-nematic phase transition of a liquid crystalline substance is of first order but the associated latent heat and volume change are very small. Therefore, similar to second order phase transitions, many properties of the isotropic liquid display critical behavior on cooling to temperatues close to the phase transition temperature T_{ni} [1]. The microscopic origin of this behavior (often called pretransitional in the liquid crystal literature) is the existence of short range orientational order among the molecules. Although macroscopically isotropic, there are pseudonematic domains in the liquid characterized by an orientational correlation length ξ (see fig 1). DeGennes has applied Landau theory to the nematic-isotropic phase transition [1] and shown that the temperature dependence of this correlation length is given by $\xi(T) = \xi_0[T^*/(T - T^*)]^{1/2} = [L/a(T - T^*)]^{1/2}$. Here ξ_0 is a molecular length which is related to the isotropic elastic coefficient L and the free energy expansion parameter A, and T^* is the virtual phase transition which is typically 1-2 $^\circ C$ below T_{ni}. Therefore right above T_{ni} the correlation length ξ is much larger than a molecular length and for a molecule like pentylcyanobiphenyl (5CB) reaches values of 100-200 Å. The relaxation time τ associated with these pseudonematic orientational fluctuations also diverges on approaching the phase transition as $\tau(T) \propto \nu[(T - T^*)]^{-1}$. Here ν is the viscosity of the sample. The validity of the Landau-deGennes (LdG) theory for the description of the bulk phase transition has been confirmed for static as well as dynamic parameters by a large number of experiments.

213
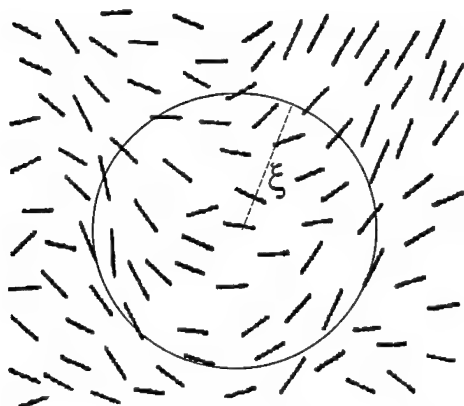
Figure 1. Schematic picture of a pseudonematic domain with a correlation length ξ.

In porous systems like Vycor glass or silica aerogels it is possible to achieve spatial restrictions well below 200 Å, the typical magnitude of the orientational correlation length at T_{ni}. Therefore we expect modifications of the behavior of a nematogenic liquid upon confinement within spatial restrictions of this kind. There are indeed several recent studies [2, 3, 4, 5] demonstrating a number of new effects in confined nematogenic liquids. The theory of critical phenomena also suggests interesting comparisons of data for the nematic-isotropic phase transition with those found for phase transitions of binary mixtures [6] and He[4] [7] inside these porous systems.

EXPERIMENTAL

5CB was purchased from Merck and filtered through a pore size of 0.2 μm, to remove dust particles. It has a well-defined bulk phase transition temperature at $T_{ni} = 35.2$ °C. The pertinent material parameters are: $T^* = T_{ni}$ - 1.1 °C, L = $17 \cdot 10^{-12}$ J/m and a = $0.132 \cdot 10^6$ J/m^{3}K. The porous sol-gel glasses used in these studies were supplied by Gel-Tech Inc. They are characterized by high specific surface areas (400-700 m^2/g) and large specific pore volumes (0.4-0.9 cm^3/g) with a well-defined narrow pore size distribution (see fig. 2). In these studies samples with average pore sizes of 25, 50 and 100 Å have been used. In general the inner surface of these pores is covered with polar OH-groups. These OH-groups can be replaced by less polar $OSi(CH_3)_2OC_2H_5$-groups allowing a modification of the surface interaction of the 5CB molecules. To distinguish surface and finite size effects, a surface-modified sample with a mean pore size of 100 Å (denoted 100 Å-M) has also been investigated. The disk-shaped glasses (10 mm diameter, 5 mm thickness) were immersed in a spectroscopic cuvette filled with isotropic 5CB and left several days to ensure complete filling. The cuvette was inserted into a variable temperature cell allowing to control the temperature within $\pm$ 0.1 K.

In the optical Kerr effect (OKE) experiment a short laser pulse with a well-defined polarization incident on the sample interacts with the polarizable molecules of the liquid. The optical field induces a dipole moment in the molecules and then exerts a torque on this induced dipole moment. Thereby the molecules are oriented preferentially parallel to the polarization of this excitation pulse. A variably time-delayed second pulse, again with a well-defined polarization, probes the decay of this orientational anisotropy. It is important to note
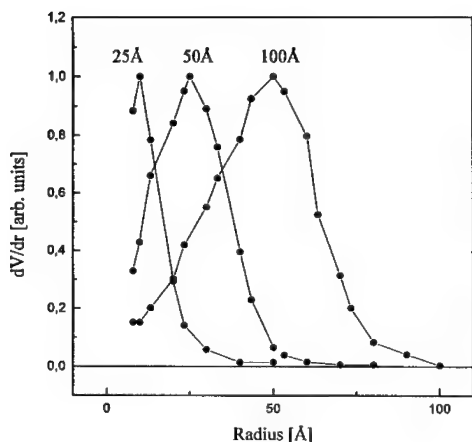
Figure 2. Pore size distribution of the investigated sol-gel-glasses as determined by nitrogen BET adsorption isotherms.

that the observable detected with the OKE is the third-order nonlinear susceptibility $\chi^{(3)}$ and the dielectric constant ϵ of the sample. That is, in contrast to e.g. NMR-investigations or fluorescence depolarization studies, this experiment monitors a macroscopic property and is sensitive to collective rotational dynamics. It is the time domain equivalent to Rayleigh wing scattering in the frequency domain [8]. We will limit here the discussion to the relaxation dynamics for $t \geq 1$ ns, i.e. we will focus on the slow pseudonematic orientational fluctuations. Similar to the bulk [9] there are fast rotational relaxation channels associated with only few molecules which will be discussed elsewhere. We have used a so-called transient grating (TG) set-up in which two excitation pulses are crossed within the sample to form an optical interfernce pattern. The probe pulse is then Bragg-scattered off the spatially modulated index of refraction in the sample. The TG approach has a number of advantages, one of them being the selective monitoring of different physical processes in the sample through appropriate choice of the polarization of pulses [10]. One major difference to the regular OKE is the fact that the signal $I(t) \propto |\chi^{(3)}|^2 \propto |G(t)|^2$ goes as the square of the dielectric response function $G(t)$ of the sample. A more detailed description of the laser system used for the TG-OKE experiments described here can be found elsewhere [11].

RESULTS AND DISCUSSION

As shown earlier [9] the relaxation of pseudonematic fluctuations in bulk 5CB is characterized by a monoexponential decay with a single correlation time τ for the whole temperature range 35-120 °C. τ diverges upon approaching the phase transition as predicted by the LdG theory (see full diamonds and solid line in fig. 3). The corresponding OKE decays of 5CB in the porous samples on the ns time scale are clearly nonexponential. Nevertheless, to get a feeling of the general trend of the reorientational dynamics in the porous samples we have calculated a mean relaxation $< \tau >$ depicted in fig. 3. A strong deviation between the data

215
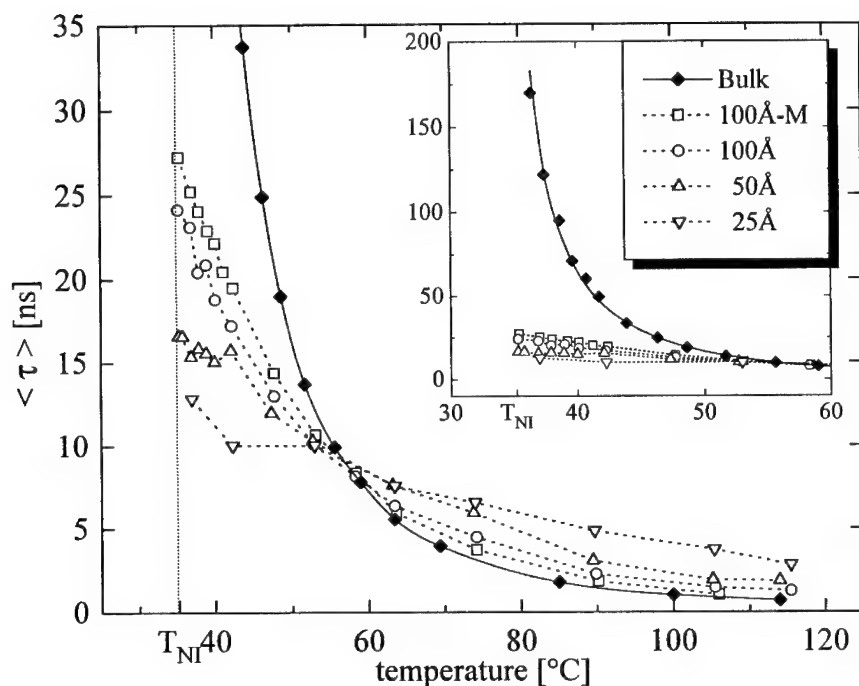
Figure 3. Temperature dependence of the mean relaxation time $< \tau >$ for 5CB bulk and 5CB in porous glasses. Dotted lines provide a guideline to the eye.

for the confined 5CB and bulk 5CB is evident. Two temperature ranges with very different behavior are observed. At temperatures above 70 $^{\circ}C$ the rotational relaxation of the confined liquid is slower than in the bulk, at temperatures below 70 $^{\circ}C$ reorientational dynamics are faster than in the bulk. As will be shown in the following the high temperature confined 5CB data can be explained by the existence of a surface layer with higher viscosity [12]. At lower temperature geometrical restriction dominates the pseudonematic fluctuations [13]. We will first discuss the high temperature results and then come back later to the low temperature data.

High temperature data / Surface interaction

Figure 4 shows a logarithmic plot of the TG-OKE signals for 5CB bulk and 5CB in a surface-modified and surface-unmodified 100 Å-glass, all taken at 106 $^{\circ}C$. Neglecting the first hundreds of ps, the bulk sample clearly exhibits a monoexponential decay. On the other hand, the nonmodified 100 Å sample is characterized by a biexponential relaxation, a first fast decay component identical with the bulk and a second distinctly slower component. This second slower component can also be detected in the surface-modified 100 Å-M sample
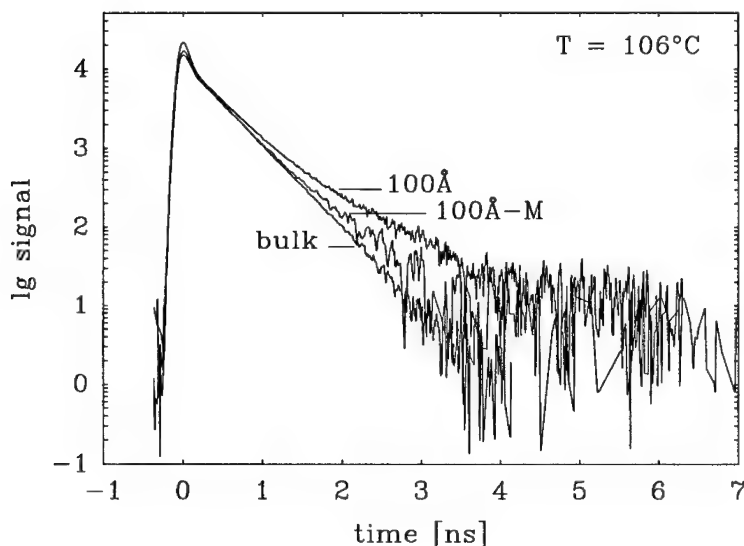
Figure 4. Logarithmic plot of the transient grating signals at T = 106 °C for bulk 5CB and 5CB in surface-modified (100 Å-M) and unmodified porous 100 Å glass.

but its amplitude is drastically reduced. This fact indicates that in the sample with the polar OH-groups there exists a distinct surface layer of 5CB molecules with slower collective rotational dynamics. This finding of a more viscous surface layer is in agreement with the pioneering OKE studies of Warnock et al. [14] as well as the NMR experiments of the Jonas group [15] for single particle reorientation of polar liquids. It should be emphasized at this point that the two relaxation components shown in fig. 4 still represent cooperative molecular reorientational dynamics.

However, in contrast to those earlier results the relaxation time of the surface component is not pore size independent as can be seen from the shallower slope for the 25 Å-sample in fig. 5. To obtain a more quantitative picture of this fact a numerical fit of the data has been carried out. There is a small oscillatory component in the TG signals most evident in the 25 Å sample. This component is due to propagating shear waves in the glass induced by impulsive stimulated Brillouin scattering. Its contribution (a damped sine wave) can easily be subtracted from the raw data to leave the pure reorientational dynamics. As mentioned before, these rotational dynamics follow a biexponential decay function

$$G(t) \ = \ A \cdot exp(-t/\tau_b) \ + \ B \cdot exp(-t/\tau_s) \tag{1}$$

with τ_b and τ_s being the relaxation times for the fast bulk contribution and the slow surface layer. The values of τ_s together with the corresponding bulk values are tabulated in table I and shown in fig. 6 for three different temperature values. Whereas the relaxation times in the 50 Å and 100 Å samples are identical within experimental error, τ_s for the 25 Å sample is significantly smaller. The activation energy which can be calculated from the temperature
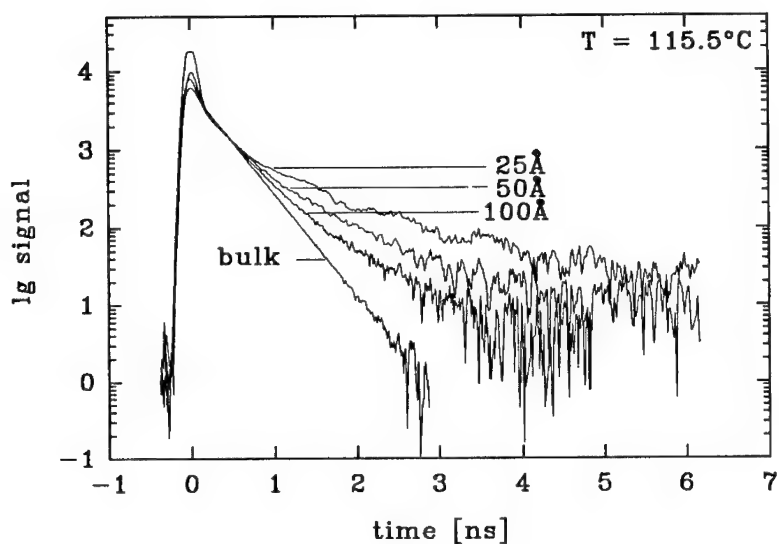
Figure 5. Logarithmic plot of the transient grating signals at T = 115.5 °C for bulk 5CB and 5CB in porous glasses with different average pore sizes.
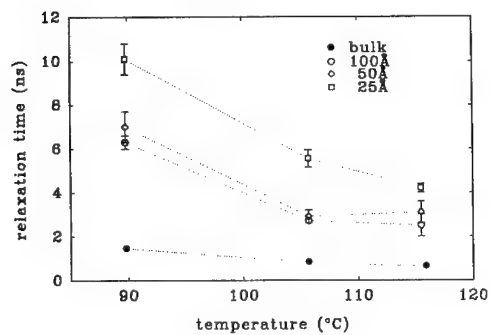
Figure 6. Temperature and pore size dependence of the surface layer relaxation time. For comparison the bulk relaxation times are also marked. Dotted lines are a guideline to the eye.

dependence is identical for τ_s in all three porous glasses and the bulk. This suggests that a kind of Debye-Stokes-Einstein relation is valid for bulk as well as surface layer. Under these circumstances the ratio of the viscosity of the surface layer to the viscosity in the bulk is six for the case of the 25 Å sample and 3-5 for the 50 Å and 100 Å samples. Again, one should keep in mind that the rotational molecular dynamics observed has cooperative character.

From the OKE amplitudes of bulk and surface layer it is possible to calculate an effective thickness of the surface layer. The ratio of the amplitudes of surface layer and bulk phase B/A is given by

		$T = 90\ ^oC$	$T = 106\ ^oC$	$T = 115.5\ ^oC$
	τ_s (ns)	10.1 ± 1.2	5.6 ± 0.5	4.2 ± 0.2
25 Å	$B/(A+B)$	0.34	0.34	0.31
	l (Å)	6.6	6.5	6.1
	τ_s (ns)	7.0 ± 0.7	2.9 ± 0.3	3.1 ± 0.7
50 Å	$B/(A+B)$	0.23	0.31	0.24
	l (Å)	8.9	9.4	9.1
	τ_s (ns)	6.3 ± 0.3	2.7 ± 0.1	2.5 ± 0.5
100 Å	$B/(A+B)$	0.12	0.18	0.15
	l (Å)	8.9	9.9	9.5
bulk	τ_b (ns)	1.46	0.84	0.66

Table I:
OKE relaxation time τ_s, relative OKE amplitude B/(A+B) and effective thickness l of the surface layer for 5CB in different pore size glasses.

$$B/A = \frac{V_s/\tau_s}{V_b/\tau_b} \tag{2}$$

where V_s and V_b are the volumes of the surface layer and the bulk phase. Assuming cylindrical pores with radius r and a surface layer with thickness l, this ratio has the form

$$B/A = \frac{\tau_b}{\tau_s} \cdot \frac{r^2 - (r - l)^2}{(r - l)^2}. \tag{3}$$

The relative amplitudes B/(A+B) obtained in our investigations as well as the layer thickness calculated from them are shown in table I. It turns out that l is independent of temperature for all three samples. Again, we find identical behavior for the 50 Å and 100 Å samples, namely a thickness $l \approx 9$ Å and a much smaller value $l \approx 6$ Å for the 25 Å glass.

The slower reorientational relaxation time and smaller thickness for the surface layer in the 25 Å sample as compared to the larger pore size glasses indicate a modification of surface layer structure as well as dynamics through the large surface curvature in the 25 Å pores. This curvature does not accommodate a thick surface layer and suppresses the mobility of the 5CB molecules close to the pore wall.

Low temperature data / Confinement effects

Quite opposite to the characteristics discussed above, in the temperature range $T_{ni} \leq$ T $\leq 70\ ^oC$ the OKE decays of 5CB confined to the porous glasses are faster than the bulk relaxation observed at the same temperature. This fact is exemplified by the OKE data at T $= 42\ ^oC$ shown in fig. 7. This figure demonstrates a number of other facts which are essentially valid at all temperatures in the range indicated above. First, there is a pronounced pore size dependence of the rotational dynamics. The smaller the pore the faster the relaxation. Second, in contrast to the high temperature results, the behavior of the surface-modified and unmodified sample with identical pore size are very similar, indicating that surface interactions are only of minor importance in the temperature range. Third, unlike the bulk, the confined liquids exhibit distinctly nonexponential OKE decays.

To rationalize the fast pseudonematic orientational fluctuations in the bulk and explain the pronounced pore size dependence shown in figs. 3 and 7 we have used different theoretical approaches and tried to simulate the OKE decays. In a first very crude model we assume that the LdG theory, so successful in the bulk, is valid without modification in the confined
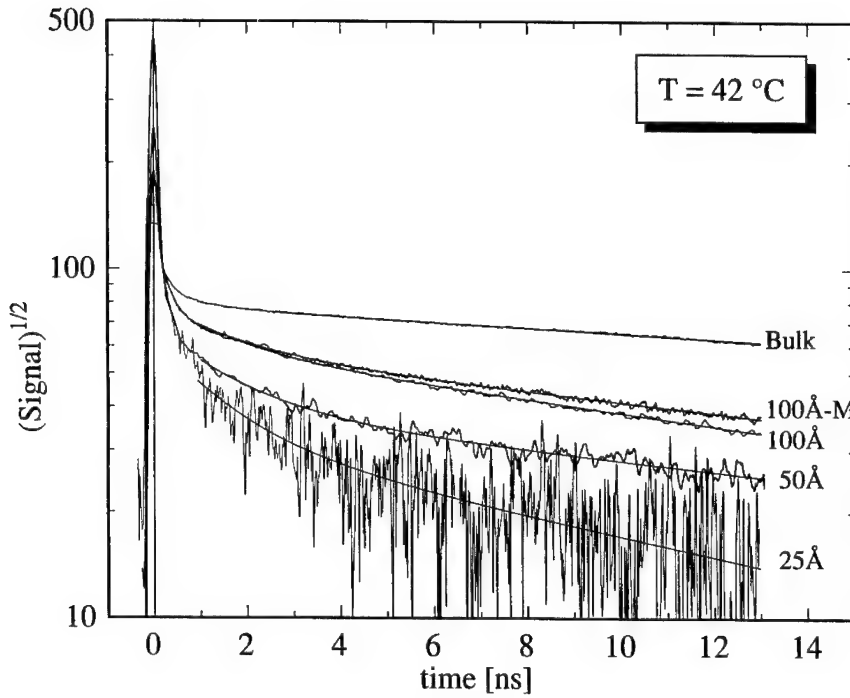
Figure 7. Logarithmic plot of the OKE decays for bulk 5CB and 5CB confined to different pore size and surface-treated sol-gel-glasses, all at 42 °C.

nematic liquid. If for a given temperature the bulk orientational correlation length ξ_b is smaller than the pore radius r_p, the correlation length ξ_c of the confined liquid is the same as ξ_b. If the pore radius is smaller than ξ_b, ξ_c is given by the pore radius r_p. That is, in this model the correlation length ξ_c is frozen or cutoff by the pore size but the relationship between correlation length and orientational fluctuation time is unchanged. The simulation of the OKE decays is complicated by the fact that in the investigated porous sol-gel-glasses there is a distribution $f(r_p)$ of pore sizes around the mean pore size (see fig. 2). That is, to obtain the OKE signal one must integrate over the pore size distribution according to

$$G(t) \; = \; \int f(r_p) \cdot \frac{1}{\tau_c(r_p)} \cdot exp\left[-\frac{t}{\tau_c(r_p)}\right] dr_p, \qquad (4)$$

where $\tau_c(r_p)$ is determined as indicated above. Although the orientational fluctuations in a given pore size relax exponentially, the distribution of pore sizes results in a nonexponential decay. We will come back to this point later. For comparison with the experimental data the mean relaxation times are depicted in fig. 8 (experiment on the left, simulation at the right). The main conclusion is that this correlation length cutoff model reproduces the drastic decrease of $< \tau >$ for the confined liquids as well as the pore size dependence. However, quantitative agreement between experiment and simulation is poor.
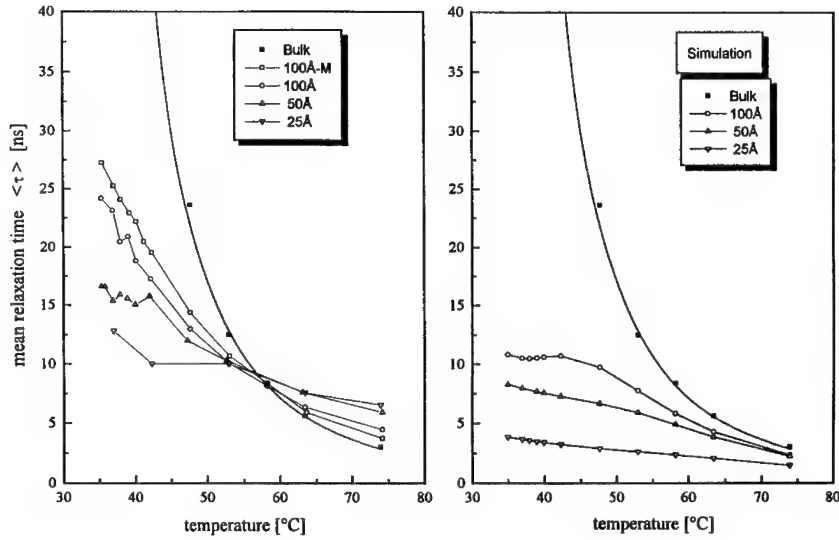
Figure 8. Temperature dependence of the mean relaxation time $< \tau >$ for 5CB bulk and 5CB in porous glasses. Left: experimental data. Right: simulated data with the correlation length cutoff model. Dotted lines provide a guideline to the eye.

The second model is based on a modified LdG ansatz as introduced by Iannachione et al. [3] to explain order parameter measurements for confined 5CB. As in the first model, independent pore segments with an effective scalar order parameter Q are assumed. In addition to the usual bulk terms the expansion of the free energy

$$F = F_0 + \frac{1}{2}a(T - T^*)Q^2 - \frac{1}{3}bQ^3 + \frac{1}{4}cQ^4 + \frac{1}{2}\frac{L}{r_p^2}Q^2 - gQ \tag{5}$$

contains two new terms $LQ^2/2r_p^2$ and gQ describing the distortion energy of the paranematic director field through the pore curvature and an ordering effect due to surface interaction, respectively.

To describe dynamics within this model a time-dependent Landau-Ginzburg description can be used as originally done by deGennes. Then the time dependence of the order parameter is given by $\nu\dot{Q} = -\partial F/\partial Q$. Introducing $Q(t) = \bar{Q} + \delta Q(t)$ one can separate time-dependent and time-independent parts and linearize with respect to the fluctuations δQ [16]. Because the paranematic order is small in the temperature range above the bulk phase transition [3], higher terms of $\bar{Q}\delta Q$ can be neglected yielding

$$\nu\delta\dot{Q} + [a(T - T^*) + \frac{2L}{R^2}]\delta Q = \delta\mathcal{F} \tag{6}$$

with $\delta\mathcal{F}$ a fluctuating force, whose precise form is not required. The solution of this differential equation yields a monoexponential relaxation of δQ with
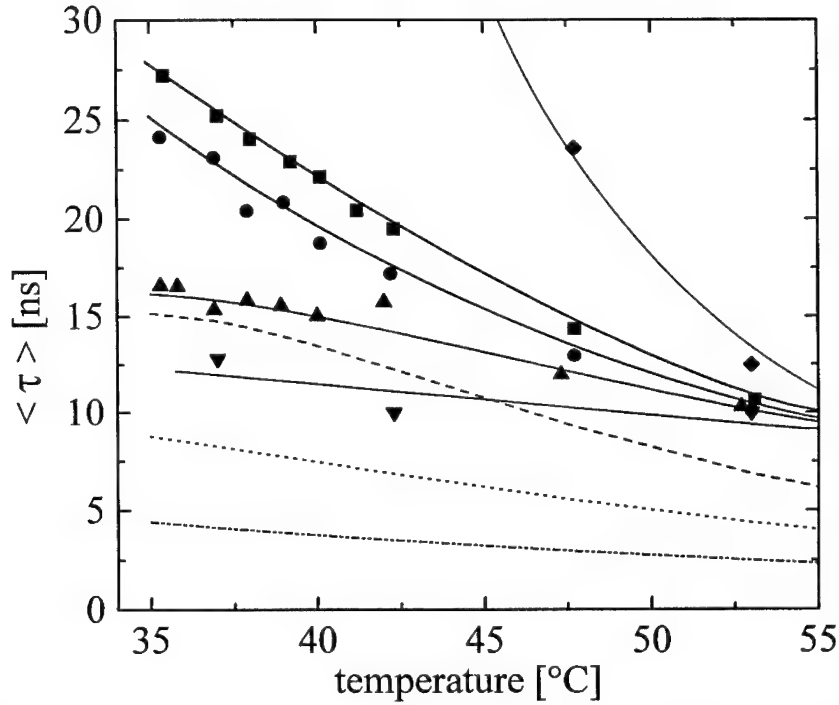
Figure 9. Comparison of the mean relaxation time for the data simulated on the basis of the modified LdG ansatz (100Å:— — — —, 50Å:- - - - - , 25Å:— - - — - - — -) and experimental data (bulk: ◇, 100Å-M: □, 100Å: o, 50Å: △, 25Å: ▽). Solid lines provide a guideline to the eye.

$$\tau = \frac{\nu}{a(T - T_R^*)} \tag{7}$$

introducing a pore size dependent $T_R^* = T^* - \frac{2L}{aR^2}$. This renormalization of T^* by including the elastic energy in the expansion is the same as found in the derivation of the static properties [3]. In this simplified approach the surface interaction g has no influence on the relaxation time τ_c.

In this modified LdG model the pore size dependence of τ is given through eq. 7. To simulate an OKE decay one has again to weight the contributions of the different pore sizes in the sample by integrating over the experimental pore size distribution $f(r_p)$ quite analogous to eq. 4. This again results in a nonexponetial decay function from which an average $< \tau >$ can be calculated. The temperature dependence of $< \tau >$ expected from the modified LdG ansatz, again together with the experimental values for $< \tau >$, are shown in fig. 9. Similar to the outcome in the correlation length cutoff model the decrease of $< \tau >$ for the confined liquid and the pore size dependence are reproduced, the absolute values of $< \tau >$ are not. The agreement between experimental and simulated data can be improved for a given pore
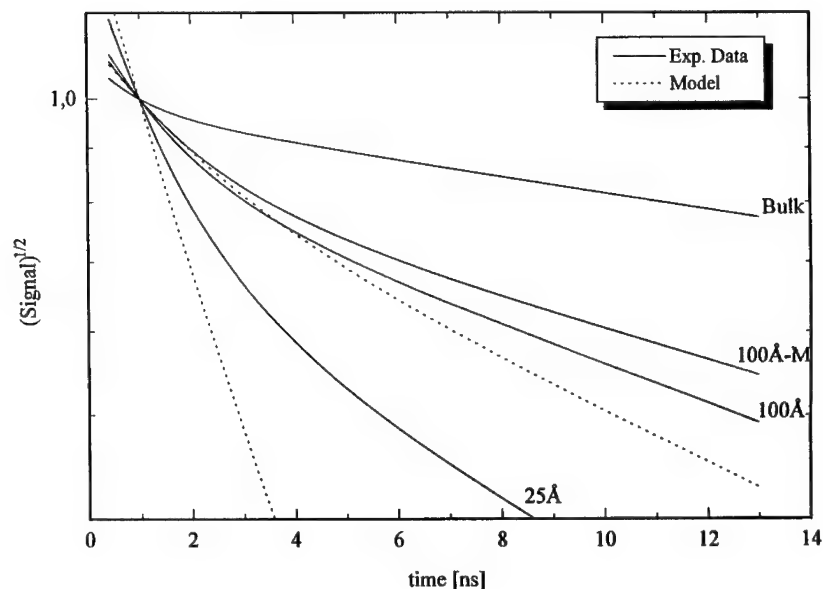
Figure 10. Time dependence of the OKE decay function at T = 42 °C. The solid lines are experimental data. The dotted lines are calculated on the basis of the modified LdG ansatz for the 100 Å (upper curve) and 25 Å porous glass (lower curve).

size if a value of L different from the bulk isotropic elastic coefficient is chosen. However, it is not possible to find a value L which would allow a satisfying fit for all porous samples at the same time. Altogether the agreement with the experimental data is not better than in the crude cutoff model discussed earlier.

Taking into account the distribution of pore sizes leads to nonexponential decays as observed experimentally. However, a closer inspection of the form of the decays for experimental data on one hand and simulated data on the other hand reveals that the nonexponentiality is much more pronounced for the experimental decays. To illustrate this point, fig. 10 shows the experimental decays for the 25 Å, 100 Å and 100 Å-M samples and simulated decays according to the modified LdG model for the 25 Å and 100 Å glasses, all at 42 °C. To achieve within the simulation a nonexponentiality comparable to the experimental one, a pore radii distribution much broader than the one calculated from BET adsorption isotherms must be used. This discrepancy indicates that for the description of pseudonematic fluctuations within the pores a model based on independent pores is not sufficient and interporous interactions must be included. We cannot rule out that there are intrinsic deviations from an exponential decay as e.g. predicted by random field models and found for temperatures below T_{ni} in a dynamic light scattering experiment by Wu et al. [4].

In this context an extension of our measurements below T_{ni} is the next goal to monitor the transition of the very fast orientational fluctuations found in our study to the extremely slow dynamics found by those authors. Another target must be the detailed comparison of correlation lengths ξ and correlation times τ in the same system to see if and at which

223

temperature the conventional scaling between the two parameters changes to an exponential one as predicted by finite size theories.

ACKNOWLEDGEMENTS

REFERENCES

1. P.G. deGennes, *The Physics of Liquid Crystals* (Clarendon Press, Oxford, 1974).

2. T. Bellini, N.A. Clark, C.D. Muzny, L. Wu, D.W. Schaefer, B.J. Oliver, Phys. Rev. Lett, **69**, 788 (1992).

3. G.S. Iannachione, G.P. Crawford, S. Žumer, J.W. Doane, D. Finotello, Phys. Rev. Lett, **71**, 2595 (1993).

4. X.L. Wu, W.I. Goldburg, M.X. liu, J.Z. Xue, Phys. Rev. Lett, **69**, 470 (1992).

5. S. Tripathi, C. Rosenblatt, F.M. Aliev, Phys. Rev. Lett, **72**, 2725 (1994).

6. S.B. Dierker and P. Wiltzius, Phys. Rev. Lett, **66**, 1185 (1991); B.J. Frisken and D.S. Cannell, Phys. Rev. Lett, **69**, 632 (1992).

7. D. Finotello, K.A. Gillis, A. Wong, M.H.W. Chan, Phys. Rev. Lett, **61**, 1954 (1988); A. Wong and M.H. Chan, Phys. Rev. Lett, **65**, 2567 (1990)

8. Y.X. Yan, K.A. Nelson, J. Chem. Phys., **87**, 6257 (1987).

9. F.W. Deeg, S.R. Greenfield, J. Stankus, V.J. Newell, M.D. Fayer, J. Chem. Phys., **93**, 3503 (1990).

10. F.W. Deeg, M.D. Fayer, J. Chem. Phys., **91**, 2269 (1989).

11. F.W. Deeg, K. Diercksen, G. Schwalb, C. Bräuchle, H. Reinecke, Phys. Rev. B, **44**, 2830 (1991).

12. G. Schwalb, F.W. Deeg, C. Bräuchle, J. Non-Cryst. Sol., **172-174**, 348 (1994).

13. G. Schwalb and F.W. Deeg, Phys. Rev. Lett., submitted.

14. J. Warnock, D.D. Awschalom, M.W. Shafer, Phys. Rev. B, **34**, 475 (1986).

15. see e.g. G. Liu, Y. Li, J. Jonas, J. Chem. Phys., **95**, 6892 (1991).

16. A. Mauger, D.L. Mills, Phys. Reb. B, **27**, 7736 (1983).

Molecular Dynamics Computer Simulations of Diffusion in Porous Silicates

GRANT S. HEFFELFINGER, PHILLIP I. POHL and LAURA J. D. FRINK
Sandia National Laboratories, Albuquerque, NM, 87185-0727

Abstract

In this work a newly developed dual control volume grand canonical molecular dynamics technique simulates the diffusion of gas in a cylindrical pore. This allows spatial variation of chemical potential and hence an accurate simulation of steady state pressure driven diffusion. The molecular sieving nature of microporous imogolite models and the Knudsen effect are discussed and compared with experimental data.

Introduction

The diffusion of gases in porous solids is governed by physical and chemical features of both the solid and the gas. The pores, for example, can be slit, ink bottle, or funnel shaped, cylindrical or some combination of these [1]. They can be ordered, as in zeolites and imogolite or disordered as in amorphous silica. The gases can be spherical or elongated, large or small, and can interact strongly with the solid or be rather inert. Describing the diffusion through porous solids with valid theories and predictive equations is essential to successful engineering of the processes in which this is involved. Porous membranes [2], catalysts [3] and thermal insulation [4] are such processes. Computer simulations can aid in understanding the structure-property relationships for fluid interactions with porous solids.

The diffusion of a species, i, in a direction, x, is related to the gradient of concentration or density, ρ, by Fick's law,

$$J_i^x = -D_i^x \frac{d}{dx} \rho_i(x). \tag{1}$$

Recently, Xiao and Wei gave a detailed analysis of the diffusion mechanisms of hydrocarbons in zeolites [5]. Their unified diffusion theory describing gaseous, liquid, Knudsen, solid and configurational (molecular sieving) diffusion, has a diffusivity expressed by

$$D = guLe^{-\frac{E}{RT}} \tag{2}$$

where g is a geometric term, u is a characteristic velocity, L the characteristic path length, and E the activation energy. The activation energy is only used for solid and configurational diffusion, and is cause for the sieving effect important in micropore separations.

To test the assumptions used in arriving at equation 2, one can employ a number of simulation techniques [6]. Their analysis included molecular mechanics to predict E, grand canonical Monte Carlo (GCMC) to simulate the concentration in model pores and analysis of

225

available pore space for different sized molecules to evaluate porosity/tortuosity effects. The focus of the present work is an alternative to this three pronged approach. That is, simulate pressure driven gas diffusion in pores, which is much more like the actual experiments carried out in laboratories developing porous materials.

It has been generally known, that the chemical potential gradient is the true driving force for diffusion [7]. To completely investigate these effects on gas diffusion, we have attempted to model diffusion driven by a chemical potential gradient in imogolite a tubular aluminosilicate (~1μm in length, ~7-10Å inner diameter). Perhaps the newest and most unique material for these computer simulations, synthesis of and adsorption experiments with imogolite have explored many possible applications which would exploit its narrow pore size distribution and unique structure. Ackerman et al completed a study of the porosity associated with natural and synthetic imogolite which included N_2, CO_2 and CH_4 adsorption, N_2 temporal adsorption and ^{129}Xe NMR [8,9]. In addition, NVT MD simulations of He/SF_6 in imogolite were conducted [6] comparing with the membrane selectivities [10].

GCMD

The Dual Control Volume Grand Canonical Molecular Dynamics (DCV-GCMD) method [11] has been used to investigate the sieving nature of microporous materials by simulating pressure-driven transport of a pure component fluid through an imogolite pore. While the DCV-GCMD method employs molecular dynamics (MD) moves throughout the system, each MD move is followed by a series of GCMC-like insertions and deletions of fluid molecules in each of two control volumes in order to maintain the chemical potential in the control volumes constant at a desired value. By measuring the flux and the gradient of the resulting steady-state density profile, the diffusitivity of each fluid component, i, in the presence of a chemical potential or pressure gradient, can be determined from Fick's law, equation 1. While DCV-GCMD has been demonstrated for binary color diffusion [11], in this work we have extended the method to model a fluid experiencing a pressure gradient while confined in a small pore. The pressure gradient is achieved for a pure component fluid simply by choosing chemical potentials in the two control volumes which produce two different fluid densities.

The fluid-fluid and fluid-wall interactions were modeled with the cut and shifted Lennard-Jones potential,

$$\phi(r) = \begin{cases} \phi^{LJ}(r) - \phi^{LJ}(r^c), & r \leq r^c \\ 0, & r > r^c \end{cases}, \tag{3}$$

where ϕ^{LJ} is the full LJ potential

$$\phi^{LJ}(r) = 4\varepsilon \left[\left(\frac{\sigma}{r} \right)^{12} - \left(\frac{\sigma}{r} \right)^6 \right], \tag{4}$$

with r^c the cut-off distance, taken to be $\sigma^{1/6}$ for all interactions. The fluid-wall LJ parameters were taken as, $\sigma_{fw}/\sigma_{ff} = 0.7723$, and $\varepsilon_{fw}/\varepsilon_{ff} = 1.0697$.

The 4224 wall atoms, which did not move, were positioned in two concentric shells of length (on the x axis) $48.0\sigma_{ff}$ and with radii of 6.0σ and 6.54446 σ_{ff}. Using cylindrical coordinates, the wall atoms were spaced $1.0\sigma_{ff}$ apart in the axial (x) direction and approximately 8.2 degrees apart in the theta direction. The theta coordinates of the wall atoms in the outer shell were shifted from those in the inner shell by 4.1 degrees.

When applying the DCV-GCMD method to some systems it is possible to choose an MD timestep that is large enough to move fluid in or out of the control volumes faster than the GCMC-like insertions/deletions can remove or add fluid to maintain the desired chemical potential. Thus it is important to know the appropriate density of the fluid at the desired chemical potential in each control volume. This can be accomplished via standard GCMC or, as we have done in this work, with a DCV-GCMD simulation that employs two control volumes which each encompass one half of the entire system (system I). Once this has been accomplished, the standard approach (system II) can be employed to develop a steady state density profile which has a smooth gradient.

In this work, systems I and II were taken to be $48.0\sigma_{ff}$ long, thus their x coordinate stretched from 0.0 to $48.0\sigma_{ff}$. Periodic boundary conditions were employed along the x axis at x = 0.0 and $x = 48\sigma_{ff}$. For system I, the two control volumes, A and B, were positioned on the x axis to extend from 0.0 to $24.0\sigma_{ff}$ and from $24.0\sigma_{ff}$ to $48.0\sigma_{ff}$, respectively. For system II, control volume A extended from $6.0\sigma_{ff}$ to $18.0\sigma_{ff}$ and $30.0\sigma_{ff}$ to $42.0\sigma_{ff}$, respectively. For both systems, each control volume encompassed the entire pore cross section (in the y and z directions see Figure 1). While we have positioned the control volumes for both systems inside the pore, they could just as easily have been positioned outside the pore, enabling one to model entrance effects.

The temperature was kept constant [11] at $kT/\varepsilon_{ff} = 1.0$, and the chemical potential of the fluid in control volumes A and B was taken to be $\mu' = 3.03$ and $\mu' = 2.23$ where,

$$\beta\mu_i' = \beta\mu_i + 3\ln\left(\frac{\sigma}{\Lambda_i}\right), \tag{5}$$

with $\beta = 1/kT$. The molecular dynamics timestep employed was $\Delta t(\varepsilon_{ff}/(m_{ff}\sigma_{ff}^2))^{1/2} = 0.001$.

After starting from 64 molecules in each control volume, system I was equilibrated for 20,000 molecular dynamics timesteps after which averages were accumulated for 60,000 timesteps. A system I configuration 40,000 timesteps after startup was saved and used as the starting point for the system II simulation which

Figure 1 Schematic of DCV-GCMD Pore Systems

Control Volume A **System I** Control Volume B

0σ 24σ 48σ

System II

0σ 6σ 18σ 30σ 42σ 48σ
Control Volume A Control Volume B

Imogolite Wall Atoms
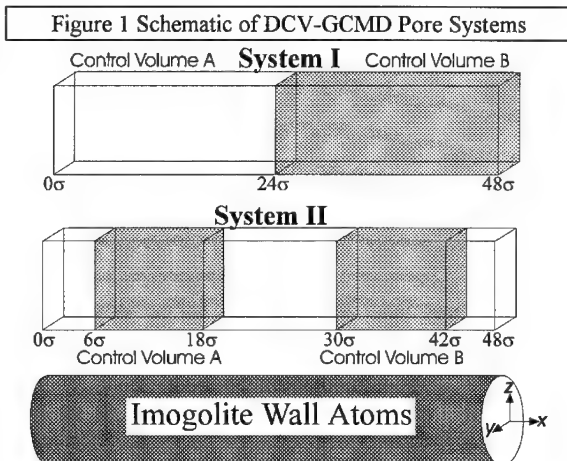
was equilibrated for 140,000 timesteps after which averages were accumulated for approximately 180,000 steps.

The algorithm employed in this work is a massively parallel version of the DCV-GCMD method of [11]. Briefly, this parallel algorithm [12] employs a superposition of two different parallel algorithms: spatial GCMC [13] and spatial MD [14]. With this parallel DCV-GCMD algorithm, simultaneous insertions/deletions can be attempted in each control volume thus for this work, 64 insertions and/or deletions were attempted in each control volume after each MD step.

Because the parallel spatial GCMC and spatial MD algorithms scale with system size and are most efficient for large systems (tens of thousands of atoms), the primary application of the parallel DCV-GCMD algorithm is to simulate such systems. While the systems studied in this work are relatively small, approximately 2200 fluid atoms and 4224 static wall atoms, they represent the first application of the new parallel DCV-GCMD algorithm. For these simulations, carried out on 32 processors of an Intel Paragon, 1 second was required to perform a single MD timestep and its associated 64 attempted insertions/deletions in each control volume.

Results

The axial density profile ($\rho(x)$), determined by averaging the number of fluid molecules in bins of $0.5\sigma_{ff}$ wide (in the x direction) and across the entire radius, is shown for both system I and II in Figure 1. From this figure, we can see that the density in control volumes A and B, $\rho\sigma_{ff}^3 = 0.4610$ and 0.4075, respectively, is nearly identical with that for system I, $\rho\sigma_{ff}^3 = 0.4612$ and 0.4076. Thus the control volume densities for system II are the proper results for the desired chemical potentials. The axial density profile in Figure 2 shows some structure, namely the saw-blade shape with periodicity of $1\ \sigma_{ff}$, evidence that the fluid moves down the pore as a row of atoms. Furthermore, it is not entirely clear from Figure 2 that the diffusion in the pore is fickean, that is, the gradients of the density profile in the regions between the control volumes are not

Figure 2 Axial Density Profiles in Pore, System 1 (dash), System II (solid)

228
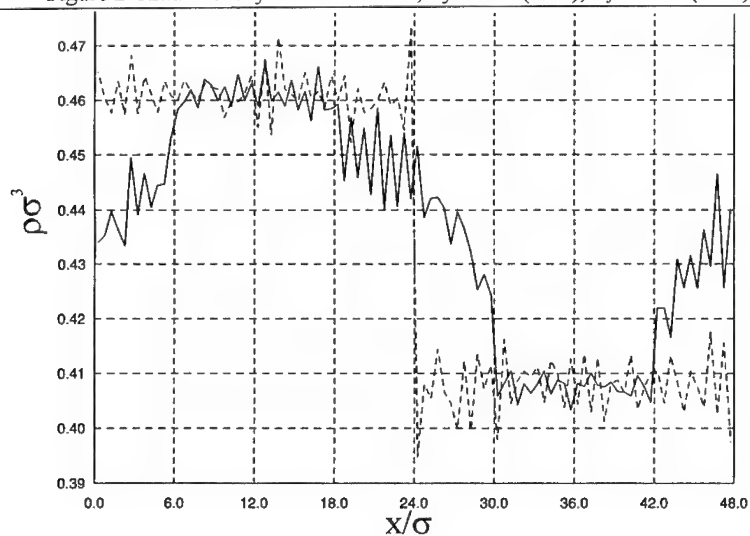
clearly linear. Extending the simulation time should answer this question conclusively.

Given the repulsive nature of the fluid-wall interaction, most of the fluid should be contained within the center of the pore (as opposed to being adsorbed on the pore wall). This is borne out by Figure 3, radial profiles of the fluid taken at $12.25\sigma_{ff}$ (solid), $25.25\sigma_{ff}$ (short dashes), and $36.25\sigma_{ff}$ (long dashes). These profiles were obtained by determining the average number of molecules in annular bins $0.5\sigma_{ff}$ wide (in the x direction) and $0.75\sigma_{ff}$ wide in the radial direction.

We can see from Figure 2 that the density profile develops two gradients between the control volumes, one which straddles the periodic boundary (x = $42.0\sigma_{ff}$ to $6.0\sigma_{ff}$) and one which does not (x = $18.0\sigma_{ff}$ to $30.0\sigma_{ff}$). By determining the slope of a straight line fit to the density profile in these two regions we have determined d ρ(x)/dx, as shown in Table I.

Figure 3 Radial Density Profiles

We have also calculated the flux via two different methods [11], the flux plane method and the control volume flux method (J^x and ζ^x, respectively):

$$J^x = \frac{j^{LTR} - j^{RTL}}{\Delta t A_{yz} N_{planes}}, \quad (6)$$

$$\xi^x = \frac{M(B) - M(A)}{4\Delta t A_{yz} N_{steps}}, \quad (7)$$

Table I Density Profiles from DCV-GCMD

Region	|slope|
18-30	2.34×10^{-3}
42-6	2.34×10^{-3}

where j^{LTR} and j^{RTL} represent the net number of fluid molecules which move through each flux plane (two were used in this work, one at x = $24.0\sigma_{ff}$ and another at the periodic boundary, x = 0 and $48.0\sigma_{ff}$) and N_{planes} is the number of flux planes (2 for this work). $M(B)$ and $M(A)$ are the net number of insertions (accepted insertions - deletions) in control volumes A and B, respectively, deltat is the MD timestep, A_{yz} is the cross sectional area of the pore, taken to be $\pi r^2_{effective}$ where $r_{effective}$ arbitrarily taken to be $6.0\sigma_{ff} - 0.5\sigma_{ww}$ ($\sigma_{ww} = 0.5445\sigma_{ff}$), and N_{steps} is the number of MD timesteps. The fluxes, calculated via both methods (reduced by multiplying by $\sigma_{ff}^3(mass_{ff}/\varepsilon_{ff})^{1/2}$), and the resulting diffusivities (reduced by dividing by $\sigma_{ff}(\varepsilon_{ff}/m_{ff})^{1/2}$), calculated via equation 1 and an average of the two density gradients (Table I), are shown in Table II.

From Table II we see that the fluxes calculated via the two methods agree quite well and yield a large value for the diffusivity, due largely to the presence of the pressure gradient.

Table II Diffusivities and Fluxes from DCV-GCMD

	flux	diffusivity
flux plane method (J^x)	0.0581	24.8
control volume flux method (ζ^x)	0.0577	24.7

Conclusions

We have demonstated the usefulness of DCV-GCMD for investigating the sieving nature of microporous materials by applying the method to a model system. Work is currently underway to apply DCV-GCMD to multicomponent fluids employing more realistic interaction potentials. In this work we tried to exhibit the power and usefulness of computer simulation in understanding gas flow in microporous solids. The theories in use for zeolites may work well for amorphous silica membranes if the pores are of molecular dimensions and can now be tested using DCV-GCMD. This simulation allows comparison with the most relevant experiments in membrane research, that is adsorption and diffusion.

Acknowledgment

References

1. Rouquerol, J.; Avnir, D.; Fairbridge, C.W.; Everett, D. H.; Haynes, J. H.; Pernicone, N.; Ramsay, J. D. F.; Sing, K. S. W.; Unger, K. K., 1994, Pure Appl. Chem., 66, 1739.
2. Brinker, C. J., T.L. Ward, R. Sehgal, N. K. Raman, S.L. Hietala, D.M. Smith, D.W. Hua, Headley, T, J. Memb. Sci., 1993, 66, 271.
3. Chen, N. Y., T. F. Degnan, and C. M. Smith, Molecular Transport and Reaction in Zeolites, 1994, VCH Publishers, Inc, New York.
4. Schaefer, D. W., MRS Bulletin, 1994, xix(4), 49.
5. Xiao, J., and J. Wei, Chem. Engr. Sci., 1992, 47(5), 1123.
6. Pohl, P. I., and D. M. Smith, 'Molecular Simulations of Gases in Porous Silicates', Paper W1-1.5, MRS Fall Mtg, Porous Materials Symposium.
7. Cussler, E., 1994, Diffusion, Cambridge.
8. Ackerman, W. C.; Hua, D. W.; Kim, Y-W.; Huling, J. C; Smith, D. M.; 1994, Chararacterization of Porous Solids III, J. Roquerel, F. Rodriguez-Reinoso, K. S. W. Sing, and K. K. Unger, eds, 735, Elsevier.
9. Ackerman, W. C.;Smith, D. M.; Huling, J. C.; Kim, Y-W.; Bailey, J. K.; and C. J. Brinker, Langmuir, 1993, 9, 1051-1057.
10. Sehgal, R; Huling, J. C.; Brinker, C. J., Proceedings of the Third International Conference on Inorganic Membranes, Worcester, MA, 1994, (in Press).
11. Heffelfinger, G. S., and F. van Swol, J. Chem Phys., 1994, 100(10), 7548.
12. Heffelfinger, G. S., in preparation, 1994.
13. Heffelfinger, G. S., and M.E. Lewitt, submitted, 1994
14. Plimpton, S. J., 1993, Fast Parallel Algorithms for Short-Range Molecular Dynamics, SAND91-1144, Prepared by Sandia National Laboratories, Albuquerque, NM.

PROBING SURFACE ROUGHNESS AND POROSITY
THROUGH ADSORPTION OF WETTING LAYERS

J. KRIM and V. PANELLA*
Department of Physics, Northeastern University, Boston, MA 02115
*Present address: Faculte' des Sciences de Luminy, Departement de Physique, Case
901 - 13288 Marseille Cedex 9, France.

ABSTRACT

We have employed a quartz microbalance technique to record adsorption isotherms
on silver and gold surfaces whose roughness has also been characterized by x-ray reflec-
tivity or scanning tunneling microscopy. We observe strikingly different behavior for
two different liquid adsorbates (oxygen and nitrogen), and attribute this to a difference
in their surface tension. Our results demonstrate the impact that capillary condensa-
tion phenomena can have on the interpretation of adsorption data, particularly with
regards to the fractal nature of the substrate. Valuable information on surface morphol-
ogy can nonetheless be obtained from adsorption isotherms, if combined with alternate
experimental techniques.

INTRODUCTION

A wide variety of surfaces and interfaces occurring in nature are well represented by
a kind of roughness associated with self-affine fractal scaling, defined by Mandelbrot in
terms of fractional Brownian motion.[1] Examples include the nanometer scale topology
of vapor-deposited films,[2] the spatial fluctuations of liquid-gas interfaces,[3] and the
kilometer scale structures of mountain terrain.[1] Physical processes which produce such
surfaces include fracture, erosion, and molecular beam epitaxy, as well as fluid invasion
of porous media.[4]

All rough surfaces exhibit perpendicular fluctuations which are characterized by
a mean-square roughness $\sigma = <z(x,y)^2>^{1/2}; z(x,y) = h(x,y) - <h(x,y)>$, where
$h(x,y)$ is the height function and $<...>$ is the spatial average over a planar reference
surface. If the surface exhibits self-affine roughness, σ will scale with the horizontal
length L sampled as $\sigma(L) \propto L^H$,[5] where $0 < H < 1$ is referred to as the "roughness"
exponent.[6] Self-affine fractals are distinguished from self-similar ("genuine") fractals by
an asymetry in the scaling behavior perpendicular to the surface, generally manifested
by an absence of surface overhangs.[7] A "local" regime may, however, be present where
below a certain crossover length, the surface is indistinguishable from a self-similar
fractal whose dimension is $D = 3 - H$ (three spatial dimensions are assumed throughout
this paper).

Regardless of the surface under study, a knowledge of the topography and rough-
ness at submicron length scales is frequently essential to gain an understanding of its

physical origins. The technique of adsorption appears to be an ideal choice for such a characterization, since it involves coating the surface with particles of *atomic* extent while still sampling the entire *macroscopic* extent of the surface. We report here adsorption isotherm results for a number of silver and gold surfaces whose roughness has previously been characterized by means of x-ray reflectivity or scanning tunneling microscopy (STM). We observe that adsorption yields ambiguous values for D and H, and does not clearly distinguish between self-affine and self-similar scaling.[8] It nonetheless remains a very powerful technique when used in conjunction with experimental probes such as STM or X-ray reflectivity, neither of which can directly detect atomic-scale surface porosity.

THEORY OF ADSORPTION ON A FRACTAL SURFACE

Pfeifer *et al*,[9] and also de Gennes,[10] proposed an adaptation of the "Frenkel-Halsey-Hill" (FHH) expression (applicable to films which completely wet planar substrates)[11] for the form of an adsorption isotherm on a fractally rough surface:

$$\ln(P/P_o) = -\frac{\alpha}{k_B T \theta^n} \tag{1}$$

The coefficient α reflects both the substrate-adsorbate and adsorbate-adsorbate van der Waals interactions,[12] T is the temperature, θ is the quantity of adsorbed material, and $n = 3/(3 - D)$. A surface with fractal dimension $D > 2$ is associated with an exponent $n > 3$ within the context of this model. Several authors have argued that the inclusion of adsorbate surface tension effects, neglected in the formulation of Eq.(1), are a necessary aspect of the data interpretation.[13-17] An extensive discussion has ensued as to whether or not such effects must in fact be included in the analysis of experimental data. This issue arises on account of the fact that the atomic scale behavior of surface tension may be different from that of the bulk. Somewhat of a consensus does however exist for the specific relations between n and D. [9,10,13-18] If surface tension effects are negligible, then for self-similar surfaces,

$$D = 3(1 - \frac{1}{n}), \tag{2a}$$

and for self-affine surfaces,

$$n = 3, \tag{2b}$$

while, if such effects are dominant, then for self-similar surfaces,

$$D = 3 - \frac{1}{n}, \tag{2c}$$

and for self-affine surfaces,

$$H = \frac{2}{n+1} \quad (H > 0.5) \quad ; \quad n = 3 \quad (H < 0.5), \tag{2d}$$

where the value $H = 0.5$ which divides the regimes in Eq.(2d) pertains to non-retarded

van der Waals forces. It has very recently been argued that the relation $H = 2/(n+1)$ in Eq.(2d) is in fact valid for all values of H.[18]

EXPERIMENTAL

Adsorption isotherms were recorded by means of a quartz crystal microbalance technique. The microbalance consists of a single crystal of quartz which oscillates in transverse shear motion with a quality factor near 10^5. Each major face is plated with a metal electrode, which is prepared by thermal evaporation, and which also serves as the substrate for the adsorption studies. For the work presented here, we produced silver films *in situ* by collimated thermal evaporation at $10^{-9} - 10^{-8}$ torr onto 1/4 inch diameter, optically polished quartz crystals held 50 cm above a boat evaporation source. The gold film was prepared commercially by evaporation onto an unpolished quartz substrate.[19]

Adsorption isotherms were carried out by transferring the sample, within the vacuum chamber, to a tip which could be cooled to 77.4 K. N_2 or O_2 gas was then admitted to the chamber, and the quantity adsorbed (proportional to oscillator frequency shift) was monitored as a function of pressure under equilibrium conditions. The crystal drive level was always adjusted to be as low as possible, so as to minimize the heating of the crystal. It was not however possible to always lower the drive level so as to eliminate all observable heating effects. In this case, we recorded the data by hand. Set quantities of gas were introduced into the system and allowed to reach equilibrium (this typically was reached after several minutes). The crystal oscillator was then turned on and, after the measurement was recorded, turned off again. Each measurement required only a few seconds. In this way, due to the slow rate of self heating, the temperature of the crystal remained sufficiently constant. All measurements were repeated at least once to check for reproducibility.

RESULTS

Silver deposited at 300K

"Flat" silver surfaces were produced by depositing films at 0.5Å/s and normal incidence onto quartz substrates held at room temperature. The surfaces of such films are in fact gentle rolling hills rather than planes,[20] but the increase in surface area (relative to that of a plane) is below the detection threshold ($\sim 10\%$) for adsorption. STM investigations of these surfaces have established that they are self-affine, with roughness exponent $H = 0.82 \pm 0.05$. The STM results are fully consistent with *in situ* synchrotron x-ray reflectivity measurements.[21] The exponent $n = 3$ is expected for adsorption on such substrates. This anticipated exponent is obtained from Eq. (2a), assuming that the adsorption data cannot distinguish between a $D = 2$ planar surface and the sample, or from Eq. (2b), assuming that the slopes of the self-affine surface are too small for surface tension effects to dominate.
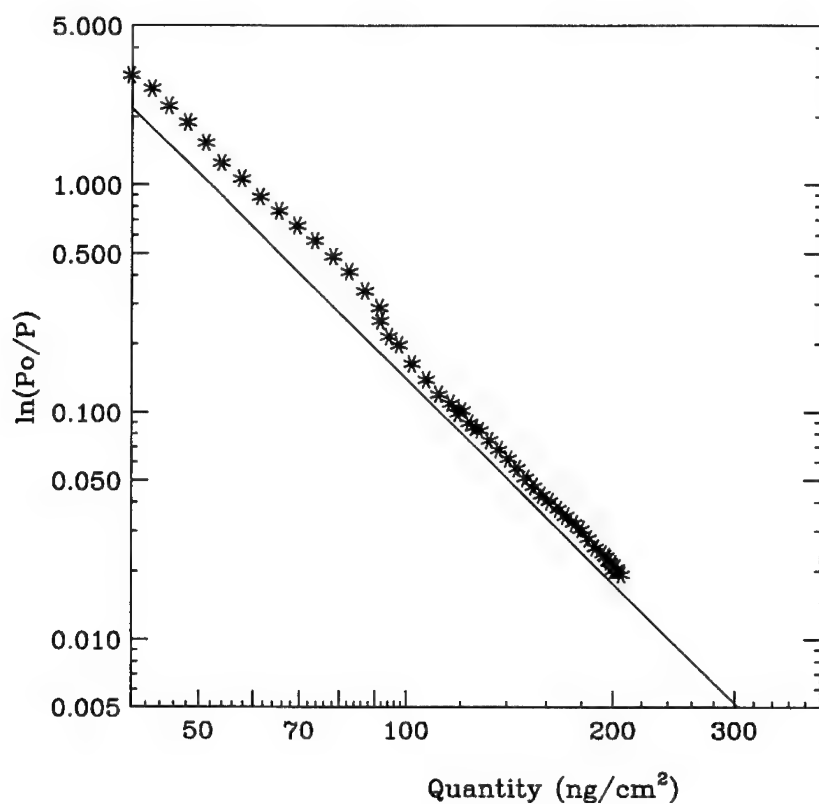
Figure 1. N_2 adsorption at T=77.4K on a 1000Å±10% silver film vapor deposited onto an optically polished quartz substrate at T=300K during the deposition. The solid line depicts theoretical prediction for adsorption onto a flat silver surface, and is characterized by $n = 3$.

Figure 1 presents nitrogen adsorption data for a 1000Å thick Ag film deposited at room temperature.[22] The data match theoretical predictions[12] for adsorption on a planar substrate (Eq. 1, with N_2/Au parameters taken from Ref. 23), with *no* adjustable parameters (solid line) , and are well fit by the exponent $n = 3$.

Silver deposited at 80K

"Rough" silver films were deposited at near-normal incidence onto a quartz substrate held at 80K. Both STM[23] and X-ray reflectivity measurements[2] recorded on such samples indicate that the samples are self-affine, with roughness exponent $H = 0.46 \pm 0.1$. The increase in surface area determined by STM is above the detection threshold for adsorption for films prepared in this manner. The exponent $n \approx 0.34$ is expected for adsorption on such substrates. This anticipated exponent is obtained from Eq. (2d), assuming that the adsorption data on these substrates will be dominated by surface tension effects.

Figure 2 presents oxygen and nitrogen adsorption data for a 1000Åthick silver film deposited at 80K and 5° off-normal incidence angle. Nitrogen and oxygen were chosen on account of the fact that the two adsorbates are extremely similar except for their surface tensions. Both are diatomic molecules, with comparable molecular diameters ($d_{O_2} = 3.58$ Å and $d_{N_2} = 3.7$ Å). The van der Waals coefficient α for the two gases is nearly the same ($\alpha_{O_2} = 1.92 \times 10^4$K Å^3 and $\alpha_{N_2} = 2.1 \times 10^4$K Å^3),[24] and yet the surface tension of liquid oxygen is almost double that of liquid nitrogen ($\gamma_{O_2} = 16.51$ dynes/cm and $\gamma_{N_2} = 8.94$ dynes/cm at T=77 K, $\gamma_{O_2} = 16.25$ dynes/cm and $\gamma_{N_2} = 8.72$ dynes/cm at T=78K)[25] . The temperature at which the measurements were carried out (T= 77.4K), is low enough to prevent oxidation of the silver. Neither nitrogen nor oxygen have dipole moments, but they do have very different quadrupole moments ($\Theta_{N_2} = -1.52 \times 10^{-26}$e.s.u. cm^2 and $\Theta_{O_2} = -0.39 \times 10^{-26}$e.s.u. cm^2).[26] A difference in quadrupolar character can give rise to a contribution to the adsorbate-adsorbent interaction, which in turn affects the shape of the isotherm in the monolayer regime, but should not affect the multilayer regime which is analyzed here. For N_2 adsorption the exponent $n = 4.7$ is found, while for the O_2 adsorption isotherm $n = 3$. The value for the oxygen data is closer to the expected result, and it could be argued that the higher surface tension of the liquid oxygen film makes oxygen data more appropriate for comparison with Eq. (2d), which assumes surface tension effects to be dominant.

Gold deposited at 300K onto rough quartz

Commercially prepared gold films deposited at room temperature onto unpolished quartz have been extensively investigated by means of STM, and have been found to exhibit self-affine scaling with $H = 0.96 \pm 0.03$.[27] The scaling occurs over at least three orders of magnitude. The rms widths of these surfaces are too large to be probed by means of x-ray reflectivity. The exponent $n = 1$ is expected for adsorption on such substrates. This anticipated exponent is obtained from Eq. (2d), assuming that the adsorption data on these substrates will be dominated by surface tension effects.
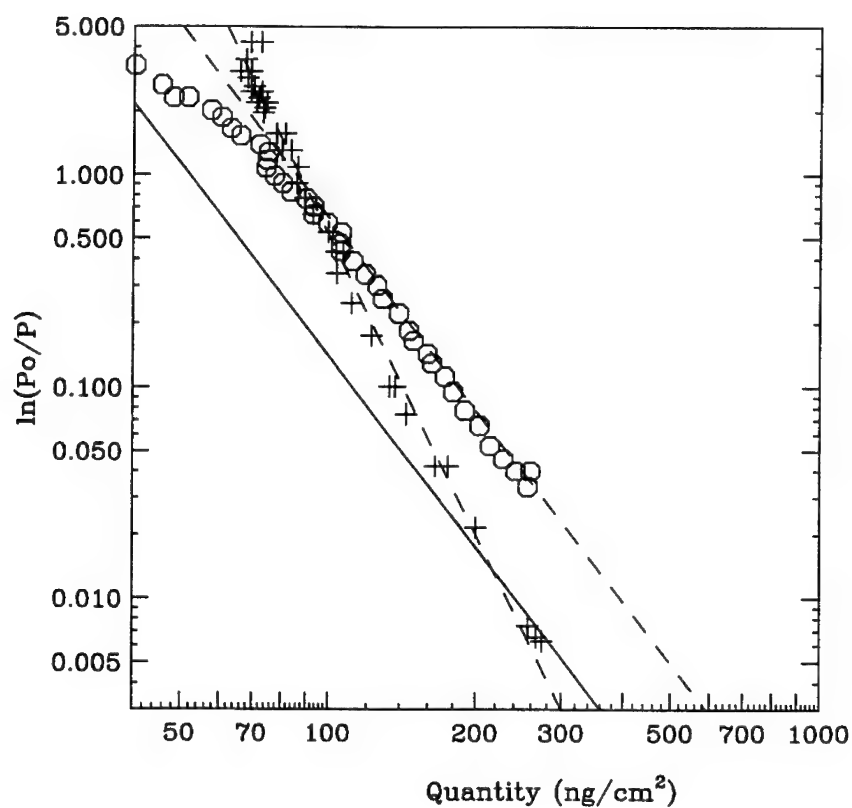
Figure 2. N_2 (+) and O_2 (o) adsorption at T=77.4K on a 1000Å±10% silver film vapor deposited onto an optically polished quartz substrate with $\theta = 5°$ and held at T=80K during the deposition. The dashed lines fitting the experimental points corresponds to $n = 4.7 (+)$ and $n = 3$ (o). The solid line depicts theoretical prediction for adsorption onto a flat silver surface, and is characterized by $n = 3$
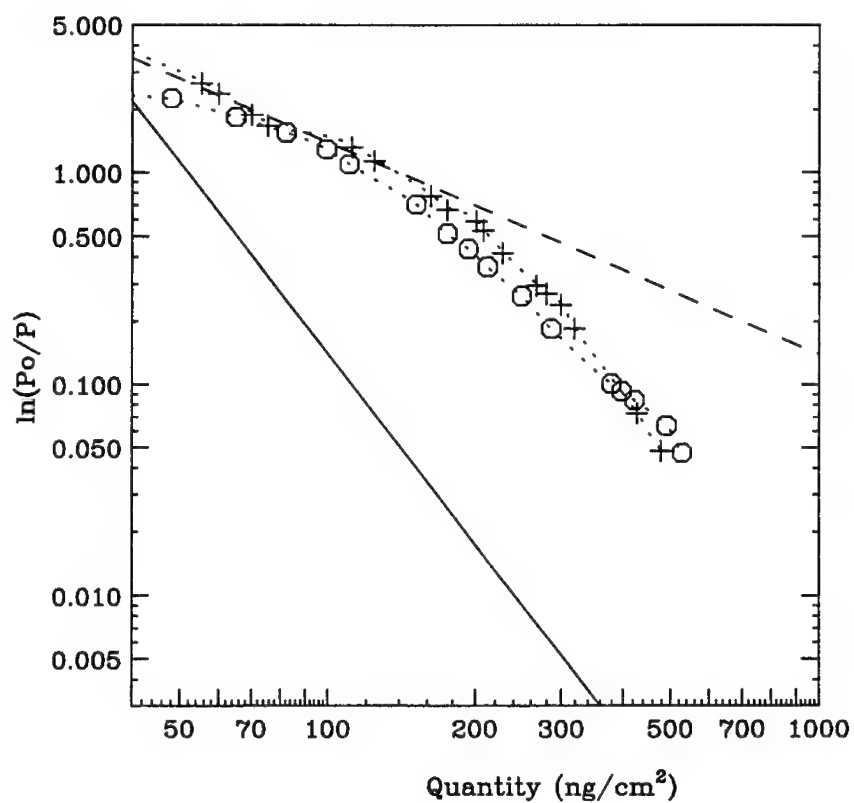
Figure 3. N_2 (+) and O_2 (o) adsorption at T=77.4K on a commercially prepared gold film deposited at 300K onto an unpolished quartz substrate. The dashed line depicts the slope $n = 1$ (see text). The solid line depicts theoretical prediction for adsorption onto a flat gold surface.

Nitrogen and oxygen adsorption on the gold surfaces are depicted in Figure 3. The data for the two adsorbents are coincident, indicating that surface tension effects may not be as dominant in this case as might be expected. Indeed, the exponent $n = 1$ is not observed. A slope of $n = 3$, the value predicted by Eq.(2b) is far more consistent with experimental observation.

DISCUSSION

We have employed a quartz microbalance technique to record adsorption isotherms on silver and gold surfaces whose roughness has also been characterized by x-ray reflectivity or scanning tunneling microscopy. In all cases the adsorption results could be argued to be consistent theoretical predictions for adsorption on self-affine surfaces. Nonetheless, it could also be argued that adsorption as the sole technique yields ambiguous values for D and H, and does not clearly distinguish between self-affine and self-similar scaling. Since the primary complication in the interpretation of adsorption data is the role of surface tension and capillary condensation, the interpretation of adsorption data is somewhat improved by recorded both nitrogen and oxygen data on the same sample. Future theoretical developments may allow for more quantitative information to be obtained. Adsorption meanwhile remains a very powerful technique when used in conjunction with experimental probes such as STM or X-ray reflectivity, neither of which can directly detect atomic-scale surface porosity.

ACKNOWLEDGEMENTS

REFERENCES

1. B. B. Mandelbrot, *The Fractal Geometry of Nature* (Freeman, New York, 1982)

2. R. Chiarello, V. Panella, J. Krim and C. Thompson, Phys. Rev. Lett. **67**, 3408 (1991)

3. J. H. Sikkenk, J. M. J. van Leeuwen, E. O. Vossnack, and A. F. Bakker, Physica **146A**, 622 (1987)

4. M. W. Mitchell and D. A. Bonnell, J. Mater. Res. **5**, 2244 (1990); E. A. Eklund *et al.*, Phys. Rev. Lett. **67**, 1759 (1991); J. Krim *et al.* Phys. Rev. Lett.**70**, 57 (1993); D. A. Kessler *et al.* Phys. Rev. Lett. **69**, 100 (1992); M. A. Rubio *et al.* Phys. Rev. Lett. **63**, 1685 (1989); V. K. Horvath *et al.* J. Phys. A **24**, L25 (1991)

5. For a review, see F. Family and T. Vicsek, *Dynamics of Fractal Surfaces* (World Scientific, Singapore, 1991)

6. J. Krim and J. O. Indekeu, Phys. Rev. E **48**, 1579 (1993)

7. F. Family and T. Vicsek J. Phys. A **18**, L75 (1985)

8. J.M. Drake, L.N. Yacullo, P. Levitz and J. Klafter, J.Chem Phys. **98**, 380 (1994)

9. P. Pfeifer, Y. J. Wu, M. W. Cole and J. Krim Phys. Rev. Lett. **62**, 1997 (1989)

10. P. G. de Gennes, in *Physics of Disordered Materials*, edited by D. Adler, H. Fritzsche, and S. R. Ovshinsky (Plenum, New York, 1985).

11. J. Frenkel, *Kinetic Theory of Liquids*, (Oxford University Press, London, 1949); G. D. Halsey, J. Chem. Phys. **17**, 520 (1949); T. C. Hill, J. Chem. Phys. **17**, 590 (1949)

12. E. Cheng and M. W. Cole, Phys. Rev. B **38**, 987 (1988)

13. M. Kardar and J. O. Indekeu, Europhys. Lett. **12**, 161 (1990); Phys. Rev. Lett. **65**, 663 (1990).

14. P. Pfeifer, J. Kenntner, and M. W. Cole, in *Fundamentals of Adsorption*, edited by A. B. Mersmann and S. E. Sholl (Engineering Foundation, New York, 1991), p. 689.

15. A. V. Neimark, Pis'ma Zh. Eksp. Teor. Fiz. **51**, 535 (1990) [JETP Lett. **51**, 608 (1990)]

16. D. Avnir and M. Jaroniec, Langmuir **5**, 1431 (1989); M. Jaroniec, X. Lu, R. Madey, and D. Avnir, J. Chem. Phys. **92**, 7589 (1990)

17. M. O. Robbins, D. Andelman, and J. F. Joanny, Phys. Rev. A **43**, 4344 (1991)

18. A.V. Neimark, Phys. Rev. B, in press

19. Sycon Instruments, Inc., East Syracuse, NY, (315)463-5297; 6 MHz quartz crystal unit for deposition rate monitors.

20. G. Palasantzas and J. Krim, Phys. Rev. Lett., in press

21. C. Thompson, G. Palasantzas, Y.P. Feng, S.K. Sinha and J. Krim, Phys. Rev. B **49**, 4902 (1994)

22. V. Panella and J. Krim, Phys. Rev. E **49**, 4179 (1994)

23. C. Mak and J. Krim, unpublished

24. S. Rauber, J. R. Klein, M. W. Cole, and L. W. Bruch, Surf. Sci. **123**, 173 (1982)

25. E. C. C. Baly and F. G. Donnan, J. of Chem. Soc. of London **81**, 907 (1902)

26. D. E. Stogryn and A. P. Stogryn, Mol. Phys. **11**, 371 (1966)

27. J. Krim, I. Heyvaert, C. Van Haesendonck and Y. Bruynseraede, Phys. Rev. Lett **70**, 57 (1993)

HYSTERESIS IN A CAPILLARY CONDENSATION SYSTEM

M. P. LILLY AND R. B. HALLOCK
Laboratory for Low Temperature Physics, Department of Physics and Astronomy
University of Massachusetts, Amherst, MA 01003

ABSTRACT

We report measurements of the hysteretic capillary condensation of liquid ^{4}He into the porous material Nuclepore. Results are presented for global and hysteretic behavior for 300 Å diameter pores. These observations deviate from the predictions of the Preisach model of independent hysteresis domains. By modifying the Preisach model so as to restrict the ability of some of the pores to drain normally we are able to model many features of the experimental data.

INTRODUCTION

In many cases, hysteresis associated with the cyclic behavior of a physical parameter can be attributed to a large number of hysteretic elements acting either independently or interacting with the other elements in the system in a complicated manner. Preisach[1] developed a simple model for predicting the shapes of the hysteresis trajectories of magnetic systems based on the behavior of independent domains. Another example of a system exhibiting hysteresis can be found in the study of adsorption and capillary condensation of a fluid in the pores of a porous material. As gas is added to a chamber containing a porous material, the chemical potential, μ, increases, a film forms on the walls of the pores, and the vapor pressure and film thickness both increase while maintaining the condition $\mu_{film} = \mu_{vapor}$. Eventually, due to a competition between the surface tension and Van der Waals forces, capillary condensation in the pores takes place. Because the liquid-vapor interface is different for filling and draining, a pore fills and drains at different values of the chemical potential, and as a result, each pore can be treated as a hysteresis element. Previous studies by Smith, Godshalk and Hallock[2] examined the global hysteretic behavior of capillary condensation of superfluid ^{4}He into the porous material Nuclepore.[3] In an effort to understand the details of the capillary condensation process in terms of various hysteresis models we have extended the measurements using the same porous material. For Nuclepore with 2000Å pores we found[4] departures from the predictions of the Preisach model. We present new experimental results for 300Å diameter pores and suggest possible modifications to the Preisach model to describe the observed hysteresis.

In our experimental system, both the porous material and the liquid have unique properties. At the experimental temperatures (T<2K), ^{4}He is a superfluid. Since the superfluid component of ^{4}He has no viscosity, very thin films (as thin as a few atomic layers) are mobile; a normal liquid would be clamped to the substrate. As a result of the ability of a thin ^{4}He film to flow, the relaxation times in the experiment are short. Nuclepore is a thin polycarbonate membrane with a high density of nearly cylindrical pores penetrating the material at a random angle, θ, normal to the surface; $0 \leq \theta < 34°$. The pore openings have a narrow distribution of diameters with a variety of sizes available. For the experiments reported here, we used Nuclepore with nominal 300 Å diameter pore openings, a thickness of 6 μm, and a density of 6×10^8 pores/cm^2. The pores are not perfectly cylindrical, but are slightly barrel

241

shaped.[5] Because all pores have access to the membrane surface we avoid the problem of pore blocking, which occurs in other systems when large pores in the interior are shielded from the sample by smaller pores. In addition, the high density of pores leads to intersections among the pores. Recent computer simulations[6] of 300 Å Nuclepore indicate intersections occur among the pores.
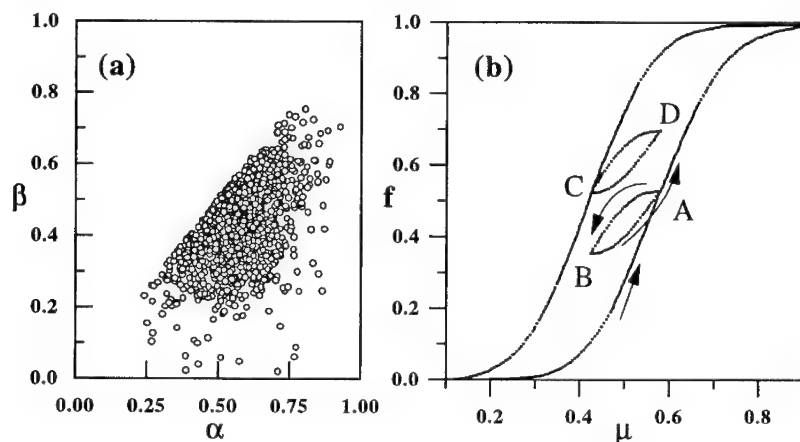
Figure 1: Preisach model demonstration of congruent subloops, (A–B–A and C–D–C).

For systems composed of a large number of *independent* hysteresis elements (e.g. pores), the overall hysteretic behavior can be explained using the Preisach model. One pore in the system will fill at a chemical potential, labeled α_0, and drain at a different chemical potential, labeled β_0, where α_0 and β_0 depend on the shape of the pore, the substrate material, and the fluid. For ^{4}He in cylindrical pores, these chemical potentials can be calculated using the framework described by Saam and Cole.[7] For a real material with a spectrum of pore shapes and sizes, the filling and draining chemical potential values of the ith pore will be labeled α_i and β_i. Using the collection of α_i, β_i pairs we can calculate the behavior of the hysteresis loop for a given evolution of the chemical potential. To illustrate the model we have created by an algorithm a set of 4000 α, β pairs shown in figure 1a. Using this, we create the filling and draining trajectory with two subloops with common endpoints, $\mu = 0.42$ and $\mu = 0.58$, displayed in figure 1b. Two features of the independent element model are demonstrated by these loops. First, each subloop returns to its parent loop at the same place where it began (points A and C in figure 1b). The second feature is the congruence of the two loops with the same chemical potential endpoints. Close examination of the two subloops, A–B–A and C–D–C reveals they are of identical shape. If an experimental system under study does not show return point memory and if two loops between the same chemical potentials are not congruent, then the hysteretic elements in the experimental system do not act independently.

EXPERIMENT

In order to study the hysteretic properties of the capillary condensation of ^{4}He into Nuclepore, we measure the amount of ^{4}He in the pores as a function of the chemical potential in the sample chamber by use of a capacitive technique. We evaporate 1000 Å Ag plates onto the top and bottom of the Nuclepore membrane. The plates do not block the pore

openings, although the Ag may modify the opening shape somewhat. When helium, which is a dielectric, enters the pores it causes a shift in the capacitance. For the 300 Å sample the measured capacitance ranges from $C_{empty} = 1410.0550$ pF for no helium in the pores to $C_{full} = 1410.7416$ pF for all of the pores capillary condensed; resolution on the capacitance measurement is $\delta C \sim 1 \times 10^{-4}$ pF.

To measure the chemical potential we take advantage of the existence of a sound mode on a superfluid ^{4}He film called third sound, which is characterized by both a temperature and thickness fluctuation. Since the velocity of third sound is related to the chemical potential in the sample chamber, measuring the velocity allows us to monitor the chemical potential. We measure[4] the time of flight, τ, required for a pulse to travel from a thermal driver to a transition edge Al bolometer. The driver, an Ag strip (300 Å thick, 150 μm wide and 2 cm long), and detector, an Al strip (same dimensions as the driver), are located on a borosilicate glass substrate separated by 0.2" and created by vacuum deposition. A third sound pulse is generated by applying a 50 μsec square voltage pulse triggered at a rate of 47 Hz to the driver. The detector is biased with a 10 μA current. The voltage across the detector is digitized and averaged for 1000 pulses. The onset of the received pulse captured by the digitizer is the measured time of flight. The time of flight is related to the chemical potential in such a way that an increasing time of flight corresponds to an increasing chemical potential[8].
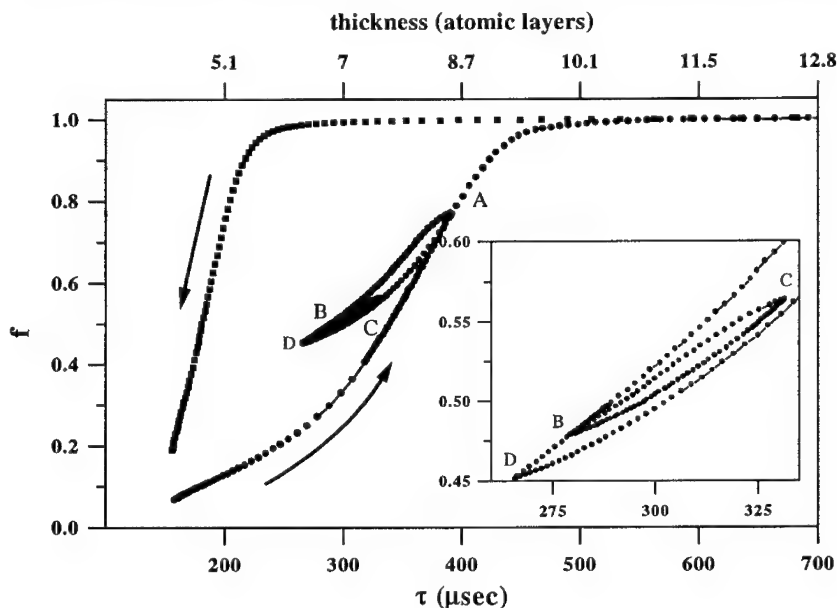
Figure 2: Experimental hysteresis loop with nested subloops for 300 Å Nuclepore.

We mount the samples on a standard cryostat insert and use a pumped bath technique with heater feedback to set the temperature at 1.370 K with a drift of ~ 3 mK during typical experimental runs. ^{4}He gas is admitted to the sample chamber at a rate which causes the thickness of the ^{4}He film on glass to increase at a rate of ~ 2 layers/hour. We remove gas at about the same rate by pumping on the sample chamber through a needle valve. Increasing the rate above a threshold causes relaxation effects; during the experiment we are careful to stay well below this threshold.

An example of the hysteretic behavior for the 300 Å Nuclepore sample is shown in figure 2.

Plotted on the vertical axis is the filling fraction,

$$f = \frac{C - C_{empty}}{C_{full} - C_{empty}},\tag{1}$$

which is approximately the fraction of the pores capillary condensed. Along the bottom axis we plot the time of flight of the third sound pulse. The corresponding thickness of a helium film on a glass substrate, calculated from the measured third sound velocity, is shown on the top axis. The lower curve (circles) is the filling trajectory. As the time of flight increases, ^{4}He condenses into the pores and the filling fraction, f, increases. At $\tau \simeq 400\mu$sec we reverse the flow of the gas and the filling fraction begins to decrease. This is the beginning of a pair of nested subloops, A–D–A and B–C–B, with the B–C–B loop magnified in figure 2 inset. Both subloops show return point memory (points A and B). After finishing the subloops, the rest of the pores in the Nuclepore fill and $f \to 1$. Upon draining (squares), the filling fraction remains near 1 until $\tau \sim 250\mu$sec, at which point it drops abruptly. This sharp corner is characteristic of desorption curves in porous media.[9] The absence of data below $\tau = 160\mu$sec (d$\sim$ 3 layers) is due to the fact that at T=1.37 K the film undergoes the Kosterlitz-Thouless[10] transition and the film becomes normal. Without superfluidity the third sound mode does not exist, and we can no longer measure the time of flight.
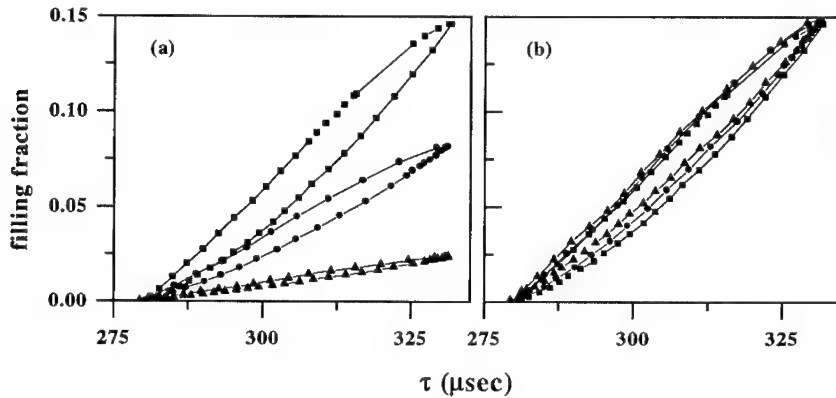
Figure 3: Subloops with left endpoints offset to overlap (a), same loops scaled so that both endpoints overlap (b).

One interesting feature of the data is the behavior of a series of subloops similar to B–C–B created so as to have the same time of flight (i.e. chemical potential) endpoints. In figure 3a we show three such subloops with endpoints $\tau_{left} = 280$ μsec and $\tau_{right} = 331$ μsec. Each subloop is performed at a different value of f_{min}, the filling fraction of the subloop's left endpoint, and then for display purposes is shifted so that the left endpoint of each subloop overlaps. For the loops shown, f_{min} =0.312, 0.476, and 0.826 for the squares, circles and triangles respectively. As f_{min} of the subloops increases, the area of the loops decreases. These loops are not congruent. When the two smaller loops are scaled (figure 3b) so that both endpoints overlap for all of the loops, we find that the resulting scaled loops are more nearly congruent with the draining curves (top of the loops) overlapping, but with the filling curves (bottom of the loops) shifted slightly for each subloop. Because these subloops between the same time of flight endpoints are not congruent, the experiment shows that the Preisach model *does not* work for this system. To make progress in the understanding of some of the experimental observations we have modified the Preisach model to account for intersections in a manner we now describe.
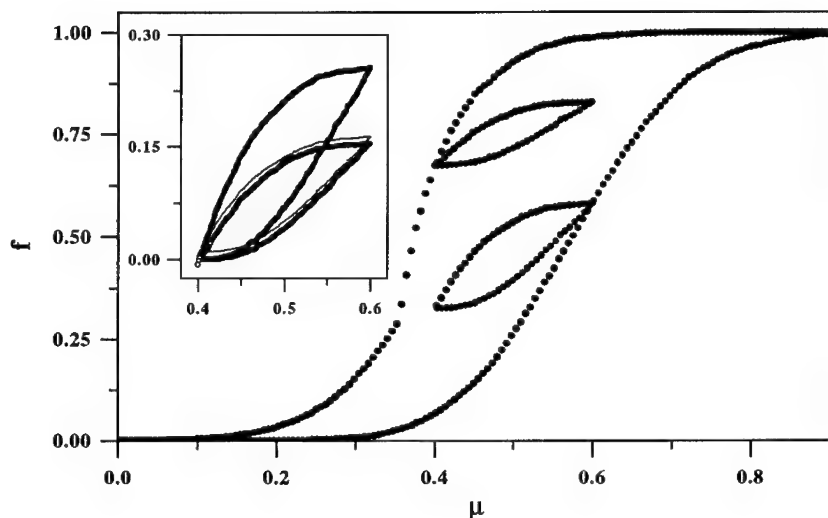
Figure 4: Results of modified Preisach model. The inset shows that *scaled* loops are congruent.

We begin with the observation that the largest loop (figure 3) occurs at the lowest filling fraction. When the pores begin to empty, additional openings due to intersections among pores become available, and as a result, the original Preisach β_i values can increase and cause some pores to drain early. The addition of more α, β pairs at a lower f enhances the size of these loops. To simulate this behavior, we have added another parameter, ϵ, to the original (α, β) where ϵ is assigned randomly from ϵ_{min} to ϵ_{max}. ϵ_i represents the degree to which intersections affect the draining of the ith pore. If $\epsilon_i > 1$, the pore behaves in the normal Preisach manner. If $\epsilon_i < 1$ then the pore drains as soon as the filling fraction drops below ϵ_i. The physical interpretation for Nuclepore is that even though all pores have access to the membrane surface, it is easier for some pores to drain through the interior interconnections; for this to occur, the surrounding connecting pores must have already emptied. Figure 4 shows the results of simulating this system with $\epsilon_{min} = 0.25$ and $\epsilon_{max} = 1.1$ using the same α_i, β_i pairs and chemical potential evolution from figure 1. The results indicate that the global draining curve is slightly sharper (the corner gets much sharper as $\epsilon_{max} \rightarrow 1^+$), and that two loops with the same chemical potential endpoints, the smaller of which occurs at a higher filling fraction, are no longer congruent. The inset to figure 4 shows the two loops with the left endpoint offset (for ease of comparison) so as to overlap. The fine line slightly offset from the smaller loop (for visibility) is the result of scaling the larger loop so that both endpoints overlap the smaller loop; this shows that scaled loops are congruent. The results of the modified Preisach model are qualitatively much closer to the actual experimental data than are the results of the original Preisach model. The scaled loops in the data seen in figure 3b are not exactly congruent, but similarities between this model and the data suggest that a change in the ability of a pore to drain may be a possible explanation of the experimental data.

CONCLUSION

We have presented hysteresis data for the capillary condensation of superfluid ^{4}He in the porous material Nuclepore. The subloops in this system show the property of return point memory and the size of subloops with the same chemical potential endpoints decreases as the filling fraction of the loop, f_{min} increases. The Preisach independent element model predicts the observed return point memory, but also predicts that subloops with the same chemical potential endpoints will be congruent. This second prediction is not seen in the data, so we conclude that due to the intersections of pores of the material, the individual hysteresis elements cannot act independently. To understand how intersections might affect the Preisach model, we have modified the model to induce draining through additional internal openings as surrounding pores drain. The results qualitatively agree with the experimental data.

ACKNOWLEDGMENTS

REFERENCES

1. F. Preisach, Z. Phys. **94**, 277 (1935).

2. D. T. Smith, K. M. Godshalk, and R. B. Hallock, Phys. Rev. B **36**, 202 (1987); K. M. Godshalk and R. B. Hallock, Phys. Rev. B **36**, 8294 (1987).

3. Nuclepore is a trademark of Costar, Cambridge, MA.

4. M. P. Lilly, P. T. Finley and R. B. Hallock, Phys. Rev. Letters **71**, 4186 (1993).

5. D. S. Cannel and F. Rondelez, Macromolecules **13**, 1599 (1980).

6. We have modeled Nuclepore using the parameters describing the pores. We calculate results for both the number of intersections/pore and the probability of percolation for the largest cluster as a function of pore size.

7. W. F. Saam and M. W. Cole, Phys. Rev. B **11**, 1086 (1975).

8. See S. J. Putterman, *Superfluid Hydrodynamics* (North-Holland, Amsterdam, 1974).

9. See, for example, J. H. Page, J. Liu, B. Abeles, H. W. Deckman, and D. A. Weitz, Phys. Rev. Letters **71**, 1216 (1993).

10. J. M. Kosterlitz and K. J. Thouless, J. Phys. C **6**, 1181 (1973).

ADSORPTION ON ROUGH SURFACES

RONALD SEGARS AND LOUIS PISCITELLE
U.S.Army Natick Research, Development and Engineering Center
Natick, MA 01760

ABSTRACT

A new model for adsorption on rough surfaces is derived.
The model predicts behavior regarding surface smoothing that
agrees well with experimental observations. Computer simulations
show the model capable of matching a wide variety of isotherm
patterns with reasonable physical constants. These simulations
also show that a significant error results in applying the
standard BET equation to adsorption data obtained on rough
surfaces.

INTRODUCTION

Since it was first published in 1938, the Brunauer, Emmett
and Teller (BET) theory of sorption equilibrium[1] has been widely
used in many fields of science. Even though the BET equation
holds only for a narrow range of vapor concentrations, it has
found extensive use in determining moisture relations in foods
and polymers[2,3,4].   It is the equation of choice for most
determinations of surface area and has recently been widely used
to determine fractal dimensions of many different materials[5,6,7,8].

One limitation of the BET theory is that it assumes the
surface on which the adsorption takes place to be perfectly
smooth. This of course is seldom the case in real systems,
especially at the molecular level, which is the length scale of
concern in physical adsorption. As molecular layers are adsorbed
onto a rough surface, one expects some of the deeper valleys to
fill in, blocking access to molecules forming the next outer
layer. Thus, the surface presented to the second forming layer
is smaller than the surface area of the adsorbent. It is
expected that succeeding adsorbed layers will likewise be smaller
than the layer previously adsorbed, at least until the surface
becomes smooth.

This smoothing behavior has been recently recognized by
other researchers, most noteworthy Fripiat and co-workers and new
theories have been presented[9,10]. In most cases these theories do
not exhibit the expected behavior in the limit of a large number
of layers and the effect of molecular size is not included. We
believe both of these limitations present serious deficiencies in
the presently available theory. A new model, which encompasses
much of the original BET work, is presented that we believe
correctly addresses both of these problems.

247

THEORY

It is obvious from their original paper that Brunauer, Emmett and Teller realized that real surfaces were not smooth and that roughness would effect the number of molecules that could be adsorbed on any given layer. They derived a general equation, Eq.(1), that contained a parameter, β, relating the number of molecules that could be adsorbed on a given layer (size of the layer) to the number of molecules that could be adsorbed in the monolayer (size of adsorbent surface).

$$\frac{V}{V_m} = \frac{CX}{1-X} \sum_{n=1}^{\infty} \beta_n \{ \frac{1-(n-1)x^n + nX^{n+1}}{1+(C-1)X-CX^{n-1}} \} . \tag{1}$$

Realizing that experimental values for β would be impossible to obtain, Brunauer, Emmett and Teller made the limiting assumptions that the surfaces were smooth and that an infinite number of layers would be adsorbed. This resulted in the well-known BET equation, Eq.(2). The more general result is found only in a footnote in the original 1938 paper.

$$\frac{V}{V_m} = (\frac{CX}{1-X}) (\frac{1}{1+(c-1)X}) . \tag{2}$$

With the advent of fractal measures for characterizing rough surfaces, it becomes possible to evaluate the parameter β. An equation relating the fractal dimension of an adsorbed surface of molecules to the fractal dimension of the adjacent adsorbed surface has been obtained. This allows use of Eq (1) and forms the basis for the new model.

Consider three levels of adsorption on a fractal surface, i, i+1 and i+2 . The surfaces have fractal dimensions of D_i, D_{i+1} and D_{i+2}, respectively, and are separated from each other at all points by a distance 2r. Surfaces i+1 and i+2 can be considered as formed by adsorbing molecules of radius r on the neighboring surface below them. Following Fripiat[9], the surface i+1 forms a 'hull' of distance 2r from surface i. The hull volume, V_i, is the volume of the molecules needed to fill this hull. For fractal surfaces, the number of molecules, N(r), of radius r needed to cover a surface scales as $(L/r)^D$ where D is the fractal dimension of the surface, and we can write the hull volume as

$$V(r) = CL^D r^{3-D} \tag{3}$$

where the constant C includes a shape factor. According to

Fripiat, this hull volume contains 'excluded' volumes and a better estimate of the layer volume, $\overline{V}(r)$, is given by the product of the surface area of the layer and the layer thickness. The area of a surface can be written as the rate of change of volume, evaluated at the surface in question, as the surface is uniformly displaced perpendicular to its plane. The volume $\overline{V}(r)$ of the i+1 layer of thickness 2r is compared to the volume of the i+1 layer determined from the i layer as r goes from 2r to 4r. After some algebra and a two-term Taylor expansion in D_i, the resulting equation for the fractal dimension of the i+1 layer is

$$D_{i+1} = (1 - Ln\frac{r}{L}) - \sqrt{(1 - Ln\frac{r}{L})^2 + 2(D_i Ln\frac{r}{L} + (D_i - 2)Ln2 - Ln(3 - D_i))}. \quad (4)$$

Equation (4) describes the smoothing that occurs as successive layers of thickness 2r are deposited on a rough surface of fractal dimension D_o. As can be seen from Eq.(4), the fractal dimension, D_{i+1}, approaches 2 as i increases.

Equation (1) requires a parameter β_i, which is the fraction of the adsorbent surface that is covered by i layers, and only i layers, of adsorbate. As discussed in Eq.(3), $N(r)$, the number of molecules of radius r that can be adsorbed on a surface of linear dimension L is given by

$$N = k(\frac{L}{r})^D. \quad (5)$$

N is a measure of the "size" of the surface and since the D's are known from Eq.(4), the size of each surface can be determined. The fractions β_i are obtained from

$$\beta_i = \frac{(\frac{L}{r})^{D_{i-1}} - (\frac{L}{r})^{D_i}}{(\frac{L}{r})^D} = (\frac{L}{r})^{D_{i-1} - D} - (\frac{L}{r})^{D_i - D} \quad (6)$$

Let the β_i's, i=1,2,3,...k represent the fraction of surface covered by each of the first k layers during which smoothing occurs and let β_n be the fraction of surface covered by n layers of adsorbate (n-k of these layers being of uniform size). Since the sum of all β's must be equal to unity, β_n is a measure of the surface of the k'th layer and is given by

$$\beta_n = (\frac{L}{r})^{D_k - D}. \quad (7)$$

All the parameters required to solve Eq.(1) except for the interaction constant, C, and the monolayer coverage V_m, which are generally obtained from adsorption data, have been determined. A computer program has been written to give the least squares fit to isotherm data where the volume adsorbed is measured versus

concentration (P/P_o). This program provides the fractal dimension of the adsorbent surface, D, the interaction constant, C, the monolayer volume, V_m, and a shape factor, K, for the best fit to a single isotherm or to several isotherms if multiple isotherm data are available.

EXPERIMENTAL

Computer-simulated data showing the fractal dimension, D, as a function of

Figure 1. Plot of Equation (4) showing the effect of molecule size (r/L) on surface smoothing.

the layer number for different sized molecules (of radius r) are shown in Fig. 1. This plot clearly shows that for a given surface roughness, D, smoothing occurs more rapidly for the larger molecules. In all cases, D approaches two as the number of layers increase. It can also be shown using either ideal (triadic Koch curve) or real surfaces that the surface area remains finite as D approaches two. This is in direct contrast to existing theories which show surface areas tending toward zero as i becomes large. This model also shows the effect of molecule size, a factor not considered in the earlier models.

To demonstrate the smoothing behavior and provide a test of Eq.(4), layers of constant thickness were drawn on a section of the triadic Koch curve. The fractal dimension of the surface of each layer was measured via the step counting method. The D-values obtained by this procedure are compared with values predicted by Eq.(4)

Figure 2. Comparison of experimental and predicted (Eq.4) D-values for the triadic Koch surface.

in Fig. 2. Agreement is reasonably good. Although not directly evident in Fig.2, the surface area of the smooth top layer is nonzero at about half the value of the initial surface.

Computer-generated isotherms were obtained for several D-values and different values of the constants C and r/L. The results of these computer simulations are shown in Fig. 3 where the volume adsorbed normalized by the volume in the monolayer is plotted against the concentration as given by the ratio of the actual pressure to the saturation pressure of the adsorbate. By choosing a value for V_m, the above isotherms can be converted to

typical experimental isotherm data where the volume of adsorbed gas is obtained as a function of the concentration, P/P_o. Analyzing these data using customary BET methods gives the standard BET values of V_m and C. The BET values of V_m divided by the correct values, i.e., the values used to generate the isotherm data, are plotted versus D in Fig. 4. The error in surface area (obtained from V_m) introduced when the BET equation is applied to rough surfaces clearly increases as D (roughness) increases.
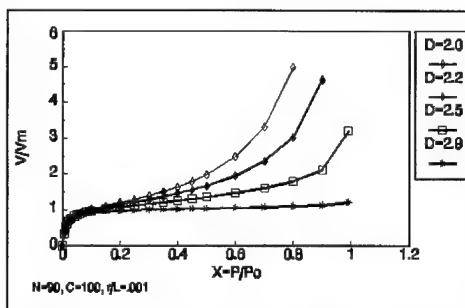
Figure 3. Typical isotherms for rough surfaces (D-values) generated by the new model.

RESULTS AND DISCUSSION

It is clear from the data in Fig. 1 that a rough adsorbent surface gradually becomes smoother as more and more layers of molecules are adsorbed. The fractal dimension of successive surfaces (increasing n) approaches two as distance from the adsorbent surface increases. It was also shown, using the ideal fractal surface of the triadic Koch curve, that the surface remains finite at a nonzero value when D=2. The observation that the surface available for further adsorption approaches a constant value is significantly different from that predicted by previous

Figure 4. Error in monolayer coverage, V_m, when standard BET plots are used on rough surfaces.

theories referenced earlier. It is also clear that the smoothing occurs more quickly, that is, in fewer layers, as the size of the molecule increases. Previous theory did not consider this effect.

The errors associated with using the standard BET equation on rough surfaces were determined as described in the previous section using the isotherms shown in Fig. 3. The values chosen for the monolayer coverage, V_m, in the model calculations are compared to the V_m values obtained from the standard linear BET plot. The ratio of the monolayer volume obtained from the linear BET plot to the monolayer volume required by the general equation is plotted in Fig. 4 vs. the fractal dimension of the rough

surface. As the fractal dimension increases, the error
introduced by the surface roughness increases significantly,
reaching 40% for moderately rough surfaces having D=2.5.
    The data in Fig.3 show that the general isotherm equation
can fit experimental isotherms that exhibit a wide range of
behaviors, ranging from the "nonwetting" behavior of super-
activated carbons to the more rapid uptake characteristic of the
standard BET equation. It remains to be shown that the
parameters that provide best fits to the various isotherms are
physically meaningful.

CONCLUSIONS

    A general isotherm equation has been found in the early
literature that with today's understanding of surface roughness
can be used to represent experimental data more accurately. The
equation requires a parameter related to the surface areas of
each layer adsorbed. A new model of rough surfaces provides
values for this parameter that computer simulations suggest are
correct and intuition dictates have the correct asymptotic
behavior. Based on the model and the computer simulations, an
estimate of the errors associated with the assumption that the
surface of the adsorbent is smooth can be made. It appears that
as the fractal dimension of the surface approaches three, the
error in monolayer coverage may exceed 50%. It is also shown
that the general isotherm equation has sufficient flexibility to
fit a wide veriety of isotherm behaviors.

REFERENCES

1. S. Brunauer, P.H. Emmett and E. Teller, J.Am.Chem.Soc. 60,309
    (1938).
2. T. Nagai and T. Yano, J. Food Sci. 55,1334 (1990).
3. S.G. Halzikiriakos and S. Avramidis, Wood Sci.and Tech.
    28,275 (1994).
4. Y. Lefebvre and C. Jolicoeur, Colloids and Surfaces 63,67
    (1992).
5. M. Jaroniec, Fuel 69,1573 (1990).
6. V.V. Kutarov and B.M. Katz, Russian J.Phy.Chem. 67,1666
    (1993).
7. R. Tsunoda, J.Colloid and Interface Sci. 152,571 (1992).
8. Y. Lefebvre, S. Lacelle and C. Jolicoeur, J.Mater.Res. 7,1888
    (1992).
9. J.J. Fripiat, L. Gatineau and H. VanDamme, Langmuir 2,562
    (1986).
10. P. Levitz, H. VanDamme and J.J. Fripiat, Langmuir 4,781
    (1988).

AN UNDERCOOLING EFFECT IN POROUS GLASS: FROM BULK TO THE CONFINED

Y. XUE*, R. MU*, D.O. HENDERSON* AND D.O. FRAZIER**
*Department of Physics, Fisk University, Nashville, TN 37208
**Space Science Laboratory, Chemistry and Polymeric Materials Branch, Marshall Space Flight Center, Huntsville, AL 35812

ABSTRACT

The Thermodynamic properties of TNT physically confined in 5, 10, and 20 nm pores were investigated by Differential Scanning Calorimetry (DSC). Depending upon the pore size and the sample condition, different aspects of the thermodynamic properties of the confined TNT were illustrated. The freezing transition of the confined TNT in 10, 20 nm pores can be triggered by excess bulk TNT on the outer surface. The sharp freezing transition of the TNT in 20 nm pores without the presence of the bulk suggests that the confined TNT maintains its interconnectivity during the transition. The confined TNT in 10 nm pores without bulk on surface failed to freeze during the cooling run up to 100 K with cooling rates ranging from 10 K/min. - 1 K/min. However, a sharp crystallization peak was observed upon heating. When the TNT is confined in 5 nm pores, the confined TNT is incapable of freezing.

INTRODUCTION

It is known that when the fluids and solids are restricted in nano-sized pores, their freezing and melting transition temperature will be depressed.[1-9] However, how and where the nucleation occurs is still not clear and sometimes controversial. In addition, how the physical confinement and surface properties modifies the confined phase structure has not been well-established. The plug model proposed by Awschalom et al.[1] predicts that the depression of freezing, melting, and solid-solid transition temperatures of the confined phases are inversely proportional to average pore size and is consistent with experimental data. This model has applied classic nucleation theory to the restricted geometry by considering the competition between the lowering the volume Gibbs free energy of the nucleus and an increase of the interfacial energy solid-wall or liquid-wall interface. In the case of freezing and melting transitions, three assumptions must be made with this model: 1) The substrate wall is more favorable a liquid-wall interface than a solid-wall interface, 2) nucleation occurs at the pore center, and 3) nucleation process is restricted in the reduced dimension. A computer simulation study[6] of molecular freezing dynamics of a Lennard-Jones liquid in a confined geometry has predicted the time development of ordering and a novel freezing mechanism. Upon cooling, the confined liquid forms layers near the pore wall and a subsequent in-plane ordering within a layer is accomplished by a sharpening of the layering in the transverse direction, which is also qualitatively supported by neutron scattering experiments of Sokol et al.[4] On the other hand, the simulation can not provide information on supercooling effects for confined fluids. Therefore, the correlation between the supercooling effect and the structure of the confined phase is lacking. The mechanism of the nucleation and growth from the supercooled and confined fluids in porous media is not understood.

The motivation of the present research is to use 2,4,6-Trinitrotoluene (TNT) as a prototype of molecular systems which exhibit large undercooling i) to illustrate how and where the solid nucleation occur in porous media when the fluid is supercooled, ii) to demonstrate how bulk TNT outside the pores alters the freezing properties of the confined, iii) to examine the percolating behavior of the confined TNT before and after freezing and melting transitions.

In the past several years, TNT has been extensively studied in our laboratory. Its thermal, optical, and TNT-metal oxide interaction properties are relatively well known. Bulk TNT exhibits supercooling effect of more than 15 K, which makes TNT a good candidate for investigating supercooling phenomena in the confined state. In addition, an understanding TNT cluster formation and cluster' thermodynamics are required the very important parameters for the design of the explosive detection devices.

EXPERIMENTAL

Gelsil porous silica glass hosts with pore diameters of d_p = 20, 10 and 5 nm were used for confining TNT. The porous silica was thoroughly cleaned according to the procedure described elsewhere[11] and the purified TNT was impregnated into the glass from molten phase.

The thermal measurements were performed with Perkin-Elmer differential scanning Calorimeter (DSC 2) and a TA Modulated DSC 2920. The measurements were made in the temperature range of 100 K - 380 K. In order to optimize the quality of the measurements, four different heating and cooling rates of 10 K/min, 5 K/min, 2 K/min, and 1 K/min were used. There were no dramatic changes observed for different ramping rates. To enhance the signal to noise ratio, 5 K/min heating and cooling rates were used throughout the measurements.

RESULTS AND DISCUSSION

Figs. 1 - 3 show the DSC thermograms of the confined TNT with and without bulk TNT on the outer surface for pore diameters of 5, 10, and 20 nm. For the TNT confined in 5 nm pores, depicted in fig. 1A, only the bulk TNT melting and freezing transitions were observed indicating that the TNT physically restricted in 5 nm pores is incapable of freezing. For the TNT confined in 10 nm pores, on the other hand, two different freezing processes were observed. The confined TNT with the bulk at outer surface in fig. 2A exhibited two melting and two freezing peaks upon the heating and cooling runs. The two broad phase transitions at lower temperature T_{mc} =323 K and T_{fc} =

Fig. 1 TNT confined in 5 nm pores with bulk on surface.

288 K are due to the melting and freezing transitions of the confined TNT, while the two sharp peaks at T_{bm} = 353 K and T_{bf} = 319 K are due to the melting and freezing transition of the bulk TNT on the outer surface. When the bulk TNT was removed, as is shown in fig. 2B, the melting curve of the confined TNT mimics the melting behavior in fig. 2A. However, upon cooling, no freezing transition was observed. In a subsequent heating run, an exothermic transition occurs at ~ 250 K before the observation of the melting transition of the confined TNT at 321 K. For TNT confined into 20 nm pores with bulk covering, as depicted in fig. 3A, two melting peaks were observed. Clearly, the broad peak at T_{cm} = 340 K is the melting transition of the confined and the sharp one at T_{bm} = 352 K is the melting transition of bulk

Fig. 2 DSC thermograms of TNT confined in 10 nm Gelsil porous glass.
A) With bulk TNT on outer surface; B) Without bulk TNT on surface.
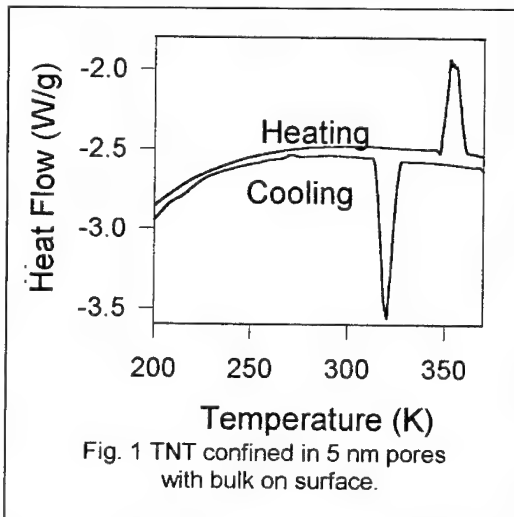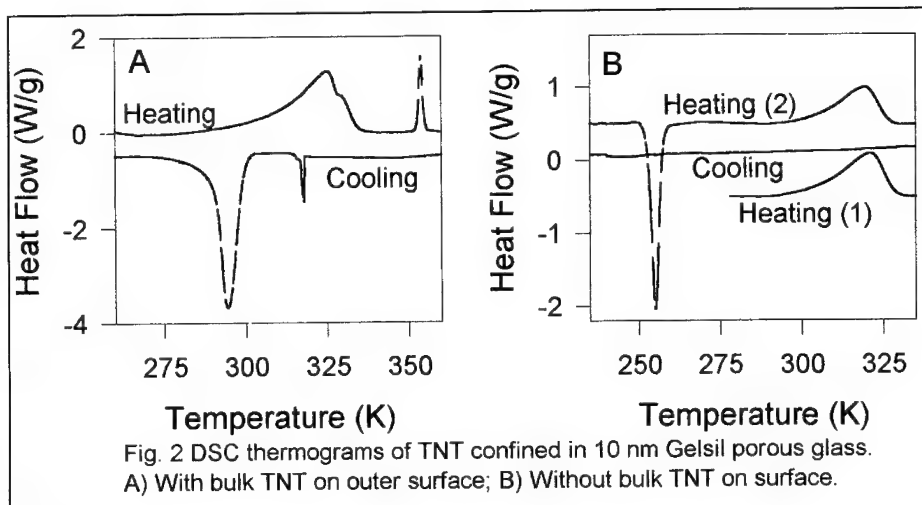
TNT. Interestingly, when the sample was cooled, only one strong and sharp transition at $T_{(b+C)f}$ = 319 K was observed suggesting that both the bulk and the confined TNT freeze at the same temperature. Fig. 3B further shows that the confined TNT without the presence of the bulk exhibits a similar broad melting transition at T_{cm} = 340 K and a sharp freezing transition at T_{cf} = 287 K rather than at 319 K.

In order to highlight our experimental observation, the present paper will only focus a few key points. A comprehensive report will be submitted to elsewhere.[10]

Fig. 3 DSC measurements of TNT confined in 20 nm porous silica glass. A)
With bulk TNT on the surface; B) Without bulk TNT on the surface.
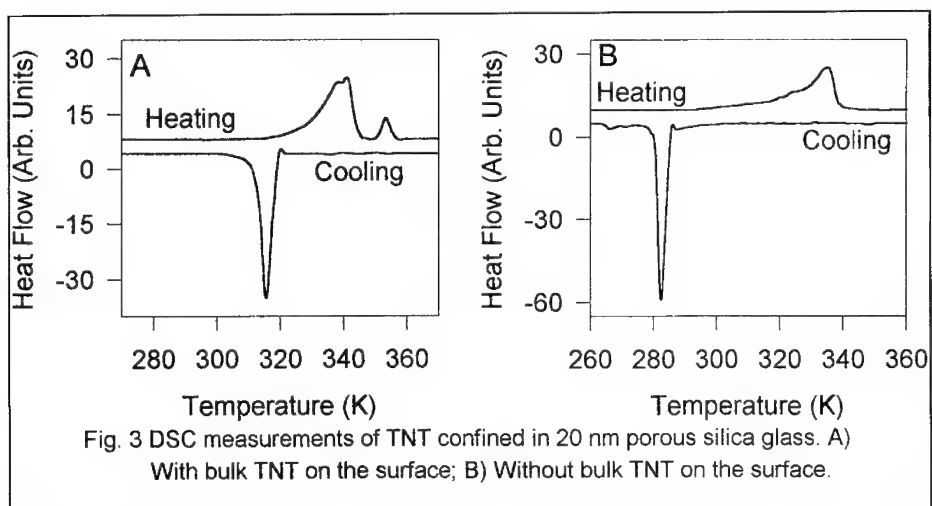
TNT Physically Confined in 5 nm Pores

As demonstrated by us[8] and others,[3,7] when a fluid or a solid is restricted in ultrasmall pores, a bulk-to-clusters crossover effect maybe observed. For TNT physically restricted in 5 nm silica pores, with and without bulk TNT covering the outer surface, only the bulk TNT melting and freezing transition resulted and no freezing and melting transitions of the confined TNT were observed indicating that the TNT in such small pores is incapable of freezing. Based upon classic thermodynamics, the freezing process consists of at least two stages; one is crystal nucleus formation and the other is crystal growth. As the system is supercooled, thermal fluctuations can lead to solid-like cluster formation. When a solid-like cluster is large enough so that its total Gibbs free energy change ($\Delta G_{total} = \Delta G_v + \Delta G_{surf}$) is equal or less than zero, the cluster becomes a critical nucleus which then can result in a freezing transition. Therefore, it may be argued that the TNT confined 5 nm pores is not able to form nuclei which may be attributed to two reasons: 1) the TNT nucleus formation requires a relatively larger cluster size with respective to smaller organic molecules, cyclohexane[2,3,7], 2) TNT is strongly adsorbed through hydrogen bonding on the silica pore surface, and therefore is not able to participate in nucleation process. This in turn reduces the number of molecules available to form a critical nucleus. Based on the orthorhombic cell parameters[14] (a = 14.991Å, b = 6.077Å, and c = 20.017 Å) of TNT single crystal, only 2 - 4 unit cells can exist across the 5 nm pores. Therefore, the TNT confined in such small pores in the cluster form rather than in a conventional solid or liquid phase. A Raman spectroscopic investigation[11] will further illustrate this point.

TNT Physically Confined in 10 and 20 nm Pores with Bulk on Outer Surface

The characteristics of the melting transitions of the confined TNT in 10 and 20 nm pore is very similar to what have been observed in other systems.[1-3] There are two melting transitions observed in both systems. The broad, lower temperature transition is due to the melting transition of the confined. For the smaller the pore sizes, the lower the melting transition becomes. The broadness of the transition can be attributed to two causes. One is due to the finite size effect (total number of the confined molecules N is finite). The other is due to the pore size distribution. However, when the systems are cooled, the TNT in 10 and 20 nm pores exhibits very different freezing behavior. For the TNT confined 10 nm pores, two freezing transitions were also observed. The sharp freezing transition at higher temperature is due to the freezing transition of the bulk, while the lower temperature transition is due to the freezing transition of the confined. For the TNT confined in 20 nm pores, on the other hand, only *one* freezing transition is observed. The total amount of the energy released during the freezing process is equal to the total intake energy of the bulk and the confined TNT during the melting transitions suggesting the bulk and the confined TNT freeze at the same time. Although the freezing transition of the fluids confined in porous media has been studied many time in the literature,[1-6] the mechanism of the freezing process is still inconsistent and is sometimes controversial. Awschalom *et al.*[1], Mu and Malhotra[2], Jackson and Mckenna[3] and Brodka *et al.*[7] suggested that the freezing transition occured in the center of the pores and the depression of the freezing temperature can be modeled with classic nucleation and growth theory in the confined dimension. Further, it is also argued that when the porous media is immersed in a pool of fluid under investigation and is undercooled. The crystallized solid phase outside the porous media can act as a seed for the confined fluid to freeze.[5,12] The degree of the solid "invasion" into the pores is dictated by the growth thermodynamics. i.e., the total Gibbs free energy change (ΔG_{total}) must be less than or equal to zero. Therefore, it is suggested that the solid invasion will be stopped at the throat[12] (the smallest pore size of the media). Based on the neutron scattering investigation of liquid O_2 and D_2 in porous vycol glass by Sokol *et al.*[4] and the computer simulation by Ma *et al.*[6], on the other hand, the results suggest that the fluids inside the pores

freeze layer by layer initiating from the wall. The results for the TNT confined 20 nm pores with bulk on the outer surface strongly suggests that the freezing of the bulk TNT indeed can trigger the freezing transition of the confined TNT inside the pores because at the bulk freezing temperature T_{bf} , all the confined TNT molecules are in the supercooled state, i.e., $T_{bf} < T_{cm}$. For the TNT in 10 nm pores, the freezing transition of the bulk TNT can trigger a small fraction of the confined TNT to freeze since only the TNT in large pores is supercooled. The TNT in small pores is still thermodynamically in favor of the liquid phase. Therefore, the freezing process is ceased by these small pores - throats. If the interconnectivity of the large pores is below their percolation threshold, then even the large pores inside of the porous glass will also remain in supercooled liquid phase. As a result, with the presence of the bulk, the confined TNT in 10 nm pores gives its own freezing transition exthothermic peak at 288 K. Therefore, the present results seem to support that 1) the solid phase can act as a seed to cause heterogeneous nucleation of the confined by penetrating into the porous media, 2) during the freezing precess, the TNT still reserves the interconnectivity - percolation, 3) nucleation occur at the center of the pores.

TNT Confined in 10 and 20 nm Pores without Bulk TNT on the Surface

As discussed in the previous paragraph, the TNT confined in 20 nm pores should render a sharp freezing transition at much lower temperature which is consistent with our experimental observation shown in fig. 3B. The sharp transition is due to the crystallization of the TNT in large pores which triggers all the confined TNT to freeze since all the confined TNT is supercooled $T_{cf} < T_{cm}$. However, when the TNT is confined in 10 nm pores, an additional feature is illustrated. That is, when the bulk TNT was removed from the outer surface of the impregnated porous glass (d_p = 10 nm), an endothermic peak was observed upon heating. When the system is cooled, no freezing transition was observed up to 100 K. This phenomena seems to be independent of cooling rate (> 1 K/min.). Upon a second heating, an endothermic and an exthothermic peak were observed. The second peak at T_{cm} = 323 K coincides with the melting transition of the confined in the first heating. Therefore, it can be argued that the peak at T = 323 K is due to the solid melting transition of the confined TNT, while the exthothermic peak at T_{cc} = 250 K is believed to be due to the crystallization. In order to understand this observation of the crystallization upon heating, two explanations may account for the present observation. In the context of the classic nucleation and growth theories,[13] for a undercooled liquid to freeze, a nucleus must first be formed. A growth process is followed. It is also known that the nucleation rate and growth rate do not follow the same temperature dependent characteristics. A freezing transition can only exist when the nucleation and growth curves overlap, which is apparently the case for bulk TNT and the confined TNT in 20 nm pores. However, as the physical dimension of the confined TNT is reduced, the confined TNT will experience two effects: one is the surface perturbation from the substrate and the other is the modification of the thermodynamic properties of the bulk. Therefore, it is possible that these two effects will shift the temperature dependent nucleation and growth curves to opposite direction. Namely, the nucleation curve shifts to a lower temperature region whereas the growth curve shifts to a higher temperature region. In fact, earlier studies[9] have suggested that the dynamic process is slowed when the fluids wet the substrate surface. As a result, the nucleation and growth curves have little overlap as the function of the temperature. Upon cooling, when the growth rate is non-zero at higher temperature, the nucleation rate is virtually zero. When the nucleation rate is non-zero, the growth rate is quenched. Therefore, no freezing transition is possible. However, during the cooling process, the nuclei have been formed. When the system is heated up to the temperature at which the growth rate is non-zero, the crystallization results. The second possible explanation is that the interfacial energy at fluid/wall interface exhibit hysteresis. That is, when the system is cooled to the crystallization temperature, say T_{cc} = 250 K, the interfacial energy σ is large.

The further cooling will result in the vitrification of the fluid TNT. The differential thermal properties, such as thermal expansion, will cause the separation of the TNT and the substrate. Therefore, the interfacial energy may be reduced. Upon heating, the reduced interfacial energy decreases the crystallization barrier which leads to the observation of crystallization at $T_{cc} = 250$ K.

CONCLUSION

Thermodynamic investigation of the TNT confined in 5, 10, 20 nm pores suggests that i) nucleation occurs at the center of the pores. ii) The freezing transition of the bulk fluid can trigger the freezing transition of the confined. iii) Although the freezing transition of the bulk has the volume reduction about 10%, the freezing transition of the confined maintains its interconnectivity. iv) When the molecular system is confined in nanopores, its nucleation and growth characteristics may also altered due to the substrate perturbation and finite size effect, which may lead to the vitrification of the confined TNT. However, the crystallization can be realized upon heating. v) For the TNT confined in pores $d_p < 5$ nm, no freezing and melting transitions were observed indicating that the confined TNT is incapable of freezing.

ACKNOWLEDGEMENT

REFERENCES

1. D.D. Awschalom, J. Warnock, Phys. Rev. B **35**, 6779 (1987); J. Warnock, D.D. Awschalom, and M.W. Shafer, Phys. Rev. Lett. **57**, 1753 (1986).
2. R. Mu and V.M. Malhotra, Phys. Rev. B **44**, 4296 (1991).
3. C.L. Jackson and G.B. Mckenna, J. Chem. Phys. **93**, 9002 (1990).
4. P.E. Sokol, W.J. Ma, K.W. Herwig, W.M. Snow, Y.Wang, J.Koplik, J.R. Banavar, Appl. Phys. Lett. **61**, 777 (1992).
5. George W. Scherer, J. Non-cryst. Solids **155**, 1 (1993).
6. W.J. Ma, J.R. Banavar, and J.Koplik, J. Chem. Phys. **97**, 485 (1992).
7. A. Brodka and T.W. Zerda, J. Chem. Phys. **97**, 5676 (1992).
8. R. Mu, F. Jin, S.H. Morgan, D.O. Henderson, and E. Silberman, J. Chem. Phys. **100**, 7749 (1994); R. Mu, D.O. Henderson, F. Jin in Determining Nanoscale Physical Properties of Materials by Microscopy and Spectroscopy, edited by M. Sarikaya, M. Isaacson, and H. K. Wickramasinghe (Mater. Res. Soc. Proc. **332**, Pittsburgh, PA, 1994)pp. XXX-000.
9. J. Klafter and J.M. Drake, Molecular Dynamics in Restricted Geometries (John Wiley & Sons, New York, 1989).
10. R. Mu, Y. Xue, D.O. Henderson, Phys. Rev. B (to be submitted).
11. R. Mu, Y. Xue, D.O. Henderson in Dynamics in Small Confining Systems, edited by J.M. Drake *et al.* (Mater. Res. Soc. Proc. XXX, Pittsburgh, PA, 1995) pp. XXX-000.
12. R. Mu "Thermodynamics and Dynamics of Physically Restricted Ultrasmall (d < 70 nm) Systems", Chap. 1, pp. 7 - 35, PhD dessertation (1992).
13. J. Zarzycki " Glasses and the Vitreous State", Cambridge Solid State Sciences Series (Cambridge University Press, 1991).
14. W.R. Carper, L.P. Davis, and M.W. Extine, J. Phys. Chem. **86**, 459 (1982).

Dielectric Relaxation in Small Confining Geometries

M. Arndt and F. Kremer

Universität Leipzig, Linnéstr. 5
04103 Leipzig, Germany

Abstract

Broadband dielectric spectroscopy (10^{-2} Hz - 10^9 Hz) is employed to study the molecular dynamics of the glassforming liquid salol (phenyl salicylate) being contained in (dielectric inactive) porous glasses with pore sizes of about 2.5 nm, 5.0 nm and 7.5 nm. Besides the bulk relaxation (I) of salol, two further dielectric loss processes are observed due to the geometrical constraint of the inner surfaces of the pores: the "interfacial relaxation" (II) and a Maxwell-Wagner polarization (III). The "interfacial relaxation" is assigned to the restricted dynamics of the molecules close to the inner surface of the pores. It shows a strong *pore-size dependence* for pores < 5 nm both in relaxation rate and dielectric strength.

1 Introduction

It is well established that glassforming liquids are strongly restricted in their molecular dynamics due to constraining geometries [1-13]. In a recent paper [14] it was shown that even in pore sizes about 10 nm the presence of large inner surfaces causes - besides the glass transition of the bulk material - a further "interfacial" relaxation. This additional relaxation is caused by molecules which are restricted in their mobility. In this paper - for the first time - the pore size dependence of the dielectrically observed molecular dynamics is studied for pores having mean diameters of 2.5 nm, 5.0 nm and 7.5 nm.

2 Experimental

Controlled porous glass (CPG) from Geltech Inc., USA was used. The glass was produced in sol-gel technology, a kind of processing in which very small collodial particles are formed in solution. In sufficient concentration these minute particles link together into chains, then into 3-D networks. The material consists of disks with a diameter of 10 mm and a thickness of 0.2 mm. The relative pore volume increases with increasing pore diameter while the inner surface decreases.
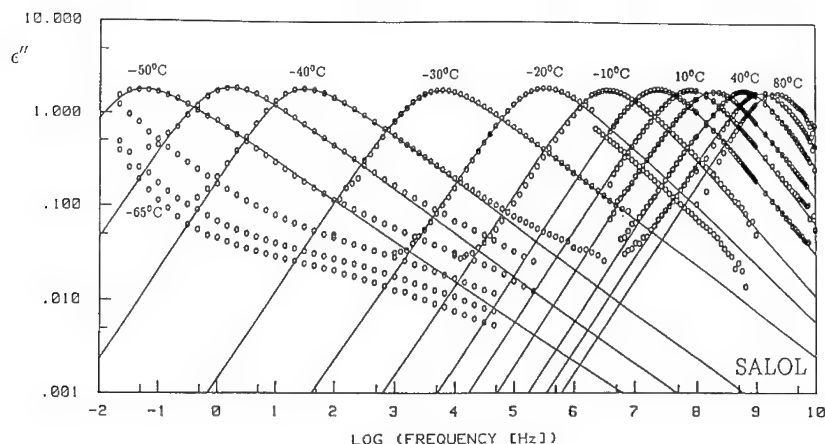
Figure 1: Relaxation loss ϵ'' vs. frequency for bulk salol at temperatures as indicated [18]

pore diameter	pore volume	surface area
[nm]	[%]	[m^2/g]
2.5	48	610
5.0	63	580
7.5	70	525

Tab. 1: Pore volume and inner surface area of the porous glasses (Geltech, Inc.)

The salol samples were obtained from Aldrich Chemical Company. After evacuating the porous glasses to 10^{-4} mbar at 570 K for 24 h to remove water and other volatile impurities, the pores were filled by capillary wetting during 48 h at 350 K. For that purpose the glassforming liquid was injected in the (closed) vacuum chamber by use of a syringe. The dielectric equipment is decribed in Refs. [14, 15].

3   Results

For bulk salol one dielectric relaxation process is observed (Fig. 1), which is assigned to the dynamic glass transition [18]. In contrast, three dielectric loss processes are observed (Fig. 2) for salol being contained in an anorganic (dielectrically inactive) porous glass. The processes are well seperated in frequency and can be described by a superposition of a conductivity contribution and three relaxation functions according to Havriliak and Negami as illustrated in Fig. 2 [16, 17]:

$$\epsilon'' = \frac{\sigma_0}{\epsilon_0} \cdot \frac{1}{\omega^s} - \sum_{k=1}^{3} \mathrm{Im}\left[\frac{\Delta\epsilon_k}{\left(1 + (i\omega\tau_k)^{\alpha_k}\right)^{\beta_k}}\right]$$

In this notation ϵ_0 is the permittivity of free space, σ_0 the DC-conductivity, $\Delta\epsilon$ the dielectric strength and τ the relaxation time. α and β describe the symmetric and asymmetric broadening of the relaxation time distribution, s is a constant between 0.5 and 1.
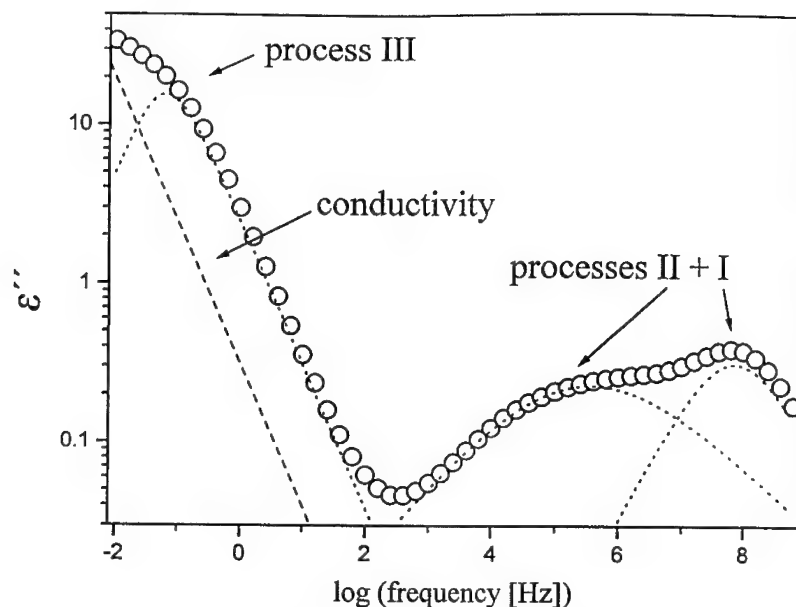
Figure 2: Dielectric loss ϵ'' vs. frequency for salol being contained in 7.5 nm pores. Temperature is 263 K. The dotted lines indicate the three superimposed loss processes. The conductivity contribution is marked as a dashed line.

Relaxation process I of salol in the porous system has at high temperatures a nearly identical temperature behaviour as bulk salol. Hence it is assigned to the relaxation of the salol molecules which behave like a free liquid. At low temperatures this process is faster than in the bulk salol, indicating that the glass transition is shifted to lower temperatures.

Temp. [K]	$\Delta\epsilon$									bulk
	2.5 nm			5.0 nm			7.5 nm			
	I	II	III	I	II	III	I	II	III	
263	0.3	2.8	-	0.4	1.8	15	1.0	1.4	24	4.3
344	-	-	16	0.5	1.4	52	-	-	88	3.5

Tab. 2: Dielectric strength for the three dielectric loss processes (–: seperation of the corresponding loss processes was not possible at this temperature) and bulk salol [18]

Relaxation process II of salol in the porous systems is decreased in its relaxation rate by about two orders of magnitude. This process is strongly broadened compared to relaxation I (see Fig. II). Relaxation II corresponds to the volume-fraction of salol in the neighbourhood of the inner surface ("interfacial relaxation" [19]). Its dielectric strength increases with decreasing pore size for diameters < 5 nm. The dielectric loss process III is not caused by a molecular relaxation but by a Maxwell-Wagner-Sillars polarization. The very high dielectric relaxation strength of this process originates from ions, which are presumably dissolved out of the porous matrix. The dielectric strength of the third process increases with increasing pore size (Fig. 3).
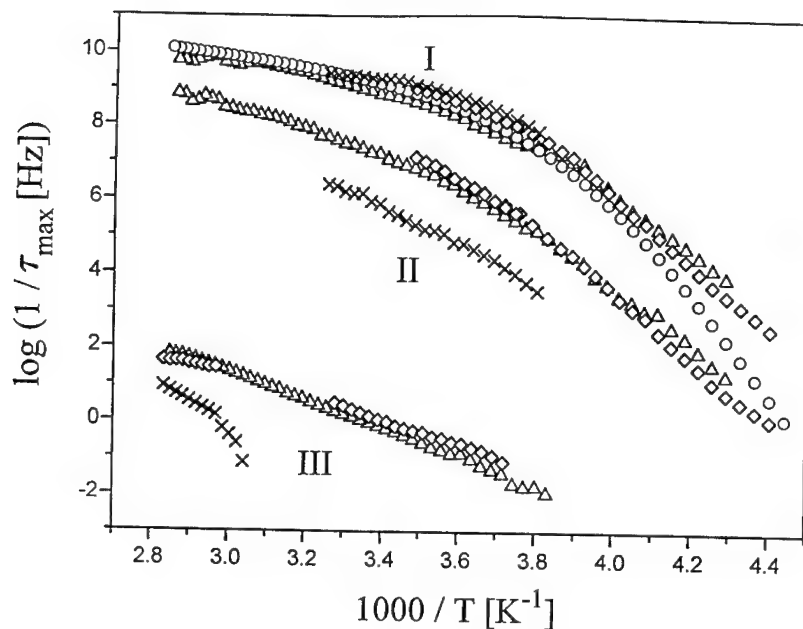
Figure 3: Relaxation time vs. inverse temperature for bulk salol (taken from Ref. [18]) and salol being contained in porous glasses of varying pore size (2.5 nm: ×, 5.0 nm: △, 7.5 nm: ◇)

The suggested interpretation of the three observed loss processes is backed (Tab. 1 and Tab. 2) by the measured dielectric strength as well: The dielectric strength of process III increases with increasing pore volume corresponding to a Maxwell-Wagner-Sillars process [20], while the dielectric strength of process II decreases. An "interfacial" relaxation process should increase with an increasing inner surface area, which is fulfilled for process II and not for process III. Assuming the thickness of the "interfacial" layer to be independent of the pore size, the dielectric strength of the bulk relaxation should decrease with decreasing pore volume as observed. The sum of the dielectric strength of processes I and II, which are interpreted as molecular relaxation processes of salol, corrected with the pore volume is comparable to the dielectric strength of bulk salol. In contrast the dielectric strength of process III does not allow a interpretation in terms of molecular relaxation.

4 Conclusions

In porous systems (pore diameter 2.5 nm, 5.0 nm and 7.5 nm) the dynamic glass transition of an organic liquid (e.g. salol) is characterized by the appearance of two relaxation processes which are well seperated in frequency. These processes correspond to the relaxation of unrestricted and constrained molecules. The assignment of the second additional process was tested by varying the pore diameter, the pore volume and the inner surface area. The relaxation of the constrained molecules shows a pronounced pore size dependence for pore sizes < 5 nm.

References

[1] J. Klafter and J. M. Drake, Molecular Dynamics in Restricted Geometries, John Wiley, New York (1989)

[2] D. Richter, A. J. Dianoux, W. Petry and J. Teixeira, Dynamics in Disordered Materials, Springer Proceedings in Physics, Vol. **38**, Springer, Berlin (1989)

[3] J. Zhang, Y. Li and J. Jonas, J. Phys. Chem. **95**, 3478 (1992)

[4] J. Zhang, G. Liu and J. Jonas, J. Chem. Phys. **96**, 3478 (1992)

[5] K. L. Ngai and G. B. Wright, Relaxation in Complex Systems, North-Holland, Amsterdam (1991)

[6] C. L. Jackson and G. B. McKenna, J. Chem. Phys. **93**, 9002 (1990)

[7] M. Urbakh and J. Klafter, J. Phys. Chem. **97**, 3344 (1993); M. Urbakh and J. Klafter in Disorder Effects on Relaxational Processes, Eds.: R. Richert and A. Blumen, Springer, Berlin (1994)

[8] E. W. Fischer, E. Donth and W. Steffen. Phys. Rev. Lett. **68**, 2344 (1992)

[9] H.-W. Hu and S. Granick, Science **258**, 1339 (1992)

[10] U. Steiner, J. Klein and L. J. Fetters, PRL **72**, 1498 (1994)

[11] S. Stampf, R. Kimmich and J. Niess, J. Appl. Phys. **75**, 529 (1994)

[12] C. L. Jackson and G. B. McKenna, J. Non-Cryst. Solids **131-133**, 221 (1992)

[13] P. Pissis et al., J. Phys. **6**, L325 (1994)

[14] J. Schller et al., Phys. Rev. Lett. **73**, 2224 (1994)

[15] F. Kremer et al., Prog. Polym. Sci. **80**, 129 (1989)

[16] S. Havriliak and S. Negami, J. Polym. Sci. Part C **14**, 99 (1966)

[17] S. Havriliak and S. Negami, S. Polymer **8**, 161 (1967)

[18] A. Hofmann, F. Kremer, E. W. Fischer and A. Schnhals, pp. 309 in Disorder Effects on Relaxational Processes, Eds.: R. Richert and A. Blumen, Springer, Berlin (1994)

[19] K. U. Kirst, F. Kremer and V. M. Litvinov, Macromolecules **26**, 975 (1993)

[20] K. W. Wagner, Arch. Elektrotech. **2**, 378 (1914)

QUENCHED MOLECULAR REORIENTATION IN CONFINEMENT

J.-P. KORB*, L. MALIER*, F. CROS*, Shu XU** and J. JONAS**
*Laboratoire de Physique de la Matière Condensée, C.N.R.S., Ecole Polytechnique, 91128 Palaiseau, France
**Department of Chemistry, School of Chemical Sciences, University of Illinois, Urbana, Illinois 61801, USA.

ABSTRACT

The effect of steric hindrance on reorientational molecular dynamics has been studied both theoretically and experimentally in well-defined geometries. We show that, even for a non-wetting fluid, confinement quenches reorientation. This is unambiguously probed by the nuclear relaxation of ^{33}S and ^{13}C in a set of calibrated porous glasses saturated with CS_2.

INTRODUCTION

Various studies have shown that topological restrictions can strongly affect molecular dynamics [1-5]. Among various experimental techniques, nuclear magnetic relaxation has proved to be a powerful tool for probing such effects. It has been shown that confinement can strongly alter both intramolecular [1, 3] and intermolecular [4, 5] relaxation rates, the former being related to reorientations, the latter, to translational diffusion. Since in non polar confined liquids, surface interactions are very weak, these effects must originate from the restricted dynamics of the confined fluid. Information on this dynamics can be obtained provided that one can answer the following theoretical questions : (i) How do the quenched molecular reorientations of a confined non polar liquid modify the nuclear relaxation ? (ii) How do the reorientational correlation times of this confined liquid depend on the average pore size ?

This paper is devoted to the dynamics of confined non-polar fluids. Our aim is two-fold : first, we address the theoretical questions and propose a model for quenched reorientations in restricted geometries and use it to evaluate the nuclear relaxation. Second, we present the application of this theory to explain the experimental pore size dependence of longitudinal relaxation rate of ^{33}S and ^{13}C of carbon disulfide (CS_2) liquid confined to a set of calibrated porous silica glasses. In these systems, the observed strong dependence of the relaxation rates on pore size clearly establishes that the reorientational motions of the fluid are modified by the geometrical confinement.

THEORY

We develop a theory of nuclear relaxation for the case of quenched molecular reorientations in geometrical confinement. Such a quench arises from the anisotropic propagation of steric hindrance due to the proximity of the confined molecules and the pore walls. We present a statistical description of the anisotropic angular orientations of a linear molecule like CS_2 in the cylindrical pore model (Fig.1a), which allows us to determine the relevant correlation times of the molecular motion. Considering the specific relaxation mechanisms, we then study the influence of such anisotropic motion on the nuclear relaxation of ^{33}S and ^{13}C.
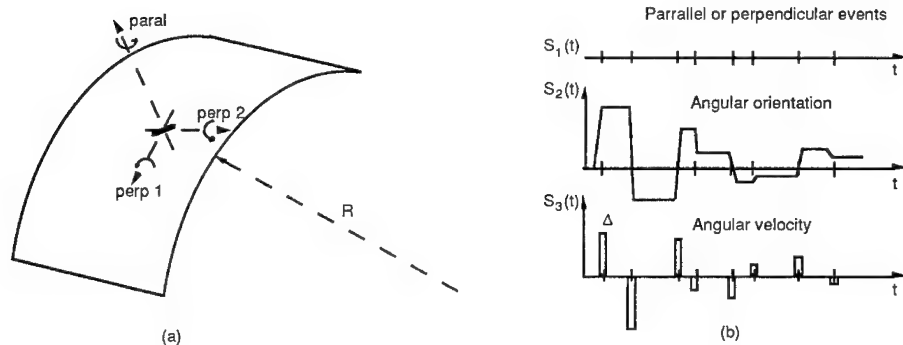
Fig. 1 a) Axes of molecular reorientations associated to the cylindrical model. b) The three random time dependent functions corresponding to the statistical model used in the text. These functions are different in the case of parallel or perpendicular events.

Description of anisotropic molecular reorientation

For modelling the reorientations of a linear molecule, we introduce the random functions $S_1(t)$ of the occurrence of reorientations and $S_2(t)$ which represents the angular orientations [6]. In the case of confined fluid, the existence of pore walls breaks isotropy and one has to distinguish the reorientations parallel ($S_{1//}$, $S_{2//}$) and perpendicular ($S_{1\perp}$, $S_{2\perp}$) to the walls. Our major hypothesis is that the parallel rotations are not hindered by the geometrical confinement : the linear molecule turns freely in the plane parallel to the pore surface. The probability per unit time that an event of $S_{1//}$ occurs is equal to the inverse of the bulk reorientational correlation time τ_b, while the probability that $n_{//}$ events occur in a time t is given by a Poisson distribution :
$P_{//}(n_{//}, t) = 1/n_{//}! \ (t/\tau_b)^{n//} \exp(-t/\tau_b)$. The expectation value for this distribution, $E(n_{//}) = t/\tau_b$, represents the average number of parallel events about the parallel axis of the cylindrical pore model (Fig. 1a). $S_{2//}(t)$ is constant between successive events of $S_{1//}$ and jumps discontinuously to an uncorrelated value when any parallel reorientation occurs (Fig. 1b). Therefore, the stationary autocorrelation function of $S_{2//}(t)$ becomes

$$\left\langle S_{2//}(t) \ S_{2//}(t+\tau) \right\rangle = \left\langle S^2_{2//} \right\rangle P_{//}(n_{//}=0, \tau) = \left\langle S^2_{2//} \right\rangle \exp\left(-\tau/\tau_b\right) \qquad (1)$$

where $<S_{2//}^2>$ represents the mean square magnitude of the parallel reorientation and $P_{//}(n_{//}=0,\tau)$ represents the probability that no parallel reorientations occur during τ. This form is generally used to describe orientation-dependent processes, and applies to a Brownian motion as well as to a jump motion [6].

For the perpendicular events $S_{1\perp}(t)$, we have to take into account the steric molecular hindrance due to the proximity of the pore surface. Basically this enhances the correlation time of the perpendicular reorientations and consequently creates the discrete occurrences of the random function $S_{1\perp}(t)$ (Fig. 1b). It results in a limitation of the total number $N_\perp$ of the perpendicular events in a given time interval {0, t}. A Poisson distribution is no longer valid for describing these bounded rotations, because the total number of events could be very large with such a distribution, and it is necessary to limit $N_\perp$. Moreover, the number of realized events $S_{1\perp}(t)$ must tend towards $S_{1//}(t)$ when the pore size increases (R->∞). These two latter

conditions are consistent with a binomial probability of having $n_\perp$ events about a perpendicular axis, in a given time t, among a total number $N_\perp$ of possible perpendicular rotations: $P_\perp(n_\perp, t)$ $= C_{N_\perp}{}^{n_\perp} p^{n_\perp}(1-p)^{N_\perp - n_\perp}$. The expectation value for this distribution is $E(n_\perp) = N_\perp p$ where p is the probability of a perpendicular rotation during a time interval $t/N_\perp$.

For an isotropic and unbounded liquid one has $E(n_\perp) \sim E(n_{//}) = t/\tau_b$, but in presence of confinement this latter relation is no more valid. Now $N_\perp$ becomes a pore size-dependent function $N_\perp(R)$ which could be written as $N_\perp(R) = E(n_{//}) f(R)$, when introducing a pore size-dependent funtion $f(R)$ which controls the number of subdivisions in the time interval $\{0, t\}$. In consequence the expectation value of the perpendicular events $S_{1\perp}$ also becomes pore size-dependent: $E(n_\perp, R) = E(n_{//}) f(R)p(R)$, where $p(R)$ is now the probability of a perpendicular rotation during a time interval of length $t/N_\perp(R)$. $S_{2\perp}(t)$ is constant between successive events of $S_{1\perp}$ and jumps discontinuously to an uncorrelated value when any perpendicular reorientation occurs during τ (Fig.1b). Therefore, the stationary autocorrelation function of $S_{2\perp}(t)$ becomes

$$\left\langle S_{2\perp}(t)\, S_{2\perp}(t+\tau) \right\rangle = \left\langle S_{2\perp}^2 \right\rangle P_\perp(n_\perp=0, \tau) = \left\langle S_{2\perp}^2 \right\rangle [1-p(R)]^{N_\perp(R)} = \left\langle S_{2\perp}^2 \right\rangle \exp[-\tau/\tau_\perp(R)], \quad (2a)$$

$$\tau_\perp(R) = \frac{-\tau_b}{f(R)\,\ln[1-p(R)]} \quad \text{with } p(R) < 1, \quad (2b)$$

introducing the pore size-dependent perpendicular reorientational correlation time $\tau_\perp(R)$.

In this model, the effect of confinement imposes some restrictions to the product $f(R)p(R)$. At the limit of an infinite medium ($R \to \infty$), $f(R) \to \infty$ and $p(R) \to 0$ while their product stays finite $f(R)p(R) \to 1$. In other words, the binomial distribution $P_\perp(n_\perp, t)$ tends to the Poisson distribution $P_{//}(n_{//}, t)$. At the other extreme, when the pore size reaches the molecular size δ, the perpendicular rotations are quenched ($f(R)p(R) \to 0$). In that latter case, it is sufficient to consider $p(R) \to 0$.

The remaining problem is now how to express the product $f(R)p(R)$ or $E(n_\perp, R)$ in a closed form. As we consider non interacting liquids, the only possibility of quenching the perpendicular rotations is the steric molecular hindrance due to the proximity of the pore walls. We model the release of this hindrance by a diffusion equation of Yukawa type describing the spatial evolution of the radial concentration $C(r, R)$ of quenched molecules, whose angular orientations are still parallel to the pore walls at a distance r to the middle of the pore :

$$\Delta C(r, R) - \chi^2 C(r, R) = 0 \quad (3)$$

where Δ is the Laplacian operator. We denote : C_0, the constant concentration of quenched molecules on the pore wall, and introduce a parameter χ (Å^{-1}) related to the extent of orientational order that describes the strength of propagation of the steric hindrance from the confining surface to the center of the pore. The solution of Eq. (3) for a cylindrical geometry is $C(r, R) = C_0 I_0(\chi r)/I_0(\chi R)$, where I_0 is the zero order modified Bessel function. It makes sense that, at the middle of the pore, the concentration of quenched molecules tends to a value smaller than C_0. For a given value of χ such concentration's value is the larger as the pore size is smaller. Now the spatial evolution of the function describing the local number of perpendicular events $S_{1\perp}$, should vary inversely to $C(r, R)$. Then the expectation value $E(n_\perp, R)$ is just the integral average of this latter local function linearly related to $C(r, R)$. From the definition : $E(n_\perp, R) = E(n_{//}) f(R)p(R)$ and according to the limiting conditions on $f(R)P(R)$ defined above, one finds :

$$f(R) = \chi R, \quad p(R) = \frac{1}{\chi R}\left[1 - \frac{2}{\chi R}\frac{I_1(\chi R)}{I_0(\chi R)}\right] \quad (4)$$

where I_1 is the first modified Bessel function.

In summary, we have proposed a model in which the anisotropic reorientation in confinement has been described quantitatively in terms of two different correlation times. The former, τ_b, deals with the reorientations parallel to the pore wall and has been considered independent of the pore size. The latter, $\tau_\perp(R)$, deals with the reorientations perpendicular to the pore wall and appears to increase significantly in presence of confinement, as shown by the expression obtained by substitution of Eq. (4) into Eq. (2b).

Nuclear relaxation through anisotropic molecular reorientation

We consider the cases where the hamiltonian $H(t)$ responsible for the relaxation is orientational dependent as it is for quadrupolar or chemical shift anisotropy relaxation through molecular reorientation. The former situation is relevant for ^{33}S while the latter occurs for ^{13}C at low temperature. As described in terms of the random functions of figure 1b, this hamiltonian is $H(t) = C[S_{2//}(t)+S_{2\perp1}(t)+S_{2\perp2}(t)]$, where C is a coupling constant. Last, the nuclear relaxation rate $1/T_1$ is simply proportional to the spectral density $J_2(\omega)$ of the autocorrelation function $G_2(\tau) = \langle H(t)H(t+\tau)\rangle$.

Assuming no correlation between the fluctuations about two different axes, one can calculate $G_2(\tau)$ and obtain the following form for $J_2(\omega)$:

$$J_2(\omega) = \frac{1}{3}\left\langle S_2^2\right\rangle\left[\tau_b + 2\,\tau_\perp(R)\right] = \left\langle S_2^2\right\rangle\tau_r(R), \tag{5}$$

in the extreme motional narrowing of the reorientation, i.e. at very low frequency $\omega\tau \ll 1$.
The overall reorientational correlation time $\tau_r(R)$ depends on the pore size through the equations (2b, 4 and 5) :

$$\tau_r(R) = \frac{\tau_b}{3}\left\{1 - \frac{2}{f(R)\,\ln[1-p(R)]}\right\} = \frac{\tau_b}{3}\left\{1 - \frac{2}{\chi\,R} \Big/ \ln\left[1-\frac{1}{\chi\,R}\left[1-\frac{2}{\chi\,R}\frac{I_1(\chi\,R)}{I_0(\chi\,R)}\right]\right]\right\} \tag{6}$$

Of course, it tends to the bulk value when $R \rightarrow \infty$.

The final step is to identify the coupling constant C, for the relaxation mechanism. In the case of quadrupolar relaxation through fast molecular tumbling, one obtains :

$$\frac{1}{T_1(R)} = \frac{2\pi^2}{5}C_Q^2\tau_r(R) \tag{7}$$

where C_Q is the quadrupole coupling constant. For relaxation of chemical shift anisotropy, one has :

$$\frac{1}{T_1(R)} = \frac{2}{15}\omega_0^2\Delta\sigma^2\,\tau_r(R). \tag{8}$$

where ω_0 is the Larmor frequency and $\Delta\sigma$ the chemical shift anisotropy.

APPLICATION TO NMR RELAXATION EXPERIMENTS FOR CS_2 CONFINED TO POROUS SILICA GLASSES

In the experimental part of this study, we show how the geometrical confinement affects the reorientational correlation times of a non polar liquid confined in calibrated porous media. More specifically, we have measured the spin-lattice relaxation rates $1/T_1$ of ^{33}S and ^{13}C of carbon disulfide (CS_2) liquid confined to a set of porous silica glasses whose pore radii range from 15 to 100 Å. CS_2 is a linear molecule with no dipole moment and it is expected not to wet the glass surface.

The very low natural abundance (0.76%) of the quadrupolar spin of ^{33}S favors the quadrupolar relaxation as the dominant mechanism of relaxation. Consequently, at any temperature, the spin-lattice relaxation rate $1/T_1$ depends on the pore size accordingly to the equation (7), with $C_Q = 13 \pm 3$ MHz [7]. The value we deduce for the bulk CS_2 at room temperature, $\tau_r(R{\to}\infty) = \tau_b = 1.77$ ps, agrees with the value of 1.62 ps obtained in recent Raman spectroscopy experiments [8]. A significant increase of $1/T_1$, hence of $\tau_r(R)$, is observed as we enhance the confinement (Fig. 2) and this is also supported by the Raman spectroscopy results. Equations (6) and (7) are used to fit the experimental data for a cylindrical geometry of pores with a single parameter χ. Its value is 0.081Å^{-1} at 293 K and varies with temperature (Fig.2). At lower temperature the precision on χ decreases due to experimental constraints.
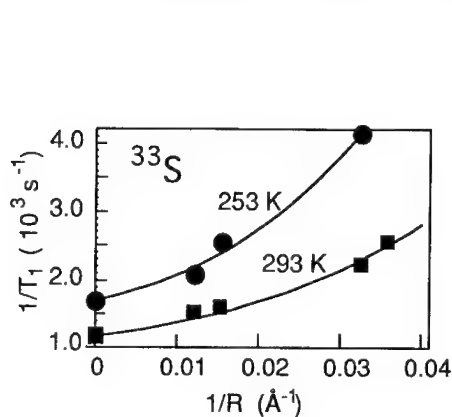
Fig. 2
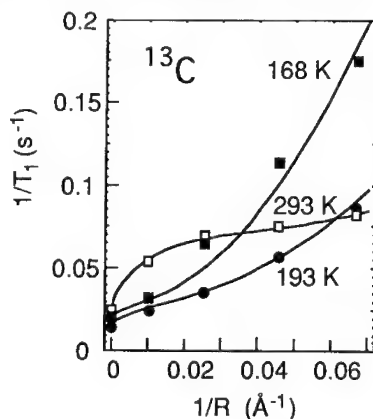
Fig. 3

Best fits (solid lines) of the pore size dependencies of spin lattice relaxation rates of ^{33}C (Fig. 2) and ^{13}C (Fig. 3) of CS_2 in set of calibrated porous silica glasses at different temperatures.

For ^{13}C, the characteristic temperature dependence of $1/T_1$ allows to separate contributions from the spin rotation and from the chemical shift anisotropy mechanisms [9]. For temperatures below 223 K, the relaxation is dominated by the chemical shift anisotropy modulated by molecular reorientation and the equation (8) is applicable, with $\Delta\sigma = 438 \pm 44$ ppm [9]. However, around the room temperature the spin rotation dominates the relaxation and the relevant random function becomes the angular velocity $S_3(t)$ [Fig. 1b] which has a different correlation function $G_3(t)$. For a given temperature, the overall $1/T_1$ is a linear combination of chemical shift anisotropy [equation (8)] and spin rotation contributions. The figure (3) shows that this accounts for the observed behavior and that the specific pore size dependencies of $1/T_1$ allows also to separate the contribution of the spin rotation and the chemical shift anisotropy.

One notes that the value $\chi = 0.084\text{Å}^{-1}$ found for ^{13}C at 293 K (Fig. 3) is quite similar to the corresponding one of ^{33}S.

Finally, the figure 4 presents the temperature dependence of the parameter χ for ^{13}C and ^{33}S, with their respective error bars. One can see that this parameter decreases with the temperature as it is expected since χ is the inverse of the propagation length of the steric hindrance due to ordering effects near the pore walls. The Arrhenius-type plot yields $E_a = 0.41$ kcal/mole. This value is not sufficiently large in comparison to kT (~0.3 to 0.5 kcal/mole) to suggest an activated energy. The precise meaning of E_a and its relation to rotational constraints are still not clear since the activation energy obtained in bulk CS_2 from ^{13}C relaxation results gives 1.5 kcal/mole.
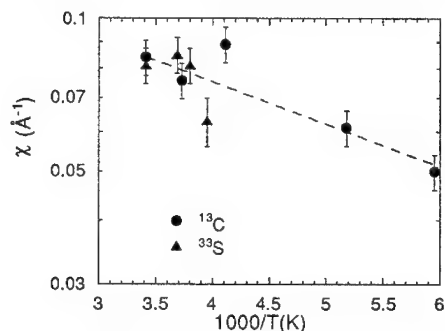
Fig. 4. Semilogarithmic plot of temperature dependence of $\chi(T)$. We have plotted on the same graph the values obtained for ^{33}S (Fig. 2) and ^{13}C (Fig. 3).

CONCLUSION

We have presented a theory of rotational molecular dynamics which, for the first time, accounts for the confinement effects on non wetting fluids. It predicts the increase of the reorientational correlation time when the pore size is decreased. Experimental nuclear relaxation data on liquid CS_2, in a set of calibrated porous silica glasses, support this prediction. This theory should also apply to other reorientation sensitive techniques where it can be helpful to probe how do topological constraints arise in the confined liquid.

ACKNOWLEDGEMENT

References

[1] G. Liu, M. Mackowiak, Y. Li and J. Jonas, J. Chem. Phys. **94**, 239 (1991).
[2] J. Warnock, D.D. Awschalom and M.W. Shafer, Phys. Rev. B**34**, 475 (1986).
[3] G. Liu, Y. Li and J. Jonas, J. Chem. Phys. **95**, 6892 (1991).
[4] J.-P. Korb, Shu Xu and J. Jonas, J. Chem. Phys. **98**, 2411 (1993).
[5] J.-P. Korb, A. Delville, Shu Xu, G. Demeulenaere, P. Costa and J. Jonas, J. Chem. Phys. **101**, 7074 (1994).
[6] R.J.C. Brown, H.S. Gutowsky and K. Shimamura, J. Chem. Phys. **38**, 76 (1963).
[7] A. Lowenstein and D. Igner, J. Phys. Chem. **92**, 2124 (1988).
[8] S.L. Wallen, Phd Thesis, University of Illinois (1994).
[9] H.W. Spiess, D. Schweitzer, U. Haeberlen and K.H. Hausser, J. Magn. Reson. **5**, 101 (1971).

OPTIMIZATION OF DIFFUSIVE TRANSPORT TO IRREGULAR SURFACES WITH LOW STICKING PROBABILITY

PETER PFEIFER*,** AND BERNARD SAPOVAL**
*Department of Physics and Astronomy, University of Missouri, Columbia, MO 65211
**Laboratoire de Physique de la Matière Condensée, Ecole Polytechnique, F-91128 Palaiseau, France

ABSTRACT

We study steady-state diffusion to an irregular membrane or catalyst surface which "annihilates" arriving particles by transfer across the membrane or chemical reaction at the surface. For diffusion in two dimensions and an arbitrary given surface, we present a simple algorithm to compute the total flux across the surface (annihilation rate) when the permeability of the membrane or reaction probability at the surface is small. The resulting flux increases with increasing surface irregularity and depends nonlinearly on the transport parameters and on the surface area. It predicts an optimal temperature, dependent on the surface irregularity, at which the flux is maximal. We illustrate this for self-similar surfaces, in which case the flux is a power law of the transport parameters and is governed by the fractal dimension of the surface.

INTRODUCTION

Considerable progress has been made recently in the understanding of transport processes in confined geometries. One process that has been studied from many different angles is mass and charge transport from a source outside the system to a geometrically irregular surface which acts as a sink (see, e.g, [1-11]). In this paper, we address the following specific case:

(i) The transport is mass transport by diffusion, with diffusion constant D, considered under steady-state conditions.
(ii) The surface is a membrane or catalyst which "annihilates" arriving particles by transfer across the membrane or chemical reaction at the surface.
(iii) The permeability of the membrane, W, or the sticking probability (reaction probability) at the surface, σ, is small (nonideal sink);
(iv) The source is near the outer boundary (circumscribing sphere) of the system, so that diffusion is confined to the pore space of the system.
(v) At the source, the concentration of the diffusing species is maintained at the constant value c_0 (number of particles per unit volume), for example by rapid transverse hydrodynamic flow.

Our goal is to compute the total flux across the surface (annihilation rate), Φ_T, as a function of D, W (or σ), c_0, and the surface geometry; and to identify conditions under which the flux is maximal (optimal transport). Clearly, the scenario (i)-(v) occurs in a wide variety of applications, and the question of optimal transport is of great practical interest. Physically, the question is to what extent the gain in flux, if one increases the surface area by making the surface more convoluted, is offset by the increase of screened, inaccessible surface regions. The two opposing effects may be described as the competition between the *transfer across the surface*, controlled by W, and the *access to the surface*, controlled by D. An increase in surface area by making the surface more convoluted increases the transfer across the surface, but reduces the access to the surface.

For fractal and other models for irregular surfaces, the problem of computing the flux under the conditions (i)-(v) has been studied previously by scaling arguments, random-walk simulations, and numerical solutions of the diffusion equation [4, 7]. Here we present a solution of the problem, for diffusion in two dimensions, that does not require to solve any differential equation, is applicable to arbitrary surface geometries, and recovers the results of the earlier case studies. The solution is obtained by performing a certain "rope walk" along the surface, translating into the diffusion context a recent method to compute the electrochemical response of an arbitrary irregular

electrode [11]. The derivation of the rope-walk algorithm given here is entirely in terms of the diffusion problem. A more detailed presentation is forthcoming [12].

THE ROPE-WALK ALGORITHM

We use the following terminology and notation. Surface, volume, area, and concentration in d dimensions are the d-dimensional counterparts of the respective notions in d = 3. The permeability W is the number of particles annihilated per unit time, surface area, and concentration at the surface (regardless of the annihilation mechanism). Thus for all d, the ratio D/W is a length. In a lattice description, with lattice constant ℓ, hopping time τ, and sticking probability σ, the diffusion constant and the permeability are given by

$$D = \ell^2/(2d\tau) \tag{1}$$
$$W = \sigma\ell/(2d\tau) \tag{2}$$

[4]. Equations (1, 2) will be used to convert results involving the macroscopic transport parameters D and W (continuum description) into results in terms of the microscopic parameters ℓ, σ, τ (discretized description). In particular, for fixed ℓ and τ, small values of W correspond to small values of σ.

The method to compute the flux Φ_T in d = 2 is as follows. We assume the surface to be given on a lattice, with lattice constant ℓ. In a high-resolution extreme, ℓ may be a few Å. The number of surface sites and the diameter of the surface (largest distance between any two sites on the surface) are denoted by N and L, respectively. We select an initial site x_0 on the surface (one of the endpoints if the surface is not closed) and walk $D/(W\ell)$ steps *along* the surface, ending up at site x_1 on the surface. This amounts to tracing out the surface with a rope of length D/W, starting at x_0 and following all the irregularities until we run out of rope at x_1. We call the walk from x_0 to x_1 a rope walk and denote the visited surface segment by $[x_0, x_1]$. The quantity of interest is the diameter L_1 of the segment $[x_0, x_1]$. From x_1, we walk another $D/(W\ell)$ steps along the surface, ending up at site x_2, and determine the diameter L_2 of the segment $[x_1, x_2]$; and so on. The walk is continued until we are back at x_0, or reach the other end if the surface is not closed. If we come to a branch point on the surface, we stay on the side of the diffusion space. This makes the walks unique and covers the surface with ropes of length D/W. The i-th rope generates a local yardstick of length L_i (i = 1, ..., n), the number of ropes being n = NℓW/D. The condition

$$\ell \leq D/W \leq N\ell \tag{3}$$

ensures that the number of steps in each rope walk is at least one and at most N. The limiting case D/W = ℓ corresponds to $\sigma = 1$ in Eq. (2), and the case D/W = Nℓ corresponds to $\sigma = 1/N$. The only thing we need from the rope walks is the average yardstick length, $\langle L_i \rangle$. The flux Φ_T is then obtained by

$$\Phi_T = Dc_0 L/\langle L_i \rangle \tag{4a}$$
$$= Dc_0 L/\{\ell f(D/(W\ell))\}, \tag{4b}$$

where f(s) is the average yardstick length measured in units of ℓ, for rope walks of s steps, $1 \leq s \leq N$. We call f(s) the structure function of the surface. It depends only on the geometry of the surface and has the elementary properties

$$1 \leq f(s) \leq s \tag{5a}$$
$$f(s) \leq f(s') \quad \text{for } s \leq s' \tag{5b}$$
$$f(N) = L/\ell. \tag{5c}$$

Property (5a) expresses that the yardstick length cannot be smaller than the lattice constant and cannot exceed the rope length; (5b) states that the yardstick length increases with increasing rope length; and (5c) says that the yardstick length equals the diameter of the surface if the surface can be covered by a single rope.

Equations (4a, b) are the final result of the algorithm, subject to the condition (3). They reduce the computation of the flux to the simple task of determining $\langle L_i \rangle$ or, equivalently, the function $f(s)$. Once $f(s)$ is known, (4b) yields the flux for all possible combinations of D and W. Before we proceed to derive the algorithm, it is useful to discuss a few properties of (4). The flux depends linearly on the concentration c_0 at the source, as it must be for a linear response. From (4) and (5a), it follows that

$$WLc_0 \leq \Phi_T \leq (DL/\ell)c_0. \tag{6}$$

The bounds (6) are easy to interpret. For fixed ℓ, L, D, the flux is lowest when the surface is flat (smallest number of surface sites). In this case, every surface site is close to the source and the flux is limited by the transfer across the surface, i.e., by how many particles can cross the surface. This gives the lower bound in (6). The flux is highest when the permeability is maximal, in which case the flux is limited by the access to the surface and depends on the surface geometry only through L (screening; see also below). This gives the upper bound in (6). Maximal permeability means $\sigma = 1$, which translates into $W = D/\ell$ by Eqs. (1, 2). Thus, the upper and lower bound in (6) coincide if the permeability is maximal; but they leave room for a wide range of flux values—with a nonlinear dependence on D and W—if the permeability is small.

In general, the flux computed from (4) depends on the lattice constant ℓ because the rope walks do so. In a lattice description as in Eqs. (1, 2), this is natural. In a continuum description, as for example when experimental values for D and W are used, this dependence may seem surprising. The reason is the following. In the continuum framework, the permeability describes the transfer across a smooth, locally flat surface. Hence, in order to treat the transfer across a surface with arbitrary shape, we have to decompose the surface into locally flat segments, which is precisely what the lattice in the rope-walk algorithm does. The lattice treats the surface as flat at length scales below ℓ and allows an arbitrary shape at scales above ℓ. If the surface is smooth at scales between ℓ and some larger length ℓ', the flux in (4) is independent of ℓ (an example is the lower bound in (6)). If the surface is irregular at scales above ℓ, the dependence of (4) on ℓ is an essential part of the dependence on surface geometry. Finally, there is also a dependence on ℓ if the surface has maximal permeability (upper bound in (6)). Its origin is the discrete nature of the transfer process at the microscopic level, which generates a physical upper limit for W. In the continuum theory, there is no such limit, i.e., the maximal value is $W = \infty$. Thus, the maximum-permeability case $\Phi_T = (DL/\ell)c_0$ in (6) is the physical version of the infinite-permeability case $\Phi_T = \infty$ in the continuum theory, and the latter may be viewed as the limit $\ell \to 0$ of the former.

DERIVATION OF THE ALGORITHM

The trajectory of a diffusing particle that is successfully annihilated at an irregular surface can be divided into two parts. First, the particle has to reach the surface. When the permeability is low, the particle is not annihilated on first contact with the surface but has to revisit the surface many times before it is annihilated. So in the second part, the particle explores the neighborhood of the site of first contact. The number of different surface sites visited during this exploration can be estimated as follows. During time t, the particle explores a region of diameter $\sqrt{Dt}$ near the surface and a surface segment consisting of s sites. The number s is determined by the condition that the annihilation probability at time t equals 1, i.e., that

$$Ws\ell t \frac{1}{(\sqrt{Dt})^2} = 1, \tag{7}$$

where $s\ell$ is the area of the segment and $(\sqrt{Dt})^{-2}$ is the concentration at time t, both in $d = 2$. The expression for the concentration follows from the fact that a random walk in $d = 2$ visits most sites in the exploration region essentially once (as opposed to infinitely many times in $d = 1$ and zero times in $d \geq 3$). Condition (7) gives

$$s = D/(W\ell). \tag{8}$$

It follows from (8) that the surface segment visited prior to annihilation equals the segment traced out by a rope walk, say the i-th one, and thus has diameter L_i. By construction, the segment annihilates a particle within distance L_i from the segment with *probability one*. That is, regardless of how small the local concentration near the segment is, the segment acts like surface with *maximal permeability*. We therefore can decompose the whole surface into segments $i = 1, ..., n$ and treat each segment as a site of a coarse-grained surface with maximal permeability and lattice constant $\langle L_i \rangle$. The diameter of the coarse-grained surface is still L, of course.

Now for an arbitrary connected surface in $d = 2$ with maximal permeability, Makarov's theorem [1] states that the active zone (also called exposed or unscreened sites), i.e., the smallest set of surface sites on which an incoming particle lands with probability one, always has fractal dimension 1 and therefore area αL, where α is a constant of order one. This is the familiar screening result that the flux across an arbitrary surface with diameter L is the same as the flux across a flat surface with area αL, for maximal W and fixed D, c_0. It leads to the following expression for the flux Φ_T:

Φ_T := flux across the original surface (arbitrary W, diameter L, lattice constant ℓ)
  = flux across the coarse-grained surface (maximal W, diameter L, lattice constant $\langle L_i \rangle$)
  = flux across a flat surface (maximal W, area αL, lattice constant $\langle L_i \rangle$)
  = $(D/\langle L_i \rangle)\alpha L c_0$,   (9)

where in the last line we have used that the maximal permeability on a lattice with lattice constant $\langle L_i \rangle$ is equal to $D/\langle L_i \rangle$, by Eqs. (1, 2) with $\sigma = 1$. Upon setting $\alpha = 1$, one obtains the result of the rope-walk algorithm, Eq. (4a). Clearly, if the permeability of the original surface is maximal, then the rope length and the coarse-graining lengths L_i are all equal to ℓ, in which case (9) reduces to Makarov's theorem or, equivalently, to the upper bound in (6).

The decomposition of the surface into segments of diameter L_i may be analyzed also quite differently, without mapping the diffusion at length scales below L_i onto a coarse-grained lattice. One singles out those segments that belong to the active zone of the surface, i.e., that participate effectively in the annihilation. By definition, each active segment is *fully accessible* to incoming diffusing particles, i.e., acts like a *flat surface segment* of s sites. This gives

$$\Phi_T = n^* W s \ell c_0,$$ (10)

where $s\ell$ is the area of the equivalent flat segment and n^* is the number of active segments. To determine n^*, we observe that at length scales larger than $\langle L_i \rangle$ the active zone looks like the active zone of a surface with maximal permeability and lattice constant $\langle L_i \rangle$. Indeed, the annihilation probability of a whole segment is equal to the landing probability on a surface site with lattice constant $\langle L_i \rangle$. Hence by Makarov's theorem, we have

$$n^*\langle L_i \rangle = \alpha L.$$ (11)

Substitution of (8) and (11) into (10) yields again (9). Thus, the two conceptually different ways of analyzing the segments visited prior to annihilation lead to one and the same result.

EXAMPLE: FRACTAL SURFACES

As an illustration of the rope-walk algorithm, we consider a self-similar surface with fractal dimension D_f $(1 \leq D_f \leq 2)$ and inner cutoff length ℓ. We assume the surface to be smooth at scales below ℓ and assume the outer cutoff to be equal to the surface diameter L. Under these hypotheses, the yardstick lengths L_i are essentially all equal and the structure function is given by

$$f(s) = s^{1/D_f} \quad \text{for } 1 \leq s \leq (L/\ell)^{D_f}.$$ (12)

The power law (12) is the mass-radius relation, where mass counts the s steps of a rope walk and the radius is the radius of the walk. We note that (12) satisfies all properties (5a-c) of a structure function. Substitution of (12) into (4b) yields

$$\Phi_T = Dc_0(W\ell/D)^{1/D_f}L/\ell \qquad \text{for } 1 \le D/(W\ell) \le (L/\ell)^{D_f}, \qquad (13a)$$

$$= \frac{p_0}{4\tau}(\sigma N)^{1/D_f} \qquad \text{for } \sigma N \ge 1. \qquad (13b)$$

Equation (13b) gives the flux in terms of the continuum parameters. Since the surface is irregular at length scales above ℓ, the dependence on ℓ is an essential part of the dependence on surface geometry. Equation (13b) expresses the flux in terms of the lattice parameters, where N is the number of sites of the fractal surface and p_0 is the number of particles per site at the source. Equations (13a, b) fully agree with numerical calculations and scaling arguments for the flux across self-similar surfaces [4, 7].

The result (13b) shows that for fixed surface geometry the flux increases with increasing diffusion coefficient as $D^{(D_f-1)/D_f}$ and with increasing permeability as W^{1/D_f}. Both dependences are manifestly nonlinear. For $D_f = 1$, the dependence on D and ℓ disappears, in agreement with the earlier remark that on a flat surface the flux-limiting factor is W and that the flux is ℓ-independent if the surface is smooth at scales above ℓ. So (13a) reproduces the flat-surface result $\Phi_T = WLc_0$, as it should be, in the limit $D_f = 1$.

Alternatively, one may keep the transport parameters fixed and consider the flux as a function of surface geometry. For example, (13a) predicts that the flux increases as $\ell^{-(D_f-1)/D_f}$ with decreasing inner cutoff ℓ. This increase may be attributed to the increase in surface area as ℓ gets smaller; but the comparison with the surface area, which grows as $\ell^{-(D_f-1)}$, shows that the flux actually increases much more slowly than the surface area. The lattice result (13b) puts this nonlinear dependence on the surface area (number of surface sites) into evidence. Perhaps the most important way in which the geometry controls the flux enters via the fractal dimension. Equation (13a) shows that the flux strongly increases with increasing D_f (at constant ℓ and L), if the permeability is low ($W \ll D/\ell$). This is in sharp contrast to the case of maximal permeability ($W = D/\ell$), where (13a) yields $\Phi_T = (DL/\ell)c_0$ without any dependence on D_f, in agreement with Makarov's theorem. Thus, (13a) puts on quantitative grounds the expectation that the flux should increase with increasing surface irregularity (all other parameters kept fixed), but only if the permeability is low.

It is interesting to note that the lattice result (13b) exhibits neither a flux increase with increasing D_f if $\sigma \ll 1$ (low permeability), nor a D_f-independent flux if $\sigma = 1$ (maximal permeability). In fact, the flux in (13b) *decreases* with increasing D_f for all values of σ. The reason is simple: if we increase D_f while keeping the number of surface sites constant, as we do in (13b), the diameter L of the surface shrinks, which according to (13a) reduces the flux. This illustrates the important point, familiar from other optimization problems on fractal surfaces [2], that optimization with respect to D_f at constant L, as in (13a), and optimization with respect to D_f at constant N, as in (13b), leads to vastly different results.

OPTIMIZATION WITH RESPECT TO TEMPERATURE

The preceding section shows that there exists a variety of ways in which one may wish to optimize the flux; that the rope-walk algorithm answers them all; and that the results are unexpectedly nonlinear in most variables. Clearly, the analysis presented in terms of fractal surfaces can be carried over to any other surface geometry. The only thing needed is the corresponding structure function f(s).

A special case of such optimization is the question whether, for a given diffusing species and a given annihilation mechanism, there exists a temperature at which the flux is a maximum. The question of temperature dependence is also of interest from the viewpoint of obtaining the function f(s) from experimental measurements. Indeed, if one measures the flux as a function of D and/or W, then (4b) yields f(s) over an according range of s values, where D and W may be varied by varying the temperature.

To explore the temperature dependence of the flux, we consider again a fractal surface and choose the example of a chemical reaction at the surface, in which gas molecules diffuse to the surface and stick by activated or nonactivated chemisorption. The hopping time then is the collision time in kinetic gas theory and the sticking probability depends on the energy difference E between the barrier to chemisorption and the barrier to desorption [13], giving rise to the following

dependences on temperature T:

$$\tau = 1/(a\sqrt{kT}) \tag{14}$$
$$\sigma = \exp(-E/(kT)) \qquad \text{for activated chemisorption } (E > 0) \tag{15}$$
$$\sigma = [1 + b\exp(E/(kT))]^{-1} \qquad \text{for nonactivated chemisorption } (E < 0), \tag{16}$$

where a, b are positive constants and k is Boltzmann's constant. For activated chemisorption, the sticking probability increases with increasing temperature; for nonactivated chemisorption, it decreases. Substitution of (14-16) into (1, 2, 13a) gives

$$\Phi_T = (1/4)\ell Lc_0 a\sqrt{kT} \exp(-E/(D_f kT)) \qquad \text{(activated)} \tag{17}$$
$$\Phi_T = (1/4)\ell Lc_0 a\sqrt{kT} [1 + b\exp(E/(kT))]^{-1/D_f} \quad \text{(nonactivated).} \tag{18}$$

Thus, in the activated case, the flux always increases with increasing T and the optimal temperature is formally infinite. It shows that an increase in D_f has the same effect as a lowering of the energy barrier E or, equivalently, an increase in temperature. For example, by going from a flat to a maximally irregular, 2-dimensional surface at temperature T, one can mimick a temperature of 2T. We think this is quite remarkable. In the nonactivated case, the flux first increases, but then drops with increasing T, if b is sufficiently large. It predicts a finite optimal temperature T*, given by

$$b^{-1}e^{-E/(kT^*)} + 1 = -2E/(D_f kT^*). \tag{19}$$

It is easy to see from (19) that T* decreases with increasing D_f (e.g., $T^* \sim -2E/(D_f k)$ for $b \to \infty$). This is the counterpart of running a high-flux reaction at low temperature on an irregular surface in the activated case. The examples demonstrate that it is possible to design optimal surface geometries and reaction temperatures with very little computational effort and that the results can equally be used to elucidate unknown surface geometries from flux vs. temperature measurements.

ACKNOWLEDGEMENTS

REFERENCES

[1] N.G. Makarov, Proc. London Math. Soc. **51**, 369 (1985).
[2] P. Pfeifer, in *Preparative Chemistry Using Supported Reagents,* edited by P. Laszlo (Academic Press, New York, 1987), p. 13.
[3] B. Sapoval, J.-N. Chazalviel, and J. Peyrière, Phys. Rev. A **38**, 5867 (1988).
[4] P. Meakin and B. Sapoval, Phys. Rev. A **43**, 2993 (1991); A **46**, 1022 (1992).
[5] R.C. Ball, in *Surface Disordering: Growth, Roughening, and Phase Transitions,* edited by R. Jullien, J. Kertész, P. Meakin, and D.E. Wolf (Nova Science Publishers, Commack, NY, 1992), p. 277.
[6] T.C. Halsey and M. Leibig, Ann. Phys. **219**, 109 (1992); M. Leibig and T.C. Halsey, J. Electroanal. Chem. **358**, 77 (1993).
[7] R. Gutfraind and B. Sapoval, J. Phys. I France **3**, 1801 (1993).
[8] P. Levitz, J. Phys. Chem. **97**, 3813 (1993).
[9] H. Ruiz-Estrada, R. Blender, and W. Dieterich, J. Phys.: Condens. Matter **6**, 10509 (1994).
[10] B. Sapoval, in: *Fractals in Biology and Medicine,* edited by T.F. Nonnenmacher, G.A. Losa, and E.R. Weibel (Birkhäuser-Verlag, Basel, 1994), p. 241.
[11] B. Sapoval, Phys. Rev. Lett. **73**, 3314 (1994).
[12] P. Pfeifer and B. Sapoval, to be published.
[13] G. Ehrlich, in *Chemistry and Physics of Solid Surfaces VII,* edited by R. Vanselow and R.F. Howe (Springer-Verlag, Berlin, 1988), p.1.

LOW-TEMPERATURE MOBILITY OF THIONINE IN A FAUJASITE CAGE

F.W. DEEG, M. EHRL AND C. BRÄUCHLE
Institut für Physikalische Chemie, Universität München, Sophienstrasse 11, D-80333 München, Germany

ABSTRACT

We have used low-temperature optical spectroscopy to characterize the guest/host interaction of thiazine and oxazine dyes encapsulated in the three-dimensional pore structure of faujasite cages. The system thionine in dehydrated zeolite-Y exhibits a thermal and optical equilibrium between two spectroscopically distinguishable species. Temperature-dependent measurements allow the determination of the energy difference and barrier between these two forms as 170 cm^{-1} and 120 cm^{-1}, respectively. The two forms are associated with two different locations/conformations of the chromophore within the faujasite pore structure. The degree of freedom responsible for the interconversion of the two forms is extremely sensitive to the relationship between molecular size and form of the void.

INTRODUCTION

Progress in chemical methods allows today the synthesis of an ever increasing number of natural and synthetic molecular sieves providing regular pore and cage structures of various shapes and Å to nm extensions [1]. These voids of different form and size represent an ideal host for the encapsulation of molecular guests. Guest/host systems of this kind are unlike more common systems as chromophore-doped glasses or molecular crystals. The molecular sieve constitutes a well-defined structurally organized environment not present in glasses and, at least in principle, gives the guest degrees of freedon not known in molecular crystals. In recent years the potential to delicately control molecular dynamics in this kind of systems has been realized by physicists as well as chemists [2].

The optical transition frequency of a chromophore is extremely sensitive to the structure and dynamics of the surrounding host. We have therefore employed traditional optical methods as well as high-resolution techniques like fluorescence line narrowing and spectral hole-burning to obtain information about adsorbate/molecular sieve systems. Our studies have focused on large organic chromophores in large void porous crystals like faujasite and $AlPO_4 - 5$. These investigations had a twofold purpose. On one hand we wanted to characterize the fundamental optical properties of these guest/host systems, e.g. homogeneous and inhomogeneous broadening mechanisms [3]. On the other hand the potential of this class of materials for optical data storage applications was evaluated [4]. Of importance is the fact if these chromophore-doped molecular sieves are dehydrated or are filled with a solvent like ethanol or water as coadsorbate. For example, spectral hole-burning is in general only possible if an additional coadsorbate forms an amorphous phase within the pores. From all systems investigated, thionine in a dehydrated faujasite host (see fig. 1) exhibits a singular low-temperature optical bistability not found in any of the other very similar guest/host systems. In the following we will illustrate the characteristics of this system and relate it to the molecular confinement in the faujasite host.
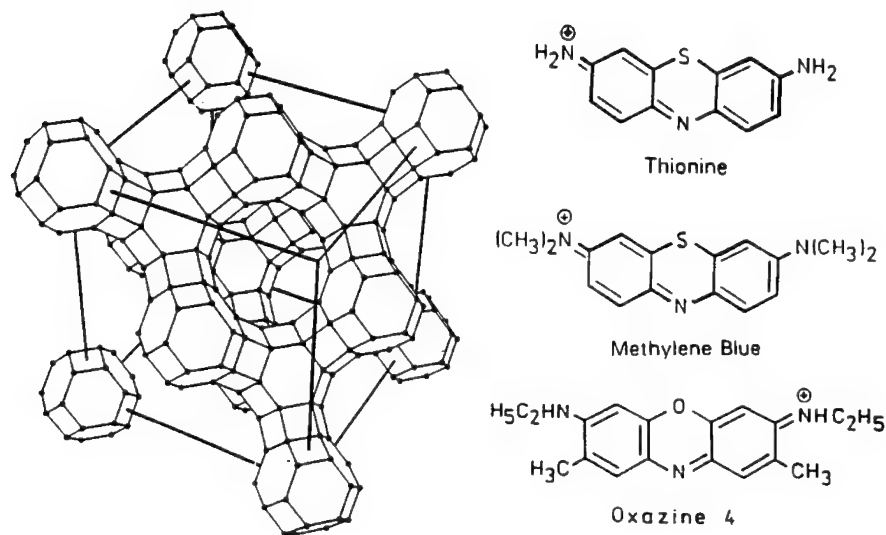
Figure 1. Schematic representation of the faujasite unit cell and the accomodated chromophores. The faujasite unit cell constant is 24.8 Å. The three-dimensional pore structure can be pictured as intersecting supercages with an overall tetrahedral symmetry. Two intersecting cages form an elongated cavity with the shape of a sand-glass. The length of this cavity is 23.7 Å, the largest diameter is 13 Å, and the bottleneck has a width of 7.8 Å.

EXPERIMENTAL

The faujasite hosts as well as the adsorbate/zeolite systems were synthesized by the groups of Profs. Schulz-Ekloff and Wöhrle in Bremen. The Si/Al ratio is 2.9 for the Na-Y zeolite. The adsorbate/zeolite samples were prepared by cation-exchange in aqueous solution. The dye concentration is about $5 \cdot 10^{-7}$ mol/g zeolite $= 1 \cdot 10^{-3}$ g/l corresponding to a population of 0.3% of the faujasite supercages. The samples were dehydrated by heating with a temperature ramp of 0.5 $°C$/min up to 120 $°C$ under the reduced pressure of 10^{-5} torr. The powderous samples were then sealed off in glass cuvettes.

RESULTS AND DISCUSSION

Whereas in general the total fluorescence intensity of a dye-doped sample decreases with increasing temperature because of the activation of radiationless relaxation channels, thionine in Na-Y exhibits the opposite behavior. At low temperature (T $\leq$ 30 K) the fluorescence yield is very low and the fluorescence excitation spectrum has a maximum at $\lambda = 640$ nm (see spectrum A in fig. 2). Upon heating the fluorescence intensity gradually increases and the excitation spectrum maximum shifts to the blue. For temperatures T $\geq$ 175 K the spectrum is stable with a maximum at $\lambda = 640$ nm (see spectrum B in fig. 2). This temperature-
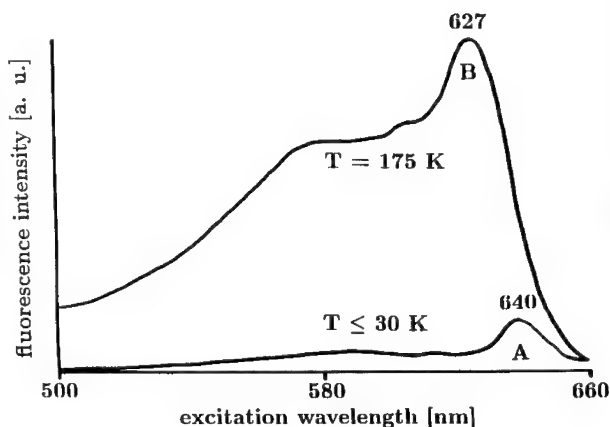
Figure 2. Fluorescence excitation spectra of $6 \cdot 10^{-7}$ mol/g thionine in dehydrated Na-Y. The two spectra correspond to the respective equilibrium of the two forms A and B at T = 175 K and T = 30 K. High- and low-temperature spectra are dominated by form B and A, respectively.

dependent change of the spectrum is reversible. However, if the sample is shock-frozen from room temperature to T $\leq$ 30 K, the high-temperature spectrum B is found. Obviously there are two spectroscopically distinguishable forms A and B of thionine in dehydrated Na-Y which can thermally convert into each other. This interconversion can also be induced optically. Following illumination of the sample at low temperature with light in the range 600-650 nm the fluorescence excitation spectrum changes from a type A spectrum into a type B spectrum.

To evaluate the energy parameters of this bistable system we have performed a number of temperature-dependent measurements. An appropriate plot [3] of the temperature-
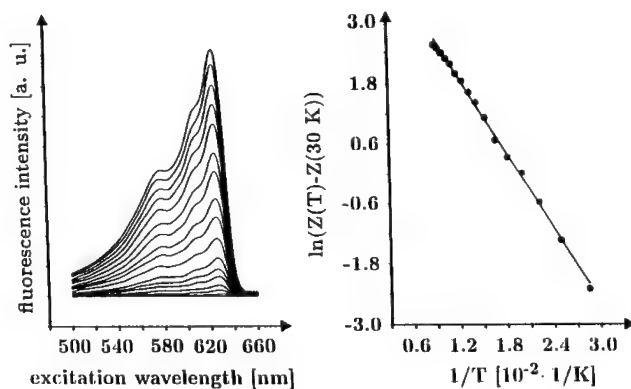
Figure 3. Left: difference between the thermal equilibrium spectrum Z(T) at elevated temperature (T = 35-110 K, in 5 K steps) and the spectrum Z_A at 30 K. Right: Logarithmic plot of Z(T) - Z_A.

279
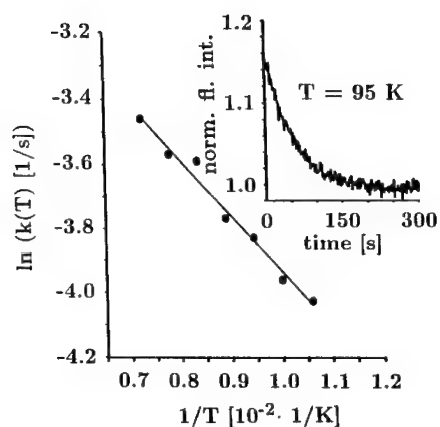
Figure 4. Arrhenius plot of the rate constant for the decay of the excess population in form B (induced by optically pumping the A → B conversion). The inset shows the decay signal at T = 95 K.

dependent intensity Z(T) of the fluorescence excitation spectrum in the temperature range 35-110 K allows a calculation of the energy difference ΔE between forms A and B (see fig. 3). From the slope in fig. 3 (right) a value of $\Delta E = 2.0$ kJ/mol = 170 cm^{-1} is found. The optically induced conversion of form A to B allows the preparation of a population excess in form B. The decay of this population excess can be followed by monitoring the decrease of the fluorescence intensity after the end of the optical pumping interval. This decrease shows a monoexponential behavior (see inset in fig. 4) and allows the determination of a decay constant. From a temperature-dependent Arrhenius plot (see fig. 4) the barrier activation energy $\Delta V = 1.4$ kJ/mol = 120 cm^{-1} for the transition B → A is determined.

Summarizing these observations the scheme of transitions and energy levels in fig. 5 can be established. To explain other pertinent experimental facts not discussed here a triplet T_1
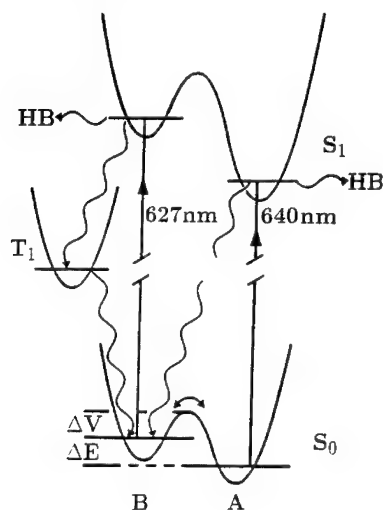
Figure 5. Optical energy and transition scheme of thionine in dehydrated zeolite Y.

280

population bottleneck and hole-burning (HB) mechanisms for both forms A and B must be assumed.

What is of more interest here is the microscopic basis for the two forms A and B and the degree of freedom linking them. The existence of two spectrally distinguishable forms and the optical and thermal interconversion are absent for the structurally and photophysically very similar but somewhat bulkier molecule methylene blue (see fig. 1) in the same host as well as a number of resembling guest/host combinations. Based on this fact we conclude that the peculiar behaviour of thionine in dehydrated zeolite Y is the result of the residual mobility of the molecule within the surrounding porous structure. For a molecule slightly larger than thionine (such as methylene blue), these degrees of freedom become frustrated by steric restraints impeding the dynamics observed in case of thionine.

Molecular modeling calculations, minimizing the overlap of van der Waals radii, revealed two sites or locations of the thionine molecule in the faujasite framework which are populated with roughly equal probability [5]. The first site is a highly symmetric conformation with a thionine molecule symmetrically occupying two neighbouring supercages (see figure 6 left). Then, the N–S axis of the central ring of thionine lies in the plane defined by the twelve-memberd oxygen ring between two supercages. In the second site the molecule is translated by about 4.5 Å from the symmetric conformation into one of the supercages (see figure 6 right). Other locations, e.g. the thionine molecule centered in the supercage seems to be very unlikely, for the length of the dye molecule exceeds the supercage diameter of 13 Å by about 3 Å. This means, both ends of the centered molecule would extend into one of the four supercage openings, which are tetrahedrally aligned with respect to the center of the cage. This is possible only if the dye molecule gives up its planarity. It should be mentioned that recently a Rietveld refinement analysis of X-ray powder diagrams has been carried out for the case of methylene blue in a faujasite cage [6]. This analysis reveals indeed two different sites corresponding to the guest/host conformations discussed here. The distribution of the methylene blue molecules between these two locations depends on the method the dye was
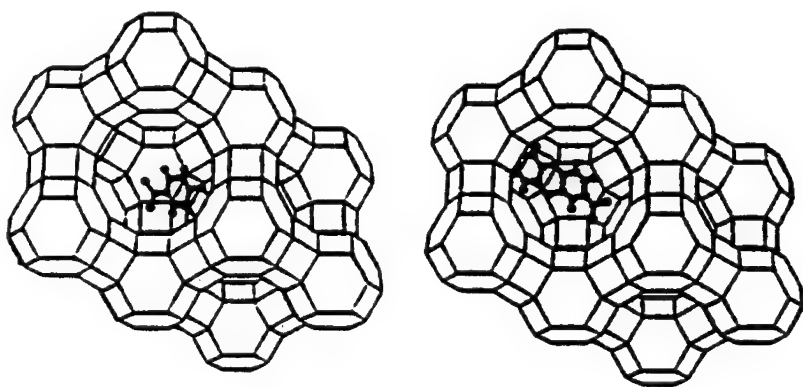
Figure 6. Schematic representation of the symmetric (left) and asymmetric location (right) of thionine in the sand-glass shaped void of two neighbouring supercages.

incorporated into the molecular sieve.

In our opinion the forms A and B found in the optical experiments are associated with the two locations/conformations described above. That is, the interconversion corresponds to a translation/rotation of the thionine molecule within the faujasite pore. For a methylene blue molecule these two locations also exist but the barrier between them is too high to be crossed at ambient temperature. We would like to note that there should be additional degrees of freedom of the encapsulated molecules which is orientation of the molecule at a given location. We think that this degree of freedom contributes to the inhomogeneous broadening of the optical spectra found in these samples.

CONCLUSIONS

The system thionine in dehydrated Na-Y demonstrates that the dynamics of molecular guests in these porous hosts depend very subtly on the relationship between size and shape of the molecule and extension and form of the surrounding void. We think that behavior of this kind can in principle be found in most chromophore/molecular sieve systems. The special properties of the thionine/Na-Y(dehydrated) system, i.e the fact that forms A and B can be separately observed and convert into each other, are due to the extremely different fluorescence yields of the two forms and the very low potential barrier between them.

ACKNOWLEDGEMENTS

REFERENCES

1. R. Szostak, Ed., *Molecular sieves, Principles of Synthesis and Identification* (Van Nostrand Reinhold, New York, 1989).

2. see e.g. J. Klafter, J.M. Drake, Eds., *Molecular Dynamics in Restricted Geometry* (Wiley, New York, 1989); V. Ramamurthy, Ed., *Photochemistry in Organized and Constrained Media* (VCH, Weinheim, 1991).

3. M. Ehrl, H.W. Kindervater, F.W. Deeg, C. Bräuchle, R. Hoppe, J. Phys. Chem., **98**, in press (1994).

4. M. Ehrl, F.W. Deeg, C. Bräuchle, O. Franke, G. Schulz-Ekloff, D. Wöhrle, J. Phys. Chem., **98**, 47 (1994).

5. R. Hoppe, PhD thesis, University of Bremen, 1992.

6. R. Hoppe, G. Schulz-Ekloff, D. Wöhrle, C. Kirschhock, H. Fuess, Stud. Surf. Sci. Catal., submitted.

A SPECTROSCOPIC AND THERMODYNAMIC INVESTIGATION OF MERCURIC IODIDE PHYSICALLY CONFINED IN POROUS GLASS HOSTS

D. O. Henderson*, R. Mu*, A. Ueda*, A. Burger*, K. T. Chen* and D. O. Frazier**
*Physics Department, Fisk University, Nashville, TN 37208
**Space Science Laboratory, Chemistry and Polymeric Materials Branch, Marshall Space
Flight Center, Huntsville, AL 35812

ABSTRACT

Raman and electronic spectra and results from differential scanning calorimetry (DSC) are reported for mercuric iodide (HgI_2) confined in four different pore-sized glass hosts. The Raman spectra reveal peaks at 39 and 141 cm^{-1} that indicate the confined HgI_2 is stabilized at 300 K in a modified orthorhombic (yellow) β-phase which is observed at 400 K for the bulk material. An additional band begins to appear at 145 cm^{-1} for pore radii smaller than 3.75 nm suggesting the presence of new phase of confined HgI_2. The DSC measurements show the melting and freezing transitions of confined β-HgI_2 are depressed from values reported for the bulk material and the depression increases as the pore size decreases. No transition is observed in the DSC measurement which could be attributed to the $\alpha\rightarrow\beta$ transition for the confined material. Evidence supporting the new phase of HgI_2 is observed in the electronic spectra of the confined HgI_2 by the appearance of an energy gap transitions located at 2.7 eV.

INTRODUCTION

The effect of size confinement on a material can often lead to a rich display of properties which differ significantly from those of the bulk.[1,2] It is well established that the thermodynamic properties of materials in restricted geometries are significantly altered from those of the bulk.[3] The melting and freezing transition temperatures of confined materials are typically depressed from the bulk and phases[4] that not observed in the bulk form may exist in the confined phase.[2] The observation of such unique phases has largely been attributed to the interfacial energy between the nanophase particle and its host.[1]

Materials in physically restricted geometries manifest changes in their optical properties. The finite size effect on semiconductors is manifested by a blue-shift in the band gap or the appearance of discrete transitions which results from the particle size being near the excitonic radius. Perturbations to external vibrational modes have been reported as well and have been explained by phonon confinement and surface phonon models,[5] while perturbations to the internal modes are understood in terms of a host guest interaction potential.

α-Mercuric iodide (red tetragonal phase) is a layered wide band gap semiconductor for which the optical, Raman and thermodynamic properties are well established.[6] Raman spectra of β-mercuric iodide and mercurous iodide (Hg_2I_2) have also been reported.[7] The lattice parameters are also known for the α- and β- forms of HgI_2.[8]

Other investigations have focused on mercuric iodide clusters in solution[9] and trapped in a zeolite cage.[10] The electronic spectra of HgI_2 solutions indicated that colloidal HgI_2 formed, but attempts to correlate the particle size and magic numbers with the observed transitions leads to large uncertainties in the number of layers and molecules which make up the cluster.[9] The results ranged from clusters made up from 12 to 38 molecules and between 1-4 layers. Some of the uncertainty stems from the fact that confinement of HgI_2 is anisotropic and the shift in the energy gap depends on the lateral dimension in the layer plane and the layer thickness. Thus, unless one

of the parameters can be constrained, no reliable particle size can be determined from the electronic spectra. The studies of HgI_2 confined in a zeolite limited the number molecules from one to five. In these studies a blue shift (with respect to the bulk) of the electronic transitions of the confined material was qualitatively explained in terms of the effective mass approximation, but no quantitative agreement could be obtained.

Although the previous studies on confined HgI_2 have indicated quantum size effects are present, there remains uncertainty in the interpretation of the electronic transitions due to lack of knowledge of the particle size. In addition, no studies have been performed for clusters larger than 38 molecules and information indicating an aggregate to bulk crossover is lacking.

Our approach is to use pore-sized glass hosts with narrow pore size distributions to restrict the size of the HgI_2 in one dimension. In the present work, we report the Raman and electronic spectra and the melting and freezing transitions of HgI_2 confined in $r_p = 10, 5.0, 2.5, 3.75$ and 1.25 nm, (where r_p is the pore radius) pore sized glasses.

EXPERIMENTAL

Geltech porous substrates ($r_p = 1.25, 2.5, 3.75, 5.0$, and 10 nm, radius) were used for confining HgI_2. The properties of the porous glasses have been reported previously.[2] Zone refined HgI_2 was used for impregnating the porous glass hosts. The impregnation can be described as follows: 1) The porous glass substrates together with a charge of zone refined polycrystalline HgI_2 were loaded into a quartz ampule with a restriction smaller that the diameter of the porous glass disk. The restriction in the ampule allows for separating the impregnated glass from the excess HgI_2. The end of ampule containing the porous glass was heated to 393 K under a vacuum of 1×10^{-3} torr for 24 h. Under these conditions water is removed for the porous glass. 2) The HgI_2 powder was transferred through the neck of the ampule to the end containing the porous glass substrate and the was heated to 540 K for 1 h. 3) While the HgI_2 was still in its molten state, the melt was separated from the impregnated glass by rotating the ampule and flowing the HgI_2 melt through the neck in the ampule. The impregnated samples were stored in evacuated ampules until any measurements were performed. Upon inspection, the impregnated porous glasses appeared yellow-green in color.

The Raman scattering measurements were carried out with a Spex Raman spectrometer equipped with a double grating monochromator and an Ar laser. The scattered light was collected at 90° to the incident beam. A resolution of 2 cm^{-1} and an integration time of 0.5 s were used throughout the measurements. Spectra were collected by scanning between 10 cm^{-1} from the exciting line (514 nm) and 1000 cm^{-1} at power of 0.5 W.

The electronic spectra for the impregnated glasses were measured with a Hitachi 3501 spectrometer equipped with a Hitachi model 132-0464 integrating sphere. All of the diffuse transmittance measurements were made at 1 nm resolution. Transmission measurements on bulk polycrystalline HgI_2 were made by spreading the powder between two fused silica windows and then heating the material to the melting point and applying a load of 11 kg on the sample. In order to obtain a spectrum of β-HgI_2, the melted sample was quickly cooled to room temperature. At this stage the sample appeared predominantly yellow indicating the presence of the orthorhombic phase of HgI_2. The spectra were immediately recorded.

The thermal analysis measurements were made with TA Instruments 2920 differential scanning calorimeter. All measurements made with samples enclosed in hermetically sealed gold pans. Both the heating and cooling runs were made between 303 and 573 K at rate of 10 K/min.

RESULTS

Figure 1 shows the Raman spectra for HgI_2 confined in various pore-sized glasses together with the spectrum of the bulk HgI_2 heated to 410 K, (above the $\alpha \rightarrow \beta$ transition). All of the spectra show two prominent peaks located at 41 and 139 cm^{-1}. However, for confined HgI_2, evidence for an additional peak near 146 cm^{-1} begins to appear for glasses with $r_p \leq 2.5$ nm. The peak at 41 cm^{-1} broadens on the low energy side and develops a long tail extending into the Rayleigh line for the glass with $r_p = 1.25$. The thermograms obtained from the DSC measurements are shown in figures 2 and 3 for the heating and cooling runs, respectively. The glass with $r_p = 10.0$ shows two endothermic transitions in the heating run at 516 and 528 K. For the 5.0 and 3.75 nm pore sized glasses, two peaks are also observed at 496 and 524 K. There is also an additional weak peak near 410 K for both the 5.0 and 3.75 nm pore sized glasses. The glass with smallest pore radius of 1.25 shows a broad poorly defined transition near 365 K, a weak peak at 410 K and another weak peak at 460 K. The thermograms for the cooling runs for the $r_p = 10.0$ nm show a single exothermic peak near 501 K while the 3.75 and 5.0 nm glasses have a strong exothermic peak at 474 K and a much weaker peak at 354 K. No transitions were observed for the glass with $r_p = 1.25$.

The electronic spectra for the HgI_2 quenched from the melt, α-HgI_2 at room temperature and the spectra for HgI_2 confined in the glasses with $r_p = 1.25, 3.75, 5.0$ nm are shown in fig. 4. The spectrum for α-HgI_2 shows the band gap to be located at 556 nm (~ 2.2 eV). The spectrum corresponding to the quenched sample shows two features; one coincides
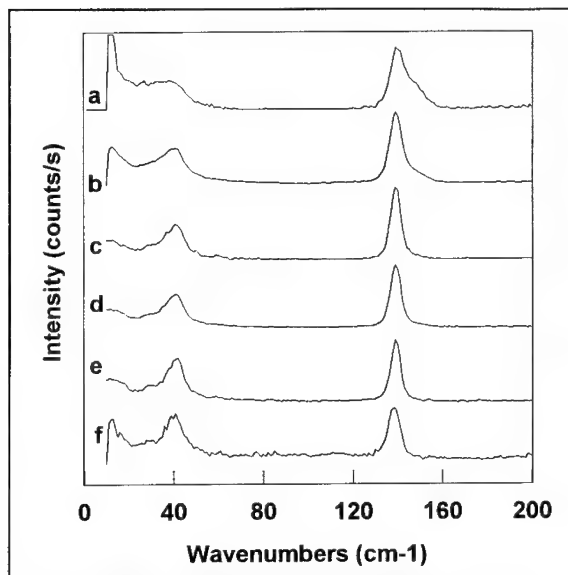
Figure 1 Raman spectra for HgI_2 confined in porous glasses with r_p= a)1.25, b)2.5, c)3.75, d) 5.0 nm e)10.0 and e) HgI_2 at 408 K
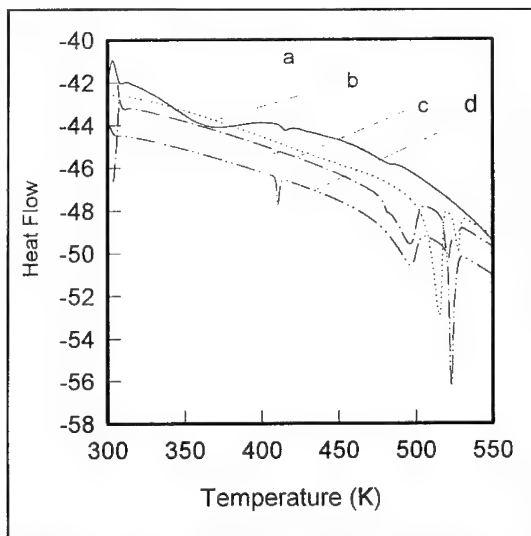
Figure 2. DSC thermograms for HgI_2 confined in porous glasses with r_p= a) 1.25, b)10.0, c) 3.75 and d) 5.0 nm.

with the 2.2 eV energy gap observed for α-HgI$_2$ and a second energy gap at 396 nm (3.1 eV). The spectra of HgI$_2$ confined in the various pore-sized glasses all exhibit features observed in spectra for α-HgI$_2$ and for the quenched sample. However, the relative intensity of the feature located at 396 nm is much weaker in the confined glasses than it is in the quenched sample. The spectra for HgI$_2$ confined in the porous glasses also exhibit a rapidly increasing strong absorption between 509 nm (2.4 eV) and 467 nm (2.66 eV). At wavelengths shorter than 467 nm the slope decreases, and then begins to increase near 430 nm (2.88 eV). This increase corresponds to the absorption onset observed for the quenched sample. No shifts were observed in absorption onset at 509 nm or in the inflection at 467 nm for the spectra of HgI$_2$ confined in the pore sized glasses. In addition, no evidence for this strong absorption between 509 and 467 nm could be found in the spectra of α-HgI$_2$ or in the quenched sample.

Figure 3. DSC thermograms for HgI$_2$ confined in porous glass with r_p= a) 1.25, b)10.0, c) 3.75, d) 5.0.

DISCUSSION

The two strong bands at 41 and 139 cm^{-1} observed in the Raman spectra for confined HgI$_2$ coincide with the same frequencies observed for β-HgI$_2$ suggesting that the confined HgI$_2$ is also in the β-phase. The absence of intense bands near 18 and 29 cm^{-1} indicate there is very little, if any α-HgI$_2$ present in the confined phase. Another possibility for the confined material based on the phase diagram of mercuric iodide is the formation of an mercury rich phase (Hg$_2$I$_2$). However, if such a phase were present, a peak should be observed at 114 cm^{-1}.[7] Thus this possibility can be eliminated.

Figure 4. Electronic spectra for HgI$_2$ confined in porous glasses with r_p= a) 5.0, b) 3.75, c) 1.25 nm, d)quenched bulk HgI$_2$ and e)α-HgI$_2$.

286

Finally, a high pressure phase (10 kbar) was reported by Adams et al.[11] and is characterized by Raman peaks at 137 and 50 cm^{-1}. The frequency of 137 cm^{-1} is very close to the frequency observed for confined and β-HgI$_2$, but the absence of a peak at 50 cm^{-1} allows us to conclude that no high pressure phase is present in the confined material.

The rather sudden appearance of the peak at 146 cm^{-1} and low frequency broadening of the 41 cm^{-1} band for HgI$_2$ confined in porous glass with $r_p \leq 2.5$ nm must be explained. Phonon confinement models predict that there should be a continuous red-shift and broadening of the confined mode as the physical dimension of the confinement decreases. This dependence is clearly not observed for the peaks at 146 and 41 cm^{-1} and another mechanism must account for the behavior of the two peaks. We suggest that the sudden onset of a the 146 cm^{-1} peak and the sudden broadening of the 41 cm^{-1} peak indicates the presence of a perturbed β-phase of HgI$_2$. Similar size confinement effects and the stabilization of a new phase have been observed for NaNO$_3$ confined in porous glass hosts.[2]

The DSC results for the heating and the cooling runs also support the presence of β-HgI$_2$ as no transition was observed which could be attributed to $\alpha \rightarrow \beta$ for confined HgI$_2$. The endothermic peak near 409 K is the $\alpha \rightarrow \beta$ transition for bulk HgI$_2$ contaminated on the porous glass surface. Similarly, the exothermic peak at 530 K is due the melting transition of bulk β-HgI$_2$. The melting transitions for confined HgI$_2$ are observed at 516, 496, and 496 K for the glasses with pore radii of 10.0, 5.0, and 3.75 nm, respectively. Such a size dependent depression in the melting transition for confined solids has been reported extensively.[3,4] The broad shallow peak near 350 K for the glass with $r_p = 1.25$ nm cannot be assigned to the melting transition of the confined material as it too low from what would expected from the 1/r dependence on melting point depression for confined solids. In addition, no freezing transition is observed for the $r_p = 1.25$. It is conceivable that the peak is due to water in the pores which was not completely removed before impregnating the glass with HgI$_2$. The cooling runs show the freezing transition for β-HgI$_2$ confined in glasses with $r_p = 10.0$, 5.0, and 3.75 nm at 501, 474 and 474 K, respectively which are depressed from the bulk freezing transition which is typically observed at 527 K. The weak feature near 354 K is due to the sluggish $\beta \rightarrow \alpha$ solid-solid phase transition of the bulk. As in the case of the heating run, no peaks were observed which could be attributed to the $\beta \rightarrow \alpha$ transition of confined HgI$_2$. It is noteworthy that the relative intensity of the melting to the $\alpha \rightarrow \beta$ transition for the bulk is roughly 6. This is approximately what we observe in the thermograms and allows us to conclude that the weak peak at 545 K is in fact due to the bulk.

α-HgI$_2$ has a band gap near 2.25 eV which agrees reasonably with the value of 556 nm (2.2eV) determined from our absorption measurements. The spectra for the quenched HgI$_2$ show an energy gap at 2.2 eV and additional one at 400 nm (3.1 eV) which we assign to the energy gap of β-HgI$_2$. The spectra for the confined HgI$_2$ also show a gap at 3.1 eV which is weak due the overlapping absorption between 509 and 430 nm. There is also the energy gap due to α-HgI$_2$ which we attribute to bulk HgI$_2$ contamination on the surface. The energy gap between 509 nm, (2.4 eV) and 467 nm (2.66 eV) which is observed only for confined HgI$_2$ cannot be attributed to a quantum confinement of the exciton. The principle reasons for this stem from the fact that quantum confinement models predict an increasing blue shift in the energy gap with a decrease in the pore size. As the energy gap was essentially invariant for all pore sizes investigated, we conclude that energy gap at 2.66 eV cannot be due to quantum confinement effects on either the α-HgI$_2$ or β-HgI$_2$. In addition, the DSC and Raman measurements indicate that the confined HgI$_2$ is probably closely related to β-HgI$_2$. Based on this observation, the energy gap at 2.66 eV cannot be attributed quantum confinement of β-HgI$_2$ as the energy shift is in the wrong direction.

Strain is known to induce shifts in the band gaps, and cause changes in selection rules due to lattice symmetry perturbations and therefore, could account for the energy gap at 2.66 eV for the confined HgI$_2$. However, if strain were the mechanism responsible for this energy gap, it would expected to be manifested in the Raman spectra as shifts in the lattice modes. The Raman spectra do not indicate such shifts, but only the appearance of new mode at 146 cm^{-1} and broadening of the 41 cm^{-1} mode into the Rayleigh line. Furthermore, if symmetry perturbations were significant

were significant, it would be expected that the Raman forbidden, infrared active mode at 180 cm^{-1} would be observed.[11] Thus, based on the Raman and electronic spectra and the DSC measurements, we suggest that confined mercuric resides in the porous glasses as a modified form of β-HgI$_2$.

Finally, it is interesting to note that a modified form of β-HgI$_2$ is stabilized in the porous glasses at room temeperature, whereas for the bulk it is observed at temperatures above 400 K. It may be that a pore radius of 10 nm is below the size required to form a critical nucleus for forming α-HgI$_2$. In this context, the studies of HgI$_2$ quantum dots and the models developed based on the band gap and lattice parameters of α-HgI$_2$ should be reconsidered in terms of parameters based on β-HgI$_2$.

Acknowledgements

References

1. S. H. Tolbert and A. P. Alivisatos, Science, **265**, 373 (1994).
2. R. Mu, F. Jin, S. H. Morgan, D. O. Henderson and E. Silberman, J. Chem., Phys., **100**, 7749 (1994).
3. D. D. Awschalom and J. Warnock, Phys. Rev., **B35**, 6779 (1987).
4. R. Mu and V. Malhotra, Phys. Rev., **B44**, 4296 (1991).
5. H. Richter, Z. P. Wang, and L. Ley, Solid State Commun., **39**, 625 (1981).
6. A. Burger, S. Morgan, H. Jiang, E. Silberman, M. Schieber, L. Van Den Berg, L. Keller, and C. N. Wagner, Nuc. Inst. Met. Phys. Res., **A283**, 130 (1987).
7. A. Rogstad, Acta Chim. Scand., **27**, 57 (1973).
8. J. B. Newkirk, Acta Metallurg., **4**, 316 (1956).
9. Z. K. Tang, Y. Nozue, and T. Goto, J. Phys. Soc. Japan, **61**, 2943 (1992).
10. O. I. Micic, M. T. Nenadovic, M. W. Peterson, and J. A. Nozik, J. Phys. Chem., **91**, 1295 (1987).
11. D. M. Adams and R. P. Appelby, Inorganica Chimica Acta, **26**, L43 (1978).

A VIBRATIONAL INVESTIGATION OF CRYSTAL NUCLEATION AND GROWTH FROM A PHYSICALLY CONFINED AND SUPERCOOLED LIQUID

R. MU, D.O. HENDERSON, Z. PAN AND Y. XUE
Department of Physics, Fisk University, Nashville, TN 37208

ABSTRACT

Temperature dependent Raman measurements were conducted on bulk and the confined 2,4,6-trinitrotoluene (TNT) in 2.5, 5, 10, and 20 nm porous silica. Two bands at 23 and 190 cm^{-1} were chosen to evaluate the structure and the melting and freezing transitions of the confined TNT in pores. The results show that the solid phase TNT confined in larger pores ($d_p > 5$ nm) forms conventional solid TNT structure, while the TNT restricted in small pores has no freezing and melting transition characteristics. The results also suggest that the freezing transition of the confined TNT starts at the pore center and the confined TNT maintains its interconnectivity during the freezing transition.

INTRODUCTION

The study of the dynamic and thermodynamic properties of confined phases in various dielectric hosts is one of the important issues in nanometer scale technology. The well characterized porous media have been used as hosts: 1) to understand the physical confinement and the surface effects of the hosts on melting, freezing, and solid-solid transitions of the restricted phases inside pores[1-9], 2) to illustrate the cluster formation and the possible mechanisms of crystal nucleation and growth in the condensed phase as well as in aqueous solution[8], 3) and to investigate molecular relaxation and diffusion in restricted geometry[9].

It is known that a physically confined fluid in ultrasmall pores can be easily supercooled. This supercooling phenomena has been attributed to the finite size effect, size-limited fluctuation, and the surface effect from the confining media. However, there is limited information available on how and where the freezing nucleation first occurs inside pores and how the crystal develops. Earlier studies[1-6] have suggested two physical models to explain the freezing transition of the confined fluids. Based on the classic nucleation and growth theories, the plug model[1] has been proposed to successfully explain the freezing and melting transition temperatures depression of the confined fluids and solids in different pore sizes. With this model, it is assumed that a) the substrate wall is more favorable liquid-wall interface than solid-wall interface, b) nucleation occurs at the pore center, and c) nucleation is restricted in one dimension. On the other hand, the computer simulation study[6] of molecular freezing dynamics of a Lennard-Jones liquid in a confined geometry suggests a different novel freezing mechanism and time development of the ordering dynamics. Upon cooling, the confined liquid forms layers near the pore wall and subsequent in-plane ordering within a layer is accomplished by a sharpening of the layering in the transverse direction. This result is also qualitatively supported by neutron scattering experiments of Sokol et al.[4] However, the simulation did not provide information on supercooling effects for confined fluids. As a result, the correlation between the supercooling effect and the structure of the confined phase is still lacking. The mechanism of the solid nucleation and growth from the supercooled and confined fluids in porous media is not understood.

Our recent thermal investigation[11] of TNT physically confined in three different pore-sized

silica glasses has provided additional information on nucleation and growth processes in a restricted dimension. The results suggest that: 1) the nucleation of the confined TNT occurs at the center of the pores, 2) the excess bulk TNT can trigger the freezing transition of the confined material in 10 and 20 nm pores, 3) the very sharp freezing transition indicates that the confined TNT maintains its interconnectivity during the freezing transition, 4) for the TNT confined in 5 nm pores, no freezing and melting transition is observed implying the TNT inside the pores is in cluster form.

In order to understand how the finite size and the surface of the confining media modifies the solid structure of the confined TNT in different pore-sized silica glasses and to compare the confined structure with the bulk, two sets of experiments have been conducted. First, temperature dependent of Raman scattering spectra of bulk TNT were investigated to search for the phonon mode of the solid TNT and the lower internal mode of TNT molecules. Then, similar measurements were conducted on the TNT confined in four different pore sizes.

EXPERIMENTAL

2,4,6-TNT was purchased from Chem Service with purity of 99.0% [+]. As-received TNT has 10 - 20% added water in it. In order to remove the added water and to further purify the sample, the TNT was transferred into a cleaned Quartz tube which connected to a mild vacuum. The tube with the sample was placed into a furnace with temperature gradient from 393 K to 300 K with the span of 9 inches. The sample was placed at the hottest spot. First, the desorbed water can be pumped out via vacuum pump. Then, the impurities and TNT, depending upon their vapor pressure and their boiling points, were condensed on to inside wall of the quartz tube in different zones. Then the tube was cut into different sections. With thermal (DSC) and optical (IR) analysis, the purest polycrystalline TNT was obtained.

Gelsil porous silica discs with pore size of 20, 10, 5 and 2.5 nm pore diameters were used for confining TNT. To clean the Gelsil, the glass was first moisturized in the humidity controlled chamber over 24 hrs before being immersed into pure water. Then, it was cut into suitable sizes for use in the experiments. The cut pieces were immersed into 30% H_2O_2 solution and heated up to 373 K for 12 hrs to remove organic contamination in the glass. The glass were then rinsed minimum of three times with 18 MΩ ultrapure water. The cleaned Gelsil is kept in the large volume of water container and ready to be used.

The impregnation of TNT into Gelsil involves two major steps. In the first step, the cleaned glass was transferred into a Quartz tube and dried under vacuum at the pressure of 10^{-5} torr the temperature of 723 K for 6 hrs. Then the temperature was reduced to room temperature and the sample tube was back-filled with ultrapure nitrogen gas. Subsequently, a sufficient amount of the purified TNT was loaded into the tube. The vacuum pump was slowly turned back on. After the 2 - 3 hrs pumping, the Quartz tube was isolated from the vacuum and the sample was heated to 363 K for 1 hr to allow for liquid TNT to flow into the pores with the help of water bath. Then, the impregnated Gelsil was cooled back to room temperature very slowly.

Temperature Dependent Raman scattering measurements of the TNT in its bulk and the confined phases were carried out with a Spex Raman spectrometer, which equipped with a double-grating monochromator and Ar^+ laser. The scattered light was collected at 90° to the incident laser beam. A homebuilt variable temperature cell was used to control the temperature with the temperature stability < ± 2 C. A typical 1 cm^{-1} resolution and 2 seconds integration time were used throughout the measurements. Spectra were collected between 10 cm^{-1} and 230 cm^{-1} from the excitation line (19436 cm^{-1}) at a power of 100 mW.

RESULTS AND DISCUSSION

Raman Scattering of Bulk TNT at 10 - 230 cm^{-1} (290 - 355 K)

In order to identify the structure of confined TNT in various pore sizes and at different temperatures, temperature dependent Raman scattering of polycrystalline bulk TNT was investigated. Fig. 1 shows a representative set of Raman spectra at different temperatures upon the heating and cooling runs. Five peaks at 23, 56, 108, 159, and 190 cm^{-1} are observed in 10 - 230 cm^{-1} region. The bands below 160 cm^{-1} disappeared when the TNT was in the liquid state, while the band at 190 cm^{-1} experienced a sudden frequency shifting and linewidth broadening. Although there has been no detailed vibrational analysis, the bands below 160 cm^{-1} may be related with lattice phonons. The low frequency Raman and Infrared study[14] of m-chloronitrobenzene single crystal suggests that the band at ~93 cm^{-1} is NO_2 torsion. Stewart et al.[13] have assigned C-N-O bend vibration at 70 cm^{-1}. It seems possible that the band at 108 cm^{-1} may be due to C-N-O bend. However, the disappearance of this band upon melting failed to support the case. Therefore, the band at 108 cm^{-1} is most likely to be the NO_2 torsion mode. The characteristics of the frequency and linewidth of the band at 190 cm^{-1} indicate that this mode may be assigned to librational modes of the NO_2 due to two reasons: 1) lattice vibrations vanish when TNT melts, and 2) the linewidth of the mode is almost doubled indicating the vibration is sensitive to its environment i.e., intermolecular interaction. Therefore, the low phonon band at 23 cm^{-1} and the NO_2 librational mode were analyzed, as shown in figs 2 & 3. The disappearance of the band at 23 cm^{-1} at 373 K during the heating suggest the melting transition. The sudden reappearance at 317 K upon cooling indicates that the bulk TNT was
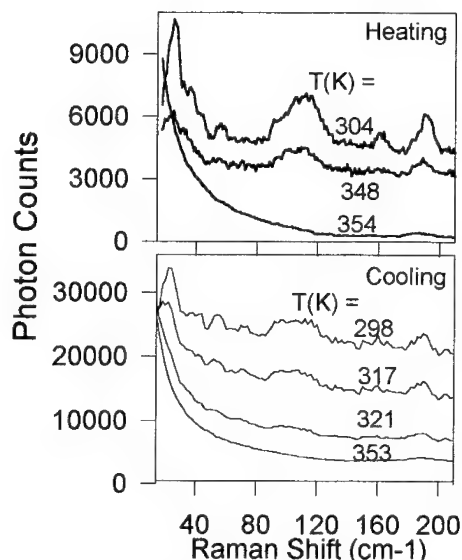
Fig. 1 Raman spectra of bulk TNT at different temperatures upon the heating and cooling.
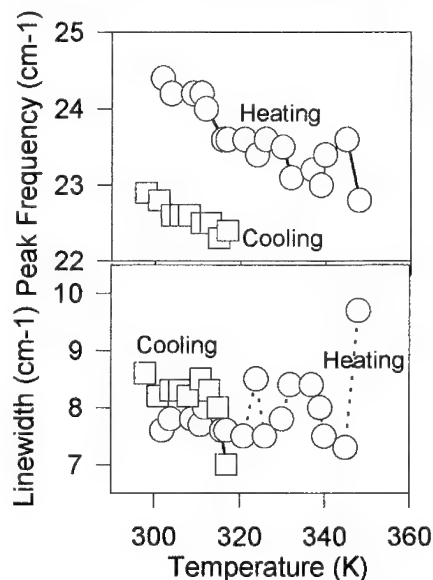
Fig. 2 Peak frequency and linewidth change as the function of temperature.

supercooled as low as 317 K before it freezes. The slight frequency down-shifting and linewidth broadening can also suggest that the polycrystalline phase formed from the supercooled liquid possesses a higher disorder than that from solution phase. The frequency shifting of the band at 190 cm^{-1} can also be related to the orderness of the solid phase formed from supercooling. Further, it is anticipated that when the TNT is confined in ultrasmall pores, the band at 23 cm^{-1} can reflect the solid structure of the TNT while the band at 190 cm^{-1} may provide information on TNT-substrate interactions.

Raman Investigation of melting and freezing transitions of the Confined TNT

As stated earlier, the confined TNT in each pore size has been subdivided into two sets. One is the sample with bulk TNT covering the surface. The other is the sample with no bulk TNT on the surface. The temperature dependent Raman scattering investigation shows that the freezing transition of the confined TNT has strong correlation with the fact that whether or not the bulk TNT is present on the sample surface. However, the melting transition of the confined TNT without bulk TNT on surface only shows the pore-size dependence. Table I has summarized the observed freezing and melting transition temperatures of the confined TNT in four different pore sizes together with the bulk TNT.
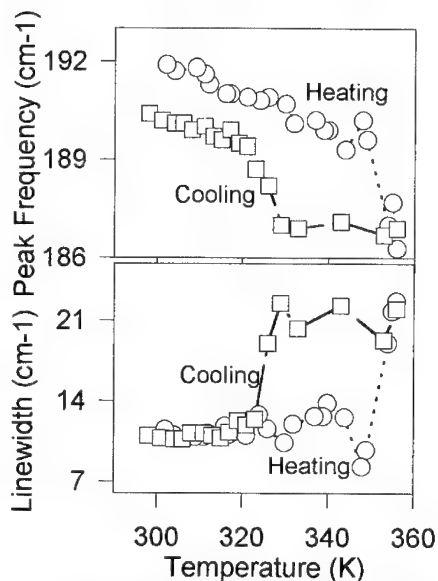
Fig. 3. Peak frequency and linewidth change as the function of temperature.

Table I
Melting and freezing transition temperatures of
bulk and the confined TNT via Raman scattering measurements

Confined TNT in d_p(nm)=	Bulk TNT	20 nm w/ bulk presence	20 nm w/o bulk presence	10 nm w/ bulk presence	10 nm w/o bulk presence	5 nm w/ & w/o bulk	2.5 nm w/ & w/o bulk
Melting	352±2K	340±2K	338±2K	323±2K	320±2K	-	-
Freezing	318±2K	319±2K	287±2K	288±2 K	?*	-	-

* as presented in ref. 11, the confined TNT in 10 nm pores can crystalize upon heating from 100 K. The crystallization temperature is at ~ 251 K, based on DSC measurements.

When the TNT is confined same pore-sized glass, regardless of the presence of bulk TNT on the surface, the same melting transition temperature of the confined TNT was observed. However, a dramatic difference was observed in the case of freezing transition temperature. The freezing transition of the confined TNT in 20 nm pores with bulk on the surface gives the same

freezing transition temperature. This suggests that the freezing transition of the bulk TNT outside the pores induces the transition of the confined TNT. At 319 K, both bulk and the confined TNT are supercooled. Once the bulk TNT was removed, the confined TNT in 20 nm pores freezes at 287 K, which is 32 K below the freezing transition in the first case. This strongly suggests that the freezing transition of the TNT in 20 nm pores without bulk on the surface follows the typical homogeneous nucleation. Therefore, the nucleation should start at the pore center. The results obtained from the TNT confined in 10 nm pores also supports the above argument. In addition, the TNT in 10 nm pores without bulk on the surface can be undercooled to 100 K without freezing. Our DSC measurements[11] show that the crystallization of the confined TNT without bulk on the surface occurs at 263 K following the heating run. This finding not only suggests that the transition is not heterogeneous, but also implies that the nucleation and growth processes have been modified. That is, the temperature dependent nucleation and growth curves are shifted away from each other resulting in little overlapping.

When the TNT is confined the pore size $d_p < 5$ nm, no solid melting and freezing transitions are observed. Clearly, the presence of the bulk TNT cannot trigger the freezing transition of the confined material. With the plug model, the TNT is confined in 5 nm pores, its freezing transition temperature is expected to be at 220 K. However, when the sample was cooled to 100 K and heated to 373 K, no transition was observed. Therefore, the TNT confined in 5 and 2.5 nm pores may be in cluster form. The critical nucleus cannot be formed in such small pore size.

Structural Characterization of the Confined TNT in Different Pore Sizes

As discussed earlier, two vibrational modes at 23 and 190 cm^{-1}, respectively were chosen to investigate the confined TNT in different pore-sized silica hosts. These two modes cannot only give the information on the phase transition, they may also provide structural characteristics of the confined TNT in pores. Table II has summarized the observed band frequencies and their linewidths for bulk TNT and the confined TNT.

Table II

The observed frequencies and the linewidths of the bands at 23 and 190 cm^{-1}

for the bulk and the confined TNT at selected temperatures[**]

Confined TNT in d_p(nm) =	Bulk TNT	20 nm w/ bulk presence	20 nm w/o bulk presence	10 nm w/ bulk presence	10 nm w/o bulk presence	5 nm w/ & w/o bulk	2.5 nm w/ & w/o bulk
Before melting	24 (8) 192 (12)	23 (6) 190 (12)	24 (5) 191 (12)	23 (5) 190 (13)	24 (5) 191 (14)	- 191 (20)[*]	- 189 (20)
After melting	- 186 (23)	- 188 (23)	- 189 (20)	- 188 (19)	- 188 (20)	- 191 (20)[*]	?
After freezing	23 (8) 190 (11)	23 (6) 190 (12)	24 (5) 191 (12)	23 (4) 191 (13)	- 190 (20)[*]	- 190 (19)[*]	?

[**] The data provided in the table are in cm^{-1}. The data outside parenthesis are the observed center frequency, while the data inside the parenthesis are the linewidths of the band.
[*] indicates that the sample shows no melting or freezing transition.

Based upon the center frequencies and the linewidths of the bands at 23 and 190 cm^{-1}, it is clear that the solid phase of the confined TNT shows a very close resemblance to that of the bulk TNT. During the melting transition, the disappearance of the band at 23 cm^{-1} indicates the

lattice phonon is destroyed. Like the bulk, the band at 190 cm^{-1} exhibits two trends. That is, the frequency of the band red-shifts by ~ 2 cm^{-1}, while the linewidth is broadened by ~ 6 - 10 cm^{-1}. In addition, the band at 190 cm^{-1} for the confined TNT seems to be less sensitive to the temperature. When the system is heated up to 375 K in all cases, the band for the confined TNT at 190 cm^{-1} is red-shifted by ~ 2 cm^{-1}, while the bulk frequency shifts by 6 cm^{-1}. It can be argued that the NO_2 groups of the confined TNT can form hydrogen-bonding with the OH groups on pore surface. Therefore, the NO_2 librational mode is further constrained by increasing the hindered rotation barrier height.

CONCLUSION

Temperature dependent Raman scattering measurements of bulk and the confined TNT in four different pore sizes suggest that a) the freezing transition of the confined TNT can be triggered by the bulk TNT on the outer surface, b) the freezing transition of the confined TNT starts at the pore center rather at the pore surface, c) the confined solid TNT retains the similar solid structure of its bulk, d) the TNT confined in 5 and 2.5 nm pores may exist in cluster form.

ACKNOWLEDGEMENT

REFERENCES

1. D.D. Awschalom, J. Warnock, Phys. Rev. B **35**, 6779 (1987); J. Warnock, D.D. Awschalom, and M.W. Shafer, Phys. Rev. Lett. **57**, 1753 (1986).
2. R. Mu and V.M. Malhotra, Phys. Rev. B **44**, 4296 (1991).
3. C.L. Jackson and G.B. Mckenna, J. Chem. Phys. **93**, 9002 (1990).
4. P.E. Sokol, W.J. Ma, K.W. Herwig, W.M. Snow, Y.Wang, J.Koplik, J.R. Banavar, Appl. Phys. Lett. **61**, 777 (1992).
5. George W. Scherer, J. Non-cryst. Solids **155**, 1 (1993).
6. W.J. Ma, J.R. Banavar, and J.Koplik, J. Chem. Phys. **97**, 485 (1992).
7. A. Brodka and T.W. Zerda, J. Chem. Phys. **97**, 5676 (1992).
8. R. Mu, F. Jin, S.H. Morgan, D.O. Henderson, and E. Silberman, J. Chem. Phys. **100**, 7749 (1994); R. Mu, D.O. Henderson, F. Jin in Determining Nanoscale Physical Properties of Materials by Microscopy and Spectroscopy, edited by M. Sarikaya, M. Isaacson, and H. K. Wickramasinghe (Mater. Res. Soc. Proc. **332**, Pittsburgh, PA, 1994)pp. XXX-000.
9. J. Klafter and J.M. Drake, Molecular Dynamics in Restricted Geometries (John Wiley & Sons, New York, 1989).
10. R. Mu, Y. Xue, D.O. Henderson, Phys. Rev. B (to be submitted).
11. R. Mu, Y. Xue, D.O. Henderson in Dynamics in Small Confining Systems, edited by J.M. Drake et al. (Mater. Res. Soc. Proc. XXX, Pittsburgh, PA, 1995) pp. XXX-000.
12. N. LeCalve, F. Romain, and B. Pasquier, J. Raman Spectrosc. **8**, 239 - 43 (1979).
13. J.J.P. Stewart, S.R. Bosco and W.R. Carper, Spectrochimica Acta **42A**, 13 (1986).

FREEZING/MELTING TRANSITION OF PHYSICALLY RESTRICTED n-DECANE

P. M. HOFFMANN* AND V. M. MALHOTRA
Department of Physics, Southern Illinois University at Carbondale, Carbondale, Illinois 62901
*Current Address: Department of Materials Science and Engineering, The Johns Hopkins
University, Baltimore, Maryland 21218

ABSTRACT

We undertook differential scanning calorimetry (DSC) measurements at 170 K < T < 300 K on
n-decane, physically confined in 8 nm (= diameter D) porous silica derivatized with various
functional groups, to understand how surface structure of the confining media affects the freezing
or melting transition of the n-decane. Though we observed a typical depression (ΔT) in the
freezing or melting transition temperature of the physically confined decane, our results failed to
manifest usual linear dependence of ΔT on D^{-1} when the expected contraction in D, due to the
presence of aminopropyl-, hexyl-, phenyl- or trimethyl-groups on the silica surface, was taken
into account. However, it is worth noting that a linear behavior was observed between ΔT and
D^{-1} if only alkane-chain derivatized hosts were considered. Our results also indicate that a large
fraction of physically confined n-decane (35 to 70 %), depending on the host silica, does not
participate either in the melting or freezing transition. The most interesting behavior observed in
the present study is the occurrence of the unusual two peaks associated with the freezing
transition of physically confined decane. This bimodal behavior is strongly dependent on the
chemistry of the confining silica host's surface.

INTRODUCTION

It is known that the physical properties of materials are profoundly changed when the length
scale is reduced to a few nanometers. In this size range the surface to volume ratio increases to a
point where surface effects start playing an increasingly important role in describing the behavior
of ultrasmall systems. As an example, the phase transformation properties of physically
restricted systems are profoundly affected. Considerable work has been reported on the freezing
and melting of various fluids in different hosts, such as porous silica glasses.[1-9] These studies
suggest that the transition temperatures are depressed and that the depression (ΔT) is proportional
to R^{-1}, where R (=pore radius) is the major length scale of the confining medium. It is also
commonly observed that the transition peaks are significantly broadened as compared to the bulk
transition peaks. It is, however, not well understood how the surface structure of the host
medium influences the depression and the broadening of the transitions of the confined fluid. To
investigate the complex dependence of the thermodynamic properties of physically confined
fluids on the chemical surface structure of the confining host, we undertook DSC measurements
on n-decane, physically confined in 8 nm porous silica, derivatized with various functional
groups.

EXPERIMENTAL TECHNIQUES

To physically confine n-decane, we used porous silica obtained from Phase Separation, Inc. (USA) as host material. The porous silica was in the form of spherical beads of 3 to 10 μm diameter. The reported average pore diameter is 8 nm. The samples were derivatized to form monolayers of different functional groups on the silica surface. We used nude (underivatized), trimethyl-, hexyl-, aminopropyl- and phenyl-derivatized silica. The monolayer coverage of chemical surface groups was confirmed by diffuse reflectance infrared spectroscopy. The pore structure of the hosts was probed by TEM and SEM technique with limited success. The TEM images confirmed, however, that the average pore diameter at the surface of the silica beads lay in the range of 5-8 nm. If an average pore diameter is assumed to be 8 nm for the nude sample, effective diameters for the derivatized samples could be calculated using diffraction data of bong lengths and angles. To impregnate the porous samples with n-decane for DSC measurements, we followed previously described procedures.[6,7] The DSC data were recorded by heating or cooling the sample at a rate of 5 K/min.

RESULTS AND DISCUSSION

Figures 1 a,b, and c depict DSC curves for cooling and heating runs of confined n-decane in the three representative host materials. The trimethyl- and phenyl- hosts give peak shapes very similar to the nude host material. It should be noted from Fig. 1 that the melting peaks of the confined n-decane have a pronounced λ-shape with a long low-temperature tail while the freezing peaks are more symmetrical. The λ-shape can be explained if we assume the temperature depression ΔT, i. e. the difference between the bulk transition temperature and the transition temperature of the confined fluid, to be proportional to the inverse of the pore diameter D_p. A symmetrical pore size distribution, e.g., a Gaussian distribution, will then result in a non-symmetrical distribution in the temperature depression ΔT with a tail on the high ΔT or low temperature T side. Mathematically, the peak shape can be expressed by:

$$n(\Delta T) = N \cdot V_{pore} \cdot \exp\left(\frac{\left(\frac{const.}{\Delta T} - D_{avg}\right)^2}{(S \cdot \delta D)^2}\right) \qquad (1)$$

$n(\Delta T)$ is the relative number of molecules that melt at some particular temperature depression. D_{avg} is the average pore diameter, δD is the characteristic spread of the pore size distribution, S represents any additional spread due to non-ideal physical properties of the system (finite thermal conductivity, etc.). V_{pore} is the pore volume, which is proportional to D^2, if we assume a fixed pore length, and N is a normalization constant. Figure 1 d shows a calculated peak for $\delta D/D = 10\%$ and $S = 5$. It can be seen that the calculated peak resembles the measured melting peaks very closely. We can also do the reverse calculation and find the apparent pore size distribution which produces a certain measured peak. Figure 2 is the result of such a calculation, obtained from the melting peak of nude silica. We note a close resemblance between this result and pore size distributions that were reported by Liu et al.[10]
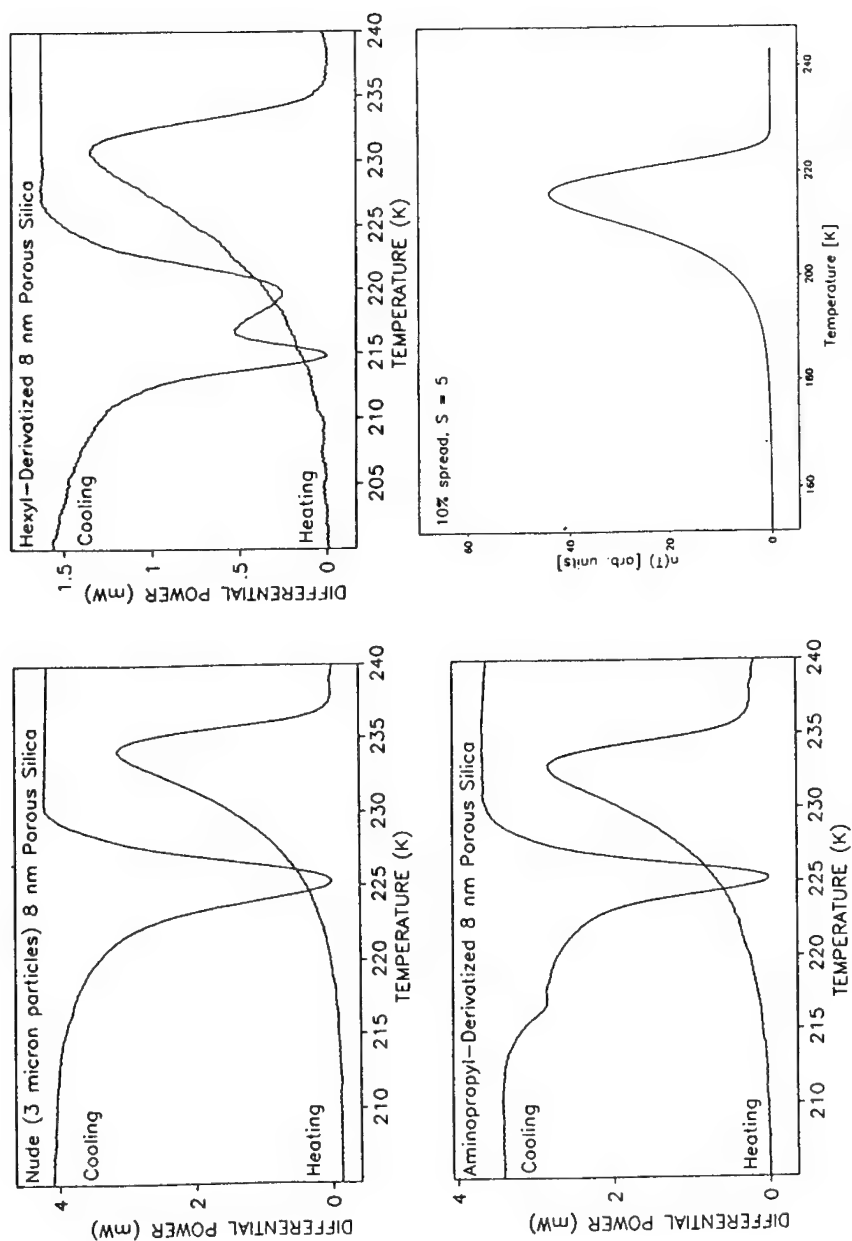
Figure 1 a-c. DSC curves of n-decane confined in nude (upper left, a), hexyl- (upper right, b), and aminopropyl-derivatized (lower left, c) silica. Figure 1 d. (lower right) Simulated DSC curves using eq. (1).
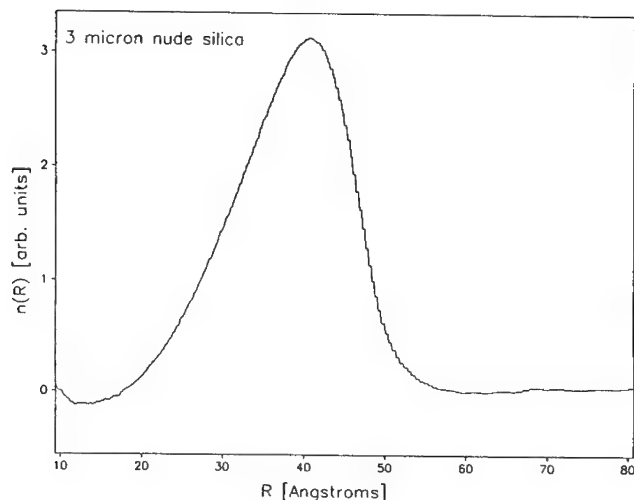
Fig. 2. Pore size distribution of nude silica calculated from the melting peak of the confined n-decane

The peak shape, however, can not be only a result of the pore size distribution since we did not observe a pronounced λ-shape for the freezing transition. The less pronounced low temperature tail in the freezing can be attributed to the fact that upon cooling the freezing in the smaller pores can be thermodynamically favored by the presence of adjacent larger pores in which the fluid is already frozen. This is not possible for the melting transition since the fluid in the smaller pore necks melts first upon heating with little influence on the melting in the larger pores.

The observed ΔT's associated with the freezing and melting transition are graphed as a function of D^{-1} in Fig. 3. We note that ΔT for the nude, hexyl- and aminopropyl-derivatized samples can be fitted to a straight line. The full width at half maximum (FWHM) of the peaks shows a very similar behavior: the FWHM corresponding to the nude, the hexyl- and the aminopropyl-derivatized samples also fit a straight line, while the FWHM for the trimethyl- and the phenyl-derivatized hosts show no correlation. From the plug model[1,3,4] we know that ΔT is proportional to the inverse of the pore diameter D^{-1}. Therefore, the spread $\delta(\Delta T)$ in ΔT should be a function of the spread in the pore diameters δD. We obtain:

$$\delta(\Delta T) = \frac{\partial(\Delta T)}{\partial D}\delta D = const. \cdot \frac{\delta D}{D} \cdot D^{-1} \qquad (2).$$

Assuming that the relative spread $\delta D/D$ is independent of the pore size, we should expect a linear D^{-1}-dependence of the FWHM. Our results suggest that this dependence only holds for the nude, hexyl- and aminopropyl-derivatized samples. The correlated behavior of these samples is surprising since their surfaces are terminated by different chemical groups, i.e., a methyl-group in the case of hexyl-sample and an amino-group in the case of the aminopropyl-sample. On the other hand the results obtained for the hexyl- and the trimethyl-derivatized samples are not correlated though the confined n-decane is influenced by terminating methyl-groups in both cases.
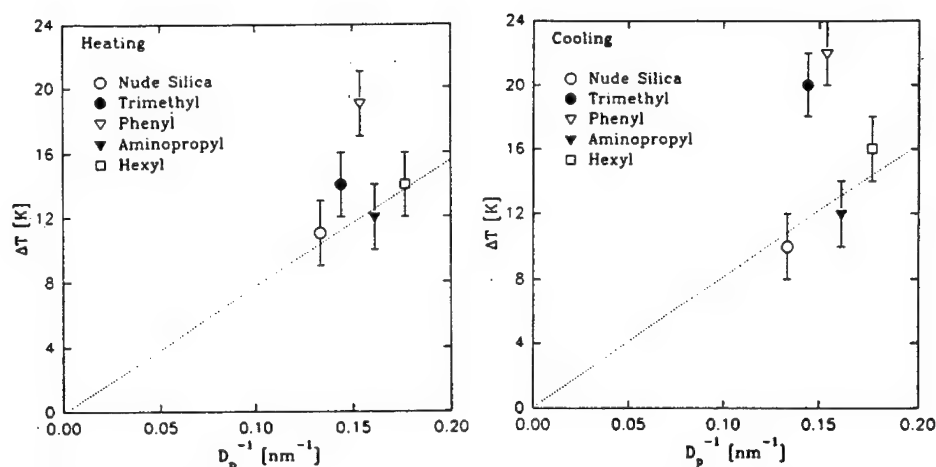
Figure 3. Temperature depression ΔT versus inverse of pore diameter D for the freezing (left) and melting (right) of the confined n-decane.

Another indication of the correlated behavior of n-decane in hexyl- and in aminopropyl-derivatized silica is the surprising observation of two peaks associated with the freezing transition of n-decane in these hosts. It seems that the influence of the chemical nature of the terminating group is negligible compared to the effect of its molecular structure since only the two alkane-chain structured derivatized hosts exhibit a similar behavior while the results obtained from the other samples indicate no correlation. The transitional properties of a confined fluids also seem to strongly depend on the structure of the fluid itself. Results on cyclohexane confined in the same range of derivatized hosts suggest no bimodal behavior.

The bimodal behavior observed in the freezing of n-decane in porous aminopropyl- and hexyl-derivatized silica can not be a result of a nonsymmetric pore size distribution or an incomplete coverage of the silica hosts surface, since two transitional peaks are observed only in the freezing but not in the melting run. Instead, it seems that the system or part of the system passes through a metastable state upon freezing, which does not exist in the case of bulk n-decane. As mentioned above, the formation of this metastable phase is linked to the alkane-chain derivatized hosts (hexyl, aminopropyl), suggesting that the formation of the metastable phase is strongly dependent on the molecular structure of the surface groups, but not on the chemical nature of their terminating groups.

We observed that a large portion of the confined n-decane did not undergo any phase transition. Using the mass of the confined and the bulk n-decane in the sample and the total observed transition enthalpy, we calculated that about 35-70 % (depending on the sample) of the confined n-decane did not participate in either freezing or melting transition. An idle, viscous layer of confined fluid close to the host surface has been repeatedly reported in the literature.[4,6] Usually such a surface layer is associated with polar fluids. However, our results indicate that even for a rather nonpolar fluid like n-decane a large portion is idle. If a large portion of idle molecules

close to the pore walls is assumed, it becomes difficult to understand how the surface structure of the host influences the transitional behavior of the confined n-decane.

REFERENCES

1. J. Warnock, D. D. Awschalom, and M. W. Shafer, Phys. Rev. Lett., **57**, 1753 (1986)
2. J. Warnock, D. D. Awschalom, and M. W. Shafer, Phys. Rev. B, **34**, 475 (1986)
3. D. D. Awschalom and J. Warnock, Phys. Rev. B., **35**, 6779 (1987)
4. D. D. Awschalom and J. Warnock, in Molecular Dynamics in Restricted Fluids, edited by J. Klafter and J. M. Drake (John Wiley and Sons, New York, 1986) p.351.
5. C. L. Jackson and G. B. McKenna, J. Chem. Phys., **93**, 9002 (1990)
6. R. Mu and V. M. Malhotra, Phys. Rev. B, **44**, 4296 (1991)
7. V. M. Malhotra, R. Mu, and A. Natarajan, in Dynamics in Small Confining Systems, edited by J. M. Drake, J. Klafter, R. Kopelman, D. D. Awschalom (Mat. Res. Soc. Symp. Proc., **290**, Pittsburgh, PA, 1993) pp. 121-126
8. E. Molz, A. P. Y. Wong, M. H. W. Chan, and J. R. Beamish, Phys. Rev B, **48**, 5741 (1993)
9. K. M. Unruh, T. E. Huber, and C. A. Huber, Phys. Rev. B, **48**, 9021 (1993)
10. G. Liu, Y. Li, and J. Jonas, J. Chem. Phys., **95**, 6892 (1991)

VESICLES AND PASSAGES BETWEEN LAMELLAS
IN L_α MEMBRANE PHASES

LEONARDO GOLUBOVIĆ
Department of Physics, West Virginia University, Morgantown, WV26506

ABSTRACT

We consider entropic effects of vesicles and passages confined between lamellas in fluid membrane lamellar (L_α) phases. We show that their presence induces attractive interactions between lamellas which strongly compete with steric repulsion in the vicinity of phase transitions from the lamellar to isotropic membrane phases. An interplay between steric repulsion and entropic interactions mediated by passages and vesicles determines the inter-lamellar distance reached at these transitions. This distance crucially depends on the membrane Gaussian bending rigidity constant.

INTRODUCTION

In recent years significant attention has been devoted to statistical physics of fluid membranes,[1] and their lamellar and random sponge-like phases.[2]-[10] Membrane fluctuations induce striking effects such as Helfrich's inter-membrane repulsion[3] stabilizing lamellar phases.[7] Free energy of this entropic ("steric") repulsion between a pair of membranes at distance l is, per unit membrane area,

$$F_{u.a.}^{steric} = const. \frac{(k_B T)^2}{\kappa l^2}, \tag{1}$$

where κ is membrane bending rigidity.[3],[4] Membrane fluctuations are essential also for understanding the lamellar phase melting which occurs when the inter-membrane distance l reaches certain maximal distance l_{max}.[5][8] De Gennes and Taupin,[8] and more recent studies[5][10] identified l_{max} with fluid membrane *persistence length* ξ_κ.[9] Recent experiments of Porte et al., however, appear to contradict this indicating that $l_{max} \ll \xi_\kappa$.[11]

Prompted by this, here we discuss effects of droplets (vesicles) and passages [as in Fig. 1a] thermally exicited in a lamellar, L_α phase of surfactant bilayer membranes. We show that their presence induces entropic *attractive* inter-membrane interactions which compete with the Helfrich's steric repulsion in Eq. (1) and limit l_{max}. We find that, in general, $l_{max} \ll \xi_\kappa$. In addition to the persistence length, $\xi_\kappa = a \; exp(4\pi\kappa/\alpha k_B T)$ (a is a molecular lengthscale, and $\alpha = 3$,[9]), we reveal another important scale $\xi_{\overline{\kappa}} = a \; exp(-4\pi\overline{\kappa}/\alpha' k_B T)$, where $\alpha' = 10/3$, and $\overline{\kappa}$ is the membrane saddle-splay ("Gaussian") rigidity constant.[12][13] We find two distinct lamellar phase behaviors: (I)*Regime A ("Passage Regime")*: For $0 < -\overline{\kappa} < \frac{\alpha'}{\alpha}\kappa = \frac{10}{9}\kappa$, one has $a \ll \xi_{\overline{\kappa}} \ll \xi_\kappa$ at low T. In this regime $l_{max} \sim \xi_{\overline{\kappa}} \ll \xi_\kappa$. For $l \approx l_{max}$, there are numerous passages connecting membranes, whereas droplets are rare. Such a lamellar phase melts either into a very dilute droplet phase, or to a sponge phase [if $||\overline{\kappa}| - \frac{10}{9}\kappa| < O(1)k_B T$]. (II) *Regime B ("Droplet Regime")*: For $-\overline{\kappa} > \frac{10}{9}\kappa$, one has $\xi_{\overline{\kappa}} \gg \xi_\kappa$ at low T. In this regime $l_{max} \sim \xi_{drop} = \xi_\kappa(\xi_\kappa/\xi_{\overline{\kappa}})^{\alpha'/(2\alpha-\alpha')} \ll \xi_\kappa \ll \xi_{\overline{\kappa}}$. For $l \approx l_{max}$ there are numerous droplets between lamellas, whereas passages are rare. Such a lamellar phase melts either into a droplet rich, globular membrane phase or to a sponge phase [if $||\overline{\kappa}| - \frac{10}{9}\kappa| < O(1)k_B T$]. Passage regime A apparently corresponds to the experimental situation in egg-lecithin lamellar states studied by Harbich et. al..[12] They observe a rise of the density of

passages, n_p, with increasing l. We suggest that this rise follows the law: $n_p \sim l^{\alpha'-2} = l^{4/3}$, for $l \ll l_{max}$.

PASSAGES AND DROPLETS

We base our study on the grand-canonocal description of fluid membrane ensembles.[4][5][10] Each membrane is characterized by the energy $E = \sigma A + E_{curv}$, where A is the membrane area, σ is the surface tension ($-\sigma a^2$ = chemical potential of surfactant molecules), and E_{curv} is the membrane curvature energy, $E_{curv} = \int dA \left[\frac{\kappa}{2} H^2 + \overline{\kappa} G\right]$, where H and G are, respectively, mean and Gaussian membrane curvature.[13] As in previous studies, we coarse-grain short-scale membrane fluctuations.[2][5][10] This induces a renormalization of the membrane bending elastic constants which attain a lengthscale dependence of the form $\kappa(L) = \frac{\alpha k_B T}{4\pi} ln\left(\frac{\xi_\kappa}{L}\right)$, and $\overline{\kappa}(L) = \frac{\alpha' k_B T}{4\pi} ln\left(\frac{L}{\xi_{\overline{\kappa}}}\right)$.[14]

First, we consider a single passage connecting two lamellas at distance l, as depicted in Fig. 1a.

(a)   **(b)**
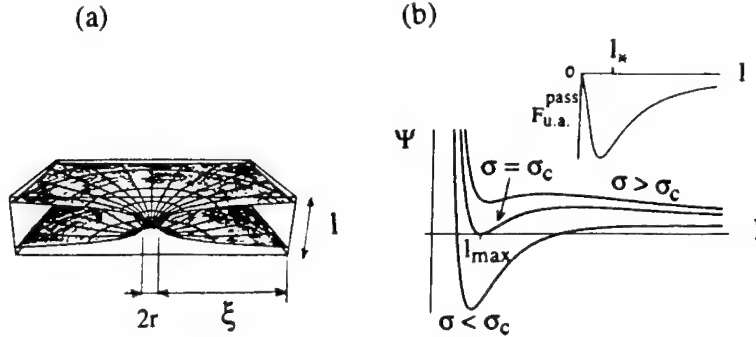
Figure 1: (a) Passage geometry. (b) Lamellar phase free energy density $\psi(l, \sigma)$ for various values of σ. Inset: Passage mediated intermembrane interaction free energy per unit area $F_{u.a.}^{pass}$.

The passage curvature energy can be estimated as

$$E_{pass} = O(1) \; \kappa(\xi)\left(\frac{r}{\xi}\right)^2 - 4\pi\overline{\kappa}(r), \tag{2}$$

where r is the size of the passage neck, and ξ is the size of the passage deformation region [Fig. 1(a)]. At distances from the neck smaller than ξ, the presence of a passage curves the membranes giving rise to the first term in (2). [15] The second term in (2) is the Gaussian curvature contribution.[12] The passage deformation region is, approximately, a catenoid.[12][15] This gives the condition $l \approx 2r \; ln(\xi/r)$ relating ξ and r in (2). With this constraint, we minimize (2) and find the equilibrium $E_{pass} = -\alpha' k_B T \; ln\left(\frac{l}{\xi_{\overline{\kappa}}}\right)$, whereas $\xi_{eq} = O(1) \; \left(\frac{\kappa(l)}{k_B T}\right)^{1/2} l / \; ln\frac{\kappa(l)}{k_B T}$, and $r_{eq} = O(1) \; l/ln(\kappa(l)/k_B T)$, for $\kappa(l) \gg k_B T$, i.e., $l \ll \xi_\kappa$. E_{pass} is dominated by the Gaussian curvature contribution to Eq. (2). E_{pass} decreases with increasing l and, moreover, becomes negative as l crosses $\xi_{\overline{\kappa}}$, whereas the passage deformation region size ξ_{eq} increases with l.

Next, consider two passages at distance R. They interact via the repulsive potential $U_{pp}(R) \approx \kappa(R)\left(\frac{r_{eq}}{R}\right)^2$,[15] for $R < \xi_{eq}$, when the passage deformation regions overlap. $U_{pp} \approx k_B T$ for $R \approx \xi_{eq}$. For $R > \xi_{eq}$, $U_{pp} < k_B T$, and the passage interaction can be

ignored. For $R < \xi_{eq}$, $U_{pp} > k_B T$. Thus, the passage interaction can be viewed as a hard core repulsion, with effective hard core size$\approx \xi_{eq}$. Two-dimensional fluid of passages, between a pair of neighbouring membranes in a lamellar phase, can be described grand-canonically by

$$Z_{pass} = \sum_{N=0}^{\infty} \frac{1}{N!} \prod_{i=1}^{N} \int \frac{d^2 \mathbf{X}_i}{\Delta A} \; e^{-H_N/k_B T}, \tag{3}$$

with $\Delta A = l^2 (k_B T/\kappa(l))^2$,[16] and $H_N = N E_{pass} + \sum_{i<j} U_{pp}(\mathbf{X}_i - \mathbf{X}_j)$. U_{pp} can be ignored when $|\mathbf{X}_i - \mathbf{X}_j| > \xi_{eq}$, i.e., when the passage number per unit area, n_p is less than ξ_{eq}^{-2}. In this *dilute* regime, (3) yields $n_p(l) \approx n_o(l) = \left(\frac{\kappa(l)}{k_B T}\right)^2 \frac{1}{l^2}\left(\frac{l}{\xi_{\overline{\kappa}}}\right)^{\alpha'} \sim l^{\alpha'-2} = l^{4/3}$. Free energy of this dilute passage fluid is, per unit membrane area, $F_{u.a.}^{pass}(l) = -k_B T n_o(l) \sim -l^{4/3}$. In the dilute regime, $n_p(l)$ *increases* as $l^{\alpha'-2} = l^{4/3}$. Such a growth of the passage density was indeed observed by Harbich et. al. in egg-lecithin membrane stacks.[12] The dilute regime occurs for $n_o \xi_{eq}^2 = (l/l_*)^{\alpha'} < 1$, with $l_* = \left(k_B T/\kappa(\xi_{\overline{\kappa}})\right)^{3/\alpha'} \xi_{\overline{\kappa}} \sim \xi_{\overline{\kappa}}$. For $l > l_*$, passage deformations regions overlap and we must take into account passage interactions. They are effectively hard core repulsions, with hard core size$\approx \xi_{eq}$. Free energy of the interacting passage fluid can be thus found by minimizing

$$F_{u.a.}^{pass}(n_p, l) = k_B T n_p \; ln\frac{n_p}{e n_o(l)} - k_B T n_p \; ln(1 - n_p \xi_{eq}^2), \tag{4}$$

over the passage density n_p. The first term in (4), alone, yields the above dilute regime results, whereas the second term is the free energy increase due to excluded volume effects. For dense passage regime, $n_o(l)\xi_{eq}^2 = (l/l_*)^{\alpha'} \gg 1$, Eq. (4) yields $n_p \approx 1/\xi_{eq}^2$, i.e., the passage separation$\approx \xi_{eq}$, whereas

$$F_{u.a.}^{pass}(l) \approx -O(1) \, \frac{k_B T}{\xi_{eq}^2} ln(n_o(l)\xi_{eq}^2) = -O(1)\frac{\alpha'(k_B T)^2}{\kappa(l)l^2} ln\frac{l}{l_*}. \tag{5}$$

$F_{u.a.}^{pass}(l)$ is sketched in the inset to Fig. 1b. For any l, to a good approximation,

$$F_{u.a.}^{pass}(l) = -O(1)\frac{k_B T}{\xi_{eq}^2} ln(1 + n_o(l)\xi_{eq}^2) = -O(1)\frac{(k_B T)^2}{\kappa(l)l^2} ln\big(1 + \big(\frac{l}{l_*}\big)^{\alpha'}\big), \tag{6}$$

reducing to the dilute regime result for $l \ll l_*$, and to (5) for $l \gg l_*$. Inset to Fig. 1b indicates that passages induce an *attractive* interaction between membrane pairs tending to keep membranes at a preferred distance $l = O(1) \, l_* \sim \xi_{\overline{\kappa}}$. Moreover, by (5) we see that, for $l > l_*$, this passage induced attraction actually *dominates* over Helfrich's steric repulsion (1). Thus, total free energy per unit area, $F_{u.a.}^{steric}(l) + F_{u.a.}^{pass}(l)$, also has a minimum at an $l = O(1)l_* \sim \xi_{\overline{\kappa}}$.

In the presence of passages, lamellar phase free energy per unit volume is $F_{u.v.}^{l.p.}(\sigma) = [\Psi(l, \sigma)]_{min(l)}$,[4] with $\Psi(l, \sigma) = \frac{1}{l}\big[\sigma + F_{u.a.}^{steric}(l) + F_{u.a.}^{pass}(l)\big]$. In the absence of the passage term, $\Psi(l, \sigma)$ has a single minimum for $\sigma < 0$, at $l = l_{eq} \sim |\sigma|^{-1/2}$. Thus, l_{eq} would diverge as $\sigma \to 0$. By de Gennes and Taupin,[8] this infinite swelling of the lamellar phase stops at a melting point where l_{eq} reaches $l_{max} \sim \xi_\kappa$ and lamellas crumple. Our inclusion of the passage free energy, however, changes this picture radically for $-\overline{\kappa} < \frac{10}{9}\kappa$ when $\xi_{\overline{\kappa}} \ll \xi_\kappa$ [Regime A], see Fig. 1b. Now l_{eq} remains finite as $\sigma \to 0$, when

$l_{eq} \to O(1)l_* \sim \xi_{\overline{\kappa}} \ll \xi_\kappa$ and the lamellar phase becomes passage rich. This passage rich lamellar phase remains stable in a range of *positive* values of σ , where a *dilute droplet phase* is typically favored.[10] For $\xi_{\overline{\kappa}} \ll \xi_\kappa$, free energy of this droplet phase is essentially zero. Thus, the lamellar phase transforms into the droplet phase when $[\psi(l,\sigma)]_{min(l)}$ goes to zero. This occurs for a *positive* $\sigma = \sigma_c = +O(1)(k_BT)^2/\kappa(l_*)l_*^2$, [see Fig. 1b]. At the transition, l reaches $l_{max} = O(1)\ l_*$. Thus $l_{max} \sim \xi_{\overline{\kappa}} \ll \xi_\kappa$ for $-\overline{\kappa} < \frac{\alpha'}{\alpha}\kappa = \frac{10}{9}\kappa$ and $||\overline{\kappa}| - \frac{10}{9}\kappa| > O(1)\ k_BT$. Under these conditions [Regime A] one thus has a strong first order phase transition between a passage rich, but *still* orientationally well ordered lamellar phase (as $l_{max} \sim \xi_{\overline{\kappa}} \ll \xi_\kappa$) and a very dilute droplet phase. Prior to this transition, passage rich smectic-lamellar phase most-likely undergoes a weaker transition to a highly anisotropic catenoid-lamellar phase in which passages form regular lattices (with the in-layer lattice constant$\approx \xi_{eq} \approx (\kappa(l)/k_BT)^{1/2}l \gg l)$. Such a structural change was indeed observed in egg-lecithin lamellar structures.[12]

Let us now consider the lamellar phase behavior in the opposite case with $\xi_\kappa \ll \xi_{\overline{\kappa}}$, occuring for $-\overline{\kappa} > \frac{10}{9}\kappa$ and $||\overline{\kappa}| - \frac{10}{9}\kappa| > O(1)\ k_BT$ [Regime B]. Then, provided $l < \xi_\kappa$, passages are very dilute. In this regime important role is played by thermally excited *droplets* (vesicles) confined between lamellas, as discussed hereafter. Curvature free energy of a single nearly spherical droplet of radius R is $E_{drop}(R) = 8\pi\kappa(R) + 4\pi\overline{\kappa}(R) = (2\alpha - \alpha')k_BT\ ln(\xi_{drop}/R)$, where $\xi_{drop} = a\ exp\big[\frac{4\pi(2\kappa+\overline{\kappa})}{k_BT(2\alpha-\alpha')}\big]$, is a new, "droplet" scale. For $2\kappa > -\overline{\kappa} > \frac{10}{9}\kappa$, one has $a \ll \xi_{drop} \ll \xi_\kappa \ll \xi_{\overline{\kappa}}$ at low T.

Next, consider a polydisperse ensemble of droplets thermally excited between two lamellas at distance l. Its grand-canonical free energy is, in a dilute limit of noninteracting droplets,[10] $F^{drop} = -k_BT \int dRd^2\mathbf{X}dz\ \rho_{drop}(R)$ with $\rho_{drop}(R) = (\Delta R)^{-4}\epsilon xp\big[-(4\pi\sigma R^2 + E_{drop}(R))/k_BT\big]$.[10] $\rho_{drop}(R)dRd^2\mathbf{X}dz$ is the number of droplets with radii in $(R, R + dR)$ and centers positioned in $d^2\mathbf{X}dz$, and $\Delta R = (k_BT/\kappa(R))^{1/2}R$ (z-direction is perpendicular to lamellas). For droplets confined between two lamellas $(2R < l)$, after integrating over z $[\int dz = l - 2R]$, we obtain the droplet free energy, per unit area of a lamella, as

$$F_{u.a.}^{drop}(l) = -k_BT \int_a^{l/2} dR\ (l - 2R)\rho_{drop}(R). \tag{7}$$

For $|\sigma|l^2/k_BT \ll 1$, we find

$$F_{u.a.}^{drop}(l) = f_{u.a.}^{drop}(l) + l\ F_{u.v.}^{d.p.}. \tag{8}$$

Here

$$f_{u.a.}^{drop}(l) = +O(1)\frac{(\kappa(l))^2}{k_BT}\frac{l^{2\alpha-\alpha'-2}}{\xi_{drop}^{2\alpha-\alpha'}} \ \sim \ +l^{2/3}. \tag{9}$$

$f_{u.a.}^{drop}(l)$ is an *attractive* interaction beween lamellas. $F_{u.v.}^{d.p.}$ in (8) is the free energy, per unit volume, of the droplet phase, $F_{u.v.}^{d.p.} = -O(1)\frac{\kappa^2}{k_BT}(a^{2\alpha-\alpha'-3}/\xi_{drop}^{2\alpha-\alpha'})$.

In the regime B, free energy of the lamellar phase is, per unit volume,

$$F_{u.v.}^{l.p.} = \left(\frac{1}{l}\big[\sigma + F_{u.a.}^{steric}(l) + F_{u.a.}^{drop}(l)\big]\right)_{min(l)}.$$

Thus, by (8), we find the *difference* between free energy densities of the lamellar and the droplet phase in the form $F_{u.v.}^{l.p.} - F_{u.v.}^{d.p.} = [\Psi(l,\sigma)]_{min(l)}$, with

$$\Psi(l,\sigma) = \frac{1}{l}\left[\sigma + F_{u.a.}^{steric}(l) + f_{u.a.}^{drop}(l)\right]. \tag{10}$$

$f_{u.a.}^{drop}(l)$ here is the droplet mediated interaction, Eq. (9). With changing σ, $\Psi(l,\sigma)$ in (10) behaves (once again) in the manner depicted in Fig. 1b. For a critical value of σ, $\sigma = \sigma_c = -O(1)(k_BT)^2/\kappa(l_{max})l_{max}^2$, when l reaches $l_{max} = O(1)\left(\frac{k_BT}{\kappa(\xi_{drop})}\right)^{3/(2\alpha-\alpha')}\xi_{drop}$, the free energy difference, $[\psi(l,\sigma)]_{min(l)}$, vanishes and the lamellar phase melts into the droplet phase. This droplet phase is actually a globular phase. The largest droplets in this phase are affected by excluded volume effects which limit their size R_{max}. Volume fraction occupied by droplets $\approx \int_a^{R_{max}} \frac{4\pi}{3}R^3\rho(R)$, is $O(1)$. This condition gives $R_{max} = O(1)\left(k_BT/\kappa(\xi_{drop})\right)^{2/(2\alpha-\alpha')}\xi_{drop}$. So, $l_{max} \sim R_{max} \sim \xi_{drop} \ll \xi_\kappa \ll \xi_{\overline{\kappa}}$, in the regime B with $-\overline{\kappa} > \frac{10}{9}\kappa$ and $|-\overline{\kappa} - \frac{10}{9}\kappa| > O(1)\ k_BT$.

On the other side, for κ and $\overline{\kappa}$ in the range $|-\overline{\kappa} - \frac{10}{9}\kappa| < O(1)\ k_BT$, one has $R_{max} \sim \xi_{drop} \sim \xi_\kappa \sim \xi_{\overline{\kappa}}$. Thus, creation of *passages between the largest droplets* (with $R \approx R_{max}$) is favored in this range. This transforms the globular phase into a sponge phase, which can be envisioned as a condensed liquid phase of droplets connected by passages. Schematic phase diagram summarizing regimes A and B is in Fig. 2.
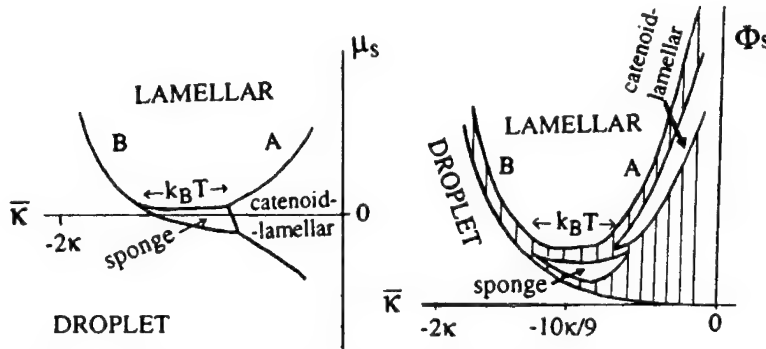
Figure 2: Schematic phase diagram of fluid membrane systems, for fixed κ, in the $(\mu_s, \overline{\kappa})$ and $(\Phi_s, \overline{\kappa})$ planes.

Phase diagram is given for a fixed $\kappa \gg k_BT$, in the $(\mu_s, \overline{\kappa})$ and $(\Phi_s, \overline{\kappa})$ planes. Here $\mu_s = -\sigma a^2$ is the surfactant chemical potential, and Φ_s is the surfactant volume fraction, $\Phi_s = a\frac{\partial F_{u.v.}}{\partial\sigma}$.[5] Membrane phases with large structural scales$\gg a$ occur only in a range of *negative* $\overline{\kappa}$, $0 < -\overline{\kappa} < 2\kappa$, in consistence with recent carefull experiments of Strey.[17] In the regime A, one has a coexistence of a very dilute droplet phase (d.p.) with a passage rich catenoid-lamellar phase (l.p.). At their coexistence, $\Phi_s^{d.p.} \sim \frac{a}{\xi_{\overline{\kappa}}}\left(\frac{\xi_{\overline{\kappa}}}{\xi_\kappa}\right)^{2\alpha} \ll \Phi_s^{l.p.} \sim \frac{a}{\xi_{\overline{\kappa}}}$.

On the other side, in the regime B, a dense droplet, globular phase coexists with a droplet rich lamellar phase. At their coexistence, $\Phi_s^{d.p.} \sim \Phi_s^{l.p.} \sim \frac{a}{\xi_{drop}}$.

Finally, let us discuss recent experimental studies of Porte et. al..[11] For their ternary system (involving a cosurfactant), $\kappa \approx 3k_B T$ [thus $\xi_\kappa \approx 300,000a$], whereas $\bar{\kappa}$ is not known. By taking that one is in the Regime A with $\bar{\kappa} = -\frac{4}{15}\kappa$ (a plausible value in the absence of cosurfactants [18]) for the lamellar phase we get $l_{max} \sim \xi_{\bar{\kappa}} \approx 100a$ and $\Phi_s^{l.p.} \approx a/l_{max} \sim 1\%$ at the coexistence with the catenoid-lamellar phase. Thus, l_{max} is some three orders of magnitude smaller then ξ_κ, in a striking consistence with the experiments.[11] The experimental $\Phi_s^{l.p.}$ varies from 5% up to 50% across the phase diagram. This variation is probably due to the cosurfactant (its amount is varied in the phase diagram). Cosurfactants are likely to affect $\bar{\kappa}$, and thus, also, $l_{max} \sim \xi_{\bar{\kappa}}$. We stress, however, that these experimental data were actually obtained at the coexistence of the lamellar with the sponge phase (rather than the catenoid-lamellar phase). Sponge phase is in Fig. 2 present in a range of $\bar{\kappa}$ around $-\frac{10}{9}\kappa$ vanishing as $T \to 0$. At room temperatures, however, this range could be wide enough to explain the stability of the sponge phase of Porte et. al..

REFERENCES

1. For a review, see Statistical Mechanics of Membranes and Surfaces, edited by D.R. Nelson, T. Piran, and S. Weinberg (World Scientific, Singapore, 1989).
2. S.A. Safran, D. Roux, M.E. Cates, and D. Andelman, Phys. Rev. Lett. **57**, 491 (1986).
3. W. Helfrich, Z. Naturforsch. **A33**, 305 (1978).
4. L. Golubović and T.C. Lubensky, Phys. Rev. **B39**, 12110 (1989).
5. L. Golubović and T.C. Lubensky, Phys. Rev. **A41**, 4343 (1990).
6. D. Roux et. al., Europhys. Lett. **11**, 229 (1990).
7. D. Roux and C.R. Safinya, J. Phys. (France) **49**, 307 (1988), and therein.
8. P.G. de Gennes and C. Taupin, J. Phys. Chem. **86**, 2294 (1982).
9. L. Peliti and S. Leibler, Phys. Rev. Lett. **54**, 1690 (1985).
10. D.A. Huse and S. Leibler, J. Phys. (France) **49**, 605 (1988).
11. G. Porte et. al., J. Phys. (France) **49**, 511 (1989); G. Porte et. al., J. Phys. II (France) **1**, 1101 (1991); M. Skouri et. al., ibid.,1121 (1991).
12. W. Harbich, R.M. Servus, and W. Helfrich, Z. Naturforsch. **33a**, 1013 (1978).
13. W. Helfrich, Z. Naturforsch. **28c**, 693 (1973).
14. See, F. David, in Ref. 1, p. 158.
15. X. Michalet, D. Bensimon, and B. Fourcade, Phys. Rev. Lett. **72**, 168 (1994).
16. L. Golubović, Phys. Rev. **E50**, 2419 (1994).
17. R. Strey, unpublished.
18. Z.G. Wang and S. Safran, J. Chem. Phys. **94**, 679 (1991),

MORPHOLOGY & EXCHANGE KINETICS IN POLYMER BRUSHES: THE PHYSICAL SIGNIFICANCE OF HYDRODYNAMIC TRANSITIONS AND STRETCHED EXPONENTIAL EVOLUTIONAL FORMS

S.D. RODGERS
Department of Chemical Engineering
Massachusetts Institute of Technology
Cambridge, MA 02139

& M. M. SANTORE*
Department of Chemical Engineering
Lehigh University
Bethlehem PA 18015

ABSTRACT

This work reexamines equilibrium and kinetic features of polymer brushes end-adsorbed onto solid substrates from solution, providing a new interpretation of previously-published experimental results and insight into the comparison between experiments and existing kinetic models. The study centers on an end-modified polyethylene oxide (PEO) which may adsorb to form a polymer brush on a hydrophobic polystyrene latex, and whose main backbone also exhibits an attraction for the surface. In a previous work, Gao and Ou-Yang claim a sharp pancake-to-brush transition with increasing surface coverage of the samples with the strongest end group attraction to the substrate, and only a delicate increase in the hydrodynamic thickness of layers whose chain ends are weakly attracted to the surface. Our reevaluation of this data, however, collapses all molecular architectures to a single curve describing the hydrodynamic thickness at different surface loadings, and which shows a relatively sharp transition for all samples. Gao and Ou-Yang have also performed kinetic exchange experiments where low molecular weight species replace preadsorbed high molecular species (with the same endgroup-surface adsorption energy), and observed stretched exponential behavior in the evolution of the hydrodynamic thickness of the adsorbed layer. We employed Milner's treatment for brush exchange kinetics, to extract equivalent phenomenological parameters for more direct comparison between fundamental parameters and experiment.

INTRODUCTION

The impact of molecular architecture on the structural and dynamic features of adsorbed polymer layers is a topic of great interest. Much work has been done with block copolymers which adsorb to form interfacial brushes, where the non-adsorbed portion of the chain extends into solution and is stretched significantly from its unperturbed radius (eg by a factor of 5 or 10).[1] A variation on this theme is the triblock copolymer whose outermost blocks are attracted to the surface. The resulting layers are thought to be comprised of loops and tails in a brush-conformation. The relative amounts of loops and tails, understandably, depends on the adsorption energy of the endgroups compared with the molecular weight of the middle portion of the backbone and the solvent quality for the middle portion of the chain. In the family of triblock copolymers are "associative thickeners," industrially-relevant water-soluble polymers containing hydrophobic moities which cause these molecules to associate into networks[2] and to adsorb onto hydrophobic surfaces at specific points in their backbone. For associative polymers containing hydrophobic end groups, the adsorption energy per end group may be weaker than that of more classical organic-soluble di- and tri-blocks.[3] The behavior of associative polymers is further complicated by attractions between their main backbone and the substrate, which have been recently demonstrated by a number of techniques.[4,5] The first question, then, is under what conditions, if any, do these associative polymers adsorb to form interfacial brushes?

Structural aspects of the adsorbed-layer-interface have long been a topic of study, with the thermodynamics leading to homopolymer train-loop-tail morphologies well-established, and the scaling behavior behind interfacial brushes equally well-accepted. The new frontier in polymer adsorption appears to be in the dynamic features of adsorbed layers and the mechanisms for their kinetic response to various stimuli, for example changes in solvent quality or the composition and concentration of the bulk solution. Whether or nor homopolymer layers are equilibrated, and how to distinguish equilibrated layers from kinetically trapped interfaces remains hotly debated.[6,7] Also of interest, for specialty architectures such as brushes, is the mechanism of dynamic exchange

between the layer and chains in free solution. To this end, Ou-Yang's group[8] has initiated work with associative polymers, where preadsorbed layers of high molecular weight are replaced by shorter chains with the same adsorption energy per end group. Stretched exponential evolution of the hydrodynamic layer thickness towards the new equilibrium was observed (after an overshoot which occurs when the preadsorbed layer momentarily swells with the shorter chains). The stretching exponent was found to increase with an increased molecular weight ratio of the original long to invading short chains, and to be nearly independent of the relative total concentrations of the long and short chains. The physical significance of the parameters in the stretched exponential model was not made clear by this work, nor was it obvious if this observed dependence of the stretched exponential parameters was in agreement or at odds with existing physical models for brush behavior. While stretched exponential behavior has been observed for homopolymer desorption and exchange, the physical significance of the phenomenological form is no clearer in this instance. Kinetic models for brush desorption and exchange, however, do exist. In this work, we reexamine the stretched exponential equivalents of diffusion-kinetic brush models and compare these trends with Ou-Yang's experimental observations.

EXPERIMENTAL BACKGROUND

Gao and Ou-Yang's adsorption work employed associative thickeners donated by Union Carbide. These molecules were comprised primarily of polyethylene glycol (PEG). Low molecular weight (8000, polydisperse) PEG's were linked together with urethane chemistry (Isophorone Diisocyanate or "IPDI") to give total nominal molecular weights ranging, over a series of samples, from 17,000 and 104,000, with an overall polydispersity near 2. Three main families of samples were employed. The first contained alkane C16 groups on both chain ends, also attached via IPDI linkages. In the second family, C12 alkane end-group hydrophobes comprised a slightly less hydrophobic architecture. The third and control architecture was comprised of the equivalent weight of PEG-urethane backbone, without the hydrophobic endgroups, with chain ends simply terminated in a hydrogen. These architectures are summarized in Figure 1, as is the nomenclature. The first part of the name-code describes the carbon content of the endgroup hydrophobe, while the second number describes the nominal molecular weight of the backbone. For example, C16AP100 applies to a sample of approximately 100,000 molecular weight with hexadecyl endgroups. Gao and Ou-Yang adsorbed these polymers onto 91 nm diameter polystyrene latex spheres.[8] The hydrodynamic layer thicknesses from Gao and Ou-Yang's work were determined by dynamic light scattering studies on dilute polystyrene latex dispersions containing the associative polymers. For studies related to structure features of the interface (eg. the pancake-brush transition) a sphere volume fraction of 2×10^{-5} was employed while in kinetic exchange studies, a volume fraction of 1×10^{-4} was employed.[8]

Other workers,[2-5,12] including ourselves, have studied molecules of parallel architectures and documented a significant interaction between the main PEG backbone and polystyrene substrates. Additionally, there is evidence that the IPDI groups also experience significant attraction to polystyrene surfaces,[4] although it is unclear if the interaction is hydrophobic in nature (as IPDI contains 10 carbons) or if specific but weak acid-base type interactions are involved.
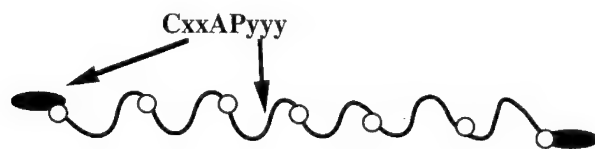

Figure 1. Molecular Architecture of the Associative Polymers from Union Carbide

STRUCTURAL ASPECTS OF THE ADSORBED LAYER:
A PANCAKE TO BRUSH TRANSITION   OR
A GLOBAL CHANGE IN HYDRODYNAMIC PROPERTIES?

A particularly exciting find documented by Ou-Yang's group[11] was the so-called 'Pancake-to-Brush Transition' which is suggested by the experimental result in Figure 2 (taken from Gao's thesis).[13] Here, three samples, all of approximately 100,000 molecular weight, but with varying endgroup hydrophobicity were studied. The graph represents the hydrodynamic thickness as a function of polymer content of a polystyrene latex dispersion with the specified number of chains per particle. Notably, those samples with the most hydrophobic end groups appear to undergo the steepest increase in hydrodynamic layer thickness with increasing associative polymer. Further, for the control sample without hydrophobic endgroups, the transition appears very gradual indeed. Such a scenario appears at first glance to be in general accord with the first order phase transition previously hypothesized by Alexander.[14]

Figure 2 suggests that the endgroup-substrate interaction is a crucial parameter in controlling hydrodynamic properties as a function of surface coverage. A closer examination of the data analysis,[13] however, reveals that such conclusions do not directly follow. Of particular note is that the polymer concentration on the x-axis of Figure 2 represents the total polymer content of the dispersion, providing no information about the relative amount of polymer that is actually on the surface, and that which remains free in solution. Indeed, it had been previously demonstrated by Jenkins,[12] via the isotherms summarized in Figure 3, that the endgroup hydrophobes enhance the adsorption of associative thickener onto polystyrene latex. (In Figure 3, the same associative polymer samples used by Ou-Yang had been previously studied by Jenkins, on a different but similar polystyrene latex. While we cannot be sure that the isotherms for Jenkins and Ou-Yang's systems are identical, we know that the isotherms applicable to Ou-Yang's system are similar to those in Figure 3, as Jenkins work was quite comprehensive, employing several latex samples.)

In order to determine if the Pancake-Brush Transition suggested by Ou-Yang's studies was truly sensitive to molecular architecture we reanalyzed Ou-Yang's data, calculating the adsorbed amount for each data point in Figure 2. This was accomplished through a mass balance on the total number of polymer chains in the system, and the equilibrium relationship between free and adsorbed chains provided by Jenkin's isotherms. For the C0AP100 and C12AP100, Jenkins isotherms were easily parameterized, as shown by the solid lines in Figure 3. The experimental isotherm for the C16AP100 sample, however, exhibits an unanticipated kink, which may be an artifact of micellization in the serum replacement experiment employed by Jenkins, or it may suggest a true surface phase transition. For this reason we attempted calculations for the C16AP100 data employing both Jenkins actual isotherm data and the parameterization in Figure 3.
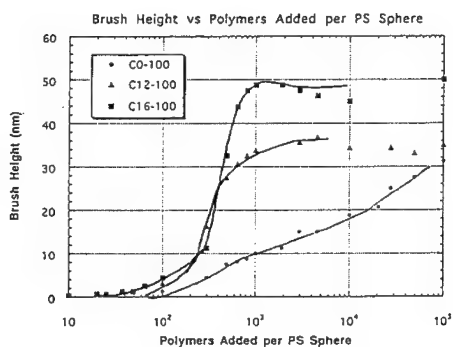

Figure 2. Brush Height of adsorbed layer as a function of added associative polymer.[13]
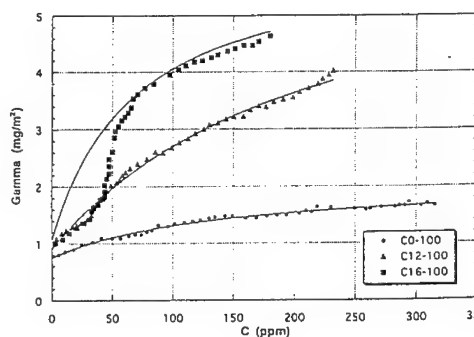
Figure 3. Adsorption Isotherm for associative polymer on polystyrene latex.[12]
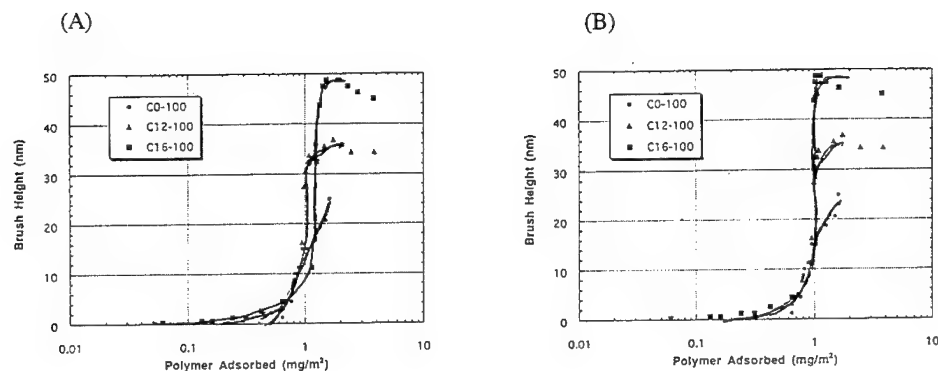
Figure 4. Hydrodynamic adsorbed layer thickness as a function of surface loading. (A) Using parameterized isotherms. (B) Using real isotherm data.

The results of our calculations are summarized in Figure 4, which shows the hydrodynamic thickness of the adsorbed layers as a function of the adsorbed amount, taking into account the partitioning of the various samples between the surface and free solution. The most striking feature of this reanalysis was that all three transitions are much more similar than originally thought, and that within experimental error, the transition occurs at approximately the same surface loading for all samples. Notably, the largest source of error in this calculation stems from the shape of the adsorption isotherm itself. With associative polymers, the shape of the isotherm is difficult to know exactly, because micellization, particle flocculation, and network formation confound separation of serum and particles via membrane and centrifugation methods. For example, we question our ability to know the flatness of the plateau region of the isotherm. Isotherms whose plateaus drift upwards (due to loosely-termed multilayer coverage, or the incorporation of additional chains into a polymer brush) tend to make the high concentration points in Figure 4 shift to the right. Conversely, flat isotherms tend to cause more vertical transitions and prevent the high concentration points from shifting to the right in Figure 4. The transition for all these samples appears near the shoulders of the isotherms (where the isotherm starts to bend from the vertical) which is similar for all three samples in Figure 3.

The near-superposition of the hydrodynamic transitions for all three samples presented in Figure 4 is not surprising. Indeed Cohen-Stuart and coworkers[15] have predicted sharp transitions for homopolymer layers with increasing surface coverage. This is because the hydrodynamic properties of an adsorbed layer are dictated primarily by the "tails," and only a few tails are required to give a significant hydrodynamic thickness. Hence, the relatively sharp transition for the C0AP100 sample parallels theory and previous hydrodynamic studies with other materials such as polyvinyl alcohol.[15] Interestingly, the hydrophobe-containing samples are not much different although the ultimate layer thickness is greater (in accord with ultimately higher surface loadings experienced with these samples.) It is unclear, therefore, whether the increase in hydrodynamic thickness for the hydrophobe containing polymers occurs because the middle of the backbone lifts from the surface as conditions become crowded, or if the associative polymer chain ends ultimately desorb, similar to the homopolymer case. Also, for the hydrophobe-containing samples, polymer-polymer associations leading to "multi layer" (loosely-termed) structures cannot be ruled out as an alternative to the brush morphology. What is clear, however, is that through enhancement of the adsorbed amount, the endgroup hydrophobes lead, ultimately, to an enhancement in the hydrodynamic thickness of the adsorbed layer.

KINETIC ISSUES: IS THERE A PHYSICAL SIGNIFICANCE
TO THE STRETCHED EXPONENTIAL DECAY
IN DESORPTION / EXCHANGE EXPERIMENTS

Gao and Ou-Yang[8] studied the evolving layer thickness in experiments where low molecular weight associative polymers displaced chains from preadsorbed layers with higher molecular weights but with the same hydrophobic endgroup. In all cases, at short times, a temporary overshoot in layer thickness was observed as the short chains swelled the preestablished brush. Then the layer thickness decreased slowly over the next several hours to the new equilibrium level. Gao and Ou-Yang varied the relative molecular weights and concentrations of the preadsorbed and invading chains and found that in all cases, the evolving brush height beyond the overshoot was satisfactorily fit to a stretched exponential. Some of their results are summarized in Table I.

Table I. Observed and Predicted Stretched Exponential Parameters

Set	Energy (kT)	N_l	N_s	loading τ	loading α	height τ	height α
Experiment 1000L-1000S	?	1140	180	?	?	0.4 hr	.53
1000L-1000S	?	1140	300	?	?	0.17	.39
1000L-3000S	?	1140	180	?	?	0.93	0.50
Milner Model-Fit	8	1140	200	0.29hr	1.16	0.07	0.54x
Closed System 1000L-1000S	9	1140	200	0.77	1.19	0.84	1.33
	8	1140	300	0.40	1.22	0.50	1.79
Closed System 1000L-3000S	8	1140	200	0.41	1.26	0.50	1.62

x denotes poor fit

Recently, Milner[10] elaborated on the kinetic brush model of Legoure and Leibler,[9] developing a treatment for the evolution of the surface loading and brush height during processes like those studied by Ou-Yang.[8] This treatment employed the potential necessary to bring a free chain into a brush, where the sticky head group enters the brush first, and is aimed towards the surface (within the range of the first "blob" of the invading chain). A Fokker-Planck equation, also accounting for drag between the invader and the brush was solved to predict the evolving flux of invading chains.

The primary difference between Milner's model and Ou-Yang's study (if the associative C16 polymers do indeed form interfacial brushes) is that the associative polymers may form brush loops in addition to regular brushes. To account for the fact that both associative thickener chain ends are "sticky" is easy if one assumes that both chain ends always adsorb: Then one simply employs 1/2 the nominal molecular weight in the kinetic models. One also has the option of neglecting the second hydrophobe on each chain altogether (we have shown that for endgroup-surface adsorption energies of up to 6kT, the configuration with one chain end adsorbed is the preferred configuration).[16] Accounting for a combination of loops and tail-brushes is more complicated and not dealt with here. Polydispersity was also an experimental complication.

Our primary objective was to attribute physical significance to the stretching exponents found by Ou-Yang's group, by comparison of Milner's model to an equivalent stretched exponential, and then by subsequent comparison of the stretched exponentials matching Milner's model to those found by Ou-Yang. We programmed the equation 17 from Milner's paper[10](not shown here because of space limitations) to predict the evolving surface concentrations of both species, and then calculated the evolving brush height employing Milner's equation 14. Over a series of runs, we varied the head-group adsorption energy, the relative concentrations of original and invading chains, and the molecular weight ratio of the original and invading chains. We ran 3 versions of the program, one which simulated behavior in an open system with a constant (high) concentration of long chains during the introduction of short invading chains, behavior in an open system where long chains were removed from the bulk solution and the concentration of short chains maintained constant, and behavior in a closed system similar to the experiments of Ou-Yang, where the adsorbed and free chains satisfied a mass balance.

Figure 5, an example of our results (also in Table I), compares the evolving brush height and surface coverage of long chains predicted by Milner's treatment, for several different head-group sticking energies. Also shown, the dashed lines indicate the best stretched exponential fits to Milner's model. Like the results in Figure 5, we found "stretching exponents" which exceeded 1, in contrast to Ou-Yangs experimental observations. (This came as a surprise, since the original desorption model of LeGoure and Leibler fit well to a stretched exponential with exponents between 0.2 and 0.8, depending on the adsorption energy.) Further, over the small range of parameters we investigated, (sticking energies from 8-10 kT, and ratio of long to short molecular weights from 2.5 to 10) the high stretching exponent was relatively invariant while the time constant of the stretched exponential showed a strong dependence on the relevant physical parameters. A slight dependence of the stretching exponent on the composition of the bulk mixture (or open vs closed system) was apparent. Further the stretching exponents for the evolution of long chain coverage and the actual brush height were different, but not by a factor of 1/3 which might be expected, since brush height follows coverage to the 1/3 power.
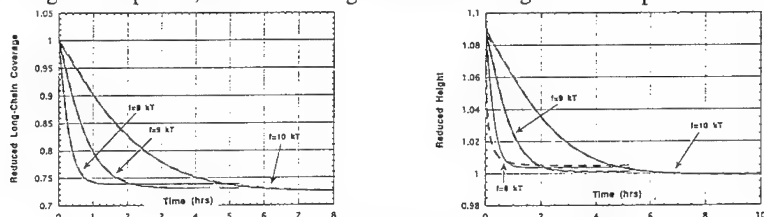

Figure 5. An example of the similarity between Milner's diffusion model(——) and the stretched exponential decay(- - -) . Here the headgroup sticking energy is varied for a closed system.

CONCLUSIONS

The two main findings from this work, (1) the collapse of hydrodynamic transitions to a similar dependence on surface coverage and (2) drastic differences between exchange kinetics observed for associative polymers and that predicted for perfect polymer brushes, suggests that layers of adsorbed associative polymer may not be simple polymer brushes. Rather their character may be closer to a hybrid of extended homopolymer (loosely-termed "multilayer") morphologies and brush behavior. An alternate explanation of the discrepancy between the kinetic results and predictions is that Milner's model has not accurately captured the rate-controlling step for exchange kinetics in brush forming systems. Equally interesting is that the equivalent stretched exponential matching a diffusion-activation brush treatment such as Milner's model contains stretching exponents exceeding unity (an "expedited exponential"), although the time constants become longer as physical parameters are adjusted to give slower processes.

REFERENCES

1. Milner, S.T., *Science* **251**, 905 (1991).
2. Sperry, P.R., Thibeault, J., and Kostansek, *Adv. Org. Coatings Sci Tech. Ser.*, **9**, 1 (1985).
3. Santore, M. M., Russel, W.B, and Prud'homme, R.K., *Farad. Disc. Chem. Soc.* **90**, 323 (1990).
4. Kelly, M.S., and Santore, M. M., *Colloids and Surfaces*, in press.
5. Haggerty, J., and Roberts, J., manuscript in preparation.
6. Dijt, J.C., Cohen Stuart, M.A., and Fleer, G.J., *Macromolecules* **27** 3219 (1994).
7. Frantz. P., and Granick, S., *Phys. Rev. Lett.*, **66**, 899 (1991).
8. Gao, Z., and Ou-Yang, H.D., *ACS Symp. Ser.* **532** 70 (1993).
9. Ligoure, C., and Leibler, L., *J. Phys. France* **51** 1313 (1990).
10. Milner, S.T., *Macromolecules* **25** 5487 (1992).
11. Gao, Z., and Ou-Yang, H.D., *J. Phys II France* **1** 1375 (1991).
12. Jenkins, R.D., Durali, M., Silebi, C.A., and El-Aasser, M.S., *J. Colloid Interface Sci.* **154** 502 (1992).
13. Gao, Z., Ph.D. Thesis. Lehigh University, 1993.
14. Alexander, S. *J. Phys. France* **38** 983 (1977).
15. Fleer, Cohen-Stuart, Scheutjens, Cosgrove, and Vincent, "Polymers at Interfaces" Chapman Hall 1993, p255.
16. Kelly, M.S., and Santore, M.M., *J. Appl. Polym. Sci.*, submitted.

MONTE CARLO STUDIES OF A COUPLED 'ELEMENTARY' REACTION-DIFFUSION SYSTEM IN ONE DIMENSION.

Anna Lin, Raoul Kopelman, Department of Chemistry, University of Michigan, Ann Arbor, MI 48109

ABSTRACT

The anomalous rate laws of diffusion limited elementary reactions in low dimensions have garnered attention over the past decade as researchers have become aware that the mean field approximation utilized in traditional kinetic rate equations is not valid in low and fractal dimensions. We use Monte Carlo simulations to study a diffusion limited system simultaneously undergoing A+B-->0 and A+A--> 0 reactions, a common situation in photochemistry. We are studying how this coupled system affects the attenuation of local fluctuations and thus the rate laws of the system in low dimensions and how these results compare to the mean field rate laws. Our results give useful guidelines for studying this type of reaction system experimentally.

INTRODUCTION

Diffusion-limited kinetics of elementary reactions occurring in confining geometries has garnered much attention and is pertinent to such applications as catalysis, energy transfer, reactions occurring at boundaries and on surfaces such as those found in ion channel membranes and on LB films ,and reactions in porous structures such as soil and rock.

The effect of local fluctuations in concentration on the rate laws of various diffusion-limited elementary reactions, mainly those of the type $A+A\rightarrow A$, $A+A\rightarrow 0$, $A+B\rightarrow C$, $A+B\rightarrow 0$ and $A+T\rightarrow T$ where A and B are different reactive species and T is a trap, have been studied using a variety of methods and under a variety of initial conditions. [1-9]

Using Monte Carlo simulations, we have studied the effect of a competing $A+A\rightarrow 0$ reaction on the already well understood kinetics of the $A+B\rightarrow 0$ batch reaction occurring in 1D. The dimerization of one of the two reactive species in an A+B reaction is a common occurrence in photochemical reactions.[10] Photochemical reactions are of particular interest to us because they are amenable to experimental realizations of batch reaction-diffusion systems with an initially random distribution of reactants.

We find that the rate law of a reaction-diffusion system, in which a dimerization reaction, $A+A\rightarrow 0$, competes with an elementary reaction, $A+B\rightarrow 0$, deviates from a 'classical' rate law in 1D. We determine the classical rate law for this set of coupled, non-linear reaction equations by simulating a reaction-diffusion system of $A+B\rightarrow 0$ and $A+A\rightarrow 0$ where the distribution of reactants is kept random at all times, the assumption that leads to 'classical' time dependencies of the rate of decay of reactants. We also report the interesting way in which this case deviates from the simpler $A+B\rightarrow 0$ case.

In almost all work done on $A+B\rightarrow 0$, for example in references 3,4,8, and 9, [Ao] = [Bo] and consequently [A(t)] = [B(t)]. Bramson and Lebowitz[6] analyze the limiting behavior of [A(t)] and [B(t)] for the $A+B\rightarrow 0$ case where [Ao] << [Bo] and Lianos and

Argyrakis[15] have addressed the A+B→B case where [Ao] << [Bo], but no previous work has shown the behavior of a system as it approaches the condition of [A] << [B], by any mechanism, from the initial condition [Ao] = [Bo].

SIMULATION METHOD

The kinetics of an A+B→0 reaction with a competing A+A→0 side reaction are studied in 1D via Monte Carlo simulations. Here A+B→0 and A+A→0 represent the formation of an inert product. Reactions studied are "batch" reactions which means that the concentrations of the two reactants, [A] and [B], at time zero is greater than the concentration of the reactants at any later time and the only way the concentration changes is by reaction (annihilation).

A random distribution of A and B particles are landed on a 10^4 site lattice with cyclic boundary conditions. The initial concentration of A and B particles is: [Ao] = [Bo] = 0.2 particle / lattice site. Excluded volume is observed; not more than one A or one B can occupy a site at any time.

All particles are allowed to move once within one time step. The diffusive motion of the particles on the lattice is realized by allowing each particle to perform an independent random walk to a nearest neighbor lattice site. After each particle is moved, a reaction is checked for. If an A and a B particle attempt to occupy the same site, both particles "react" and are removed from the lattice. If an A particle attempts to move onto a site already occupied by an A particle, both particles are removed from the lattice with a pre-set probability; they "react" a certain per cent of the time. If they are not removed then no reaction has occurred and neither particle is moved from its original position. If a B particle attempts to move onto a site already occupied by a B particle, it is not moved in that time step.

Two types of simulations, "stirred"[11,12] and "unstirred", are done. "Stirred" simulations are those where all particles remaining on the lattice after each time step are re-randomized and thereby stirred' Each re-randomization results in the formation of local fluctuations in the concentration of A and B particles, as is found in any random distribution, but it prevents the attenuation of those fluctuations in time since each distribution, as time advances one step, is independent of the previous one. The rate of decay of [A] we call classical in this case because there is a random distribution of particles at each time step, an assumption implicit in classical reaction kinetics. In "unstirred" simulations the particles are not re-randomized after each time step. Therefore, the initial local fluctuations implicit in the random distribution of particles at time t = 0 will be attenuated over time, resulting in larger and larger spatially segregated domains of A particles and B particles. The unstirred cases are typical simulations of diffusion-limited reactions[13] and the rate law should be effected by dimension while the stirred cases simulate the reaction of a distribution of particles that is random over all time and thus the rate law should be independent of dimension and agree with the classical rate law.

RESULTS AND DISCUSSION

The original motivation for these simulations was to determine if an anomalous rate law still persists; if segregation of reactants still persists to the extent that it results in anomalies in the rate law, when an A+B→0 type reaction is coupled with a

competing A+A→0 reaction. This is of particular interest because experimental realizations of batch A+B→0 or A+B→C reactions requires a fast reaction but a reaction that will not start to proceed until the two reactants are randomly mixed and convection is quenched. The satisfaction of both of these criterion in a chemical reaction is best met by the class of reactions know as photochemical reactions.

$$A + B \rightarrow \text{no reaction}$$
$$A + h\nu \rightarrow A^*$$
$$A^* + B \rightarrow 0$$
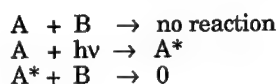
where 0 represents and inert product. It is common, in this type of reaction, for a competing dimerization reaction of the photoexcited species to exist concurrently with the predominant A+B reaction.

$$A^* + A \rightarrow 0$$

The set of non-linear, coupled differential equations describing the reaction

$$d[A]/dt = -k_1[A][B] - k_2[A]^2$$

$$d[B]/dt = -k_1[A][B]$$

where [A] and [B] are the concentrations of A and B particles respectively, are not easy to solve analytically.

Using Monte Carlo simulations, we study the effect of a competing dimerization reaction, which we assume to be effectively modeled by an elementary A+A→0 reaction , on the kinetics of an elementary A+B→0 reaction under batch conditions. To determine the classical time dependence of a rate law for this system, which assumes a random distribution of reactants at all times, we simulate a stirred system in which all particles remaining on the lattice after each time step are randomly re-landed. We compare these results to those obtained for 'unstirred' simulations -- simulations where the movement of the A and B particles is a function only of each particle's random walk on the lattice. We propose that if there is a difference in the time dependence of the decay of A particles, for example, in the stirred and unstirred cases, then there is an anomaly in the rate law of this reaction system that arises from the inability of diffusion to keep the system effectively mixed. We studied this system in 1D where any existing anomalies should be the greatest since the diffusive motion of the particles is more restricted than in higher dimensions[14].

The results we obtained for the system in 1D are summarized graphically in Figure 1. All simulations pictured in Fig. 1 are done on 10^4 site 1d lattices with initial concentrations of 0.2 particle / lattice site for both A and B particles. Pictured as diamonds are the simulation results for A+B→0 only. The solid line is for reference and has a slope of 1.00. The hollow points are data for the stirred reaction system A+B→0. We obtain the classical time dependence $[A] \sim t^{-1}$. The solid points are data that show the anomalous, dimension dependent time dependence of A+B→0, $[A] \sim t^{-d/4}$, in this case, $\sim t^{-1/4}$. The data represented by squares is data for A+B→0 with A+A→0 occurring with a probability $p=10^{-4}$. For this relatively low probability of A+A reaction, there is little deviation from the simple A+B→0 case and the Zeldovich regime, where $\sim t^{-1/4}$, exists in the "unstirred" case (solid squares) while in the stirred case the rate law appears to be classical (hollow squares).

**A+B-->0 with A+A-->0 Side Reaction
on a 10,000 Site 1d Lattice**
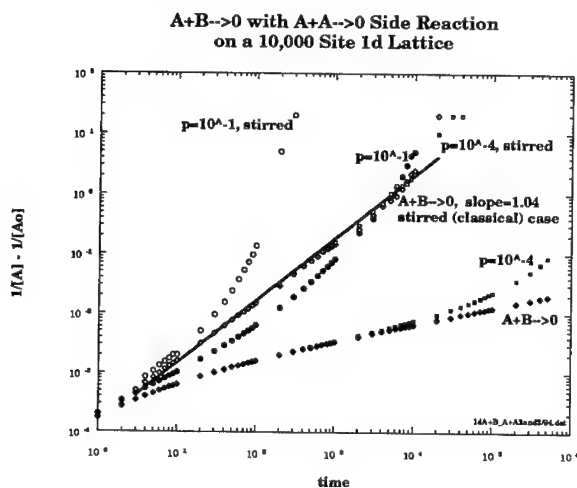
Figure 1: Time dependence of the decay of the concentration of a particles, [A] in 1D for: A+B→0, A+B→0 stirred; A+B→0 with competing A+A→0 dimerization occurring with probability 10^{-4} and 10-1, stirred and unstirred cases. The "stirred" case should model classical reaction kinetics and thus be dimension independent. For low probability of dimerization (i.e.. 10^{-4}) the Zeldovich regime is observed.

**A+B-->0 with A+A-->0 Side Reaction
10^4 site 1d lattice**
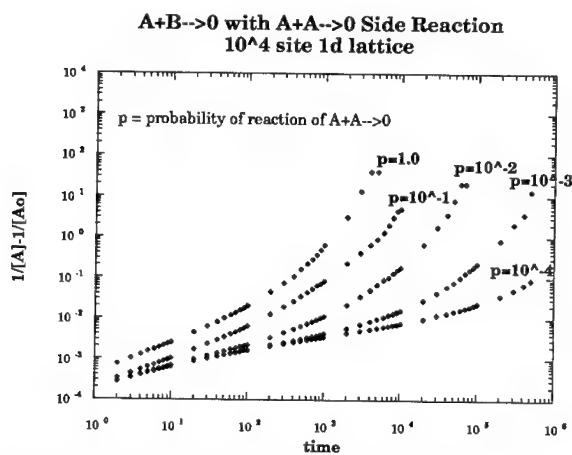
Figure 2: Effect of different probabilities of reaction of the A+A→0 dimerization on the time dependence of the decay of [A] for the A+B→0 A+A→0 competing system.

316

If the probability of the A+A reaction is increased one or more orders of magnitude the Zeldovich regime is never reached (Fig. 2).

STIRRED A+B-->0 with A+A-->0 side reaction occurring with Probability = 1.0, 10^-4, 10^-3, 10^-2, 10^-1 10^4 site 1d lattice
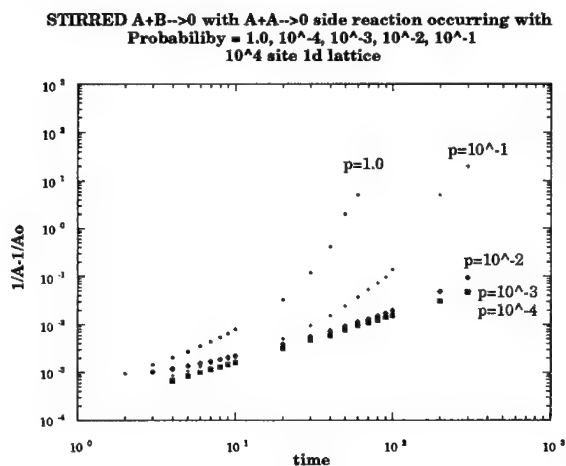
Figure 3: Effect of different probabilities of reaction of the A+A→0 dimerization on the time dependence of the decay of [A] for the *stirred* A+B→0 A+A→0 competing system. Stirring models classical behavior of the system.

A+B-->0 with A+A-->0 side reacton occurring with Probability = 10^-3 on 10^4 site 1D lattice
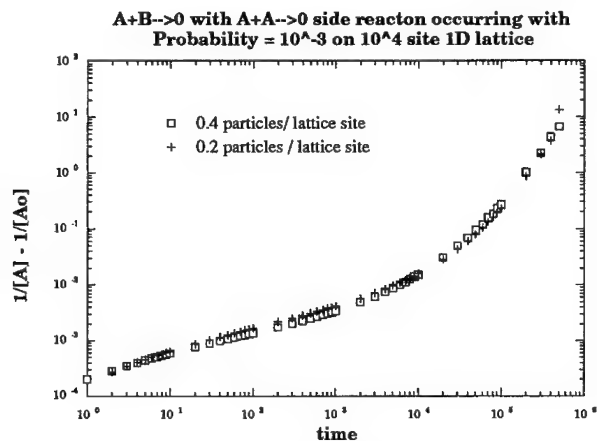
Figure 4: Finite size effects. The exponential tails for higher orders of the probability of the dimerization reaction A+A are not caused by finite size effects.

even on larger lattices (Fig. 3) indicating that the exponential tail of the decay is not due to finite size effects. For p = 10^{-3} and 10^{-2} there is a time dependence for the

decay of [A] intermediate between Zeldovich behavior and the long time exponential behavior exhibited by this system.

While the Zeldovich regime is never reached for probabilities of the competing A+A reaction higher than the order of 10^{-4}, there is substantial deviation between the stirred and unstirred simulations for a given probability indicating that the rate law of the A+B→0 reaction occurring concurrently with a competing A+A→0 dimerization reaction is dimension dependent in 1D.

The effects of the A+A→0 reaction appear only after a time on the order of the probability of the A+A reaction (see Fig. 4).

SUMMARY

In 1D, the effect of a competing dimerization reaction, A+A→0, on the rate law of an elementary A+B→0 reaction is negligible if the probability of dimerization is on the order of 10^{-4} or less. If the probability of dimerization is greater than order 10^{-4}, the Zeldovich regime is not observed. However, in a diffusion-limited reaction system the time dependence of the decay of [A] (concentration of A) , is effected by the dimension in which it occurs as is shown by comparing results for 'stirred' and 'unstirred' simulations in 1D. Thus, anomalous rate laws for the decay of [A] should be observable for an A+B→0 reaction occurring concurrently with an A+A→0 reaction.

REFERENCES

1.   R. Kopelman, *Science* **241**, 1620-1626 (1988).
2.   A. A. Ovchinnikov, Y. B. Zeldovich, *Chemical Physics* **28**, 215-218 (1978).
3.   D. Toussaint, F. Wilczek, *J. Chem. Phys.* **78**, 2642 (1983).
4.   K. Kang, S. Redner, *Phys. Rev. Lett.* **52**, 955 (1984).
5.   E. Clement, L. M. Sander, R. Kopelman, *Physical Review A* **39**, 6455-6465 (1989).
6.   M. Bramson, J. Lebowitz, *J. Stat. Phys.* **62**, 297 (1991).
7.   R. Schoonover, D. Ben-Avraham, S. Havlin, R. Kopelman, H. G. Weiss, *Physica A* **171**, 232 (1991).
8.   P. Argyrakis, R. Kopelman, K. Lindenberg, *Chemical Physics* **177**, 693-707 (1993).
9.   K. Lindenberg, P. Argyrakis, R. Kopelman, *J. Phys. Chem.* **98**, 3389-3397 (1994).
10.   J. M. Coxon, B. Halton, *Organic Photochemistry*. e. a. Ebsworkth. E., Ed., Cambridge Chemistry Texts (Cambridge University Press, 1974).
11.   P. Argyrakis, R. Kopelman, *J. Phys. Chem.* **91**, 2699-701 (1987).
12.   P. Argyrakis, R. Kopelman, *journal of physical chemistry* **93**, 225-229 (1989).
13.   P. Argyrakis, *Computers in Physics* **6**, 525-529 (1992).
14.   P. Argyrakis, R. Kopelman, *J. Phys. Chem.* **93**, 225 (1989).
15.   P. Lianos, P. Argyrakis, *J. Phys. Chem.* **98**, 7278-7283(1994).

STUDY OF AN A+2B--->C REACTION-DIFFUSION SYSTEM WITH INITIALLY SEPARATED COMPONENTS

Andrew Yen and Raoul Kopelman, Department of Chemistry, University of Michigan, Ann Arbor, MI 48109-1055

ABSTRACT

The presence of a reaction front is a characteristic feature of a variety of physical, chemical and biological processes[1,2]. A chemical reaction exhibits a front (spatially localized region where concentration of product is non zero), provided the diffusing reactants are separated in space. We study the reaction front dynamics of a termolecular A+2B--->C reaction with initially separated components in a capillary. The reaction tetra+2Ni^{2+}--->1:2 complex is used[3], where 'tetra' is disodium ethyl bis(5-tetrazolylazo) acetate trihydrate. We measure and compare with theory the dynamic quantities that characterize the kinetic behavior of the system: the global reaction rate R(t), the location of the reaction center $x_f(t)$, the front's width w(t), and the local production rate $R(x_f,t)$. The non-classical nature of this dynamical system is confirmed.

INTRODUCTION

Interest in reaction fronts has greatly increased since it was realized that pattern formation in the wake of a moving front is quite a general phenomenon. Reaction front dynamics play a crucial role in the pattern formations in the multistep Belousov-Zhabotinksii reactions and Liesegang ring formation[1,2]. The latter is thought to be a complex process of interplay between the dynamics of the reaction front and the nucleation kinetics of the precipitate.

Analytical work on the diffusion-reaction system with initial separated components was first done on the A+B--->C type reaction by Galfi and Racz[4] and later by Taitelbaum et al[5,6,7]. The generalized nA+mB--->C reaction was also studied[8]. We are interested in the A+2B--->C type reaction because we can study it experimentally. For A+2B--->C reaction we can use the following scaling argument to determine the time exponents of the dynamic quantities. The argument is based on that the width of the reaction front will grow as t^α and the rate at the center of the reaction front ,$R(x_f,t)$, will decrease as $t^{-\beta}$. The number of C particles formed in the reaction zone in a unit time is equal to the number of A particles entering the zone. The number of A particles entering the zone per unit time is equal to the current, j, which is propotional to the diffusion length ($t^{1/2}$).

$$w(t)R(x_f,t) \sim t^{\alpha-\beta} \sim t^{-1/2}$$

The second relationship comes from the average values of A particles and B particles in the reaction zone is proportional to $wt^{-1/2}$. The production rate of C is

$$R \sim ab^2 \sim \frac{w^3}{t^{3/2}} \sim t^{3\alpha - 3/2} \sim t^{-\beta}$$

Solving for a and b we get $\alpha=1/4$, $\beta=-3/4$ which means the width grow faster than A+B--->C case and the local rate decrease faster than the A+B--->C case. Our experimental results support the analytical prediction[8].

EXPERIMENTAL

We studied the reaction tetra+2Ni^{2+}--->1:2 complex under initially separated conditions. Optical measurements can be used to monitor the dynamic quantities of the reaction. A computerized system will be used for this purpose (Fig 1)[9]. The system consists of a halogen lamp, a solenoid with two filters (420 nm and 540 nm) , a PMT, and a stepping motor. The on-off of the lamp and solenoid are controlled through the parallel port of the computer and the movement of the stepping motor are controlled via a stepping motor controller. The light source, solenoid with two filters, slit unit and detector are fixed on the stepping motor and the glass reactor is fixed over the slit unit but separated from all other units. The PMT is connected to the a/d board of the computer to convert the analog data into digital data and then stored on a computer.
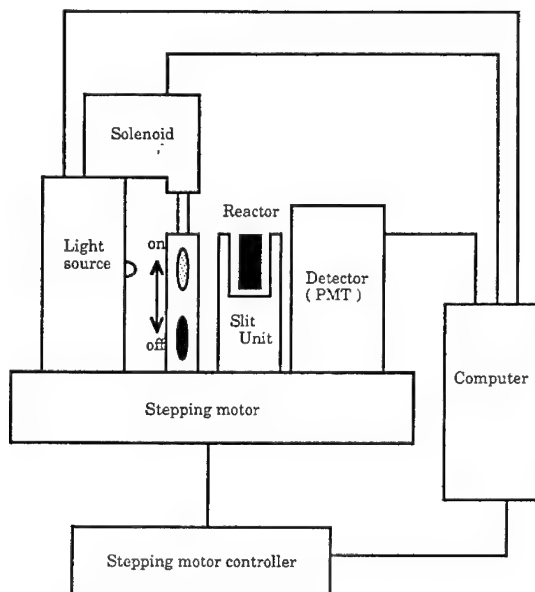
Fig. 1 Schematic diagram for experimental set-up for absorbance measurement along the reaction front domain

Reactions were run in a 4x2 mm rectangular tube reactor. We use as reactants,1.06x10^{-3} M Ni^{2+} and 3.38x10^{-5}M 'tetra' in 0.3% gel solution as reactants. the purpose of adding agarose is to increase the viscosity and thus prevent covection. At room temperature the two reactants were initially separated in the glass reactor. A sharp boundary is formed at t=0. The absorption wavelength for tetra is 420 nm and was 540 nm for the product. The first scan along the reaction front starts after 7 minutes. The time interval between scans increases from the order of 5 minutes to the order of 100 minutes. The profiles of absorbance versus distance x are obtained at different times.

RESULT AND DISCUSSION

A typical pattern is shown in Fig 2. The width of the reaction front is measured from the half-width of each profile. To determine the time exponent for width we plot width vs time on a log-log scale (Fig 3). The global rate is determined from the baseline corrected integrated area of the differential peak, divided by the appropriate time interval. We calculated the time exponential for global rate by plotting ln global rate vs ln t (Fig 4). The local rate exponents were obtained form subtraction of the width component from the global rate component.
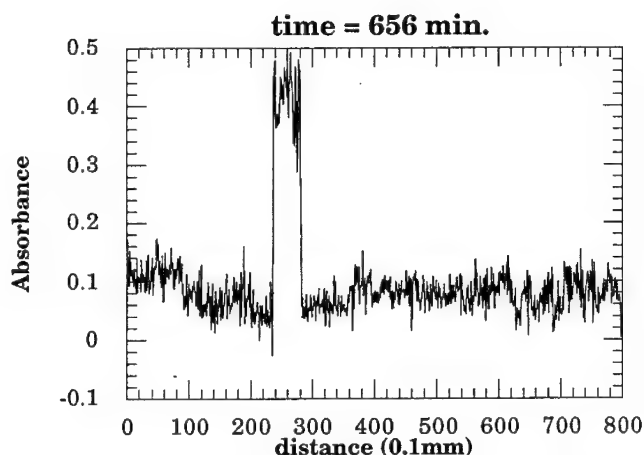
Fig. 2 A typical profile of Absorbance (arbitrary units) of Ni^{2+}-'tetra' complex vs. distance, recorded at t = 656 mintues.
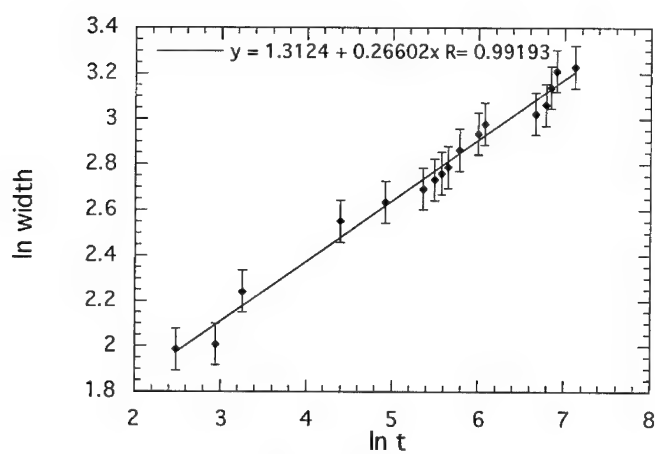
Fig. 3 ln w vs. ln t
The width is measured from the half width of each profile.
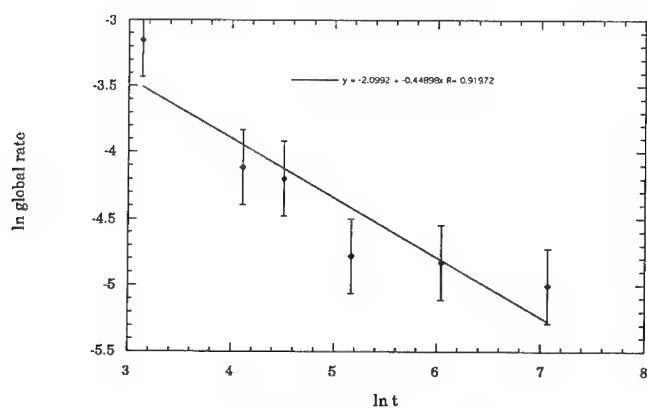
Fig. 4 ln global rate vs. ln t
The global rate is found from baseline corrected intergrated area devided by
appropriate time interval.

From the linear fits for Fig 3 and Fig 4. We obtained components for width and global rate to be 0.266 and 0.449, respectively, which are consistent with the prediction from the scaling argument (0.25,0.5). The experimental exponent for the local rate is 0.717 compare to 0.75 predicted by theory.We found this system to have non-classical nature. However it has different exponents, compared with the simpler A+B--->C type reaction[3,10,11]. We hope that the understandind of reaction diffusion system like this will help us to understand more complicated phenomena, such as pattern formation and oscillating chemical systems.

REFERENCE

1. H. K. Henisch, *Crystals in Gels and Liesegang Rings*. (Cambridge University Press, Cambridge, 1988).
2. J. D. Murray, *Mathematical Biology*. Biomathematics (Springer_Verlag, 1993), vol. 19.
3. H. Jonassen, V. Chamblin, V. Wagner, Jr and R.Henry, *Anal. Chem.*,**30**, 1660 (1958).
4. L. Galfi, Z. Racz, *Physical Review A*, **38**, 3151-3154 (1988).
5. H. Taitelbaum, S. Havlin, J.E. Kiefer, B. Trus and G.H Weiss, *Journal of Statistical Physics*, **65**, 873-891 (1991).
6. H. Taitelbaum, Y.-E. L. Koo, S. Havlin, R. Kopelman, G. H. Weiss, *Physical Review A*, **46**, 2151-2154 (1992).
7. H. Taitelbaum, *Physica A*, **200**, 155-164 (1993).
8. S. Cornell, M . Droz, B. Chopard, *Physical Review A*, **44**, 4826-4832 (1991).
9. Y.-E. L. Koo, R. Kopelman, *Journal of Statistical Physics*, **65**, 893-918 (1991).
10. Y.-E. Koo, R. Kopelman, *Israel Journal of Chemistry*, **31**, 147-157 (1991).
11. Z. Jiang, C Ebner, *Physical Review A*, 42, 7483 (1990).

ACKNOWLEGEMENT

REACTANT CORRELATION EFFECTS STUDY OF HYDROGEN ISOTOPE EXCHANGE REACTION ON SUPPORTED METAL CATALYSTS.

Inchan Choi and Raoul Kopelman
Department of Chemistry,University of Michigan, Ann Arbor, Michigan 48109

ABSTRACT

Non-classical results due to reactant correlation effects have been observed in the study of Monte Carlo simulations of the $A_2 + B_2 \rightarrow 2AB$ reaction. These simulation results, interpreted by the Pair Density Analysis method and the experimental kinetic studies, may provide an explanation of the early time anomalous kinetic behavior of the catalytic hydrogen isotope exchange reaction exhibited for surface-diffusion limited conditions on alumina supported platinum islands.

INTRODUCTION

The hydrogen isotope exchange reaction (i.e., $H_2 + D_2 \rightarrow 2HD$) on platinum catalysts has been known as a simple bimolecular second order reaction.[1] However, the reaction may have a non-classical kinetic character for supported platinum catalysts. The first reason is the effectively low dimensionality if the reaction occurs on the surface of small, 25Å by 25Å (which is 5x5 platinum atoms) islands of metal catalyst. The second one is reactant correlation. Reactants land as a pair and then dissociate into atoms. Initially, hydrogen atoms are strongly correlated to each other and so are deuterium atoms. These correlations inhibit the production of HD molecules because of an enhanced probability for H_2 and D_2 recombination. The hydrogen and deuterium atoms are not correlated with each other and their relative distances are randomly distributed in spite of the H_2 and D_2 correlation.

In this paper, non-classical kinetic behavior due to low dimensionality and the reactant self correlation was studied by Monte Carlo simulations. Also, to understand the anomalous kinetic behavior, a new pair density analysis technique was introduced.

SIMULATION

Monte Carlo simulations of the reaction $A_2 + B_2 \rightarrow P$ (with P = AA, BB, and AB) were studied for 1-dimensional and 2-dimensional systems. The Random Walk method was employed to simulate the surface diffusion and the same energy for each site was used. Low reactant concentration (e.g., 2 or 3 %) was used to accentuate diffusion effects. Finally, two different landing methods (e.g., geminate and correlated) were employed.

For geminate landing, A and B particles will land as AA and BB pairs (i.e., at neighboring sites) at the beginning. After the landing, the particles perform a random walk around the lattice. When a particle walks into another particle, a molecule is formed. The latter will leave the site and land at another pair of empty sites. Thus, the system has always the same total number of particles (i.e., the total number of each particle, A or B, remains constant). However, nearest neighbor pair densities (e.g., the number of AA, BB, or AB pairs) will change in time.

RESULTS AND DISCUSSION

Geminate Landing

Here, we will introduce three different nearest neighbor distance distributions: (1) Random (2) Correlated (3) "Anti-correlated" (Fig. 1). When a system has the random distribution, it will show the classical reaction order of 2. With the correlated distribution, the reaction order will be 1.[2] Depletion of the nearest neighbors will give the "anti-correlated" distribution. Its reaction order will be dimensionality dependent, and will be 3 in one dimension.[3] Our system will initially have HH and DD geminate landings. At later time, it will have all three (i.e., HH, DD, and HD) geminate landings as more HD molecules form. Therefore, at early time, HH and DD pairs will have a correlated distance distribution whereas HD will have a random distribution. At later time, all three will have
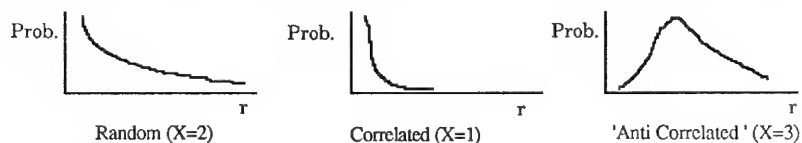
Figure 1.   Nearest Neighbor Distance Distribution

the random distribution as the initial HH and DD correlations are forgotten because of surface diffusion. Obviously, there will be changes in the HH and DD distribution in the intermediate time. What about the HD distribution? Will it remain without changes?

Simulation results for two dimensions (i.e., 100x100 square lattice) are given in Fig 2. The rates and reaction orders show classical results. Xaa and Xbb, the reaction orders for H_2 and D_2 molecule production, start at the geminate value of 1 and increase to the random distribution value of 2. Xab, the reaction order for the HD molecule, starts at 2 and remains at 2. This indicates that the HD distance distribution remains random without
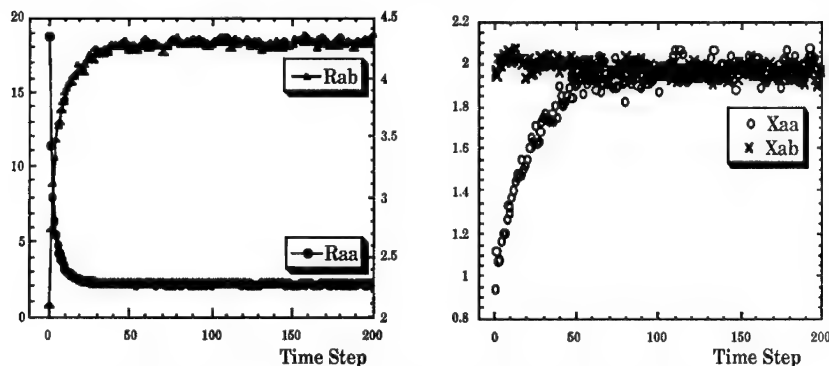
Figure 2. Reaction Rates and Orders in Two Dimensions

change from the start to the end. However, the results for one dimension (i.e., 1X10,000 lattice) are different (Fig. 3). There is an overshooting in Rab, the rate of HD production,

and the Xab in the intermediate time is different from 2. The X values being smaller than 2 at intermediate times tells that somehow the initial random distribution has shifted to the correlated distribution side and been recovered at longer time. These anomalous results in 1-dimension are of particular interest since the kinetic behavior for many-islands systems resembles that in one dimensional system.
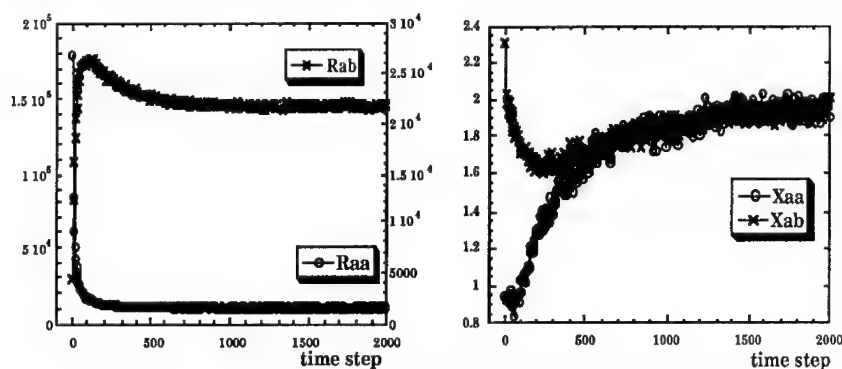
Figure 3.   Reaction Rates and Orders in One Dimension

A new analysis technique which compares pair densities (e.g., nearest neighbor pair, linear next nearest neighbor pair, non-linear next nearest neighbor pair) to reaction rates fits the rate curves very well. In one dimension, rates can be written as follows:

$$Raa = 1/2 \ [AA] + 1/4[A0A]$$
$$Rab = 1/2 \ [AB] + 1/4[A0B]$$

and in two dimensions, rates can be written as follows:

$$Raa = 1/4 \ [AA] + 1/8 \ [A9A] + 1/16[A0A]$$
$$Rab = 1/4 \ [AB] + 1/8 \ [A9B] + 1/16[A0B]$$

where [AA] represents the nearest neighbor pair density; [A0A] represents the linear next nearest neighbor pair density; and [A9A] represents the non-linear next nearest neighbor pair density in two dimensions, etc. Using the above rate equations, the rate curves were fitted (Fig. 4).

Monitoring the pair densities may also help us to understand the anomalous kinetic behavior. The strange overshooting in Rab in one dimension (Fig. 3) may be related to a rapid AB pair density increase. In one dimension, the jumping probability of a particle in each direction is 1/2, and thus half of the AA pairs disappears with each step. In the meantime, some new AA pairs are created either by surface diffusion or by landing, and thus the AA pair density will reach steady state. The initial AB pair density is close to zero (cf. there is a small number of the AB pairs randomly created by landing) but the AB pair density increases due to diffusion. Also, half of the created pairs will disappear due to the diffusion, and thus the AB pairs will reach the steady state too.

Since the jumping probability in two dimensional systems is 1/4 in each direction, 75% of the pairs in two dimensions (comparing to 50% in one dimension) will disappear

due to the diffusion. This causes a slower increase of the AB pair density in the two dimensional systems than that in the one dimensional systems. This may be the reason for the absence of the overshooting in the two dimensions. To prove the point, more simulations were studied in one dimensional systems. The survival ratio of the created AB pairs was decreased by lowering either the jumping probability or the reaction probability
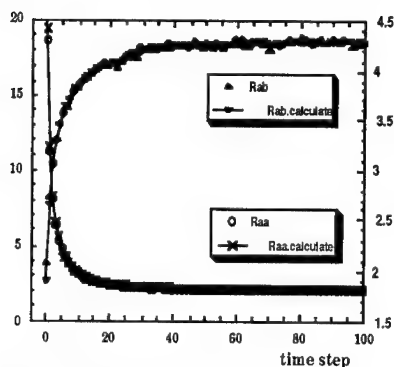
Fig. 4 Rates and Calculated Rates
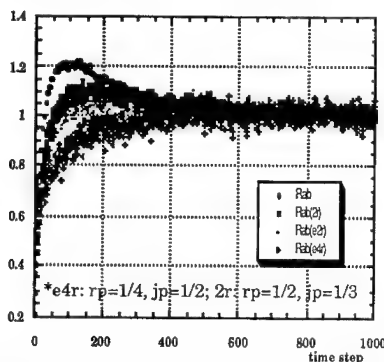
Fig. 5 Disappearance of Overshooting

or both. As can be seen from Figure 5, the overshooting disappears as the survival ratio of the AB pair decreases.

Correlated Landing

The reactant correlation effects in one dimension have been studied by employing the correlated landing method.

CR1 (Correlated landing with one space in between, e.g., A0A landing)

The shape of the Raa curve (Fig. 6) is very similar to that of the geminate landing
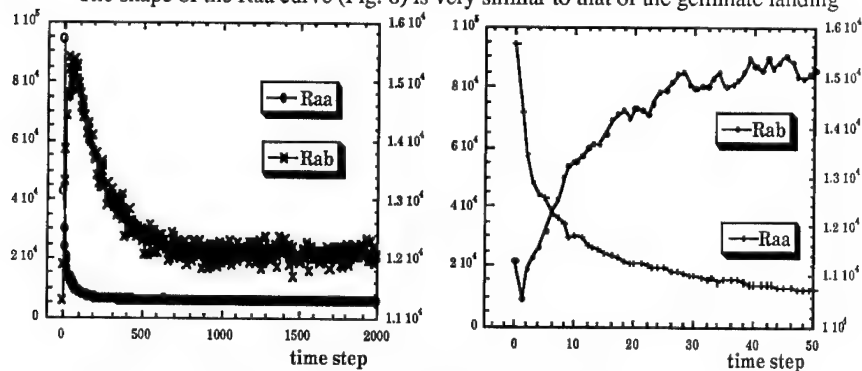
Figure 6. Overall and Early Time Rates for CR1

(i.e., CR0 or AA landing), but the magnitude is smaller. For the first step, A0A pairs have a 25% chance to react and form an A2 molecule. Therefore, the survival ratio of the original A0A pair will be 75%. For the second step, 25% of the survived A0A will react, and thus the magnitude will be less than that for the first step.

The Rab for the first step is the contribution from the AB pairs randomly created due to landing. These pairs also have a 25% chance for the reaction, 25% chance of the formation of A00B pairs and 25% chance to survive as the AB pairs. For the second step, the 25% of the survived AB pairs will react. After the second step, the AB pairs created due to surface diffusion will dominate the reaction.

CR2 (Correlated landing with two spaces in between, e.g., A00A landing)

For the first step, there will be no A2 molecule formation from the landed A00A pairs, but 25% of them will form AA pairs. For the second step, an 1/8 of the original pair will have a chance to react and 3/16 will form AA pairs. For the third step, the original pair contribution to the reaction and formation of the AA pair will be much less, and thus the rate will decrease (Fig. 7).

Rab at the first step is the contribution from randomly generated AB pairs due to landing as in the CR1 case. The larger magnitude for the CR2 than for the CR1 tells us that the less AA correlation results in the less inhibition of the AB molecule formation.
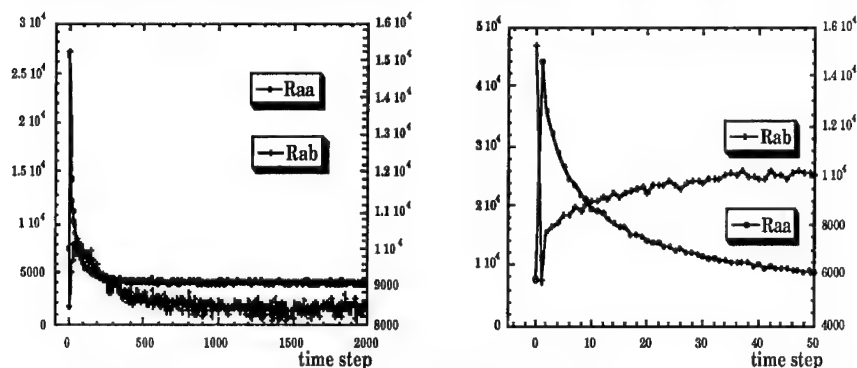
Figure 7. Overall and Early Time Rates for CR2

CR10 (Correlated landing with ten spaces in between)

The shapes of the rate curves for CR10 look very interesting (Fig. 8). According to the chart (Fig 9), a first AA pair formed from the original pair will appear after step 5, and the number of these pairs increases in time. Thus, the first reaction by the original landed pairs will occur at step 6, and Raa due to the original pairs will increase after step 6. The decrease of the rate at the beginning (i.e., from step one to step five) indicates that the contribution from the randomly created AA pairs (by landing) is lost rapidly.

The Rab rapidly decreases to the steady state, and the overall shape is similar to that of the random landing of a single particle. This tells us that the steady state distribution for this case is 'anti-correlated'. At the beginning, the system has a random AB pair distance

distribution created by landing (in this case, reactant pairs with ten spaces in between do not interfere). However, the reaction of a nearest neighbor pair and its return as a correlated pair (i.e., a pair with ten spaces in between) by landing will shift the distribution to the 'anti-correlated' distribution side.
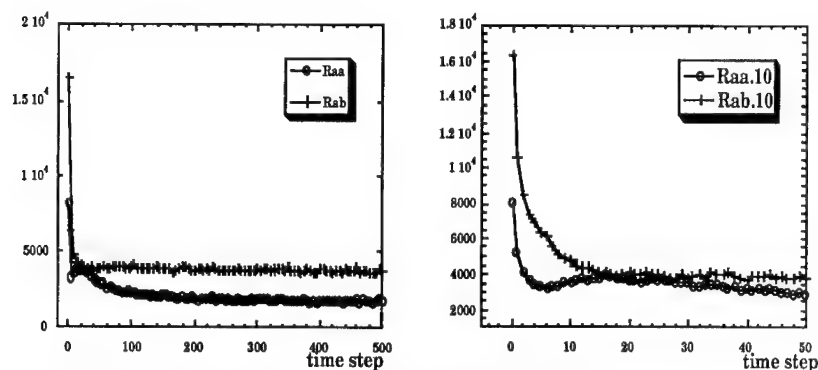
Fig. 8   Overall and Early Time Rates for CR10
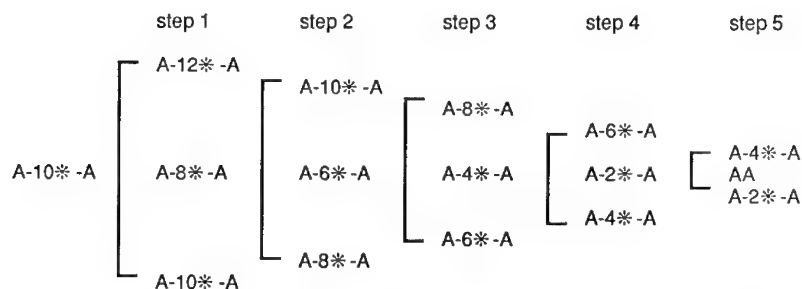
Fig. 9   Changes of CR10 Pairs in Time   (cf. A-2✻-A = A00A)

<u>CR3, 4, 6, 8</u> (Correlated landing with 3, 4, 6, and 8 spaces in between)

The rate curves are in between CR2 and CR10. They clearly show that the early time high Raa values are the consequence of the reactant correlation and also, show how the correlation effects decrease as the correlated landing space increases. The same Raa values for the first step in these landings clearly indicate that the first step reaction is the consequence of the randomly created AA pairs (Fig. 10). The shape of the Rab curves with correlated length of 5 or larger are similar to that of the CR10 case.

330
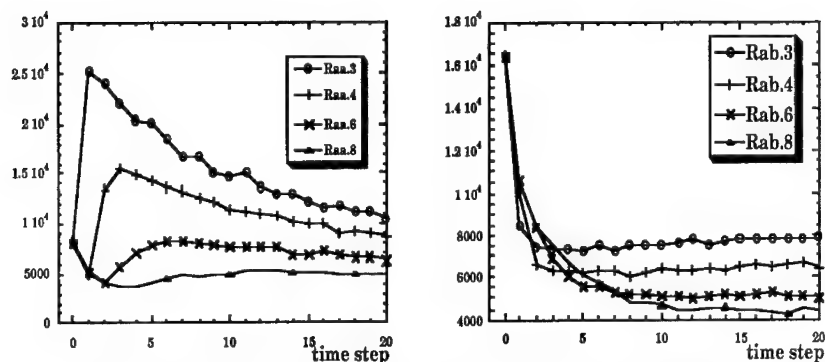
Figure 10. **Early Time Rates for CR3, CR4, CR6, CR8, and CR10**

In two dimensions, the correlations are more rapidly lost, and thus the effects are less obvious. However, the results are similar to those in one dimensional systems and they may also be analyzed by the pair density analysis method.

CONCLUSION

Reactant correlation has caused "anomalous" (non classical) results in the Monte Carlo simulations of the $A_2 + B_2 \rightarrow 2AB$ reaction in 1-dimensional and 2-dimensional systems. Geminate landing results interpreted in terms of the pair densities provide a better understanding for the kinetic behaviors of the hydrogen isotope exchange reaction on alumina supported platinum catalysts.

ACKNOWLEDGMENT

REFERENCES

1   G. C. Bond, 'Catalysis by Metals', Academic Press, London (1962).
2   L. Li, Ph. D. Thesis, The University of Michigan (1989).
3   R. Kopelman, SCIENCE, **241**, 1620-1626 (1988).

MOLECULAR MOTION THROUGH A FLUCTUATING BOTTLENECK

N. EIZENBERG AND J. KLAFTER
School of Chemistry, Tel Aviv University, Israel.

ABSTRACT

Molecular motion in a series of cavities dominated by time dependent bottlenecks is studied as a model for molecular pathways in biomolecules. The problem is formulated by coupled rate and Langevin equations and is shown to be equivalent to n-dimensional reaction-diffusion equation where n is the number of cavities visited by the molecules. Results are presented for two cavities and a comparison is made between steady state and non steady state results.

INTRODUCTION

Environmental effects on rate processes in complex dynamical systems, such as biomolecules, have drawn much interest in recent years, with emphasis on studies of escape over fluctuating barriers[1-2]. In this work we analyze the motion of molecules in a time dependent environment that involves crossing several geometrical barriers which act as bottlenecks. Following a recent work of Zwanzig[1], we assume that crossing a geometrical barrier is proportional to the cross-sectional area of the bottleneck. Environmental fluctuations change the cross-sectional area and thus affect the rate of passage. We model a molecular pathway as a motion in a series of cavities separated by bottlenecks. Transitions back and forth between the cavities occur until the molecule finally escapes through the outermost bottleneck. This description may apply to the motion of small molecules through proteins, as indicated by recent molecular dynamics simulations[3-4].

A single bottleneck model leads to a one-dimensional reaction-diffusion equation with a quadratic sink term, which admits an exact solution[5]. The model parameters are λ, the damping coefficient (the rate in which a fluctuation of the bottleneck radius decays) and k, the coefficient of the passage rate. The model results in a non-exponential decay of the molecular concentration at short times and changes to an exponential decay at long times. The effective rate coefficient of the exponential decay is proportional to $(k\lambda)^{1/2}$ in the limit of small λ. Assuming that the damping coefficient λ is inversely proportional to the solvent viscosity η (recent experiments[6] have shown that the rate of conformational relaxation in myoglobin is inversely proportional to η), the effective rate coefficient is therefore proportional to $\eta^{-1/2}$ in the limit of large η. This result agrees with experimental observations by Beece et al[7], which suggest that the rate constant of the long time decay is proportional to $\eta^{-\alpha}$ with α in the range of 0.4-0.8. Similarly, the main parameters of our model for several bottlenecks are the damping coefficients and the coefficients of the passage rates associated with each bottleneck. The two-bottleneck model is shown to lead to a two-dimensional reaction-diffusion equation for the molecular concentration which is solved numerically for different values of the model parameters. In particular, we are interested in the dependence of the decay of the molecular concentration on the two damping coefficients.

THE MODEL

We assume that a pathway of a molecule moving in protein can be described as a motion in a series of cavities separated by bottlenecks. The model is illustrated in Fig. 1. The cavities are numbered as 1,2,3,... and the radii of the bottlenecks are denoted by x,y,z,... , respectively. The rates of passage between cavities, {K(r)}, are proportional to the cross-sectional areas of the bottlenecks

$$K(r) = k_r r^2 \qquad K_{-1}(r) = k_r^* r^2 \quad , r = x, y, z, \ldots \tag{1}$$
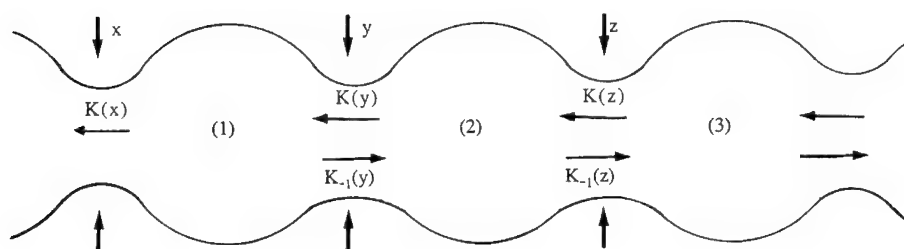
Fig. 1 Illustration of a molecular pathway as a series of cavities separated by bottlenecks.

We consider molecular motion in the presence of two serial bottlenecks, which are the two left most bottlenecks in Fig. 1. The molecular concentrations in cavities (1) and (2) are denoted as C_1 and C, respectively. Assuming a steady state for the molecular concentration C_1 we obtain

$$\frac{dC}{dt} = -K_q(x, y)C \qquad , \qquad K_q(x, y) = k_y \frac{x^2 y^2}{x^2 + qy^2} \qquad q \equiv k_y^* / k_x \tag{2}$$

Under the steady state approximation the rate of escape is controlled by the ratio between the back transition and the escape outside. The limit of $qy^2 \ll x^2$ corresponds to a situation in which the back transition is negligible in comparison with the transition out to the solvent. In this limit the escape rate is determined by the dynamics of the inner bottleneck and $K_q(x, y) \cong k_y y^2$. In the limit of $qy^2 \gg x^2$ the rate of escape is determined by the dynamics of the outer bottleneck and $K_q(x, y) \cong k_y q^{-1} x^2$. In both limits the molecular motion is governed by passage through a single bottleneck and Zwanzig's model is recovered. For intermediate values of qy^2/x^2 the escape rate depends on both x and y.

The radii of the bottlenecks are assumed to satisfy the following Langevin equations

$$\frac{dx}{dt} = -\lambda_x \frac{\partial V(x, y)}{\partial x} + F_x(t) \qquad \frac{dy}{dt} = -\lambda_y \frac{\partial V(x, y)}{\partial y} + F_y(t) \tag{3}$$

where F(t), the Markovian random noise, and the damping term λ are related by the fluctuation dissipation theorem. We assume V(x,y) to be a two-dimensional harmonic potential,

$V(x,y)=(x^2+y^2)/2$. In this potential there is no coupling between the bottlenecks radii. This is obviously a simplified potential since the radii may be correlated, as indicated by molecular dynamics simulations[3]. We intend to address this problem in future work.

An equivalent representation of Eqs. 2 and 3 is through a two dimensional reaction-diffusion equation[8-9] with $K_q(x,y)$ as the sink term

$$\frac{\partial \overline{C}(x,y;t)}{\partial t} = \lambda_x \frac{\partial}{\partial x}\left(\frac{\partial \overline{C}}{\partial x} + x\overline{C}\right) + \lambda_y \frac{\partial}{\partial y}\left(\frac{\partial \overline{C}}{\partial y} + y\overline{C}\right) - K_q(x,y)\overline{C} \qquad (4)$$

Here $\overline{C}(x,y;t)$ is the noise-averaged concentration for given values of x and y. A reflecting boundary condition is imposed at x=0 and y=0. The initial distribution function is set equal to the Gaussian equilibrium distribution function in the absence of the sink term. The quantity of physical interest is the averaged concentration $<C(t)>$

$$\langle C(t) \rangle = \int dx \int dy \, \overline{C}(x,y;t) \qquad (5)$$

The effects of the fluctuations on the rate process are reflected in the decay of $<C(t)>$.

The above procedure that led to Eq. 4 can be easily generalized for molecular pathways in the presence of n bottlenecks placed in a row. Assuming a steady state for the molecular concentration in all cavities except for the innermost, we obtain a single rate equation with an n-dimensional decay rate, coupled to a set of n Langevin equations describing the motion of n bottlenecks radii. This yields a reaction-diffusion equation of spatial dimension n.

RESULTS

In our work we solved numerically the two bottlenecks model, Eq. 4, with the sink terms:

$$K_{0.1}(x,y) = k_y \frac{x^2 y^2}{x^2 + 0.1 y^2} \qquad ; \qquad K_1(x,y) = k_y \frac{x^2 y^2}{x^2 + y^2} \qquad (6)$$

which correspond to q=0.1 and q=1 in Eq. 4. $K_1(x,y)$ describes a situation in which the coefficient of the back transition is equal to that of the escape outside, while for $K_{0.1}(x,y)$ it is ten times smaller.

We have studied the two bottlenecks model, with the above sink terms, in the following cases:

(1) The case in which the outer bottleneck is in thermal equilibrium ($\lambda_x \rightarrow \infty$) and therefore the rate of escape depends solely on the dynamics of the inner bottleneck. In this case Eq. 4 reduces to a one-dimensional reaction-diffusion equation. The sink term in this equation is the two-dimensional sink $K_q(x,y)$ averaged over the equilibrium distribution of x, which is the radius of the inner bottleneck.

(2) The case of different damping coefficients, where Eq. 4 is solved for various values of the damping coefficient λ_y, with λ_x kept constant. In this case our main purpose is to study the two-bottlenecks model in the limits $\lambda_y \ll \lambda_x$ and $\lambda_y \gg \lambda_x$. In these limits the smaller damping coefficient is expected to control the escape process[9].

(3) The case of equal damping coefficients, $\lambda_x = \lambda_y = \lambda$. This case may correspond to a situation in which both bottlenecks are affected in a similar way by the solvent viscosity.

We consider first the change in the equilibrium rate coefficient ,K_{eq}, due to the additional bottleneck. In the limit of large damping coefficients, $\lambda_x, \lambda_y \gg 1$, the distribution function $\overline{C}(x,y;t)$ remains close to the equilibrium distribution function at all times. In this limit $<C(t)>$ decays exponentially with a rate coefficient K_{eq}, which is the average of the sink term over the equilibrium distribution function of x and y.

$$K_{eq} = (2\pi)^{-1} \int dx \int dy \, K_q(x,y) \, e^{-(x^2+y^2)/2} \tag{7}$$

For $K_{0.1}(x,y)$ we obtain $K_{eq}=0.577k_y$ and $K_1(x,y)$ gives $K_{eq}=k_y/4$ These values are smaller than the single bottleneck result[1], $K_{eq}=k_y$. For three bottlenecks, with equal coefficients of the passage rates $k_x=k_y=k_y^*=k_z^*$, we obtain $K_{eq}=k_z/9$. Thus, K_{eq} decreases as expected with the number of bottlenecks.

The reaction-diffusion equations have been solved using the Crank-Nicholson[10] method both in one and two dimensions. The size of the grid was chosen such that $\Delta x = \Delta y = 0.03125$ in the space domain. The grid in the time domain was chosen such that $\Delta t = 0.0002$ at short times ($t \leq 1$), when the decay is relatively fast, and $\Delta t = 0.001$ at later times. Smaller time steps were used for large damping parameters ($\lambda > 10$ in our work). In order to test our numerical procedure we solved Zwanzig's model[1] for the one-dimensional case and its extension, $K(x,y)=k_x x^2 + k_y y^2$, for the two-dimensional case. In both cases there was an excellent agreement between the numerical and the exact solutions.

The validity of the steady state approximation has been checked for the three parameter ranges we studied. We have solved the full system of two coupled two-dimensional reaction-diffusion equations, which is obtained from our model without the steady state approximation. This has been done for the two sink terms in Eq. 6 and several values of the damping coefficients. Our results show that the steady state is realized in the limit of k_x , $k_y^* \gg k_y$. In this limit the effective rate coefficient approaches the steady state result, and therefore is independent of the specific values of k_y^* and k_x and depends only on their ratio q. The approach to the steady state result depends on the damping coefficients. For example, in the case of $\lambda_x = \lambda_y$ we have found that for smaller damping coefficients the steady state is realized for smaller values of k_y^* and k_x. In addition, we have found that in the limit in which the steady state is realized, the molecular concentration in the innermost cavity, C, is approximately equal to the total concentration in both cavities (that is, $C_1 \ll C$). Therefore, our results for $<C(t)>$, obtained under the steady state approximation, may be relevant to experimental realizations in protein systems. A full report of these results will be given elsewhere.

The general dynamical behavior of $<C(t)>$ obtained for the two-bottlenecks model is similar to that of the single-bottleneck model: a non exponential decay at short times that changes to an exponential decay at long times with an effective rate coefficient K_{eff}

$$\langle C(t) \rangle \cong e^{-K_{eff} t} \tag{8}$$

As mentioned in the introduction, the dependence of the effective rate coefficient on the damping parameters is of particular interest. In what follows we present our results for K_{eff} of the two-bottlenecks model for various damping coefficients.

<u>Results for different damping coefficients</u>

In this section the two-bottlenecks model is studied for different values of the damping coefficient λ_y, keeping λ_x constant and equal to 1. We have solved Eq. 4 numerically with the sink terms $K_{0.1}(x,y)$ and $K_1(x,y)$. The effective rate coefficient was obtained from the long time exponential decay of $<C(t)>$ for different λ_y values. The time in which the exponential decay sets in depends on λ_y. For $\lambda_y = 0.0005$, which is the smallest λ_y we chose, the exponential decay was recovered at $t > 30$. For larger values of λ_y the exponential decay was observed at earlier times. Fig. 2 presents the plots of $\log_{10}K_{eff}$ vs. $-\log_{10}\lambda_y$, obtained with the sink terms $K_{0.1}(x,y)$ (squares) and $K_1(x,y)$ (triangles), both with $k_y=10$. The solid line is the single-bottleneck result of Zwanzig with $k=k_y$ and $\lambda=\lambda_y$.

In the limit of large damping, $\lambda_y \gg 1$, K_{eff} becomes independent of λ_y. In this limit the radius y is in thermal equilibrium and the rate coefficient depends only on λ_x. In the opposite limit, where λ_y is small and $\lambda_y \ll \lambda_x$, K_{eff} is proportional to $\lambda_y^{1/2}$ and independent of λ_x. In this limit the three curves in Fig. 2 coincide and the single bottleneck result is recovered with y as the bottleneck radius. Similar results are obtained in the opposite case, in which λ_y is kept constant and λ_x is varied. We conclude that in the limits in which one of the two damping coefficient is much smaller that the other, the smaller damping coefficient controls the escape process.
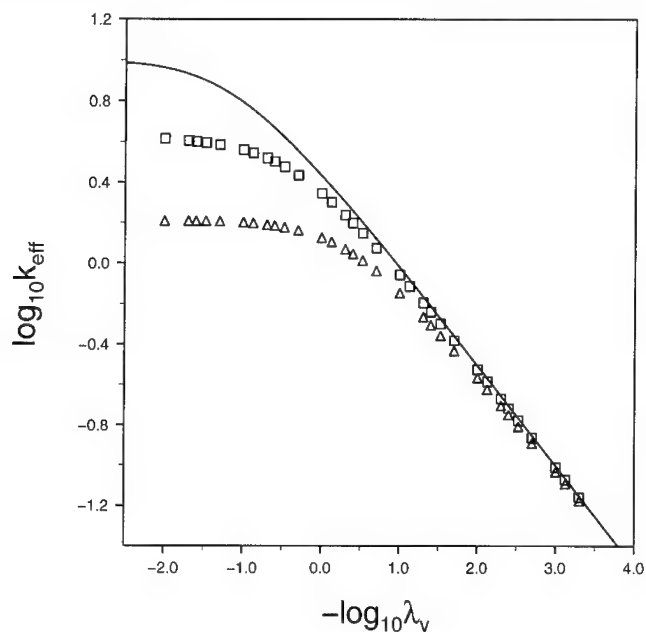
Fig. 2 $\log_{10}K_{eff}$ obtained with the sink terms $K_{0.1}(x,y)$ (squares) and $K_1(x,y)$ (triangles), with $\lambda_x=1$, vs. $-\log_{10}\lambda_y$. The solid line is the same plot obtained with the quadratic sink term k_yy^2.
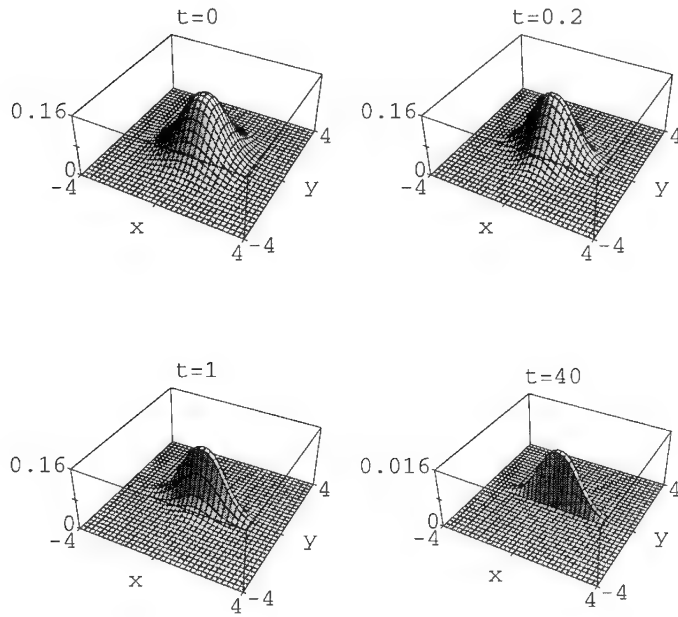
Fig. 3 The distribution function $\overline{C}(x,y;t)$ obtained with the sink term $K_1(x,y)$, $\lambda_y=0.0005$ and $\lambda_x=1$, at different times.

In order to demonstrate the main conclusion of this section, which is the approach to the single-bottleneck limit as one of the damping coefficients becomes much smaller than the other, we have plotted the distribution function $\overline{C}(x,y;t)$ obtained with $K_1(x,y)$, $\lambda_y=0.0005$ and $\lambda_x=1$ at different times. The plots are presented in Fig. 3. The initial distribution function is the Gaussian equilibrium distribution function. Notice the different decay patterns along the x and the y directions as $\overline{C}(x,y;t)$ evolves in time. Along the x direction $\overline{C}(x,y;t)$ remains close to a Gaussian, while along the y direction it becomes narrower. This is due to the different damping coefficients which correspond to a fast diffusion process along the x direction and a slow one along the y direction. At long times $\overline{C}(x,y;t)$ survives only in a narrow region along the y axis. In this region $K_q(x,y) \cong k_y y^2$ and therefore the single bottleneck result is obtained.

Results for equal damping coefficients

In this section the two-bottlenecks model is studied in the case of equal damping coefficients, such that $\lambda_x = \lambda_y = \lambda$. We have solved Eq. 4 numerically with the sink terms $K_{0.1}(x,y)$ and $K_1(x,y)$ for different values of λ. The effective rate coefficient was obtained from the single-exponential decay of $<C(t)>$.

As expected, the effective rate coefficient becomes independent of the damping in the limit of large damping. In this limit both the radii x and y are in thermal equilibrium and K_{eff} approaches K_{eq}, which is defined in Eq. 7 as the average of the sink term over the equilibrium distribution function of x and y. In the limit of small damping we obtained that $K_{eff} \propto \lambda^{1/2}$ for the two sink terms $K_{0.1}(x,y)$ and $K_1(x,y)$. In this limit the single bottleneck result is recovered only for K_{eff} with the sink term $K_{0.1}(x,y)$. In this case the decay of the distribution function $\overline{C}(x,y;t)$ is faster along the x direction due to the asymmetry of the sink term with q=0.1. At long times $\overline{C}(x,y;t)$ survives in a narrow region along the y direction. In this region $K_{0.1}(x,y) \cong k_y y^2$ and therefore the single bottleneck result is obtained.

REFERENCES

1. R. Zwanzig, J. Chem. Phys. **97** 3587 (1992)
2. J. Wang and P. Wolynes, Chem. Phys. Lett. **212** 427 (1993); Chem. Phys. **180** 141 (1994)
3. R. F Tilton Jr, U. C. Singh, S. J. Weiner, M. L. Connolly, I. D. Kuntz Jr, P. A. Kollman, N. Max and D. A. Case, J. Mol. Biol. **192** 443 (1986); R.F Tilton Jr, U. C. Singh, I. D. Kuntz Jr and P. A. Kollman, J. Mol. Biol. **199** 195 (1988)
4. R. Elber and M. Karplus, J. Am. Chem. Soc. **112** 9161 (1990)
5. G. H. Weiss, J. Chem. Phys **80** 2880 (1984)
6. A. Ansari, C.M. Jones, E. R. Henry, J. Hofrichter and W. A. Eaton, Science **256** 1796 (1992)
7. D. Beece, L. Eisenstein, H. Frauenfelder, D. Good, M. C. Marden, L. Reinisch, A. H. Reynolds, L. B. Sorensen and K. T. Yue, Biochemistry **19** 5147 (1980)
8. N. Agmon and J. J. Hopfield, J. Chem. Phys. **78** 6947 (1983); J. Chem. Phys. **79** 2042 (1983)
9. B. Bagchi and G. R. Fleming, J. Phys. Chem. **94** 9 (1990); C. S. Poornimadevi and B. Bagchi, Chem. Phys. Lett. **168** 276 (1990)
10. W. H. Press, Numerical Recipes, (Cambridge university press 1986)

FRAGMENTATION OF HIGHLY CHARGED METALLIC CLUSTERS

ESTELA BLAISTEN-BAROJAS, YIBING LI, and A. BELENKI
CSI/ Institute for Computational Sciences and Informatics, George Mason University, Fairfax, VA 22030

ABSTRACT

Multiply charged metal clusters undergo fission at a certain size. This critical size can be predicted by the liquid drop model when some modifications are taken into consideration. In this work we revise the asymmetric liquid drop model (ALD) and modify it for the alkali metals. This modification addresses those fragmentation channels in which a parent cluster with charge Ze fissions into two fragments. One of the fragments is small and singly charged whereas the second fragment is large and carries the rest of the charge. A different energetic balance equation is presented in which the ionization energy of a single atom and the energy of formation of a small cluster are included. Results and comparison to experiments is provided for Na and Cs clusters. Prediction of the critical size of Na and Cs clusters with Ze>7 is part of the discussion.

The complexity of problems connected with formation, stability, structure, and phase transformations of charged metallic clusters have gained significant theoretical interest in the last few years. An example is the dramatic structural transformations taking place in small atomic clusters due to the excess off positive charge in a confined space.[1] Clusters of a given size can only support a maximum amount of charge before fission occurs.[2-4]

Experimental data collected during the last years[5-14] give quantitative results on the Coulomb induced fission phenomenon.[4] Although theoretical work[2-4] indicates that competition between evaporation and Coulomb processes might contribute to the fission process, there exists considerable controversy concerning the symmetric versus asymmetric fragmentation arising from fission. The liquid drop model[15] (LDM) has mainly been ruled as inadequate to describe the fission reaction.[16,17] Instead, for Na clusters an amazingly simple relation, $N_c=(Z+1)^3$, seems to relate Z,charge on a cluster, with the "critical size" N_c (smallest observed cluster supporting a charge Z).[13] Approximately the same rule is followed by Cs clusters[14] with charges up to 7. In both experiments Martin et al. could not elucidate if fragmentation followed a symmetric or asymmetric channel and attempted to estimate the value of the energy barrier needed for a cluster to evaporate neutral atoms.[2] Fission and evaporation are then two competing processes. The picture that emerges from these studies is the following. If the Coulomb repulsion is larger than the evaporation barrier, then the cluster undergoes fission at the critical size. If the opposite is true, then the cluster will evaporate atoms until the balance between evaporation barrier and Coulomb repulsion is reversed.

On the other hand, the fission experiments of Saunders[8,9] on Au clusters caused by collisions with Kr atoms do not follow a simple rule. The critical size for doubly charged Au clusters was found to be 9 and 26 for triply ionized clusters. In this work Saunders indicates that fission is dominated by the asymmetric channel in which one of the fragments is a singly ionized trimer. Simulations on small doubly charged Na clusters also indicate asymmetric fragmentation with a singly charged trimer being a favored product. [18]

<u>Liquid drop model:</u>

The liquid drop model assumes that the cluster binding energy is counterbalanced by a repulsive Coulomb energy. The cluster is a classical charged continuum with finite surface. Namely, the energy of a cluster of radius R, N atoms, and charge Ze is

$$E_{LD} = E_b N + 4\pi\sigma R^2 + (Ze)^2/2R \qquad (1)$$

where E_b is the bulk binding energy/atom, σ is the surface tension and $R = r_{sw}N^{1/3}$, with r_{sw} being the Wigner-Seitz radius. In LD for symmetric fragmentation (SLD), the fissility parameter $f = E_{Coulomb}/2 E_{Surf}$ should satisfy the condition $f < 0.351$ for the parent cluster to be stable. The maximum allowable value of f defines then the minimum size at which a cluster fissions.

<u>Asymmetric Liquid Drop Model</u>

The LD might be modified by assuming that a cluster fissions into two spherical clusters of different sizes N_1 and N_2 with charges Z_1e and Z_2e when the balance of energies after and before fission

$$E_{final}-E_{initial} = 4\pi\sigma (R_1^2 + R_1^2 - R^2) + 0.5 e^2 (Z_1^2/R_1 + Z_2^2/R_2 - Z^2/R) \quad (2)$$

changes sign from positive to negative. Here R, R_1 and R_2 are the radii of the parent cluster and of the two cluster fragments. The radius of the parent cluster is $R = r_{sw}N^{1/3}$ and the corresponding radii of fragments 1 and 2 are $R_i = r_{sw}N_i^{1/3}$ Thus,

$$\Delta E = E_{final} - E_{initial} = \Gamma [N_1^{2/3} + (N_2^{2/3} - N^{2/3})] +$$

$$+ [Z_1^2/N_1^{1/3} + Z_2^2/N_2^{1/3} - Z^2/N^{1/3})] \qquad (3)$$

where $\Gamma = 8\pi\sigma (r_{sw})^3/e^2$ and energies are given in units of $e^2/2r_{sw}$.

Energetic balance occurs at a certain cluster size and fixed Z, defining a critical size N_c for asymmetric fission when ΔE is minimum and positive. Then, if

$$\Delta E > 0 \quad \text{no fission occurs}$$

$$(4)$$

$$\Delta E < 0 \quad \text{fission occurs.}$$

The critical size N_c corresponding to a channel N_1, N_2, Z_1, Z_2 is then obtained by minimizing the positive difference ΔE with respect to N_1 for every pair Z, Z_1. The minimization process is carried out numerically.

This model will be referred as asymmetric LD (ALD). The fissility parameter is f=-1. In Table 1 we give the ALD calculated values of N_c and N_1 when $\sigma = 200$ erg/cm^2 for Na (74 erg/cm^2 for Cs) and r_{sw}=2.08 A for Na (2.98 A for Cs). In this model the best fission channels favor a small singly charged fragment and a large cluster with charge Z-1.

Table 1. Critical sizes and most probable channels of fission for Na clusters and Cs clusters under the ALD model. Experimental results are after Ref. 13 and 14.

Z	Na exp [13,14]	N_c (ALD)	(N_1, Z_1)	Cs exp [14]	N_c (ALD)	(N_1, Z_1)
2	27	31	6,1	19	28	5,1
3	63	116	4,1	49	107	3,1
4	123	299	3,1	94	276	3,1
5	206	616	3,1	155	567	3,1
6	310	1101	3,1	230	1012	3,1
7	445	1790	3,1	325	1644	3,1

Modified Asymmetric Liquid Drop Model

Neither SLD or ALD fully describe the Coulomb induced fission because evaporation processes that modify the initial and/or final states are absent from either description. There is however another effect that we consider more important. In the process of asymmetric fission, the parent cluster needs to supply an 'energy of formation' of the two fragments. As in ALD, we assume that the fission channel results into two clusters one of which is singly charged. The energy of formation of the fragments contains two parts, the ionization energy and the energy necessary to reconstruct the system.

When a cluster is just about to undergo fission the system is far from thermodynamic equilibrium. Besides, experimental factors such as warming upon ionization indicate that the cluster temperature might be high at the moment of fission. Under this situation entropic effects should be important. In this paper we assume that a high temperature deformation mode sets in as a function of the the number of atoms in the parent cluster. In this mode there is a contraction of the cluster density in a large region of the parent cluster compensated by a density expansion in a smaller region. Under these circumstances, the energetic balance favoring fission is such that

$$\Delta E = \Delta E_c + \Delta E_s + \varepsilon(N)_{N_1} = 0 \tag{5}$$

where the Coulomb energy balance is

$$\Delta E_c = (Z_2^2/N_2^{1/3} - Z^2/N^{1/3}) + IP \tag{6}$$

and the surface energy balance is

$$\Delta E_s = \Gamma (N_2^{2/3} - N^{2/3}) \tag{7}$$

Here IP is the atomic ionization potential of the material under consideration. The reconstruction energy $\varepsilon(N)_{N_1}$ is a function that depends parametrically on N_1. We assume a simple linear dependence of this function with N:

$$\varepsilon(N)_{N_1} = \rho (N_1) N \tag{8}$$

This new model is referred as *modified asymmetric liquid drop* MALD. The zero order MALD model is recovered when the reconstruction energy $\varepsilon(N)_{N_1}$ is zero. A similar balance as Eq.. (6)

for sodium clusters has been considered[17] in the past where instead of the IP energy the bulk work function was included as a constant energy.

Critical sizes for Na and Cs clusters obtained in the zero order MALD are reported in Table 2, where IP_{Na}=5.14 eV and IP_{Cs}=3.89 eV. As is evident, these results are in better agreement with experiment for $Z<5$ than the ALD results . However, for $Z>4$ the critical sizes obtained within the zero order MALD become worst with increasing Z. Our next step is to allow for a non-vanishing reconstruction energy $\varepsilon(N)_{N_1}$ and to fit the value of the parameter ρ to the experimental results.[13,14] The parametric dependence of $\varepsilon(N)_{N_1}$ with N_1 can also be determined from the fit. We found that the best fitted value ρ (7) = 0.028 eV is the same for both Na and Cs and the small singly charged cluster has $N_1 = 7$. Results for N_c are reported in Table 2. The agreement with experiment is excellent. Prediction of N_c for $Z>7$ is also reported in the table.

Table 2. Critical sizes and most probable channels of fission for Na and Cs clusters under the MALD model.

	Na			Cs		
Z	N_c(zero order)	N_c (MALD)	(N_1, Z_1)	N_c(zero order)	N_c (MALD)	(N_1, Z_1)
2	22	22	7,1	14	14	7,1
3	62	57	7,1	47	43	7,1
4	154	125	7,1	115	94	7,1
5	310	218	7,1	228	161	7,1
6	591	328	7,1	399	241	7,1
7	875	448	7,1	615	329	7,1
8	1319	575	7,1	924	422	7,1
9	1890	704	7,1	1373	517	7,1
10	2606	835	7,1	1890	613	7,1

In Fig. 1 we give a three dimensional representation of the balance equation, Eqs. (5-8), for Cs when Z=6 and N_1=7. The cut defines a line of critical sizes. In Figs. 2 it is shown the

Cs, Z=6
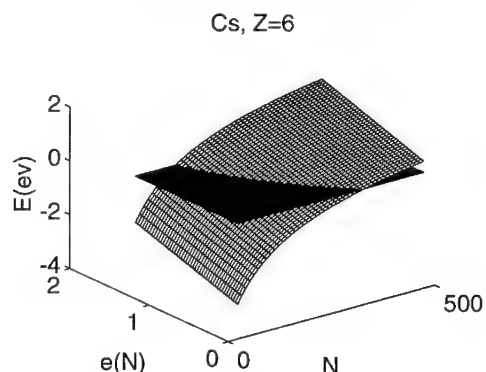
Fig. 1 Three dimensional representation of the balance equation Eqs. (5-8) for cesium clusters with charge 6. The cut defines a line of critical sizes.

behavior of ΔE with N. In these figures the values where the curves cut the abscissa correspond to the N_c obtained in the zero order MALD. The straight line represents $\epsilon(N)$ for $N_1=7$. Values of N where $\epsilon(N)$ cuts ΔE give our best estimation for the critical sizes N_c.
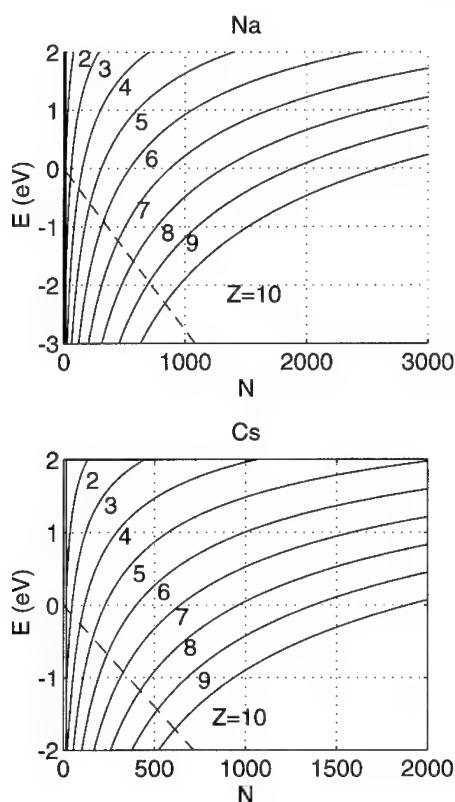
Fig. 2 Energy difference $\Delta E_c + \Delta E_s$ as a function of N (the size of the parent cluster) for Z=2 through 10 (continuous lines) and reconstruction energy $\epsilon(N)$ for $N_1 = 7$ (dashed line). (top) Na clusters; (bottom) Cs clusters.

We have presented a simple model that modifies the LD by including both the ionization energy of the material under study and the energy of reconstruction when the parent cluster fissions. At the moment of fission, this reconstruction energy is carried away by the fragments as kinetic energy. This phenomenon has been mentioned[12] in the experimental work. Finally, our prediction of asymmetric fragmentation where one of the fragments is a singly small cluster is in agreement with the dynamical simulations[18] of small Na clusters.

Exploratory Molecular Dynamics simulations of Lennard Jones clusters with 50 to 60 atoms show that when the charge is localized, the dynamically preferred fragmentation channel generates either a small singly charged cluster and a large one with the rest of the charge, or a bare charged atom and a large cluster with some evaporated atoms.[19]

ACKNOWLEDGMENT

REFERENCES

1. S. Sugano, in Microclusters, edited by S. Sugano, O. Nishina, S. Ohnishi (Springer, Berlin, 1987),p. 226; Microcuster Physics (Sringer, Berlin, 1991).
2. S. Sugano, A. Tamura, Y. Ishii, Z. Phys. D, 12, 213 (1989).
3. M. Nakamura, Y. Ishii, A. Tamura, S. Sugano, Phys. Rev. A, 42, 2267 (1990).
4. N. Nakamura, Z. Phys. D., 19, 149 (1991).
5. O. Echt, in Physics and Chemistry of Small Clusters, edited by P. Jena, B. K. Rao, and S. N. Khanna (Plenum Press, New York, 1987).
6. C. Brechignac, Ph. Cahuzac, F. Carlier, M. de Frutos, Phys. Rev. Lett. 64, 2893 (1990).
7. C. Brechignac, Ph. Cahuzac, F. Carlier, J. Leygnier, A. Sarfati, Phys. Rev. B, 44, 11386 (1991).
8. W. A. Saunders, Phys. Rev. Let., 64, 3046 (1990).
9. W. A. Saunders, N. Dam, Z. Phys. D, 20, 111 (1991).
10. I. Rabin, C. Jackschath, W. Schulze, Z. Phys. D, 19, 153 (1991).
11. N. G. Gotts, P. G. Lethbridge, A. J. Stace, J. Chem. Phys., 96, 408 (1992).
12. U. Naher, H. Gohlich, T. Lange, T. P. Martin, Phys Rev. Lett, 68, 3416 (1992).
13. T. P. Martin, U. Naher, H. Gohlich, T. Lange, Chem. Phys. Lett., 196, 113 (1992).
14. U. Naher, S. Frank, T. P. Martin, Z. Phys D, 31, 191 (1994).
15 N. Bohr and J. A. Wheeler, Phys. Rev., 56, 426 (1939).
16 M. P. Iniguez, J. A. Alonso,M. A. Aller, L. C. Balbas, Phys. Rev., 34, 2152 (1986).
17. M. Seidl, K. H. Mciwes-Broer, M. Brack, J. Chem. Phys., 95, 1295 (1991).
18. R. N. Barnett, U. Landman, G. Rajagopal, Phys. Rev. Lett., 22, 3058 (1991).
19. N. Bakaltchev and E. Blaisten-Barojas, CSI/GMU Report (1993), unpublished.

MICROWAVES FOR REDUCTION OF IRON
ORE PELLET BY CARBON

IDALIA GOMEZ AND JUAN A. AGUILAR
Universidad Autónoma de Nuevo León, Facultad de Ingeniería Mecánica y Eléctrica, Apartado
Postal 076"F", Cd. Universitaria, San Nicolás de los Garza, N.L. CP. 66450, México

ABSTRACT

Results of reducibility tests of reduction conducted on iron ore pellets by carbon are presented in this work. Work done is centered on reduction kinetics by carbon with conventional heat supply (heat transfer process) compared with reduction kinetics where heat is supplied by microwaves to whole volume. Ore used in this work is called "Alzada" which has reducibility characteristics well known, and is often used as standard for comparison. Importance of using actual pellet instead of dust is pointed. This work is part of a project related with microwaves for reduction of metallic oxides.

Introduction

Obtention of a metal from its oxide is a process called reduction, and in order to conduct this process it is necessary to provide energy to the system. The most common way is fire or electricity. There are, since a couple of decades, some studies on microwave applications for supplying energy for non metallic transformations, and just lately metallurgist people is working in this field[1,2]. It is possible to visualize the reduction of iron ore with solid carbon as a system where carbon monoxide (CO) is removed as fast as it is produced. In this work the importance of solid carbon in contact with the oxide is much smaller than the production of carbon monoxide from it by Boudouard reaction, which gives a CO/CO_2 mixture. According to thermodynamic properties of this reaction ($C + CO_2 = 2CO$), it is possible to have an atmosphere of pure carbon monoxide at high temperatures, above 1000°C. Necessary heat to conduct the reduction process is supplied in this case by microwaves, even when the product is a metal.

The objective of this work is to demonstrate that iron ore has the capacity to absorb energy from microwaves and, therefore, it is possible to conduct the reduction process with microwaves as a power source.

Reduction process

Once that carbon monoxide is produced by Boudouard reaction, reduction of an iron ore pellet is divided in two steps[3,4,5]:
a)   Diffusion of CO through external core.
b)   Chemical reaction in external core/oxide interface.
These steps correspond to a topochemical reduction following scheme on figure 1 which shows such condition.
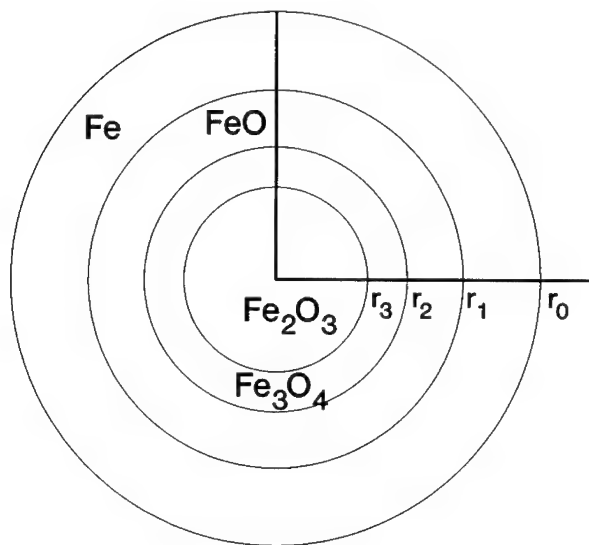
Figure 1   Scheme of a pellet showing reaction interfaces.

This figure shows an spherical pellet with three well defined reaction interfaces, r_0 is the outside radius, r_1, r_2 and r_3 are respectively the interfaces where reduction from wustite (FeO) to metallic iron (Fe), magnetite (Fe_3O_4) to wustite and hematite (Fe_2O_3) to magnetite are taking place. The reduction begins with the reduction of hematite to magnetite, this magnetite is then reduced to wustite and finally this one to metallic iron. The reactions for each stage are:

$$r_3: \quad 3Fe_2O_3 + CO = 2Fe_3O_4 + CO_2$$
$$r_2: \quad Fe_3O_4 + CO = 3FeO + CO_2$$
$$r_1: \quad FeO + CO = Fe + CO_2$$
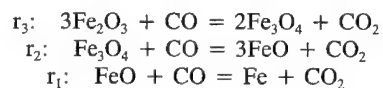
Normally chemical reaction and diffusion are both controlling[6,7] the process, but at high temperatures, above 800°C, diffusion control becomes more important.

Experimental procedure

Carbothermic reduction tests with microwaves were conducted in a conventional microwave oven (2450 MHz, 800 Watts), while conventional reduction tests were conducted in an electric resistance furnace at 1100°C. Both, pellet and carbon, were placed inside a crucible made of zirconium oxide. Several tests were conducted for determining carbon/hematite weight ratio, this ratio was 3.5. High purity carbon (99.99%) was used, pellet (3.8 gr. and radius 0.6 cm) is a typical ore coming from a mine located in the mexican state of Colima, chemical pellet composition is: Total Fe 66.5 wt%, Fe^{+2} 0.64 % and gange 5.3 % (gange composition: 37 % CaO, 11% MgO, 38% SiO_2, 14 % Al_2O_3).

For reduction with microwaves, several tests were carried out in order to know the right place inside the oven to set the crucible, according with physics, the right place must be in the Fresnel zone. Then, the oven was programmed for different times, and when this time was reached, the specimen was removed and chemically analyzed. Kinetic diagrams (reduction degree against time) were constructed with this information.

For reduction in a conventional furnace, it was heated up until desire temperature was reached and stabilized, after that, the crucibles with specimens were placed inside the furnace, and removed one by one according to the experimental design. Diagrams like those ones builded for microwave reduction were also constructed.

In all cases, scanning electronic microscopy was employed to observe the specimens.

Results and discussion

Results of microwave tests are presented in figure 2. This figure shows points that correspond to carbon/hematite weight ratios of 3.5, the obtained points are those which are on the curve builded with a validated computer model[8] simulating the reduction with CO at 1100°C. Ratios greater than 3.5 exhibit same behavior, while ratios below 3.0 are not enough for reduction. Conventional tests conducted in the same conditions (ratio equals 3.5) follow the simulated curve. Collected data show that reduction with microwaves has same behavior than conventional one, but in the first case reduction process stops when reduction degree is about 40%. This situation will be discussed later.
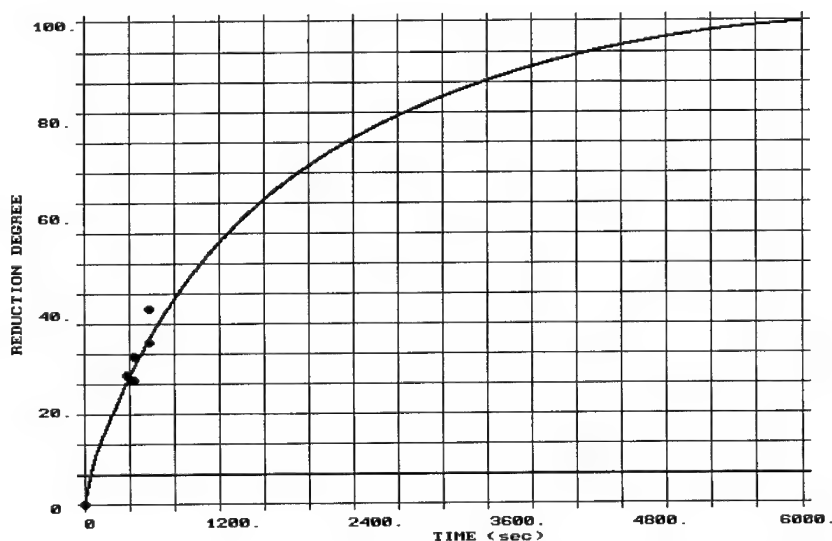

Figure 2   Reduction degree against time for microwave at 800 watts, and conventional heating at 1100°C (see text).

In order to make a realistic comparison between microwave and conventional reduction it is necessary to estimate which is the temperature in the pellet while reduction is being conducted. There is no problem for having a kinetic curve for conventional reduction, because it is easy to measure temperatures in a conventional furnace, and besides, it is possible to use a validate model for describing reduction. Temperature measurement inside a microwave field is a challenge[9]. Thermocouples do not work in this condition, and optic pyrometry just gives surface temperatures. One way to estimate temperatures is to identify and analyze the different phases that are present in the pellet, and verify if they are melted or solid, and according with their properties estimate the temperature. Figure 3 is a photo taken to an specimen exposed for 10 minutes, there are metallic iron and melted fayalite (Fe_2SiO_4). Melting points are respectively 1537°C and 1217°C, which shows that minimum temperature was about 1200°C.
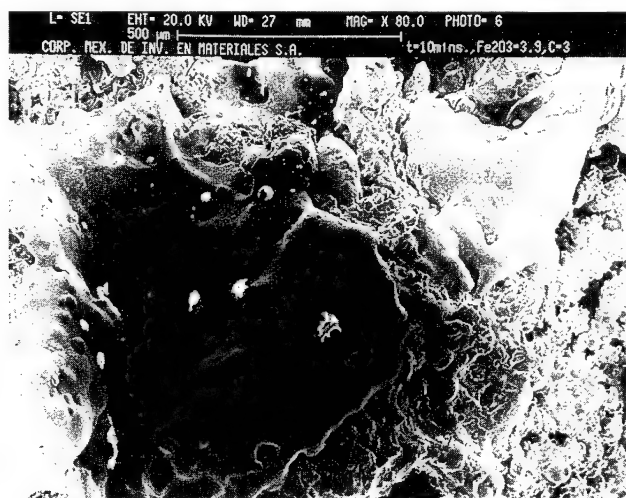
Figure 3   Specimen reduced with microwaves for 10 minutes, bright drops are melted fayalite.

Figure 4 also shows fayalite over iron. Taking reaction with CO it is possible to calculate that thermodynamic equilibrium makes easer to conduct reduction at low temperatures rather than high, this explains why simulated curves between 1100°C and 1500°C with CO are almost the same. This situation makes possible to compare tests conducted with microwaves at certain power against tests conducted conventionally at certain temperature. Accepting that diffusion is controlling step on reduction rate, when metallic iron appears on the surface, it melts and covers the pellet, and stops reduction, besides melted fayalite closes pores, porosity decreases, and this also stops reduction. Used material is not homogeneous, then dielectric properties, which are responsible of heating, are different, and some places in the pellet heats in a different manner. With above information, it is possible to say that direct reduction is achieved at about 1300°C, reduced iron is a small film of about 0.5 mm covering the pellet, this film is melted by Joule effect. Figure 5, shows this reduced and melted iron.
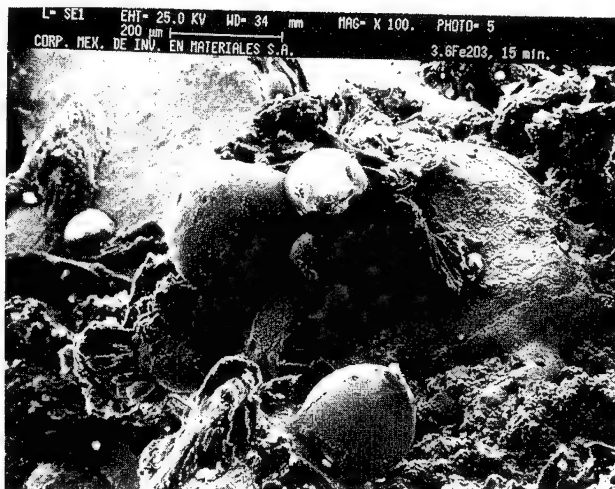
Figure 4   Specimen reduced with microwaves for 15 minutes, bright drops are melted fayalite.
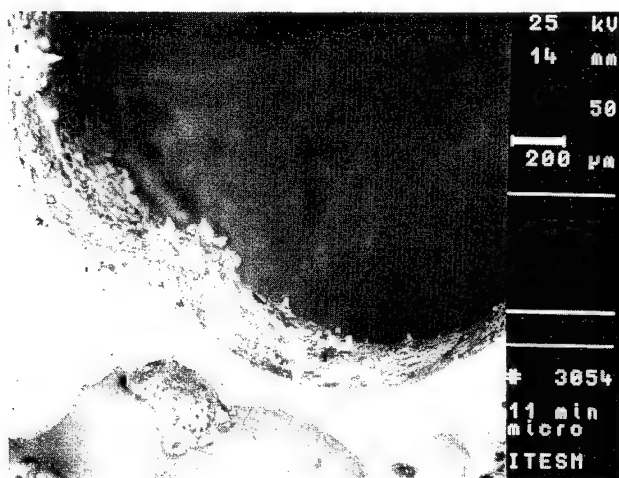
Figure 5   Film of melted iron.

Conclusions

Obtained results permit to put down the following conclusions:

Iron oxides absorb microwaves, therefore it is possible to supply them energy for heating or for conducting a reduction process.

Due to diffusion control, reduction is topochemical, in this way reduction rate is practically the same for both, microwave and conventional reduction. Due to pellet size temperature difference inside and outside pellet is small.

Reduction stops because of melted iron covers pellet surface and avoid CO diffusion, besides other phases formation with different properties could stop reduction. i.e. it is harder to remove oxygen from fayalite than from wustite.

Size pellet allows to study this situation, which is harder to evaluate in dust.

References

1.	N. Standish and H. Worner, Journal of Microwave Power and Electromagnetic Energy 1990, 59
2.	N. Standish and W. Huang, S.I.J. International, **31** (3), 241 (1991)
3.	W. Baukloh and R. Durrer, Stahl und Eisen, **54**, 673 (1934)
4.	J. O. Edtrom, Journal of the Iron and Steel Institute, **175**, 289 (1953)
5.	Von Bougdandy and H.J. Engell, The reduction of iron ores, (Springer-Verlag, Berlin, 1971)
6.	T.G. Cox and F.R. Sale, Iron and Steelmaking, 1974, 234
7.	P. Tiwari and D. Bandyopadhyay, Iron and Steelmaking, **19** (6), 464 (1992)
8.	J. Aguilar, Kinetic constants for description of iron ore reduction,(7th International Symposium on Transport Phenomena in Manufacturing Processes, **7**, Acapulco, México 1994, 126
9.	J. Binner, Materials World, 1993, 152

Acknowledgements

THE ESCAPE OF PARTICLES FROM A QUANTUM WELL

JAMES P. LAVINE
Microelectronics Technology Division, Eastman Kodak Company,
Rochester, NY 14650-2008

ABSTRACT

The escape rate is calculated for an electron in a one-dimensional potential well. First-order time-dependent perturbation theory is used with solutions of Schrödinger's equation and a set of coupled rate equations is numerically solved. The time evolution of an ensemble of one-electron systems is followed and the fraction of systems that remain in a bound state is found to decay exponentially as time passes. The characteristic time constant for the decay grows exponentially with an increase in the well depth. This is analogous to Kramers' result for the classical escape problem.

1. INTRODUCTION

Particles eventually escape confinement within a potential well. It is useful to determine whether the time scale for escape is nanoseconds or years, especially if the escape rate controls the operation of an electronic device [1,2] or an atomic process such as diffusion. Kramers [3] provided an elegant solution to the classical problem. Formal quantum mechanical approaches [4,5] do not appear to yield simple estimates or trends.

The present work develops one-dimensional models within first-order time-dependent perturbation theory. Schrödinger's equation is solved for the bound states of an electron in a square well with an infinite barrier on one side. A time-dependent perturbation causes transitions of the electron between the energy levels. The time evolution of an ensemble of one-electron systems is followed through the solution of a coupled set of rate equations [6]. The fraction of systems that remain in a bound state is found to decay exponentially as time passes. The characteristic time constant for the decay grows exponentially with an increase in the well depth. This is analogous to Kramers' result for the classical escape problem [3].

The model is described in Section 2. Numerical results are presented

in Section 3. Conclusions are contained in Section 4.

2. RATE EQUATIONS

The ideal model is pictured in Fig. 1a. The electron starts in the shallow well on the left and is tracked until it enters the deep well on the right. The present calculations are less ambitious and treat the escape of the electron from the shallow well of Fig. 1b by a straightforward application of quantum mechanics [7]. Tunneling is ignored.

Schrödinger's equation yields the bound state wave functions for the square well of depth $-V_0$ and width L. Let n label the bound state of energy $-E_n$ with n = 1 the ground state. The energy levels for a series of well depths are shown in Fig. 2 for L = 0.02 μm. The levels are generally further apart as the binding energy decreases.
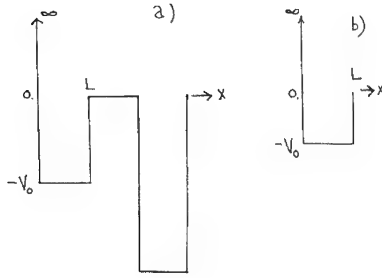
Fig. 1. Potential wells. (a) Ideal model. (b) Simplified model.
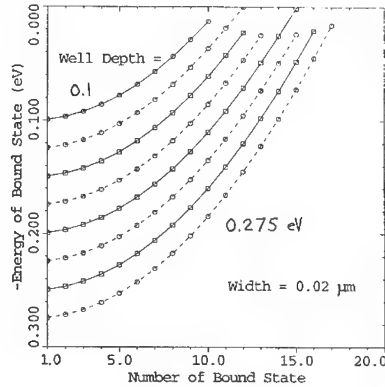
Fig. 2. Bound state energies for varying well depth and L = 0.02 μm. Successive curves vary by 0.025 eV.

Transitions from state n to state m are driven by the perturbation

$$V(x,t) = V_p[x(L - x)/L^2] \, gt \, e^{-t/t_0} \qquad . \qquad (1)$$

This permits a closed-form evaluation of the transition probabilities

$W_{mn}(t) = |a_m(t)|^2$ with [7]

$$a_m(t) = (1/\hbar) \int_0^t <m|V|n> \, e^{i(E_m - E_n)t'/\hbar} \, dt' \; + \; \delta_{mn} \qquad , \qquad (2)$$

and $\hbar$ is Planck's constant divided by 2π. Selected transition probabilities are shown in Figs. 3 and 4 for $V_0 = 0.2$ eV, $L = 0.02$ μm, $t_0 = 0.3 \times 10^{-13}$ s, $t = 1.0 \times 10^{-13}$ s, $g = 1/t_0$, and $V_p = kT$, the thermal energy at 300 K. This is intended to simulate thermally-driven escape. There are 15 bound states for this V_0 and L.

The rate equation approach also needs expressions for transitions from a bound state at $-E_n$ to the continuum ($E > 0$.). These are assumed to be $e^{-E_n/kT}$ in analogy to the thermal ionization probabilities developed in Section 10 of [8]. Spontaneous emission is included by assuming its ratio to stimulated emission is $e^{\Delta E_{mn}/kT} - 1$, where ΔE_{mn} is the energy difference between the two bound states. The set of coupled rate equations is now solved by an explicit numerical approach with a time step of 1×10^{-13} s. All systems of the ensemble start at $t = 0$. with their electron in the ground state. The fraction of the ensemble in each bound state is then available as a function of time. Fig. 5 shows selected results for the parameters of Figs. 3 and 4. The electrons that escape are those that enter the continuum and their fraction appears on the graph as the 16th state.
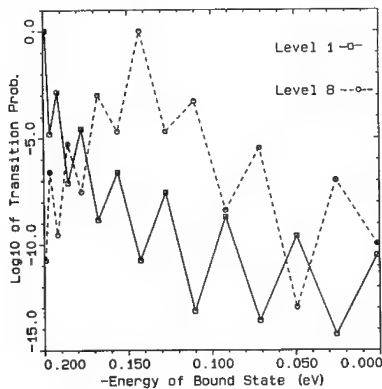
Fig. 3. Transition probabilities from the n = 1 and n = 8 bound states. $V_0 = 0.2$ eV and L = 0.02 μm.
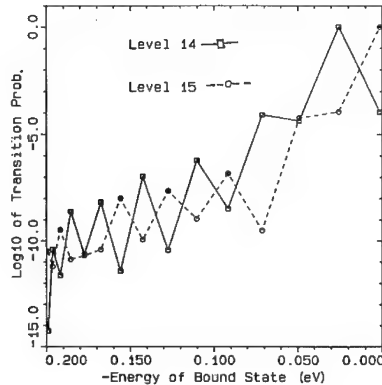
Fig. 4. Transition probabilities from the n = 14 and n = 15 bound states. $V_0 = 0.2$ eV and L = 0.02 μm.

3. NUMERICAL RESULTS

Representative numerical results are presented to illustrate the time

scale for electron escape from a square well. The parameters are those used in Section 2. An electron that enters the continuum is assumed to escape, so recapture is ignored for now. Fig. 6 shows how the fraction, f, of the ensemble with a bound electron decays as a function of time. The decay is exponential and a characteristic time constant τ is extracted from the slope, so f(t) is proportional to $e^{-t/\tau}$. The magnitude of τ is affected by the bound to continuum transition probability. For example, if this is taken to be $(V_p/V_0)^2 \ e^{-E_n/kT}$, then Fig. 7 results. A comparison with Fig. 6 shows that the time scale for escape is longer. This point is made more graphically in Fig. 8, which shows τ versus the well depth V_0.
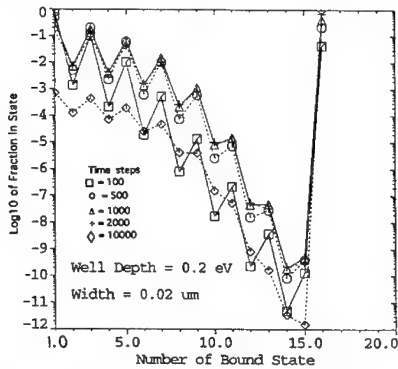
Fig. 5. Bound state populations for selected times. Level 16 = escaped. V_0 = 0.2 eV and L = 0.02 μm.
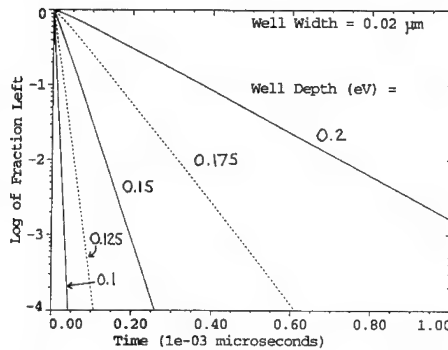
Fig. 6. Fraction left bound vs. time. V_0 varies and L = 0.02 μm.
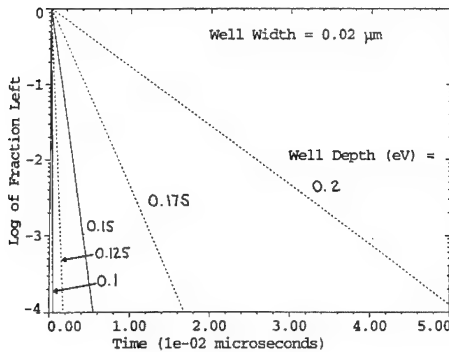
Fig. 7. Fraction left vs. time. The bound-to-free model differs from that of Fig. 6. V_0 = 0.2 eV and L = 0.02 μm.
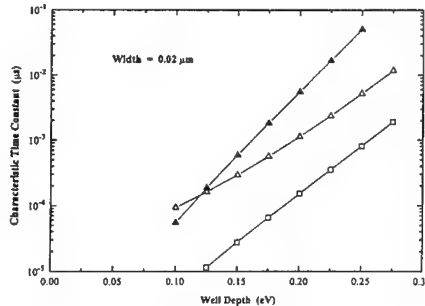
Fig. 8. Characteristic time constant vs. well depth V_0. The bound-to-free model varies. L = 0.02 μm.

The open squares ($\square$) are based on Fig. 6 and the solid triangles ($\blacktriangle$) are from Fig. 7. The open triangles ($\triangle$) are for a bound-to-free transition probability of $[(V_0 - E_n)/V_0]e^{-E_n/kT}$.

The curves in Fig. 8 demonstrate that the τ are approximately proportional to $e^{+V_0/rkT}$ with r = 1.1, 0.84, and 1.5, respectively. The latter 2 curves depart from linearity as V_0 increases. The thermionic emission theory [9] leads to τ proportional to $e^{+V_0/kT}$. The above results are all for a well width of 0.02 μm. If the well width is varied with V_0 = 0.2 eV, then the τ is found to vary linearly with L, as shown in Fig. 9. This dependence was also found earlier [9].

Fig. 9. Characteristic time constant vs. well width L for V_0 = 0.2 eV. The simplest bound-to-free model is used.
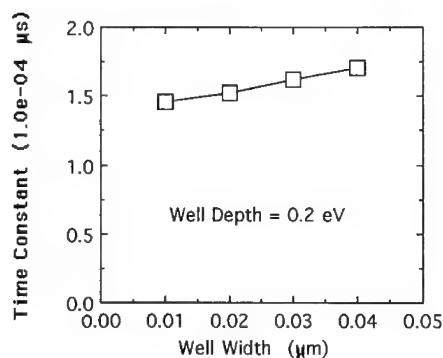
Recapture of free electrons may be permitted after each time step. This is most easily done by returning a fraction of the ensembles with a free electron to a selected bound state. Another fraction of the continuum ensembles may be considered to have diffused to x = L, and hence, escaped. These 2 changes are introduced together. The second fraction is taken to be $1 - e^{-\Delta t/t'}$ with Δt the time step, $t' = 4L^2/\pi^2 D$, and D = 12.929 cm^2/s. This form comes from classical diffusion with a sink at x = L [10]. These changes do not affect the decay curves unless the recapture is to a deeply-bound state. In the latter case, the escape is slowed significantly.

4. CONCLUDING REMARKS

Simple models are used to explore the electron escape rate from a potential well. The dependence of the characteristic time constant τ on the well depth and width resemble those found for the thermionic

emission model [9]. τ increases exponentially with an increase in well depth. This result resembles Kramers' for the classical escape problem [3]. The current calculations are not completely self-consistent in that bound-to-free and free-to-bound transitions are included on an ad hoc basis. Future work needs to remedy this as these terms affect τ and to extend the model to the double well case. The connection with numerical results for the classical escape problem [11] should also be determined.

References
1. E.K. Banghart, J.P. Lavine, J.M. Pimbley, and B.C. Burkey, COMPEL **1 0**, 205 (1991).
2. C.-Y. Tsai, L.F. Eastman, Y.-H. Lo, and C.-Y. Tsai, Appl. Phys. Lett. **6 5**, 469 (1994).
3. H.A. Kramers, Physica **7**, 284 (1940).
4. V.I. Mel'nikov, Physics Reports **2 0 9**, 1 (1991).
5. W.H. Miller, Ber. Bunsenges. Phys. Chem. **9 5**, 389 (1991).
6. W. Pickin, Phys. Status Solidi B **9 7**, 431 (1980).
7. W. Greiner, Quantum Mechanics An Introduction, (Springer-Verlag, Berlin, 1993), Sect. 11-4.
8. V.N. Abakumov, V.I. Perel', and I.N. Yassievich, Fiz. Tekh'. Poluprovodn. **1 2**, 3 (1978) [Sov. Phys. Semicond. **1 2**, 1 (1978)].
9. H. Schneider and K. v. Klitzing, Phys. Rev. B **3 8**, 6160 (1988).
10. H.S. Carslaw and J.C. Jaeger, Conductance of Heat in Solids, 2nd ed. (Oxford University Press, Oxford, 1959), p. 97.
11. J.P. Lavine, E.K. Banghart, and J.M. Pimbley, in Dynamics in Small Confining Systems, edited by J.M. Drake, J. Klafter, R. Kopelman, and D.D. Awschalom (Mater. Res. Soc. Proc. 290, Pittsburgh, PA, 1993) pp. 249-254.

CERAMIC-LIKE MATERIALS FROM WASTE INDUSTRIAL GYPSUM

E. HERLING, MARCELI CYRKIEWICZ AND JACEK KLESZEWSKI
Hercyrkle Environmental Projects Corp., 20 East 63 Street, New York, NY 10021

ABSTRACT

This paper presents a new method for preparing composites of phosphogypsum, a chemical industry waste, and synthetic (polyester, epoxide and vinyl ester) resins. These composites, after thermal improvement of the phosphogypsum, are called CLM (ceramic-like materials). They are characterized by highly desirable physical, chemical, mechanical and strength-related properties which enable there usage as anti-corrosive coatings for storage tanks and as durable floor coatings in many branches of industry.

INTRODUCTION

Of the chemical wastes currently produced world wide, phosphogypsum is the most abundant. Phosphogypsum is a byproduct of the production of phosphoric acid from both apatite and phosphorite ores. Each ton of phosphoric acid produced yields nearly 5 tons of waste phosphogypsum which is either stock- piled on land or dumped in the sea. In either case phosphogypsum continues to be a major environmental disposal challenge[1-4]. There have been a number of studies focused on identifying the properties of the phosphogypsum waste (composition, radioactivity, etc.)[1-8] and its utilization as an inexpensive filler in construction materials[1,2].

The major constituent of phosphogypsum is hydrated calcium sulfate. The extraction of phosphoric acid from apatite ore:

$$3Ca_5F(PO_4)_3 + 10H_2SO_4 + 10n \cdot H_2O \longrightarrow 6H_3PO_4 + 10CaSO_4 \cdot nH_2O + 2HF \qquad (1)$$

or from phosphorite ore:

$$Ca_3(PO_4)_2 + 3H_2SO_4 + 2H_2O \longrightarrow 2H_3PO_4 + 3CaSO_4 \cdot 2H_2O, \qquad (2)$$
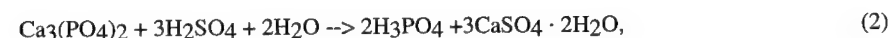
is achieved using a sulfuric acid leach. The waste phosphogypsum contains varying amounts of impurities that effect its use as a filler and determine its potential as a radioactive hazard[4-

8]. Taking as an example phosphogypsum produced from Russian apatite ore the average composition is:

$CaSO_4$	74.8 wt.%
Crystallization water	19.0
Phosphates converted to P_2O_5	1.6
Rare earth elements	1.3
SiO_2	1.1
Magnesium compounds converted to MgO	0.6
Al_2O_3	0.3
Fluorine	0.2
TiO_2	0.2
Potassium converted to K_2O	0.1
Sodium converted to Na_2O	0.1
Organic compounds	0.04
Fe_2O_3	0.03

and it exhibits the properties:

relative moisture at 323K	28 to 36%
specific surface	2100 cm^2/g
pH	2.0 to 3.3

Our measurements indicate that, depending on the origin of the apatite or phosphorite deposits, phosphogypsum may also contain small amounts of strontium (Sr), cerium (Ce), lanthanum (La), neodymium (Nd), praseodymium (Pr), yttrium (Y), samarium (Sm), gadolinium (Gd) and even smaller amounts of europium (Eu), terbium (Tb), dysprosium (Dy), holmium (Ho) and ytterbium (Yb). Phosphorite ores may also contain trace amounts of radioactive elements such as: uranium (^{238}U), radium (^{226}Ra), thorium (^{232}Tr) and potassium (^{70}K) in the amount of approximately 10^{-12} Curie/g. It has been shown that the concentration of trace lanthanides entrained in the phosphogypsum can be significantly reduced by a sulfuric acid leaching process[3]. If the residual phosphates, fluorides and sodium are not removed the phosphogypsum is less suitable for use in the manufacture of construction materials[3]. The residual lanthanides can be linked to the problem of the release of radioactive radium (^{222,226}Ra) which has been suggested to be responsible for lung cancer in some sectors of the worlds population[4-8].

We have developed methods for combining phosphogypsum and resins to produce what we refer to as CLM (ceramic-like materials). These material are prepared from an improved phosphogypsum which is believed to be composed of a complex chemical compound of the general form:

$$[CaSO_4 \cdot CaO \cdot P_2O_5 \cdot M_x(SO_4)_y \cdot (P_2O_5) \cdot M_xO_y], \qquad (3)$$
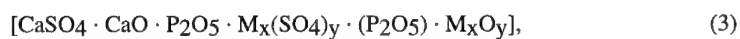
where M is a metal impurity. These new composite materials may help to address the challenge of reducing the volumes of waste phosphogypsum by providing materials with a broader range of industrial applications[9].

PREPARATION AND CHARACTERIZATION OF CLM

The production of CLM begins with a process for treating the crude waste phosphogypsum before it is combined with the resin. The crude starting material is thermally treated at 600K until the properties of the phosphogypsum are modified. The principal changes are reduced moisture and decomposition of orthophosporic acid, which is accompanied by a neutralization reaction leading to a pH of 7 to 7.5. Our results, as proposed in eq.(3), suggest that the thermal treatment yields a complex chemical compound which is not identical to any form of anhydrous or hydrated calcium sulfate. This is supported by our the x-ray diffraction measurements on apatite phosphogypsum and gypsum (Nida-Gips). Figure 1 shows the powder diffraction of three samples and it is clear that the apatite phosphogypsum differs in composition and structure from both the building gypsum and the dihydrous calcium sulfate ($CaSO_4 \cdot 2H_2O$). These data lead us to conclude that the thermally treated phosphogypsum used to prepare CLM is a mixture of different compounds, which are of the general form:

$$(CaSO_4 + M_x(SO_4)_y + M_x(PO_4)_y) \, nH_2O \qquad (4)$$
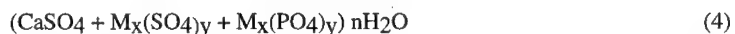
where n is the number of hydrated water molecules bound to the crystal lattice of the complex, x and y are the number of atoms and molecules in a particular compound and M are metal impurities other than calcium.

The CLM is prepared using the thermally treated phosphogypsum and synthetic polymer resins. The proportions of phosphogypsum and resin used allow us to vary the

final mechanical, electrical, and chemical properties of the CLM. CLM composites have been prepared using a variety of resins including epoxide, polyester and vinyl ester. The typical composite contains between 20-50 v% resin with the remaining fraction being phosphogypsum. A small amount of hardener is added to each system to initiate the polymerization. The composite is partially cured in 30-40 minutes and fully cured in 48 hours. Since the CLM forms only after the hardener is added it is possible to mix the resin and phosphogypsum and store the mixture for extended periods (i.e.. 2-3 months).

We believe that the properties of the CLM are determined inpart by a chemical reaction between the phosphogypsum composite and the resin during curing. The phosphogypsum is therefore not just a filler material as is the case in other synthetic resin based mixtures. The exact chemical processes that take place are not yet fully recognized. However it is believed that the rare-earth elements present in the phosphogypsum may play a significant role in this reaction process.

The range of mechanical strength and chemical resistance properties exhibit by CLM are:

a) Specific weight of 1.4 to 1.5
b) compression strength up to 1200 kg/cm^2 (17,000 psi), or 5 to 8 times greater that concrete
c) tensile strength on bending from 200 to 400 kg/cm^2 (2800 to 5700 psi), or 12 to 25 times greater than concrete
d) impact strength from 2 to 4 KJ/m^2 (0.95 to 1.0 ftlb/in^2)
e) abrasion on the boehme disk of 0.9 to 1.5 mm (0.035 to 0.047 in.), or 4 times less than concrete
f) shrinkage between 0.11 and 0.16%
g) linear coefficient of thermal expansion between 24 to 26 ppm/deg C (13 to 27 ppm/deg F)
h) cold water absorption from 0.09 to 0.61%
i) thermal conductivity between 0.4 to 0.5 W/m C (0.9 to 1.1BTU/h ft deg F)
j) electrical resistance approximately 2.5 x10^{16} ohm/cm
k) breakdown strength approximately 40Kv/mm
l) adhesion to a variety of surfaces is excellent (class 1)
m) exposure to 300 hours of salt spray with no deterioration
n) immersion in concentrated sulfuric acid for14 days at 80C with not detrimental effect
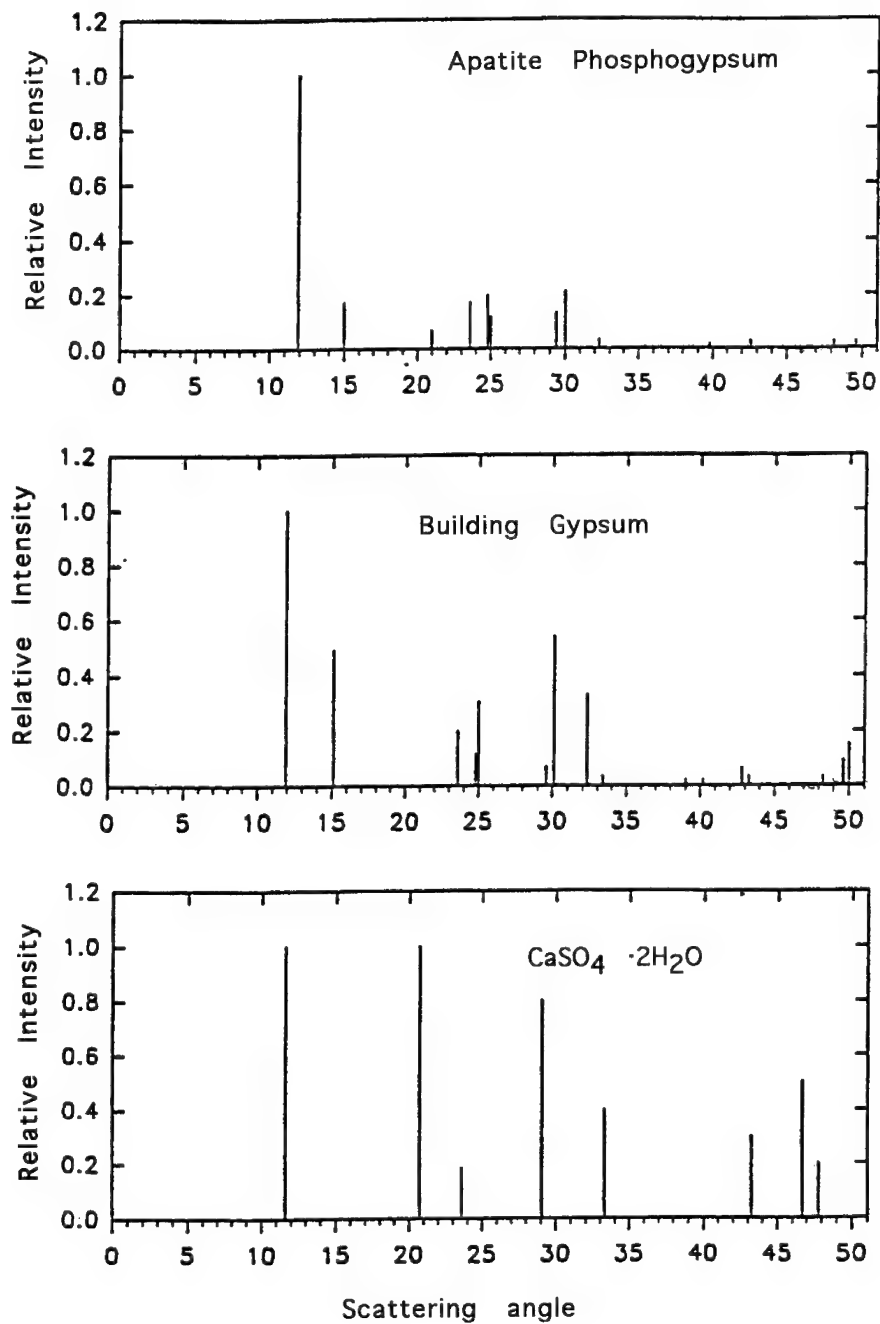
Figure 1

One of principal concerns of CLM type materials is the potential risk from exposure to radioactivity. Because waste phosphogypsum produced from apatite ore contains trace quantities of Radium the composite can contain measurable amounts of ^{222}Ra which is trapped in the pore space. The presence of ^{222}Ra can be measured and standards have been established which set the admissible levels. Our measurements of CLM made from apatite phosphogypsum filler indicate a level four times lower than the admissible level of 185 Bq/Kg. The values for CLM are comparable to values reported for cement and red bricks which are completely safe with regard to radiation exposure.

CONCLUSIONS

Our results todate on composite materials prepared using waste phosphogypsum and polymer resins demonstrate that the mechanical strength and chemical resistance properties of these composites are significantly better than many of the more common building materials currently in use. CLM appears to be a complex composite with properties that reflect strong chemical interactions between the phosphogypsum and the polymer resins. Although the exact nature of these chemical interactions remain to be more completely understood our results strongly suggest that this synergism between filler and binder can be exploited further to produce other materials with a wide range of possible industrial applications.

REFERENCES

1. D. Saylak, A.M. Gadalla and C.C. Yung, Ind. Eng. Chem. Res. **27,** 707 (1988)
2. A.M. Gadalla, D. Saylak and A.L. Lindner, J. Am. Ceram. Soc.**73**, 2255 (1990)
3. A. Jarosinski, et. al., Pol. Tech. Rev. **4**, 8 (1993)
4. H.B. Van der Heijde, P.-J. Klijn and W.F. Passchier, Radiat. Prot. Dosim. **24**, 419 (1988)
5. H. Lettner and F. Steinhausler, Radiat. Prot. Dosim. **24**, 415 (1988)
6. I. Othman and M. Mahrouka, Radiat. Prot. Dosim. **55**, 299 (1994)
7. J. Uyttenhove and R. Lapere, Radiat. Prot. Dosim. **24**, 435 (1988)
8. E.M. Hussein, Health Physics **67**, 280 (1994)
9. Patent Application (Poland), P-283240, P-299472, P-299473 and P-303058

DIFFUSION-CONTROLLED REACTIONS IN MICELLAR SYSTEMS

MASANORI TACHIYA[*] AND ALEXANDER V. BARZYKIN[**]
National Institute of Materials and Chemical Research, Department of Physical Chemistry
Tsukuba, Ibaraki 305, Japan
[*]Also affiliated with the University of Tsukuba, Department of Chemistry
[**]On leave from the Institute of Chemical Physics at Chernogolovka, Russia

ABSTRACT

Reaction kinetics in micellar solutions are studied theoretically with an emphasis on diffusion-controlled luminescence quenching. Different spatial arrangements of reactants within individual micelles are analyzed and a general method for treating diffusion-controlled reactions in a finite volume employing an effective potential approximation is developed. Several models are considered for the exchange of reactants between micelles including migration mediated by the bulk phase and successive multiparticle hopping through transient channels connecting micelles during their sticky collisions. These results are combined in a general stochastic theory of reaction kinetics in micellar solutions with exchange. The theory is further extended to reactions in clusters of micelles using a continuous time random walk approach. Once the principal features of micellar kinetics are understood, one can extract important structural and dynamic information on the aggregates and their guest molecules by analyzing suitably designed experiments.

INTRODUCTION

Reactions in self-aggregated assemblies of amphiphilic molecules, such as normal or reversed micelles, vesicles, and microemulsions, continue to attract a great deal of current research activity mainly for the following reasons. First, proper organization of reactants by their solubilization in suitable microheterogeneous environments enables one to catalyze and control a wide variety of practically important reactions, mostly photoprocesses.[1-3] The second reason is that simple indicator reactions may serve as a tool to investigate the embedding structures themselves.[4-7]

Normal micelles formed in aqueous surfactant solutions are approximately spherical, a few nanometers in diameter, and contain about a hundred monomer surfactants.[8] The surface of a micelle is composed of the surfactant polar head groups and, possibly, of the bound counterions. The hydrocarbon chains constitute the core. Microviscosity of the micellar interior is rather high hindering the mobility of solubilized molecules. Similar structures are formed in polymer-surfactant and block polymer solutions.[9] Other examples of self-associated microdisperse systems are closed bilayer structures or vesicles[1] and microemulsions.[10] A water-in-oil microemulsion consists of water droplets solubilized in oil by a monolayer of surfactant molecules. These droplets are sometimes referred to as reversed micelles. In the formulation of reaction kinetics in microdisperse systems, it is important that micelles form well-defined finite volume domains where reactants are confined. The size distribution of micelles is typically narrow and they may be approximately considered as monodisperse.

While the micellar aggregates are thermodynamically stable, they are essentially dynamic structures displaying complex formation-breakdown processes, including coalescence-fragmentation and monomer exchange with the surrounding aqueous phase.[8,11,12] This dynamic nature gives rise to intermicellar migration of solubilized molecules so that the number of reactants in a micelle continuously fluctuates.[13,14] The residence time of solubilizates in micelles is roughly in the

microsecond range. Reactants are nonuniformly distributed among the micelles. Since the average number of guest species per micelle is typically low and comparable to the fluctuation, the occupation statistics is very important in such systems and a deterministic model of kinetics, which considers only the average, cannot be applied.

The basic idea in analyzing reaction kinetics in microdisperse systems is to separately consider the process within a finite volume and then to take the occupation statistics and the dynamics of reactant exchange into account. When reaction is considerably faster than solubilizate exchange, each micelle acts as a cage, and the overall kinetics can be obtained by averaging the microscopic intramicellar kinetics with a given number of reactants over the equilibrium statistical distribution of reactants among the micelles. This is no longer valid if reaction and exchange occur on comparable time scales, and one has to use a stochastic approach to properly treat the migration-induced fluctuations.[15]

A number of good reviews on reaction kinetics in micellar systems and related topics have appeared in the literature.[4-7,15,16] The scope of the present contribution is focused on recent advances in theory in this field. For the most part we consider diffusion-controlled reactions and, more specifically, luminescence quenching as a typical example. We start from describing the diffusion-controlled reaction kinetics within individual micelles for different spatial arrangements of reacting species. Various exchange mechanisms of reactants between micelles are further discussed and a general stochastic theory for analyzing migration-influenced reaction kinetics in micellar solutions is presented. Finally, we consider reactions in systems with a higher level of organization, namely, in micellar clusters, using a continuous time random walk approach.

DIFFUSION-CONTROLLED REACTION WITHIN A MICELLE

Reaction kinetics under diffusion-limited conditions are usually described in terms of the pair survival probability $W(r, t)$, which is defined as the probability that an isolated pair of reactants with initial separation r is extant at time t. In a homogeneous solution, the relative motion of reactants can be separated and $W(r, t)$ satisfies the backward diffusion equation with appropriate boundary conditions.[17] The experimental observables are related to the configurational average of $W(r, t)$ over the initial equilibrium distribution of reactants. Separating the relative motion is no longer straightforward in nonhomogeneous media and requires a certain symmetry of the system. Exact analytical solution in terms of an infinite series of exponential eigenfunctions for a pair of particles confined to a spherical volume is available in two cases where: (i) one reactant is immobile at the center, whereas the other moves freely within the sphere;[18,19] and (ii) both reactants diffuse on the spherical surface.[19-21] For the parameter values typical of micellar systems, the decay of the survival probability is well approximated by a single exponential in both cases. The same conclusion has been drawn from numerical random-walk simulations also for the situation where both reactants move freely within the micelle,[22,23] and it has been shown that the transient effects at very short times (less than about 10 ns) become noticeable only for large values of the encounter distance $a > 0.2R$, with R being the micelle radius. It is reasonable to expect similar temporal behavior for any spatial arrangement of reactants in a small spherical volume.

It is possible to evaluate the geminate reaction kinetics for arbitrary nonhomogeneous distribution of reactants without solving the underlying diffusion problem exactly. The method takes advantage of the effective potential approximation.[24] The basic idea is in correlating the equilibrium distance distribution function $f(r)$ with the effective potential of interaction between the particles $V_{eff}(r)$ as follows: $f(r) = \exp[-\beta V_{eff}(r)]$, where $\beta = (k_B T)^{-1}$. This potential incorporates the effect of nonhomogeneity in the sense that the relative diffusive motion of the particles

interacting via $V_{eff}(r)$ in the absence of reaction leads to the correct spatial distribution at equilibrium. The pair survival probability is then assumed to satisfy the generalized one-dimensional backward equation

$$\frac{\partial W}{\partial t} = D\left(\frac{\partial^2 W}{\partial r^2} + \frac{f'}{f}\frac{\partial W}{\partial r}\right),$$ (1)

where D is the coefficient of relative diffusion. The standard boundary conditions apply, namely, immediate recombination at encounter distance a and reflection from the outer barrier erected at a maximum feasible separation b.

Since the decay of the pair survival probability in a restricted space such as the micellar interior is generally well described by a single exponential, it is reasonable to make use of the mean reaction time approximation.[20,25] Equation satisfied by the mean reaction time $\tau(r)$ of the pair having an initial separation r is derived by integrating Eq. (1) over time. After averaging the solution over the initial distribution we obtain the final expression for the mean reaction time

$$\tau = \frac{R^2}{D}\int_a^b dr f^{-1}(r)\left[\int_r^b dx f(x)\right]^2\left[\int_a^b dr f(r)\right]^{-1}.$$ (2)

Hereafter the micelle radius R is used as a unit of distance and the parameters a, b, and r are dimensionless.

The distribution of distance between two point particles confined to a spherical volume can be calculated using the method of characteristic functions[26]

$$f(r) = \frac{2r}{\pi}\int_0^\infty dq\,\frac{\sin(rq)}{q}\int_0^1 dx\,\rho_1(x)\frac{\sin(qx)}{x}\int_0^1 dy\,\rho_2(y)\frac{\sin(qy)}{y},$$ (3)

where $\rho_i(r)$ denotes the normalized radial distribution of the individual particle ($i = 1,2$) corresponding to its hydrophobic potential. The distance distribution function in Eq. (3) is normalized so that $\int_0^2 dr f(r) = 1$. Finite dimensions of the particles can be incorporated by multiplying $f(r)$ by the Heaviside function $\theta(r - a)$. Let us now consider two simplest examples of a spherical distribution: a surface distribution, $\rho_s(r) = \delta(1 - r)$, and a uniform distribution, $\rho_u(r) = 3r^2\theta(1 - r)$. The pair distance distribution function for three possible combinations of given individual spatial arrangements can be immediately calculated from Eq. (3): $f_{ss}(r) = \frac{1}{2}r$, $f_{su}(r) = \frac{3}{4}r^2(2 - r)$, and $f_{uu}(r) = \frac{3}{16}r^2(2 - r)^2(4 + r)$. The final results are illustrated in Fig. 1 where the pseudo-first-order reaction rate constant (the reciprocal of τ) is plotted as a function of the encounter distance. In the radially symmetric situation with one reactant fixed at the center, cu, the effective potential approximation yields the exact result. This is not the case for reactions on the micellar surface, but still the discrepancy is not pronounced, especially for small values of a. The effective potential approximation for τ_{uu} can be compared with the bulk reaction approximation.[22,23] The latter assumes that the rate constant in a micelle is given by the product of the bulk second-order Smoluchowski rate constant $4\pi aD$ and the reactant concentration, which may be defined as the reciprocal volume of the micelle available for diffusion, $3/4\pi(1 - a^3)$.

The solubilizates are unlikely located in a micelle at random, but rather are distributed with the probability density having a maximum at a certain distance r_0 from the center.[27] The corresponding radial distribution may be approximated to be Gaussian, $\rho_g(r) \propto r^2\exp\{-[(r - r_0)/\sigma]^2\}$, being characterized not only by the average but also the variance. Similar arguments apply to the
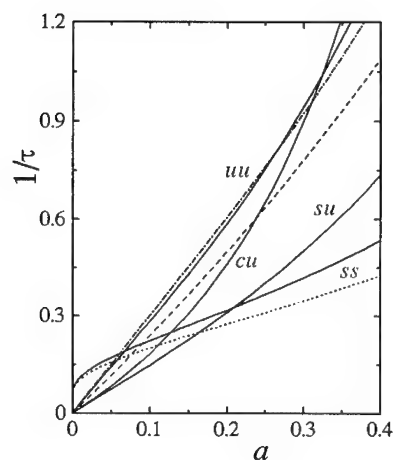
Fig. 1. The plot of $1/\tau$ as a function of a in the effective potential approximation (full lines) for several spatial arrangements of reactants in a spherical micelle (abbreviations attached). The dotted line represents the exact solution for ss problem. The dashed and dash-dotted lines correspond to the results of numerical simulations and the bulk reaction approximation, respectively, for uu arrangement. The rate constant is given in units of D/R^2, and a is in units of R.

surface distribution, which should be modified to include the penetration depth of a particle into a micelle. In this case, the first approximation leads to the exponential distribution. A very interesting behavior of the rate constant is observed when the distribution is changed from the δ-type to the uniform, as illustrated in Fig. 2. For example, $1/\tau_{sg}$ shows a maximum at a certain value of σ if the average location of the gaussian particle is near the surface. When $1 - r_0 > a$, the dependence of $1/\tau_{sg}$ on σ displays a sort of "induction period".
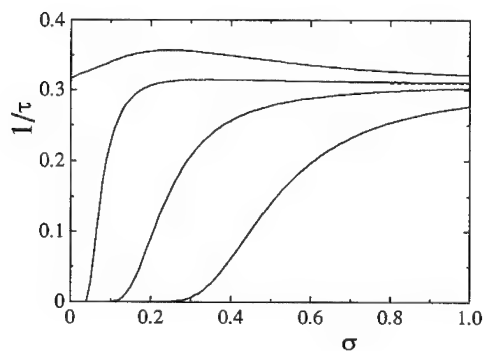
Fig. 2. The rate constant $1/\tau$ as a function of the width parameter σ for sg arrangement of reactants in a spherical micelle for several values of $r_0 = 1$, 0.7, 0.5, and 0 (top to bottom) with $a = 0.2$. The dashed line shows the ultimate value of $1/\tau$ for su ($\sigma \to \infty$).

The kinetics of intramicellar reactions involving several reactants can be evaluated in terms of τ if the reactants act independently. For instance, when an excited probe is present in a micelle together with n quenchers, its survival probability decays with the pseudo-first-order rate constant n/τ.[18,28] This statement provides a basis for the stochastic treatment of luminescence quenching in the micellar ensemble.[15]

OCCUPATION STATISTICS. EXCHANGE MECHANISMS

The number of reactants varies from micelle to micelle and fluctuates with time. The equilibrium distribution is determined exclusively by molecular interactions, no matter what processes are involved in establishing it.[29] The statistical description of an equilibrium system is performed in terms of its partition function, following the grand canonical approach. For dimensionless noninteracting particles distributed among monodisperse micelles, the occupation statistics is Poissonian

$$P_n(\overline{n}) = (\overline{n}^n/n!)\exp(-\overline{n}), \tag{4}$$

where $P_n(\bar{n})$ is the probability for a micelle to contain $n \geq 0$ particles given the mean occupancy number $\bar{n}$. The assumptions leading to the Poisson distribution are justified, in most cases, at low values of $\bar{n}$. When the concentration of particles is increased, the interactions manifest themselves skewing the distribution. The initial distortion can be described in terms of the virial expansion. For high occupancies, the excluded volume effect comes into play and a finite limit to the number of particles a micelle is able to accomodate has to be taken into account. Within the lattice gas formulation, volume exclusion leads to the binomial distribution.[30] However, it does not account for solute-surfactant interactions, which often induce changes in micelle size upon solubilization.[6]

The solute molecules are, in general, partitioned between the micellar pseudophase and the bulk aqueous phase. In equilibrium, the chemical potentials for the two phases are equal. Using this condition one can calculate the mean occupancy number $\bar{n}$ as a function of the overall concentration of the particles in solution [C]. Neglecting interactions between the particles we obtain

$$\bar{n} = \frac{[C]}{[M]}\{1 + \exp(-\beta h)\}^{-1}, \tag{5}$$

where [M] is the micelle concentration and h is the hydrophobic potential or the average energy gain due to solubilization of one particle. [M] is usually determined as the difference between the total surfactant concentration and the critical micellar concentration, divided by the average aggregation number. Clearly, strongly hydrophobic compounds with $\beta h \gg 1$ are solubilized completely so that $\bar{n} = [C]/[M]$.

The equilibrium micelle occupancy distribution and the interphase partitioning of the solute molecules are dynamically maintained by various exchange mechanisms. The process by which the particles migrate between micelles and the aqueous phase is usually represented by[31]

$$M_{n-1} + A \xrightleftharpoons[nk_-]{k_+} M_n, \tag{6}$$

where M_n stands for a micelle with n particles and A denotes a particle in the bulk phase. The definition of the rate constants is clear from the scheme. It can be verified that the interphase exchange mechanism in Eq. (6) leads to the Poisson distribution.[31] Comparing the average derived from the kinetic scheme with Eq. (5) we obtain the fundumental relation for the equilibrium constant

$$\exp(\beta h) = k_+[M]/k_- . \tag{7}$$

The micelles can also exchange their contents through collisions with temporary merging in accordance with the following scheme[32]

$$M_n + M_m \xrightarrow{k_c} Q(n|m) \xleftrightarrow{k} Q(j|n+m-j) \xrightarrow{1/\tau_c} M_j + M_{n+m-j}, \tag{8}$$
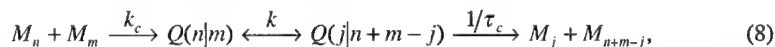
where $Q(n|m)$ denotes a cluster of two fused micellar compartments containing n and m particles, respectively. The first process in Eq. (8) represents the diffusion of two micellar aggregates toward each other followed by their merging and opening of the fluctuating channels in the interfacial layer. The second stage involves successive one-particle hopping through these channels with the frequency k. After the elapsed time τ_c, the connecting channels close and the cluster breaks up. The hopping dynamics are governed by a stochastic master equation whose solution gives the probability $Q_j(n|m,t)$ of finding j particles in the micelle, that originally contained n particles, at time t after its merging with M_m. The overall transition probability $\omega_j(n|m,\tau_c)$ of M_n to M_j

upon collision with M_m can be defined as a time integral of $Q_j(n|m,t)$ multiplied by the probability that connecting channels still exist, viz., $(1/\tau_c)\exp(-t/\tau_c)$. The transition probability happens to be a function of only one dimensionless parameter $k\tau_c$. The variation of $\omega_j(n|m,k\tau_c)$ with $k\tau_c$ is illustrated in Fig. 3. Two limiting situations are important. If $k\tau_c \ll 1$, only one-particle transitions are actually realized[33]

$$\omega_j(n|m,k\tau_c \ll 1) = [1-(n+m)k\tau_c]\delta_{j,n} + k\tau_c(n\delta_{j,n-1} + m\delta_{j,n+1}), \qquad (9)$$

where δ is the Kronecker delta. In the limit of $k\tau_c \to \infty$, complete randomization of the cluster contents takes place and the binomial distribution is eventually reached

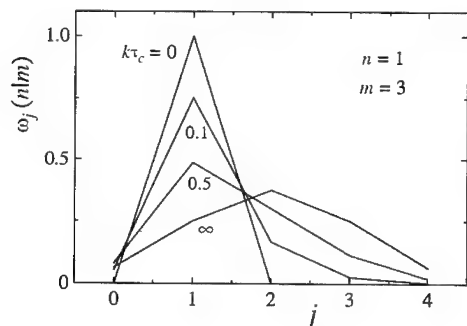$$\omega_j(n|m,\infty) = \binom{n+m}{j} 2^{-(n+m)}. \qquad (10)$$

Fig. 3. A plot of the transition probability $\omega_j(n|m,k\tau_c)$ from M_n to M_j upon collision with M_m for several values of $k\tau_c$ (the numbers attached).

This process is known as fusion-fission in the literature and usually assumes demolishing of the interfacial layers between micelles at contact.[14,33] It is useful to define the total transition probability $\omega_j(n)$ from M_n to M_j as a sum of $\omega_j(n|m,k\tau_c)$ over all possible values of m with the weight $P_m(\bar{n})$. This quantity is normalized and satisfies the detailed balance equation.

The collisional hopping exchange mechanism can be generalized to a multicomponent system provided the components migrate independently. In this case, the overall time-dependent probability function is given by the product of the corresponding component probabilities. We have considered here only the exchange mechanisms that neglect any kind of interaction between the particles and, therefore, lead to the Poisson distribution law. Interactions modify both the equilibrium and the dynamics of the system. For instance, the excluded volume effect results in a decrease of the rate constant for entry of a particle into a micelle as the number of particles already contained in that micelle is increased.[34]

STOCHASTIC MODEL FOR LUMINESCENCE QUENCHING IN MICELLES

We now turn to reaction dynamics in a statistical ensemble of micelles and consider luminescence quenching as a typical example. In a time-resolved luminescence quenching experiment one monitors the luminescence intensity of probe molecules excited by a short light pulse as a function of time in the presence of quenchers. The excitation efficiency is normally low that allows one, regarding a micellar solution, to neglect the possibility for two excited probes to ever share a micelle. We consider here strongly hydrophobic probe molecules dissolved exclusively in micelles. The excitation dynamics are governed by the following general scheme[35]

$$M_j^* \xrightarrow{k_e\,\omega_n^*(j)} M_n^* \xrightarrow{1/\tau_0 + nk_q} M_n, \qquad (11)$$
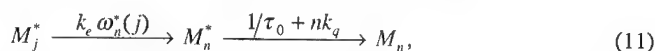
where M_n^* stands for a micelle that contains an excited probe and n quenchers, τ_0 is the self-de-

cay lifetime and determines the relevant time scale on which the dynamics have to be studied, and k_q is the first order rate constant for intramicellar quenching (inverse of the mean reaction time). The self-decay term is factored out in further analysis and we thus concentrate on the excited state deactivation solely due to migration-assisted luminescence quenching. The first process in Eq. (11) includes all possible exchange mechanisms of reactants where the excitation is conserved; k_e is the corresponding rate constant and $\omega_n^*(j)$ is the total transition probability. In the case of collisional exchange, $k_e = k_c[M]$ gives the frequency of micellar collisions. It equals k_- defined in Eq. (6) for exchange through the aqueous phase.

Theoretical interest is focused on the survival probability $F(t)$ of excited probes at time t after δ-pulse excitation. When migration occurs on a much longer time scale than reaction, one can calculate $F(t)$ by averaging the exponential intramicellar decay function over the initial Poisson distribution of quenchers among micelles containing excited probes

$$\ln F(t) = -\bar{n}\left[1 - \exp(-k_q t)\right]. \tag{12}$$

In general, the survival probability has to be found as a solution to the matrix stochastic master equation associated with the scheme in Eq. (11). An exact analytical solution can be derived for a one-particle exchange mechanism by using the generating function technique.[36] In the case where probes are immobile and stay in originally photoselected micellar compartments during the excited state lifetime we have [31,37]

$$\ln F(t) = \ln g(t) = -A_1 t - A_2\left[1 - \exp(-A_3 t)\right], \tag{13}$$

where $A_1 = k_- k_q \bar{n}/(k_- + k_q)$, $A_2 = \bar{n} k_q^2/(k_- + k_q)^2$, and $A_3 = k_- + k_q$. For collisional exchange, $k_- = k_e k \tau_c$. When both quenchers and probes are mobile, the decay function is the inverse transform of[38-41]

$$\hat{F}(\varepsilon) = \hat{g}(\varepsilon, A_1 + k_-^p)\left[1 - k_-^p \hat{g}(\varepsilon, A_1 + k_-^p)\right]^{-1}, \tag{14}$$

where $\wedge$ denotes the Laplace transform, viz., $\hat{F}(\varepsilon) = \int_0^\infty dt\, F(t)\exp(-\varepsilon t)$, k_-^p is the exit rate for the probe, and $g(t)$ is given by Eq. (13) with A_1 replaced by $A_1 + k_-^p$. In the time domain, Eq. (14) transforms into an infinite exponential series. A useful approximate model including one-particle migration of probes and quenchers and exchange by a fusion-fission process has been developed on the basis of an assumption that the variance of the distribution of quenchers among the micelles with excited probe remains linearly related to the average at all times, as it is for the Poisson distribution.[33,42] The decay is then described, to a good degree of accuracy, by Eq. (13) with a generalized interpretation of the parameters A_i. This approximation is justified only for small $\bar{n}$.[38]

The effect of general multiparticle hopping exchange during sticky collisions between micelles on the excited state deactivation kinetics can be analyzed by solving the master equation numerically.[35] The results are illustrated in Fig. 4. The initial stage is exponential and migration independent, $F(t) = \exp(-\bar{n} k_q t)$. The decay is quenching controlled and remains exponential at all times with the same initial rate constant if migration is very fast, $k_e \gg k_q$ ($\tau_c \neq 0$). On the other hand, when migration is very slow, the decay asymptotically approaches a constant, $F(t) = \exp(-\bar{n})$. This corresponds to $P_0(\bar{n})$ in the Poisson statistics and implies that excited probes survive only in micelles which initially contain no quenchers. In the intermediate regime, where quenching and exchange occur on comparable time scales, the effect of migration is pronounced at long times leading to different exponential asymptotics. The larger the ratio of k/k^p,
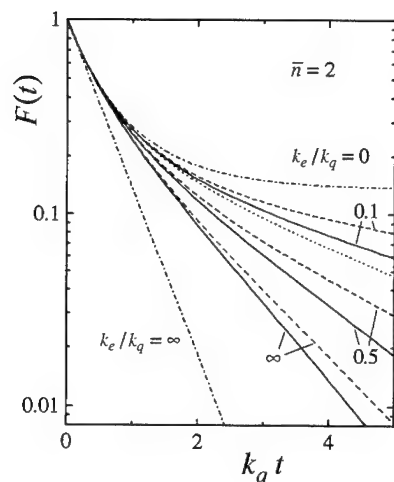
Fig. 4. Time decay of the excited probe survival probability $F(t)$ for the collisional exchange mechanism of quenchers (———) and probes (– – –) with $k_e/k_q = 2$ and $(k + k^p)\tau_c = 0.1, 05,$ and ∞ (the numbers attached) for the Poisson distribution of quenchers among the micelles with the average $\bar{n} = 2$. The decay for infinitely fast and infinitely slow migration, as compared with quenching is also included (– · –). The decay for a one-particle quencher migration mechanism with $k_-/k_q = 0.2$ (· · ·) should be compared to the curve with $k_e/k_q = 2$ and $k\tau_c = 0.1$. Multiparticle hops still affect the long time behavior. Note that self-decay is omitted.

the faster is the decay as long as $k + k^p$ and k_e are held constant. Here k^p is the probe hopping frequency defined similarly to k in Eq. (8).

So far we have assumed that no quenching occurs during fusion of colliding micelles. However, if the reaction is diffusion-controlled, it evolves on a similar time scale as the mixing of reactants within a transient micellar dimer, which process is also based on diffusion. The hopping model for collisional exchange described by Eq. (8) allows the reaction to be considered simultaneously in a straightforward way.[35] The resulting transition probability corrected on reaction is no longer normalized. For example, in the limit of $k\tau_c \to \infty$ we obtain for the fusion-fission mechanism

$$\omega_j^*(n|m, \infty) = \binom{n+m}{j} 2^{-(n+m)} \left[1 + \tfrac{n+m}{2} k_q \tau_c\right]^{-1}. \tag{15}$$

The transition probability including reaction during micellar collisions can further be used in the overall kinetic scheme of the migration-assisted luminescence quenching, provided τ_c is sufficiently small so that the solution is indeed monodisperse. We have considered strongly hydrophobic completely solubilized probe molecules. The solubility and reaction in the bulk phase can be readilty taken into account, as well as the interphase migration of the probes that occurs via a one-particle mechanism.[43]

The above models all concern the initial equilibrium distribution of reactants. In certain cases, especially when the solubilization dynamics are of interest, it is preferable to monitor the relaxation to equilibrium using stopped- or continuous-flow concentration jump techniques. Not only luminescence quenching, but any indicator reaction is usable. Normally the reaction is deliberately selected so as not to be the limiting step in the overall exchange-controlled process. The time course of such an instantaneous reaction in a nonequilibrium compartmentalized molecular ensemble undergoing collisional hopping exchange has been fully described using a stochastic approach.[44,45]

LUMINESCENCE QUENCHING IN MICELLAR CLUSTERS

For microemulsions with ionic amphiphiles, a percolative transition of the conductivity is observed with increasing temperature, revealing the formation of micellar clusters.[46] While micelles undergo clustering due to attractive interactions, they retain their individual closed structure.[46,47] Small clusters are present already in dilute microemulsions below the percolation threshold.[48] At the threshold, loose fractal clusters are formed, while well above the percolation point the clus-

ters have a compact character[49] and may even transform into a bicontinuous structure for a certain composition of the microemulsion.[50] Clustering also takes place upon approaching the clouding temperature, above which the solution is critically separated into two microemulsion phases of different composition. Similar phenomena occur in normal micellar solutions.[51]

It has been experimentally observed that luminescence quenching kinetics in micellar clusters have three well separated stages.[48] A rapid initial deactivation of excited probes by cohabitant quenchers occurs within the micelles where they were originally excited. After this fast stage is finished, the excitations produced in micelles without quenchers only survive. They are further slowly deactivated due to quenchers present in surrounding micelles within the same cluster. Reactants have to perform a random walk over the cluster by hopping between the micelles that are in direct contact until they can meet and react. The final stage of deactivation, apart from the natural decay, may involve exchange between different clusters.

At short times and/or at sufficiently high quencher concentrations, when the reactants make at most one step before reacting, the deactivation dynamics can be described by[52]

$$M^*_{x,y} \xleftarrow{\ jk_p\ } M^*_{j,n-1} \xleftarrow{\ jnk_-\ } M^*_{j,n} \xrightarrow{\ 1/\tau_0 + nk_q\ } M_{j,n}, \tag{16}$$
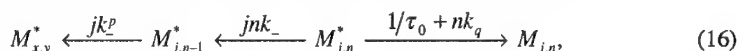
where $M^*_{j,n}$ denotes a micelle with j direct contacts containing an excited probe and n quenchers. The local cluster connectivity is assumed to be a discrete random variable independent of time and the number of reactants in the micelle.[53] The stochastic master equation corresponding to the scheme in Eq. (16) can be solved using the generating function method. The model predicts the three-stage kinetics in the limit of fast quenching. However, it neglects the concentration depletion effect. The average number of quenchers in micelles surrounding the one with excited probe is assumed to remain constant with time, while it is actually decreased, since the more quenchers the surrounding micelles contain, the faster is the excited state decay.

An alternative approach takes advantage of the continuous time random walk formalism.[54] Here we consider the so-called target problem, i.e., the deactivation of static excitations by randomly walking quenchers.[55] The target problem is exactly solvable in terms of the random walk generating function,[56] allowing us to relate the ensemble averaged survival probability $F(t)$ to the underlying cluster structure[57]

$$F(t) = \exp[-\bar{n}S(t)], \tag{17}$$

where $S(t)$ is given by the inverse Laplace transform of[54]

$$\hat{S}(\varepsilon) = \frac{k_q}{\varepsilon^2}\left[1 + \frac{k_q}{\lambda + \varepsilon} G\left(0, \frac{\lambda}{\lambda + \varepsilon}\right)\right]^{-1}, \tag{18}$$

λ being the stepping frequency (k_- times the lattice coordination number) and $G(0, z)$ the generating function for all walks which start and end at the origin. The methods of evaluating $G(0, z)$ for regular lattices are well known.[56] According to Eq. (18), the initial stage of the decay ($\varepsilon \to \infty$) is independent of migration, $F(t) = \exp(-\bar{n}k_q t)$. If quenching is very fast, $k_q \gg \lambda$, as typically is the case, the decay can be described by Eq. (12) in the time range of $\lambda t \ll 1$, corresponding to a rapid deactivation in individual micelles. The long-time asymptotics ($\varepsilon \to 0$) depend strongly on the dimensionality and the cluster structure. As an example, for a simple cubic lattice in three dimensions we have

$$S(t) \propto \lambda k_q t \left[\lambda + G(0,1)k_q\right]^{-1}, \tag{19}$$

where $G(0,1) = 1.516386$. The leading term of the expansion in one, $S(t) \propto (8\lambda t/\pi)^{\frac{1}{2}}$, and two dimensions, $S(t) \propto \pi \lambda t/\ln \lambda t$, is independent of the quenching rate constant k_q.[49] These behaviors resemble the Smoluchowski type expressions resulting from the diffusion equation approach.[17,58] Our derivations can be extended to walks on self-similar structures with dilatation symmetry, i.e., fractals.[59] Asymptotically, we have $S(t) \propto c (\lambda t)^{\tilde{d}/2}$ with a k_q-independent prefactor c for $\tilde{d} < 2$ and $S(t) \propto c(k_q) \lambda t$ for $\tilde{d} > 2$, where $\tilde{d}$ is the so-called spectral or fracton dimension.[60]

The survival probability in a finite cluster of N sites is also given by Eq. (17) leading, however, to different asymptotics[54]

$$\ln F(t) \propto -\overline{n}_c \left[1 - \exp(-k_{cq}t)\right], \tag{20}$$

where $\overline{n}_c = \overline{n}N$ is the average number of quenchers per cluster and $k_{cq} = \left(\lambda k_q/N\right)\left[\lambda + \phi(0,1)k_q\right]^{-1}$ is the effective intracluster quenching rate constant; $\phi(0,z) = G(0,z) - 1/N(1-z)$ is finite in the limit of $z \to 1^-$. Eq. (20) reveals dynamic scaling in micellar clusters.[48] Indeed, at long times the clusters act as individual micelles where the decay function is given by Eq. (12). Eventually, all the sites are explored and $F(\infty) = P_0(\overline{n}_c)$, i.e., the probes survive only in clusters without quenchers. We have considered monodisperse clusters. In reality, a distribution of cluster sizes is rather likely. The observable is then given by the average of $F(t,N)$ over this distribution. The general solution of the target problem is also valid for the trapping problem (mobile probe) in the limit of low quencher concentration ($\overline{n} \ll 1$).[57]

CONCLUDING REMARKS

Reactions in microdisperse systems exhibit rich dynamic behaviors depending on various factors. This review has considered the evolution of the diffusion-controlled reaction kinetics from the process in an isolated finite volume to the exchange-mediated reaction in a statistical ensemble of microreactors. We have discussed the effects of local spatial arrangement of reacting species, occupation statistics, as well as different mechanisms of reactant migration in normal microdisperse solutions and in clustered structures. Several points, however, have fallen beyond the scope of the present article. Firstly, all our derivations have been based on the assumption of noninteracting reactants and monodisperse micelles. Interactions modify the equilibrium distribution of reactants and the dynamics of exchange. The effect of hard-sphere interactions, accounting for the limited micelle solubilization capability, on the luminescence quenching kinetics has been studied in detail.[61,62] Although the size distribution of microdispersions is typically narrow, the micelles are in fact polydisperse and subject to spontaneous size fluctuations. The polydipersity is generally expected to become extensive with increasing surfactant concentration or upon addition of special counterions to the solution.[63,64] Luminescence quenching theory in polydisperse micellar systems has been advanced in the absence of reactant migration allowing one to relate an apparent aggregation number to the quencher concentration and the parameters of the weight distribution.[65,66] Besides size fluctuations, variations in micellar shape are also viable. For instance, micelles can undergo a sphere-to-rod phase transition under appropriate conditions. Diffusion-controlled reactions in rod-like micelles have been treated theoretically for simple spatial arrangements,[67-70] the calculations showing the strong deviation from Eq. (12) type of decay, even in the absence of polydispersity effects which in reality would be inevitable in these systems. For ionic amphiphiles, the formation-breakdown process of the micellar aggregates is accompanied by continuous charge fluctuations[71] that may have a considerable effect on reactant ex-

change. In an encounter of oppositely charged micelles, there would be an additional electric field influencing the diffusive passage through connecting channels. Another point, relevant in time-resolved luminescence measurements, is the effect of irradiation intensity. An important conclusion drawn from the general consideration is that the stochastic model of luminescence quenching for multiple occupancy of excited probes leads to the same decay function as in the case of low excitation efficiency reviewed here, provided that intramicellar reaction still follows the pseudo-first-order kinetics.[72] A great deal of work has been done in studying other processes in micellar systems which are not diffusion-controlled. The most important example is the long-range dipole-dipole electronic energy transfer.[27,73-78] Since the singlet excited states are normally short-lived, the excitation transfer occurs between static chromophore molecules. The process is very sensitive to the spatial arrangement of the energy donors and acceptors. Direct excitation transfer from donors to acceptors can be accelerated by donor-donor transport within a micelle or between different micelles. Once the general features of reaction kinetics in microdisperse systems are understood, one can extract important structural and dynamic information on the aggregates and their guest molecules by analyzing suitably designed experiments. New theoretical efforts are in progress to handle more complex systems of molecular organization.

REFERENCES

1. J.H. Fendler, *Membrane Mimetic Chemistry* (Wiley, New York, 1982).
2. K. Kalyanasundaram, *Photochemistry in Microheterogeneous Systems* (Academic Press, Orlando, 1987).
3. V. Ramamurthy, R.G. Weiss, and G.S. Hammond, Adv. Photochem. **18**, 67 (1993).
4. R. Zana, in *Surfactant Solutions: New Methods of Investigation,* edited by R. Zana (Sufactant Sci. Ser. **22,** Marcel Dekker, New York, 1987), p. 241.
5. M. Van der Auweraer, F.C. De Schryver, in *Structure and Reactivity in Reverse Micelles,* edited by M.P. Pileni (Elsevier, Amsterdam, 1989), p. 70.
6. M. Almgren, in *Kinetics and catalysis in microheterogeneous systems,* edited by M. Grätzel, K. Kalyanasundaram (Surfactant Sci. Ser. **38,** Marcel Dekker, New York, 1991), p. 63.
7. M.H. Gehlen and F.C. De Schryver, Chem. Rev. **93**, 199 (1993).
8. N.J. Turro, M. Grätzel, and A.M. Braun, Angew. Chem. Int. Ed. Engl. **19**, 675 (1980).
9. T. Cao, P. Munk, C. Ramireddy, Z. Tuzar, and S.E. Webber, Macromolecules **24**, 6300 (1991).
10. S.-H. Chen, S.-L. Chang, and R. Strey, J. Chem. Phys. **93**, 1907 (1990).
11. E.A.G. Aniansson, S.N. Wall, M. Almgren, H. Hoffmann, I. Kielmann, W. Ulbricht, R. Zana, J. Lang, and C. Tondre, J. Phys. Chem. **80**, 905 (1976).
12. K.D. Danov, N.D. Denkov, D.N. Petsev, I.B. Ivanov, and R. Borwankar, Langmuir **9**, 1731 (1993).
13. J. Lang, R. Zana, and S. Candau, Ann. Chim. **77**, 103 (1987).
14. P.D.I. Fletcher and D.I. Horsup, J. Chem. Soc. Faraday Trans. **88**, 855 (1992).
15. M. Tachiya, in *Kinetics of Nonhomogeneous Processes,* edited by G.R. Freeman (Wiley, New York, 1987), p. 575.
16. M. Almgren, Adv. Colloid Interface Sci. **41**, 9 (1992).
17. M. Tachiya, Radiat. Phys. Chem. **21**, 167 (1983).
18. M. Tachiya, Chem. Phys. Lett. **69**, 605 (1980).
19. M.D. Hatlee, J.J. Kozak, G. Rothenberger, P.P. Infelta, and M. Grätzel, J. Phys. Chem. **84**, 1508 (1980).
20. H. Sano and M. Tachiya, J. Chem. Phys. **75**, 2870 (1981).
21. M. Van der Auweraer, J.C. Dederen, E. Geladé, and F.C. De Schryver, J. Chem. Phys. **74**, 1140 (1981).
22. U. Gösele, U.K.A. Klein, and M. Hauser, Chem. Phys. Lett. **68**, 291 (1979).
23. G. Rothenberger and M. Grätzel, Chem. Phys. Lett. **154**, 165 (1989).
24. A.V. Barzykin and M. Tachiya, J. Chem. Phys. **99**, 7762 (1993).
25. A. Szabo, K. Schulten, and Z. Schulten, J. Chem. Phys. **72**, 4350 (1980).
26. A.V. Barzykin, Chem. Phys. **155**, 221 (1991).
27. M.N. Berberan-Santos and M.J.E. Prieto, J. Chem. Soc. Faraday Trans. 2 **83**, 1391 (1987).
28. D.A. McQuarrie, C.J. Jachimowski, and M.E. Russel, J. Chem. Phys. **40**, 2914 (1964).

29. A.V. Barzykin, Chem. Phys. **161**, 63 (1992).
30. J. Güémez, S. Velasco, and A.C. Hernández, Physica A **152**, 243 (1988).
31. M. Tachiya, Chem. Phys. Lett. **33**, 289 (1975).
32. A.V. Barzykin and M. Tachiya, Chem. Phys. Lett. **216**, 575 (1993).
33. M. Almgren, J.E. Löfroth, and J. Van Stam, J. Phys. Chem. **90**, 4431 (1986).
34. T.F. Hunter, Chem. Phys. Lett. **75**, 152 (1980).
35. A.V. Barzykin and M. Tachiya, J. Phys. Chem. **98**, 2677 (1994).
36. D.A. McQuarrie, Adv. Chem. Phys. **15**, 149 (1969).
37. P.P. Infelta, M. Grätzel, and J.K. Thomas, J. Phys. Chem. **78**, 190 (1974).
38. M. Tachiya, Can. J. Phys. **68**, 979 (1990).
39. M.H. Gehlen, M. Van der Auweraer, and F.C. De Schryver, Photochem. Photobiol. **54**, 613 (1991).
40. M.H. Gehlen, M. Van der Auweraer, S. Reekmans, M.G. Neumann, and F.C. De Schryver, J. Phys. Chem. **95**, 5684 (1991).
41. A.V. Barzykin, Chem. Phys. Lett. **189**, 321 (1992).
42. M.H. Gehlen, M. Van der Auweraer, and F.C. De Schryver, Langmuir **8**, 64 (1992).
43. A.V. Barzykin and I.K. Lednev, J. Phys. Chem. **97**, 2774 (1993).
44. M. Tachiya and M. Almgren, J. Chem. Phys. **75**, 865 (1981).
45. T.A. Hatton, A.S. Bommarius, and J.F. Holzwarth, Langmuir **9**, 1241 (1993).
46. A. Maitra, C. Mathew, and M. Varshney, J. Phys. Chem. **94**, 5290 (1990).
47. J. Zhang, J.L. Fulton, and R.D. Smith, J. Phys. Chem. **97**, 12331 (1993).
48. R. Jóhannsson, M. Almgren, and J. Alsins, J. Phys. Chem. **95**, 3819 (1991).
49. M. Almgren and R. Jóhannsson, J. Phys. Chem. **96**, 9512 (1992).
50. D. Vollmer, J. Vollmer, and H.-F. Eicke, Europhys. Lett. **26**, 389 (1994).
51. B. Lindman and H. Wennerström, J. Phys. Chem. **95**, 6053 (1991).
52. A.V. Barzykin and M. Tachiya, J. Phys. Chem. **98**, 9950 (1994).
53. M.H. Gehlen, Chem. Phys. Lett. **212**, 362 (1993).
54. A.V. Barzykin and M. Tachiya, Phys. Rev. Lett. (in press).
55. A. Blumen, G. Zumofen, and J. Klafter, Phys. Rev. B **30**, 5379 (1984).
56. E.W. Montroll and G.H. Weiss, J. Math. Phys. **6**, 167 (1965).
57. G. Zumofen, A. Blumen, and J. Klafter, J. Chem. Phys. **82**, 3198 (1985).
58. A.V. Barzykin and M. Tachiya, J. Chem. Phys. **99**, 9591 (1993).
59. S. Havlin and D. Ben-Avraham, Adv. Phys. **36**, 695 (1987).
60. A. Blumen, J. Klafter, B.S. White, and G. Zumofen, Phys. Rev. Lett. **53**, 1301 (1984).
61. M. Tachiya, J. Chem. Phys. **76**, 340 (1982).
62. A.V. Barzykin, J. Phys. Chem. **96**, 9074 (1992).
63. M. Almgren, J. Alsins, J. Van Stam, and E. Mukhtar, Prog. Colloid Polym. Sci. **76**, 68 (1988).
64. G.G. Warr, L. Magid, E. Caponetti, and G. Martin, Langmuir **4**, 813 (1988).
65. M. Almgren and J.E. Löfroth, J. Chem. Phys. **76**, 2734 (1982).
66. G.G. Warr and F. Grieser, J. Chem. Soc. Faraday Trans. 1 **82**, 1825 (1986).
67. M. Van der Auweraer and F.C. De Schryver, Chem. Phys. **111**, 105 (1987).
68. M. Van der Auweraer, S. Reekmans, N. Boens, and F.C. De Schryver, Chem. Phys. **132**, 91 (1989).
69. J. Alsins and M. Almgren, J. Phys. Chem. **94**, 3062 (1990).
70. M. Almgren, J. Alsins, E. Mukhtar, and J. Van Stam, J. Phys. Chem. **92**, 4479 (1988).
71. D. Bratko, C.E. Woodward, and A. Luzar, J. Chem. Phys. **95**, 5318 (1991).
72. A.V. Barzykin and M. Tachiya, Chem. Phys. Lett. **221**, 81 (1994).
73. M.N. Berberan-Santos, M.J.E. Prieto, and A.G. Szabo, J. Chem. Soc. Faraday Trans. **88**, 255 (1992).
74. J.M. Drake, J. Klafter, and P. Levitz, Science **251**, 1574 (1991).
75. M.D. Ediger, R.P. Domingue, and M.D. Fayer, J. Chem. Phys. **80**, 1246 (1984).
76. K.U. Finger, A.H. Marcus, and M.D. Fayer, J. Chem. Phys. **100**, 271 (1994).
77. A.V. Barzykin, N.S. Barzykina, and M.A. Fox, Chem. Phys. **163**, 1 (1992).
78. A.V. Barzykin and M. Tachiya, J. Chem. Phys. (in press).

REACTION-DIFFUSION MODEL FOR THE A+A → 0 REACTION

KATJA LINDENBERG*, RAOUL KOPELMAN** and PANOS ARGYRAKIS[†]
*Department of Chemistry and Biochemistry and Institute for Nonlinear Science, University of California at San Diego. La Jolla, CA 92093-0340
**Departments of Chemistry and Physics, The University of Michigan, Ann Arbor, MI 48109
[†]Department of Chemistry, The University of Michigan, Ann Arbor, MI 48109 and Department of Physics, University of Thessaloniki, GR-54006 Thessaloniki, Greece

ABSTRACT

We formulate an approach to the $A + A \rightarrow products$ reaction based on a reaction–diffusion model. We construct the first equations in a moment hierarchy whose first two members are the global density of A particles and the pair correlation function. We terminate the hierarchy by relating the three–particle correlation function to two–particle correlation functions and thereby obtain a set of coupled equations that turns out to be linear and hence analytically tractable.

This approach leads naturally to the proportionality of the rate of the reaction to the pair correlation function evaluated at $r = a$, where a is the diameter of the reacting particles. It also confirms the relation between anomalous kinetics and the deviation of the pair correlation function from that associated with a random distribution of particles.

Numerical simulations in one and two dimensions that support our theory are presented in a companion paper in this session.

INTRODUCTION

The diffusion–limited annihilation reaction $A+A \rightarrow products$ has been the subject of intense theoretical, numerical, and experimental study over the past decade [1–30]. The "anomalous" behavior of this reaction in Euclidean dimensions $d \leq 2$ (and more generally in fractal systems of dimension $d_s \leq 2$, where d_s is the spectral dimension) is by now clearly established. These anomalies are apparent both in batch reactions [7,8, 27–30], where one observes the decay of an initial distribution of A particles, and in steady–state reactions [3–5, 9, 14–17, 22, 24, 28], where one continually supplies the system with A particles and one observes the characteristics of the steady state. In the batch reaction, the anomaly shows up in the exponent X in the rate law $\dot{\rho} = -k\rho^X$, where $\rho(t)$ is the global density of A particles as a function of time. "Classical" chemical kinetics of well–stirred reactions yields $X = 2$, whereas the observed *asymptotic* rate law for this system yields $X = 1 + d_s/2$ for $d_s < 2$ with logarithmic corrections for $d_s = 2$. In the steady–state reaction, the anomaly appears in the reaction law $Q = \rho_{ss}^X$, where Q is the rate at which A particles are continually injected in the system and ρ_{ss} is the steady–state density. Again, "classical" chemical kinetics yields $X = 2$ whereas the observed reaction law for the $A + A \rightarrow 0$ system is again $X = 1 + d_2/2$ for $d_s < 2$ with logarithmic corrections for $d_s = 2$. Note that the similarity in the behavior of the batch and steady–state exponents for the $A + A$ reaction contrasts with the $A + B$ reaction, where the two behave quite differently and where even the critical dimensions for classical behavior are different for the two types of experiments.

It is by now well understood that rate laws are a direct reflection of the *spatial* distribution of particles. In particular, the classical rate law reflects a random Hertzian distribution, that is, one in which the probability that the nearest neighbor of a given particle is to be found at a distance r in a given direction peaks at $r = 0$ (suitably modified if the particles have a finite size). It is this continual supply of close pairs of particles even as they react that is embodied in the usual bimolecular rate law. Any form of thorough stirring ensures this supply [22]; diffusion in sufficiently high dimensions is a thorough stirring mechanism. However, in low dimensions diffusion becomes ineffective. The anomalous rate laws are then a direct consequence of the deviation of the spatial distribution in these systems from a random one. Indeed, it is well established numerically that the distribution of particles in the $A + A$ system after long times in the batch reaction, or in the steady state, is almost lattice–like in low Euclidean dimensions, with very

few nearby pairs. The reaction thus slows down relative to its rate in the well–stirred system, and this slowing down is reflected in the higher exponents in the rate laws.

Although these behaviors are well understood qualitatively and numerically, the underlying theories are still not complete. Most of the theoretical arguments are based on scaling approaches that yield the correct exponents. Exact results for the $A + A \rightarrow products$ batch reaction have been obtained for one and two dimensions in the classic papers of Torney and McConnell [4] and for one dimension also by Elyutin [6]. For the steady–state problem an exact solution in one dimension was obtained by Racz [8], and also by Peacock–López and Keizer [12] based on Keizer's general theory of fluctuations around the steady state. A related problem, the $A + A \rightarrow A$ "coagulation" reaction, has also been considered theoretically, numerically, and experimentally. This system has been solved asymptotically in one dimension by Spouge [15] and, more recently, for all times by Doering and Ben Avraham [18], both for the batch reaction and the steady–state reaction.

The theoretical methods used in these approaches are powerful but rather specific. A theoretical approach that is appealing because of its generality is a reaction–diffusion formalism such as has been used extensively in the $A + B \rightarrow 0$ problem [14, 17, 31]. Herein we generalize the reaction–diffusion equation to be applicable to the $A + A$ problem [17] and obtain from it a hierarchy of equations involving increasing numbers of particles. This hierarchy is truncated at the two-particle level, and we solve the resulting set of equations to obtain the global density of A particles and also the spatial distribution as reflected in the pair correlation function. We apply our approach to both the batch reaction and to the steady–state problem.

In the next section we present our reaction–diffusion model, obtain the first equations of the hierarchy implied by this model, and implement our approximation to break the hierarchy. The result is a closed set of equations for the global density of A particles and for the pair correlation function of the particles. In the following section we solve these equations for a batch reaction and in the subsequent section we do so for the steady state in the presence of sources. We end with a summary and some concluding remarks.

THE MODEL

Consider a d–dimensional Euclidean space on which A particles at an initial average density ρ_o diffuse freely. Two A particles annihilate, $A + A \rightarrow 0$, when they come in contact at a distance a between their centers. We wish to calculate the law that governs the decay of the density $\rho(t)$ of A particles as a function of time as well as a measure of the interparticle separation that underlies the rate law.

We begin by defining the local density $\rho(\mathbf{r}, t)$ of A particles at space point $\mathbf{r}$ and time t,

$$\rho(\mathbf{r}, t) \equiv \sum_i^{N(t)} \delta(\mathbf{r} - \mathbf{r}_i(t)), \tag{1}$$

where $\mathbf{r}_i(t)$ denotes the position of particle i at time t and $N(t)$ is the total number of particles in the system at time t. The average "one-particle" (global) density introduced earlier is then

$$\rho(t) \equiv \frac{N(t)}{V} \equiv \langle \rho(\mathbf{r}, t) \rangle_{\mathbf{r}} \tag{2}$$

where V is the volume of the system. We also introduce the average two–particle density function

$$f(\mathbf{r}, t) = \langle \rho(\mathbf{r}', t) \rho(\mathbf{r}' + \mathbf{r}, t) \rangle_{\mathbf{r}'} \tag{3}$$

and the average three–particle density function

$$F(\mathbf{r}, \mathbf{r}', t) = \langle \rho(\mathbf{r}'', t) \rho(\mathbf{r}'' + \mathbf{r}', t) \rho(\mathbf{r}'' + \mathbf{r}' + \mathbf{r}, t) \rangle_{\mathbf{r}''}. \tag{4}$$

The subscripted brackets indicate an average over configuration space:

$$\langle F(\mathbf{r}') \rangle_{\mathbf{r}'} \equiv \frac{1}{V} \int d\mathbf{r}' \, F(\mathbf{r}'). \tag{5}$$

378

The two–particle function by definition satisfies the identity

$$\langle f(\mathbf{r}, t) \rangle_{\mathbf{r}} = \frac{1}{V} \int d\mathbf{r} \, f(\mathbf{r}, t) = \rho^2(t). \tag{6}$$

For a random distribution of point particles $f(\mathbf{r}, t) = \rho^2(t)$. The three–particle density function satisfies the identities

$$\frac{1}{V} \int d\mathbf{r}' \, F(\mathbf{r}', \mathbf{r}'', t) = \rho(t) f(\mathbf{r}'', t); \qquad \frac{1}{V} \int d\mathbf{r}'' \, F(\mathbf{r}', \mathbf{r}'', t) = \rho(t) f(\mathbf{r}', t);$$

$$\frac{1}{V^2} \int d\mathbf{r}' \int d\mathbf{r}'' \, F(\mathbf{r}', \mathbf{r}'', t) = \rho^3(t). \tag{7}$$

For a random distribution $f(\mathbf{r}, \mathbf{r}', t) = \rho^3(t)$.

It is convenient to introduce the pair correlation function

$$g(\mathbf{r}, t) \equiv \frac{f(\mathbf{r}, t)}{\rho^2(t)}. \tag{8}$$

This function is of course normalized to unity, $\langle g(\mathbf{r}, t) \rangle_{\mathbf{r}} = 1$, and for a random distribution of point particles $g(\mathbf{r}, t) = 1$. Similarly, the three–particle correlation function is defined by

$$G(\mathbf{r}, \mathbf{r}', t) \equiv \frac{F(\mathbf{r}, \mathbf{r}', t)}{\rho^3(t)} \tag{9}$$

and is also normalized to unity, $\langle \langle G(\mathbf{r}, \mathbf{r}', t) \rangle_{\mathbf{r}} \rangle_{\mathbf{r}'} = 1$.

We start with a generalized form of the usual reaction–diffusion equation for the local density cite-burlatskii,ourlonger:

$$\frac{d}{dt} \rho(\mathbf{r}, t) = D\nabla^2 \rho(\mathbf{r}, t) - k \int d\mathbf{R} \rho(\mathbf{r}, t) \rho(\mathbf{r} + \mathbf{R}, t) \delta(R - a) + Q(\mathbf{r}, t), \tag{10}$$

where D is the diffusion coefficient, k is the local reaction rate coefficient, and $Q(\mathbf{r}, t)$ is a source term modeling external sources if the system is open. This equation says that the local density of A's changes through diffusion, through the reaction of the A particle in question with another A particle a distance a away from it, and through external sources. Equation (10) is not the usual local equation, but that is the price that must be paid to deal with the $A + A$ reaction in this language. We will only consider space–independent sources, $Q(\mathbf{r}, t) = Q(t)$.

The evolution equation for the global density $\rho(t)$ is obtained by integrating (10) over $\mathbf{r}$ and dividing by the volume. With the definitions (2), (3), and (8) we find

$$\dot{\rho}(t) = -k\Omega_d a^{d-1} f(a, t) + Q(t) = -k\Omega_d a^{d-1} \rho^2(t) g(a, t) + Q(t), \tag{11}$$

where the dot denotes a time derivative and Ω_d is the solid angle in d dimensions. We have implemented statistical spatial isotropy and the consequent dependence of $f(\mathbf{r}, t)$ only on $|\mathbf{r}| = r$ and not on angles. Here and subsequently we simply replace a vectorial argument by a scalar argument, $h(\mathbf{r}) = h(r)$, when a function is known not to depend on the orientation of $\mathbf{r}$.

Equation (11) is the first equation in a hierarchy. It is of the standard form

$$\dot{\rho}(t) = Q(t) - J(t) \tag{12}$$

where the source term $Q(t)$ is zero for a batch reaction and where $J(t)$ is the reaction term. The rate law (12) is of the standard "classical" bimolecular form if the pair correlation function $g(a, t)$ is independent of time. "Anomalous" behavior is therefore reflected in the time dependence of the pair correlation function.

The second equation in the hierarchy is that of the two–particle density function or of the pair correlation function. To construct this equation consider the rate of change of the product of two densities:

$$\frac{d}{dt} [\rho(\mathbf{r}, t) \rho(\mathbf{r} + \mathbf{r}', t)] = \dot{\rho}(\mathbf{r}, t) \rho(\mathbf{r} + \mathbf{r}', t) + \rho(\mathbf{r}, t) \dot{\rho}(\mathbf{r} + \mathbf{r}', t)$$
$$-k \, \rho(\mathbf{r}, t) \rho(\mathbf{r} + \mathbf{r}', t) \delta(r' - a). \tag{13}$$

The derivative on the left is a total derivative, that is, it represents all the different ways in which this product can change. The first two terms on the right represent the possible changes in each of the two densities in the product due to diffusion and due to the reaction of a particle at $\mathbf{r}$ with a third particle and of a particle at $\mathbf{r} + \mathbf{r}'$ with a third particle. The $\dot{\rho}$'s in these two terms are thus given by (10). The last term on the right represents the direct reaction of the two particles in question, the one at $\mathbf{r}$ and the one at $\mathbf{r} + \mathbf{r}'$. Substituting (10) into (13) yields

$$\frac{d}{dt}[\rho(\mathbf{r},t)\rho(\mathbf{r}+\mathbf{r}',t)] = -k\rho(\mathbf{r},t)\rho(\mathbf{r}+\mathbf{r}',t)\delta(r'-a) + \rho(\mathbf{r}+\mathbf{r}',t)\left(D\nabla^2_\mathbf{r}\rho(\mathbf{r},t)\right.$$

$$-k\int d\mathbf{R}\rho(\mathbf{r},t)\rho(\mathbf{r}+\mathbf{R},t)\delta(R-a)\Big) + \rho(\mathbf{r},t)\left(D\nabla^2_{\mathbf{r}+\mathbf{r}'}\rho(\mathbf{r}+\mathbf{r}',t) + Q(t)\right.$$

$$-k\int d\mathbf{R}\rho(\mathbf{r}+\mathbf{r}',t)\rho(\mathbf{r}+\mathbf{r}'+\mathbf{R},t)\delta(R-a) + Q(t)\Big). \tag{14}$$

The subscripts on the operators ∇^2 indicate the variable with respect to which these operators are to be evaluated. Integrating (14) over $\mathbf{r}$ and dividing by V we obtain

$$\begin{aligned}\dot{f}(\mathbf{r}',t) &= -kf(\mathbf{r}',t)\delta(r'-a)\\ &+\frac{D}{V}\int d\mathbf{r}\left(\rho(\mathbf{r}+\mathbf{r}',t)\nabla^2_\mathbf{r}\rho(\mathbf{r},t) + \rho(\mathbf{r},t)\nabla^2_{\mathbf{r}+\mathbf{r}'}\rho(\mathbf{r}+\mathbf{r}',t)\right)\\ &-k\int d\mathbf{R}\,\delta(R-a)\left(F(\mathbf{r}',\mathbf{R},t)+F(-\mathbf{r}',\mathbf{R},t)\right) + 2Q(t)\rho(t).\end{aligned} \tag{15}$$

The second term on the right can be integrated by parts twice and the derivatives with respect to $\mathbf{r}$ can be converted to derivatives with respect to $\mathbf{r}'$ so that we can write

$$\begin{aligned}\frac{D}{V}\int d\mathbf{r}\,\rho(\mathbf{r}+\mathbf{r}',t)\nabla^2_\mathbf{r}\rho(\mathbf{r},t) &= \frac{D}{V}\int d\mathbf{r}\left[\nabla^2_\mathbf{r}\rho(\mathbf{r}+\mathbf{r}',t)\right]\rho(\mathbf{r},t)\\ &= \frac{D}{V}\int d\mathbf{r}\,\nabla^2_{\mathbf{r}'}\rho(\mathbf{r}+\mathbf{r}',t)\rho(\mathbf{r},t) = D\nabla^2_{\mathbf{r}'}f(\mathbf{r}',t).\end{aligned} \tag{16}$$

The third term on the right of (15) can be dealt with similarly:

$$\frac{D}{V}\int d\mathbf{r}\,\rho(\mathbf{r},t)\nabla^2_{\mathbf{r}+\mathbf{r}'}\rho(\mathbf{r}+\mathbf{r}',t) = \frac{D}{V}\int d\mathbf{r}\rho(\mathbf{r},t)\nabla^2_{\mathbf{r}'}\rho(\mathbf{r}+\mathbf{r}',t) = D\nabla^2_{\mathbf{r}'}f(\mathbf{r}',t). \tag{17}$$

Combining these results in (15) we then have

$$\begin{aligned}\dot{f}(\mathbf{r}',t) &= -kf(\mathbf{r}',t)\delta(r'-a) + 2D\nabla^2 f(\mathbf{r}',t)\\ &- k\int d\mathbf{R}\,\delta(R-a)\left[F(\mathbf{r}',\mathbf{R},t)+F(-\mathbf{r}',\mathbf{R},t)\right] + 2Q(t)\rho(t).\end{aligned} \tag{18}$$

This equation is an exact consequence of our starting model — no further approximations have yet been made.

It is more convenient to write (18) in terms of the pair correlation function $g = f/\rho^2$ and the three particle correlation function $G = F/\rho^3$. These substitutions followed by division by $\rho^2(t)$ (and relabeling $\mathbf{r}'$ as $\mathbf{r}$) immediately gives

$$\begin{aligned}2\frac{\dot{\rho}(t)}{\rho(t)}g(\mathbf{r},t) + \dot{g}(\mathbf{r},t) &= -kg(\mathbf{r},t)\delta(r-a) + 2D\nabla^2 g(\mathbf{r},t) + \frac{2Q(t)}{\rho(t)}\\ &- k\rho(t)\int d\mathbf{R}\,\delta(R-a)\left[G(\mathbf{r},\mathbf{R},t)+G(-\mathbf{r},\mathbf{R},t)\right].\end{aligned} \tag{19}$$

This is the second equation in our hierarchy.

Our approximation to break the hierarchy consists of writing the three–particle correlation function as a product of two two–particle correlation functions:

$$G(\mathbf{r},\mathbf{R},t) \approx g(\mathbf{r},t)g(\mathbf{R},t). \tag{20}$$

Note that (20) preserves the correct normalization to unity for $G(\mathbf{r}, \mathbf{R})$. We further note the two identities

$$g(-\mathbf{r}, t) = g(\mathbf{r}, t) \tag{21}$$

and

$$\int d\mathbf{R}\delta(R - a)g(\mathbf{R}, t) = \Omega_d a^{d-1}g(a, t), \tag{22}$$

and recall the rate equation (11) so that

$$-k\Omega_d a^{d-1}g(a, t) = \frac{\dot{\rho}(t)}{\rho^2(t)} - \frac{Q(t)}{\rho^2(t)}. \tag{23}$$

Substitution of (20)–(23) into (19) then yields the much simpler equation

$$\dot{g}(\mathbf{r}, t) = 2D\nabla^2 g(\mathbf{r}, t) - kg(\mathbf{r}, t)\delta(r - a) + 2\frac{Q(t)}{\rho(t)}[1 - g(\mathbf{r}, t)]. \tag{24}$$

Equation (24) together with the rate equation (11) then constitute our closed set of equations.

As noted earlier, $-k\Omega_d a^{d-1}g(a, t)$ is our effective rate coefficient for the reaction. If $g(a, t)$ is asymptotically constant then (11) is asymptotically an ordinary second order rate law that leads to the usual classical results for well-stirred reactions. If, on the other hand, $g(a, t)$ turns out to be time dependent at long times then the rate law is "anomalous." The classical vs. anomalous behavior of the system should also become apparent in the asymptotic behavior of the pair correlation function. If the system behaves classically then the spatial distribution of particles should become essentially random and $g(\mathbf{r}, t)$ should $\rightarrow 1$ at long times independent of $\mathbf{r}$ (except for small corrections due to the finite radius a of the particles). Anomalous behavior is associated with a deviation from this uniform distribution, a deviation that persists even in the limit $a \rightarrow 0$. Indeed, simulations [30] show that for $d < 2$ there is a dearth of near neighbors surrounding any given particle and it is this depletion that causes the reaction to slow down. This depletion should show up as a decrease of $g(\mathbf{r}, t)$ as a function of r as $r \rightarrow 0$. We expect to find such behavior for $d < 2$, while for $d > 2$ the pair correlation function is expected to be essentially constant.

BATCH REACTIONS

For batch reactions $Q = 0$. Our two hierarchy equations then reduce to

$$\dot{\rho}(t) = -k\Omega_d a^{d-1}g(a, t)\rho^2(t) \tag{25}$$

and

$$\dot{g}(\mathbf{r}, t) = 2D\nabla^2 g(\mathbf{r}, t) - kg(a, t)\delta(r - a). \tag{26}$$

Equation (26) is a simple linear equation that can easily be solved by Fourier transformation. With the transformation conventions (assuming periodic boundary conditions)

$$\widehat{g}_{\mathbf{n}}(t) = \frac{1}{L^{d/2}} \int d\mathbf{r}\, g(\mathbf{r}, t)e^{-2i\pi\mathbf{n}\cdot\mathbf{r}/L} \tag{27}$$

where $L^d = V$ and $\mathbf{n}$ is the d-tuple of integers $n_1, n_2, \ldots, n_d$, and

$$g(\mathbf{r}, t) = \frac{1}{L^{d/2}} \sum_{n_1,\ldots,n_d=-\infty}^{\infty} \widehat{g}_{\mathbf{n}}(t)e^{2i\pi\mathbf{n}\cdot\mathbf{r}/L}, \tag{28}$$

we find

$$g(\mathbf{r}, t) = g_\circ(\mathbf{r}, t) - k \int_0^t dt'\, g(a, t')K_d(\mathbf{r}, t - t'). \tag{29}$$

Here

$$g_o(\mathbf{r}, t) = \frac{1}{L^{d/2}} \sum_{n_1,\ldots,n_d=-\infty}^{\infty} \widehat{g}_{\mathbf{n}}(0) e^{-(8D\pi^2 n^2/L^2)t} e^{2i\pi\mathbf{n}\cdot\mathbf{r}/L}$$

$$= \frac{1}{L^d} \sum_{\mathbf{n}} \int d\mathbf{r}' g(\mathbf{r}', 0) e^{-2i\pi\mathbf{n}\cdot(\mathbf{r}'-\mathbf{r})/L} e^{-(8D\pi^2 n^2/L^2)t}$$

$$\equiv \sum_{\mathbf{n}} g_{o,\mathbf{n}}(\mathbf{r}, t) \tag{30}$$

is the pair correlation function for a purely diffusive process, and

$$K_d(\mathbf{r}, t) = \frac{1}{L^{d/2}} \sum_{n_1,\ldots,n_d=-\infty}^{\infty} H_{d,\mathbf{n}}(t) e^{-(8D\pi^2 n^2/L^2)t} e^{2i\pi\mathbf{n}\cdot\mathbf{r}/L}$$

$$\rightarrow \frac{1}{(2\pi)^{d/2}} \int d\mathbf{q}\, e^{i\mathbf{q}\cdot\mathbf{r}} e^{-2Dq^2 t} H_d(\mathbf{q}) \tag{31}$$

with

$$H_1(q) = \frac{2}{(2\pi)^{1/2}} \cos qa, \tag{32}$$

$$H_2(\mathbf{q}) = \frac{2\pi a}{(2\pi)} J_0(qa), \tag{33}$$

$$H_3(\mathbf{q}) = \frac{4\pi a^2}{(2\pi)^{3/2}} \frac{\sin qa}{qa}. \tag{34}$$

$J_0(z)$ is a Bessel function of the first kind, and (31) is the large volume limit.

The $\mathbf{n} = 0$ term in (30) is fixed by the normalization of g regardless of the size of the system:

$$g_{o,0}(\mathbf{r}, t) = \frac{1}{V} \int d\mathbf{r}' g(\mathbf{r}', 0) = 1. \tag{35}$$

This $\mathbf{r}$–independent non-decaying contribution dominates the long–time behavior of $g_o(\mathbf{r}, t)$ since all the other contributions decay with time. Indeed, if the initial distribution is uniform, then $g(\mathbf{r}, 0) = 1$ (except for a small region of radius a around $\mathbf{r} = 0$), and $g_o(\mathbf{r}, t)$ remains exactly equal to unity for all time.

Since (29) is a convolution, its time Laplace transform according to

$$\widetilde{F}(s) = \int_0^{\infty} dt\, e^{-st} F(t) \tag{36}$$

is particularly simple and useful:

$$\widetilde{g}(\mathbf{r}, s) = \widetilde{g}_o(\mathbf{r}, s) - k\widetilde{g}(a, s)\widetilde{K}_d(\mathbf{r}, s). \tag{37}$$

The integral of (37) over angles can now be used to solve for the unknown quantity $g(a, t)$ that appears on the right hand side of (37) by setting $r = a$. One readily obtains

$$\widetilde{g}(a, s) = \frac{\widetilde{g}_o(a, s)}{1 + k\widetilde{K}_d(a, s)}. \tag{38}$$

The long-time behavior of $g(a, t)$ *regardless of initial condition* (and indeed its behavior for all time for a uniform initial condition) is thus obtained from

$$\widetilde{g}(a, s) = \frac{1}{s[1 + k\widetilde{K}_d(a, s)]}. \tag{39}$$

The Laplace transform of the pair correlation function according to (37) then is

$$\widetilde{g}(r, s) = \widetilde{g}_o(r, s) - \frac{k\widetilde{g}_o(a, s)\widetilde{K}_d(r, s)}{k\widetilde{K}_d(a, s) + 1}. \tag{40}$$

Further discussion requires that we evaluate the functions K_d explicitly, which in turn must be done separately for each dimension. In one dimension we find (with $r = |x|$, where x is the usual Cartesian coordinate):

$$K_1(r,t) = \frac{1}{2\sqrt{2\pi Dt}} \left[e^{-(r-a)^2/8Dt} + e^{-(r+a)^2/8Dt} \right].$$ (41)

Laplace transformation of $K_1(r,t)$ followed by a small-s expansion readily leads to

$$\widetilde{g}(a,s) \sim \frac{\sqrt{2D}}{k\sqrt{s}} + O(\sqrt{s}) \sim \frac{\sqrt{2D}}{k\sqrt{s}}.$$ (42)

The inverse transform of (42) is

$$g(a,t) \sim \frac{\sqrt{2D}}{k\sqrt{\pi t}}$$ (43)

This immediately gives for (25) with $d = 1$ and $\Omega_1 = 2$

$$\dot{\rho}(t) = -2\frac{\sqrt{2D}}{\sqrt{\pi t}}\rho^2(t),$$ (44)

that is, a rate coefficient proportional to $t^{-1/2}$. From (44) we deduce that

$$\rho(t) = \frac{1}{4}\sqrt{\frac{\pi}{2D}}t^{-1/2}$$ (45)

and consequently

$$\dot{\rho} = -\frac{16D}{\pi}\rho^3.$$ (46)

Such a third-order rate law in one dimension has been found using a variety of other approaches and also from simulations. Note that the rate coefficient is entirely determined by the diffusion coefficient D and is otherwise independent of the size a of the particles and of the local rate coefficient k. This observation is also borne out by numerical simulations.

The spatial distribution of reactants is now found from (40). It simplifies the final results to note that for diffusion-controlled reactions k is large, i.e., $kK_1(a,s) \sim k/(2Ds)^{1/2} \gg 1$ except for very large values of s (which only affects the shortest time behavior). We thus set

$$\widetilde{g}(r,s) \sim \frac{1}{s}\left(1 - \frac{\widetilde{K}_1(r,s)}{\widetilde{K}_1(a,s)}\right).$$ (47)

Further, no important physical information is lost by setting $a = 0$ in this expression — as in the rate law, the finite size of the particles here does not play an important role. We then have

$$\widetilde{g}(r,s) \sim \frac{1}{s}\left(1 - e^{-(s/2D)^{1/2}r}\right),$$ (48)

whose inverse Laplace transform is

$$g(r,t) = \mathrm{erf}\left(\frac{r}{2\sqrt{2Dt}}\right).$$ (49)

This expression is exactly of the desired form: at large values of r, $g(r,t) \to 1$, so that there is no long-range order in the system. For small r, however, there is definite structure in the pair correlation function. A depletion region around each reactant particle grows in time as $t^{1/2}$. Note also that this result is normalized correctly.

In two dimensions we obtain

$$\widetilde{K}_2(r,s) = \frac{a}{2D}I_0(a\sqrt{s/2D})K_0(r\sqrt{s/2D})$$ (50)

where I_0 and K_0 are modified Bessel functions and $r \geq a$. For small s

$$\widetilde{K}_2(r,s) \sim \frac{a}{2D}\left[\ln 2 - \gamma - \frac{1}{2}\left(\frac{r^2 s}{2D}\right)\right]$$ (51)

where $\gamma = 0.577\ldots$ is the Euler constant. The leading contribution in s to $\widetilde{g}(r,s)$ is

$$\widetilde{g}(r,s) \sim -\frac{4D}{kas\ln\left(\frac{r^2 s}{2D}\right)}. \tag{52}$$

This expression does not lend itself to the calculation of a useful analytic form for $g(a,t)$ and hence for the rate law. In particular, the rate law is certainly not a simple power. Indeed, in the absence of the logarithmic term in the denominator of (52) we would find that $g(a,t) \sim constant$ independent of t and an associated classical rate law $\dot{\rho} \sim -\rho^2$. The logarithmic contribution leads to the well-known logarithmic correction to the classical rate law in two dimensions and to logarithmic deviations from a uniform spatial pair correlation function.

In three dimensions we readily find

$$K_3(r,t) = \frac{a}{2r}\frac{1}{\sqrt{2\pi Dt}}\left[e^{-(a-r)^2/8Dt} - e^{-(a+r)^2/8Dt}\right]. \tag{53}$$

Laplace transformation followed by small s expansion leads to

$$\widetilde{g}(a,s) \sim \frac{1}{s(1+ka/2D)} + O(s^{-1/2}). \tag{54}$$

The inverse transform of (54) is

$$g(a,t) \sim \frac{1}{1+ka/2D}, \tag{55}$$

that is, a constant rate coefficient for long times. Equation (25) with $d = 3$ and $\Omega_d = 4\pi$ then yields the classical rate law

$$\dot{\rho} = -\frac{4\pi a^2 k}{1+ka/2D}\rho^2. \tag{56}$$

Note that the rate coefficient depends explicitly on the size a of the particles and that there is no reaction if the particles are point particles.

The spatial distribution of reactants is found from (40). For $(s/2D)^{1/2}a \ll 1$, $k/2Ds \gg 1$, and $a \le r$ we obtain

$$\widetilde{g}(r,s) \sim \frac{1}{s}\left[1 - \frac{a}{r(1+2D/ka)}e^{-(s/2d)^{1/2}r}\right], \tag{57}$$

and inverse Laplace transformation of this expressions immediately yields

$$g(r,t) \sim 1 - \frac{a}{r(1+2D/ka)}\text{erfc}\left(\frac{r}{2\sqrt{2Dt}}\right) \tag{58}$$

where $\text{erfc}(z)$ is the complementary error function. The spatial distribution thus approaches a uniform one (except for corrections of order a) and indeed remains uniform for all time if $a = 0$. In particular, there is no growing depletion zone. This result is of course well known from numerical simulations.

STEADY STATE REACTIONS

In this section we consider the *steady state* when there are sources present, that is, when $Q \neq 0$ and $\dot{\rho} = 0$. Our two hierarchy equations then become

$$Q = k\Omega_d a^{d-1}\rho^2 g(a) \tag{59}$$

and

$$0 = 2D\nabla^2 g(\mathbf{r}) - kg(\mathbf{r})\delta(r-a) + \frac{2Q}{\rho}[1-g(\mathbf{r})], \tag{60}$$

where the absence of a time argument where there was one previously denotes the steady state.

Equation (60) can be solved by Fourier transformation. In this solution, the $\mathbf{n} = \mathbf{0}$ term must be separated out explicitly and the remaining sum can be converted to an integral in the large V limit. We find:

$$g(\mathbf{r}) = 1 - \frac{1}{(2\pi)^{d/2}} \frac{Q}{2\Omega_d a^{d-1} \rho^2} \int d\mathbf{q}\, e^{i\mathbf{q}\cdot\mathbf{r}} \frac{H_d(\mathbf{q})}{Dq^2 + \frac{Q}{\rho}}. \tag{61}$$

This result agrees with that of Clément et al. [23].

In one dimension (again with $r = |x|$, where x is the usual Cartesian coordinate) Eq. (61) leads to

$$g(r) == 1 - \frac{1}{8}\sqrt{\frac{Q}{D\rho^3}} \left(e^{-|r-a|\sqrt{Q/D\rho}} + e^{-|r+a|\sqrt{Q/D\rho}} \right). \tag{62}$$

This together with the relation (59), $Q = 2k\rho^2 g(a)$, constitutes the solution of the steady–state problem. We find

$$Q = 16D\rho^3. \tag{63}$$

Corrections of $O(a)$ have been dropped in this result, which again agrees with the result of Clément et al. [23]. Finally, substitution in (62) then yields for the spatial distribution

$$g(r) = 1 - \frac{1}{2} \left(e^{-4\rho|r-a|} + e^{-4\rho|r+a|} \right). \tag{64}$$

Thus, in the steady state there is again a depletion zone around each reactant particle. The size of this region is inversely proportional to the steady–state density ρ of reactants.

As in the batch reaction, the two dimensional expression for the pair correlation function in the steady state,

$$g(r) = 1 - \frac{Qa}{D\rho^2} I_0(a\sqrt{D/\rho}) K_0(r\sqrt{D/\rho}), \tag{65}$$

does not lend itself to algebraic manipulation or indeed to any simple analytic expression for Q as a function of the steady–state density ρ nor for the steady state spatial distribution $g(r)$. In particular, there are again logarithmic deviations from classical behavior that we do not pursue explicitly. It is, however, straightforward to establish that again our results agree with those of Clement et al. [23].

In three dimensions Eq. (61) becomes

$$g(r) = 1 - \frac{1}{16\pi ar}\sqrt{\frac{Q}{D\rho^3}} \left(e^{-|r-a|\sqrt{Q/D\rho}} - e^{-|r+a|\sqrt{Q/D\rho}} \right) \tag{66}$$

which in turn immediately leads to

$$Q = 8\pi a D\rho^2 \tag{67}$$

where corrections of $O(a)$ have been dropped. More specifically, we have assumed that the steady state density is very much smaller than full occupancy, i.e., that $8\pi a^3\rho \ll 1$. This result agrees with the result of Clément et al. The spatial distribution of reactants in the steady state obtained from (66) with (67) with this condition and with $r \geq a$ finally is

$$g(r) = 1 - \frac{a}{r} e^{-(r-a)(8\pi a\rho)^{1/2}}. \tag{68}$$

Thus, in three dimensions there is no depletion zone in the steady state - the distribution is essentially uniform.

SUMMARY AND CONCLUSIONS

We have formulated an approach to the $A+A \rightarrow products$ reaction that is based on a reaction–diffusion equation frequently used for the $A + B$ problem but requiring appropriate generalization for the $A + A$ problem.

Starting from this reaction–diffusion equation, we have constructed the first equations in a moment hierarchy whose first two members are the global density of A particles and the pair correlation function.

385

We terminate the hierarchy via an approximation that relates the three–particle correlation function to two–particle correlation functions and thereby obtain a set of coupled equations that turns out to be linear and hence analytically tractable.

This approach leads naturally to the proportionality of the rate of the reaction to the pair correlation function evaluated at $r = a$, where a is the diameter of the reacting particles. In other words, the reaction rate is proportional to the probability that two A particles are sufficiently close. In the more traditional approach based on the Smoluchowski theory for trapping phenomena, the reaction rate is instead proportional to the *gradient* of the pair correlation function. Elsewhere [33] we have discussed in some detail the differences and essential similarities between these points of view and their consequences. When the local reaction rate coefficient k is large, both approaches lead to essentially equivalent results [34]; differences become more important as k decreases.

In a companion paper in this session [35] we present extensive numerical simulations in one and two dimensions in order to check our predictions. Our results confirm the well-known anomalous rate law in one dimension (the anomalies are marginal in two dimensions) and the proportionality of the reaction rate to the two-particle correlation function. Our simulations serve to stress an important point brought forth by the theory: the rate of the reaction is determined entirely by the spatial distribution of a very small shell of particles around a given reactant particle. In the lattice simulations, the rate is entirely determined by the distribution of nearest and next nearest pairs. In the continuum formulation this translates into the distribution of reactants that are very close (in physical contact) with a given reactant particle. Anomalous kinetics is a direct reflection of the deviation of the spatial distribution of this small shell from a random configuration. Our simulation results also confirm the predicted distance and time scaling of the pair correlation function in one dimension.

ACKNOWLEDGEMENTS

REFERENCES

1. M. Bramson and D. Z. Griffeath, Wahrscheinlichkeitstheorie Gebiete **53**, 183 (1980); Annals of Probability **8**, 183 (1980).

2. P. W. Klymko and R. Kopelman, J. Lumin. **24/25**, 457 (1981); J. Phys. Chem. **86**, 3686 (1982).

3. P. W. Klymko and R. Kopelman, J. Phys. Chem. **87**, 4565 (1983).

4. D. C. Torney and H. M. McConnell, J. Phys. Chem. **87**, 1441 (1983); Proc. Roy. Soc. London A **387**, 147 (1983); D. C. Torney, J. Chem. Phys. **79**, 3606 (1983).

5. J. Keizer, J. Chem. Phys. **79**, 4877 (1983); R. Kopelman, J. Hoshen, J. S. Newhouse, and P. Argyrakis, J. Stat. Phys. **30**, 335 (1983); A. Blumen, J. Klafter, and G. Zumofen, Phys. Rev. B **27**, 3429 (1983); P. G. de Gennes, Chem. R. Acad. Sci. Paris **296**, 881 (1983); P. Evesque, J. Phys. **44**, 1217 1983; P. Evesque and J. Duran, J. Chem. Phys. **80**, 3016 1984; K. Kang and S. Redner, Phys. Rev. Lett. **52**, 955 (1984); R. Kopelman, P. W. Klymko, J. S. Newhouse, and L. Anacker, Phys. Rev. B **29**, 3747 (1984); P. Meakin and H. E. Stanley, J. Phys. A **173**, L17 (1984); L. W. Anacker, R. Kopelman, and J. S. Newhouse, J. Stat. Phys. **36**, 591 (1984); J. S. Newhouse, P. Argyrakis, and R. Kopelman, Chem. Phys. Lett. **107**, 48 (1984); K. Kang, P. Meakin, J. H. Oh, and S. Redner, J. Phys. A **17**, L665 (1984).

6. P. V. Elyutin, J. Phys. C **17**, 1867 (1984).

7. L. W. Anacker and R. Kopelman, J. Chem. Phys. **81**, 6402 (1984); L. W. Anacker, R. P. Parson, and R. Kopelman, J. Phys. Chem. **89**, 4785 (1985).

8. Racz, Z., Phys. Rev. Lett. **55**, 1707 (1985).

9. K. Kang and S. Redner, Phys. Rev. A **32**, 435 (1985); Y. Elskens and H. L. Frish, Phys. Rev. A **31**, 3812 (1985); J. S. Newhouse and R. Kopelman, Phys. Rev. B **31**, 1677 (1985); R. Kopelman, J. de Physique C **7**, 9, 1985; G. Zumofen, A. Blumen, and J. Klafter, J. Chem. Phys. **82**, 3198 (1985); D. Ben-Avraham and S. Redner, Phys. Rev. A **34**, 501 (1986); J. S. Newhouse and R. Kopelman, J. Chem. Phys. **85**, 6804 (1986); R. Kopelman, S. Parus, and J. Prasad, Phys. Rev. Lett. **56**, 1742 (1986); R. Kopelman, J. Stat. Phys. **42**, 185 (1986); L. Peliti, J. Phys. A **19**, L365 (1986); D. Ben-Avraham, J. Stat. Phys. **48**, 315 (1987); A. A. Lushnikov, Phys. Lett. A **120**, 135 (1987); S. Redner, D. Ben-Avraham, and B. Kahng, J. Phys. A **20**, 1231 (1987).

10. R. Kopelman, Philos. Mag. B **56**, 717 (1987); J. Prasad and R. Kopelman, J. Phys. Chem. **91**, 265 (1987); Phys. Rev. Lett. **59**, 2103 (1987).

11. P. Argykaris and R. Kopelman, J. Phys. Chem. **91**, 2699 (1987); L. Li and R. Kopelman, J. Lumin. **40/41**, 688 (1988).

12. E. Peacock–López and J. Keizer, J. Chem. Phys. **88**, 1997 (1988).

13. D. Balding, P. Clifford, and N. J. B. Green, Phys. Lett. A **126**, 481 (1988).

14. S. Kanno, Prog. Theoret. Phys. **79**, 1330 (1988).

15. J. L. Spouge, Phys. Rev. Lett. **60**, 871 (1988); *ibid* 1885.

16. V. Kuzovkov and E. Kotomin, Rep. Prog. Phys. **51**, 1479 (1988).

17. Find the right ones

18. C. R. Doering and D. Ben-Avraham, Phys. Rev. A **38**, 3035 (1988); Phys. Rev. Lett. **62**, 2563 (1989).

19. A. Blumen, G. Zumofen, and J. Klafter, in *Fractals, Quasicrystals, Chaos, Knots and Algebraic Quantum Mechanics*, eds. A. Amann et al. (Kluwer, New York, 1989) p. 21.

20. R. Kopelman, Science **41**, 1620 (1988).

21. R. Kopelman, S. J. Parus, and J. Prasad, in *Excited State Relaxation and Transport Phenomena in Solids*, eds. J. L. Skinner and M. D. Fayer, special issue of Chem. Phys. **128**, 209 (1988); Z. Cheng, S. Redner, and F. Leyvraz, Phys. Rev. Lett. **62**, 2321 (1989); R. Kopelman, S. J. Parus, and Z-Y. Shi, in *Dynamical Processes in Condensed Molecular Systems*, eds. J. Klafter, J. Jortner, and A. Blumen (World Scientific, Singapore, 1989) p. 231; S. J. Parus and R. Kopelman, Phys. Rev. B **39**, 889 (1989); S. J. Parus and R. Kopelman, Mol. Cryst. Liq. Cryst. **175**, 119 (1989).

22. P. Argyrakis and R. Kopelman, J. Phys. Chem. **93**, 225 (1989).

23. E. Clement, L. M. Sander, and R. Kopelman, Phys. Rev. A **39**, 6472 (1989).

24. J. Prasad and R. Kopelman, Chem. Phys. Lett. **157**, 535 (1989); L. A. Harmon and R. Kopelman, J. Phys. Chem. **94**, 3454 (1990); P. Argyrakis and R. Kopelman, Phys. Rev. A **41**, 2114 (1990); J. Prasad and R. Kopelman, J. Lumin. **45**, 258 (1990); R. Kopelman, C. S. Li, and Z-Y. Shi, J. Lumin. **45**, 40 (1990).

25. R. Kopelman, L. W. Anacker, E. Clement, L. Li, and L. Sander, J. Lumin **45**, 323 (1990).

26. S. J. Parus and R. Kopelman, J. Lumin. **45**, 43 (1990); Z-Y. Shi and R. Kopelman, J. Lumin. **45**, 275 (1990); R. Kopelman, in *Dynamical Processes in Condensed Molecular Systems*, eds. A. Blumen, J. Klafter, and D. Haarer (World Scientific, Singapore, 1990) p. 173; T. Ohtsuki, Phys. Rev. A **43**, 6917 (1991).

27. V. Privman, J. Stat. Phys. **69**, 629 (1992).

28. L. Li and R. Kopelman, J. Phys. Chem. **96**, 8079 (1992); Z-Y. Shi and R. Kopelman, Chem. Phys. **167**, 149 (1992); P. Argyrakis and R. Kopelman, Phys. Rev. A **45**, 5814 (1992).

29. Z-Y. Shi and R. Kopelman, in *Dynamics in Small Confining Systems*, eds. J. M. Drake, J. Klafter, R. Kopelman, and D. D. Awshalom, MRS Symposium Proceedings **290**, 279 (1993).

30. P. Argyrakis and R. Kopelman, Phys. Rev. A **41**, 2114 (1990); *ibid* 2121.

31. K. Lindenberg, B. J. West, and R. Kopelman, in *Noise and Chaos in Nonlinear Dynamical Systems*, eds. S. Capelin and F. Moss (Cambridge University Press, 1989) and references therein; K. Lindenberg, B. J. West, and R. Kopelman, Phys. Rev. A **42**, 890 (1990); K. Lindenberg, B. J. West, and R. Kopelman, Phys. Rev. Lett. **60**, 1777 (1988).

32. M. von Smoluchowski, Z. Phys. Chem. **92**, 129 (1917).

33. K. Lindenberg, P. Argyrakis, and R. Kopelman, to be published.

34. N. G. van Kampen, Int. J. Quant. Chem. **16**, 101 (1982).

35. P. Argyrakis et al., companion paper.

EXPERIMENTAL STUDY OF A REACTION-DIFFUSION SYSTEM IN A CAPILLARY: COMPLEX BEHAVIOR OF A SEEMINGLY SIMPLE SYSTEM

Anna Lin, Andrew Yen, Yong-Eun Koo and Raoul Kopelman, University of Michigan, Ann Arbor, MI. 48109.

ABSTRACT

We study a reaction-diffusion system within the confines of a thin capillary tube. Xylenol orange and Cr^{3+} are introduced into a capillary tube from opposite ends and meet in the middle forming a reaction front. Unequal initial concentrations of the reactants causes the center of the reaction front to move in time. Characteristics of the front such as the width of the reaction zone, w, the position of the center of the front, x_f, the global reaction rate, R, and the local reaction rate, $r(x_f,t)$ are determined by continuously monitoring the product concentration in space vs. time. We observe crossover of the global rate from classical to non-classical behavior and a splitting of the reaction front.

INTRODUCTION

Chemical reaction fronts are copious in nature[1,2]. Liesegang rings and traveling chemical waves such as seen in the Belousov-Zhabotinskii reaction are examples of such chemical reaction fronts. Understanding the dynamics, dictated by the initial conditions, at the front may help elucidate the mechanism of at least some types of crystal growth in gels, chemical pattern formation and oscillating chemical systems among other phenomena associated with a chemical reaction front.

The non-equilibrium, asymptotic dynamics of a reaction front formed via initial segregation of the reactants of a binary reaction have been studied theoretically[3-9] and experimentally[10,11]. Characteristics of the front such as the width of the reaction zone, w(t), the position of the center of the front, $x_f(t)$, the global reaction rate, R(t), and the local reaction rate, $r(x_f,t)$, were determined for a simple binary reaction system with the initial conditions $a=a_0$ and $b=0$ for $x<0$ and $a=0$, $b=b_0$ for $x>0$; see figure 1. The asymptotic time dependencies of these dynamic parameters obtained experimentally[10] : $w \sim t^{0.17\pm0.05}$, $x_f \sim t^{-0.51\pm0.06}$, $r \sim t^{-0.70}$ and $R \sim t^{-0.53\pm0.07}$ agree quite well with the theoretical predictions[3] $w \sim t^{1/6}$, $x_f \sim t^{-1/2}$, $r \sim t^{-2/3}$ and $R \sim t^{-1/2}$.

However, the above mentioned work only addresses behavior of the front in the long time limit. Taitelbaum et al.[5,6] have worked out a perturbation analysis of the reaction front dynamics that is valid in the short time limit and predicts a variety of nontrivial crossovers and different universality classes for the dynamics of the front at early times.

Experimentally, using a reaction-limited system as opposed to diffusion-limited system enables us to observe some of these short time regime behaviors. In particular, we have observed for the first time the predicted crossover of the global rate from $t^{1/2}$ to $t^{-1/2}$ at early time.

Our choice of a reaction-limited reaction, xylenol orange $+ Cr^{3+} \rightarrow 1:1$ complex, also exhibits behavior of the reaction front not previously predicted. Namely, it

exhibits an apparent splitting of the reaction front which has prompted further (analytical) work in this area and requires the development of an extension of the existing theory.
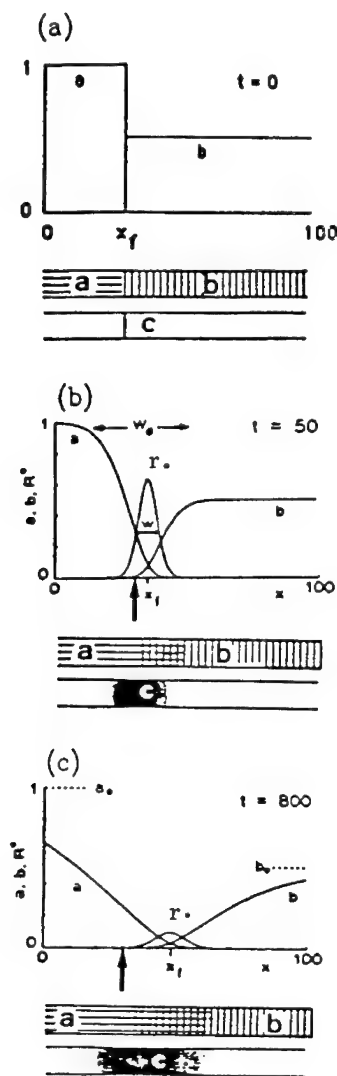

FIG. 1. The motion of the reaction front. Length (x), time (t), densities (a,b) of the reagents (A,B), and the magnified production rate ($r^* = 100r = 100kab$) of C are scaled to be all dimensionless. As an initial condition, we use a=1, b=1 for x<30, and a=), b=0.5 for x > 30. The t=0 postion of the reaction front is shown with an arrow.

Parts b. and c. are numerical results to a set of reaction diffusion equations.[3]

EXPERIMENTAL

1.0x10^{-5} M Cr^{3+} and 5x10^{-4} M xylenol orange samples are prepared by boiling solutions of the two reactants with 0.8% gelatin and 0.8% Ficoll. The pH of each solution is adjusted and the samples are frozen over a period of days.   Once removed from the freezer, samples are stored in a refrigerator and are equilibrated to room temperature before they are used in an experiment(see Fig.2).

Gelatin is used to increase the viscosity of the samples. This helps to prevent convection and aids us in forming a sharp initial reaction boundary. The Ficoll is used to inhibit fungal growth.   Gelatin solutions of the two reactants, xylenol orange and Cr^{3+}, are injected into opposite ends of a thin capillary reaction vessel.   The two reactant solutions meet in the center of the vessel forming a reaction front at time, t=0.

Optical absorption measurements are used to monitor the dynamic quantities of the reaction front. An automated system consisting of a halogen lamp, two band pass filters (440 nm and 570 nm --reactant (xylenol orange) and product absorbance ranges respectively) which are alternated using a solenoid , a PMT, and a stepping motor is used. The lamp and the solenoid are controlled through the parallel port of a computer and the movement of the stepping motor is controlled via a stepping motor controller. The light source, solenoid with two filters, slit unit and detector are fixed on the stepping motor. A glass capillary reaction vessel fits into the slit unit located in front of the PMT, which interfaces with the computer via an a/d board.

The first scan of the capillary reaction vessel starts after one minute. Each scan takes ~35 seconds. The vessel is scanned in the direction of the motion of the reaction front over a distance of 80 mm. The spatial resolution of the experiment is 0.1 mm. Consecutive scans of the reactant and product profiles are taken over the course of the run. The time interval between scans ranges from the order of minutes to the order of hours.
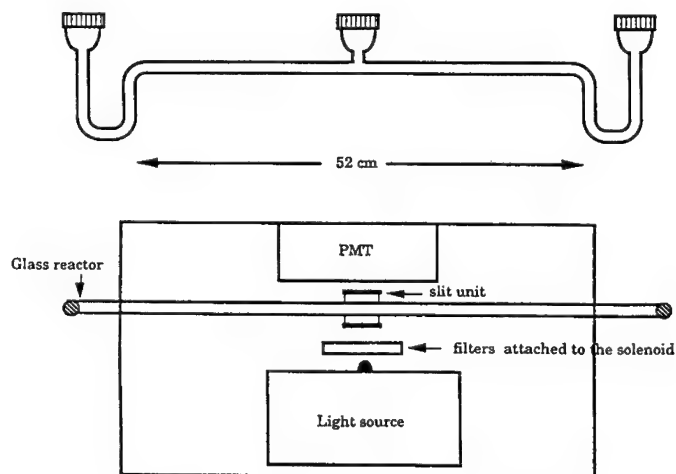

Fig. 2

Top view of the experimental set-up for absorbance measurement

RESULTS AND DISCUSSION

Using the slow complexation reaction of xylenol orange + $Cr^{3+} \rightarrow$ 1:1 complex we are able to study the short time regime kinetic behavior of the reaction front. This 'short time' regime behavior occurs over a period of hours in our experiments.

Unequal initial concentrations and unequal diffusion constants of the reactants xylenol orange and Cr^{3+} causes the center of the reaction front to move in time. We observed a change in direction of the movement of the center of the reaction front[6,15](see Fig.3).
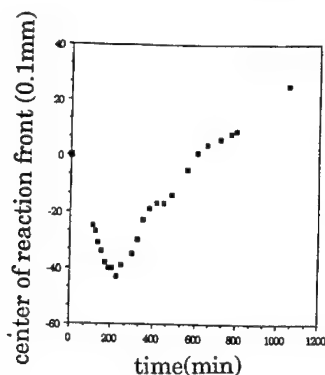
Fig. 3: Plot of position of the center of the reaction front, x_f, vs. time. The motion of x_f is non-monotonic in time.

We determine the global rate by calculating the area difference of consecutive product profiles divided by the time interval and observe, for the first time the predicted crossover[5] of the global rate of reaction from $t^{1/2}$ to $t^{-1/2}$ (see Fig. 4).
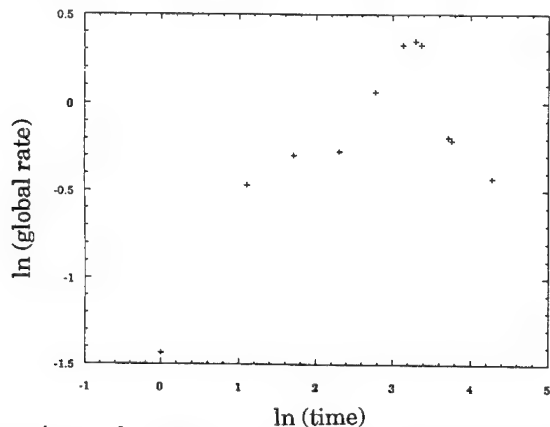

Fig. 4: Experimental results for ln (global rate) vs. time. "Global rate" is the rate of the product formation over the whole space. We see a crossover of the global rate as predicted by the theory.

This crossover is to be expected if one considers that, in a slow, reaction-limited system at early times, a relatively small amount of mixing will have occurred and reactive effects will be small compared to those of diffusion. Later, the reactive effects will dominate resulting in the crossover from the reaction-limited regime, $t^{1/2}$, to the diffusion-limited regime, $t^{-1/2}$.

The reaction, xylenol orange + $Cr^{3+} \rightarrow$ 1:1 complex, exhibits more complicated behavior than is predicted analytically for a simple, reaction-limited, bimolecular reaction where the two reactants are initially separated in space along the net diffusion coordinate. Namely, the reaction front exhibits a splitting of the reaction front which is not predicted by the original theory for reaction-diffusion systems with initially segregated reactants.
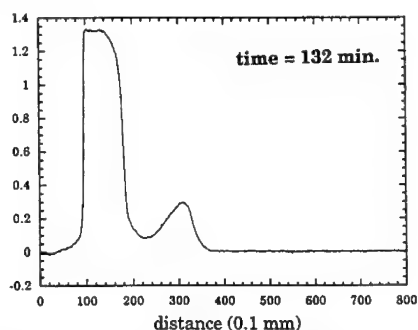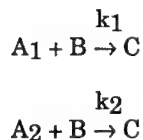

Fig. 5 : An absorbance profile of the reaction front showing that the front is split.

A new model[13,14] has been proposed to account for the splitting pattern that we observe at the reaction front. In this model, the elementary reaction: $A + B \rightarrow C$, is replaced with

$$A_1 + B \overset{k_1}{\rightarrow} C$$

$$A_2 + B \overset{k_2}{\rightarrow} C$$

where A_1 and A_2 are different forms of the same species and $k_1 \neq k_2$. Under the condition of initially segregated reactants A (A_1 and A_2) and B, Taitelbaum et al.[14] have determined via simulations that, if the concentration of A_1, a_1, is much smaller than the concentration of A_2, a_2, ($a_1 << a_2$) and $k_1 >> k_2$, interesting behavior, not predicted for the more simple $A + B \rightarrow C$ case, occurs.

The most striking change in the reaction front behavior using this model is an apparent splitting of the reaction front. We observe this splitting qualitatively in our experimental results (See Fig. 5.). To understand the similarity of our experimental conditions to those of the proposed model we note that there are ten different ionic forms of xylenol orange as a function of pH[12]. At the pH of 4.5-5.0, under which our experiments were done, two forms of xylenol orange can coexist and react with Cr^{3+}

with different reaction constants. The products of these two reactions, because they are very similar in structure, could be indistinguishable by our detection technique. Thus, the formation of two reaction fronts over time appears to be a splitting of the reaction front. More details of this are given in reference [14,16].

In summary, we observe a cross-over in the global reaction rate as predicted by analytical results, the non-monotonic movement of the center of the reaction front and our data are consistent with a new model which predicts a splitting of the reaction front.

ACKNOWLEDGMENTS

REFERENCES

1. H. K. Henisch, *Crystals in Gels and Liesegang Rings*. (Cambridge University Press, Cambridge, 1988).
2. J. D. Murray, *Mathematical Biology*. Biomathematics (Springer_Verlag, 1993), vol. 19.
3. L. Galfi, Z. Racz, *Physical Review ,A* **38**, 3151-3154 (1988).
4. S. Cornell, M. Droz, B. Chopard, *Physical Review A,* **44**, 4826-4832 (1991).
5. H. Taitelbaum, S. Havlin, J. Kiefer, B. Trus, G. Weiss, *Journal of Statistical Physics* **65**, 5/6, 873-891 (1991).
6. H. Taitelbaum, Y.-E. L. Koo, S. Havlin, R. Kopelman, G. H. Weiss, *Physical Review A,* **46**, 2151-2154 (1992).
7. M. Araujo, H. Shlomo, G. H. Weiss, H. E. Stanley, *Physical Review A,* **43**, 5207-5213 (1991).
8. S. Havlin, M. Araujo, H. Larralde, A. Shehter, H. E. Stanley, *Fractals,* **1**, 405-415 (1993).
9. Z. Jiang, C. Ebner, *Physical Review A* **42**, 7483 (1990).
10. Y.-E. L. Koo, R. Kopelman, *Journal of Statistical Physics,* **65**, 893-918 (1991).
11. Y.-E. Koo, R. Kopelman, *Israel Journal of Chemistry,* **31**, 147-157 (1991).
12. B. Rehak and J. Korbl, *Collection Czechoslov. Chem. Commun.,* **25**, 797 (1960).
13. B. Vilensky, H. Taitelbaum, *to be published.*
14. H. Taitelbaum, et al., *to be published.*
15. Y.-E. Koo, R. Kopelman, A. Yen and A. Lin, *MRS Symp. Proc.,* **290**, 273 (1993).
16. H. Taitelbaum, et al., this symposium, *to be published.*

GLOBAL REACTION RATES FROM LOCAL CLUSTER DISTRIBUTIONS

PANOS ARGYRAKIS[*], RAOUL KOPELMAN[**] and KATJA LINDENBERG[#]
[*] Department of Chemistry, University of Michigan, Ann Arbor, MI 48109-1055
and Department of Physics, University of Thessaloniki, 54006 Thessaloniki Greece
[**]Departments of Chemistry and Physics, University of Michigan, Ann Arbor, MI 48109-1055
[#]Department of Chemistry and Biochemistry and Institute for Nonlinear Science, University of California at San Diego, La Jolla, CA 92093-0340

ABSTRACT

The well-known model reactions A+A-->0 and A+B-->0 are examined in terms of the microscopic geometric arrangements of the reactants that may possibly lead to reaction. The reaction takes place only upon physical short-ranged collision of the reactants. Different dimensionalities are examined, and for each one of these arrangements all possible arrangements of the reactants are enumarated. Then, the frequency (probability) is taken into account, and an overall rate is formed. This rate is monitored in the course of the reaction in the simulation calculation and compared to the overall rate derived the traditional way from the densities. These two rates agree very well. Finally, the pair correlation functions are calculated as a function of time from the simulation data, and they are also in good agreement with previous studies.

INTRODUCTION

This paper is accompanying the paper (paper I) published earlier in this volume [1], which reported on some new aspects of the bimolecular model reactions, a topic that has been extensively reported upon in the past several years [See references in previous paper]. The anomalous rate law exhibited for reactions in low dimensions is well known, and it is discussed in detail in the previous paper. The new picture reported here gives a quantitative explanation of the spatial distributions of the reacting particles. It is well understood today that the anomaly exhibited is due to specific reasons: For the reaction of similar particles (A+A --> 0) the reason is the formation of a depletion zone in the vicinity of each surviving particle as the reaction proceeds, an effect of very poor "stirring" of particles provided by diffusion. For the reaction of dissimilar particles (A+B-->0) the reason is the segregation of each species from the other, leading to the aggregation of each species, with the end result that the reaction proceeds only at the interface of the aggregates. A main point in paper I was the derivation of a non-Smoluchowski reaction term, relating the reaction to the pair-correlation function rather than its derivative. Our simulations in this paper are designed to check on this point, as well as on the functional form of the pair-correlation function derived in I. Here we probe in more detail the relative positions of the reacting particles. We take into consideration all spatial arrangements that lead to a reaction. For each arrangement we give a proper weight, according to its probability of occurrence. The overall "global" rate can then be derived from the sum of all contributions leading to reaction. Each quantity is also monitored separately in the calculation.

METHOD OF CALCULATION

The numerical simulations of the chemical reactions are performed using the conventional Monte-Carlo techniques described in our earlier papers [2]. Briefly, lattices of size L=1,000,000 sites (1-dim), and L=2,000x2,000 sites (2-dim) are generated. Particles are placed at random positions on the lattice with a stipulation that only one particle can occupy a given site at any time. All particles are placed before the reaction starts (no particle source, i.e. "batch" type). Cyclic boundary conditions are utilized. The reaction proceeds in the usual way. The particles diffuse on the lattice by performing independent forced random walks to nearest neighbor sites. When two particles step onto the same site they react, which means that they are removed from the system. Cyclic boundary conditions are employed at the ends of the lattice for the random walk as well. We monitor the particle density as a function of time for times up to 10,000 steps, which immediately yields the global rate of the reaction. In addition we monitor in 1-dim the number of A-A pairs (two particles on adjacent sites), and the number of A-0-A pairs (two particles separated by only one empty site). For 2-dim lattices we again monitor the A-A and A-0-A pairs, but in addition we also monitor the bent A-0-A pair, bA-0-A, meaning the case where the two A-0 bonds form a 90 degree angle (as opposed to the straight line A-0-A case), which is present as well in the square-lattice topology. The pair (position) correlation function is calculated at a fixed time t in the following way: For every particle we count n, the number of all other particles present in a sampling interval Δr which is at a distance r away from the particle (point of origin). Typically $\Delta r = 10$ sites, and we may go up to r = 1000 sites. We do this in both directions (right and left) from the point of origin, and for all particles present, N. We average the result for all these situations. The correlation function is properly normalized and given here as:

$$g(r,t) = \frac{n}{\Delta r} 2Nr$$

where N is, as above, the total number of particles present in the system, n is the number of particles in the sampling interval of length Δr, and ρ is the density at the time of measurement. Thus g(r,t) gives the normalized probability of finding at time t a particle at distance r away, given that a particle is present at the origin.

RESULTS

Fig. 1 shows the data for the 1-dim A+A reaction. Several single and pair densities, and combinations of pair densities are plotted, as marked. The instantaneous reaction rate obviously depends only on the instantaneous nearest and next-nearest pairs. Using elementary probability arguments, we predict it to be linear with ρ_{AA} + 1/2 ρ_{A0A}. The simulations seem to bear this out, as from the 6 curves plotted the best agreement is received for this function. We notice that there is also a simple relation between ρ_{AA} and ρ_{A0A}. It is also obvious from the figure that the reaction rate is proportional to ρ^3, the non-classical result, rather than to ρ^2. This means that the pair densities ρ_{AA} and ρ_{A0A} do not have a ρ^2 dependence, even at low ρ, in contrast to random distribution statistics [3]. The 2-dim case is analogous to the
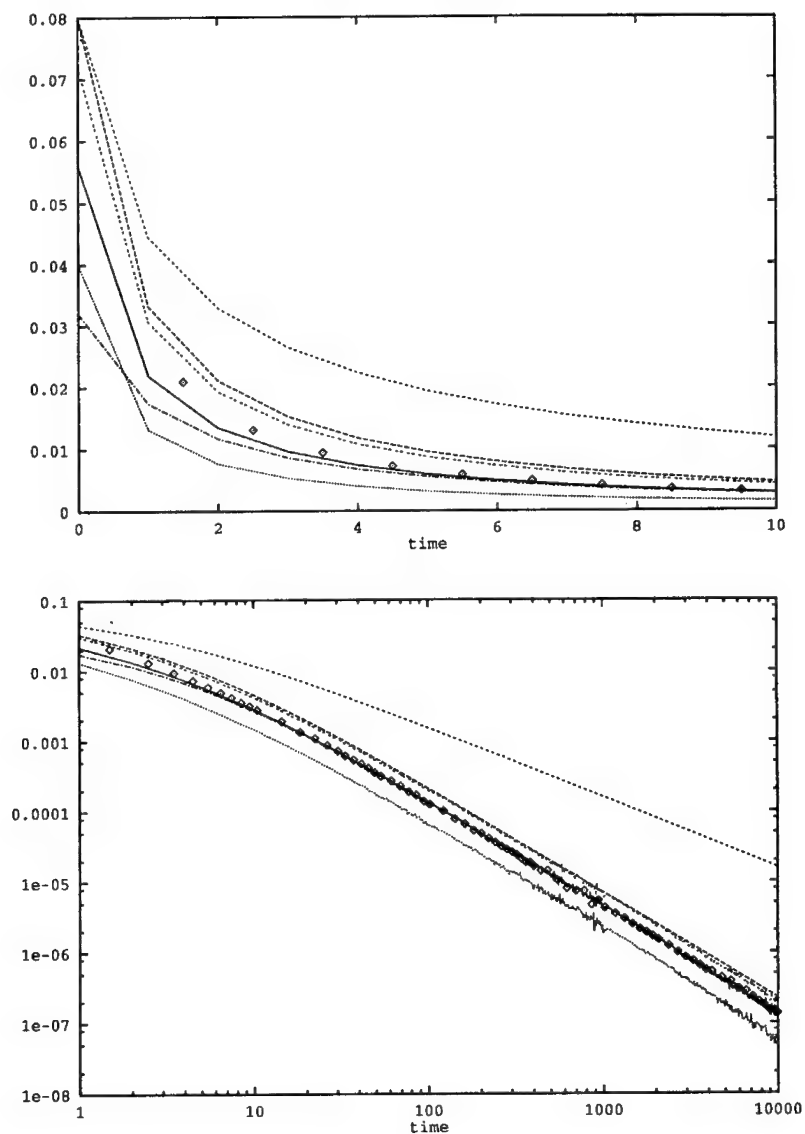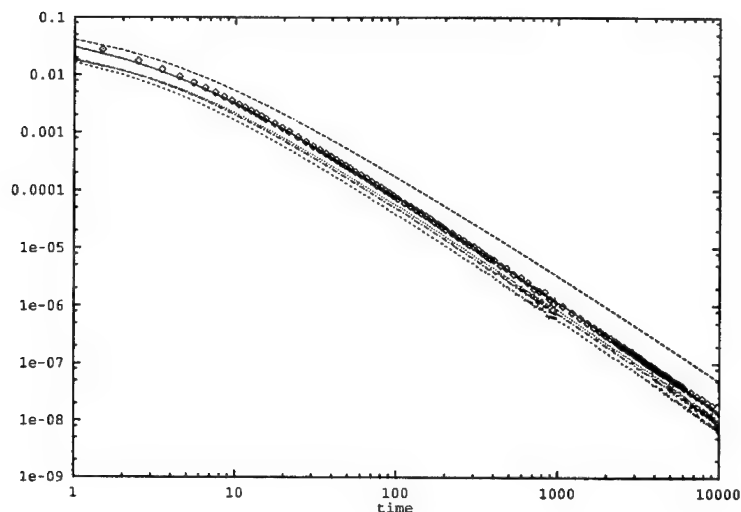
Figure 1: Plot of the rate of the reaction A+A vs. time (diamonds) for 1-dim lattices. Also plotted (top to bottom, right hand side) are the quantities: (i) $2\rho^2$, (ii) $10\rho^3$, (iii) $(\rho_{A0A} + \rho_{AA})$, (iv) $(\rho_{AA} + 1/2\ \rho_{A0A})$, (v) ρ_{A0A}, and (vi) ρ_{AA}. Here the lattice size is $L = 100,000$ sites, $\rho_0 = 0.2$, and 1,000 runs were averaged. Part (a) is a linear plot of the early time behavior (up to 10 steps), and part (b) is a log-log plot, covering a larger range.

Figure 2: Plot of the rate of the reaction A+A vs. time (diamonds) for 2-dim lattices. Also plotted (top to bottom) are the quantities: (i) $2\rho^2$, (ii) $(\rho_{AA} + 1/4\, \rho_{A0A} + 1/2\, \rho_{bA0A})$, (iii) ρ_{bA0A}, (iv) ρ_{A0A}, and (v) ρ_{AA}. Here the lattice size is L = 100,000 sites, $\rho_0 = 0.2$, and 1,000 runs were averaged.

1-dim one. The density behavior is shown in Fig. 2. Here the rate seems to agree with $\rho_{AA} + 1/4\, \rho_{A0A} + 1/2\, \rho_{bA0A}$, again as expected from elementary arguments. However, here the classical rate law (ρ^2 dependence) only differs by a logarithmic correction from the correct one [1]. Both the 1-dim and 2-dim case demonstrate the applicability of our "non-Smoluchowski" reaction term (eq. 11 of paper I). They also demonstrate the simplicity of this approach.

The correlation function g(r,t) can be calculated from the particle positions at certain fixed times t [4]. It is shown in figure 3 for several different fixed times, ranging from t = 100 steps to t = 10^6 steps. One notices that at long times the lines have more noise. This is because there are fewer particles left and the statistics is not so good as at early times. As expected, at large values of r, for all lines, g(r,t) =1, as there is no long-range order in the system. The interesting features occur at small r, as shown in figure 3. A depletion region forms around each particle and grows with time. This is seen from the several curves which, for longer times, need a larger r to reach the asymptotic value of g(r,t) =1. If we assume that (eq. 49 of paper I) is correct, then we can scale all curves corresponding to different times by the function:
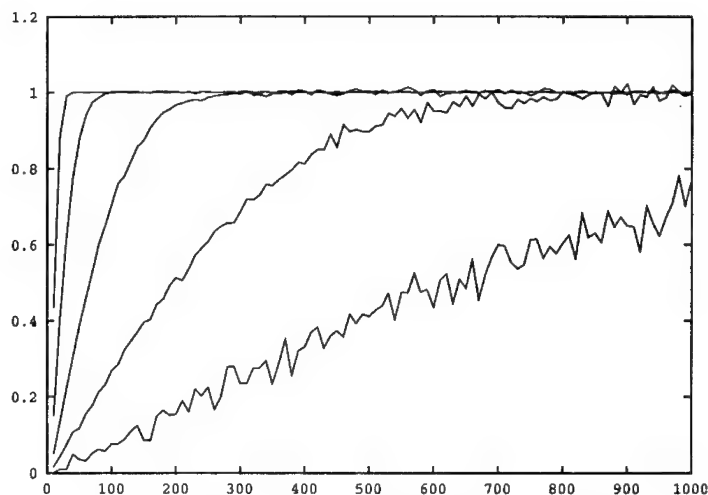
$$r/[2(Dt)^{1/2}]$$

398

Figure 3: Correlation function g(r,t) vs. the distance r for several different times in the course of the reaction A+A: t = 100, 1000, 10,000, 100,000, and 1,000,000 steps (left to right). The initial reaction density is $\rho_0 = 0.8$, the 1-dim lattice size is 1 million sites, and 500 realizations were averaged. The sampling interval Δr for the function calculation is $\Delta r = 10$ sites.
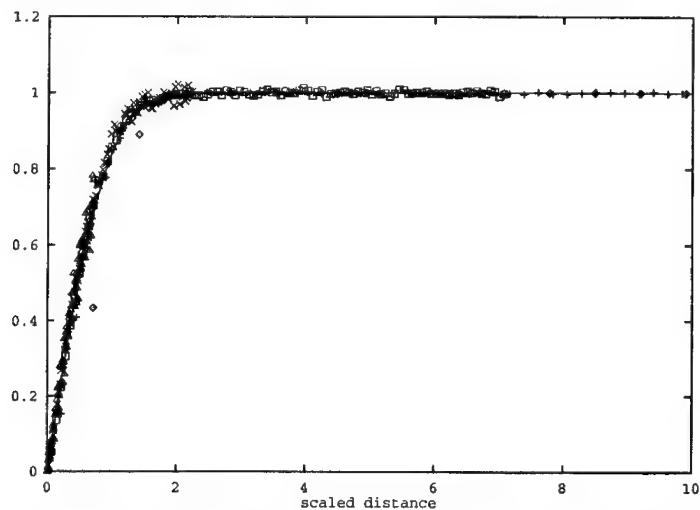

Figure 4: The correlation function vs. the scaled distance for the A+A reaction. The x-axis here is $r/[2(Dt)^{1/2}]$, where D is the diffusion coefficient (here D = 1/2).The data is the same as used in the previous figure. All five simulation curves fall right onto the theoretical continuous line which is derived from eq. 49 of paper I. The only possible exception is the early time (100 steps) short r points (diamonds).
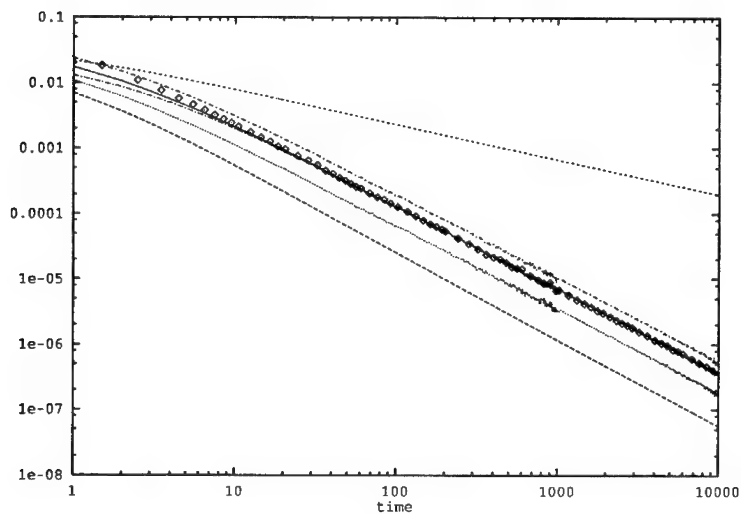
Figure 5: Plot of the rate of the reaction A+B vs. time (diamonds) for 1-dim lattices. Also plotted (top to bottom, right hand side) are the quantities: (i) ρ^2, (ii) $\rho_{A0B}+\rho_{AB}$, (iii) ($\rho_{AB} + 1/2\rho_{A0B}$), (iv) ρ_{A0B}, (v) ρ_{AB}, and (vi) $100\rho^5$. Here the lattice size is L = 100,000 sites, ρ_0 = 0.2 of each species, and 1000 runs were averaged.
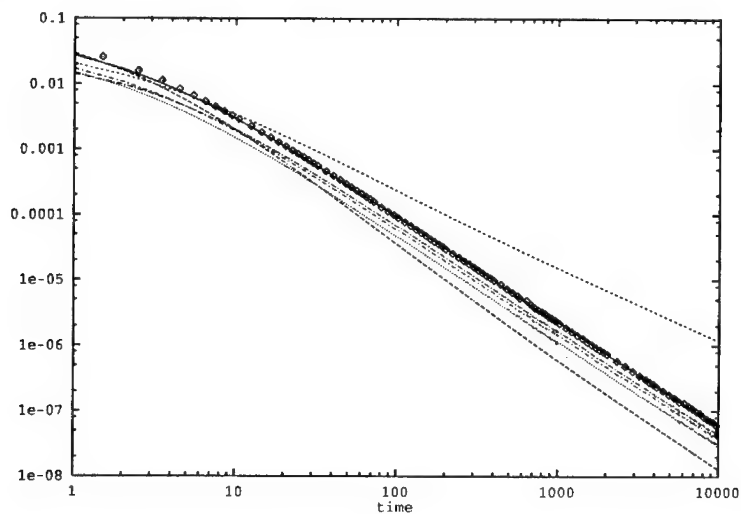

Figure 6: Plot of the rate of the reaction A+B vs. time (diamonds) for 2-dim lattices. Also plotted (top to bottom) are the quantities: (i) ρ^2, (ii) ($\rho_{AB} + 1/4$ $\rho_{A0B} + 1/2$ ρ_{bA0B}), (iii) $10\rho^3$, (iv) ρ_{bA0B}, (v) ρ_{A0B}, and (vi) ρ_{AB}. Here the lattice size is L = 100,000 sites, ρ_0=0.2 of each species, and 1,000 runs were averaged.
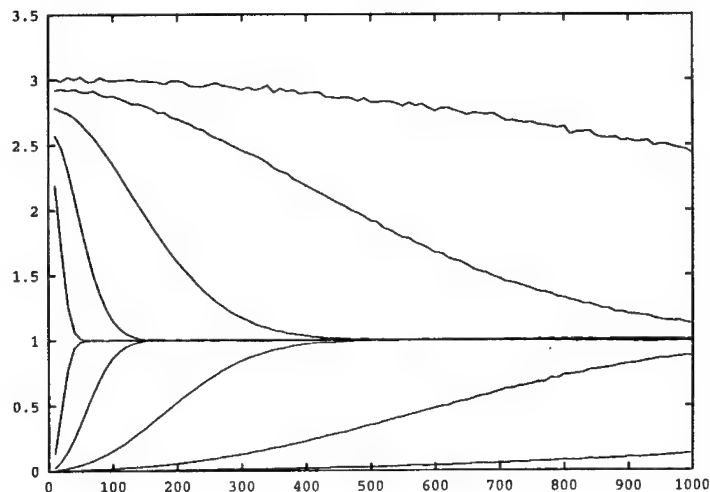
Figure 7: Correlation function g(r,t) vs. the distance r for several different times in the course of the reaction A+B: t = 100, 1000, 10,000, 100,000, and 1,000,000 steps (left to right). The initial reaction density is $\rho_0 = 0.4$ of each species, the 1-dim lattice size is 1 million sites, and 500 realizations were averaged. The sampling interval Δr for the function calculation is $\Delta r = 10$ sites. The top curve is for like-like particle correlation, the bottom curve for like-unlike correlations.
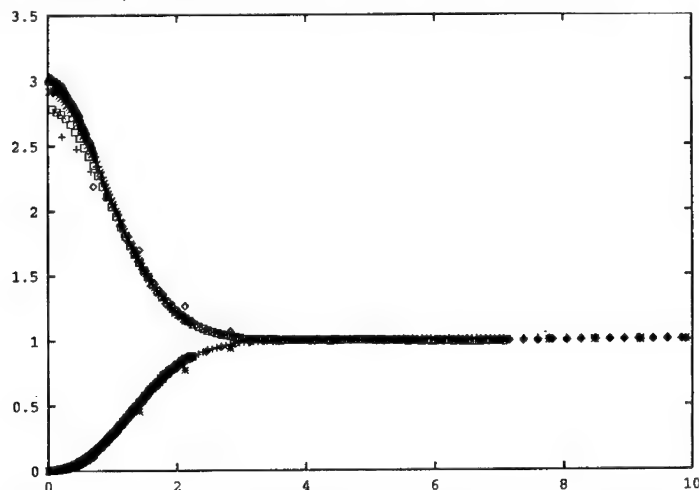

Figure 8: The correlation function vs. the scaled distance for the reaction A+B. The x-axis here is $r/[2(Dt)^{1/2}]$, where D is the diffusion coefficient (here D = 1/2).The data is the same as used in the previous figure. All five simulation curves for the like-unlike correlations (bottom curve) fall right onto the theoretical continuous line which is derived from eq. 49 of paper I. The only possible exception is the early time (100 steps) short r points (diamonds).

which is the argument of the error function in that equation. This is done in figure 4, where the x-axis now is $r/[(2t)^{1/2}]$ Here we used $D=1/2$ for 1-dim, and the y-axis is identical to the previous figure. We emphasize here that the scaling is very good, and that these curves are in very good agreement with the error function (eq. 49 of ref. 1), except for a factor of square root of 2.

Figs. 5-8 show the results for the A+B case. Several combinations of densities are plotted, and the best agreement is received for the function: $\rho_{AB} + 1/2\ \rho_{A0B}$ (1-dim lattices), and $\rho_{AB} + 1/4\ \rho_{A0B} + 1/2\ \rho_{bA0B}$ (2-dim lattices), as expected from simple probability arguments.

DISCUSSION AND CONCLUSIONS

Based on simulations we find a clear-cut correlation between the instantaneous reaction rate and the instantaneous pair densities. The non-classical kinetics is thus expressed by the non-randomness of the pair distributions. This is fully consistent with the derivation of the analytical theory [1] and in contrast with the Smoluchowski reaction term. However, the linear relation between nearest and next-nearest neighbors (e.g. AA and A0A) means that the difference $(\rho_{AA} - \rho_{A0A})$ is also linear with the reaction rate. The latter may explain why the Smoluchowski reaction term, given by the gradient of the pair density, accounts almost as well [1] for the reaction term (within a constant), for the A+A reaction. Finally, our simulations agree quite well with the analytical result [1] for the pair-correlation function in one dimension.

ACKNOWLEDGMENTS

REFERENCES

(1)K.Lindenberg, R.Kopelman, and P.Argyrakis, article in this volume.
(2)K.Lindenberg, R.Kopelman, and P.Argyrakis, J.Phys.Chem., In press.
(3)J.Hoshen and R.Kopelman, Phys. Stat. Sol. B, 81,479(1977).
(4)A. Blumen, S. Luding, and I. M. Sokolov, J. Stat. Phys. 65, 849 (1991).

SCALING OF REACTION FRONTS
IN THE PRESENCE OF DISORDER

Mariela Araujo

Intevep S.A. Apartado 76343, Caracas 1070A. Venezuela

ABSTRACT

A study of the dynamics of the reaction front that appears in diffusion-reaction systems of the form $A + B \rightarrow C$ with initially separated reactants in the presence of quenched disorder is presented. The scaling of the width of the front w is analyzed as a function of the "disorder strength" and the dimensionality of the system. It is shown that disorder strongly affects the width exponent α, $w \sim t^{\alpha}$ even for $d \geq 2$, where the mean field approximation is known to be valid. The scaling of the nearest neighbor distance, midpoint fluctuations and concentration profiles near the center of the front, are also studied.

INTRODUCTION

Reaction front dynamics for reactions of the form $A + B \rightarrow C$ have attracted considerable interest in recent years [1-13]. The interest stems out not only from its applications in many areas such as heterogenous catalysis, biological, and physical systems [16], but also from the anomalous behavior observed in low dimensional systems, that is not yet completely understood. The reactive species A and B are transported by diffusion, and when in contact react instantaneously to produce the inert species C. Most of the previous work on this reaction, have studied the case where both reactants are initially randomly mixed (homogeneous initial conditions)[1-13]. The segregated case, in which the reactants are initially separated in space has also been considered, although less extensively. In either case, fluctuations are important at low dimensionality [4,8,11]. In segregated systems, reactions take place in a localized region called the "reaction front", whose dynamics is studied here.

The reaction front is generally described in terms of two exponents α and β, that indicate how its width and height change asymptotically with time, $w \sim t^{\alpha}$, $h \sim t^{\beta}$. Without disorder, and for $d \geq 2$, it has been shown that the kinetics of the system is well described by a set of mean-field type of equations [1,4]

$$\frac{\partial c_i}{\partial t} = D_i \frac{\partial^2 c_i}{\partial x^2} - k c_i c_j \tag{1}$$

where $c_i \equiv c_i(x,t)$ for i = A,B are the concentrations of reactants A and B at position x and time t respectively, $D_{A,B}$ are the diffusion constants and k is the reaction constant. The reaction front profile is given by $R(x,t) \equiv k c_A c_B$ and has the asymptotic form [4] $R(x,t) \sim t^{-2/3} \left(x/t^{1/6}\right)^{3/4} \exp[-2/3(\lambda x/t^{1/6})^{3/2}]$. Thus, the

width scales with time as $w \sim t^{\alpha}$ with $\alpha = 1/6$. The height of the front scales as $h \sim t^{-\beta}$ with $\beta = 2/3$. These values were also obtained using scaling arguments, and confirmed by experiments and simulations [1-13].

The situation is not so simple for reactants "confined" to one dimension. For $d = 1$ eqn. (1) does not hold, because the reaction term can not be written as a product of the average reactant concentrations. It was found [11] that α lays in the range $1/4 \leq \alpha \leq 1/3$, depending on the moment at which the width is calculated. These two numerical values are associated with two related quantities: the $1/4$ is related to the scaling of the nearest neighbor distance between particles A and B ($l_{AB} \sim t^{1/4}$), and the $1/3$ with the fluctuations in the location of the midpoint between these particles. On the other hand, recent work by Cornell [14] suggest that the reaction front scales with $\alpha = 1/4$. The origin of the difference between the exponents in $d = 1$ and those in higher dimensions is due probably to fluctuations in the location of the front, which are important in low dimensions and are neglected in the mean field approach.

In this paper we study how the width of the reaction zone is affected by the presence of strong quenched disorder, effectively reducing the diffusion constants of the A and B particles. We also study the concentration profiles of the reactants, and their scaling near the center of the reaction front.

FRONT AND CONCENTRATION PROFILES

We consider systems with two types of particles, A and B, that diffuse on a lattice. Initially the A's occupy the sites located to the left of the origin, whereas the B's occupy the right hand side. The A and B particles have the same diffusion constant $D_A = D_B$, and are initially in the same concentration $c_o = 1$. The lattice has a quenched disorder, represented in the following way: at each lattice site, there is a disorder variable, τ, taken from a power law distribution $p(\tau) = \nu \tau^{\nu-1}$, with $0 < \nu < 1$ and $0 < \tau < 1$. Each time a particle "attempts" to move, a random number between 0 and 1 is generated and compared with the value of the disorder variable at the site where the particle is in, if it is less or equal to it, it will move to a neighbor site with equal probability, else it stays in. In this case, the mean squared displacement scales as $\langle x^2 \rangle \sim t^{2/d_w}$, with the diffusion exponent d_w, $d_w = (1+\nu)/\nu$ for $d < 2$, and $d_w = 2/\nu$ for $d \geq 2$) and $d_w \geq 2$ [17]. If any two A and B particles meet on a site, they immediately react to produce an inert species C. The dynamics of the C particles does not affect the diffusion and/or reaction of particles A's and B's. The reaction front $R(x,t)$ is defined as the average number of C particles produced at position x and time t, thus it is the localized region where reactions take place.

To measure the width of $R(x,t)$ we calculate the spatial moments of the reaction front. Since $D_A = D_B$, the center of the reaction zone remains stationary at the origin. In our simulations, we start with a disorder configuration and let the system

evolve up to a given time. At each unit of time a particle is selected at random and it given the chance to move to any of its neighbor sites. After moving all the particles on average, the occurrence of reactions is checked for. Averages are taken over many ($\sim 10^4$) disorder configurations. The integral in time of the reaction front (which is the concentration profile of the inert C particles, $C_c(x,t)$) is measured in the simulations. The moments of the front are calculated $\langle |x|^q \rangle^{1/q}$ for $q > 0$.

$$\langle |x|^q \rangle \equiv 2 \frac{\int_0^\infty x^q R(x,t) dx}{\int_o^\infty R(x,t) dx} \sim t^{1/d_w} \frac{d}{dt} \int_o^\infty x^q C_c(x,t) dx \qquad (2)$$

We find that for particles confined to $d = 1$

$$\langle |x|^q \rangle^{1/q} \sim t^{\alpha(\nu)}. \qquad (3)$$

The moments of the reaction front appear to follow a simple scaling relation with an exponent that depends on the strength of disorder. This is shown in Figure 1.
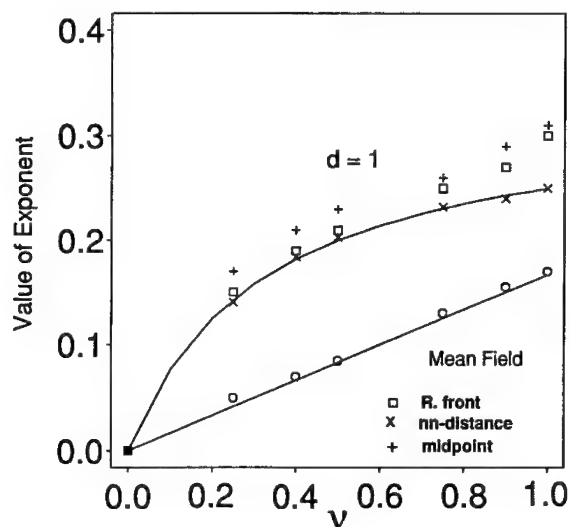

Figure 1. Values of α from the second moment of the reaction front for confined ($d = 1$), and mean field systems ($d \geq 2$). Solid lines correspond to empirical prediction from scaling of l_{AB}. The values of the exponents σ and δ of the scaling of l_{AB} and $m(t)$ for $d = 1$ are also shown.

The scaling behavior of the concentration profiles of species A and B near the origin was also studied. It was found that

$$C_i(t) \sim \left(x/t^{1/d_w}\right)^\gamma, \tag{4}$$

with γ depending on ν according to the empirically determined relation $\gamma = (1 + \nu)/2(2 - \nu)$. This scaling form is clearly appreciated in Figure 2, where data for $d_w = 5(\nu = 1/4)$ is shown for times from 2000 to 32000 unit steps.

As in Ref. [11], we find that in order to properly describe the behavior of the reaction zone for particles confined to $d = 1$, one needs to study the fluctuations of two quantities: the distance between the rightmost A particle and the leftmost B, which we call the nearest neighbor distance l_{AB}, and the midpoint $m(t)$. Note that reactions may occur in between the position of these two extreme particles,– just at $m(t)$–, and provided that $l_{AB} = 0$. We found that the scaling of moments of l_{AB} and $m(t)$ with time involve a single exponent, namely

$$\langle l_{AB}^q(t) \rangle^{1/q} \sim t^\sigma \qquad \xi(t) \equiv \langle m^q(t) \rangle^{1/q} \sim t^\delta, \tag{5}$$

with σ and δ dependent on disorder. Empirically we determined the relation $\sigma = \nu/(1 + 3\nu)$. Figure 1 shows the dependence of these two exponents as a function of the disorder parameter ν.

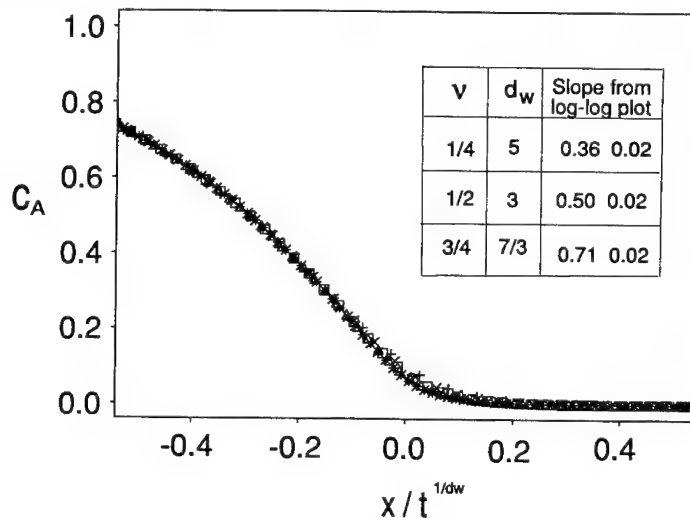| ν	d_w	Slope from log-log plot	
1/4	5	0.36	0.02
1/2	3	0.50	0.02
3/4	7/3	0.71	0.02

Figure 2. Scaling plot of the concentration profile of species A, $C_A(x,t)$ (near the center of the front) as a function of the reduced variable $x/t^{1/d_w}$ for $d_w = 5(\nu = 3/4)$ and times $t = (2, 4, 8, 16, 32) \times 10^3$ unit steps. The inset shows γ values from the slope of log-log plot (See eqn.(4)).

For $d \geq 2$, we did simulations on a lattice with quenched disorder, and found that as for the case without disorder, the kinetics is well described by the set of mean field reaction diffusion equations (1), where the reaction term is proportional to the product of the average concentration of reactants. The presence of disorder is accounted in the same way as for $1D$ systems. The mean field equations (1) are discretized and the reactant concentrations A and B, are calculated as a function of time by first considering solely the diffusive step with the disorder restriction, and then taking into account possible reactions. The reaction front R is calculated following Taitelbaum et al. [5], and from it, we calculate the width of the reaction zone using different moments, i.e., $w = \langle x^q \rangle^{1/q}$ for $q > 0$. It is found that the same scaling with time is obtained for any $q > 0$ ($w \sim t^\alpha$) with α also dependent of the disorder strength, as shown in Figure 1. Empirically, we find the relation $\alpha(\nu) = \nu/6$. For $d \geq 2$ the relation between d_w and the disorder exponent is $d_w = 2/\nu$. For the scaling of the concentration profiles near the center of the front we find a simpler relation, $c_i(x,t) \sim x/t^{1/d_w}$. Within the time range studied here deviations from this form were not observed.

DISCUSSION AND CONCLUSIONS

We have found that quenched disorder from a power law distribution strongly affects the exponent α that describes how the width of the reaction front scales asymptotically with time. The scaling of a related quantity, l_{AB} (the nearest neighbor distance between A and B particles), sets a lower bound for the value of this exponent. This is also the case for the same systems without disorder [11], and there is suggesting evidence that the scaling of this quantity gives the scaling of the reaction front in the asymptotic limit [15]. For systems in $d \geq 2$, an implicit assumption is that just one length scale describes the typical nearest neighbor distance. From the numerical data there is no clear indication of the existence of multiscaling of the reaction from in the presence of disorder, as appear to be the case for confined systems without disorder.

The scaling of the concentration profiles near the center of the front is severaly modified for $1D$ systems. A similar scaling in concentration profiles and nearest-neighbor distance was found in the trapping problem on a disordered lattice by Taitelbaum et al. [18].

For any dimension, we found that as the disorder strength increases, i.e, d_w increases, the width exponent α becomes smaller. This is explained by the fact that for very strong disorder the particles practically do not diffuse, and therefore the reaction zone does not grow.

The scaling relation between α and β, the width and height exponents of the reaction front, and the flux of particles at its center is still valid [1-2,6-9]. For disordered systems it is written in terms of the diffusion exponent d_w, as $\alpha - \beta = 1/d_w - 1$.

ACKNOWLEDGMENTS

REFERENCES

[1] L. Gálfi and Z. Rácz, Phys. Rev. A **38**, 3151 (1988).

[2] Z. Jiang and C. Ebner, Phys. Rev. A **42**, 7483 (1990).

[3] E. Ben-Naim and S. Redner, J. Phys. A **25**, L575 (1992).

[4] H. Larralde, M. Araujo, S. Havlin, and H.E. Stanley, Phys. Rev. A **46**, 855 (1992).

[5] H. Taitelbaum, S. Havlin, J. Kiefer, B.L. Trus, and G.H. Weiss, J. Stat. Phys. **65**, 873 (1991).

[6] Y.E. Koo, L. Li, and R. Kopelman, Mol. Cryst. Liq. Cryst. **183**, 187 (1990); Y.E. Koo and R. Kopelman, J. Stat. Phys. **65**, 893 (1991).

[7] H. Larralde, M. Araujo, S. Havlin and H.E. Stanley, Phys. Rev. A **46**, R6121 (1992).

[8] S. Cornell, M. Droz, and B. Chopard, Phys. Rev. A **44**, 4826 (1991).

[9] B. Chopard, M. Droz, T. Karapiperis, and Z. Rácz, Phys. Rev. E **47**, 40 (1993).

[10] S. Havlin, M. Araujo, H. Larralde, A. Shehter and H.E. Stanley, Fractals **1**, 475 (1993).

[11] M. Araujo, H. Larralde, S. Havlin and H.E. Stanley, Phys. Rev. Lett. **71** 3592 (1993).

[12] S. Redner and F. Leyvraz, J. Stat. Phys. **65**, 1043 (1991) ; F. Leyvraz and S. Redner, Phys. Rev. A **46**, 3132 (1992).

[13] S. F. Burlastsky. Teor. Eskp. Kim. **14**, 483 (1978) ; P. Meakin and H.E. Stanley, J. Phys. A **17**, L173 (1984) ; K. Kang and S. Redner, Phys. Rev. Lett. **52**, 955 (1984).

[14] S. Cornell, preprint 1994.

[15] B.P. Lee and J. Cardy, preprint 1994.

[16] D. Avnir and M. Kagan, Nature **307**, 717 (1984); G.T. Dee, Phys. Rev. Lett. **57**, 275 (1986); B. Heidel, C. M. Knobler, R. Hilfer and R. Bruinsma, Phys. Rev. Lett. **60**, 2492 (1986); R. E. Liesegang, Naturwiss, Wochensch **11**, 353 (1896) ; T. Witten and L. Sander, Phys. Rev. Lett. **47**, 1400 (1981) ; R. A Ball, Ausr. Gemmol. **12**, 89 (1984).

[17] S. Havlin and D. Ben-Avraham, Adv. in Phys. **36**, 695 214(1987).

[18] H. Taitelbaum and G.H. Weiss, Phys. Rev. E, **50**, 2357 (1994).

REACTION KINETICS AT A FLUCTUATING SURFACE: PROTON EXCHANGE IN PROTEINS

T. GREGORY DEWEY
Department of Chemistry, University of Denver, Denver, CO 80208.

ABSTRACT

Experimental data for the exchange of protons between proteins and the aqueous solvent is re-examined using a fractal model. The fraction of protons unexchanged from the protein, f, is seen to follow a stretched exponential, $f \sim \exp\left\{-(t/\tau)^{\alpha}\right\}$ at long times. For the protein, lysozyme, data over a range of temperatures were considered and accurate fits were obtained with a single, unadjusted scaling exponent, α. The time constant, τ, followed an Arrhenius law and gave an activation energy comparable to that obtained for free peptide exchange. A model is proposed where proton exchange occurs as a result of solvent reacting at the fractal surface of the protein. The protein itself is not treated as static but has units that diffuse to the surface. The diffusion of these units in the long time domain is assumed to be classical. In this model the scaling exponent, α, is related to the spectral dimension of the system. Treating the problem as a reaction of the type A+B→C in a confined region, the exponent is given by: $\alpha = (3 - d_s)/4$ where d_S is the fractal surface dimension of the protein. Using the value of 2.17 previously established for the surface dimension of lysozyme, data at 6 different temperatures could be fit with the corresponding α of 0.21. These results show that the fractal structure of a protein can influence diffusional processes of small molecules associating with the protein.

HYDROGEN EXCHANGE IN PROTEINS

With the initial success of X-ray crystallography in biochemistry, there became a view of proteins as static, rigid structures. A number of kinetic experiments served to dispel this view [1]. One of these was the observation of exchange of hydrogen atoms from a protein to the aqueous solvent. Hydrogen exchange in proteins is a hydroxyl or hydronium ion-catalyzed process that occurs over many orders of magnitude in time. Even groups that appear buried in the X-ray structure are capable of exchanging with the solvent. Thus, this experiment reveals the dynamic nature of the solution structure of a protein. There have been a number of models developed over the years to describe the kinetics of such exchange processes [1]. Most of these involve a description of a distribution of rate constants and, often, do not provide a physical picture of the process. Recently, an attempt was made to relate the surface morphology of the protein, via its fractal surface dimension, to the scaling exponent in a

stretched exponent [2]. This model provides an excellent fit to hydrogen exchange data in lysozyme over a wide temperature range. It is also consistent with data from the peptide, pancreatic trypsin inhibitor. In the present work, we enumerate the assumptions of the previous model and provide a more rigorous outline of the theoretical justification for the assumptions. Hydrogen exchange reactions have reasonably large activation energies (approximately 20 kcal/mole) and, therefore, are "chemically-controlled" reactions. For proteins such reactions occur in a restricted geometry and are characterized by time-dependent rate constants. Consequently, a complete kinetic model must incorporate both diffusive and chemical steps within a single formalism. Such a kinetic model should have general application to chemically-controlled reactions in restricted geometries.

Hydrogen exchange is often monitored by observing the "out-exchange" of tritium. Initially, a protein is exposed to tritiated water for an extended period of time. It is then removed from this environment and put into normal water. At fixed time periods, the protein is removed and the amount of tritium remaining on the protein is measured by scintillation counting. Figure 1a and 1b shows the results of such an experiment (data from [3]). The data is for the protein, lysozyme with (1b) and without (1a) an enzymatic inhibitor bound to it. Bound molecules tend to restrict the dynamics of the protein. As can be seen in both cases, the
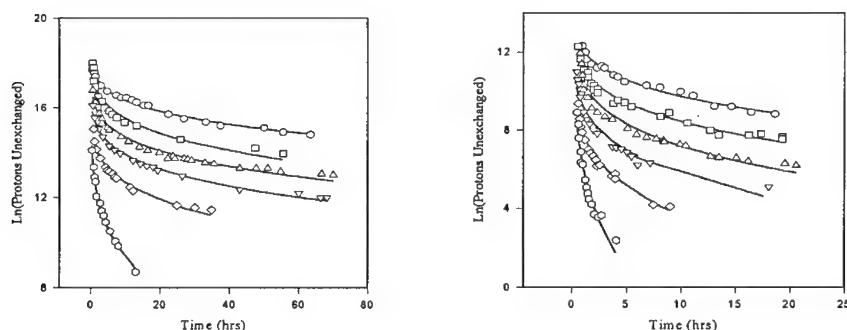

Figure 1. Plot showing the proton exchange kinetics of lysozyme. Log of the concentration of unexchanged protons versus time is shown for six different temperatures. Figure 1a is lysozyme with an inhibitor bound. Figure 1b is without inhibitor. From top to bottom the temperature is 2 °C (O), 10 °C(□), 16 °C (Δ), 23 °C (∇), 31 °C (◊) 41 °C (○). Solid lines are curves obtained from a two parameter, non-linear least squares fit to a stretched exponential (Eq. 4) with the parameter, α, held fixed at 0.21 for all temperatures.

plots of log(tritium unexchanged) versus time shows considerable curvature. This is indicative of a stretched exponential dependence and these data points are accurately fit by such a function. This dependence occurs over a wide temperature range. The major contribution to the exchange reaction is from hydrogens in the amide backbone of the protein. The reaction is of the type, A+B→C+D, where A is the tritiated amide linkage in a protein, B is H_3O^+ (or OH$^-$ depending upon the pH), C is the amide linkage with a hydrogen replacing the tritium

and D is TH_2O^+ (or OT^-). The time course of the reaction can be represented by a macroscopic rate law that has a time-dependent rate constant:

$$-\frac{d[A]}{dt} = k(t)[A][B] \qquad (1)$$

where the brackets represent the concentration of the respective species and the rate constant, k, is a function of time. Since experiments are carried out in buffered solutions, [B] is essentially a constant and the reaction is pseudo-first order in A.

Time-dependent rate constants appear frequently in reaction kinetics in inhomogeneous or restricted environments. From theoretical arguments and computational results, it is seen that the rate constant scales with time as a fractional power law [cf. 4-7]:

$$k(t) = k't^{-h} \qquad (2)$$

where k' is a time-independent constant and the exponent h is restricted to values between 0 and
1. This exponent is related to the spectral dimension, $\bar{d}$, of the system and the functional form will depend on the universality class of the reaction. For instance, in the case of A+B→ C+D, it is seen that $h = 1 - \bar{d}/4$ [cf. 6]. The exponent is given by:

$$1 - h = \bar{d}/4 = d_f/2d_w \qquad (3)$$

where d_f is the fractal dimension of the spatial region that the reaction occurs and d_w is the walk dimension. The walk dimension characterizes the diffusion of the reactants and is related to the mean squared displacement, r^2, by: $r^{d_w} \sim t$. The right hand side of Eq. 3 has been derived from general theoretical considerations [cf. 4-7].

In previous work, this formalism was used to interpret data as in Figure 1 [2]. Thus, Eq. 3 provides a means of predicting the time course of the data in Figure 1. For the pseudo-first order conditions of interest in hydrogen exchange, Eq. 1 can be directly integrated to give a stretched exponential. The expression is of the form: $[A] \propto \exp\left\{-(t/\tau)^{1-h}\right\}$ where τ is a reciprocal rate constant. To estimate *(1-h)*, the following the assumptions are made:

1. The solvent does not penetrate the protein core.

2. Protein side chains make excursions into the boundary volume as a result of fluctuations in protein structure.

411

3. As a consequence of 1 and 2, the reaction must occur in the boundary volume. The fractal dimension of the boundary volume is given by: $d_f = 3 - d_s$ where d_s is the surface dimension of the protein. The boundary volume is the complementary space of the surface fractal. The fractal surface dimension of lysozyme was previously determined in a careful study [8] and found to be 2.17. Thus, the fractal dimension of the reaction volume is 0.83.

4. The walk dimension of the solvent is 2. The solvent diffuses normally to the reaction volume.

5. In the long time limit, the walk dimension of protein side chains is also 2. Protein side chains will diffuse through fluctuations in the protein structure. This is akin to monomer diffusion in polymer melts [cf. 9]. In this latter case, the short time diffusion will be anomalous while the long time limit will be classical, i.e., $d_w = 2$. It is proposed that proteins will show comparable behavior.

With the assumptions of the model, it is seen that $1 - h = (3 - d_s)/4 \approx 0.21$. The curves in Figure 1 were fit using a non-linear least squares routine to an equation of the form:

$$f = A \exp\left\{-(t/\tau)^{0.21}\right\} \tag{4}$$

where f is the fraction of tritium unexchanged, A and τ, are adjustable parameters. As is seen from Figure 1, accurate fits can be obtained at all temperatures using a fixed, unadjusted exponent. The parameter A represents the fraction of tritium at time t=0. As can be seen from Figure 1, comparable values for A will be obtained at all temperatures. It is not anticipated that the protein's solution structure would vary significantly over this temperature range, because structural sensitive properties, such as enzymatic activity, are not compromised. Consequently, it is unlikely that their are any gross morphological changes in the enzyme. It is, therefore, anticipated that the fractal surface dimension will be insensitive to changes in temperature and it is unlikely that the scaling exponent will have a large temperature dependence.

Arrhenius plots derived from the fitted relaxation times are shown in Figure 2. From the slopes of these plots, activation energies of 18±3 kcal/mole without bound inhibitor and 24±4 with bound inhibitor were obtained. These are comparable to the value of 17.5 kcal/mole observed for proton exchange in free peptides [10]. For aqueous solutions under these conditions, it is anticpated that approximately 4 kcal/mole of the activation energy is due to viscosity effects and the remainder is due to the chemical barrier. It is then seen that in addition to accurately fitting the data in Figure 1, the temperature-dependence of the relaxation times give realistic value for the activation barrier. It is interesting to note that the addition of the inhibitor to the enzyme, has only a small effect on the activation energy. In general, it is thought that binding a substrate to an enzyme greatly restricts the flexibility of the protein chains. This effect appears in the entropy of activation rather than in the activation energy.

Figure 2. Arrhenius plots obtained from fitting the data in Figure 1 to Eq. 4. Top line (circles) is lysozyme with bound inhibitor and bottom line (squares) is without.
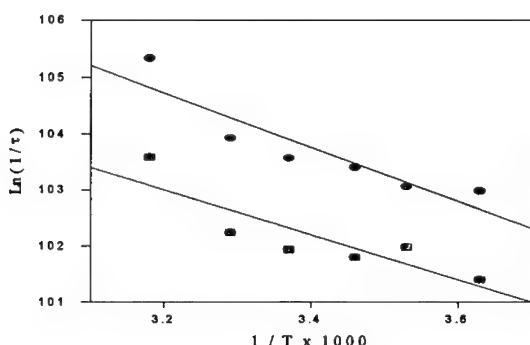
ROLE OF DIFFUSION IN CHEMICALLY-CONTROLLED REACTIONS

The activation parameters observed in Figure 2 and also those observed for simple peptides in solution are much higher than expected for diffusion-controlled reactions in aqueous solutions. Yet the formalism of Eq. 2 and 3 pertains to diffusion-controlled reactions. The reaction is also unusual in that reactants diffuse to but do not diffuse within the "reaction volume". This is a consequence of the boundary volume having a dimensionality less than one. To accommodate these features, a more detailed kinetic model must be developed than described above. To account for the "chemical-control" of the reaction a standard and general description of solution phase reactants is used. The reaction is considered to occur in two steps. First, the reactants diffuse into the vicinity of each other to form an "encounter" or "outer sphere" complex. This complex is often viewed as the two reactants separated by their respective solvation spheres. This step will be strictly diffusion-controlled and, when appropriate, will follow the rate law dictated by Eq. 1 and 2. The second step of the reaction involves the collapse of the outer sphere complex to the final product. This is the chemically controlled step. In cases where the chemical step is very fast, the overall reaction will be diffusion-controlled. With traditional homogeneous phase kinetics, very slow chemical steps will drastically reduce the influence of the diffusive process on the rate of the reaction. As will be seen in the present work, this will not be the case for chemically controlled reactions that have time-dependent diffusional steps. Because of the decreasing rate constant in Eq. 2 decreases with time, a time domain will always exist were the reaction achieves the diffusion limit.

This mechanism for this two step processes is given by:

$$A + B \underset{k_{-1}}{\overset{k_1}{\longleftrightarrow}} A \bullet B \underset{k_{-2}}{\overset{k_2}{\longleftrightarrow}} C \qquad (4)$$

where $A \bullet B$ is the encounter complex and the rate constants with positive (negative) subscripts are forward (reverse) reactions. The diffusive steps (k_1 and k_{-1}) will be time-dependent and the constants characterizing the chemical steps, (k_2 and k_{-2}), are time-independent rate constants. These constants are dictated by the nature of the potential energy surface of the chemical process. A consequence of chemical-control is that the diffusive step is reversible. Reversible diffusion controlled reactions have not received the considerable attention as irreversible ones, yet there is a significant literature in this area [11-14]. The theoretical development for determining the forward reaction can often be adapted by a change of boundary conditions to consider the reverse reaction [cf. 11, 15]. Kang and Redner [6] derived the time dependent rate constant in Eq. 2 from scaling arguments and conservation considerations. For the diffusion-controlled reaction of the type (A+B), a constant of motion of the system is ([A(t)]-[B(t)]). The conservation of this quantity is exploited to yield Eq. 2. In the current, reversible, chemically-limited mechanism ([A(t)]-[B(t)]) is still a constant of motion and Kang and Redner's arguments still hold. Thus, the rate constant k_1 takes the form $k_1(t) = k_1' t^{-h}$. One could argue for a comparable dependence for k_{-1}. An equilibrium constant, K_1, can be determined for the formation of the outer sphere complex using general arguments [12, 15]. This will be a time-independent quantity and is equal to k_1/k_{-1}. Thus, the reverse rate will be: $k_{-1} = k_1' t^{-h}/K_1$ and an identical scaling is retained for the diffusive dissociation of the complex as for the association. Alternatively, one could justify this dependence from an approach comparable to Kang and Redner [6]. For the reaction A+B$\leftrightarrow$C+D, there are now two constants of motion; ([A(t)-B(t)]) and ([A(t)]+[C(t)]). From the first constant and a scaling Ansatz, one has $[A(t)] \sim t^{h-1}$. This dependence implies that Eq. 2 is the functional form for the forward rate constant. A second conservation relationship gives: $[C(t)] = C_{tot} - A(t) = C_{tot} - A' t^{h-1}$ where C_{tot} is the total amount of reactant present and A' is a constant. The form derived from this second relationship implies an identical scaling of the reverse constant as for the forward rate constant.

To derive an expression for the diffusional steps in the above process, the formalism and results of a kinetic problems treated by Zwanzig and Szabo are examined [16]. They considered the problem of ligands in the bulk solution diffusing and binding to receptors partially covering the surface of a sphere. This time-dependent treatment of the problem considers the diffusive interference of different receptors on the sphere. It proves convenient to define the Laplace transform of the diffusive rate constant, $\hat{k}(s)$, by:

$$\hat{k}(s) = \int_0^\infty e^{-st} k(t) dt \tag{5}$$

In this problem, two diffusional fluxes were considered: flux to the surface of the sphere and flux to the receptors. It was shown that the Laplace transform of the overall, diffusive rate constant could be related to the respective transforms of rate constants associated with these two diffusive steps. This gives:

$$\frac{1}{\hat{k}(s)} = \frac{1}{\hat{k}_{sphere}(s)} + \frac{1}{\hat{k}_{receptor}(s)} \qquad (6)$$

where $\hat{k}_{sphere}(s)$ is the Laplace transform of the bimolecular rate constant for a ligand colliding with a sphere. It is given by:

$$\hat{k}_{sphere}(s) = \frac{4\pi RD}{s}\left(1 + R\sqrt{\frac{s}{D}}\right) \qquad (7)$$

where D is the sum of the diffusion constants of the sphere and the ligand and R is the radius of the sphere. In the original work, the receptor was taken to be a partially absorbing disk and an appropriate expression was derived for that situation [16].

Equation 6 is actually quite general and can be used to describe rate processes that proceed through multiple domains. For our purposes, the boundary volume of the protein is considered to be the "receptor", $\hat{k}_{bv}(s) = \hat{k}_{receptor}(s)$. From dimensional arguments of the preceding section, one has:

$$\hat{k}_{bv}(s) \propto s^{-\bar{d}/4} \qquad (8)$$

The long time regime will correspond to the region where $s \rightarrow 0$. From Eq. 6 it is readily seen that this is the regime where $\hat{k}_{bv}(s)$ will dominate. Under these conditions, the diffusional rate constant in the forward direction will be given by: $k_1(t) = k_1't^{-h} = k_1't^{1-\bar{d}/4}$. To account for the time course of the reaction in this time regime, one must consider the effects of the reversibility of the reaction and the influence of the chemical steps. As argued above, the diffusional dissociation step will have a comparable time-dependence as the association step. In the long time limit, one then has: $k_{-1}(t) = k_{-1}'t^{-h} = k_{-1}'t^{1-\bar{d}/4}$.

For simplicity, the kinetic behavior under conditions in which the reaction intermediate, A•B has achieved a steady state is now considered. This, of course, is different from determining the steady state rate law for the overall reaction. In this latter case, anomalous reaction orders are obtained (cf. 4) and the rate constants are time-independent. Applying the steady state condition to the intermediate, one has:

$$\frac{d[A \bullet B]}{dt} = 0 = -(k_{-1}(t) + k_2)[A \bullet B] + k_{-2}[C] + k_1(t)[A][B] \qquad (9)$$

Eq. 9 is used to determine the steady state concentration of [A•B] and in conjunction with the other microscopic rate laws allows one to determine the macroscopic rate constant used in Eq. 1:

$$k_f(t) = \frac{k_1(t)k_2}{k_{-1}(t) + k_2} \tag{10}$$

Interestingly, Eq. 10 is the time domain analog of Eq. 6. Indeed, one can introduce chemical steps into diffusive theories of reaction kinetics and obtain equations of the form of Eq. 6 in which one of the rate constants is due to the "chemical" step (cf. [14]). In the present work, this approach is avoided because it can result in unrealistic stationary state behavior for the system. The alternate approach of treating the chemical and diffusive steps separately and solving the respective differential equations for the system is given in the next section.

For acid or base-catalyzed hydrogen exchange processes carried out in buffered solutions, the pH will be constant and, thus, pseudo-first order conditions will be fulfilled. Under such conditions, Eq. 1 can be integrated to give:

$$-\ln\left(\frac{[A(t)]}{[A(t_0)]}\right) = \int_{t_0}^{t} k_f(t)[B]dt = \int_{t_0}^{t} \frac{k_1'[B]k_2 t^{-h}}{k_2 + k_{-1}'t^{-h}}dt \tag{11}$$

where Eq. 10 has been used and the explicit time dependence has been introduced in the rightmost equality of Eq. 11. The lower limit of the integral is set to a time, t_0, reflecting the fact that $t>1$ for rate constants defined by Eq. 2. After a change of variables, the right hand side of Eq. 17 can be reduced to a standard integral (17) and gives:

$$-\ln\left(\frac{[A(t)]}{[A(0)]}\right) = (k_1'k_2 t/k_{-1}')F(1,1/h;1+1/h;-k_2 t^{-h}/k_1') - (k_1'k_2 t_0/k_{-1}')F(1,1/h;1+1/h;-k_2 t_0^{-h}/k_1') \tag{12}$$

where F is the hypergeometric function. The rightmost term in Eq. 12 is merely a constant and all the time dependence is contained in the first term. It is instructive to examine the asymptotic properties of Eq. 12. Using the series expansion for the hypergeometric function, the behavior of Eq. 12 at short time is obtained. This limit gives:

$$-\ln\left(\frac{[A(t)]}{[A(0)]}\right) \sim (k_1'k_2 t/k_{-1}') - \frac{2k_1'k_2^2 t^{h+1}}{k_{-1}'^2}\left(\frac{1}{h+1}\right) + \vartheta(t^{h+2}) \tag{13}$$

where ϑ represents the order of the term. Thus, at short time the concentration of the limiting reactant decays exponentially. To obtain the long time limit, the hypergeometric function is first transformed using standard linear transformation equations and is then expanded in a series. This is accomplished using:

$$F\left(1,1/h;1+1/h,-k_2 t^h/k'_{-1}\right) = \frac{\Gamma(1+1/h)\Gamma(1/h-1)}{\Gamma^2(1/h)}\left(k_2 t^h/k'_{-1}\right)^{-1} F(1,1-1/h;2-1/h;(k_2 t^h/k'_{-1})^{-1})$$

$$+\frac{\Gamma(1+1/h)\Gamma(1-1/h)}{\Gamma^2(1)}\left(k_2 t^h/k'_1\right)^{-1/2} F(1/h,0;1/h;-(k_2 t^h/k'_{-1})^{-1}) \tag{14}$$

After a series expansion in the limit of large t, one obtains:

$$-\ln\left(\frac{[A(t)]}{[A(0)]}\right) \sim \left(k'_1 t^{1-h}/(1-h)\right) + \vartheta(t^{-1}) + \vartheta(t^{1-2h}) \tag{15}$$

Thus, the long time behavior follows a stretched exponential with exponent equal to 1-h. This is the same long time behavior that is seen for a diffusion-controlled bimolecular reaction. This is not surprising as the reaction is forced to the diffusion limit at long time by virtue of the decreasing rate constants, $k_1(t)$ and $k_{-1}(t)$. Thus, it is seen that diffusion will have a profound effect on the time course of a reaction, even for reactions that are initially chemically-controlled. The short time behavior is a simple exponential rather then the power law behavior seen in diffusion-controlled kinetics. However, this comparison is not appropriate. In the present case, the short time behavior represents the time domain after a steady state has been achieved by the intermediate. This is not necessarily comparable to the short time regime commonly investigated in diffusional kinetics. The present derivation is readily adapted to give the time course of the reverse reaction and an identical functional form is obtained. In the next section a more general treatment is presented that gives approximate expressions for the transient behavior.

TRANSIENT BEHAVIOR OF THE REACTION

To investigate the transient behavior of the mechanism in Eq. 4, a system of non-homogeneous linear differential equations must be solved. These equations are of the form:

$$\dot{x}(t) = A(t) \bullet x(t) + b(t) \tag{16}$$

where the dot represents a time derivative and $\mathbf{x}$ and $\mathbf{b}$ are column vectors and $\mathbf{A}$ is a 2X2 matrix. In practice, equations of the form of Eq. 16 are not easily solved and approximation techniques are often required. The explicit form of Eq. 16 for the present problem is:

$$\begin{pmatrix} \dot{x}_1 \\ \dot{x}_2 \end{pmatrix} = \begin{bmatrix} -a_{11} & -a_{12} \\ -a_{21}t^{-h} & -a_{22}t^{-h} \end{bmatrix} \begin{pmatrix} x_1 \\ x_2 \end{pmatrix} + \begin{pmatrix} b_1 \\ b_2 t^{-h} \end{pmatrix} \tag{17}$$

where $x_1 = [C], x_2 = [A], a_{11} = k_2 + k_{-2}, a_{12} = k_2, a_{21} = k_1[B] + k_{-1}, a_{22} = k_{-1}$ and the non-homogeneous terms are $b_1 = k_2 C_{tot}, b_2 = k_{-1} C_{tot}$. In solving ordinary differential equations, one often seeks to reduce the order of the differential equation. In the present case, it proves convenient to revert to a higher order form. This results in a fortuitous cancellation of the b terms. Eq. 17 can be represented as a second order equation, giving:

$$\ddot{x}_1 + (a_{11} + a_{22}t^{-h})\dot{x}_1 + (a_{11}a_{22} - a_{12}a_{21})t^{-h}x_1 = 0 \tag{18}$$

Differential equations of the form of Eq. 18 are often conveniently solved with series techniques. Because of the term in t^{-h}, the equation has an irregular singular point. Under certain circumstances, cases of irregular singular points are more readily handled using a Liouville transformation [18]. First, Eq. 18 is transformed to remove the first order term. This is achieved by the following transformation:

$$x_1 = \exp\left\{-\frac{1}{2}\int(a_{11} + a_{22}t^{-h})dt\right\}y \tag{19}$$

This gives a differential equation of the form:

$$\ddot{y} = q(t)y \tag{20a}$$

where

$$q(t) = \frac{1}{4}(a_{11} - a_{22}t^{-h})^2 - \frac{h}{2}a_{22}t^{-h-1} + a_{12}a_{21}t^{-h} \tag{20b}$$

In regions where q(t) is a slowly varying function, the Liouville (or WKB) transformation provides an accurate solution to Eq. 20a. This transformation gives (18):

$$y = C_1 q(t)^{-1/4} \exp\left\{ \int q(t)^{1/2} dt \right\} + C_2 q(t)^{-1/4} \exp\left\{ -\int q(t)^{1/2} dt \right\} \qquad (21)$$

where the constants C_1 and C_2 are determined from the boundary conditions. Using Eq. 19 and 21, the time course of the reaction is readily determined.

The limiting behavior of this solution provides an interesting comparison to the results of the previous section. In the long time limit, the a_{11} term will dominate q(t) and one has $q(t) = \frac{1}{4} a_{11}^2$. This gives:

$$y = C_1 (2/a_{11})^{1/2} \exp\left\{ -\frac{a_{22}}{2} t^{1-h} \right\} + C_2 (2/a_{11})^{1/2} \exp\left\{ -a_{11} t - \frac{a_{22}}{2} t^{1-h} \right\} \qquad (22)$$

The second term on the right hand side of Eq. 22 will decay faster then the first. Therefore, in the long time limit a stretched exponential is obtained. This is identical to the dependence seen for the steady state solution of the previous section. The short time limit is somewhat more difficult to handle. For the Liouville transformation to provide an accurate solution q(t) must be a slowly varying function. This will not be the case as t→0. However, Eq. 2 is also no longer valid in this limit as the more complicated dependence given by Eq. 6 is now needed. The asymptotic behavior of the Liouville transformation can be explored in the regime where q(t) is rapidly varying. This short time regime will retain a power law dependence even under chemical control. However, the exponent differs from that expected for a diffusion-controlled reaction. For this latter case, one has $y \sim t^{h-1}$. Chemical control gives power law behavior but with an exponent that decays more slowly and which depends on the specific values of the rate constants. The behavior in this regime is currently under investigation.

SUMMARY

In this work, a model for hydrogen exchange kinetics in proteins [2] is examined in detail. In this model hydrogen exchange reactions occur in the boundary volume surrounding the protein. Hydroxyl or hydronium ions from the bulk aqueous solution penetrate this volume to catalyze the reaction. Protein fluctuations bring exchangeable groups into this volume. The time-course of the loss of exchangeable groups from the protein follows a stretched exponential over a wide range of temperatures. The scaling exponent is obtained using the fractal surface dimension of the protein. Data for the protein, lysozyme, are accurately fit with this model without adjustment of this exponent over a range of tempertures. Thus, the model provides a direct link between the structure (fractal surface dimension) and dynamics (spectral dimension) of a protein. It allows one to predict solution kinetics scaling laws from X-ray crystal structures.

This work examines the effect of chemically-slow steps on reactions with time-dependent diffusive behavior. A general, solution phase mechanism is considered where an "encounter complex" is formed. The diffusive steps of the reaction are analyzed as if the protein were a sphere with target or receptor regions in the boundary volume. The rate constant for the boundary volume association dominates the diffusive modes. For reversible, chemically controlled reactions, it is argued that the dissociative diffusive step will have an identical time-dependence as the associative step. Under steady state conditions for the encounter complex, two scaling regimes exist. The short time regime is characterized by an exponential decay of reactant concentration. The long time regime is the stretched exponential expected for diffusion-controlled reaction. In the long time regime, the diffusive steps will become slow compared to the chemical steps and the reaction ultimately achieves diffusion control. The early transient phase of the reaction can be treated by solving the differential equations associated with the reaction mechanism. Asymptotic forms of this solution exhibit a power law behavior similar to diffusion-controlled reactions, except that exponents are smaller. This results in a decrease in reactant concentration that varies more slowly with time.

BIBLIOGRAPHY

1. G.R. Welch, The Fluctuating Enzyme (John Wiley & Sons, New York, 1986).
2. T.G. Dewey, Proc. Natl. Acad. Sci. USA (in press,, 1994).
3. R.R. Wickett, G.J. Ide, and A. Rosenberg, Biochemistry **13**, 3273 (1974).
4. R. Kopelman, Science **241**, 1620 (1988).
5. G. Zumofen, A. Blumen, and J. Klafter, J. Chem. Phys. **82**, 3198 (1985).
6. K. Kang, and S. Redner, Phys. Rev. Lett. **52**, 955 (1984).
7. S.Havlin, in The Fractal Approach to Heterogeneous Chemistry, edited by D. Avnir, (Wiley, Chichester, 1989) Chap. 4.1.1.
8. P. Pfeifer, U. Welz, and H. Wippermann, Chem. Phys. Lett. **113**, 535 (1985).
9. P. deGennes, J. Chem. Phys. **76**, 3316 (1982).
10. S.W. Englander, and A. Poulsen, Biopolymers 7, 329 (1969).
11. N. Agmon, J. Chem. Phys. **81**, 2811 (1984).
12. A. Szabo, J. Chem. Phys. **95**, 2481 (1991).
13. N. Agmon, and A. Szabo, J. Chem. Phys. **92**, 5270 (1990).
14. S. Lee, and M. Karplus, J. Chem. Phys. **86**, 1883 (1987).
15. M. Eigen, Zeitschrift Phys. Chem. (Frankfurt) **12**, 176 (1954).
16. R. Zwanzig, and A. Szabo, *Biophys. J.* **60**, 671 (1991).
17. I.S. Gradshteyn, and I.M. Ryzhik, Tables of Integrals, Series and Products (Academic Press, New York, 1980) pp.285.
18. F.W.J. Olver, Asymptotics and Special Functions (Academic Press, New York, 1974) pp. 190-195.

SUBSTRATE-DEPENDENT FEATURES OF POLYETHYLENE OXIDE (PEO) ADSORPTION FROM AQUEOUS SOLUTION: COMPETITIVE ADSORPTION VERSUS SURFACE RELAXATIONS

M. M. SANTORE and V. A. REBAR
Department of Chemical Engineering
Lehigh University Bethlehem PA 18015

ABSTRACT

This work employed total internal reflectance fluorescence (TIRF) to examine the adsorption kinetics of polyethylene oxide (PEO) on silica from aqueous solution in controlled shearing flow. Studies with PEO, fluorescently labeled such that TIRF tracked the chain number on the surface, exhibited an overshoot in the early stages of adsorption. This overshoot was not seen with other polymers such as polyvinyl alcohol, and hydroxyethyl cellulose, possibly because these other polymers were labeled such that TIRF measured the interfacial mass. Indeed, reflectometry studies of PEO adsorption, sensitive to interfacial mass, showed no overshoot. This suggests that the overshoot results from the selectivity of the surface for high molecular weight populations within a polydisperse sample. Initially short chains adsorb because they diffuse to the surface quickly. At longer times, higher molecular weight chains reach the surface and replace the short chains. This evolution occurs as the mass coverage increases (according to reflectivity) but the number of adsorbed chains, and hence the TIRF signal decrease at long times. A study of the impact of the molecular weight distribution confirmed this hypothesis.

Several complications to the molecular weight selectivity hypothesis, however, arose: First, the same PEO samples which overshot during adsorption on silica showed no overshoot on a polystyrene substrate. This suggested that the ability to overshoot was governed by the substrate-segment interactions, even though the molecular weight distribution within the sample determined the overshoot shape. Further, the effect of transport conditions (wall shear rate, bulk polymer concentration) were not completely consistent with the molecular weight competition hypothesis, which was based on surface-solution equilibrium, taking into account transport-limited rates of adsorption. Finally certain runs, where the adsorption process was interrupted by solvent flow and later allowed to proceed, never reached the full coverage seen for uninterrupted runs. Hence, the surface coverage and possibly the chain configurations can depend on the history of the adsorption process, a feature which points to surface relaxations and non-equilibrium structures.

INTRODUCTION

The adsorption, desorption, and exchange kinetics of polymers from solution onto solid surfaces is a topic of recent fundamental interest. Whether desorption and exchange kinetics reflect a transport-limited approach to equilibrium or if these phenomena are governed by surface kinetics and trapped non-equilibrium states remains a topic of debate. Indeed, depending on the particular system, there is evidence for both mechanisms of kinetic control.[1,2] The adsorption kinetics of PEO have been well documented, at least in terms of the evolution of interfacial mass. The current findings suggest that PEO kinetics should be dictated by the transport-limited approach to equilibrium. This was recently demonstrated by Fleer in a study of bimodal (in terms of molecular weight) mixtures where the surface composition followed the independently-determined bimodal adsorption isotherms, with kinetics dominated by transport considerations.

Our own studies with PEO adsorption focus on the evolution of interfacial chain number in addition to the surface excess in terms of interfacial mass. Originally, we had intended that total internal reflectance fluorescence (TIRF), when used to study systems with one fluorescent label on each chain, could directly track the interfacial chain number and therefore measure certain adsorption and exchange processes more precisely than reflectivity. In our initial work with PEO adsorption onto silica from aqueous solutions, we observed an overshoot in the early stages of the adsorption kinetics. Closer studies revealed that such overshoots occurred regardless of the ionic conditions of the experiments, and independent of the particular dye employed to label the PEO (both fluorescein and rhodamine have been tested). The overshoot was not seen, however, for other polymers such as polyvinyl alcohol, and hydroxyethyl cellulose, possibly because these chains were randomly labeled such that the TIRF signal reflected the interfacial mass. The

421

overshoot was also absent in PEO adsorption runs on a polystyrene substrate, suggesting that the segment-substrate interactions were key in generating an overshoot, and providing a second reason why the other polymers did not show overshoots. Even with the complication that the segment-substrate interactions were important in causing overshooting phenomena, the leading hypothesis for the overshoot still had to do with the molecular weight selectivity of the surface. In polydisperse samples such as ours, the short chains diffuse to the substrate first and adsorb. When the longer chains arrive, the short ones are displaced. While such processes may occur at constant or increasing surface mass, the interfacial chain number decreases, giving an overshoot. The purpose of this investigation was to determine the importance of the molecular weight distribution in the overshooting behavior, and establish the extent to which interfacial relaxations and trapped surface states were important.

EXPERIMENTAL

The experiments presented here employ total internal reflectance fluorescence (TIRF), a technique which concentrates the excitation light for a fluorescence study into an exponentially-decaying evanescent wave near the interface between a polymer solution and the substrate onto which the polymer adsorbs. TIRF measures the surface excess of fluorescently-labeled polymer chains, while chains bearing no fluorescent labels are invisible to TIRF. The concepts of TIRF[3,4] and the details of our home-built TIRF apparatus[5] have been described elsewhere. The important features of our apparatus were that a 488 nm. Ar+ ion laser was used for excitation and emissions measured above 540 nm. The evanescent wave decay length was 63 nm. The adsorption experiments took place in a shearing flow cell[6] with an adjustable wall shear rate.

For these studies, polyethylene oxide and polyethylene glycol molecular weight standards from Polymer Labs and Polysciences were employed, with reported molecular weights of 97,000 and 20,000 and polydispersities less than 1.06. The 97,000 sample was fluorescein-labeled with one tag on each chain by isothiocyanate chemistry.[5] The purification procedure included dialysis to remove unattached fluorescent labels. After several weeks in dialysis, the molecular weight distribution of the 97,000 sample was seen to decrease and broaden slightly. Over the next several months, the sample was used in other experiments. Finally, when the experiments presented here were run, the molecular weight distribution was broad, with an average near 55,000 and populations as low as 10,000, as determined by GPC. Despite the change in molecular weight, this sample will still be referred to as "97K". The narrow molecular weight 20K sample was dialyzed and stored wet only for a few weeks and retained its narrow molecular weight distribution. Also used in this study was a dialyzed 400,000 molecular weight polydisperse sample from Aldrich which was of distinctly higher molecular weight than the 97K sample.

For the 97K labeled but degraded sample, we presumed that the degradation was by random chain scission. Indeed no evidence was found for the removal of the fluorescent label from the chains. Notably, if all the chains were of uniform length at the time of labeling, and if these chains degraded randomly, the sample studied here contained some chains of random length less than 97,000 molecular weight, with one fluorophore on each chain. The rest of the sample was assumed to be comprised of unlabeled chains having the same molecular weight distribution as the labeled fraction. Extensive studies by us have shown that the fluorescein label had no detectable effect on the surface excess, as determined by adsorption isotherms on silica beads.

Acid treated microscope slides comprised the substrate for the adsorption studies detailed here. ESCA analysis revealed that acid-treated glass closely resembled silica. Adsorption studies were conducted in pH 7.4 phosphate buffer[5] which enhances the fluorescein emissions. The high ionic strength of the solutions (0.173 M) also ensured that electrostatic repulsion between the negatively-charged silica surface and the negatively charged fluorescein label was screened. The details of the experimental procedure and control studies demonstrating the negligible effect of fluorescein labeling and the extent of the ionic effects are detailed elsewhere.[7]

RESULTS

Figure 1 illustrates an overshoot for a buffered 50 ppm 97K PEO solution flowing past a silica flat at a wall shear rate of 40 s^{-1}. This example illustrates the typical overshoot features: a sharp

almost linear rise to the maximum and then a slow decay. The extent and duration of the decay varied with the concentration of the bulk solution and the wall shear rate. Small overshoots, with a drop whose size was 5% of the maximum signal were seen for bulk concentrations exceeding 200 ppm while large overshoots with drops whose magnitudes approached 2/3 of the maximum were seen for the most dilute solutions (2 ppm). The decay process lasted from 20 minutes (for samples with high bulk concentrations) to over 24 hours for dilute samples. Similar PEO samples, labeled and unlabeled, polydisperse and of narrow molecular weight distribution have also been studied by reflectometry, employing a homebuilt internal reflection reflectometer.[8] While the shape of an adsorption trace was clearly influenced by the molecular weight distribution within the sample (with broader molecular weight distributions giving more rounded shoulders and a slower and longer lasting increase to the ultimate coverage), no overshoot was ever observed. Hence, the overshoot is an observation isolated to the TIRF method, and may reflect chains leaving the surface after the peak, or a slow reconformation which influences the quantum yield of the label.

Figure 1. Typical Adsorption Run 50 ppm 97K PEO adsorbing onto silica from buffer at a wall shear rate of 40 s^{-1}.

Figure 2 illustrates sequential injections (meaning that a particular polymer solution is made to flow continuously past the substrate until the next solution is introduced) of 97K PEO solutions, at a wall shear rate of 8 s^{-1}. In Figure 2a, the concentrations are 2 ppm, 10 ppm, 20 ppm, 35 ppm, and 50 ppm, with solvent introduced between each polymer solution. Each polymer solution sees the surface for 45 minutes and then the solvent is flushed through the cell for 45 minutes. The most dilute solution gives the largest overshoot, with the size of the overshoot decreasing as the concentration of the bulk solution increases. As a point of reference, the adsorption isotherm for this system is inserted into Figure 2b. The initial rise of the isotherm is fairly steep, followed by a shoulder near 50 ppm, and a flat plateau at higher coverages. Comparing the overshoot kinetics to the isotherm, one realizes that the overshoot is greatest where the isotherm is steepest, and then almost disappears as the plateau is reached. Figure 2b illustrates a second sequence of injections, with concentrations of 50 ppm, 100 ppm, 200 ppm, and 6255, ppm, all on the isotherm plateau.

Figure 2. Sequential Adsorption Studies of 97K labeled PEO adsorbing onto silica at a wall shear rate of 8 s^{-1}. Buffer solutions are injected for 45 minutes between each polymer solution. Arrows indicate the injection of new polymer and buffer solutions. **(A)** 2 ppm PEO, 10 ppm, 20 ppm, 35 ppm, 50 ppm. **(B)** 50 ppm, 100 ppm, 200 ppm, and 6255 ppm.
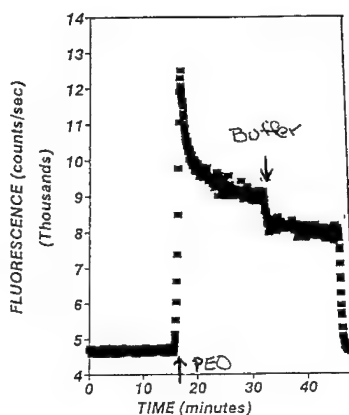
Here, the bulk polymer concentration is fairly high such that in the flow cell there are free polymer chains which penetrate the evanescent zone near the surface and therefore contribute to the signal. When the cell is flushed with solvent, however, the signal drops back to a level which reflects only the adsorbed chains. Hence, in Figure 2b, the overshoot occurs only for the injection where the adsorption has occurred, at 50 ppm. At 100 ppm and greater, the system is on the plateau of the isotherm and no further chains adsorb. Hence, from a comparison of Figures 2a and 2b, one concludes that the overshoot occurs only for situations where new chains add to the surface: on the initial rise of the isotherm, or for the first injection where the bulk concentration is on the plateau of the isotherm. The question remains as to whether the signal decrease is due to surface relaxations or the removal of low molecular weight species from the surface, a point that was difficult to determine directly.

To further determine whether the signal drop after the maximum was due to changes altering the fluorescein quantum yield or due to removal of chains (and their labels) from the surface, a series of experiments were performed, in which an additional injection was made at the maximum of the overshoot (per the arrows in Figure 3). Figure 3a illustrates an uninterrupted run with 97K PEO at 2 ppm and a wall shear rate of 8 s^{-1}. In Figure 3b, buffer solution was injected at the arrow and a much more gradual decrease follows. Hence it is concluded that while some desorption/relaxation may occur as the TIRF signal increases, the addition of chains from the bulk solution are instrumental in causing the fluorescence decrease. In Figure 3c, an unlabeled 2 ppm sample of Aldrich 100K polymer (also allowed become polydisperse with age) has been injected at the arrow, while in Figure 3d, a 2 ppm unlabeled 20K (narrow molecular weight) cut has been injected at the arrow. Figure 3c is very similar to Figure 3b, suggesting that if new chains are added to the surface during the signal decrease, only very few need to be added to cause the drop. Figure 3d is also similar to Figures 3a and 3c, but the drop in Figure 3d may appear slightly more extensive. (It is not clear if these fine details are real or if Figures 3a, 3c, and 3d should be considered identical within experimental error.) Still to be determined is whether chains leave the surface during the signal decrease. It is clear that some new chains add to the interface at this time.
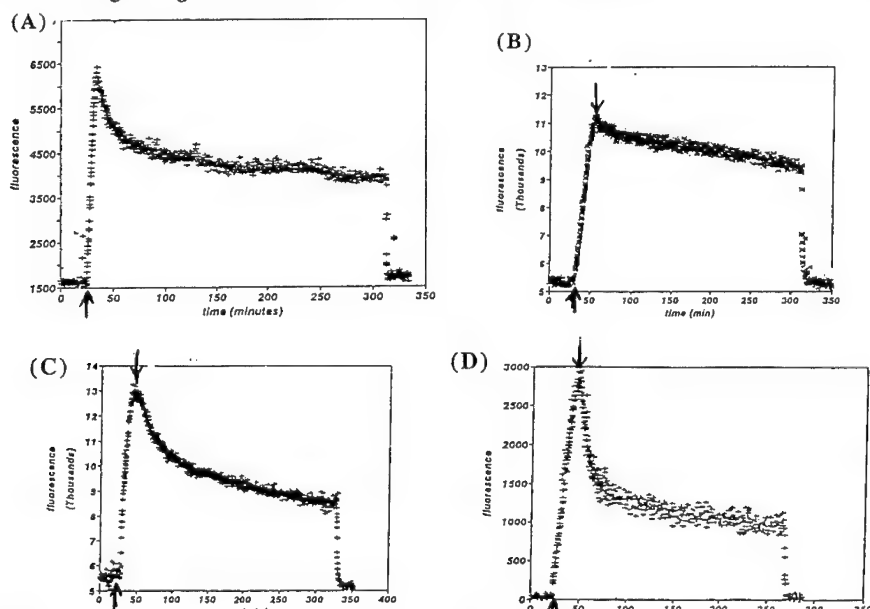

Figure 3. Adsorption runs at 8 s^{-1} wall shear rate, beginning with 2 ppm 97K labeled PEO. Arrows indicate the injection of new solutions. **(A)** experiment runs without interruption. **(B)** buffer is injected at the maximum. **(C)** 2 ppm 100K unlabeled polymer solution is injected at the maximum. **(D)** 2 ppm 20K unlabeled polymer solution is injected at the maximum.
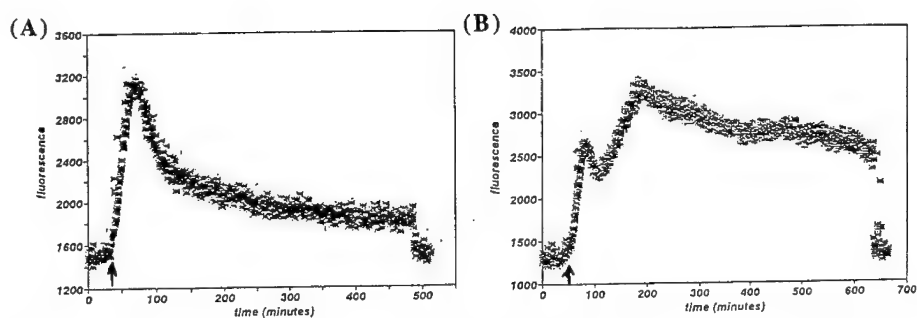
Figure 4. Adsorption runs at 0.8 s⁻¹ wall shear rate with 50/50 mixtures totaling 2 ppm PEO: (A) mixture of labeled 97K and unlabeled 400K sample. (B) mixture of labeled 97K and unlabeled 20K sample. Arrows remind reader that a single injection occurs in each of these runs.

To further illustrate the molecular weight effects, in Figure 4, mixtures of labeled and unlabeled chains have been injected at the beginning of the experiment. In Figure 4a, a 50/50 mixture of 400K(unlabeled) and 97K(labeled) PEO is injected and seen to given an extensive decrease after the maximum, indicating that higher molecular weight species are indeed favored on the surface at long times. In Figure 4b, a 50/50 mixture of the 20K (narrow molecular weight, unlabeled) and 97K sample (labeled) with a total concentration of 2ppm is injected at 0.8 s⁻¹ and two overshoots are seen. This can be explained if the lowest molecular weight population of the 97K labeled sample diffuses to the surface fastest and adsorbs. Then at intermediate times, the narrow 20K unlabeled cut adsorbs and some of the low molecular weight labeled chains are displaced. At longer times, the higher molecular weight populations within the 97K sample finally reach the surface, and as they adsorb, some of the unlabeled 20K chains are displaced and the signal increases. At the longest times, the highest molecular weight populations are preferred on the surface, and the smaller chains continue to desorb, causing a signal decrease.

A final point in Figure 5 suggests that there is more happening than a simple exchange between the various molecular weight populations. Here 2 ppm of the labeled 97K PEO sample are introduced at 0.8 s⁻¹, conditions which should have given an overshoot. The run is interrupted at 20 minutes by flowing solvent, before the system has reached the maximum. Then after the initially adsorbed chains have been subjected to flowing solvent for 9 hours, the original polymer solution is reinjected, giving only a small overshoot. First, it is clear that the expected coverage, based on the previous run in Figure 3a is never achieved. Hence, the number of chains on the surface, or their configurations (which potentially affect the quantum yield of the fluorescein) appear to be history dependent.
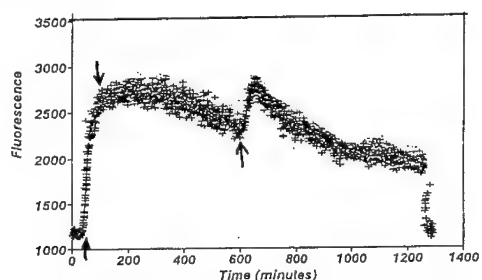

Figure 5. Adsorption of 2 ppm labeled 97K PEO at 0.8 s⁻¹ wall shear rate. Run is interrupted before reaching the maximum by continuous buffer flow. Polymer solution flow is later resumed.

425

DISCUSSION

At this point, the extent to which molecular weight competition and surface relaxations cause the overshoot remains to be quantified. The ultimate experiment, clearly, is to run a test case with a labeled sample of very narrow molecular weight distribution. This option is not available because PEO samples degrade during the minimal purification time needed to remove free labels from the test solutions, and preservatives serve as contaminants.

Even without this crucial experiment there is evidence that molecular weight competition and exchange processes do not tell the whole story. For example, we have been unable to superpose overshoots by scaling the x-axis on the rate of chain arrival (time * wallshear$^{1/3}$), an observation which argues against transport-limited rate processes controlling what is essentially an equilibrium phenomenon. Certain aspects of our observations are also at odds with expectations for chain spreading on the surface: If chains are added to a surface slowly, they should have time to spread and prevent the arrival of new chains, thus decreasing the overshoot; however, the slow runs (0.8 s-1, 2 ppm polymer) show the most dramatic overshoots. When the rate of chain arrival is completely interrupted for several hours in Figure 5, the history dependence is obvious. Hence any relaxations, if they occur, last several hours.

A final idea is that lateral interactions between adsorbed chains influence the quantum yield. In Figures 3c and 3d, however, the signal reduction occurs without the addition of new fluorophores to the surface: Only new PEO has been added. Fluorescein-PEO interactions have also been shown to reduce the fluorescein quantum yield;[7] however, it remains to be determined how such interactions develop, if they do indeed develop. For instance, reflectometry studies (not illustrated here) show minimal addition of new material to the surface during the time when the TIRF signal decreases. Hence one might conclude that the development of fluorescein-PEO interactions, if they occur, are enhanced by densification of the layer or other restructuring, which is essentially a surface relaxation. Hence, all our explanations of the overshoot rely on a combination of molecular weight competition and very slow surface relaxation phenomena.

CONCLUSIONS

This work examined the origin of overshoots measured by TIRF for the adsorption of PEO onto silica from aqueous solution but not seen via TIRF for the adsorption of other polymers onto silica, or for PEO onto polystyrene substrates. Further, reflectivity studies of the same system showing a TIRF overshoot did not show an overshoot in interfacial mass. Hence the overshoot could be explained by exchange between various molecular weight populations within a polydisperse sample, directly causing a decrease in the number of chains at the surface at long times. Our experiments confirmed these expectations for the impact of molecular weight, but also revealed that certain history-dependencies applied. For runs with signal increases lasting 45 minutes or less, the history dependence was difficult to see, but more obvious when runs were interrupted for several hours. In addition to desorption of low molecular weight chains (limited by transport or surface kinetics) directly causing the reduction in fluorescence, a second explanation for the fluorescence reduction was put forth: The surface-rate-controlled development of lateral interactions among chains reducing the quantum yield through fluorophore - PEO interactions. Hence, while the molecular weight distribution determined the shape of the overshoot, surface controlled kinetics apply and non-equilibrium behavior can be obtained.

REFERENCES

1. Dijt, J.C., Cohen Stuart, M.A., and Fleer, G.J., *Macromolecules* **27** 3219 (1994).
2. Frantz. P., and Granick, S., *Phys. Rev. Lett.*, **66**, 899 (1991).
3. Caucheteux, I., and Hervet, H., Jerome, R., and Rondelez, F., *J. Chem. Soc. Faraday Trans.* **86** 1369 (1990).
4. Hlady, V., and Andrade, J.D., *Colloids and Surfaces* **32** 359 (1989).
5. Kelly, M.S., and Santore, M. M., submitted to *Colloids and Surfaces*.
6. Lok. B., Cheng. Y.L. and Robertson, C.R., *J. Coll. Int. Sci.* **91** 87 (1983).
7. Rebar, V.A., and Santore, M. M., Manuscript in progress for *J. Coll. Int. Sci.*
8. Fu. Z.L., and Santore, M. M. *Progress Reports of Lehighs Polymer Interfaces Center* **7** (1994).

STATIC AND DYNAMIC PERTURBATIONS OF DROPLET MICROEMULSION BY CONFINEMENT AND ADSORPTION OF POLYMER

JYOTSANA LAL*, BELA FARAGO** AND LOIC AUVRAY*
*Laboratoire Leon Brillouin, CEN -Saclay, 91191 Gif-Sur-Yvette, Cedex, France.
**Institute Laue Langevin, Grenoble, France.

ABSTRACT

The effects induced on the structure and dynamics of dilute microemulsion droplets by the confinement of polymer chains inside the droplets and by the adsorption of polymer on the surfactant shells from the outer continous phase were studied. The local structure changes were observed by small angle neutron scattering (SANS). The curvature fluctuations and the size distribution of the droplets increase for both chains inside and outside by different possible mechanisms, an induced size polydispersity minimizing osmotic stresses in the first case, a lowering of the film rigidity in the second one. Neutron spin echo techniques (NSE) were also used to probe the shape fluctuations of the same droplets with and without polymer. A sharp characteristic peak due to the contribution of the l=2 mode is exhibited by the spectrum of relaxation times as a function of wavevector q. The height of this peak is decreased with the addition of polymer. i.e. the fluctuation of the l=2 modes are dampened with the addition of polymer. The effect on the elastic coefficient K of the surfactant layer will be discussed below.

INTRODUCTION

The interaction (attraction or repulsion) of polymers with flexible surfactant layers may modify strongly the elasticity and the shape fluctuations of the layers [1,2,3]. These effects have important applications in food industry, cosmetics, oil recovery, but are still poorly understood. We have recently started to study them by using microemulsions as model systems. Microemulsions in particular, allow the polymer to be localized in different geometries and solvents, polar, non-polar, and different types of polymer surfactant interactions can be probed: hydrophobic, hydrophilic, attractive or repulsive. We have characterized several systems [4] where we could study the following questions :

i) to what extent can non-adsorbing chains be confined inside the microemulsion droplets, how they probe the elastic properties of the layers, what are the induced structural changes?

ii) what are the effects of the polymer on the droplet structure and interactions when the chains are adsorbed on them from the outer continous phase?
The first question has in fact already been investigated in references [5,6,7,8] by conductivity measurements, light scattering, fluorescence techniques [5,6] and SANS [7,8] at a rather macroscopic level. The second question has never been studied before to our knowledge.

The main observation made in our first static small angle neutron scattering experiments, reported in ref. [4], is that the polymer chains, present inside or outside the droplets, strongly deform their structure. One can in first approximation express

quantitatively these induced deformations in term of an increase of the apparent size polydispersity of the droplets. Here we attempt to go beyond this simple characterization and try to distinguish and analyse more precisely the change of size and of shape of the droplets. It is a difficult task, but it can be done in principle in several ways:

i) one can first observe the static scattering intensities in different contrast conditions by adjusting the neutronic indices of refraction using mixtures of hydrogenated and deuterated compounds so that the polymer is invisible and the scattering signal arises either from the core of the droplets or just from the surfactant layer. A particular model of fluctuating polydisperse droplets can be used and one can check if each signal is consistent with it . More generally, the different asymptotic behaviors of the intensity at large scattering vector can be related by well-defined expressions to the local curvature deformations of the droplets.

ii) one can also perform quasi-elastic neutron scattering experiments using the Neutron Spin Echo (NSE) technique. Pioneering experiments [9] have already shown that it is an efficient mean to analyse the different modes of fluctuation of droplet microemulsions in the time range 1-50 ns at a length scale of a few nanometers. A comparison with the theoretical dynamic structure factor $S(q,t)$ of fluctuating droplets calculated by Safran and Milner a few years ago [10] may then yield quantitative informations on the elastic constants of the surfactant layer, in particular its bending rigidity K.

The first aim of this article is to describe in a critical way the applications of these methods to our different systems of microemulsions : the bare one and the one with confined and adsorbed polymer. We also compare our observations with the predictions of existing theories [1,2].

EXPERIMENTAL PROCEDURES

Composition of the Samples

POLYMER INSIDE -   The polymer confinement studies were performed mainly with Poly(ethyleneglycol) (PEG) in water-in-oil microemulsions made of cyclohexane (a non solvent of PEG), SDS (Sodium DodecylSulfate), butanol as cosurfactant and brine at two salinities $I = 5.8\%$ (1M) and 9% (in g/cm^3). These two values of the ionic strength yield a different spontaneous curvature of the surfactant layer C_0. I=1M is the optimal salinity of the Winsor system associated with the constituants and should correspond to a very small or vanishing spontaneous curvature [4]. $I = 9\%$ provides on the other hand a large spontaneous curvature stabilizing water in oil phases. We vary the droplets radius R (determined by the water to surfactant ratio W/S in ml/g), the polymer concentration in water expressed here by the average number of chains per droplet, n and the polymer molecular weight (M_w=10000 (Aldrich polydispersity =1.08). The maximum number of chains per droplet depends on the droplets radius and polymer molecular weight.. For M=10000, n_{max}=1.5 at R=50Å (W/S=2, I=5.8 and 9%), it increases to n_{max}=2 at R=75 Å (W/S=3, I=5.8%).

POLYMER OUTSIDE-   We have studied oil in water microemulsions (O/S), ϕ=4% (cyclohexane/brine(1%)/SDS, pentanol), where we have dissolved a water soluble polymer called PNIPAM (poly-N-isopropylacrylamide synthetized in the laboratory, M_w=10^6, c=$5X10^{-3}$), known for interacting strongly with pure SDS

Small angle neutron scattering (SANS)

The scattering from the droplets both in core and shell contrast were measured in Saclay (PACE spectrometer)[4]. The measurements were done in several different configurations to study different ranges of scattering vector from 5×10^{-3} to 0.2 Å^{-1}. Water which scatters isotropically was used to normalize the intensities.

Neutron spin Echo (NSE)

The neutron spin echo experiments were done on the Saclay's instrument MESS. The samples (also measured by static SANS) were observed in shell contrast: hydrogenated SDS, deuterated water and mixture of hydrogenated and deuterated cyclohexane matching the water core of the droplets. For this experiment deuterated PEO (Mw=10000) which is invisible in the deuterated core of the droplets, was used. It is known from ref.[9] that the observations in shell contrast are more sensitive to the shape fluctuations of the droplets than the one in core contrast. For the experiments with PNIPAM, we left the polymer ,which could not be deuterated, unmatched. We employed a neutron wavelength of $\lambda=6$Å, resulting in the time window of 0-18 ns. NSE directly measures the normalized intermediate scattering function $I(q,t)/I(q,0)$ as a function of time t, in the wave-vector range corresponding from .02 to .12 Å^{-1}.

FLUCTUATIONS OF THE DROPLETS FROM STATIC EXPERIMENTS

1)Effects of droplets fluctuations on the scattering intensity

The scattering intensity by a set of independant monodisperse spheres (core) $i_c(q)$ or shells (film) $i_f(q)$ at concentration c is well known and given by the following expressions

$$i_c(q) = cV_c^2(\Delta n)^2[3(\sin qR - qR\cos qR)/(qR)^3]^2 \tag{1}$$

$$i_f(q) = c(4\pi R^2)^2 d^2(\Delta n)^2[\sin qR/(qR)]^2 \tag{2}$$

V_c is the volume of the droplet core, d the shell thickness, the Δn are contrast factors.
In each case, the expression is the sum of two terms, a monotonous decaying term and a non monotonous term oscillating around zero. For example:

$$i_f(q) = c(4\pi R^2)^2 d^2(\Delta n)^2(1/2(qR)^2)[1 - \cos 2qR] \tag{3}$$

Any deviations from the system being monodisperse (fluctuations of size) or spherical (fluctuation of shape) will modify each of these terms.

Fluctuations of size are taken into account by averaging the intensity over a given size distribution. A Schultz-Flory distribution of the droplets radii $f(R)=AR^z\exp(-(Z+1)R/<R>)$ is usually chosen for the sake of simplicity [15], A is a normalization constant, $<R>$ is the average droplet radius, and Z a polydispersity parameter. The width of the size distribution, i.e. the r.m.s. average $\delta R=<(R-<R>)^2>^{1/2}$, is related to Z by $\delta R/R= 1/(Z+1)^{1/2}$. The main effect of the averaging is to damp and partially suppress the oscillating term of the intensity .

There is uptill now no general way of calculating the effect of the shape fluctuations on the scattering intensity in the whole range of scattering vectors. Safran and Milner have developed a perturbation approach that we will use to analyse the Neutron Spin Echo data and that will be discussed in the second part of this article. The shape of fluctuating droplets is described in term of spherical harmonics Y_{lm}, each mode lm having a dimensionless amplitude u_{lm}. One can then perform a perturbation expansion of the intensity in the u_{lm} up to the second order. One must be however aware that this expansion is in fact an expansion in qRu_{lm}, so that the calculation is valid only in the limit of small scattering vectors or small fluctuations. This expression nevertheless allows to analyse precisely the smearing of the intensity by small shape fluctuations.

There is however another approach, complementary to the one of Safran-Milner, which is valid in the range of large scattering vectors. It focusses on the effect of the shape fluctuations on the monotonic part of the intensity at large q. When the scattering vector q is much larger than the typical curvature of the oil-water interface, the scattering intensity can be calculated (up to the oscillating term) as if one had a flat interface. In core contrast, one recovers the classical Porod's behaviour, $i_c(q) \approx q^{-4}$ and for a microemulsion film of finite thickness d , one gets in film contrast $i_f(q) \approx q^{-2}$. Deviations from these asymptotic behaviors are observed when q becomes of the same order of magnitude as the local curvature of the interface.When scattering from the core is considered, these curvature corrections (which are positive and depend on a quadratic average of the principal curvatures of the surface) vary as q^{-6} and were first derived by Kirste and Porod [11]. Likewise, curvature corrections can be developed in the case of scattering from a shell. Many people recently performed this calculation independantly [12,13,14]. One obtains the following expressions describing the asymptotic behaviour of the intensity scattered by the surfactant layer (of thickness d) , valid in the range $qR_c>>1$, $qd<<1$:

$$q^2 i_f(q) = 2\pi c_s \Sigma d^2 (\Delta n)^2 \{ 1 - <(C_1-C_2)^2>/8q^2 \} \qquad (4)$$

$\Delta C^2 = <(C_1-C_2)^2>$ is the quadratic average of the difference between the principal curvatures of the surfactant layer, it reveals the droplets asphericity and shape fluctuations. This expression predicts that the $q^2 i(q)$ plateau is reached from below if these oscillations of the droplets form factor are averaged

2) Analysis in term of size polydispersity

Classically the analysis of the static scattering by fluctuating droplets has always been performed only in term of size polydispersity using a Schultz-Flory distribution [15,16]. As a matter of fact, the data are very often well fitted by models of polydisperse spheres. There is however a debate about the significance of the polydispersity parameter z or $\delta R/R$ that one can draw from the analysis. It has been in particular argued that this parameter in fact incorporates all the contributions from both size and shape fluctuations [16]. We think that this may be true in the case of core contrast: it is well known that one can fit the spectrum of an ellipsoid by a model of polydisperse spheres, but this should not be true in principle for the scattering from shells because one violates the asymptotic behavior (1), if the asphericity of the fluctuating droplets is large.

We have applied this analysis in term of polydisperse spheres to our data. We have observed that the spectra in core contrast could be totally fitted by assuming polydisperse spheres with a Schultz-Flory distribution. The value of the corresponding z parameter are reported in table I. As one can already observe it qualitatively on the spectra, the W/O microemulsions without polymer are already very polydisperse and fluctuating, z is small (z≈8 for W/S=2) while the O/W microemulsion is more monodisperse (z=22). In both cases, the effect of adding polymer is to increase the apparent polydispersity (z goes down to 5 for W/S=2 and to 14 for O/S=2). The situation is less clear and satisfying with the spectra observed in film contrast. Models of polydisperse water in oil shells cannot fit the whole range of scattering vectors. One possible explanation is the existence of apparent attractive interactions between the water droplets. The values given in table I are obtained by fitting only the large angle behavior, at qR>2.5. We also note that for the W/O samples, the z values that we obtain are larger than the one obtained from the core contrast. The trend is however the same : confined polymer increases the droplets polydispersity. Even for the less fluctuating oil in water shells, the agreement is not perfect. Here however the z values between core and shell are consistent. It seems that when the fluctuations of size or shape are relatively small, it is safe to interpret the data only in term of size polydispersity. However, when they are large (what is the case of W/O microemulsions) a more detailled analysis has to be made. Possibly, the shape fluctuations do not contribute in the same way to the apparent polydispersity index z in core and film contrast.

3)Possible deviations from sphericity

We now attempt to analyse the asymptotic behavior of the film spectra using expression (4). Since the curvature correction varies as q^{-4}, we expect to observe a straight line with an extrapolated negative intercept proportionnel to ΔC^2 by plotting $q^4 i_f(q)$ vs q^2. This is indeed the case (Figures 1 and 2). Even if the values of the intercept are small, they are measurable. However the uncertainty on them are large and a word of caution has to be applied, because of the possible effect of the background subtraction and spurious oscillations of the form factor, which are not included in expression (4).

In Figure 1 we draw the scattering spectra of the W/O microemulsions with and without confined polymer in this $q^4 i_f(q)$ vs q^2 representation. For the sample w/s=2 without polymer we measure $\Delta C^2 = 1.21 \times 10^{-2} \text{Å}^{-2}$, whereas when a single polymer chain is confined within the droplets, one gets $\Delta C^2 = 0.87 \times 10^{-2} \text{Å}^{-2}$. It thus seems the asphericity in the average droplet shape is slightly less with polymer inside.

The relative effect is larger with the oil in water droplets (Figure 2). The observed value of the parameter ΔC^2 is $0.55 \times 10^{-2} \text{Å}^{-2}$ for the sample without polymer with a large uncertainty because of the oscillations of the droplets form factor. The asymptotic behavior is much better defined when the polymer is adsorbed, we measure $\Delta C^2 = 2.88 \times 10^{-2} \text{Å}^{-2}$. This directly implies that polymer adsorption increases the shape fluctuations of the surfactant layer. Such an effect has been predicted theoretically but is still a subject of controversy [1,2] : reversible polymer adsorption could indeed decrease the surfactant film rigidity K [4].

It thus seem that one can detect shape fluctuations from static scattering experiments.
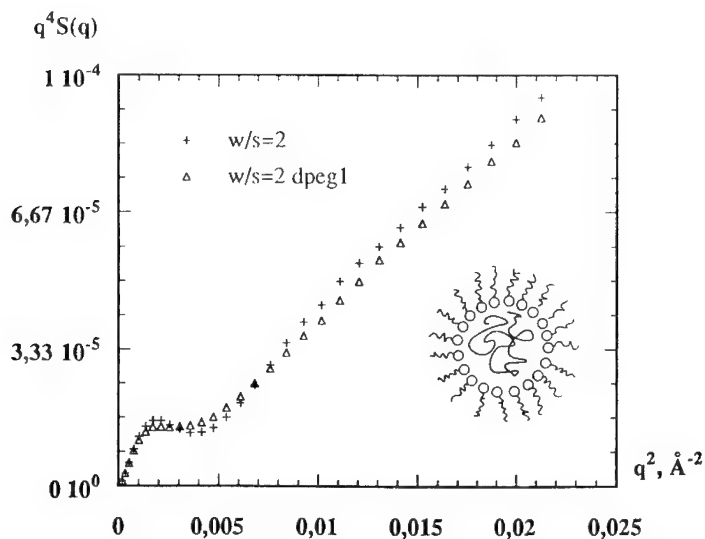
Figure 1. $q^4 i_f(q)$ vs q^2 plot for water in oil microemulsion with and without polymer.

4)Summary

The change of in shape fluctuations seems to be weak with polymer inside. Clearly here the distribution of the droplets volumes should be the most important parameter which controls in first approximation the balance between the confinement free energy of the chains and the droplets elastic energy [4] and the effect of size polydispersity are more important. One may estimate, in agreement with our observations, that one or several chains imposing a local monomer concentration c_p cannot enter in a single droplet if c_p is larger than c_p^* and the film rigidity is of order $k_B T$. We interpret the induced size polydispersity by

a mechanism in which it might be more favourable for the system to form larger droplets containing two or more chains while some smaller droplets would be empty. This induced polydispersity then depends on the spontaneous curvature of the surfactant layer, and should decrease if C_0 is larger. This conclusion is in agreement with our observations that for higher ionic strength I = 9% , w/s=2, the polydispersity parameter z changes from 7 to 5.3 with one chain of PEG inside as opposed to for I=5.8% where z changes from 8 to 5, when measured in core contrast.. Thus at higher ionic strength corresponds to higher values of C_0, the polymer induces less relative polydispersity. Confining polymer is thus a sensitive way to probe the elasticity of surfactant film.
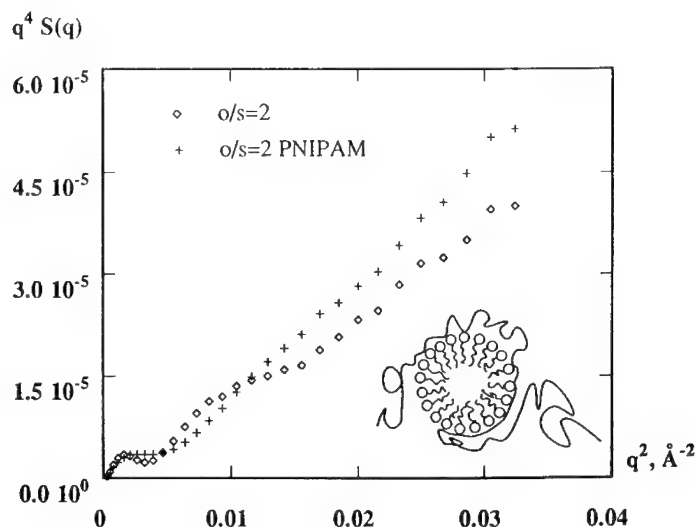
Figure 2. $q^4 i_f(q)$ vs q^2 plot for oil in water microemulsion with and without polymer.

The effect of adsorbed polymer is more difficult to analyse. Adsorption of polymer certainly exerts stresses on the droplets which may deform their shape. It is at first sight difficult to unravel this effect from the prediction of lowering the surfactant layer rigidity. In any case, separating size and shape fluctuations only from the static data is a difficult task, at our present stage of knowledge. This was one of our motivation to perform spin echo experiments.

FLUCTUATIONS OF THE DROPLETS FROM DYNAMIC NSE EXPERIMENTS

As discussed in reference [9] NSE directly measures the normalized intermediate scattering function $I(q,t)/I(q,0)$. The small fluctuations around a time averaged spherical shell can be written as follows

$$I(q,t)=\langle exp[-D_t q^2 t] \; V(\delta\rho)^2 \; [f_0(qR)+\Sigma_{l\geq 2} \; (2l+1/4\pi) \; f_l(qR)\langle|u_l|^2\rangle exp[-t/\tau_l] \;] \rangle_R \qquad (5)$$

where the time independent part $f_0(qR=x)$ is expressed in terms of Bessel functions (j's)

$$f_0(x)=j_0(x)^2+j_0(x)\Sigma_{l\geq 2} \; (2l+1/4\pi)\langle|u_l|^2\{[\;2-x^2+l(l+1)]\; j_0(x)-2xj_1(x)\} \qquad (6)$$

$$f_l(x)=[(l+2)j_1(x)-xj_{l+1}(x)]^2 \qquad (7)$$

here D_t is the diffusion of the center of mass of the droplets, V is the volume of the surfactant shell, u_l is the fluctuation amplitude of the lth mode, corresponding to lth spherical harmonics, τ_l is the relaxation time of the lth mode.

As a first step, we did a very simple analysis of the data of the NSE signal as a function of decay times, where we see that simple exponential fits work at low q's and for short times for $qR>\pi$. We start to see a deviation from single exponentials at $qR>\pi$. At small q's we observe the motion of the droplet as a whole, at large q's, $qR>\pi$ we start to be sensitive to the internal shape fluctuations of the droplets. As explained in [9], at $qR=\pi$ the contribution of the static form factor of the shell reaches its minimum meanwhile the form factor of the l=2 mode is at its maximum. Therefore at $qR=\pi$, the scattering is dominated by the contribution of the l=2 mode. In the plot $D_{eff}(q)$, the effective diffusion constant , as a function of wavevector q, we observe a characteristic peak due to the contribution of the mode l=2.

In our case the interests lies in the mode l=0 (polydispersity) and l=2 which dominate the NSE data. We can deduce the values of the amplitudes of the l=0 mode which, we assume, is related to the polydispersity index z of the Flory-Schultz distribution of scattering from array of polydisperse spherical shells, obtained from the static experiments.

$$<\delta r^2/r^2>=1/z+1=u_0^2/4\pi \qquad (8)$$

The amplitudes of the fluctuation are related to the elastic parameters of the fluctuating surfactant shell by the calculation of Safran and Milner [10]. For the modes l=0 and l=2 the amplitude is given by

$\langle|u_0|^2=kT/2K(6-A)$ and $\langle|u_2|^2=kT/4KA$, where $A=4R/R_s-3K/K_g$

434

where K is the elastic curvature modulus, K_g is the saddle splay modulus and R_S is the spontaneous curvature. The relaxation time of the l=2 mode is then given by the equality $\tau_2=(\eta R^3/KA)55/24$, where η is the viscosity.

$I(q,t)/I(q,0)$
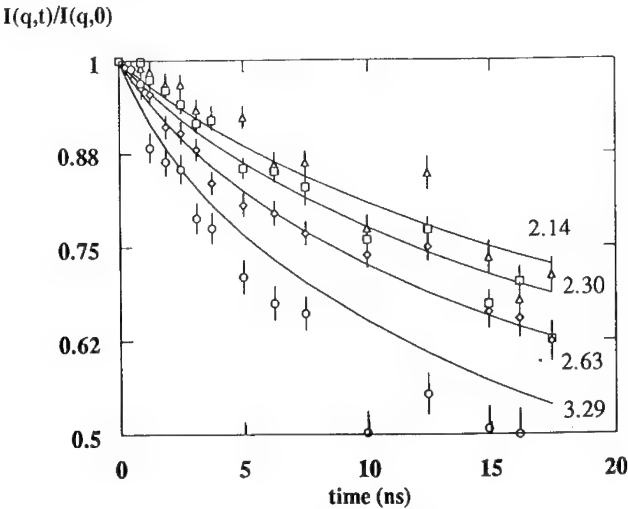
Figure 3. Spin echo signal as function of time for various qR values for a single chain of polymer DPEG $M_w=10^4$ confined inside water in oil microemulsion w/s=2.

Table I

R_{mean} Å	D_o cm²/s	Z_{core}	Z_{shell}	viscosity η cp	K (kT)	U_o	A	τ_2 ns	U_2
w/s=2, 35	2.4×10^{-7}	8	13.4	1.6×10^{-2}	1	0.93	5.43	7.06	0.215
w/s=2 dpeg1, 36	2.2×10^{-7}	5	8.4	1.8×10^{-2}	1	1.16	5.63	8.34	0.210
w/s=3 51	0.9×10^{-7}	5	14.2	1.0×10^{-2}	0.9	0.91	5.33	15.46	0.228
w/s=3 dpeg2 57	1.3×10^{-7}	3	9.4	1.3×10^{-2}	0.9	1.09	5.54	26.99	0.223
o/s=2 48	1.9×10^{-7}	22	22.2	1.1×10^{-2}	5.0	0.74	5.81	2.33	0.093
o/s=2 pnipam 47	1.2×10^{-7}	14	13.7	1.7×10^{-2}	1.65	0.92	5.69	10.59	0.164

435

For a quantitative intrepretation of the data we use the results in [9]. We do a numerical simulation of the data using the difference of scatterring from two spheres of finite thickness d for the static part of the expression (in our case d=15 Å extracted from the SANS data). For the static part, we use the scattering from an unperturbed sphere given by $[3j_1(qR)/qR]^2$ averaged over the proper size polydispersity. For the dynamic part we use the whole expression given by Safran and Milner.

The final results of two such fits with and without polymer are shown with the experimental data in Figures 3 and 4, where we have plotted the effective diffusion coefficient as a function of the wavevector q. The parameters obtained from such a fit are given in Table I. R_{mean} and z are obtained from the SANS data. D_0 the value of the effective diffusion coefficient in the limit q—>0 was measured by dynamic light scattering.

In the case of Figure 3 we show the results of a single chain of polymer confined inside the water in oil droplets. With polymer the height of the effective peak is decreased, i.e. the fluctuations of the mode l=2 are diminished by the presence of the polymer inside the droplet. The rigidity K of the surfactant layer remains unperturbed (table I) what changes is the effective viscosity felt by the surfactant layer in the presence of the polymer. It is the dissipative term i.e. the viscosity which is effected due to the polymer. Our fit does not agree very well with the data at the largest q values, this may be either due to the existence of a scale dependant dissipation or to the failure of the Safran Milner calculation. We also note that the amplitude of the mode l=2, remains more or less uneffected by the presence of polymer. This confirms our analysis that the most important effect of the confined chains is to act on the droplets polydispersity.
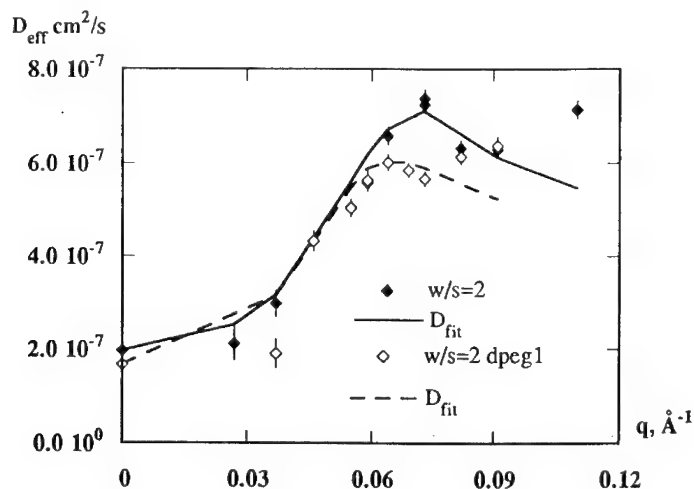
Figure 4. D_{eff} as a function of q. Experimental points (symbols). Numerical fits (lines). For w/s=2, with polymer inside (open symbols) and without polymer (solid symbols).

In Figure 5 we consider the case of the inverse oil in water microemulsion, where the hydrosoluble polymer PNIPAM is present in the continous phase. Our fit does not describe

the data very well. Nevertheless, the parameters of such a fit , the best possible are shown in Table I. There is an increase in the local viscosity felt by the fluctuating surfactant layer and the coefficient of rigidity K is decreased in the presence of polymer, however, the initial value K=5kT seems too large even for this rather monodisperse sample. We observe also that the amplitude of the mode l=2 increases in the presence of polymer. This confirms that the adsorbed polymer deforms the shape of the droplets, as hinted by the static spectra, and that this deformation could be related to a decrease in the film rigidity. At last we also remark that for both polymer inside and outside the relaxation time of the mode l=2 is smaller with polymer than without, as one could expect. However, we are lacking a precise model for the relaxation of the fluctuations of the droplets in presence of polymer.
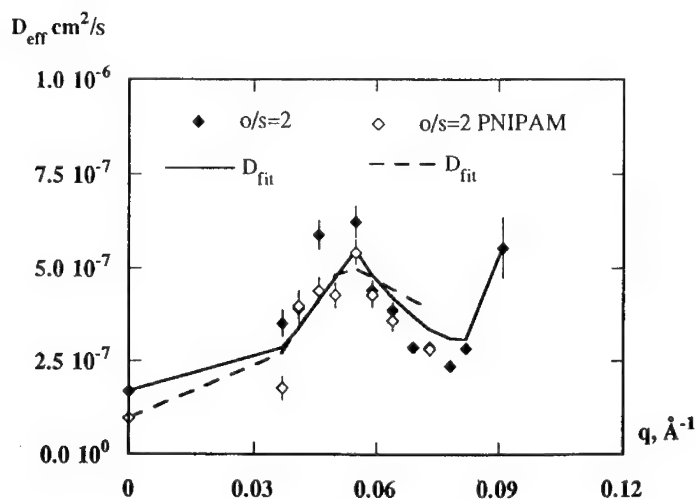
Figure 5. D_{eff} as a function of q. Experimental points (symbols). Numerical fits (lines). For o/s=2, with polymer inside (open symbols) and without polymer (solid symbols).

CONCLUSION

The statics data by SANS corresponds to the time averaged values over all modes of deformation, whereas by NSE we principally probe the fluctuations of the mode l=2. It is

satisfying to note that our observations, which are mainly qualitative, indicate the same trends in both cases. A lot of theoretical and experimental work however remains to be done to improve the methods of analysis of the data, both in statics and dynamics experiments, in order to separate better size and shape fluctuations and get quantitative measurements of the surfactant film elastic parameters and of the effects of polymer on them.

ACNOWLEGDEMENT

REFERENCES

1. P.G. de Gennes, J. Phys. Chem. **94,** 8407 (1990).

2. J. T. Brooks, C. M. Marques, M. E. Cates, Europhys. Lett. **14,** 713 (1991).

3. H. Ringsdorf, J. Venzmer, F. M. Winnik, Angew. Chem. Int. Ed. Engl. **30,** 315 (1991).

4. J. Lal and L. Auvray, J. Phys. II France **4,** 1 (1994).

5. P. Lianos, S. Modes, G. Staikos, andW. Brown, Langmuir, **8,** 1054 (1992).

6. M. J. Saurez, H. Levy and J. Lang, J. Phys. Chem. **97,** 9808 (1993).

7. S. Radiman, L.E. Fountain, C. Toprakcioglo, A. de Vallera and P. Chieux, Progr. Coll. Polym. Sci., **81,** 54 (1990).

8. J. T. Brooks and M. E. Cates, Chem. Phys. **149,** 97 (1990).

9 B. Farago, D. Richter, J. S. Huang, S. A. Safran, S. T. Milner, Phys. Rev. Lett. **65,** 3348 (1990)..

10. S. T. Milner and S. Safran, Phys. Rev. A, **36,**4371 (1987).

11. R. Kirste and G. Porod, Koll. Z., Z. fur Polym. 184, **1** (1962).

12. L. Auvray, also credited to T. Crowley, Ph. D; Thesis Oxford (1984).

13. M. Teubner, J. Chem. Phys. **92** 4501 (1990).

14. A. Onuki, Phys. Rev. A **45** 3884 (1990).

15. M. Kotlarchyk, S. H. Chen, J. Chem. Phys. **79,** 2461 (1983).

16. F. Sicoli, D. Langevin, L.T. Lee, J. Chem. Phys. **99,** 4759 (1993)

A POPULATION BALANCE ANALYSIS OF SUBSTRATE DISTRIBUTION EFFECTS ON ENZYMATIC REACTION RATES IN REVERSED MICELLES

T. ALAN HATTON* AND ANDREAS S. BOMMARIUS**
*Department of Chemical Engineering, Massachusetts Institute of Technology, Cambridge MA 02139
**Organic and Biological Chemistry R&D, Degussa, D-63403 Hanau, Germany

ABSTRACT

A population balance analysis of the statistical distribution of substrates over reversed micelles indicates the importance of accounting for concentration fluctuations within the micelles in interpreting observed enhancements in enzymatically-catalysed reactions in reversed micellar media. When the reactions are slow relative to the rates of solubilizate exchange via micellar coalescence and redispersion processes, analytical solutions to the detailed population balance equations are obtained, and the connection between Michaelis-Menten kinetics in reversed micellar media and bulk aqueous solution is made. It is shown that the finite occupancy number of the micelles at low water content leads to a statistical distribution of substrates over the micelle population, and that this can give rise to changes in the apparent reaction kinetics, even in the absence of changes in the intrinsic reaction parameters themselves. The model predictions are in good qualitative agreement with reported experimental results.

INTRODUCTION

Reversed micelles are thermodynamically stable water-in-oil microemulsions in which surfactant-coated, nanometer-scale water droplets are dispersed in a continuous organic phase. There has been much interest in the encapsulation of enzymes within the water pools of reversed micellar solutions, as they show significant potential as reaction media for the biocatalytic synthesis of lipophilic compounds.[1,2] The simplest of enzymatic reaction schemes can be represented by the equation

$$E + S \underset{k_{-1}}{\overset{k_1}{\rightleftharpoons}} ES^* \overset{k_2}{\rightarrow} E + P$$
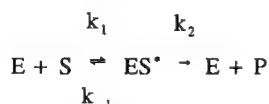
where E, S and P represent enzyme, substrate and product, respectively, and ES* is the enzyme-substrate complex. The rate of product formation can be derived assuming equilibrium for the binding of the substrate to the enzyme

$$\frac{d[P]}{dt} = \frac{k_2[E][S]}{K_{S,aq} + [S]}$$

where $K_{S,aq} = k_{-1}/k_{1,aq}$ is the Michaelis-Menten constant.

It is found that the values obtained for the two reaction parameters in reversed micellar media depend strongly on the molar water-to-surfactant ratio, $\omega_0 = [H_2O]/[Surf]$, in the reversed micellar solution.[3,4] Various reasons have been suggested for this behavior, including the possibility of changes in enzyme structure with changing amount of water present. Rahaman and Hatton,[5] however, concluded that the size of the protein-filled micelle remains constant as the water content of the microemulsion is changed, and that it is only the empty micelle size that changes. Thus, the environment sensed by the enzyme is not dependent on water content, and therefore neither should be the intrinsic reaction parameters. Here, we propose that the effects observed are a consequence of the statistical distribution of the substrate molecules over the micelle population, and the way this is affected by the changing water pool properties of the *empty* micelles as ω_0 is altered.

GENERAL POPULATION BALANCE MODEL

Substrate molecules are assumed to be distributed unevenly over empty micelles containing no enzymes (e), filled micelles containing free enzyme (f), and filled micelles containing enzyme-substrate complexes (f^*). These micelles exchange contents through coalescence of two micelles to form a transient dimer, which then breaks apart again to form two new micelles, with a consequent redistribution of the substrate molecules. We define $p_e(k)$, $p_f(k)$ and $p_{f^*}(k)$ to be the fractions of the total number of micelles, N, that contain k free substrates in no enzyme-, free enzyme-, and enzyme-substrate complex-containing micelles, respectively. These distributions depend in a complex manner on the intermicellar exchange rates, and the various rate processes associated with the enzymatically-catalyzed reaction. We develop here a population balance analysis that accounts for the dynamic exchange and reaction processes, and use this analysis to explore the effects of the reversed micellar medium on the overall reaction kinetics.

When two micelles coalesce and redisperse again the substrates in the initial micelles are redistributed over the two newly-formed micelles in a non-uniform way. The rate of production of the empty micelles containing k substrates is determined partly by the rate at which these micelles are formed as a result of coalescence and redispersion of empty micelles containing j substrates, $Np_e(j)$, and those containing m substrates, $Np_e(m)$, such that one of the newly formed micelles contains k substrates. These interactions are governed by a second order rate constant, k_{ex}. Other contributions to the overall balance on empty micelles containing k substrates include similar interactions between the empty and filled micelles, which, for convenience, we assume here also to be characterized by the constant k_{ex}, and loss of these micelles by coalescence with all other micelle types in the system. The probability that a substrate reports to the newly-formed empty micelle when a filled and empty micelle coalesce and redisperse is denoted by λ.

In addition to the exchange processes similar to those described above, enzyme-filled micelles with k free substrates can be formed by the three routes associated with (i) dissociation of an enzyme-substrate complex in a micelle containing $k-1$ free substrates, (ii) the loss of this micelle-type by association of a substrate with the enzyme, and (iii) the release of a product by an enzyme-substrate complex in an f^*-type micelle containing k free substrates.

For the rate of formation by reaction of complex-containing reversed micelles with k free substrates, we need to allow for (i) the loss of these micelles due to dissociation to form a free enzyme in a micelle with $k+1$ substrates, (ii) the formation of these micelles by the association of a substrate with an enzyme in a micelle initially containing $k+1$ substrates, and (iii) loss due to product formation from the complex in a micelle containing k substrates.

The population balance equations that result from this set of assumptions are

$$\frac{dp_e(k)}{d\tau} = \frac{1}{2}\sum_{j=0}^{\infty}\sum_{m=k-j}^{\infty} p_e(j)p_e(m)\binom{j+m}{k}\left(\frac{1}{2}\right)^{j+m}$$

$$\sum_{j=0}^{\infty}\sum_{m=k-j}^{\infty} p_e(j)\left[p_f(m)+p_{f^*}(m)\right]\binom{j+m}{k}\lambda^k(1-\lambda)^{j+m-k}-p_e(k) \tag{1}$$

$$\frac{dp_f(k)}{d\tau} = \sum_{j=0}^{\infty}\sum_{m=k-j}^{\infty} p_f(j)[\tfrac{1}{2}p_f(m)+p_{f^*}(m)]\binom{j+m}{k}\left(\frac{1}{2}\right)^{j+m}$$

$$\sum_{j=0}^{\infty}\sum_{m=k-j}^{\infty} p_f(j)p_e(m)\binom{j+m}{k}\lambda^k(1-\lambda)^{j+m-k}-p_f(k) \tag{2}$$

$$+k_1\left[K_sp_{f^*}(k-1)-\gamma_k kp_f(k)\right]+k_2p_{f^*}(k)$$

440

$$\frac{dp_{f*}(k)}{d\tau} = \sum_{j=0}^{\infty}\sum_{m=k-j}^{\infty} p_{f*}(j)[\tfrac{1}{2}p_{f*}(m)+p_f(m)]\binom{j+m}{k}\left(\tfrac{1}{2}\right)^{j+m}$$

$$\sum_{j=0}^{\infty}\sum_{m=k-j}^{\infty} p_{f*}(j)p_e(m)\binom{j+m}{k}\lambda^k(1-\lambda)^{j+m-k}-p_{f*}(k)$$

$$-k_1\left[K_S p_{f*}(k)-\gamma_{k+1}(k+1)p_f(k+1)\right]-k_2 p_{f*}(k) \tag{3}$$

where $\tau = k_{ex}Nt$, and $K_S = k_{-1}/k_1$. Note that K_S and k_1 are based on number concentrations and not molar concentrations as used for $K_{S,aq}$ and $k_{1,aq}$. The rate constants k_1 and k_2 have been normalised with respect to Nk_{ex}. The 'activity coefficient' γ_k is defined to recognise the different statistical weighting factors associated with placing k substrates in the filled and empty micelles, and is shown later to depend on λ.

Under reaction-limited conditions, the removal of substrate from the system is slow relative to the redistribution rates of the substrate over the micellar population, and an equilibrium distribution exists over this population. Thus, our problem reduces to the steady state system of equations with the irreversible reaction terms suppressed (i.e., $k_2 \approx 0$). The equations can be solved subject to the constraints on the fraction of enzyme-containing micelles, ϕ, and the average micellar occupancy number, μ,

$$\sum_{k=0}^{\infty}\left[p_f(k)+p_{f*}(k)\right]=\phi; \qquad \sum_{k=1}^{\infty} k\left[p_e(k)+p_f(k)+p_{f*}(k-1)\right]=\mu$$

It can be shown that solutions satisfying this set of equations are

$$p_e(k) = (1-\phi)\frac{(\lambda\psi)^k e^{-\lambda\psi}}{k!}; \qquad p_f(k) = \frac{\phi}{(1+\psi/K_S)}\frac{[(1-\lambda)\psi]^k e^{-(1-\lambda)\psi}}{k!}$$

$$p_{f*}(k) = \frac{\phi(\psi/K_S)}{(1+\psi/K_S)}\frac{[(1-\lambda)\psi]^k e^{-(1-\lambda)\psi}}{k!}; \qquad \gamma_k = \frac{1}{(1-\lambda)} \tag{4}$$

where

$$\psi = \frac{\mu-(\xi K_S+\phi)+\sqrt{[\mu-(\xi K_S+\phi)]^2+4\xi K_S\mu}}{2\xi} \tag{5}$$

with $\xi = (1-\phi)\lambda+\phi(1-\lambda)$. The function ψ is a measure of the relative distribution of the substrates over the filled and empty micelles, and is the root of the material balance equation.

RELATION TO THE MICHAELIS-MENTEN EQUATION

The rate of product formation is

$$\frac{d[P]}{dt} = k_2 N \sum_{k=0}^{\infty} p_{f*}(k) = \frac{k_2[E]\psi}{K_S+\psi} \tag{6}$$

where it has been noted that $\phi = [E]/N$. While this is in the familiar form of the Michaelis-Menten equation, the concentration, ψ, is not experimentally accessible. We can express this equation in

terms of the substrate concentration $[S]_{mic} = \mu/VN_A$, (N_A is Avogadro's number) based on the average micellar water pool volume, $V = (1-\phi)V_e + \phi V_f$, by multiplying top and bottom by the ratio $(\mu/\psi)/VN_A$:

$$\frac{d[P]}{dt} = \frac{k_2[E][S]_{mic}}{K_{S,app} + [S]_{mic}} \tag{7}$$

The apparent Michaelis-Menten constant, $K_{S,app}$, can be identified as

$$K_{S,app} = \left(\frac{\mu}{\psi}\right)\frac{K_S}{VN_A} = \left(\frac{\mu}{\psi}\right)\frac{V_f/V}{(1-\lambda)}K_{S,aq} \tag{8}$$

on recognizing that $K_S = \gamma W_f N_A K_{S,aq}$. Note, however, that this constant is not consant at all, as the ratio (μ/ψ) will, in general, be a function of concentration, μ (and hence also $[S]_{mic}$). This has important ramifications with regard to the estimation of kinetic parameters using traditional methods such as Lineweaver-Burke plots.

We can expand (μ/ψ) in a Taylor series about $\mu = 0$ to get

$$\left(\frac{\mu}{\psi}\right) = \left(\frac{\mu}{\psi}\right)_{\mu=0} + \frac{d}{d\mu}\left(\frac{\mu}{\psi}\right)_{\mu=0}\mu + \dots \tag{9}$$

and neglect terms second order and higher in μ. On substituting this expansion in equation (7), and rearranging, we find

$$\frac{d[P]}{dt} = \frac{k_2^*[E][S]_{mic}}{K_{S,app}^* + [S]_{mic}} \tag{10}$$

where k_2^* and $K_{S,app}^*$ are the measured kinetic parameters, and are given by

$$\frac{k_2^*}{k_2} = 1 + \frac{\phi/K_S}{(1-\phi)\lambda + \phi(1-\lambda)}; \qquad \frac{K_{S,app}^*}{K_{S,aq}} = \frac{\upsilon/(1-\upsilon) + \phi/(1-\phi)}{\lambda/(1-\lambda) + \phi/(1-\phi)}\left(\frac{k_2^*}{k_2}\right) \tag{11}$$

respectively. These equations are valid for $\mu \ll 1$. For $\mu \geq 1$, where ψ/μ is constant, $k_2^*/k_2 = 1$, and the result for $K_{S,app}^*$ still holds. $\upsilon = V_e/(V_e + V_f)$..

NUMERICAL EXAMPLE

Rahaman and Hatton[5] have shown that the filled micelle size remains essentially unchanged as the total water content of a reversed micellar solution is varied, and that an increasing water content is reflected in an increase in empty micelle size. With this constraint, geometric arguments yield

$$\rho = \frac{R_e}{R_f}\frac{W_0 - (1-\rho_P^3)\alpha}{(1-\alpha)}; \qquad \frac{\phi}{1-\phi} = \frac{\alpha}{1-\alpha}\left[\frac{W_0}{1-\alpha} - (1-\rho_P^3)\frac{\alpha}{1-\alpha}\right]^2$$

442

where $\alpha=(4\pi R_f{}^2/f_S)(N_f/N_{S,total})$, and $W_0=\omega_0/(R_f f_S/3v_w)$. The size of the filled micelle, R_f, is assumed to be constant at 33Å. The head group area of the surfactant is f_s (60Å^2), and v_w is the volume of a water molecule (30Å^3). R_e is the radius of the empty micelle, while $\rho_P=R_P/R_f$, with R_P being the protein radius (21Å). $N_f/N_{S,total}$ is the molar enzyme-to-surfactant ratio.

The only undefined parameter in the model formulation is λ. As the empty micelle decreases in size, the fraction of free water within the micelle core decreases, the effective environment seen by the substrate molecule is less favourable for its solublisation, and hence the partitioning towards the filled micelles becomes increasingly favoured. Thus, we expect λ to decrease with decreasing water content. For illustrative purposes, we assume that this parameter varies with W_0 according to

$$\lambda/(1-\lambda) = W_0^n \upsilon/(1-\upsilon) = W_0^n \rho^3/(1-\rho_p^3)$$

For $n=0$, this expression reduces simply to that of passive partitioning, in which the probability that a substrate enters a given micelle is dependent only on the relative volumes of the two water pools, i.e., the solvent quality of the water is the same for both micelle types.

DISCUSSION

The ψ/μ ratio is shown in Figure 1 as a function of the average micelle occupancy number, μ, where it is evident that only at very low occupancy numbers is this ratio a function of μ, and that for average occupancy numbers greater than about 0.4-0.5, this ratio has an asymptotic value determined by the distribution factor, λ. It is evident from the results depicted in Figure 2 that these low occupancy numbers are attained under realistic experimental conditions, but only for W_o values less than about 0.5. Under these conditions, then, we expect k_2^*/k_2 to differ from unity. This is seen to be true in Figure 3, where the model predictions for two different exponents n are in
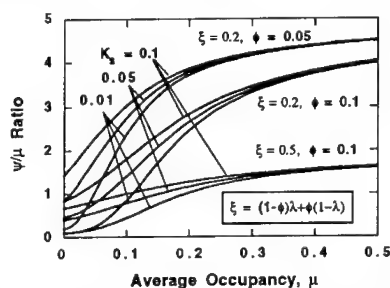
Figure 1 The ratio ψ/μ depends on the average occupancy of the micelles, μ.
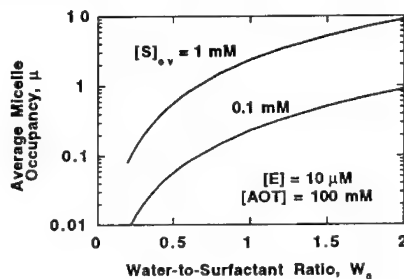
Figure 2 The average occupancy number is small for low micellar phase water content

good qualitative agreement with experimental results reported by Fletcher et al.[4] Note that the model predictions are indicated by solid lines for the region over which they are valid; the dotted lines indicate the model predictions over the range of parameter values where the assumption of low μ no longer holds.

The effect of overall water content on the apparent first order rate parameter is shown in Figure 4 for different exponents n. For $n=0$, there is no effect of W_0 on the rate constant, since this corresponds to a passive partitioning of the substrate between the micelle types. For $n>o$, the substrate partitioning favors initially the empty micelle, but with increasing W_0, the conditions within the empty micelle are more hospitable towards the substrate molecule. It is interesting to

note that even with this simple model of the substrate distribution over the different micelle types, we are able to capture the general features of the reaction rate behavior at low water contents reported, e.g., by Barbaric and Luisi.[3] The model predictions can certainly be improved by using a more detailed model for λ. For instance, the exponent n would be expected to decrease to zero at the higher water contents ($W_0 > 0.75$, say), and here we would not expect the reaction rate to depend on W_0. Such refinements are beyond the scope of the present study, but are currently under consideration.
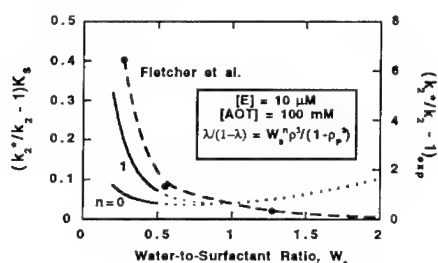
Figure 3 The effect of micellar phase water content on the turnover number, k_2
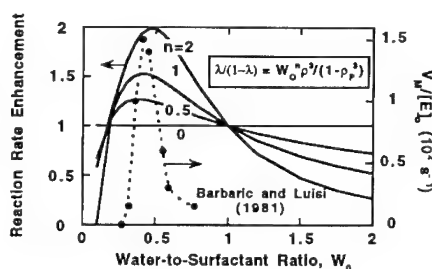
Figure 4 The enzyme activity depends on the micellar phase water content

CONCLUSIONS

The statistical distribution of substrate molecules over a reversed micelle population has been shown to cause changes in both the apparent turnover number, k_2^*, and the apparent reaction velocity, $k_2^*/K_{S,app}^*$, in a manner consistent with experimental observations of a number of research groups around the world. These effects are particularly important at low water contents where the number of micelles formed is large, such that the average occupancy per micelle is very low. Thus, it can be concluded that many of the features observed in experimental reaction rate measurements can be attributed to simple partitioning phenomena owing to the different solvation environments afforded by the different micelle types, and need not necessarily be due to changes in the active pocket of the enzyme, structural perturbations, or other interpretations (some of which are aphysical) advanced by many researchers in this area. This idea is appealing in light of the experimental measurements of Rahaman and Hatton that indicate the filled micelle does not change in size as the water content is changed, and therefore neither should the environment felt by the enzyme.

ACKNOWLEDGEMENTS

REFERENCES

1. P.L. Luisi, Angew. Chem., Int. Ed. Engl. **24**, 439 (1985)
2. J.W. Shield, H.D. Ferguson, A.S. Bommarius, T.A. Hatton, I&EC Fundam. **25**, 603 (1986)
3. S. Barbaric, P.L. Luisi, J. Am. Chem. Soc. **103**, 4239 (1981)
4. P.D.I. Fletcher, R.B. Freedman, J. Mead, C. Oldfield, B.H. Robinson, Colloids Surf. **10**, 193 (1984)
5. R.S. Rahaman, T.A. Hatton, J. Phys. Chem. **95**, 1799 (1991)

DYNAMICS OF FERROELECTRIC AND NEMATIC LIQUID CRYSTALS CONFINED IN POROUS MATRICES

FOUAD M. ALIEV
Department of Physics and Materials Research Center, PO BOX 23343, University of Puerto Rico, San Juan, PR 00931-3343, USA

ABSTRACT

We performed dielectric spectroscopy measurements to study dynamics of collective modes of ferroelectric (FLC) and molecular motion of nematic (NLC) liquid crystals with polar molecules confined in silica macroporous and microporous glasses with average pore sizes of 1000 Å (volume fraction of pores 40%) and 100 Å (27%) respectively. For FLC the Goldstone and the soft modes are found in macropores. The rotational viscosity associated with the soft mode is about 10 times higher in pores than in the bulk. These modes are not detected in micropores although low frequency relaxation is present. The last one probably is not connected with the nature of liquid crystal but is associated with surface polarization effects typical for two component heterogeneous media. The difference between the dynamics of orientational motion of the polar molecules of NLC in confined geometries and in the bulk is qualitatively determined by the total energy F_s of the interaction between molecules and the surface of the pore wall, which is found $F_s \approx 10^2 erg/cm^2$.

INTRODUCTION

Investigations of condensed matter in porous matrices have revealed various new properties and effects not observed in the same substances when they are in the bulk [1-10]. The difference between the surface and bulk properties, as well as finite size effects, are manifested most strikingly in the case of liquid crystals (LC) [11-16]. This is due to the fact that LC are "soft" systems because the energy responsible for long-range orientational order is fairly small. The substrates between which a layer of LC is confined can exert their influence on the LC up to distances L which may reach several thousand angstrom[11]. Investigations of LC in pores of sizes less than L should, in principle, provide information on the interfacial properties of these LC. Generally all aspects of the physical properties of LC in restricted geometries were studied on nematic LC, and just in a few papers static properties of smectic phase were studied [14]. While it is well known that restricted geometries have a significant effect on the ordering and phase transition of nematic liquid crystals [12-14] there has been a little work performed to characterize the influence of confinement on dynamics of LC [15,16]. There are at least two factors influencing on the dynamics of fluids or liquid crystals in confinement: surface interaction and geometrical effects. The confinement can break the symmetry of the bulk phase, and change viscosity, that can lead to a modification of dynamics. In the case of polar liquid-crystal molecules, the substrate may induce a polar order and give rise to the polarization effects , which can also be due to a gradient of the order parameter and inhomogeneity of orientation. Clearly, the bent nature of the pore may induce these effects in porous matrices. We performed dielectric, DSC and X-ray scattering measurements to study the influence of the confinement on the dynamics, phase transitions and structure of a FLC imbibed inside silica porous glasses with thoroughly interconnected and randomly oriented pores. The influence of the confinement and interface on the orientational mobility of NLC molecules were investigated by dielectric spectroscopy.

SAMPLES

The matrices were the same as we used previously to investigate concentration fluctuations of binary liquid mixtures in macropores[8] and orienetational susceptibility of ne-

matic liquid crystal in micropores[13]. Porous silicate glass can be used as an ideal matrix to study the influence of a temperature on the surface effects that occur at the interface between the glass and some other material. Since the structural characteristics of these matrices are nearly independent of the temperature, all observable effects when the temperature is changed can be attributed to the change in the physical properties of the second component (LC). Moreover, silica porous glass matrix has practically negligible electrical conductivity, and its dielectric permittivity is independent of the temperature and frequency for a wide range of frequencies. Macroporous and microporous matrices with thoroughly interconnected and randomly oriented pores with average pore sizes of 1000 Å (volume fraction of pores 40%) and 100 Å (27%) respectively, were prepared from the original sodium borosilicate glasses. The sodium borate phase was removed by leaching, and the matrix framework consisted of SiO_2. The FLC we used was SCE 12 synthesized by BDH Ltd. through E.M. Industries. The phase transitions temperatures of SCE 12 in the bulk are: $SmC^* \, 66°C \, SmA^* \, 81°C \, N \, 121°C \, I$. Nematic liquid crystals were 5CB and cyanophenyl ester of heptilbenzoic acid, i.e. cyanophenyl heptylbenzoate (CPHB). The dipole moment μ of the 5CB molecule is $5D$, and it is parallel to the longitudinal axis of the molecule ($\beta = 0$, where β is the angle between the dipole and the long axis of a molecule); and for CPHB $\mu = 6.1D$ and $\beta = 16°$. The temperatures of phase transitions of 5CB and CPHB in the free state are $T_{CN} = 295K$ and $T_{NI} = 308K$ (5CB), and $T_{CN} = 316.5K$ and $T_{NI} = 328.1K$ (CPHB). In dielectric measurements the samples were porous glass plates, of dimension $2 \times 2 \times 0.1 cm$; they were heated to $450°C$ and pumped out; this was followed by impregnation with the liquid crystals from an isotropic melt.

FERROELECTRIC AND NEMATIC LIQUID CRYSTALS IN PORES

The main purpose of this paper is to study dielectric relaxation in confined FLC, and we use X-ray and DSC as additional methods to establish existence of layered structures (X-ray scattering) and the phase transition (X-ray and DSC). Using X-ray scattering it was found that at temperatures below $52°C$, the distance d_p between layer spacing of FLC in pores depends on temperature and increases from $d_p \approx 28.3 Å$ at $25°C$ up to $d_p \approx 29.7 Å$ at $\approx 52°C$. In the temperature range $52°C \leq T \leq 80°C$, $d_p \approx 29.7 Å$ and is constant. For the bulk FLC in temperature range $25°C \leq T \leq 67°C$, d_b varies within limits $28.1 Å \leq d_b \leq 31.2 Å$ and is characteristic of SmC^* phase. In temperature range $67°C \leq T \leq 80°C$, $d_b = 31.2 Å$ and corresponds to SmA^* phase. For FLC confined in pores there is not enough information to make a conclusion about types of smectic phases: are they SmC^* and SmA^* or SmC and SmA? Therefor, below we will call smectic phases in pores simply SmC and SmA. DSC measurements show a bump covering a broad temperature region $42°C \leq T \leq 52°C$ in the plot of heat flow versus temperature. This bump is connected with a smeared phase transition and the temperature $\approx 50°C$ could be attributed to phase transition from SmC to SmA. This transition temperature shows a significant shift ($\Delta T \sim 15°C$ from the bulk transition temperature. Detailed arguments for these conclusions and analyses of X-ray and DSC measurements will be published separately.

Having identified the existence of layered structures of Sm C and Sm A types and very broad phase transition between these phases in pores we turned our attention to study the dynamics of the Goldstone and the soft modes by dielectric spectroscopy. Measurements of the real ϵ' and imaginary ϵ'' parts of the complex dielectric permittivity in frequency range of $1 Hz$ to $5 MHz$ at different temperatures were carried out by Schlumberger Technologies the 1260 Impedance/Gain-Phase computer controlled Analyzer. The quantities measured directly were the permittivities ϵ'_{syst} and the dielectric loss factors ϵ''_{syst} of the two-phase heterogeneous systems comprised of a matrix and a liquid crystal. We had calculated the permittiviy of the second phase (liquid crystal) using Bottcher's theory $\epsilon_{syst} = \epsilon_m + 3\omega\epsilon_{syst}/(\epsilon - \epsilon_m)/(2\epsilon_{syst} + \epsilon)$, where ϵ_m and ϵ are dielectric constant of matrix material and liquid crystal; ω is volume fraction of pores. A satisfactory theory may first of all alter the absolute values of dielectric

permittivity of liquid crystal but it should have less effect on the nature of the temperature and frequency dependencies which are discussed below. We found two regions of dielectric dispersion for FLC in macropores. The first one (low frequency) region we attribute to the Goldstone mode and the second - to a soft mode. As an example of low frequency measurements, Fig. 1 shows real and imaginary parts of the permittivity versus frequency in SmC phase.
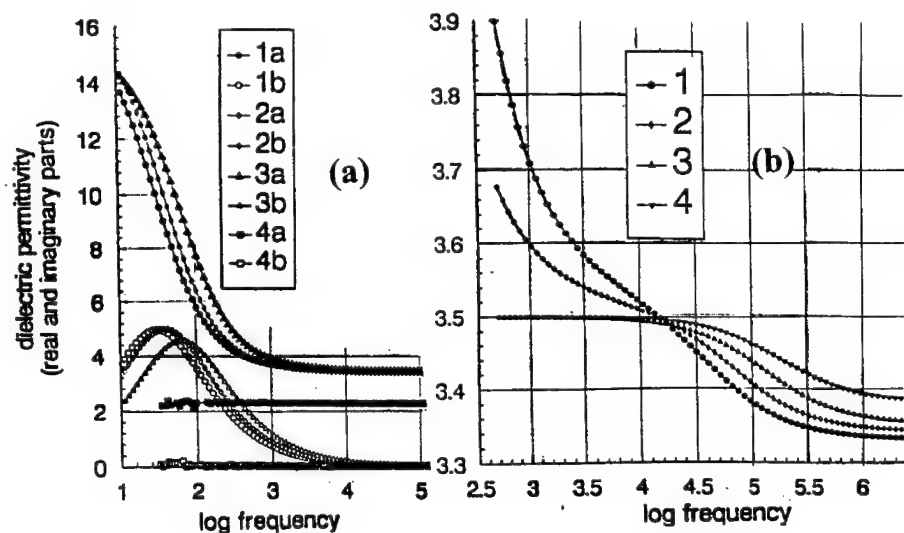

Figure 1: FLC in macropores. (a): Low frequency relaxation of ϵ' (1a,2a,3a) and ϵ'' (1b, 2b, 3b) at different temperatures: (1, 1a) - 21; (2, 2a) - 25; (3, 3a) -35°C. 4a and 4b-ϵ' and ϵ'' for empty matrix; (b): Dispersion curves ϵ' due to the soft mode as a function of frequency at different temperatures: 1-45, 2- 55, 3-70, 4-80°C

At first sight, one might be tempted to attribute low frequency dispersion to the Maxwell-Wagner (M-W) mechanism, which arises in heterogeneous materials. In the case of spherical inclusions with electric conductivity σ in a nonconducting medium ($\sigma_m = 0$ the relaxation time governed by the M-W mechanism, is $\tau = \epsilon_0(2\epsilon_m + \epsilon + \omega(\epsilon_m - \epsilon))/\sigma(1 - \omega)$, where $\epsilon_0 = 8.854 \times 10^{-12} F/m$. We estimate that in the case of the investigated samples the dispersion due to M-W polarization should be manifested at frequencies $f \leq 10^3 Hz$. This is the reason why the relaxation times obtained at frequencies $f \geq 10^3 Hz$ should be regarded as the dipole properties of the investigated LC in porous matrices. Two possibilities for the explanation of low frequency dispersion (the Goldstone mode or M-W mechanism) can be distinguished by studying the temperature dependence of the dielectric permittivity. The low frequency contribution to dielectric permittivity decreases with increasing temperature and at temperature $\approx 50°C$ is much smaller than in temperature region below $\approx 40°C$ (see Fig.1b). This behavior is consistent with interpretation of the feature as the superposition of the Goldstone mode (which vanishes at critical temperature) and dispersion resulting from the M-W mechanism (the contribution from M-W mechanism exists at all temperatures). The overlapping of the Goldstone mode and M-W dispersion does not make possible the quantitative analysis of the Goldstone mode, and the data at Fig.1a are qualitative indications of the Goldstone mode connected with tilted layered structure identified from X-ray measurements. At the same time, then temperature approaches $\approx 50°C$ the second

relaxational process, corresponding to the soft mode, appears and at temperatures above phase transition temperature determined from X-ray scattering and DSC measurements this mechanism dominates. Again, like in X-ray scattering and DSC measurements, dielectric measurements do not show existence of sharp phase transition between SmC and SmA phases and the Goldstone mode contribution completely disappears (Fig.1b) at high enough temperatures. Plotting ϵ'' as a function of ϵ' (the Cole-Cole diagrams) enables us to separate the dispersion regions and to determine the values of the permittivities which in the second dispersion region were static and at the same time corresponded to the "high-frequency" plateau for the first dispersion region. The Cole-Cole diagrams indicate that for LC in pores the parameters α, which represent empirically the spectrum of the relaxation times, vary from 0.2 to 0.35, and then there is a spectrum of relaxation times. This is due to the fact that the properties of the surface layers begin to vary at distances of the order of molecular dimensions, and depending on the distance from the surface of a pore, the various layers of LC can have different relaxation times. This procedure was performed for all the samples and permits the use of the Debye equation for complex permittivity ϵ^*, modified by Cole and Cole, to describe it frequency dependence:

$$\epsilon^* = \epsilon_\infty + \sum_{j=1}(\epsilon_{js} - \epsilon_\infty)/(1 + i4\pi f \tau_j)^{1-\alpha_j}, \tag{1}$$

where ϵ_∞ is the high-frequency limit of the permittivity, ϵ_{js} the low-frequency limit, and τ_j the mean relaxation time. A graphical fitting enables us to determine ϵ_{js} and τ_j. Using Bottcher's formula and equation (1) we have determined quasistatic ϵ_{As} and high frequency ϵ_∞ values for soft mode, and temperature dependence of the soft mode dielectric strength $\Delta\epsilon_A = \epsilon_{As} - \epsilon_\infty$. The expressions of the soft mode dielectric strength $\Delta\epsilon_A$ and the relaxation time τ_A of the bulk SmA^* phase are well known [17]:

$$(\Delta\epsilon_A)^{-1} = (a/\epsilon^2 C^2)(T - T_c) + Kq^2/\epsilon^2 C^2, \tag{2}$$

$$\tau_A^{-1} = a(T - T_C)/\eta_\Theta + Kq^2/\eta_\Theta. \tag{3}$$

In these equations a is the coefficient contained in the temperature dependent term of Landau expansion of the free-energy density, C is linear-coupling between polarization and tilt angle, ϵ is the dielectric constant of the system in the high frequency limit, $K = K_3 - \epsilon\mu^2$, where K_3 is bend elastic constant and μ is the flexoelectric coupling constant. For bulk FLC, with helix pitch p, q is the wave vector of the pitch: $q = 2\pi/p$. For the liquid crystal confined in pores, distortions of FLC can exist, and it is naturally to assume that in this case q corresponds to the wave vector of the distortions, characterized by liner size $\approx$ pore size. The results for FLC in macropores show that temperature dependencies of $1/\Delta\epsilon_A$ and τ_A^{-1} are linear. We found that the slope of experimental $\Delta\epsilon_A^{-1}(T)$ dependence $d(1/\Delta\epsilon_A)/dT = \alpha/\epsilon^2 C^2$ is equal to ≈ 0.04, and assigning typical value $a = 3.5 \cdot 10^4 Nm^{-2}K^{-1}$ we can estimate the rotational soft mode viscosity. Temperature dependence of η_Θ, calculated by using equations (2),(3) and experimental data on temperature dependencies of $(\Delta\epsilon_A)^{-1}$ and τ_A^{-1} obeys the Arrhenius equation and η_Θ changes in the interval $(8.5 - 2.9) Ns/m^2$ in temperature interval $(45 - 80)°C$. Note that estimated values of viscosity are about 8 - 10 times higher than the typical corresponding viscosities of the bulk FLC. It is possible to estimate q from the formulas (2) and (3) at $T = T_C$ using the measured values of $\Delta\epsilon_A$, τ_A and assigning a typical value of $K = 3.4 \cdot 10^{-12}N$. The both formulas give approximetly the same value of $q \approx 7.4 \cdot 10^{10}m^{-1}$. This value corresponds to linear size $l \approx 85Å$. This result is surprising as one expects the natural length scale to be the pore size. One of the possible explanations of this result could be existence of modulated structure, which consists of periodically bent smectic layers with conserved local symmetry. The characteristic wavelength of this structure [18] roughly can be estimated as $\lambda \sim (\pi d\xi)^{1/2}$, where d is the pore size and the penetration length $\xi \sim (5 - 10)Å$. The result is $\lambda \sim 10^2 Å$. It should be noted that the calculation of this smaller length scale ($l \approx 85Å$) arises from a theory that does not contain

any contributions from the surface.

In micropores x-ray measurements show the existence of a frozen layered structure but no temperature dependence of layer spacing and no phase transitions are observed. The Goldstone and the soft modes are not detected in micropores although one low frequency dispersion process is present. The last one probably is not connected with the nature of liquid crystal but is associated with surface polarization effects typical for two component heterogeneous media.

Dielectric properties of NLC were studied in the frequency range 100 Hz-20Mz. The dependence of $\langle \epsilon \rangle$ on the frequency is shown in Fig. 2 for 5CB in micropores and in macropores, and for CPHB in micropores. It is evident that all curves of $\langle \epsilon \rangle$ are relaxational in character
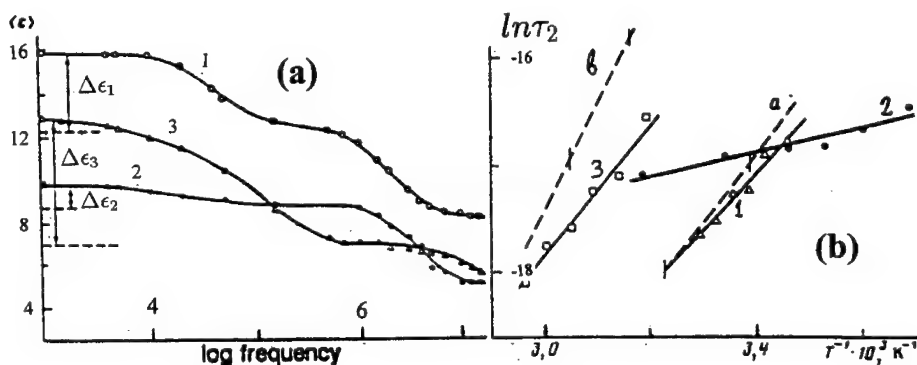
Figure 2: (a):Frequency dependence of $\langle \epsilon \rangle$ at $T = 290K$: 1) 5CB in micropores; 2) 5CB in macropores; 3) CPHB in micropores. The dashed horizontal lines are the values of $\langle \epsilon_s \rangle$ for the second dispersion region; (b): Dependence of $\ln \tau_2$ on the reciprocal temperature: a) 5CB; b) CPHB; 1) 5CB in micropores; 2) 5CB in macropores, 3) CPHB in micropores

and exhibit three regions of the permittivity dispersion. The low-frequency (first) region of the dispersion is not present in nematic liquid crystals in the free state. The relaxation times for the second dispersion region are plotted in Fig.2b as a function of reciprocal temperature. The dashed lines in Fig.2b represent the relaxation times for 5CB and CPHB in the free state., corresponding to the rotation of molecules. The main difference between the behavior of NLC in pores and the behavior in the free state is the existence of a low-frequency dispersion region, absent in the free state and characterized by relaxation times $\tau \sim 10^{-6}s$. The relaxation times τ_2 for the second region were close to τ for the free state, but the temperature dependence of τ_2 was weaker in both micropores and macropores. All these properties and the temperature hysteresis of $\langle \epsilon \rangle$ measured at the frequency of 1kHz can be explained using the assumption that the internal surface of the pore induces polar order of smectic type in the surface layer located close to the wall. It is evident from Fig.2b that the dependence of $\ln \tau_2$ on T^{-1} is linear and may be described by the relation $\tau = \tau_0 \exp(U/kT)$, where U is the activation energy. This activation energy is equal, in barrier theories, to the difference in potential energy of the stable orientations $\theta = 0$ or π and the highest potential energy of intermediate orientation ($\theta = \pi/2$) (where θ is the angle between the director and the dipole). There is no polar ordering in the free state; and therefore, the orientations $\theta = 0$ and $\theta = \pi$ are equally probable. The values of the activation energies of the investigated nematic liquid crystals in the free state were found to be $U_{1f} = 8.8 \times 10^{-13} erg$ for 5CB and $U_{2f} = 14 \times 10^{-13} erg$ for CPHB. The interaction of nematic LC molecules with the surface (characterized by the interaction energy U_0) is equivalent to the interaction with an external

field producing a polar order close to the surface, stabilizing one orientation ($\theta = 0$) and correspondingly changing U_f to $U_f + U_0$. For $\theta = \pi$ the potential becomes to $U = U_f - U_0$ and corresponds to the activation energy. The activation energies U_i, corresponding to the dependencies $\tau_2(T)$ in micropores are: $U_1 = 1.7 \times 10^{-13} erg$ (5CB) and $U_2 = 8.5 \times 10^{-13} erg$ (CPEH). A comparison of U_f and U_{0i} gives the energy of the interaction of molecules with the surfaces of the pores $U_{0i} = U_f - U_i$, and these values were $U_{01} = 7.1 \times 10^{-13} erg$ (5CB) and $U_{02} = 5.5 \times 10^{-13} erg$ (CPHB). These estimates are only qualitative; it would be reasonable to assume that $U_0 \approx 5 \times 10^{-13} erg$. Bearing in the mind that the number of molecules per cm^2 is $n_s \approx (2-3) \times 10^{14} cm^{-2}$, we found that the surface energy of the nematic liquid crystal $F_s = U_0 n_s$, should be $F_s \sim 10^2 erg/cm^2$. Another argument in support of existence of polar ordering at the wall is the low-frequency dispersion. It is natural to assume that the ratio of low-frequency increments $\Delta\epsilon_2'$ and $\Delta\epsilon_1'$ corresponding to curves 2 and 1 in Fig.4 is proportional to the volume fraction g of the polar ordered surface layer (thickness l) in the macropores, if all the molecules in the micropores belong to this layer. Then, if the macropore is modeled by a cylinder of radius R, $\Delta\epsilon_2/\Delta\epsilon_1 \approx 1 - (R-l)^2/R^2$. Using the experimental values $\Delta\epsilon_1 = 3.5$, $\Delta\epsilon_2 = 1$ determined at the same temperature and $R \approx 500 \mathring{A}$, we find that $l \approx 75 \mathring{A}$.

REFERENCES

1. D.D.Awschalom, J.Warnock, Phys.Rev.,**B35**, 6779 (1987).
2. *Molecular Dynamics in Restricted Geometries*, ed. by J.Klafter and J.M.Drake (Wiley, New York, 1989).
3. J.M.Drake, J.Klafter, Physics Today **43**(5), 46, (1990).
4. C.L.Jackson and G.McKenna, J.Chem.Phys., **93**, 9002, (1990).
5. G.Liu, Y.Li, J.Jonas, J.Chem.Phys., **95**, 6892, (1991).
6. P.A.Thompson, G.S.Grest, Phys.Rev.Lett.,**68**, 3448, (1992).
7. M.C.Goh, W.I.Goldburg, Ch.M.Knobler, Phys.Rev.Lett., **58**, 1008, (1987); S.B.Dierker, P.Wiltzius, ibid.,**66**, 1185, (1991); B.J.Frisken, D.S.Cannell, ibid.,**69**, 632, (1992).
8. F.M.Aliev, W.Goldburg, X-l.Wu, Phys.Rev.E. **47**, R3874, (1993).
9. *Dynamics in Small Confining Systems*, edited by J.M.Drake, J.Klafter, R.Kopelman and D.D.Awschalom, Material Research Society Symposium Prosidings, v.290, (Material Research Society, Pittsburgh, 1993).
10. J.Schuller, Yu.B.Mel'nichenko, R.Richert, E.W.Fisher, Phys.Rev.Lett., **73**, 2224, (1994).
11. K.Miano, Phys.Rev.Lett., **43**, 51, (1976); B.Jerome, Rep.Prog.Phys., **54**, 391, (1991).
12. D.Armitage, F.P.Price, Chem.Phys.Lett., **44**, 305 (1976), MCLC, **44**, 33, (1978), M.Kuzma, M.M.Labes, ibid., **44**, 100, (1983); G.S.Iannacchione, G.Crawford, S.Zumer, J.W. Doane, D.Finotello,Phys.Rev.Lett., **71**, 2595, (1993).
13. S.Tripathi, C.Rosenblatt, and F.M.Aliev, Phys.Rev.Lett., **72**, 2725, (1994).
14. T.Bellini, N.A.Clark, Ch.D.Muzny, L.Wu, C.W.Garland, D.W.Schaefer, B.J.Oliver, Phys. Rev.Lett., **69**, 788, (1992); N.A.Clark, T.Bellini, R.M. Malzbender, B.N.Thomas, A.G.Rappaport, C.D.Muzny, D.W.Schaefer, L.Hrubesh, ibid.**71**, 3505, (1993).
15. F.M.Aliev, M.N.Breganov, Sov. Phys. JETP, **68**, 70, (1989); F.M.Aliev, MCLC, **243**, 91, (1994); F.M.Aliev, J.Kelly, Ferroelectrics, **151**, 263, (1994).
16. X-l.Wu, W.I.Goldburg, M.X.Liu, J.Z.Xue, Phys.Rev.Lett., **69**, 470, (1992).
17. R.Blinc, B.Zeks, Phys.Rev.,**A18**, 740, (1978).
18. N.A.Clark, R.Meyer, Appl.Phys.Lett., **22**, 493,(1973); M.Delaye, R.Ribotta, G.Durand, Phys.Lett., **A44**, 139,(1973).

INITIALLY SEPARATED REACTION-DIFFUSION SYSTEMS

HAIM TAITELBAUM[1], BARUCH VILENSKY[1],
YONG-EUN LEE KOO[2], ANDREW YEN[2], ANNA LIN[2] AND RAOUL KOPELMAN[2]
1. Department of Physics, Bar-Ilan University, Ramat-Gan, Israel
2. Department of Chemistry, University of Michigan, Ann Arbor, MI 48109

ABSTRACT

Characteristics of the $A + B \to C$ reaction-diffusion system with initially separated components are studied theoretically and experimentally. When the reaction is slow, the two species will mix before reacting. This leads to a series of crossovers from a rich initial behavior to an asymptotic time behavior. The crossovers depend on the system parameters, such as the diffusion coefficients and initial densities of the two species.

In this paper we review our recent studies on this system. We elaborate on a theoretical study of momentum effects, and then focus on theoretical explanations of two experimental phenomena: 1) Non-universal and non-monotonic motion of the reaction front center. The latter occurs when one of the reactants has larger diffusion coefficient but smaller initial density. 2) Existence of more than one front. This occurs when two different transformations of the same reactant (on one of the sides of the system), react with the reactant on the other side with a different reaction constant - the majority slowly, but the minority much faster.

INTRODUCTION

The kinetics of the $A + B \to C$ reaction-diffusion process is very sensitive to initial conditions. Systems with *initially uniformly mixed* reactants have been widely studied theoretically, but such a condition is difficult to achieve in a real chemical system. On the other hand, systems with *initially separated* components are more readily amenable to experimental studies. The initial separation of reactants leads to formation of a dynamic reaction front, which is a spatially localized region with non-zero reactant production. The presence of such a reaction interface is a characteristic of many processes in nature, and has recently attracted much research interest [1-26].

The following set of mean-field-type reaction-diffusion equations for the local concentrations ρ_a, ρ_b has been assumed to describe the initially-separated $A + B \to C$ reaction-diffusion system [1] :

$$\dot{\rho}_a = D_a \nabla^2 \rho_a - k \rho_a \rho_b \tag{1a}$$

$$\dot{\rho}_b = D_b \nabla^2 \rho_b - k \rho_a \rho_b \tag{1b}$$

where D_a, D_b are the diffusion constants, and k is the microscopic reaction constant. The equations are subject to the initial separation condition along the x axis,

$$\rho_a(x,0) = a_0 H(x), \qquad \rho_b(x,0) = b_0[1 - H(x)], \tag{1c}$$

where a_0, b_0 are the initial densities and $H(x)$ is Heaviside step function. This means that initially the A's are uniformly distributed on the right side ($x > 0$), and the B's - on the left ($x < 0$). This mean-field description has been argued by Cornell *et al* [8] to be valid above an upper critical dimension $d_{up} = 2$.

The local production rate of C, defined as the reaction term in Eq.(1),

$$R(x,t) = k\rho_a(x,t)\rho_b(x,t), \tag{2}$$

is the basis for defining all dynamic quantities of interest. For example, the global reaction rate, $R(t)$, is the spatial integration over $R(x,t)$, the center of the reaction front, $x_f(t)$, is defined as the position where $R(x,t)$ has a maximum, the width of the front, $w(t)$, is defined through its second moment, and the height of the front is simply the local rate at x_f, denoted by $R(x_f,t)$.

RESULTS

Two main analytical methods have been used to study the model system. The first is a *scaling theory* by Gálfi and Rácz [1], which is valid in the asymptotic time limit. They assume a scaling form for $R(x,t)$, from which they obtain the asymptotic behavior of the above-mentioned quantities. The second analytical approach is a *perturbation theory* by Taitelbaum *et al* [5,6], which is valid for relatively short times, when very little reaction takes place before the species become effectively mixed. The perturbation expansion is based on a description of the initial behavior using a small dimensionless reaction constant, given by

$$\epsilon = \frac{k}{\sqrt{a_0 b_0 D_a D_b}}. \tag{3}$$

The combination of the results from these two theoretical methods is reflected in a series of crossovers from the initial to the asymptotic behavior of the kinetic properties of the reaction front. These crossovers depend on the microscopic reaction constant, as well as on the ratios of diffusion coefficients and initial densities of the two species. For example, the global reaction rate $R(t)$ changes dramatically from an initial $t^{1/2}$ increase to a final $t^{-1/2}$ decrease, at time proportional to k^{-1} [5]. In practice, when k is very small, these crossovers take place on a real time scale of *hours*, thus providing a useful means to extract microscopic parameters from macroscopic experiments.

In Table I we summarize the crossover from the short-time limit to the asymptotic behavior for characteristics of the reaction front in the initially-separated system. All of these results have been confirmed by various numerical methods [2-5].

Table I: A summary of the crossover behavior of the reaction front properties in the initially-separated $A + B \rightarrow C$ reaction-diffusion system.

quantity	notation	short-time	long-time
global rate	$R(t)$	$t^{1/2}$	$t^{-1/2}$
center of front	$x_f(t)$	non-universal	$t^{1/2}$
width of front	$w(t)$	$t^{1/2}$	$t^{1/6}$
local rate at x_f	$R(x_f,t)$	const.	$t^{-2/3}$

The initially-separated system has attracted further theoretical interest during the last five years. In the context of the mean-field results, Larralde et al [12] have found an asymptotic expression for $R(x,t)$ for the case of symmetrical system parameters. Results for systems below the upper critical dimension $d_{up} = 2$, in particular in one dimension, have been obtained by several groups, and are reviewed by Havlin, Stanley and coworkers [15,16]. Ben-Naim and Redner [11] have studied the system under steady-state conditions. Droz and coworkers [7-9,18] have focused on the generalized system $mA + nB \rightarrow$ inert, and, in this symposium, Yen et al [25] provide the first experimental study of $A+2B \rightarrow C$ with initially-separated reactants. Chopard et al [17] have studied the system with the possibility of a reversible reaction. Interesting scaling anomalies have been reported by Araujo et al [19]. Vilensky et al [22] have recently studied the effects of incorporating momentum into the system, which will be described in the next section. Results for the process taking place on a percolation cluster at criticality have been given in [5], and Araujo, in this symposium [26], has presented results for a system with quenched disorder.

MOMENTUM EFFECTS

Vilensky et al [22] have recently studied momentum effects in the system. The inclusion of momentum results in an additional early-time regime in which the global reaction rate can increase $linearly$ with time. Hence one expects the possibility of seeing three types of behavior of the reaction rate as a function of n (the number of steps), an initial regime in which the reaction rate increases proportional to n, followed by an increase proportional to $n^{1/2}$ at later times, and a final regime in which the reaction rate falls off proportional to $n^{-1/2}$. The occurrence of these three types of behavior is manifest in Fig. 1.

The physical system is modeled in [22] in terms of a persistent random-walk, which is the discrete analog of the telegrapher's equation. In this case the reaction constant k and the velocity (or the momentum) v that appear in the continuum model are replaced by the probabilities θ and α respectively. The times at which crossovers occur between the three types of scaling behavior are most naturally expressed in terms of two parameters which may be interpreted as discrete times: $1/\theta$ and $1/(1-\alpha)$. The first of these, the average number of encounters between two unlike particles required to produce a reaction is a measure of the efficiency of the reaction. The second parameter is the average number of steps before a reversal of direction occurs and measures the tendency of the dynamical behavior to approach the regime in time beyond which the system can be regarded as being diffusive. The interplay between these two characteristic times determines the number of regimes that can appear in the behavior of R_n as a function of n. Thus, when the average reaction time is greater than the time at which the diffusive regime is reached, we might expect to see three regimes with proportionalities to $n, n^{1/2}, n^{-1/2}$, as is the case in Fig. 1. On the other hand, if the reaction efficiency is relatively high, so that the reaction time is smaller than the persistence time, it is possible that only the first, or linear, regime appears, followed by an immediate transition to the decrease in R_n without a visible increase in the reaction rate proportional to $n^{1/2}$. Such a case is illustrated in Fig. 2. When the persistence parameter is sufficiently large the rate will tend to have a flat region as a function of n since unreacted particles tend to meet at a constant rate. An extreme case of this phenomenon is shown in Fig. 2 for $\alpha = 1$ for which the reaction rate eventually becomes a constant. With less than complete persistence the reaction rate always reaches times at which it falls off as $n^{-1/2}$.
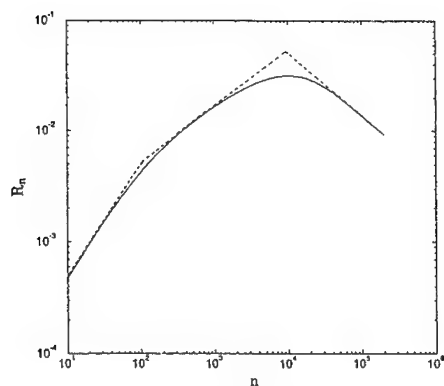
- **Fig. 1:** The global reaction rate R_n as a function of step number n with persistence probability $\alpha = 0.99$ and reaction probability $\theta = 10^{-4}$. Tangent lines with slopes 1, 1/2 and -1/2 illustrate the three regimes.
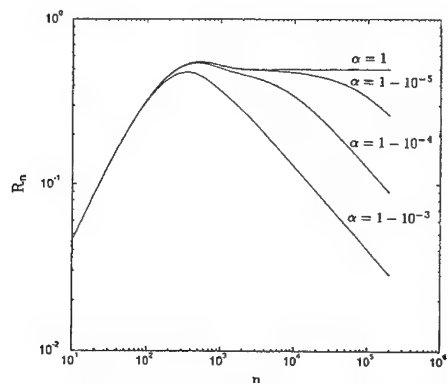
- **Fig. 2:** The global reaction rate R_n as a function of n for reaction probability $\theta = 0.01$ and increasing degrees of persistence. For $\alpha \to 1$ the reaction rate is asymptotic to a constant.

EXPERIMENTS

The experimental studies of the initially-separated system are based on optical absorbance measurements of the reactants and the product [3,21,23-25]. In order to test the *asymptotic* predictions, Koo and Kopelman [3] have chosen the inorganic bimolecular reaction $Cu^{2+}+$ "tetra" $\to 1 : 1$ complex (in a gel solution), where "tetra" is the molecule disodium ethyl bis(5-tetrazolylazo)acetate trihydrate. This reaction is instantaneous, which means that k is large, and the reaction passes immediately to the asymptotic diffusion-limited regime. With these materials, the asymptotic results for the global reaction rate $R(t)$, the width $w(t)$, and the reaction front center $x_f(t)$ have been confirmed.

However, in order to test the *crossover* predictions, one has to use *slow* reactions. For this purpose, Kopelman and co-workers [5,21,23,24] chose the reaction $Cr^{3+} + X.O. \rightarrow 1:1$ complex in gel, where X.O. is the dye Xylenol Orange. In general, the experimental results have confirmed the crossover predictions, as is discussed in the companion paper by Lin *et al* [24], in particular with respect to the global production rate $R(t)$. The experimental results also exhibit one of the most striking phenomenon of the initially-separated system which is the non-monotonic motion of the reaction front center [5]. The front changes its direction of motion along the separation axis after reaching an extremum position, as is shown in Fig. 3. Indeed, such a behavior is predicted by the perturbation analysis. In what follows we review the interesting results for the non-universal behavior of the reaction front center in the short-time limit, which has already been mentioned in Table I.
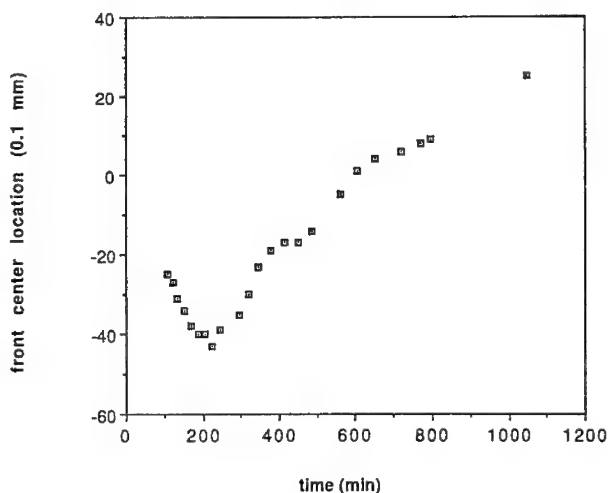
- **Fig. 3:** Experimental results of the reaction center location x_f (in units of 0.1 mm) as a function of time (min), for the $Cr^{3+} + X.O. \rightarrow 1:1$ complex system. From [5].

KINETICS OF THE REACTION FRONT CENTER

The center of the reaction front, x_f, is defined as the position where the local rate $R(x,t)$ is a maximum. The general expression for x_f is found after maximization of $R(x,t)$ and expansion around the initial position $x = 0$, and is given by

$$x_f(t) \simeq \frac{\frac{1}{\sqrt{\pi}}\left(\frac{1}{\sqrt{D}} - \sqrt{D}\right) t^{-1/2} + \epsilon M(D,r) t^{1/2}}{\frac{1}{\pi} t^{-1} + \epsilon N(D,r)} \tag{4}$$

where

$$D = \sqrt{\frac{D_a}{D_b}}, \qquad r = \sqrt{\frac{a_0}{b_0}}, \tag{5}$$

and M, N are time-independent constants, with a non-trivial dependence on D and r.

455

The behavior of x_f has been found to be extremely sensitive to the parameters $\{D, r\}$ as is summarized in Table II. Apart from the symmetric trivial case ($x_f = 0$ for all times), there can be as many as four different universality classes for describing the kinetics of the front in the little reaction regime, and as many as three distinguishable regimes in time.

In general, the earliest time behavior is $x_f \sim t^{1/2}$ (provided that $D \neq 1$), the asymptotic one is also $x_f \sim t^{1/2}$, and the different universality classes are mainly found in the intermediate time regime. When $D = 1$ (and $r \neq 1$), the first term in the numerator vanishes, and the center of the front remains fixed in position at the earliest times. As time increases, the next term in the numerator becomes significant, and $x_f \sim \epsilon t^{3/2}$, prior to the crossover to the asymptotic $t^{1/2}$ behavior. This intermediate behavior is observable experimentally when the reaction constant is small enough. If also $r = 1$, than M vanishes and $x_f = 0$ for all t, as it should be due to symmetry.

Table II: A summary of the various time-dependences of x_f, the center of the reaction front, as a function of the system parameters D and r.

$\{D, r\}$	short times	intermediate times	long times
$\{D = 1, r = 1\}$	0	0	0
$\{D = 1, r \neq 1\}$	0	$t^{3/2}$	$t^{1/2}$
$\{D \neq 1, r = 1\}$	$t^{1/2}$	$t^{1/2}$	$t^{1/2}$
$\{2 + \sqrt{3} > D > 1, r < 1\}$ or $\{1 > D > 2 - \sqrt{3}, r > 1\}$	$t^{1/2}$	$t^{3/2}$ - non-monotonic	$t^{1/2}$
$\{D > 1, r > 1\}$ or $\{D < 1, r < 1\}$	$t^{1/2}$	$t^{3/2}$	$t^{1/2}$

The most interesting feature of x_f, is, of course, the possibility of the non-monotonic motion along the separation axis. The mathematical expression of this feature is that the function $x_f(t)$ has some extremum point as a function of time. The time t^* for which $x_f(t)$ has such an extremum point depends on D and r, through the rather cumbersome expressions for M and N. However, it turns out that t^* will be positive, and thus with a physical meaning, only if the parameters D and r satisfy the double condition $\{D > 1$ and $r < 1\}$, or, equivalently, $\{D < 1$ and $r > 1\}$. In fact, if D is too large ($D > 2 + \sqrt{3} \approx 3.73$) or too small ($D < 2 - \sqrt{3} \approx 0.27$), t^* will be negative, and x_f will not have a physical extremum point, independent of the value of r. But if we restrict ourselves to values of D not too far from 1, than we can write $\{D > 1, r < 1\}$ (or the opposite), as the condition which ensures the change of the direction of motion of the front.

This result can be physically understood. Suppose, e.g., that $D_a > D_b$ and $a_0 < b_0$. At very early times diffusion effects are dominant, and the direction of motion is determined by the penetration of the A-species to the left, B-side of the system. Later on, the reaction comes into play, and the species with higher concentration, B, will govern the direction of motion, which will be towards the right, A-side. Note that this result involves both two lowest orders in ϵ, so one expects the transition of the front from one direction to the other to occur at a rate proportional to $t^{3/2}$. Indeed, in the experiment whose results are plotted in Fig. 3, the parameters were 5 x $10^{-5} M$ Xylenol Orange (diffusion constant 3.5 x 10^{-10} m^2/sec), and 7.5 x 10^{-4} M Cr^{3+} (diffusion constant 2.7 x 10^{-10} m^2/sec), so that $D = 1.14$ and $r = 0.26$ in accord with the requirements for an extremum position. In addition, one can clearly see that the change of direction occurs at a rate much higher than the asymptotic $t^{1/2}$. This formal short-time limit behavior takes place at time $t = 223$ min, which is definitely quite long. This is because of the very small reaction constant k in this chosen system, so that the corresponding small parameter ϵ defined in Eq.(3) is extremely small, and the short-time limit is extended over an easily measurable time interval.

TWO REACTION FRONTS

Recently, while repeating the experiments with Xylenol Orange, some different and challenging results have been obtained. The first is the global rate which exhibits more than one crossover as a function of time (as is seen in Fig. 4), and the second, which is also very surprising, is the existence of more than one localized front, as is exemplified by the two peaks in the set of "snapshots" of the local production rate $R(x, t)$ as a function of x for various times in Fig. 5.
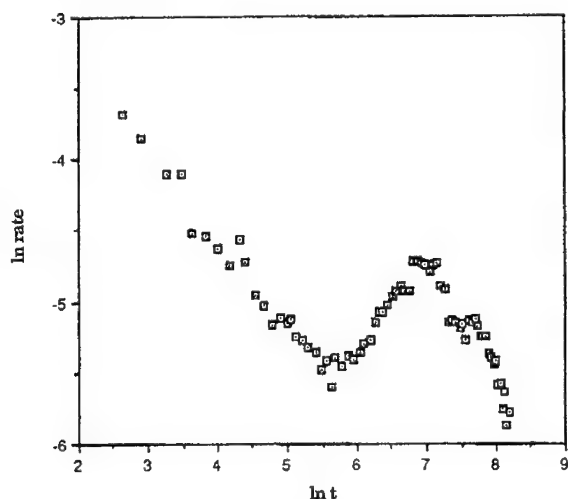
- **Fig. 4:** Experimental results of the global reaction rate $R(t)$ as a function of time, with more than one crossover.
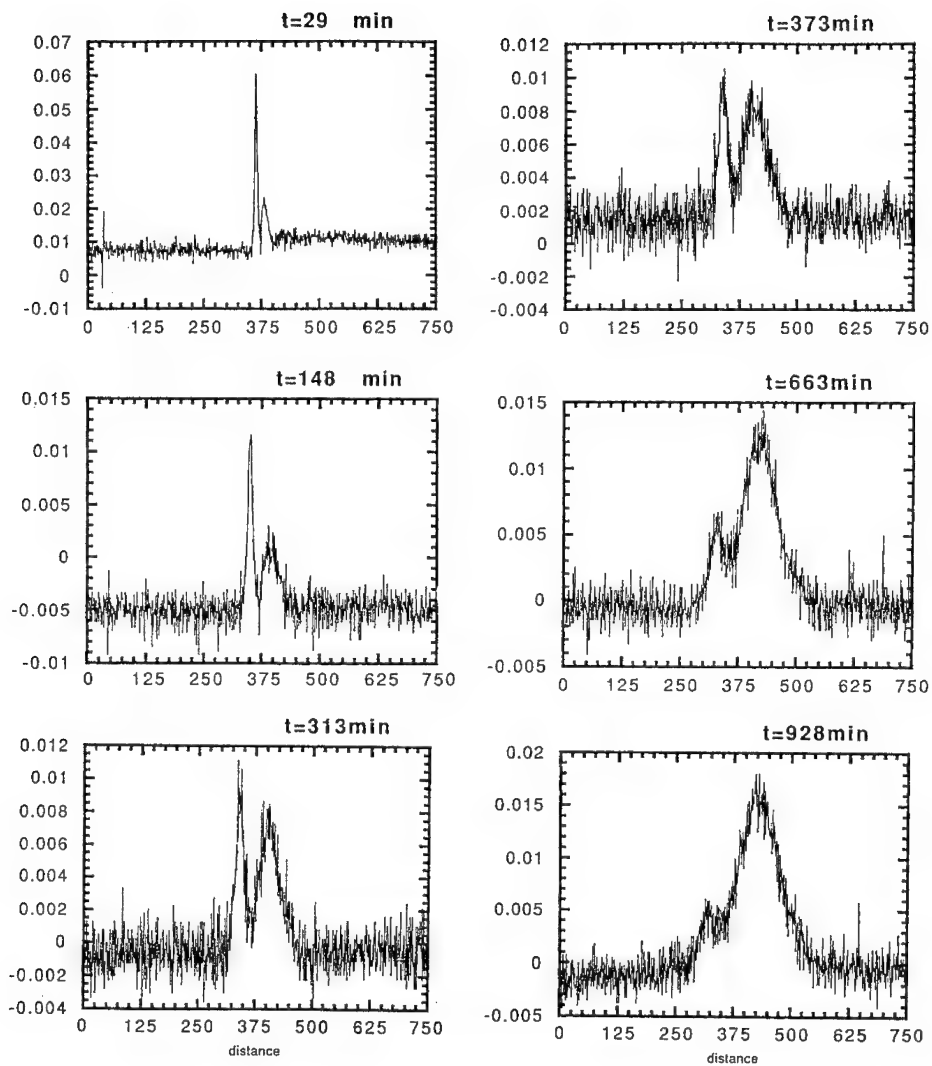
Fig. 5: Set of experimental "snapshots" of the absorbance profiles of the product at various times. These represent the local production rate $R(x,t)$. The distance is given in units of 0.1 mm, and the initial position of the front is at 375.

Our explanation of these results is based on the idea that there may be more than a single species on one of the sides of the system, i.e. there exist two *similar* species A_1 and A_2 on the right side and a single species B on the left side. By similar species we mean that most of their properties are the same, but each of them is assumed to react with B with a *different* reaction constant, so that the reaction scheme is

$$A_1 + B \overset{k_1}{\to} C_1 \qquad (6a)$$

$$A_2 + B \overset{k_2}{\to} C_2. \qquad (6b)$$

The products C_1 and C_2 are assumed to be either identical or at least have similar spectra, so that they are indistinguishable by the detector in the experiment. Thus, the local reaction rate of this system will be a superposition of the form

$$R(x,t) = k_1 \rho_{a_1}(x,t)\rho_b(x,t) + k_2 \rho_{a_2}(x,t)\rho_b(x,t). \qquad (7)$$

We have studied this system by means of numerical calculations. The main conclusion is that the results resemble those of the experiments, provided that k_1 and k_2 differ by several orders of magnitude, and the faster reacting A_i species is only a very small fraction of the A's. Namely, the main reaction is indeed the slow one, but there exist a very small fraction of slightly different version of A which reacts much faster with B. In Fig. 6 we show the results for a system with reaction constants $k_1 = 1$, $k_2 = 10^{-4}$, and initial densities $a_1 = 3\%$, $a_2 = 97\%$ of the A's, which clearly look like the experimental results in Fig. 4. It can be seen that the faster reaction (with A_1) decays after time proportional to k_1^{-1}, and the second one is slowly developing up to time k_2^{-1} where the second crossover occurs. The ratio of the A densities ensures that there is enough material left for the slower process. The superposition of these two processes is also reflected in the spatial behavior of the local rate $R(x,t)$, as is shown in Fig. 7. The dominant peak at early times comes from the fast front. Later, as this reaction diminishes, the slower one starts to build up, and finally becomes the dominant one in the asymptotic regime. The remarkable agreement with the experimental results in Fig. 5 speaks for itself.
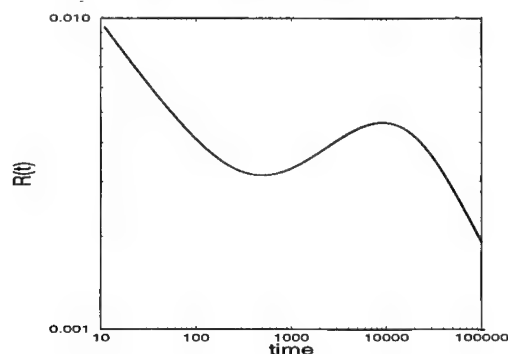
- **Fig. 6:** Numerical results of the global rate $R(t)$ as a function of time for the double-reaction scheme of Eq.(6). Parameters are $k_1 = 1$, $k_2 = 10^{-4}$ and $a_1 = 3\%$, $a_2 = 97\%$.
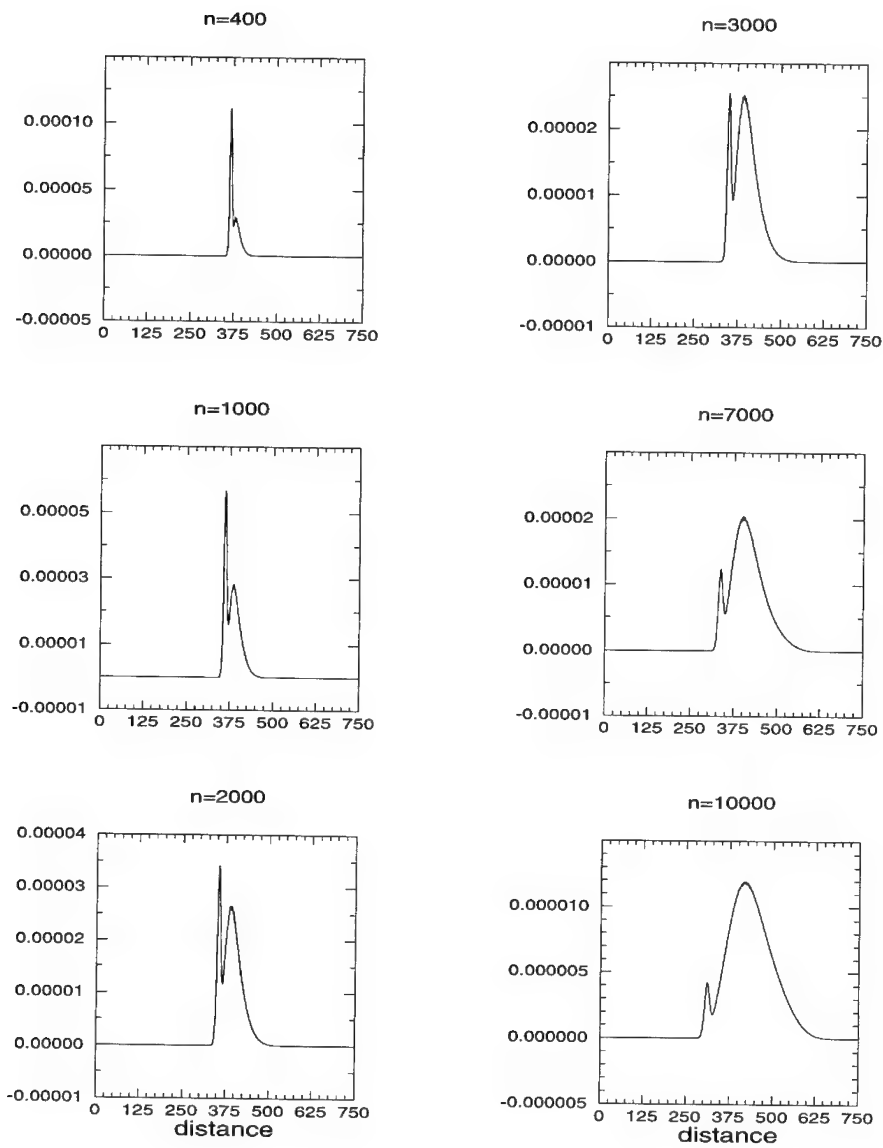
Fig. 7: Numerical results for the time evolution of the spatial profile of the local production rate $R(x,t)$, for the parameters of Fig. 6.

However, referring to the experiments, the question is *who are* these A_1 and A_2 in the specific experimental system. Naturally, one would think about various sources of impurities or defects which result in a non-ideal experimental system. However, A_1 and A_2 should be somehow related, since they must yield the same, or at least a very similar product upon reacting with B.

In order to answer this question, we notice that one of the parameters that plays a crucial rule in such reactions is the pH of the solution. The reaction under study ($Cr^{3+}+$ X.O. $\rightarrow$ 1 : 1 complex) is known to be very highly pH-dependent. Back in 1960, Řehák and Körbl [27] performed a physico-chemical study of Xylenol Orange. They show that X.O. can appear in *ten* different ionic transformations as a function of the pH of the aqueous solution. The percentage of each chelate as a function of pH is shown in Fig. 8. Indeed, for pH=4.5, which was the average pH in most of our experiments, one can see that there exist simultaneously two forms of X.O., 3% of H_4XO^{2-}, and 97% of H_3XO^{3-}, which is exactly the expected picture for the relative portions of the A_i's in the two-front system. Note that the two transformations differ only by a single proton, thus one expects that the diffusion coefficients are the same, the product of the bimolecular reaction is the same, and the only difference, which can be explained on chemical grounds, is the very different reaction constant which represents the reaction efficiency.
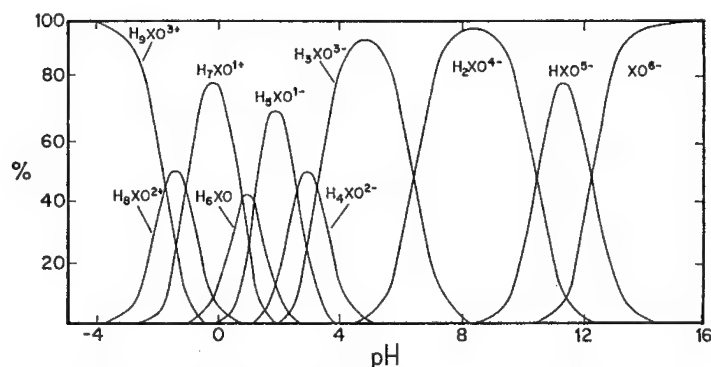
Fig. 8: Percentage of each ionic transformation of Xylenol Orange as a function of the pH of the solution. After Řehák and Körbl [27].

SUMMARY

In summary, we have presented various characteristics of the reaction-diffusion system $A+B \rightarrow C$ with initially separated components, which exhibits a series of crossovers from an initial to an asymptotic time behavior. We have discussed theoretically momentum effects. Then we have focused on the kinetics of the reaction front center and showed that its motion can be classified into four different universality classes, depending on the system parameters. In particular, we showed that the front can exhibit a non-monotonic motion, which occurs when one of the species has larger diffusion coefficient but smaller initial density. In addition, we have discussed the case of a two-front system, which results from a simultaneous presence of two similar species on one of the sides of the system, an example of which is the case of two ionic transformations of the same molecule.

REFERENCES

[1] L. Gálfi and Z. Rácz, Phys. Rev. A, **38**, 3151 (1988).

[2] Y.E. Koo, L. Li and R. Kopelman, Mol. Cryst. Liq. Cryst., **183**, 187 (1990).

[3] Y-E.L. Koo and R. Kopelman, J. Stat. Phys., **65**, 893 (1991).

[4] Z. Jiang and C. Ebner, Phys. Rev. A, **42**, 7483 (1990).

[5] H. Taitelbaum, S. Havlin, J.E. Kiefer, B. Trus and G.H. Weiss,
        J. Stat. Phys., **65**, 873 (1991).

[6] H. Taitelbaum, Y-E.L. Koo, S. Havlin, R. Kopelman and G.H. Weiss,
        Phys. Rev. A, **46**, 2151 (1992).

[7] B. Chopard and M. Droz, Europhys. Lett., **15**, 459 (1991).

[8] S. Cornell, M. Droz and B. Chopard, Phys. Rev. A, **44**, 4826 (1991).

[9] S. Cornell, M. Droz and B. Chopard, Physica A, **188**, 322 (1992).

[10] M. Araujo, S. Havlin, H. Larralde and H.E. Stanley,
        Phys. Rev. Lett., **68**, 1791 (1992).

[11] E. Ben-Naim and S. Redner, J. Phys. A, **25**, L575 (1992).

[12] H. Larralde, M. Araujo, S. Havlin and H.E. Stanley,
        Phys. Rev. A, **46**, 855 (1992).

[13] H. Larralde, M. Araujo, S. Havlin and H.E. Stanley,
        Phys. Rev. A, **46**, R6121 (1992).

[14] M. Araujo, H. Larralde, S. Havlin and H.E. Stanley,
        Physica A, **191**, 168 (1992).

[15] S. Havlin, M. Araujo, H. Larralde, H.E. Stanley and P. Trunfio,
        Physica A, **191**, 143 (1992).

[16] S. Havlin, M. Araujo, H. Larralde, A. Shehter, H.E. Stanley,
        Fractals, **1**, 405 (1993).

[17] B. Chopard, M. Droz, T. Karapiperis and Z. Rácz,
        Phys. Rev. E, **47**, R40 (1993).

[18] S. Cornell and M. Droz, Phys. Rev. Lett., **70**, 3824 (1993).

[19] M. Araujo, H. Larralde, S. Havlin and H.E. Stanley,
        Phys. Rev. Lett., **71**, 3592 (1993).

[20] H. Taitelbaum, Physica A, **200**, 155 (1993).

[21] Y-E. Koo, R. Kopelman, A. Yen and A. Lin,
        Mat. Res. Soc. Symp. Proc., **290**, 273 (1993).

[22] B. Vilensky, S. Havlin, H. Taitelbaum and G.H. Weiss,
        J. Phys. Chem., **98**, 7325 (1994).

[23] H. Taitelbaum, in "Diffusion Processes", A. Pekalski, ed.,
        Lecture Notes in Physics, vol. **438**, (Springer, Berlin, 1994), pp. 77-89.

[24] A. Lin, A. Yen, Y-E. Koo and R. Kopelman,
        Mat. Res. Soc. Symp. Proc., **366**, this symposium.

[25] A. Yen and R. Kopelman, Mat. Res. Soc. Symp. Proc., **366**, this symposium.

[26] M. Araujo, Mat. Res. Soc. Symp. Proc., **366**, this symposium.

[27] B. Řehák and J. Körbl, Collection Czechoslov. Chem. Commun., **25**, 797 (1960).

Author Index

464

Subject Index

adhesion force, 33
adsorption, 231, 247, 421
alkali metals, 341
alkanes, 15
anisotropic self-diffusion, 207
anomalous, 319, 377
area fraction, 27
asymmetric liquid drop, 341
atomic
    force microscopy, 71
    scale structure, 141
Au(111), 63

BET equation, 247
bimodal equation, 295
binary
    fluid, 57
    mixture, 141
biomolecules, 333
brush exchange kinetics, 307
buckling transitions, 163

capillary, 389
    condensation, 33, 231, 241
chemical reaction, 271
clusters, 173
competitive adsorption, 421
complex structure, 179
confined
    colloidal monolayers, 163
    fluids, 113, 129
confinement, 27, 101, 265, 283, 289, 295, 427, 445
contact
    angle, 39, 51
    line, 51
continuous time random walk, 365
correlation length, 27
critical size, 341

depinning, 51
de-wetting, 71
dielectric
    constant, 77
    spectroscopy, 259
diffusion, 225, 271
    limited (controlled), 319, 365, 409
digital images, 163
dynamic critical phenomenon, 51

electrokinetics, 201
electroosmosis, 201
electrorheological fluids, 155
ellipsometry, 183
enzymes, 439
escape rate, 353

faujasite, 277
fcc lattice, 141

field-cycling NMR, 189
fission, 341
flow, 101
fluctuating barriers, 333
fluid
    films, 39, 101
    membrane, 301
fractal, 247, 271
freezing/melting transition, 295
friction force microscopy, 113
frictional forces, 129

geometrical barrier, 333
glass
    forming salol, 259
    transition temperature, 183
glassy transformations, 173
global reaction rates, 395
growth
    dynamics, 57
    exponent, 57
guided x-rays, 3

hydrodynamic thickness, 307
hydrogen isotope exchange, 325
hysteresis, 241

interconnectivity, 253
interfacial structure, 63
iron ore pellet, 347
isotherm, 247
isotropic-nematic transition, 213

kinetics, 179, 347

lamellar phase, 301
light scattering, 155
liquid(-)
    crystals, 445
    solid transition, 123
local fields, 77
luminescence quenching, 365

mercuric iodide, 283
micelle system, 179, 365
microemulsions, 95, 427
microwaves, 347
molecular dynamics, 57, 173, 225
molecularly thin films, 123
moment hierarchy, 377

n-decane, 295
nanorheology, 113
nanoscale structure, 141
NMR field-gradient diffusometry, 189
non-wetting fluid, 265
nuclear relaxation, 265

optical Kerr effect, 213